**UNIVERSITÉ CLERMONT AUVERGNE**
**ÉCOLE DOCTORALE DES SCIENCES FONDAMENTALES**

# THÈSE
présentée pour obtenir le grade de

# Docteur d'Université
Spécialité de doctorat: phsique des particules

Par **Halime SAZAK**
Laboratoire de Physique de Clermont, CNRS/IN2P3

# Measuring the CP Violation Phase $\gamma$ in open charm B decays at LHCb

soutenu publiquement le 16 décembre 2022

**Jury :**

| | |
|---|---|
| **M. Anton POLUEKTOV** | **Rapporteur et Examinateur** |
| Directeur de Recherche CNRS, CPPM Marseille, | |
| **Mme. Isabelle RIPP-BAUDOT** | **Rapporteur et Examinatrice** |
| Directrice de Recherche CNRS, IPHC Strasbourg | |
| **M. Jean ORLOFF** | **Examinateur** |
| Professeur des Universités, LPC Clermont | |
| **M. Niels TUNING** | **Examinateur** |
| Senior Researcher, NIKHEF Amsterdam | |
| **Mme. Stefania RICCIARDI** | **Examinatrice** |
| Research Scientist, STFC Rutherford Appleton Laboratory | |

**Directeur de thèse :** **M. Vincent TISSERAND**
Directeur de Recherche CNRS, LPC Clermont

# DECLARATION

Here I declare that this thesis contain the results of my own work my, except where the explicitly reference is point out for the works of other people.

# ACKNOWLEDGEMENTS

**To my dear family**

# ABSTRACT

This thesis presents the study of the measurement of the CKM angle $\gamma$ through two possible analysis at LHCb: first analysis, from the measurement of $B_s^0 \to \tilde{D}^{(*)0}\phi$ decay, where the notation $\tilde{D}^0$ stands for either a $D^0$ or a $\bar{D}^0$ meson reconstructed in sub-decay mode: $K\pi\pi^0$, while the $\phi$ decays to $K^+K^-$; the second analysis, from the more conventional decay mode $B^- \to D^0 K^{*-}$, where $D^0$ decays to $K^-\pi^+$ (RS), $K^-K^+$, $\pi^-\pi^+$, $\pi^-K^+$ (WS) and $K^{*-}$ is reconstructed in $K^-\pi^0$. Both measurements for the decay modes using proton-proton collision based on an integrated luminosity of $9.0\,\text{fb}^{-1}$ collected by the LHCb detector during Run 1 & Run 2, accumulated over years 2011 to 2018.

Key words: LHCb detector, charmed $B_s^0$ decays, direct CP violation, neutral pions

# Contents

# Glossary

- **AUC** : Area Under ROC Curve.

- **BSM** : Beyond the Standard Model.

- **BDT** : Boosted Decision Tree.

- **CALO** : Calorimeters .

- **CERN** : European Organisation for Nuclear Research (Organisation européenne pour la recherche nucléaire).

- **CF** : Cabibbo Favored.

- **CKM** : Cabibbo-Kobayashi-Maskawa matrix.

- **CP** : Charge conjugation and Parity symmetry.

- **CPU** : Central Processing Unit.

- **DCS** : Doubly Cabibbo suppressed.

- **DTF** : Decay Tree Fitter.

- **ECAL** : Electromagnetic Calorimeter.

- **FD** : Flight Distance.

- **GIM** : Glashow-Iliopoulos-Maiani mechanism.

- **HCAL** : Hadronic Calorimeter.

- **HLT** : High Level Trigger.

- **IP** : Impact Parameter.

- **IT** : Inner Tracker.

- **KS** : Kolmogorov-Smirnov test.

- **LHC** : Large Hadron Collider.

- **LHCb** : Large Hadron Collider Beauty Detector.

- **MC** : Monte Carlo.

- **MLP** : Multi-Layer Perceptron.

- **MVA** : Multivariate Analysis.

- **NN** : Neural Network.

- **NP** : New Physics.

- **OT** : Outer Tracker.

- **PDF** : Probability Density Function.

- **PDG** : Particle Data Group.

- **PID** : Particle identification.

- **PS** : Pre-Shower.

- **PV** : Primary Vertex.

- **RICH** : Ring Imaging Cherenkov detectors.

- **ROC** : Receiver operating characteristic curve.

- **SCS** : Singly Cabibbo suppressed.

- **SM** : Standard Model

- **SPD** : Scintillator Pad Detector.

- **SPS** : Super Proton Synchrotron.

- **SV** : Secondary Vertex.

- **TT** : Tracker Turicenis.

- **TIS** : Triggered independently of signal.

- **TOS** : Triggered on signal.

- $p_T$ : Transverse momentum.

- **QCD** : Quantum Chromodynamics.

- **QED** : Quantum Electrodynamics.

- **VELO** : Vertex Locator.

# 1 Introduction

The angle $\gamma$ is one of the three angles that makes up the Cabibbo-Kobayashi-Maskawa (CKM) matrix [1] defined as $\arg[-V_{ud}V_{ub}^*/V_{cd}V_{cb}^*]$. The angle $\gamma$ is a complex phase of the complex number $\bar{\rho} + i\bar{\eta}$ is found to be necessary to explain CPV in Kaons by Kobayashi and Maskawa in 1973, thus it is a fundamental parameter of the Standard Model (SM). Precise determination of the angle $\gamma$ (the precision is expected to reach $1°$ level) is one of the main goals of the LHCb experiment and flavour physics to determine the violation of charge-parity (CP) symmetry. The measurement can be achieved by exploiting the interference of decays that proceed via the $b \to c\bar{u}s$ and $b \to u\bar{c}s$ tree-level amplitudes, where the determination of the relative weak phase $\gamma$ is not affected by theoretical uncertainties. Hence the $\gamma$ angle measurement through the tree level provides a standard model(SM) benchmark to probe the consistency with loop-level measurements sensitive to the new physics.
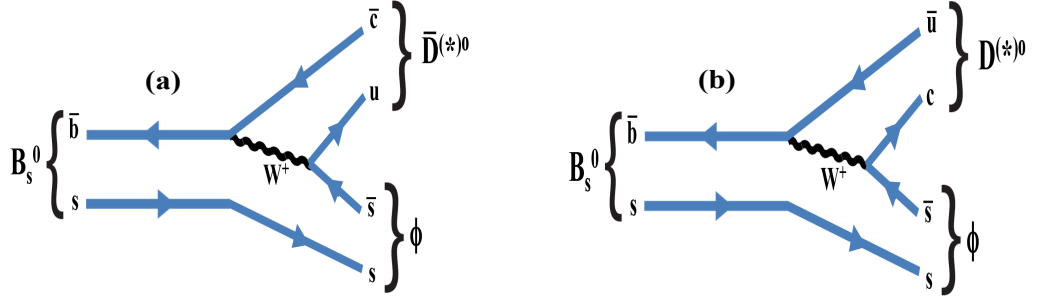


Figure 1.1: Feynman diagrams for (a, left) $B_s^0 \to \overline{D}^{(*)0}\phi$ and (b, right) $B_s^0 \to D^{(*)0}\phi$ decays.

Different methods can be utilized to measure the $\gamma$ angle. LHCb has obtained the best precision on the CKM angle $\gamma$ by combining the measurements from several $B$ decay modes using the full Run 1 and Run 2 LHCb data. The precision on $\gamma$ angle is found to be $\gamma = (65.4^{+3.8}_{-4.2})°$ [2] and this result is the most accurate determination to date by a single experiment (to be updated soon). A combination on the $\gamma$ angle has been obtained with the new and updated inputs in the charged $B^\pm$, neutral $B^0$ decays and in the $B_s^0$ measurements based on only $B_s^0 \to D_s^\mp K^\pm$ [3], $B_s^0 \to D_s^\mp K^\pm \pi^+\pi^-$ [2] decay modes. The last two analysis in $B_s^0$ decay use time-dependent methods and therefore strongly rely on

the B-tagging capabilities of the LHCb experiment. The most recent combination on $\gamma$ from the $B_s^0$ measurements is $\gamma = 80° \pm 12$ level of precision and this is the most probable value but high wrt to the $B^+$ and $B^0$ measurements. A $2\sigma$ tension between the charged $B^\pm$ and $B_s^0$ results was observed.

In a recent sensitivity study [4] on $\gamma$, it has been shown that these results can be improved by another alternative measurement with time-integrated untagged rate of $B_s^0 \rightarrow \overline{D}^{(*)0}\phi$ in various neutral D meson sub-decays [[5, 6, 7]]. The most precise measurement on the $\gamma$ angle has been performed through the decay of $B_s^0 \rightarrow \overline{D}^{(*)0}\phi$ whose observations were published by the LHCb experiment in 2013 [8] and 2018 [9]. This analysis relies on sensitivity to $\gamma$ from $B_s^0 \rightarrow \tilde{D}^{(*)0}\phi$ mode where $\tilde{D}^{(*)0}$ notation stands for the $D^0$ and $\overline{D}^0$ meson. Sensitivity to $\gamma$ comes from the interference between two colour-suppressed diagrams shown in Figure 1.1. The sensitivity analysis relied on rough extrapolation based on the analysis which was designed for the non-resonant measurement of $B_s^0 \rightarrow \overline{D}^0 K^+ K^-$ branching fraction [9]. It was demonstrated that the precision on $\gamma$ can be reached from $8°$ to $19°$. With the LHCb increased data Run 1- 3 dataset ($23\,\text{fb}^{-1}$ in 2025) and ultimately a precision on $\gamma$ is expected to be $2°$ to $7°$ level of precision with HL-LHC LHCb dataset ($300\,\text{fb}^{-1}$ in 2038). For the $\gamma$ measurement, neutral $D$-meson reconstructed in the following sub-decay modes: quasi flavour-specific final states: $K\pi$, $K3\pi$, $K\pi\pi^0$ and CP-eigenstate final states: $KK$ and $\pi\pi$ have been studied, whose yields are estimated using realistic assumptions based on measurements from LHCb [

In this thesis, two different decay channels for the $\gamma$ measurement are studied. One is aforementioned channel in the sensitivity study [4] $B_s^0 \rightarrow \overline{D}^{(*)0}\phi$ and the second decay channel $B^- \rightarrow D^0 K^*$ where $D^0$ decays to $K\pi$, $KK$ and $\pi\pi$ and $K^*$ decays to $K^{*-} \rightarrow K^-\pi^0$ which is more conventional method uses GLW [[10], [11] and ADS [[12], [13]] approaches. The sensitivity to the CKM angle $\gamma$ can be obtained in $B^\pm \rightarrow \tilde{D}^0 K^{*\pm}$ decays from interference between favoured $b \rightarrow c$ and color-suppressed $b \rightarrow u$ transitions displayed in Figure 2.9.
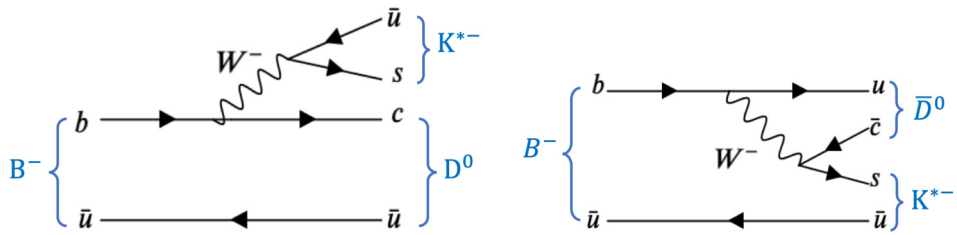


Figure 1.2: Feynman diagrams for $B^- \rightarrow D^0 K^{*-}$ ($K^-\pi^0$) decay (left) and $B^- \rightarrow \overline{D}^0 K^{*-}(K^-\pi^0)$. The interference between tree amplitudes favored $b \rightarrow c$ (Vcb) and color suppressed $b \rightarrow u$ (Vub).

This analysis is a complementary for an other published result by LHCb [14] with the same decay channel where $K^{*-}$ decays to $K_S^0\pi^-$ with the decays of the $D^0$ meson to $K^-K^+$, $\pi^-\pi^+$, $\pi^-K^+$, $K^-\pi^+\pi^-\pi^+$, $\pi^-\pi^+\pi^-\pi^+$ and $\pi^-K^+\pi^-\pi^+$ [15]. Measurements

on the CKM angle $\gamma$ and observables sensitive to $\gamma$ angle were performed by exploiting the data recorded between 2011 and 2016. The details concerning these analysis will be discussed in the corresponding sections.

In this present work, optimisation on the sub-decay modes indicated above for each decay channel has been studied. The accurate measurement of the CKM angle $\gamma$ is obtained by analysing the the full dataset (Run 1 & Run 2) corresponding to integrated luminosity of $3.2\,\mathrm{fb}^{-1}$ collected by LHCb detector at center-of-mass energies of 7 and $8\,\mathrm{TeV}$ from 2011 to 2012 and of $5.9\,\mathrm{fb}^{-1}$ at center-of-mass energies of $13\,\mathrm{TeV}$ from 2015 to 2018 years. For $B_s^0 \to \overline{D}^{(*)0}\phi$ decay, the selection requirements which were used for the branching fraction measurements of $B_s^0 \to \overline{D}^0 K^+ K^-$ [9] are revisited and according to the decay modes of interest, they are rearranged. The yields from neutral D meson decays to $K\pi\pi^0$ are obtained.

This thesis is organised as follows. In Chapter 1 presents the introduction part about CKM angle $\gamma$ measurements through the decay modes: $B_s^0 \to \overline{D}^{(*)0}\phi$ where $D^0$ decays to $K\pi\pi^0$ and $B^- \to D^0 K^*$ where $K^{*-}$ decays to $K^-\pi^0$. In Chapter 2 the Standard Model of particle physics and their interactions are explained. In Sec. 2.1 Yukawa interactions and Sec. 2.2 Cabibbo-Kobayashi-Maskawa (CKM) matrix and unitarity conditions are detailed. In Sec. 2.3 and in Sec. 2.4, informations about the CP violation and the CKM angle $\gamma$ are provided. In Chapter 3 technical details of the LHC and LHCb detector performance are presented.

In Chapter 4 $B_s^0 \to \overline{D}^{(*)0}\phi$ analysis are detailed. In Sec. 4.1 a motivation is given for the decay of interest. In Sec. 4.2 corresponding dataset selections and in Sec. 4.3 event selections are presented. Sec. 4.4 details the specific selections with respect to the specific sub-decay mode $K\pi\pi^0$. In Sec. 4.5 initial selections for the $B_s^0$ and $D^0$ mesons are presented. Multivariate analysis (MVA) for $B_s^0 \to \overline{D}^{(*)0}\phi$ are shown in Sec. 4.6. In Sec. 4.7 gives the Particle identification (PID) requirements. In Sec. 4.8 veto studies are explained. Sec. 4.9 presents the studies on the multiple candidates. In Sec. 4.10 extraction of the yields from the $B_s^0 \to \overline{D}^{(*)0}\phi$ and $K\pi\pi^0$ are obtained. In Sec. 4.11 and Sec. 4.12 efficiencies and systematic sources of the related mode are given. Final part in Sec. 4.13 the result of the extraction of CKM angle $\gamma$ from $B_s^0 \to \overline{D}^{(*)0}\phi$ are detailed and Conclusion is given in Sec. 4.14 for the $B_s^0 \to \tilde{D}^{(*)0}\phi$ analysis.

In Chapter 5 gives the detail about the second measurement on the CKM angle $\gamma$ through $B^\pm \to \tilde{D}^0 K^{*\pm}$ decay mode. In Sec. 5.1 gives the motivation for the analysis of the related mode $B^\pm \to \tilde{D}^0 K^{*\pm}$. Dataset and event selections are given In Secs. 5.2 and 5.3. In Sec. 5.4 background contributions to the measurement are detailed. In Sec. 5.5 extraction of the yields of $B^+$ and $B^-$ are given. Measurement of the CP asymmetry for the interested decay mode are presented in Sec. 5.6. In Secs. 5.7 and 5.8 the study for the efficiency and the systematics are performed. In Sec. 5.9 the results for the CP observables are presented. In Sec. 5.10 the extraction of the CKM angle $\gamma$ from the $B^\pm \to \tilde{D}^0 K^{*\pm}$ decay is detailed and in Sec. 5.11 conclusion for the $B^\pm \to \tilde{D}^0 K^{*\pm}$ is given.

# 2 The Standard Model of particle physics and their interactions

The Standard Model (SM) of particle physics is today's diligent theory that explains the fundamental particles of matter and how they interact through corresponding mediator particles under the electromagnetic, weak and strong forces represented by three gauge symmetry groups which SM relies upon. This is characterized by

$$SU(3)_C \otimes SU(2)_L \otimes U(1)_Y \tag{2.1}$$

where the $SU(3)_C$ represents the symmetry group for strong interactions (QCD) and $SU(2)_L \otimes U(1)_Y$ is responsible for weak and electromagnetic forces.

Fundamental particles are characterized by their masses, lifetime, charges and spin-parity[*] quantum numbers. Fermions which obey Fermi-Dirac statistics [[16]] have half-integer spin-1/2, spin-3/2, etc..., while bosons which obey Bose-Einstein [[17]] have integer spin-0, spin-1, etc... The table for the fundamental particles of the SM are given as in the Figure 2.1: fermions are sorted in three generations as quarks, leptons together with their antiparticles (antiquarks and antileptons) and mediators which are gauge bosons act as the force carriers: gluons (eight massless) and photon (one massless photon) are responsible for the strong and electromagnetic interactions; $W^{\pm}$, $Z^0$ are for the weak interactions and the Higgs which is the only scalar boson[†] which complete the SM picture.

Nevertheless, SM seems to encapsulate the everything of the subatomic world, it is not able to complete the whole picture of the universe with its limitations. While the universe covers lots of mysteries to be solved, there has to be provided answers to open questions such as a dark matter candidate (27%), dark energy (68%), gravitational interactions and asymmetry between the matter and antimatter (baryon asymmetry) which are beyond the SM's scope. At this stage, in order to test the SM or reach the limits beyond SM, direct searches or indirect searches where the deviations observed from the SM expectations show up. These are explained by the Cabibbo-Kobayashi-Maskawa (CKM) matrix which describes the flavor-changing in weak interactions of quarks (u,c,t),(d,s,b) in the SM.

---

[*]intrinsic property of all elementary particles in quantum mechanics

[†]It is the instance of a field where the mass is generated for fundamental particles including the Higgs Boson itself.

Figure 2.1: Table of fundamental particles and forces of the Standard Model.

## 2.1 The Yukawa couplings

The weak interaction is responsible for the flavour mixing takes place between the different generations of quarks. The mixing derived from the differences between the mass eigenstates (flavour eigenstates) and the weak eigenstates. Within the frame of SM, the masses and the mixing arise from the Yukawa couplings which describes the interactions between the Higgs scalar field and fermion Dirac fields. The Lagrangian considering the quark field can be written as

$$\mathcal{L}_Y^{Quarks} = -Y_{ij}^d \bar{Q}_{Li}^I \phi d_{Rj}^I - Y_{ij}^u \bar{Q}_{Li}^I \phi^* u_{Rj}^I - h.c. \tag{2.2}$$

where L is for left and R is for right, $Y^{u,d}$ represents 3x3 Yukawa arbitrary complex matrix elements, scalar Higgs field is given with $\phi$; $i, j$ are the indices for quarks generations and h.c. is for the hermitian conjugate. The quark doublets matrix for the left-handed and the right-handed up and down quark singlets: $u_R^I$, $d_R^I$ are given like:

$$Q_L^I = \begin{pmatrix} U_I \\ D_I \end{pmatrix}, u_R^I = \begin{pmatrix} u_I \\ 0 \end{pmatrix}, d_R^I = \begin{pmatrix} 0 \\ u_I \end{pmatrix}$$

This Yukawa Lagrangian equation 2.2 for the quark field can be written with respect to the quark mass matrice through the unitary gauge

$$\mathcal{L}_Y^{mass} = -\bar{u}_{LI} m_{ij}^d u_{Rj} - \bar{d}_{LI} m_{ij}^u d_{Rj} - h.c. \tag{2.3}$$

where $m_{ij}^d$ and $m_{ij}^u$ represent the mass matrices for down and up quarks sequentially. With respect to the weak interaction Yukawa matrices are non-diagonal. After the spon-

7

taneous symmetry breaking, where the electroweak $SU(2)_L U(1)_Y$ symmetry merge the U(1) electromagnetic symmetry and thus the W and Z bosons acquire the masses, vacuum expectation value (vev) acquired by the Higgs field can be written

$$\phi = \begin{pmatrix} \phi^+ \\ \phi^0 \end{pmatrix} \rightarrow \frac{1}{\sqrt{2}} \begin{pmatrix} 0 \\ \nu \end{pmatrix}, \tilde{\phi} = \begin{pmatrix} \phi^0 \\ -\phi^- \end{pmatrix} \rightarrow \frac{1}{\sqrt{2}} \begin{pmatrix} \nu \\ 0 \end{pmatrix} \tag{2.4}$$

In order to write the Yukawa Lagrangian for the mass eigenstates basis, mass matrices should be diagonal and real by using $V_{L,R}^q$ unitary matrices where q is for u and d quarks and the mass terms related with scalar Higgs vev is defined

$$M_{diagonal}^u = V_L^u m_u V_L^{u\dagger} (\nu/\sqrt{2})$$

$$M_{diagonal}^d = V_L^d m_d V_L^{d\dagger} (\nu/\sqrt{2})$$

$$M_{diagonal}^u = V_R^u m_u V_R^{u\dagger} (\nu/\sqrt{2})$$

$$M_{diagonal}^d = V_R^d m_d V_R^{d\dagger} (\nu/\sqrt{2})$$

Through these diagonal matrices, the mass eigenstates can be written as :

$$u_{L,R} = V_{L,R}^u u^{L,R}$$

$$d_{L,R} = V_{L,R}^d d^{L,R}$$

within the context of these transformation the Yukawa Lagrangian for the quark charged current can be interpreted like

$$\mathcal{L}_Y^{mass} = -\frac{g}{\sqrt{2}} (\bar{u}, \bar{c}, \bar{t})_L \gamma^\mu (V_L^{(u,c,t)\dagger} V_L^d)_{ij} d_L W_\mu^+ + \frac{g}{\sqrt{2}} (\bar{d}, \bar{s}, \bar{b})_L \gamma^\mu (V_L^{(d,s,b)\dagger} V_L^u)_{ij} u_L W_\mu^- \tag{2.5}$$

where g is for the charged current and the matrix $V_L^{u\dagger} V_L^d$ introduces the Cabibbo-Kobayashi-Maskawa (CKM) matrix which arises from the Yukawa interactions of quarks.

## 2.2 The Cabibbo-Kobayashi-Maskawa (CKM) matrix and unitarity conditions

The Cabibbo-Kobayashi-Maskawa (CKM) complex 3x3 matrix $V_{CKM}$ [[1]] and [[18]] which is written as follows :

$$V_{CKM} = \begin{pmatrix} d' \\ s' \\ b' \end{pmatrix} = \begin{pmatrix} V_{ud} & V_{us} & V_{ub} \\ V_{cd} & V_{cs} & V_{cb} \\ V_{td} & V_{ts} & V_{tb} \end{pmatrix} \begin{pmatrix} d \\ s \\ b \end{pmatrix}$$

where $d', s', b'$ are the weak eigenstates, while $d, s, b$ are for their mass eigenstates.

In the framework of the SM, the CKM matrix is a unitary and complex matrix including eighteen parameters with its nine real and nine complex elements and this is reduced to four free parameters as a consequence of unitarity $(V_{CKM}V_{CKM}^\dagger = V_{CKM}^\dagger V_{CKM} = \mathbf{1})$ and relative unobservable five arbitrary quark phases. As a consequence this end up with three mixing angles and one imaginary part known as CP violating phase in the CKM matrix decsribing the weak interactions of quarks. The CKM matrix can be parametrized in several possible ways. In many CKM-related analysis, the representation is expressed in terms of Particle Data Group (PDG) and the Wolfenstein parameterisation [19]. Regarding PDG parameterisation these parameters are : three Euler angles $\Theta_{23}$, $\Theta_{13}$, $\Theta_{12}$ and $\delta$ is the complex (imaginary) parameter which provides the only source of CP violation where the subtle difference between matter and anti-matter can be explained in the SM[‡]. The most common representation can be written as

$$V_{CKM}(PDG) = \begin{pmatrix} c_{12} & s_{12} & 0 \\ -s_{12} & c_{12} & 0 \\ 0 & 0 & 1 \end{pmatrix} \begin{pmatrix} c_{13} & 0 & s_{13}e^{i\delta_{13}} \\ 0 & 1 & 0 \\ -s_{13}e^{i\delta_{13}} & 0 & c_{13} \end{pmatrix} \begin{pmatrix} 1 & 0 & 0 \\ 0 & c_{23} & s_{23} \\ 0 & -s_{23} & c_{23} \end{pmatrix}$$

$$\begin{pmatrix} c_{12}c_{13} & s_{12}c_{13} & s_{13}e^{-i\delta_{13}} \\ -s_{12}c_{23} & c_{12}c_{23} & s_{23}c_{13} \\ s_{12}s_{23} - c_{12}c_{23}s_{13}e^{i\delta_{13}} & -c_{12}s_{23} & c_{23}c_{13} \end{pmatrix}$$

where $c_{ij} = cos\theta_{ij} =$ and $s_{ij} = sin\theta_{ij}$ $(i, j = 1, 2, 3)$.

And these parameters can also simply be written in respect of the Wolfenstein parameterisation $V_{CKM}$ where all the CKM elements are expressed in terms of power of $\lambda$

$$V_{CKM}(Wolfenstein) = \begin{pmatrix} 1 - \frac{\lambda^2}{2} & \lambda & A\lambda^3(\bar{\rho} - i\eta) \\ -\lambda & 1 - \frac{\lambda^2}{2} & A\lambda^2 \\ A\lambda^3(1 - \bar{\rho} - i\eta) & -A\lambda^2 & 1 \end{pmatrix} + \mathcal{O}(\lambda^4)$$

where its real parameters are denoted as $A, \rho, \lambda$ where $\lambda$ is the sine of the Cabibbo angle $\sin\theta_c$ where it is small $\lambda = V_{us} \approx 0.22$ and $\eta$ is for the imaginary part (source of CP violation effects). $A, \rho, \eta$ can be expressed as

$$s_{23} = A\lambda^2,$$

$$s_{13}e^{-i\delta_{13}} = A\lambda^3(\rho - i\eta)$$

---

[‡]The CP violation was observed in 1964 in neutral K meson decays and following this observation James Cronin and Val Fitch are rewarded with a Nobel prize in 1980 [20]

The diagonal elements of the CKM matrix are so near to unity (1) whereas off-diagonal elements are much smaller ( $V_{ud} \gg V_{us} \gg V_{ub}$) and with respect to the angles ($\theta_{12} \gg \theta_{23} \gg \theta_{13}$)). This is arise from the hierarchy between the magnitudes of the CKM matrix elements and it can be derived that the quark flavour transitions between the same generations are more probable.

The corresponding best fit values of the CKM parameters in the $(\bar{\rho}, \bar{\eta})$ plane are given in terms of the Wolfenstein parameterisation Table 2.1.

| Parameter | Value |
|---|---|
| $\lambda$ | $0.2250 \pm 0.00067$ |
| $A$ | $0.826^{+0.018}_{-0.015}$ |
| $\bar{\rho}$ | $0.159 \pm 0.010$ |
| $\bar{\eta}$ | $0.348 \pm 0.010$ |

Table 2.1: The latest fits for the CKM parameters in terms of Wolfenstein parameterisation. The values of parameters are taken from [18].

The CKM matrix elements are fundamental parameters of the SM can be measured experimentally [18] since this is the purpose of CKMfitter and UTfit to over-constrain them from many different measurements and coherence test of the CKM mechanism within the frameworks of the SM. Various decay processes contribute the measurements to extract the magnitude of the matrix elements. The matrix is displayed in Figure 2.2 gives the decay processes where the matrix elements' values can be determined
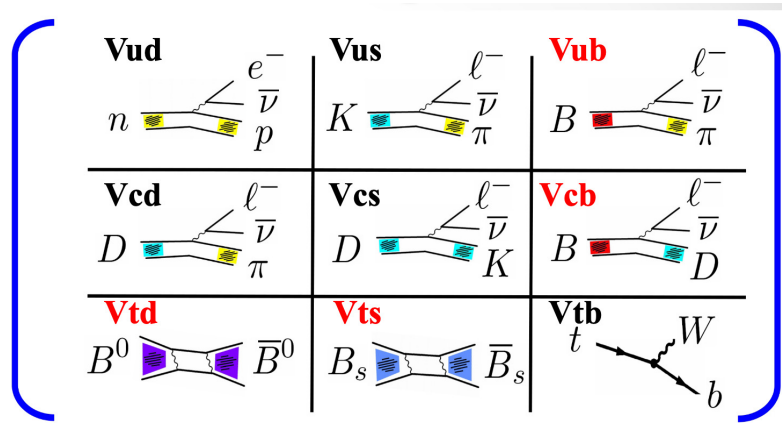


Figure 2.2: Decay processes to extract the CKM elements.

- $|V_{ud}|$

Super-allowed nuclear beta decay, neutron decay, pion beta decay are considered to extract the value of $|V_{ud}|$ CKM matrix element. Current most precise value

is determined through the super-allowed $0^+ \to 0^+$ nuclear beta decays which are pure vector $n \to pe^- \bar{\nu}_e$ [18]. The magnitude of the $|V_{ud}|$ is obtained as

$$V_{ud} = 0.97373 \pm 0.00031.$$

- $|V_{us}|$

Measurement for the CKM matrix element $|V_{us}|$ can be proceed through semileptonic kaon decays $K \to \pi l^- \bar{\nu}_l$ and hadronic tau decays $\tau^- \to K^- \nu_\tau$. $|V_{us}|$ can be also determined with the ratio of $|V_{us}/V_{ud}|$. This ratio $|V_{us}/V_{ud}|$ can be measured through the ratio of decay constants for $K^+ \to \mu^+ \nu_\mu(\gamma)/\pi^+ \to \mu^+ \nu_\mu(\gamma)$ decay modes where $\gamma$ specify that radiative decays are included [18]. With the derivation of the branching ratio of interested decay, combining this with lattice QCD calculation of form factors gives the value of $V_{us}$ CKM element as

$$V_{us} = \lambda = 0.2243 \pm 0.0008.$$

- $|V_{cd}|$

The value of the CKM matrix element $V_{cd}$ can be measured through the semileptonic D decays $D \to \pi l \nu$, $D \to K l \nu$ and leptonic decays $D^+ \to \mu^+ \nu$ and $D^+ \to \tau^+ \nu$. In case of semileptonic decay measurement, the value obtained for the $|V_{cd}|$ is limited by the uncertainties from the lattice QCD calculations of $D \to \pi$ form factor [18]. The value can also be determined via di-muon production from deep elastic neutrino scattering. With these determination, the value is found

$$V_{cd} = 0.221 \pm 0.004.$$

- $|V_{cs}|$

Direct determination of the value for $|V_{cs}|$ element can be through the measurements of semileptonic D meson decays $D \to K l \nu_l$ and leptonic $D_s^+ \to \mu^+ \nu_\mu$. In order to measure in semileptonic decays D and leptonic decay $D_s^+$ lattice QCD calculations of the D form factor and $D_s^+$ are taken into account [[18]]. For the semileptonic measurement, form factor of $D \to K l \nu_l$ is obtained through the lattice QCD calculations. By combining the obtained form factor value for the semileptonic decay with the measurements from CLEO-c [[21], Belle [22], BABAR [23]] and BESIII [[24], [25]] $V_{cs}$ element is determined with a dominant theoretical uncertainty from the form factor calculation. This value is compatible but less precise from the one obtained via leptonic decays. The value for the $V_{cs}$ is obtained by averaging the two measurement as:

$$V_{cs} = 0.975 \pm 0.006.$$

11

- $|V_{cb}|$

  As for $|V_{cb}|$, determination of the value is proceed through exclusive and inclusive semileptonic B mesons decays to charm $B \rightarrow Dl\nu_l$ [18]. From this measurements $|V_{cb}|$ is determined as:

$$V_{cb} = 0.0408 \pm 1.4$$

- $|V_{ub}|$

  The value for the $|V_{ub}|$ can be determined from exclusive $B \rightarrow \pi l\nu$ and inclusive semileptonic $B \rightarrow X_u l\nu$ decays. The measurement through $B \rightarrow X_u l\nu$ decay is complicated because of the large background from $B \rightarrow X_c l\nu$ decay mode and it strongly depends on the decay rate of the b quark mass [18]. Extracting $|V_{ub}|$ from exclusive $B \rightarrow \pi l\nu$ is done with the calculation of the form factor of this mode from lattice QCD and light cone sum rules. The combination from these two measurements gives the value of the $V_{ub}$ as

$$V_{ub} = 0.00382 \pm 0.20$$

- $|V_{td}|$ **and** $|V_{ts}|$

  The values of $|V_{td}|$ and $|V_{ts}|$ can't be determined through the tree level decays of top quark where t and b transitions happen. The $|V_{td}|$ and $|V_{ts}|$ values can be accessed through the oscillation frequencies of the $B^0 - \bar{B}^0$ and $B_s^0 - \bar{B}_s^0$ systems, respectively. For these processes the precision is limited due to the theoretical uncertainties in hadronic effects by lattice QCD. The current precise values for both $|V_{td}|$ and $|V_{ts|}$ [18] are

$$V_{td} = 0.0086 \pm 0.2,$$

$$V_{ts} = 0.0415 \pm 0.9$$

- $|V_{tb}|$

  The determination of $|V_{tb}|$ value is possible through the branching ratios [18]

$$\mathcal{R} = \frac{\mathcal{B}(t \rightarrow Wb)}{\mathcal{B}(t \rightarrow Wq)} = \frac{|V_{tb}|^2}{\left(\sum_q |V_{tq}|^2\right)} = |V_{tb}|^2, \tag{2.6}$$

where q is b, s, d from top decays. And it can be also measured from the single top production cross section from $p\bar{p}$ collision and the values for $|V_{tb}|$ has been determined by CDF and DØ collaborations. Currently the average value by Tevatron and LHC is

$$V_{tb} = 1.014 \pm 0.029$$

**Unitarity conditions**

There are six unitary conditions provided by the off-diagonal elements of the CKM matrix. Each of the conditions are represented by the triangles and the shape of them are different from each others. In the complex plane the condition for the CKM matrix can be provided by a triangle called as an Unitarity Triangle (UT). Two of those six conditions which is linked to the unitarity formed by the first and third columns and by the third and first row of the CKM matrix are given respectively

$$V_{ud}V_{ub}^* + V_{cd}V_{cb}^* + V_{td}V_{tb}^* = 0. \tag{2.7}$$

$$V_{td}V_{ud}^* + V_{ts}V_{us}^* + V_{tb}V_{ub}^* = 0. \tag{2.8}$$

These triangles don't have a side much shorter than the other four triangle. And the unitarity conditions are important for the decay of $B_d$ and $B_s$ mesons. The sides of the triangle are represented by the terms of this equation above 2.7: $V_{ud}V_{ub}^*$, $V_{cd}V_{cb}^*$, $V_{td}V_{tb}^*$ where each side is rescaled by best-known term $V_{cd}V_{cb}^*$ [18]. The unitarity triangle is shown in Fig. 2.3 and $(\bar{\rho}, \bar{eta})$ labels the apex of the triangle.
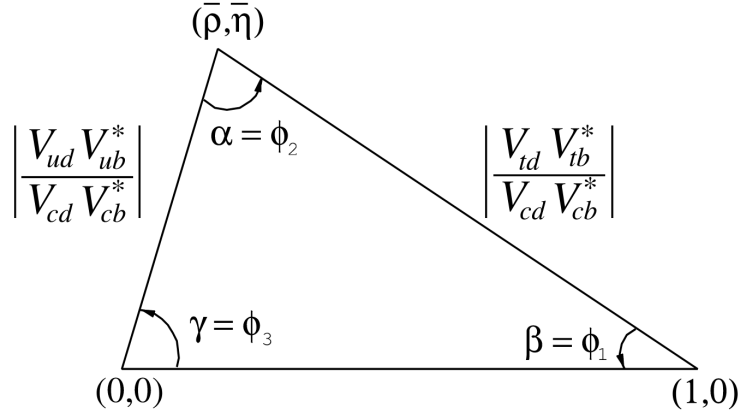


Figure 2.3: The unitarity triangle of CKM in the complex plane. Each side and the angles of the triangles are given in terms of the CKM matrix elements.

The apex and the angles of the unitarity triangle [26] are defined as

13

$$\bar{\rho} + i\bar{\eta} \equiv [-\frac{V_{ud}V_{ub}^*}{V_{cd}V_{cb}^*}],$$

$$\alpha \equiv arg[-\frac{V_{td}V_{tb}^*}{V_{ud}V_{ub}^*}],$$

$$\beta \equiv arg[-\frac{V_{cd}V_{cb}^*}{V_{td}V_{tb}^*}],$$

$$\gamma \equiv [-\frac{V_{ud}V_{ub}^*}{V_{cd}V_{cb}^*}],$$

When the sides of the CKM unitarity triangle meet, the values of the angles sum up to $\alpha + \beta + \gamma = (173 \pm 6)°$ [18]. And the interior area of the triangle is directly related to the amount of the CP violation in the SM.

One of the main goal of LHCb is to overconstraint the CKM Unitarity triangle by measuring the CKM parameters precisely by combining the constraints determined from various decay processes. These constraints are the angles $\alpha, \beta, \gamma$; the lengths of the sides of the triangle $|V_{ub}|$ and $\Delta m_d$, $\Delta m_s$ which gives the mass difference between two mass eigenstates, determined the frequency of oscillations of $B_d^0 - \bar{B}_d^0$ and $B_s^0 - \bar{B}_s^0$. The last constraint comes from the $\varepsilon_K$. The constraints from the latest global fits from the CKMfitter group is shown in Fig. 2.4.

## 2.3 The CP violation

This part reviews the violation of the CP symmetry where C and P imply discrete symmetries charge conjugation which shows a transformation of a particle to its antiparticle and a parity reversal (space inversion) respectively. In the SM of particle physics, the CP violation arises from a weak phase(complex phase) which has been explained by the CKM matrix describes the flavour mixing of the quarks in the previous section 2.2. Both electromagnetic and strong interactions conserve C, P and CP. The study of CP violation is crucial in the understanding of our current matter-dominated universe than the one was in existence with equal amount of matter and antimatter during the Big Bang. According to the Sakharov conditions which was proposed in 1967 [27] and confirmed in a more recent, elaborated work [28]. There are three ingredients requisite to create this inequality between matter and antimatter which is also known as baryon asymmetry in the Universe:

1. **Non-conserved baryon number :** this is the first barrier condition implies that the conservation of the number of baryons in the interactions must be violated. This is a demanded condition to have excess of baryon numbers over anti-baryons.
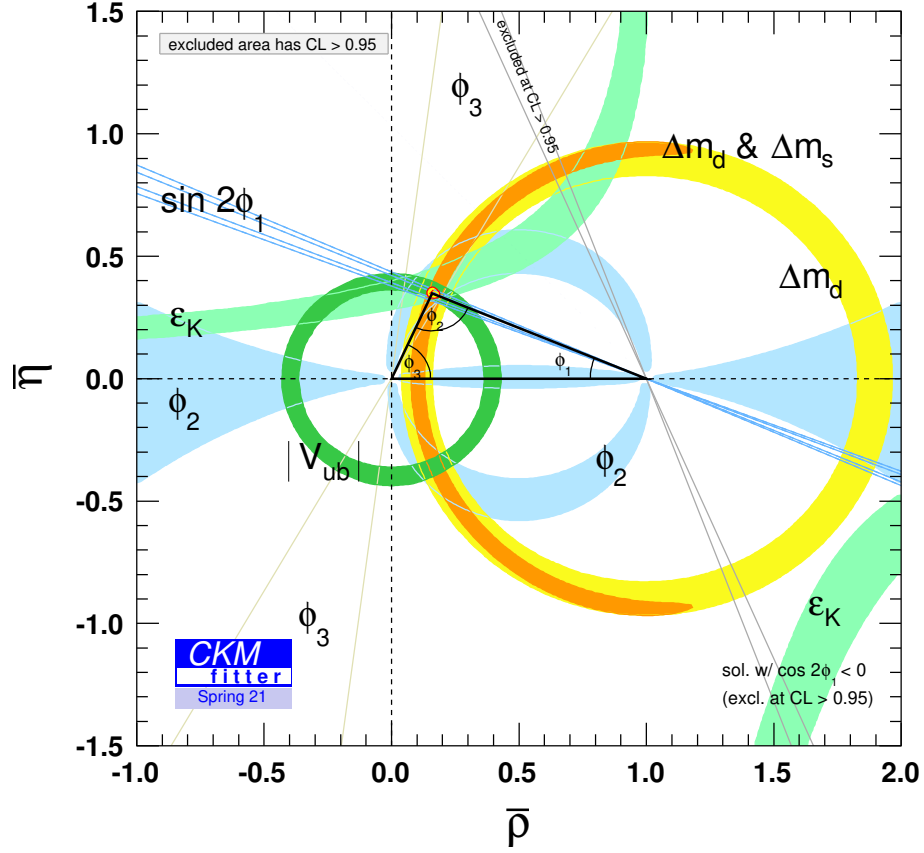
Figure 2.4: Global fit of the unitarity triangle and constraints in the $(\bar{\rho}, \bar{\eta})$ plane from the CKMfitter group (frequentist statistical approach).

2. **Charm (C) and Charm-Parity (CP) violation :** C and CP symmetries is necessary to be violated. First observation of this condition was in the Kaon system in 1964 [29].

3. **Going out of thermal equilibrium :** Interactions should happen out of the thermal equilibrium. This condition explained the situation in the early of the universe.

These conditions are enough to understand the baryogenesis phenomenon (explains imbalance between matter and antimatter). For the first condition there is no evidence for the observation of baryon number violation so far [30]. The second one C-symmetry and CP-symmetry violation is the most subtle requirement of Sakharov's in order to digest the absolute difference between matter and antimatter. So far, while the CPV was observed in neutral kaon decays (1994), beauty decays(2002 $e^+e^-$ B-factories BaBar experiment at PEP-II at Stanford Linear Accelerator Center(SLAC) California,USA and

15

Belle experiment at KEKB accelerator in Tsukuba, Ibaraki Prefecture, Japan, designed to study B-hadron decays) and charm decays (LHCb 2019) , the amount of CPV is far from satisfying the disparity matter-antimatter in the Universe.

This difference can be investigated in three ways in the SM :

- **CP violation in decay**

  This type of violation occurs when the amplitude $A_f$ of a particle (B) decays to a final state $f$ has different magnitudes from the amplitude for an antiparticle $(\bar{B})$ $\bar{A}_{\bar{f}}$ decays to final state $\bar{f}$. The condition is provided by

  $$|A_f| \neq |\bar{A}_{\bar{f}}| \tag{2.9}$$

  And the asymmetry for this CP violation is given with

  $$A_{CP(f\bar{f})} = \frac{\Gamma(\bar{B} \to \bar{f}) - \Gamma(B \to f)}{\Gamma(\bar{B} \to \bar{f}) + \Gamma(B \to f)} = \frac{1 - |\bar{A}_{\bar{f}}/A_f|^2}{1 + |\bar{A}_{\bar{f}}/A_f|^2} \tag{2.10}$$

  This violation is known as a direct CP violation and placed both charged and neutral b hadron decays. In this thesis direct CPV is studied with the B decay channels: $B_s^0 \to D^{(*)0}\phi$ and $B^- \to D^0 K^{*-}$.

- **CP violation in mixing**

  This type of CP violation can be proceed in mixing of the neutral B system (B factories: Babar and Belle) and neutral kaon system. It is represented through the box diagrams where oscillations occur between $B_{s,d}^0$ and $\bar{B}_{s,d}^0$ processes. The CP violation in mixing appears when two neutral mass eigenstates can not be choosen to be CP eigenstates, they differ from each others and CP violation occurs when

  $$\frac{|p|}{|q|} \neq 1$$

  where p and q are complex coefficients, this shows the asymmetry among the transitions of $B^0 \to \bar{B}^0$ and $\bar{B}^0 \to B^0$. CP violation is expected to be very small $(< 10^{-4})$ in mixing.

- **CP violation in the interference**

  Following the first two CP violation types, last type of CP violation occurs in neutral B decays when there is a phase difference between decay $(B \to f, \bar{B} \to \bar{f})$

and mixing $(B^0_{s,d}, \bar{B}^0_{s,d} \rightarrow f)$ processes. The CP violation in interference occurs when

$$\lambda_f = arg(\frac{q}{p}\frac{\bar{A}_{\bar{f}}}{A_f}) \neq 0 \qquad (2.11)$$

CP violation in mixing and CP violation in the interference (decay with mixing , decay without mixing) are called as "indirect CP violation" as well.

## 2.4 The CKM angle $\gamma$

One of the challenge of the flavor physics is to measure the $\gamma$ angle which is the complex phase of the CKM matrix $\gamma \propto -arg(V_{ub})$ and only source which provides information about the CP violation. And eventually the $\gamma$ angle is not least well known angle anymore. It verifies very well now and provides a concrete benchmark ("Standard candle") of the SM with respect to the processes which are affected by and sensitive to New Physics (NP) phenomena. That's why it is important to determine this angle precisely by combining as much measurements as possible from different B-meson decays. It can be measured through both tree-level processes (direct measurement)(CKM angle $\gamma$ is the only angle can be measured via tree level) and loop-level processes (indirect measurement). Figure 2.5 shows the latest global CKM fit for the direct measurements and indirect measurements respectively.
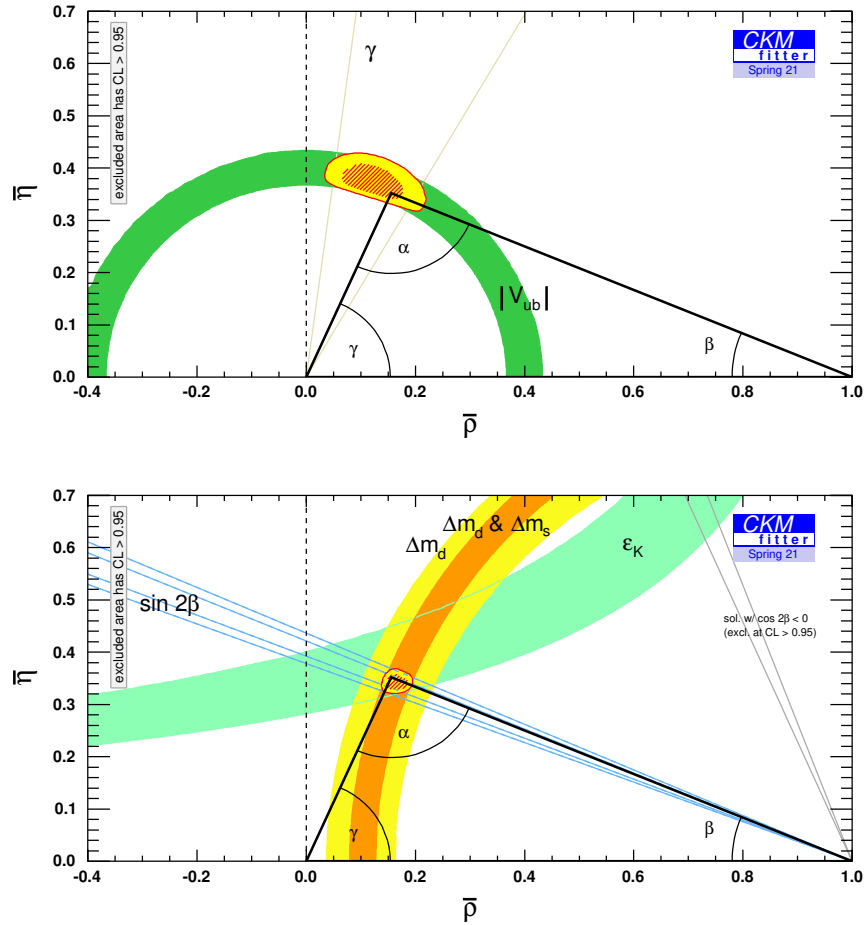


Figure 2.5: Constraints on the unitarity triangle from tree-level observables (top) and loop-level observables (bottom) from the CKMfitter group (frequentist approach) [31].

Direct measurements comes with the negligible theoretical uncertainties since they

have no involvements from loop-induced measurements which are sensitive to physics effects beyond the SM where they appear as virtual particles in loops. So far the indirect precision on the $\gamma$ angle through the global coherence test of the SM is found to be $\gamma(indirect) = (65.5^{+1.1}_{-2.7})^{\circ}$ [31] in a frequentist approach by the CKMfitter group, while a companion Bayesian method UTfit determines it to be $\gamma = (65.8 \pm 2.2)$ [32] which shows a good agreement. The reference value of $\gamma$ comes from direct measurement is important to be compared to the values from indirect measurement and any inconsistency between these two values would be a clear indication of NP. Therefore a direct measurement with a precision on $\gamma$ at the level of $1^{\circ}$ or better is highly desirable to validate the SM in the CKM sector. The last combined value on $\gamma$ angle from direct measurement is achieved to be $\gamma(direct) = (65.4^{+3.8}_{-4.2})^{\circ}$ [2] by LHCb (new $\gamma$ combination is obtained to be $\gamma(direct) = (63.8^{+3.5}_{-3.7})^{\circ}$ by LHCb experiment [33]) and this is so far the most precise value on $\gamma$ angle provided by a single experiment. Combination of the measurements from different decays and sub-degree level of processes from beauty and charm sectors to reach the $4^{\circ}$ level are given in Table 2.2 (taken from [2]) are important to achieve the stringest precison test on the $\gamma$. The combination involves 151 observables in total to determine 52 free parameters (new $\gamma$ combination [33] with 173 observables and 52 parameters), and the fit quality is tested with toy studies to be found 84% [2].

Figure 2.6 taken from [2] shows the latest $\gamma$ combination distributions obtained from different B meson species: $B^{\pm}$, $B^0$ and $B^0_s$. Between the charged and neutral B decays, a 2.2 $\sigma$ difference was observed. It can be seen that the combination is mostly driven by the charged $B^{\pm}$ decays to $B^{\pm} \to DK^{\pm}$ where D is accessible both $D^0$ and $\bar{D}^0$ decays and the Confidence Level (CL) for these initial B meson species are displayed in Table 2.3. Various methods are studied based on the D meson final states to measure the observables to measure the sensitivity to $\gamma$.

| B decay | D decay | Ref. | Dataset | Status since [34] |
|---|---|---|---|---|
| $B^{\pm} \to Dh^{\pm}$ | D$\to h^+h^-$ | [35] | Run 1&2 | **Updated** |
| $B^{\pm} \to Dh^{\pm}$ | D$\to h^+\pi^-\pi^-\pi^-$ | [36] | Run 1 | As before |
| $B^{\pm} \to Dh^{\pm}$ | D$\to h^+h^-\pi^0$ | [37] | Run 1 | As before |
| $B^{\pm} \to Dh^{\pm}$ | D$\to K_s^0 h^+h^-$ | [38] | Run 1&2 | **Updated** |
| $B^{\pm} \to Dh^{\pm}$ | D$\to K_s^0 K^{\pm}\pi^{\mp}$ | [39] | Run 1&2 | **Updated** |
| $B^{\pm} \to D^*h^{\pm}$ | D$\to h^+h^-$ | [35] | Run 1&2 | **Updated** |
| $B^{\pm} \to DK^{*\pm}$ | D$\to h^+h^-$ | [40] | Run 1&2(*) | As before |
| $B^{\pm} \to DK^{*\pm}$ | D$\to h^+\pi^-\pi^+\pi^-$ | [40] | Run 1&2(*) | As before |
| $B^{\pm} \to Dh^{\pm}\pi^+\pi^-$ | D$\to h^+h^-$ | [41] | Run 1 | As before |
| $B^0 \to DK^*$ | D$\to h^+h^-$ | [42] | Run 1&2(*) | **Updated** |
| $B^0 \to DK^*$ | D$\to h^+\pi^-\pi^+\pi^-$ | [42] | Run 1&2(*) | **New** |
| $B^0 \to DK^*$ | D$\to K_s^0\pi^+\pi^-$ | [43] | Run 1 | As before |
| $B^0 \to D^{\mp}\pi^{\pm}$ | $D^+ \to K^-\pi^+\pi^+$ | [44] | Run 1 | As before |
| $B_s^0 \to D_s^{\mp}K^{\pm}$ | $D_s^+ \to h^+h^-\pi^+$ | [45] | Run 1 | As before |
| $B_s^0 \to D_s^{\mp}K^{\pm}\pi^+\pi^-$ | $D_s^+ \to h^+h^-\pi^+$ | [46] | Run 1&2 | **New** |
| D decay | Observable(s) | Ref. | Dataset | Status since [34] |
| $D^0 \to h^+h^-$ | $\Delta A_{CP}$ | [[47],-[48]] | Run 1&2 | **New** |
| $D^0 \to h^+h^-$ | $y_{CP}$ | [49] | Run 1 | **New** |
| $D^0 \to h^+h^-$ | $\Delta Y$ | [[50],-[51]] | Run 1&2 | **New** |
| $D^0 \to K^+\pi^-$ (Single Tag) | $R^{\pm}, (x'^{\pm})^2, y'^{\pm}$ | [52] | Run 1 | **New** |
| $D^0 \to K^+\pi^-$ (Double Tag) | $R^{\pm}, (x'^{\pm})^2, y'^{\pm}$ | [53] | Run 1&2(*) | **New** |
| $D^0 \to K^{\pm}\pi^{\mp}\pi^+\pi^-$ | $(x^2+y^2)/4$ | [54] | Run 1 | **New** |
| $D^0 \to K_s^0\pi^+\pi^-$ | $x, y$ | [55] | Run 1 | **New** |
| $D^0 \to K_s^0\pi^+\pi^-$ | $x_{CP}, y_{CP}, \Delta x, \Delta y$ | [56] | Run 1 | **New** |
| $D^0 \to K_s^0\pi^+\pi^-$ | $x_{CP}, y_{CP}, \Delta x, \Delta y$ | [57] | Run 2 | **New** |

Table 2.2: Measurements from beauty and charm (bottom part of the table) sectors used in the $\gamma$ combination. Table is taken from [2] shows the new and updated results since the previous $\gamma$ combination [34]. Dataset given with (*) represents Run 2 including only 2015 and 2016.

| Species | Value [°] | 68.3% CL | | 95.4% CL | |
|---|---|---|---|---|---|
| | | Uncertainty | Interval | Uncertainty | Interval |
| $B^+$ | 61.7 | +4.4 -4.8 | [56.9, 66.1] | +8.6 -9.5 | [52.2, 70.3] |
| $B^0$ | 82.0 | +8.1 -8.8 | [73.2, 90.1] | +17 -18 | [64, 99] |
| $B_s^0$ | 79 | +21 -24 | [55, 100] | +51 -47 | [32, 130] |

Table 2.3: $\gamma$ combination results within the corresponding Confidence Level (CL) from the B meson species. Table is taken from [2].
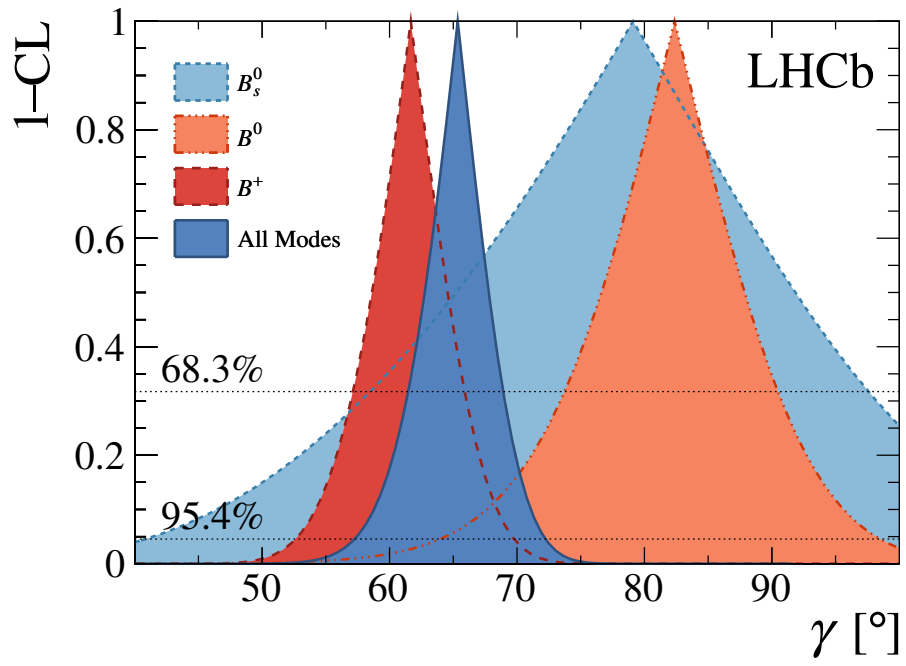
Figure 2.6: $\gamma$ measurements from different B meson flavours. $B_s^0$ meson (light blue), $B^0$ meson (orange), charged B meson (red) and the combination from all flavours is given (dark blue).

## 2.4.1 The CKM $\gamma$ angle from tree-level decays

The sensitivity to angle $\gamma$ (phase of V_ub) in B decays is obtained using the interference between the $b \to c\bar{u}s$ and $b \to u\bar{c}s$ decay amplitudes at tree level diagrams, where the D meson decays to the same final state $[D^0/\bar{D}^0]$ as shown in corresponding Feynman diagrams in Figure 2.7.
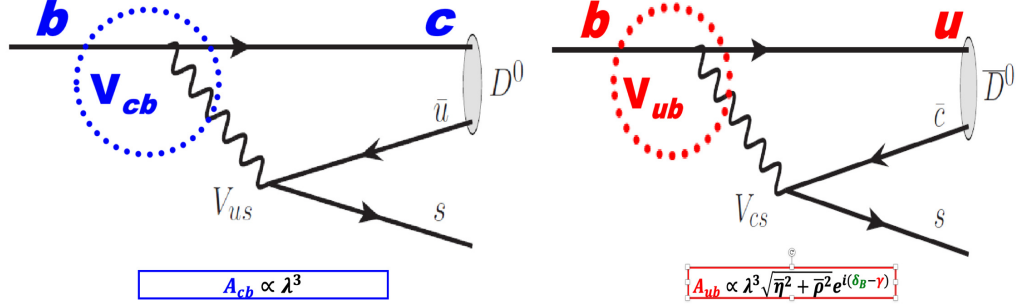


Figure 2.7: Feynman diagrams. Tree level diagrams mediate via $b \to c\bar{u}s$ and $b \to u\bar{c}s$ transitions.

where the amplitude of the $b \to c\bar{u}s$ and $b \to u\bar{c}s$ transitions are proportional to Eq. 2.12 and Eq. 2.13.

$$A_{cb} \propto \lambda^3 \tag{2.12}$$

$$A_{ub} \propto \lambda^3 \sqrt{(\bar{\eta})^2 + (\bar{\rho})^2} e^{i(\delta_B - \gamma)} \tag{2.13}$$

and the total amplitude is obtained by sum of these two amplitudes $A_{ub}$ and $A_{cb}$

$$A = A_{cb} + A_{ub} \tag{2.14}$$

The relative strong phase and relative weak phase between the two decay amplitudes are given by $\delta_B$ and $\gamma$ respectively. The magnitude of the ratio between the amplitudes of the $b \to c\bar{u}s$ and $b \to u\bar{c}s$ transitions is given by $r_B$. The $r_B$ parameter has a crucial importance for the $\gamma$ measurements. The sensitivity to $\gamma$ is governed by the size of the $r_B$

$$r_B \equiv \frac{A_{ub}(b \to u)}{A_{cb}(b \to c)}. \tag{2.15}$$

If the $r_B$ parameter is small, the experimental sensitivity to $\gamma$ becomes small. The precision on $\gamma$ correspond to

$$\gamma \propto \frac{1}{r_B}$$

For each B decay modes $r_B$ is considered with the different values.

For this thesis study, two different analysis are presented. The sensitivity to $\gamma$ angle is presented in time-integrated measurements in the $B_s^0$ systems where neutral strange B-meson decays to $B_s^0 \to \tilde{D}^{(*)0}\phi$ and $B^{\pm}$ systems where charged B-meson decays to $B^{\pm} \to \tilde{D}^0 K^{*\pm}$ are considered. Both measurements provide theoretically clean path to extract the weak phase $\gamma$ angle.

### 2.4.1.1    Measurement with $B_s^0 \to D^{(*)0}\phi$ decay

The $B_s^0$ measurement involved in the latest $\gamma$ combination [2] based on time-dependent and B-tagging analysis of two decay modes : the sensitivity on $\gamma$ from $B_s^0 \to D_s^{\pm} K^{\pm}$ decay with only Run 1 (this measurement will be improved using the full dataset in the new $\gamma$ combination study) $\gamma = (128^{+17}_{-22})^{\circ}$ [45] and for $B_s^0 \to D_s^{\mp} K^{\pm} \pi^{\pm} \pi^{\mp}$ with Run 1 + Run 2 dataset is $\gamma = (44 \pm 12)^{\circ}$ [46]. This leads to a combination $\gamma \sim (79^{+21}_{-24})^{\circ}$ level of precision given in Table 2.3 [2] and seems the most probable value but high with respect to the measurements from $B^+$ and $B^0$. In a recent sensitivity study [4] we have shown that there is another different method to determine the angle $\gamma$ which uses untagged $B_s^0 \to \tilde{D}^{(*)0}\phi$ decays, where you can find the information about the CP violation in the time-integrated rate of $B_s^0 \to \tilde{D}^{(*)0}\phi$ (or of $B^0 \to D\phi$) [[5, 6, 7]]. And it is known that this decay can itself be sufficient to determine the $\gamma$ with the various $D$-meson final state [4]. Sensitivity to $\gamma$ angle in $B_s^0 \to \tilde{D}^{(*)0}\phi$ is studied from the interference between $b \to c$ and $b \to u$ transitions [4], and the both corresponding Feynman diagrams are color-suppressed are displayed in the Figure 2.8. The formalism for the $B_s^0 \to \tilde{D}^{(*)0}\phi$ analysis are explained in the sensitivity study to $\gamma$ given in [4] and also explained in Appendix A.
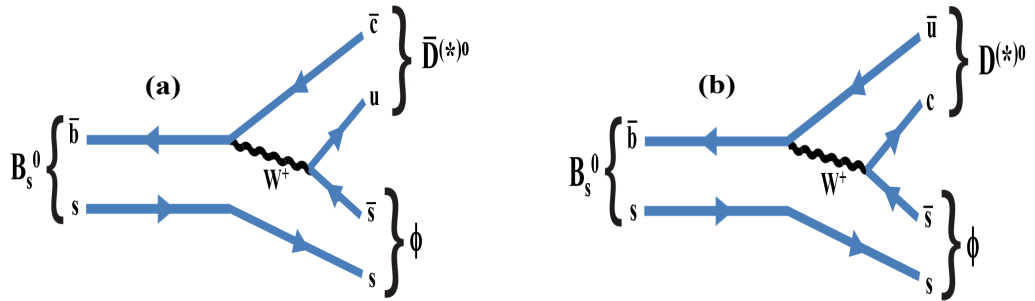


Figure 2.8:    Feynman diagrams for (a, left) $B_s^0 \to \overline{D}^{(*)0}\phi$ and (b, right) $B_s^0 \to D^{(*)0}\phi$ decay. The sensitivity comes from the two interfering diagrams based on $V_{cb}$ (left) and $V_{ub}$ (right) CKM matrix elements.

where the ratio of the interference between $b \to c$ and $b \to u$ decay amplitudes is expected to be large due to the two color suppressed diagrams (r_B from 20 % to 50 %) [4]. For the measurement of the angle $\gamma$ from $B_s^0 \to \tilde{D}^{(*)0}\phi$, five sub-decay modes where the neutral $D^0$ meson decays are considered: $K\pi, K3\pi, KK, \pi\pi, K\pi\pi^0$. For this analysis, we study $B_s^0 \to \tilde{D}^{(*)0}\phi$, where $D^0$ meson decays to $K\pi\pi^0$ sub-decay. The analysis will be elaborated in Chapter 4.1.

### 2.4.1.2 Measurement with charged $B^\pm \to \tilde{D}^0 K^{*\pm}$ decays

In order to measure the sensitivity to $\gamma$ angle and obtain the hadronic (physics) parameters of the decay: $r_B$ and $\delta_B$, a charged B decay measurement $B^\pm \to \tilde{D}^0 K^{*\pm}$ has been studied previously by a former PhD student Anita Nandi for her PhD thesis [15] and published [58] and [59], with the D meson decays to two-body and four-body final states $K^-\pi^+$, $K^-K^+$, $\pi^-\pi^+$, $K^-\pi^+\pi^-\pi^+$, $\pi^-\pi^+\pi^-\pi^+$, $\pi^-K^+\pi^-\pi^+$ and, where $K^{*\pm}$ reconstructed in $K_s^0\pi^\pm$ using the datasets Run 1 and Run 2 (2015&2016). Within the scope of this thesis, we revisit and study this decay mode of $B^\pm \to \tilde{D}^0 K^{*\pm}$, where $\tilde{D}^0$ decays to two body final states $K^-\pi^+, K^-K^+, \pi^-\pi^+$ and $K^{*\pm}$ is reconstructed in another decay $K^\pm\pi^0$ with the full datasets Run 1 and Run 2. Details concerning this analysis will be presented in Chapter 5. The extraction of the CKM angle $\gamma$ can be obtained in $B^\pm \to \tilde{D}^0 K^{*\pm}$ decays exploiting the interference between favoured $b \to c$ and color-suppressed $b \to u$ transitions. The related Feynman diagrams are given in Figure 2.9.
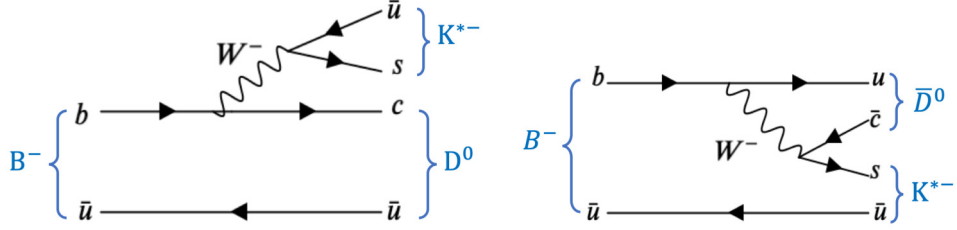


Figure 2.9: Feynman diagrams for $B^- \to D^0 K^{*-}$ ($K^-\pi^0$) decay (left) and $B^- \to \bar{D}^0 K^{*-}(K^-\pi^0)$. The interference between tree amplitudes favored $b \to c$ (Vcb) and color suppressed $b \to u$ (Vub).

The amplitude of $B^- \to D^0 K^{*-}$ and $B^- \to \bar{D}^0 K^{*-}$ decays can be written as:

$$A(B^- \to D^0 K^{*-}) = a \tag{2.16}$$

$$A(B^- \to \bar{D}^0 K^{*-}) = a r_B^{DK^*} e^{i\delta_B e^{-i\gamma}} \tag{2.17}$$

and with their conjugates:

$$A(B^+ \to D^0 K^{*+}) = b \tag{2.18}$$

$$A(B^+ \to \bar{D}^0 K^{*+}) = b r_B^{DK^*} e^{i\delta_B e^{+i\gamma}} \tag{2.19}$$

where $r_B$ is the magnitude of the ratio of the amplitude of the decay mode, $\delta_B$ is the strong phase difference between two decay modes: $B^- \to DK^{*-}$ and $B^+ \to DK^{*+}$ and the CP-violation phase $\gamma$. The sensitivity to CKM angle $\gamma$ is derived by the ratio of the amplitudes $r_B$. The parameters can be determined experimentally.

In order to measure the $\gamma$ and hadronic parameters (physics parameters) $r_B$ and $\delta_B$ with $B^\pm \to \tilde{D}^0 K^{*\pm}$, various methods and approaches depending on the D-meson final state decays and here three of them will be explained: GLW (Gronau-London-Wyler) [[60], [61], ADS (Atwood-Dunietz-Soni) [62], [63] and GGSZ (Gri-Grossman-Soffer-Zupan) [64]].

### 2.4.1.3   The GLW method

GLW method which is named after the theorists Gronau-London-Wyler [[60], [61]]. This approach using D meson final states, where D stands for $D^0$ and $\bar{D}^0$ are reconstructed in two-body CP-even eigenstates: $\pi^-\pi^+$ and $K^-K^+$ and CP-odd states e.g. $K_s^0\pi^0$, $K_s^0\omega$, $K_s^0\pi^0$. The angle $\gamma$ is determined from the $B^\pm \to \tilde{D}^0 K^{*\pm}$ decay. The interference diagrams for GLW strategy is displayed in Figure 2.10.



Figure 2.10: Diagram shows the $B^\pm \to DK^\pm$ decay, where D decays $\pi^+\pi^-$ and $K^+K^-$ decay modes of GLW method to increase sensitivity on $\gamma$.

An easy analogy can be made with the Young's double slit experiment to manifest the phenomenon of the interference see Figure 2.11. The experiment comprise a light waves and aimed at a barrier with two slits located and this wave produces an interference in the double slit and their interference pattern appears on a screen placed opposite sides of two slits. In our case this light source is the decay amplitudes of particles: number of the B mesons: $B^+$ and $B^-$. And two slits are represented by the decay diagrams (Feynman diagrams) which shows two possible paths for the decay of the B mesons towards the same projection point on the screen, in our case i.e. the final state. And the $r_B$ parameter represents the ratio of the size of the slits $A_{cb}$ and $A_{ub}$. GLW method is sensitive to the $\gamma$ angle but since the interfering amplitudes are in different size, the ratio $r_B$ tends to be small.
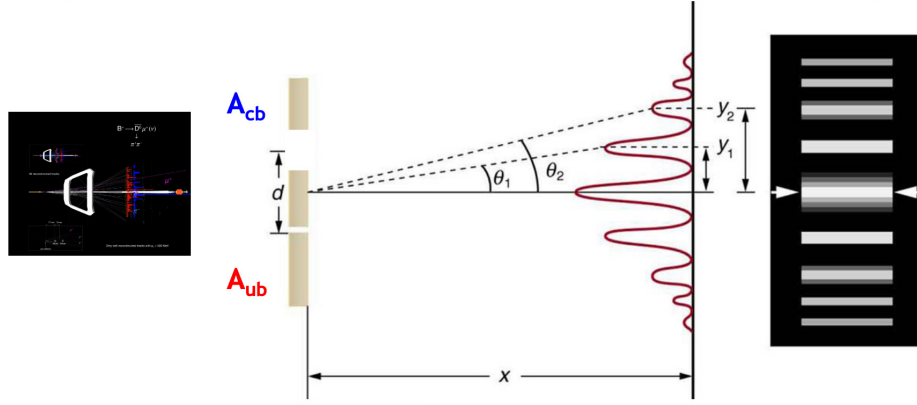
Figure 2.11: Young's double slit experiment to explain GLW method.

The observables for the GLW are generally expressed regarding the ratio of charged rates $R_{CP\pm}$ and the charge asymmetry $A_{CP\pm}$ where $CP\pm$ referees to $K^+K^-$ and $\pi^+\pi^-$. The asymmetry and ratio are:

$$A_{CP\pm} = \frac{\Gamma(B^- \to D^0{}_{CP\pm}K^{*-}) - \Gamma(B^+ \to D^0{}_{CP\pm}K^{*+})}{\Gamma(B^- \to D^0{}_{CP\pm}K^{*-}) + \Gamma(B^+ \to D^0{}_{CP\pm}K^{*+})} \qquad (2.20)$$

$$R_{CP\pm} = \frac{\Gamma(B^- \to D^0{}_{CP\pm}K^{*-}) + \Gamma(B^+ \to D^0{}_{CP\pm}K^{*+})}{\Gamma(B^- \to D^0K^{*-}) + \Gamma(B^+ \to D^0K^{*+})} \times \frac{\mathcal{B}(D^0 \to K^-\pi^+)}{\mathcal{B}(D^0 \to_{CP\pm})} \qquad (2.21)$$

where $D^0{}_{CP\pm}$ refers to CP-eigenstates of $D^0$ meson $D^0{}_{CP\pm} = (D^0 \pm \bar{D}^0)/\sqrt{2}$ and the ratio scaled by the branching fraction. Taking into account the Equations 2.20 and 2.21 and neglecting $D^0 - \bar{D}^0$ mixing and considering the $r_B$ which is the magnitude of the ratio of the amplitudes for the decay processes $B^- \to D^0K^{*-}$ and $B^- \to \bar{D}^0K^{*-}$ and the strong phase $\delta_B$ between these amplitudes, these equations 2.20 and 2.21 can be expressed as follows:

$$R_{CP\pm} = 1 \pm 2r_B cos(\delta_B)cos(\gamma) + r_B^2 \qquad (2.22)$$

$$A_{CP\pm} = \pm\frac{2r_B sin(\delta_B)sin(\gamma)}{R_{CP\pm}} \qquad (2.23)$$

it can be seen that $A_{CP\pm}$ relates to the quantify the difference between the number of events $B^+$ and $B^-$ which is directly proportional to the $r_B$ and the $\gamma$. In this case we have four observables as $R_{CP+}$, $R_{CP-}$, $A_{CP+}$, $R_{CP-}$ and three physical parameters: $\gamma$, $r_B$, $\delta_B$. And these parameters can be determined through these four observables. According to these equations 2.20 and 2.21 we also express

$$R_{CP+}A_{CP+} = R_{CP-}A_{CP-} \qquad (2.24)$$

26

And one of these observables can be calculated from the other three. We then have three unknown physical parameters and three independent equations, which remains soluble. But we know that the LHCb detector does not allow reconstruction of the CP modes because these modes like $D^0$ decays to $K_s^0\pi^0$, $K_s^0\eta$, $K_s^0\omega$ and $K_s^0\eta'$ always include a $K_s^0$, a $\pi^0$ and a $\gamma$ which are difficult to detect.

We have two observables for three unknown parameters, consequently we need to use another method to quantify the parameters. According to that we build the observables with the GLW method as

$$A_{CP\pm} = \frac{N(B^- \to CP_\pm) - N(B^+ \to CP_\pm)}{N(B^- \to CP_\pm) + N(B^+ \to CP_\pm)} \tag{2.25}$$

$$R_{CP\pm} = \frac{N(B^- \to CP_\pm) + N(B^+ \to CP_\pm)}{N_{non-CP}} \times \frac{\epsilon_{non-CP}}{\epsilon_{CP\pm}} \tag{2.26}$$

where N express $N(B^- \to CP_\pm)$ the number of decay of $B^- \to D^0_\pm K^{*-}$ and $N(B^+ \to CP_\pm)$ gives the number of decay of $B^+ \to D^0_\pm K^{*-}$. $N(non-CP)$ shows the number of events of the decay of $B^\pm \to D^0 K^{*-}$ where $D^0 \to K^-\pi^+$. And $\frac{\epsilon_{non-CP}}{\epsilon_{CP\pm}}$ display the relative efficiency of the non-CP decay of $D^0 \to K^-\pi^+$.

#### 2.4.1.4   The ADS method

The ADS method [[12], [13]] accounts for the interference between the favoured $b \to c$ transition followed by Doubly-Cabibbo Suppressed (DCS) decay, where $D^0$ to $K^+\pi^-$ and $b \to u$ is followed by the Cabibbo-Favoured (CF) decay, where $\bar{D}^0$ to $K^+\pi^-$ and the normalization mode is considered as $D^0$ to $K^-\pi^+$ [59]. Figure 2.12 shows the interference diagram for the ADS method. There are two parameters for the ADS method: $r_B$ and $\delta_B$ where the magnitude of the ratio of amplitudes between $D^0$ and $\bar{D}^0$ and the corresponding relative strong phase respectively.
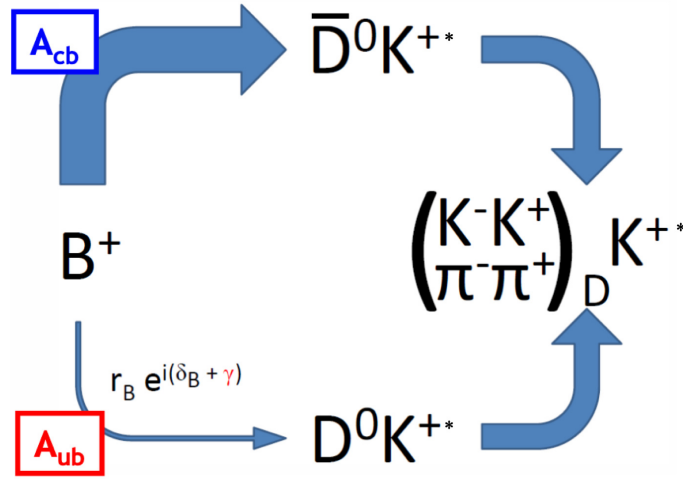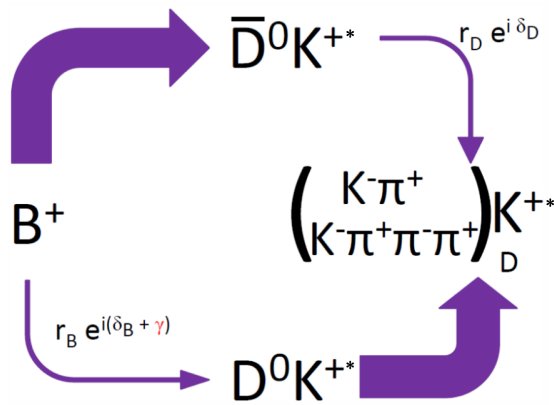


Figure 2.12: Diagram shows the $B^\pm \to DK^\pm$ decay, where D decays $K^-\pi^+$ and $K^-\pi^+\pi^-\pi^+$ decay modes of ADS method to increase sensitivity on $\gamma$.

With the ADS method, the amplitudes of two interfering diagrams have the same order of magnitude which provides the large asymmetry. The analogy with the double slit like interference for the ADS method is also displayed in Figure 2.13. Differently from GLW method it can be seen that there is another screen with a smaller slit just behind the large slit in the first screen to compensate Doubly Cabibbo suppressed D decay (DCS).
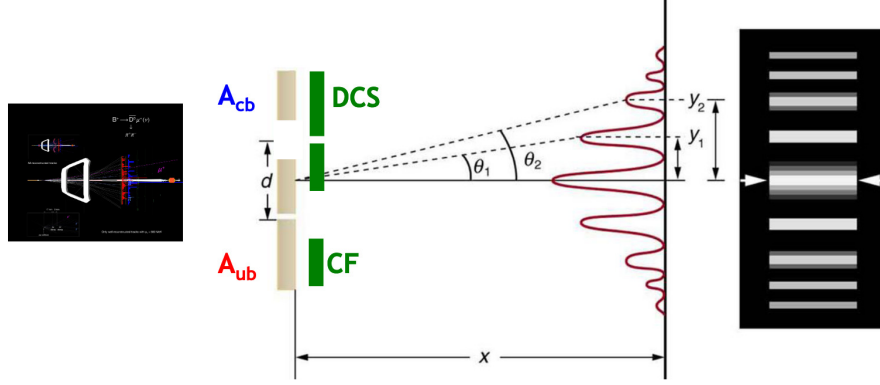


Figure 2.13: Young's double slit experiment to explain ADS method. It shows the enhanced interference. First line with two slits shows the allowed and suppressed and in order to compensate there is another screen with a smaller slit DCS and larger CF behind the large slit in the first screen.

The amplitude for the $\bar{D}^0$ and $D^0$ decays is given by

$$A(\bar{D}^0 \rightarrow K^+\pi^-) = b \tag{2.27}$$

$$A(D^0 \rightarrow K^+\pi^-) = br_D\epsilon^{i\delta_D} \tag{2.28}$$

where $\delta_D$ and $r_D$ are the relative phase and the ratio of the magnitudes between the interfering decay amplitudes $D^0 \rightarrow K^+\pi^-$ and $\bar{D}^0 \rightarrow K^+\pi^-$. We define two CP-violating observables:

$$A_{ADS} = \frac{\Gamma(B^- \rightarrow D(K^-\pi^+)K^{*-}) - \Gamma(B^+ \rightarrow D(K^+\pi^-)K^{*+})}{\Gamma(B^- \rightarrow D(K^-\pi^+)K^{*-}) + \Gamma(B^+ \rightarrow D(K^+\pi^-)K^{*+})} \tag{2.29}$$

and this 2.29 can be written as:

$$= \frac{2r_Br_D\sin(\delta_B + \delta_D)\sin\gamma}{R_{ADS}} \tag{2.30}$$

$$R_{ADS} = \frac{\Gamma(B^- \rightarrow D_{ADS}K^{*-}) + \Gamma(B^+ \rightarrow D_{ADS}K^{*+})}{\Gamma(B^- \rightarrow [K^-\pi^+]_{D^0}K^{*-}) + \Gamma(B^+ \rightarrow [K^+\pi^-]_{\bar{D}^0 K^{*+})}} \tag{2.31}$$

and can be expresses as

$$= r_B{}^2 + r_D{}^2 + r_Br_D2\cos(\delta_B + \delta_D)\cos\gamma \tag{2.32}$$

where contrary to what we had in the GLW method, this method require the knowledge of the hadronic paraters $r_D$ and $\delta_D$ charm D-meson. ADS method provides large interference hence a better sensitivity to $\gamma$. We have three unknown physical parameters to be determined experimentally with four observables for $D^0$ decays to $K^-\pi^+$ (RS) and $K^+\pi^-$ (WS). Concerning this observables the ADS can be defined in a similar with the ones for the GLW method:

$$A_{ADS} = \frac{N(B^-, WS) - N(B^+, WS)}{N(B^-, WS) + N(B^+, WS)} \tag{2.33}$$

$$R_{ADS} = \frac{N(B^-, WS) + N(B^+, WS)}{N(B^-, RS) + N(B^+, RS)} \tag{2.34}$$

Here, N($B^\pm$, WS) gives the number of the decay $B^\pm \to [WS]_D K^{*\pm}$ and N($B^\pm$, RS) gives the number of the decay $B^\pm \to [RS]_D K^{*\pm}$ where RS correspond to the decay of $D^0$ meson to $K^-$ has the same sign with the $K^{*-}$ of the $B^-$ meson decay and WS corresponds to the the different signs. And the equation can be written in terms of efficiencies:

$$R^\pm = \frac{N(B^\pm \to D^0 K^*(WS))}{N(B^\pm \to D^0 K^*(RS))} \times \frac{\epsilon_{sel}(K\pi)}{\epsilon_{sel}(\pi K)} \tag{2.35}$$

And here experimentally efficiency values of $K\pi$ and $\pi K$ are similar and that's why the ratio can be taken 1, from that point the observable are measured

$$R_{ADS} = \frac{R^+ + R^-}{2} \tag{2.36}$$

$$A_{ADS} = \frac{R^- - R^+}{R^- + R^+}. \tag{2.37}$$

### 2.4.1.5   The GGSZ method

There is another method so-called GGSZ (Giri-Grossman-Soffer-Zupan) Method [64] which is also known as Dalitz plot analysis. This method is a mixture of GLW + ADS methods and it used to extract $\gamma$ angle based on $B^\pm \to DK^\pm$ decays, where D decays to self-conjugate three body decays i.e. $K_S^0 \pi\pi$, $K_S^0 K^+K^-$. The method exploit the Dalitz plot structure of the decays $K_S^0 \pi\pi$, $K_S^0 K^+K^-$ [[65], [38]]. This method gives the most stringent constraint on the $\gamma$ angle. In this thesis GGSZ method is not involved.

# 3 The LHCb experiment

In this thesis, the presented analysis is performed using the data collected by the Large Hadron Collider beauty (LHCb) experiment which is one of the major experiment located at the Large Hadron Collider (LHC). This chapter gives the overview of the facilities at the LHC and the LHCb detector and its sub-detectors during Run 1 and Run 2 period. And it also describe the upgrade of the LHCb experiment during the 2018-2022 years for Run 3 period.

## 3.1   The Large Hadron Collider

The Large Hadron Collider (LHC) is built beneath the border between Switzerland and France near Geneva city as the world's most powerful and highest energy particle accelerator [[66], [67]]. It consists of 27 km ring of superconducting magnets located around 100 metres underground circular tunnel which placed the previous Large Electron-Positron Collider from 1989 to 2000 at CERN, Conseil Européen pour la Recherche Nucléaire (European Organization for Nuclear Research) [68]. The LHC is designed to collide proton beams with center-of-mass energy $\sqrt{s} = 14$ TeV. It is only one part of the accelerator complex which has a series of machines that boost the particles' energy to the higher enough level before reaching the next accelerator and finally LHC. After electrons stripped from hydrogen atoms to obtain protons, the protons enter the first chain, a linear accelerator, called LINAC2* that accelerates protons to the energy of 50 MeV and then injects proton beams into an another accelerator called the Proton Synchrotron Booster (PSB). The (PS) Booster forms the proton bunches accelerate to 1.5 GeV and sent to the next chain called Proton Synchrotron where pushes the beam up to the energy of 25 GeV. After being accelerated to the enough level of energy, they sent to the another accelerator called Super Proton Synchotron (SPS) where they are accelerated to 450 GeV. From this point, they are finally injected to the LHC where one beam travelling clockwise and the other one going counterclockwise up to 6.5 TeV. When the two beams arrives the maximum energy which they can, they collide at one of the four experiments located at the LHC. Figure 3.1 : ATLAS [[70], CMS [71], LHCb [72] and ALICE [73]. The Compact Muon Solenoid (CMS) detector and the A Toroidal LHC ApparatuS (ATLAS) detector are general-purpose of

---

*During the Run 3 period, the LINAC2 replaced by the LINAC4. The main goal of the LINAC4 is to increase the beam energy from 50 MeV (LINAC2) to 160 MeV (LINAC4) and increase the brightness of the beam from the PS Booster by a factor of 2 [69].

detectors. They are considered to study the Standard Model (SM) Higgs boson searches and physics beyond the SM. ALICE detector is specialized in heavy-ion collisons. In this thesis, data collected by the Large Hadron Collider beauty (LHCb) experiment during Run 1 and Run 2 period is analysed, detailed in the next section 3.2
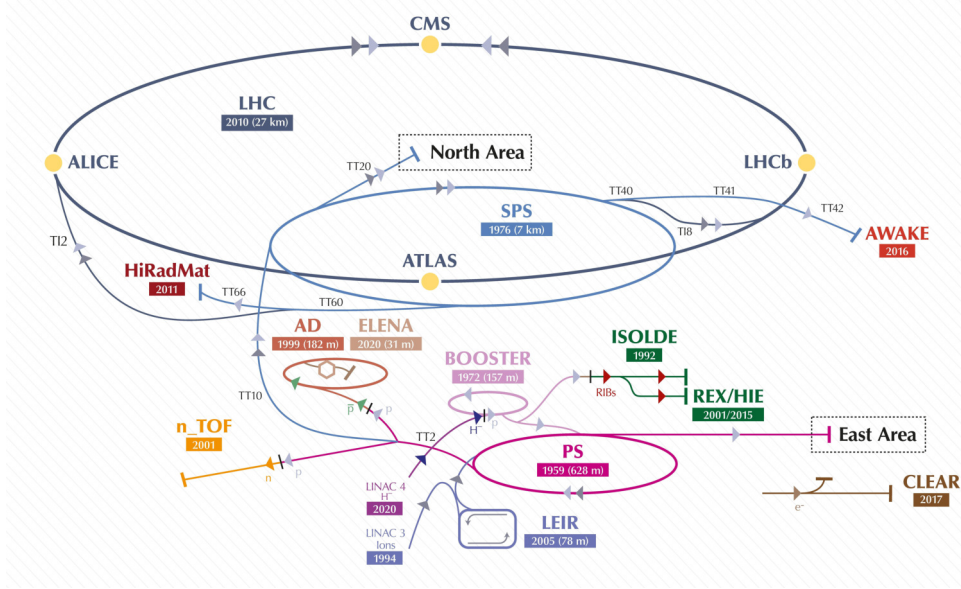


Figure 3.1: Schematic view of the CERN accelerator complex. The four main experiments are shown at the interaction points: ATLAS, CMS, LHCb, ALICE. LINAC2 is replaced by the LINAC4 accelerator during Run 3 period. LINAC3 and the Low Energy Ion Ring (LEIR) are for the heavy ion acceleration [74] Figure is taken from [75].

## 3.2 The Large Hadron Collider beauty (LHCb) detector

The LHCb detector exploit the maximum production of (heavy quarks) $b\bar{b}$ and $c\bar{c}$ pairs in the forward (backward) direction at higher energies (at $\sqrt{s} = 14\,\text{TeV}$) while it covers the small polar angles from the beam axis as shown in Figure 3.2 [72]. Inside the LHCb acceptance, Figure 3.2 shows that about 25% of $b\bar{b}$ pairs are produced. Because of this feature of LHCb, it is designed in different shape than of other LHC detectors which are cylindrical shape like ATLAS, CMS and ALICE. The LHCb detector is a single-arm spectrometer in a forward region with an angular covarage of 15-300(250) mrad in the horizontal(vertical) plane with respect to the beam axis [76], corresponding to a pseudorapidity[†] interval of $2 < \eta < 5$ defined as

---

[†]Particles falling in the LHCb acceptance.

31

$$\eta = -ln[tan\frac{\theta}{2}] \tag{3.1}$$

where $\theta$ is the angle between the particle momentum and the beam axis.

The LHCb detector is dedicated to focus to the study of particles containing b or c quarks to probe CP violation and rare decays of heavy flavours with higher precision [77]. During Run 1 and Run 2, LHCb has collected data of $pp$ collisions corresponding to a total integrated luminosity of 9 $fb^1$ at collision energy of 7, 8 and 13 TeV. The layout of the detector is given in Figure 3.3 and as is shown, LHCb is made up of a tracking system including a VErtex LOcator (VELO) [78] and four tracking stations (TT, T1, T2, T3) on upstream and downstream of the magnet respectively [79]. Two Cherenkov detectors (RICH2 and RICH2) [80], an electromagnetic calorimeter (ECAL), a hadronic calorimeter (HCAL) and a muon system (M1-M5) [81].
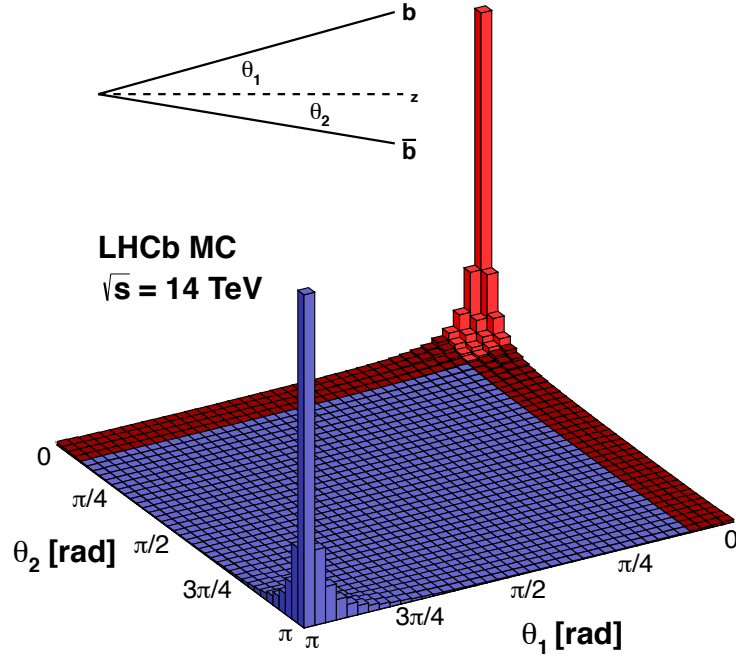


Figure 3.2: Angular distribution of $b$ and $\bar{b}$ quarks in the LHCb acceptance at $\sqrt{s} = 14\,\text{TeV}$ with $\theta_1$ and $\theta_2$ being the angle between the quark and the beam axis. Red region shows the acceptance by the LHCb detector. Reproduce from [82].
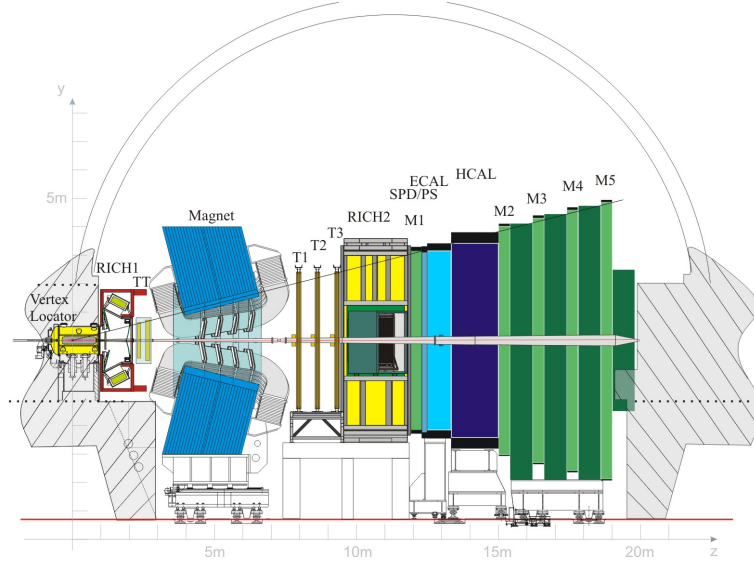
Figure 3.3: A schematic view of the LHCb experiment.

## 3.2.1   Tracking System

LHCb tracking system consists of three sub-detectors: VErtex LOcator (VELO), dipole magnet and four tracking stations: TT and T1-T2-T3. Figure 3.4 shows the sketch of various track types passing through the VELO along with the TT, T1-T2-T3 tracking stations where the tracks are reconstructed inside the acceptance of LHCb. For the most physics analysis downstream and long tracks are considered. The other types are for the detector studies. Track types are given in Appendix B.

### 3.2.1.1   VErtex LOcator

VErtex LOcator system (VELO) is the first detector which is a precise silicon-strip detector surrounds the proton-proton interaction point inside the LHCb [72]. The VELO of LHCb provides high spatial resolution of vertices of proton-proton interactions and the displaced decay vertices of charm and beauty hadrons [78]. The schematic view for the VELO is shown in the Figure 3.5. It has a critical importance for the detector as its location precisely at the pp collision point and specifically to identify and reconstruct primary and secondary vertices of track coordinates. It splits into two retractable halves and compose of 42 silicon modules settled along the beam axis. Each side of the beam line containing 21 modules at a distance of 7 mm and composed of two planes of 300 $\mu m$ thick silicon micro-strip sensors. The modules providing a measurement of the radial distance from the beamline R, and azimuthal angle, $\Phi$ sensors along the beam line respectively. Figure 3.6 shows the geometry of the $R$ and $\Phi$ sensors [72]. With the first upgrade during the Long Shutdown 2 (LS2), VELO is upgraded its silicon micro-strip sensors based on detectors to silicon micro-strip pixels to cope with the larger occupancies at the increased luminosities.
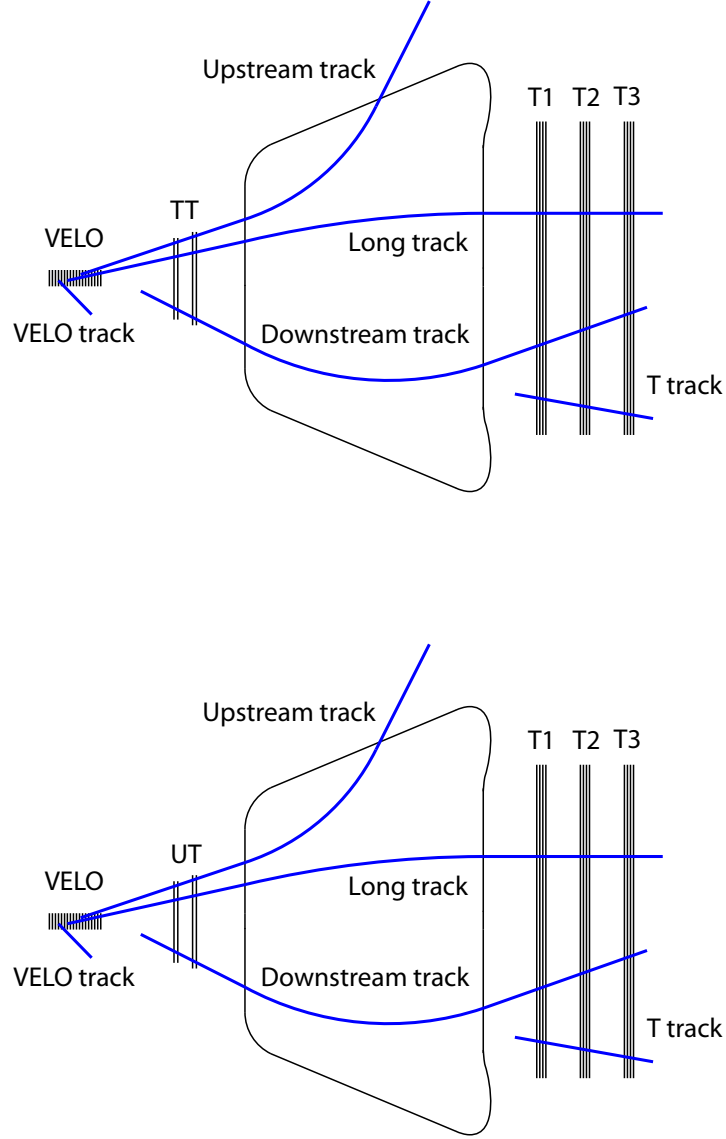
Figure 3.4: The different types of track which pass through the LHCb tracking system. Tracks which only register hits within the VELO are classified as VELO tracks and tracks which register hits only in the VELO and TT tracker are known as Upstream tracks. Tracks which register hits only in the TT and T1-3 stations are known as Downstream tracks and those only passing through the T1-3 stations are known as T tracks. Tracks which pass through all elements of the tracking system are known as Long tracks. Track types for the LHCb Run 1 and 2 (Top) and track types for the LHCb Upgrade (bottom) for Run 3. Figures are taken from [83] and [84] respectively.
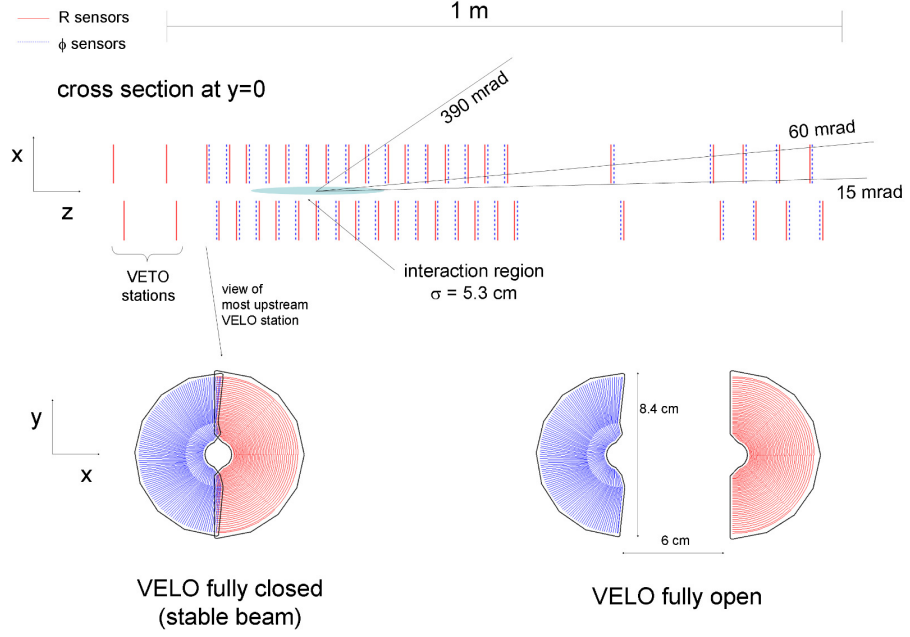
Figure 3.5: Illustration of a layout of the VELO. ($\phi$ sensor in blue and R-sensor in red) Figures are taken from [72].
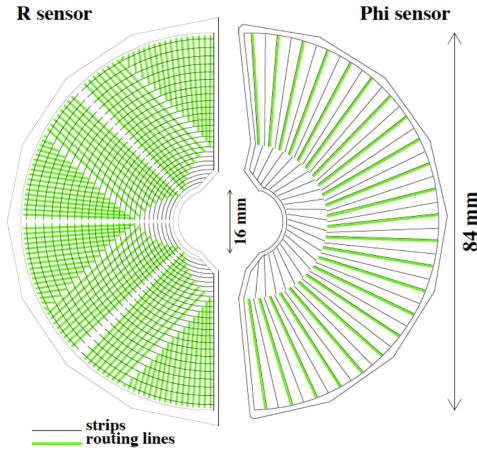


Figure 3.6: The geometry of the $R$ (left) and $\Phi$ (right) silicon micro-strip sensors of the silicon modules composing the VELO. Inner most strips are 8mm from the beam line and outer most 42mm away from the beam line. Figure is from [85].

### 3.2.1.2 Dipole magnet

The LHCb warm dipole magnet is providing momentum measurement of charged particles generating the bending power. As it is shown in the Figure 3.3, it is settled between the

TT and T1, T2, T3 tracking stations. The Figure 3.7 shows the layout of the magnet and it can be seen that the strength of the magnetic field of 4 Tm in the central region of the x-y plane along the z-axis. This provides the tracking detectors to measure the momentum of charged particles with a precision of about 0.4% for momenta up to 200 GeV/$c$.
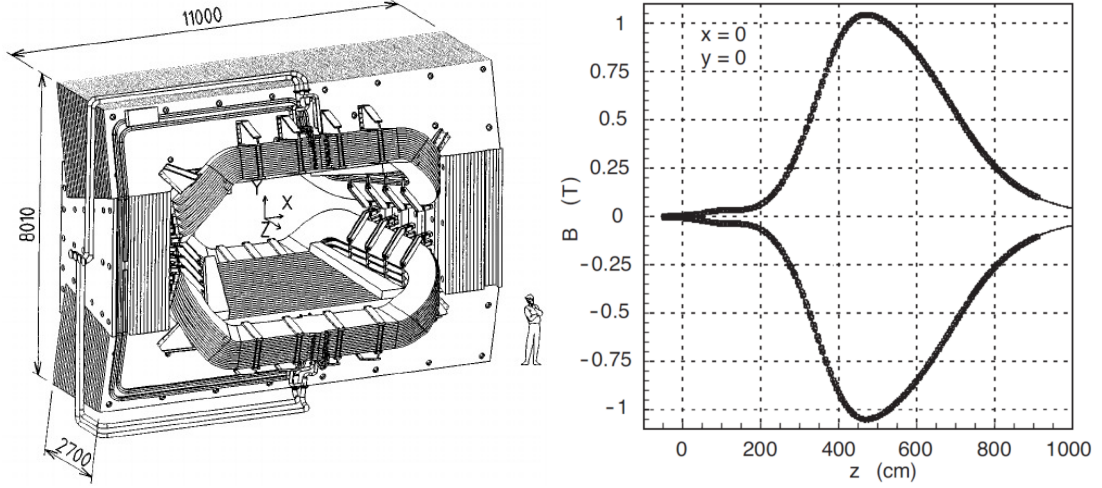


Figure 3.7: The layout of the LHCb Dipole magnet, where the interaction point lies behind the magnet (left) and (right) magnetic field along the $z$ axis. Figures are taken from [72].

#### 3.2.1.3 Tracking stations

The tracking system of the LHCb detector also consist Silicon tracker (ST) with its of four tracking stations : TT and T1-T2-T3 Turicensis. Turicensis Tracker(TT)[‡] which is a silicon-microstrip detector with a low signal-to-noise ratio placed upstream of a dipole magnet and after RICH-1 detector. It consists of 150 cm in width and 130 cm in height planar stations settled in a $x - u - v - x$ order (each station with $x - u$ and $v - x$ order) where $x$ layers located vertically while $u$ and $v$ layers are tilted by $\pm 5°$. Figure 3.8 ([86]) shows the layout of the TT. It has a full coverage of LHCb acceptance. The other three tracking stations T1, T2, T3 with Inner Tracker (IT) [87] and Outer Tracker (OT)[§] which use silicon-microstrip detector and straw tubes respectively located downstream of the magnet and before RICH-2. During the first upgrade IT and OT are replaced by a single tracking system based on scintillating fibres (SCiFi). IT is located in the area close to the beam and OT covers the outer region of the LHCb acceptance. The layout for IT and OT is illustrated in Figures 3.9 and 3.10 taken from [72]. The Figure 3.4 represents the track types and positions of the each track in different tracking systems in LHCb detector. The tracking system provides a measurement of momentum, p, of charged particles with a relative uncertainty that varies from 0.5% at low momentum to 1.0% at 200 GeV/$c$.

---

[‡]as a part of the upgrade TT tracker is replaced by Upstream Tracker(UT)

[§]the LHCb Outer Tracker (OT)is a drift-chamber detector [88]

The minimum distance of a track to a primary vertex (PV), the impact parameter (IP), is measured wit a resolution of $(15 + 29 ./p_T)\mu m$, where $p_T$ is the component of the momentum transverse to the beam, in GeV/$c$ [89].
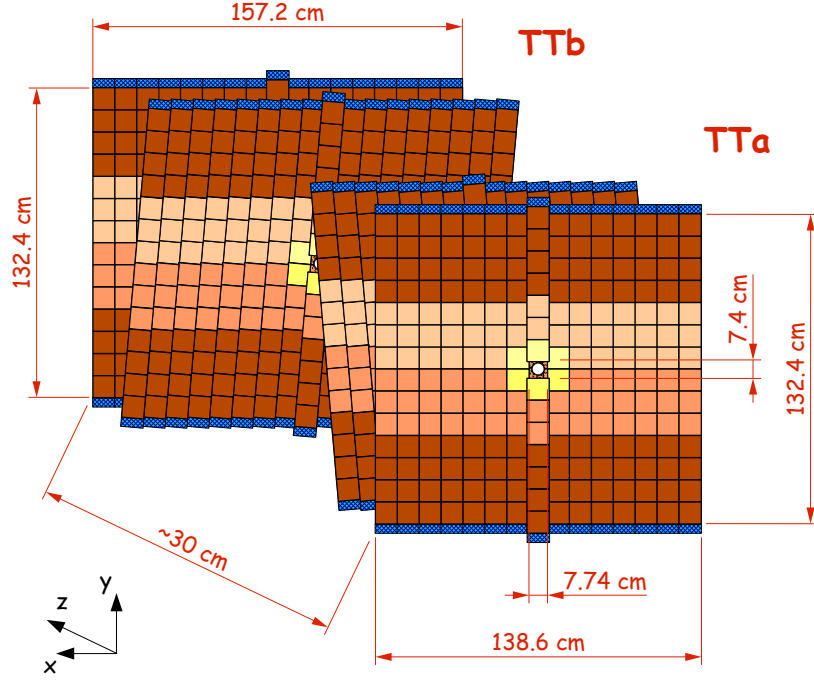


Figure 3.8: Layout of the four detection layers of the TT station. Figure is taken from [86].
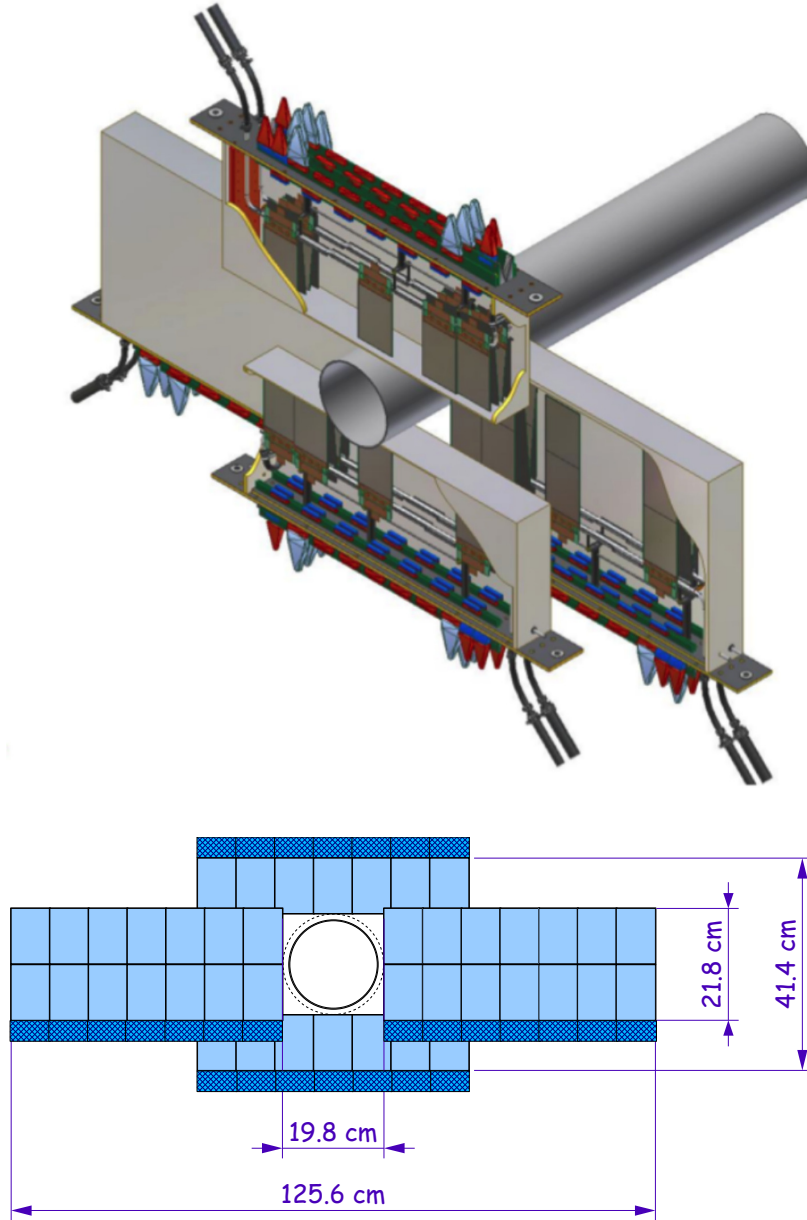
Figure 3.9: IT surround the beam pipe (top) and the layout of the IT station (bottom).

With the first upgrade (during LS2) of the LHC for Run 3, LHCb's main tracking systems VELO and four tracking stations: TT, T1, T2, T3 ([[90], [91]]) are replaced by the new type of tracking stations with a new silicon micro-strip Upstream Tracker (UT) and Scintillating Fibre Tracker (SCiFi) respectively. Details will be given in the following sections 3.2.4.
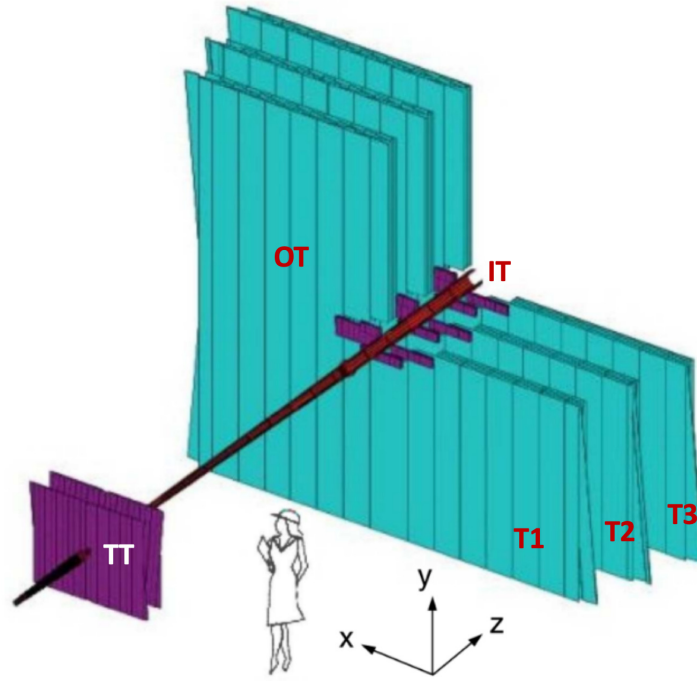
Figure 3.10: Layout of the T-stations(T1, T2, T3) with their IT and OT detectors. Outer tracker coats the large part of the tracking volume.

### 3.2.2 Particle identification

Particle identification (PID) system is essential provided by the RICH detector, the Calorimeter (CALO) which splits into: Electromagnetic (ECAL) and Hadronic (HCAL) calorimeter and Muon stations (M1-M5). These sub-systems come up with useful PID informations for physics analysis. RICH (RICH1 and RICH2) sub-detectors play a key role for the $\pi/K$ separation for the physics analysis.

#### 3.2.2.1 The Ring Imaging Cherenkov detectors (RICH)

LHCb has two Ring Imaging Cherenkov (RICH) detectors designed for particle identification of charged different hadrons, protons, pions and kaons. The identification of charged particles are provided by measuring emissions of Cherenkov radiation[¶] over a wide momentum range (2-100 GeV/$c$) [92]. The are two sub-detectors, RICH 1 and RICH 2 are located upstream and downstream of the LHCb magnet 1 and 10m away from the interaction point respectively. The RICH 1 detector designed to identify particles at low-momentum $1 - 60$ GeV/$c$ with a better performance using two radiators: $C_4F_{10}$ gas and aerogel while RICH 2 performs better at high momentum $15 - 100$ GeV/$c$ using only $C_4F_{10}$ [93]. During Long Shutdown(LS1) for LHC Run 2, the aerogel was removed and each detector used a single gas radiators. Particle optimisation was done using $C_4F_{10}$

---

[¶]charged particles emit Cherenkov radiation when they travel trough a transparent medium (water or air) faster than a light does

39

by RICH 1 and $CF_4$ by RICH 2. The Figure 3.11 shows the schematic view of the LHCb RICH detector (left side) and the Cherenkov angle as a function of the momentum for different particles (right side). The RICH detectors are overhauled during the Long Shutdown 2 (LS2) for the Run 3 period.
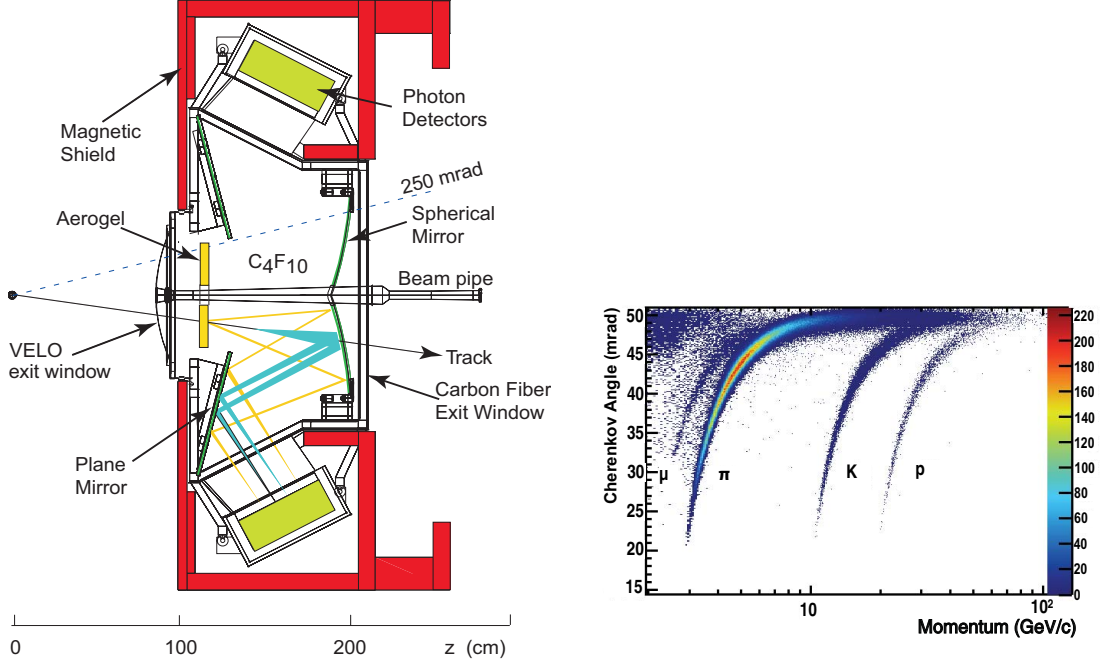


Figure 3.11: (Left) A schematic view of the RICH detectors and (Right) reconstructed Chrenkov angle as a function of track momentum in RICH [92].

### 3.2.2.2 Calorimeters

The LHCb calorimeters are designed to identify of hadrons, electrons, photons, neutrons and responsible to measure the energies and positions of these particles passing through the detector. It consist of four types of sub-detectors : Scintillator Pad Detector (SPD), the Pre-Shower detector (PS), Electromagnetic Calorimeter (ECAL) and Hadronic Calorimeter (HCAL). The Figure 3.12 displays the layout of the LHCb calorimeter. The SPD and PS are two planes of scintillator pads with high granularity, separated by a 2.5 radiation lengths lead sheet [94]. The SPD/PS are responsible to identify electrons from charged hadrons and neutral pions. First plane SPD is charged to spot if the incoming particles are charged or neutral while PS is responsible for separating electro-magnetic and hadronic showers.

Figure 3.13 shows the interaction of the particles within the various parts of the detector. Each tracks left by the particles are used to identify the signature of the particles and discriminate them. Electrons and photons are identified in the ECAL, while neutrons, protons and hadrons in HCAL. ECAL uses a technology alleged "Shashlik" with 3312 modules and 6016 channels which consists of thick scintillator tiles and lead plates, which
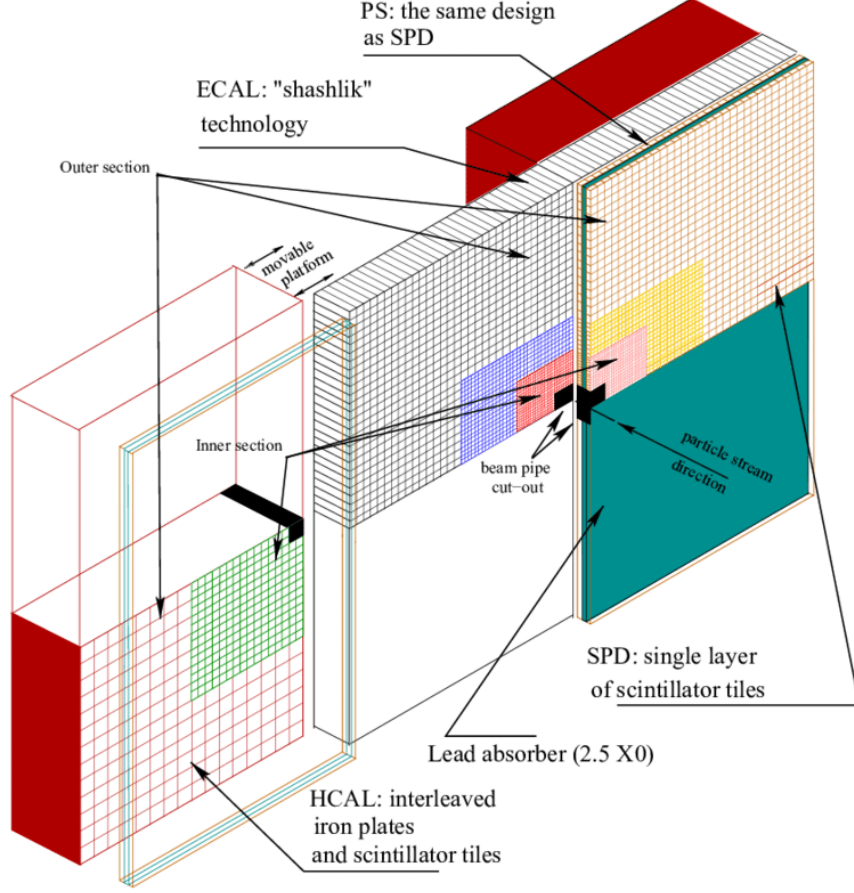
Figure 3.12: The layout of the calorimeter system.

replaced with iron plates in case of HCAL as in seen in Figure 3.12 The energy resolution for the ECAL and the HCAL is provided as respectively

$$\frac{\sigma_E}{E} = \frac{10\%}{\sqrt{(E)}} \oplus 1\% \tag{3.2}$$

$$\frac{\sigma_E}{E} = \frac{69 \pm 5\%}{\sqrt{(E)}} \oplus 9 \pm 2\% \tag{3.3}$$

where $E$ denotes energy of the particle in GeV.

The calorimeters have an importance for the analysis of two decay channels are mentioned in this thesis: $B_s^0 \to \tilde{D}^{(*)0}\phi$, where $D^0$ decays to $K\pi\pi^0$ and $B^- \to D^0 K^{*-}$, where $K^{*-}$ decays to $K^{*-} \to K^-\pi^0$ and contain $\pi^0$ decays to $\pi^0 \to \gamma\gamma$ represents roughly half of the decay products of the pp collision leading to a huge amount of combinatorial background which need a special treatment in the analysis and the reconstruction of the

41

neutral pions carry out by ECAL. They are reconstructed from two photons as in the one single cluster which is known as 'merged $\pi^0$' or in two separate clusters known as 'resolved $\pi^0$' in ECAL [95].
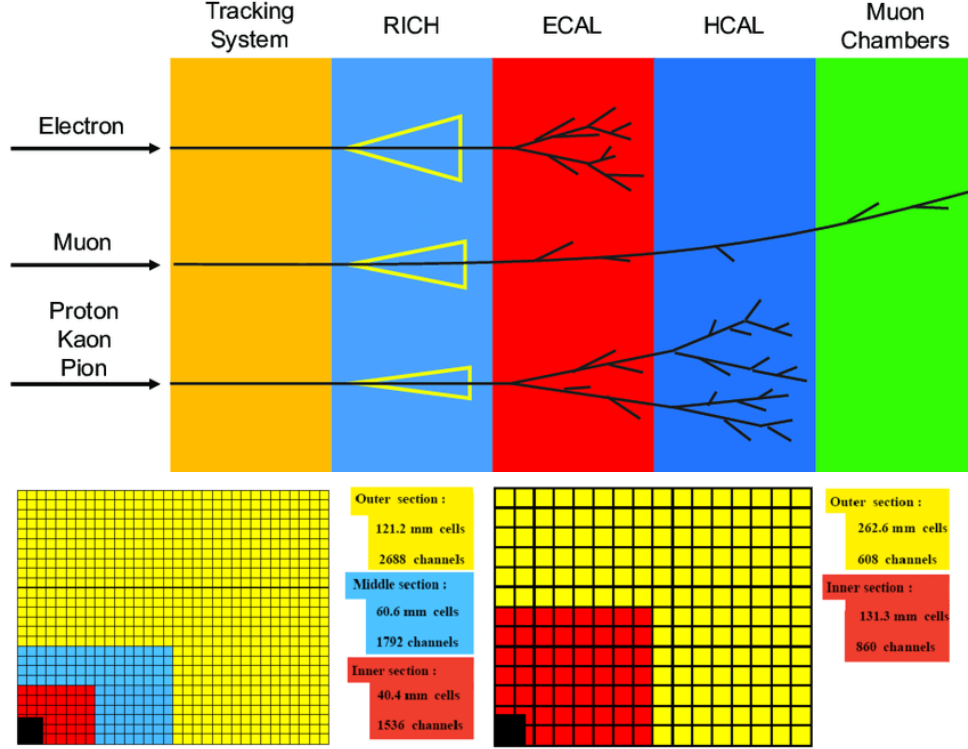


Figure 3.13: The schematic view of the different layers of the calorimeter system. Bottom figure is for lateral segmentation of the SPD-PS-ECAL (left) and HCAL (right) respectively.

### 3.2.2.3 Muon Systems

The Muon detection system is composed of five rectangular Multi-Wire Proportional Chamber (MWPC)stations (M1-M5) as shown in Figure 3.14 [81]. The stations (MWPC) are filled with a CO2/CF4/Ar gas mixture (55/5/40 in volume). The purpose of this configuration is to discriminate muons against to copious hadronic background and measure their momenta. A muon candidate is reconstructed by aligning hits in each of these five stations [96]. It is crucial to provide powerful identification and triggering of particle decays into a final state with high $p_T$ muons. The first muon station M1 is positioned in front of the calorimeters and in such a way it can detect not only muons but also any charged particles to improve the $P_T$ measurement. The other four M2-M5 stations are established downstream the calorimeters and separated by 80 cm thick iron filters which is acting as absorber stopping all particles except muons and neutrinos.

42
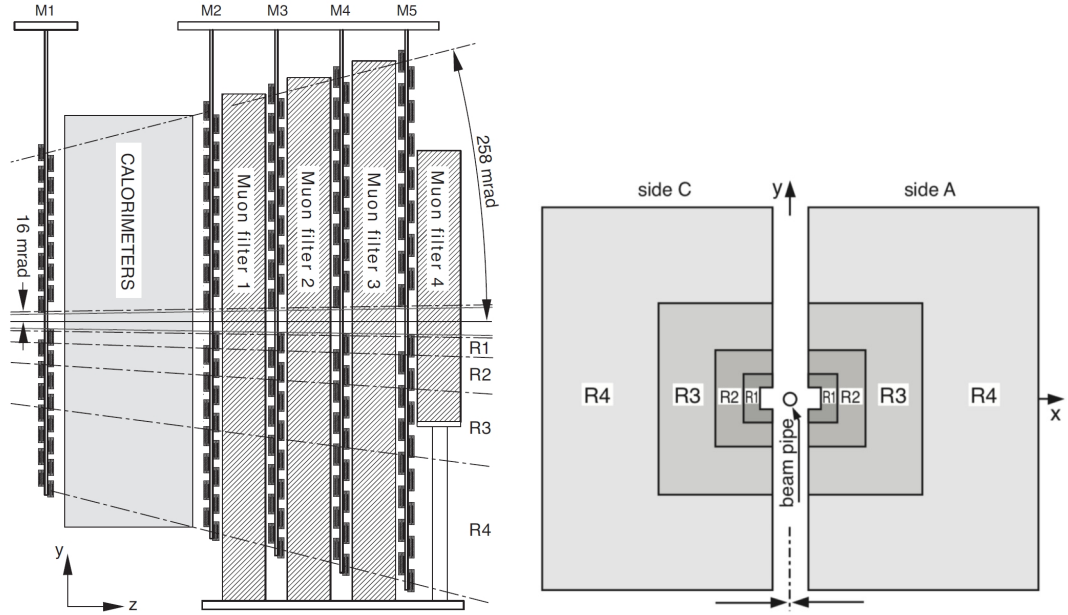
Figure 3.14: Side-view layout of the muon system consists of muon stations M1-M5 (left) split into regions R1-R4 (right) [81].

### 3.2.3 The trigger system

The online event selection is performed by the trigger system [97]. The trigger system is the key to select the doable amount of events and reject the backgrounds of interest for b-physics studies. It consists of two stages: an initial stage is implemented in hardware stage known as first level L0 online trigger and this is followed by the second stage which is known as offline software High-Level Trigger (HLT) which selects the interesting events in two different steps: High Level Trigger 1 (HLT1) and High Level Trigger (HLT2). This two stage is following each others and needed to reduce the rate of events up to a few kHz of data to be stored. The trigger layout of L0 and HLT for Run 1 and Run 2 is shown in Figure 3.15.

#### 3.2.3.1 The L0 trigger

The Level-0 trigger (L0) implemented in the front-end electronic FPGAs based board has maximum output rate of the read-out system to reduce the rate of the selected events (the bunch crossing rate) from 40 MHz to below 1 MHz which is the maximum rate can be read out the full detector. As shown in Figure 3.16, It accommodates three components: the pile-up VELO system, the L0 Calorimeter and the L0 Muon trigger which uses information from five muon stations. The L0 Calorimeter trigger process the information deposited in the SPD, PS, ECAL and HCAL to trigger the selection of events by with high transverse energy and transverse momentum. During Run3, LHCb's L0 trigger will be removed and based fully software HLT running at 30 MHz collision frequency to cope with the increased
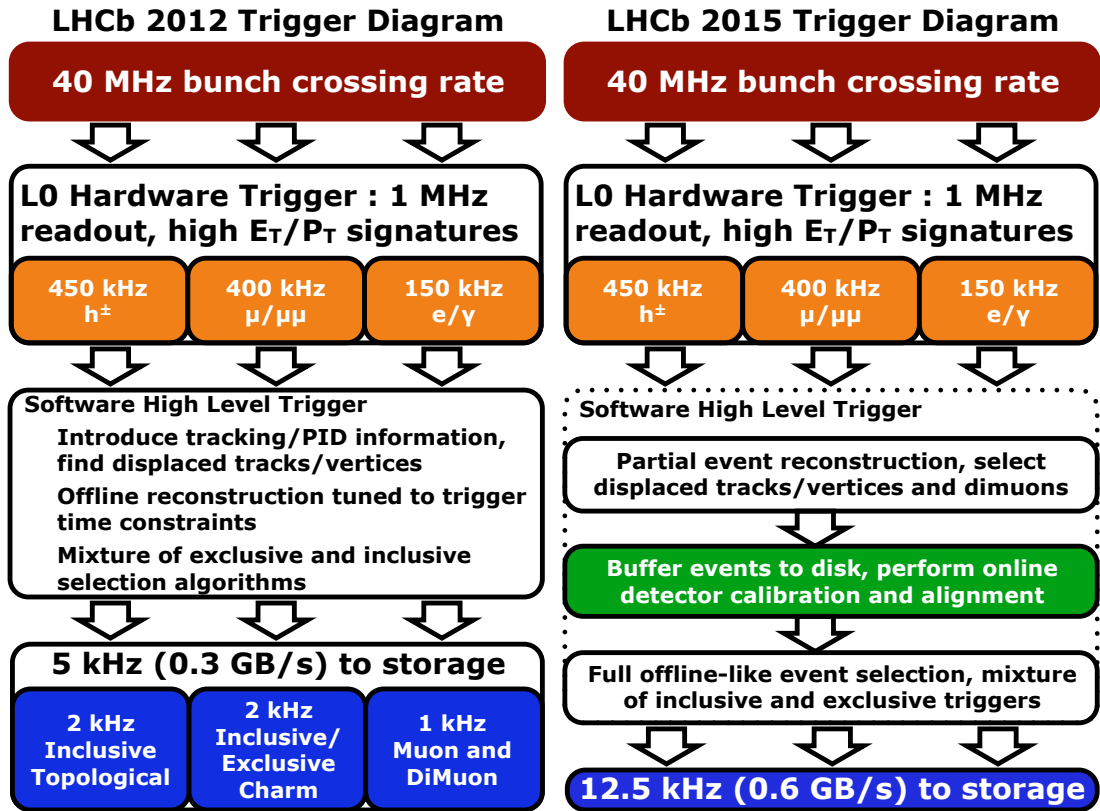
Figure 3.15: The trigger sketch in Run 1 (left), Run 2(right).

rate of signals and to classify the quality of the signal.
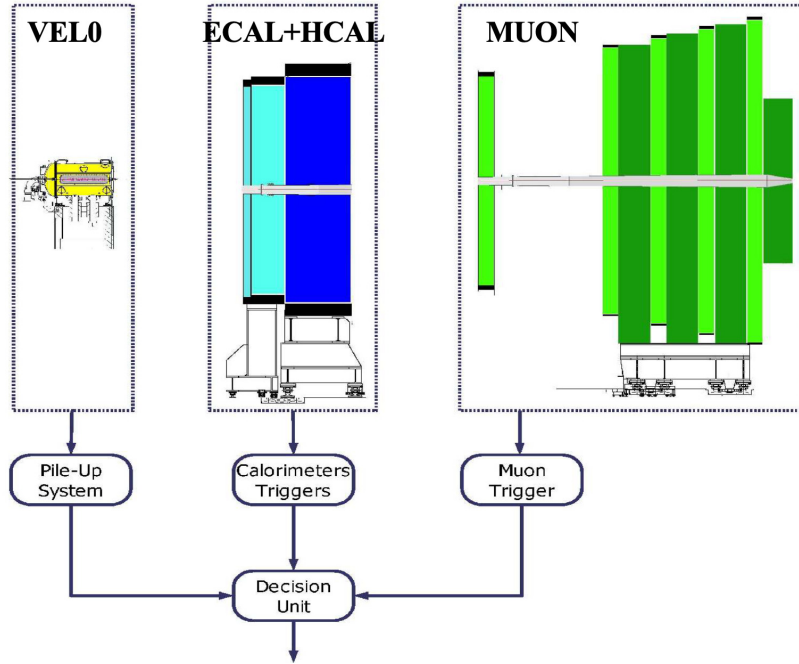
Figure 3.16: Layout of the L0 trigger.

### 3.2.3.2 The high level trigger (HLT)

After the events passing the L0 trigger, the farther selection of the events and the confirmation for the full event reconstruction for the offline analysis given by the software based trigger HLT. The HLT is implemented in C++ executable running on a processor farm which requires significant computing power [98], which holds 16 000 CPU cores. The HLT is responsible to reduce the further event rate within few kHz limit for the storage. It is split in two parts: HLT1 and HLT2.

The first part of the software trigger system is HLT1 which performs a partial event reconstruction and inclusive selections of the signal candidates. It reduces the event selection rate from 1 MHz to 50 kHz. HLT1 triggers uses the informations coming from the VELO and tracking stations. The events selected by the HLT1 pass to the second stage of HLT trigger known as HLT2 which completes full offline reconstruction of the particles with $p_T > 300$ MeV/$c$. The last part of the trigger system is HLT2 which performs full event reconstruction with a set of inclusive and exclusive selections to reduce the output rate of 2 kHz to further process offline reconstruction and analysis.

## 3.2.4 The upgrade Phase I of the LHCb detector

The LHCb detector showed an excellent performance during the years of Run 1 and Run 2 using 9 $fb^{-1}$ pp collison data at center-of-mass energies 7, 8, 13 TeV with its instantenous luminosity of $\mathcal{L} = 4 \times 10^{32} cm^{-2} s^{-1}$. This performance however was in need to be improved in order to reach the crucial studies which are limited in statistically. For

this reason with the major upgrade phase I[∥] between the years of 2019 and 2022 with the aim to collect $50\,\mathrm{fb}^{-1}$ of data by 2028 (Run 3 - Run 4) operate at higher luminosity by a factor 5 with respect to the Run 2, $\mathcal{L} = 2 \times 10^{33} cm^{-2} s^{-1}$. With this upgrade the LHCb detector is entirely changed, particularly all tracking elements of the detector, to operate at 40 MHz bunch crossing rate without the use of hardware trigger [99] and implemented fully software flexible trigger which uses the information from all sub-detectors. In order to maintain, all the front-end electronics of the sub-detectors are replaced and upgraded. In Figure 3.17 LHCb detector after the upgrade of tracking, particle identification and trigger system is shown:
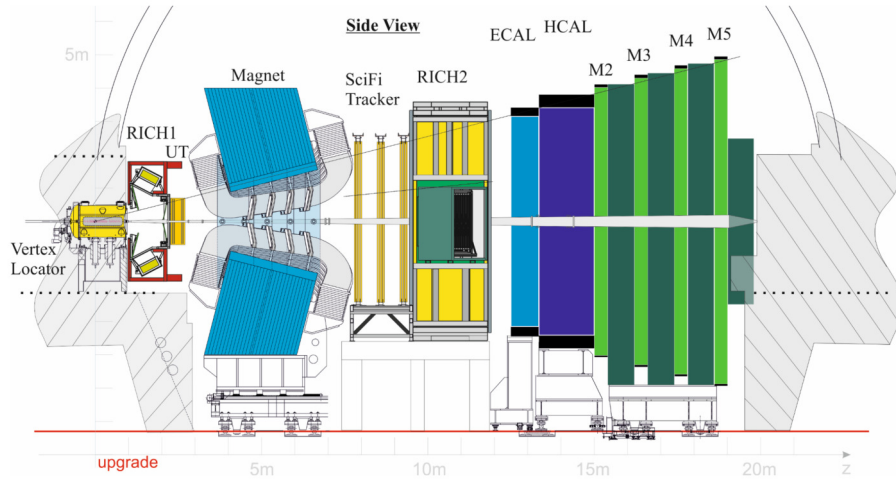


Figure 3.17: Schematic side-view of the LHCb upgrade I detector . Figure is obtained from [99] and [100].

Further sections upgrades for the detector elements are given:

- **Vertex Locator (VELO) upgrade:**

  VELO is replaced with upgraded VELO consists of 26 tracking modules based on hybrid silicon pixel detectors arranged horizontally around the LHC beam line. The new VELO's active area is closer to the beam axis of 5.1 mm contrary to previous distance of 8.4 mm. It consists of pixel-tracking layers which provide improved hit resolution and fast track reconstruction to the software trigger. Figure 3.18 shows the overview of the VELO

- **Upstream Tracker (UT) upgrade:**

---

[∥]Upgrade I is divided into 2 phases: Upgrade Phase Ia and Upgrade Phase Ib. Upgrade Phase Ia is started with the Run3 while Upgrade Phase Ib will start with the Run 4 data taking period.
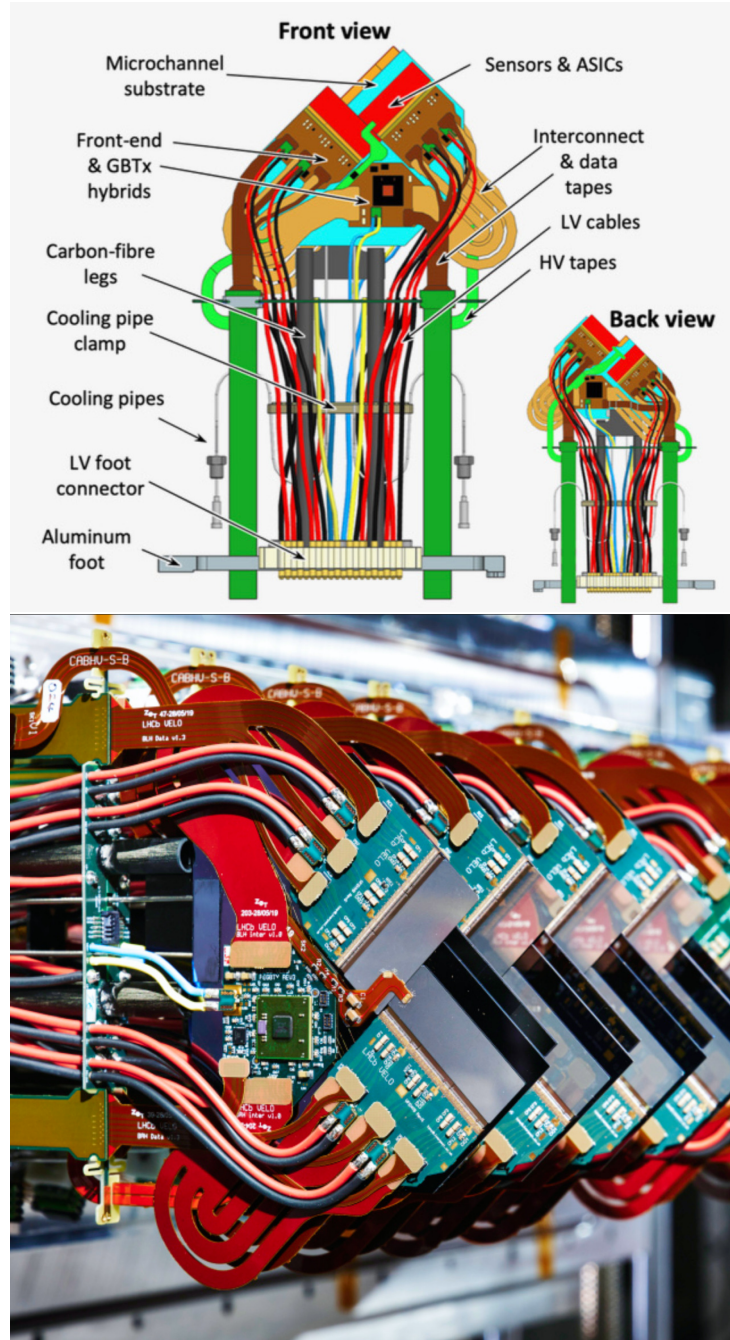
Figure 3.18: Schematic view of the module layout with the hybrid pixel sensors (two on each side) (top) and upgraded LHCb VELO modules (bottom). Figures are taken from [101] and [102].

Previous Tracker Turicensis (TT) is replaced by the new silicon strip (Si-strip) tracking detector Upstream Tracker (UT) which has a finer granularity [100] installed before the magnet, It is composed of four layers (X, U, V, X) of silicon-microstrip

sensors. Each layers are approximately of 2 $m^2$ area with 1000 silicon modules mounted on a C frame with a total of 68 staves which are integrated with CO2 cooling tubes [103]. Sensors are placed on both sides of the staves which are closer to the beam pipe and covers LHCb's larger area compared to the previous TT. The second and third layers are rotated by ±5. In order to cope with the upstream occupancy UT sensors has better acceptance compared to the TT. In Figure 3.19, modules and their establishment in planes and staves are shown with their sensors are readout.
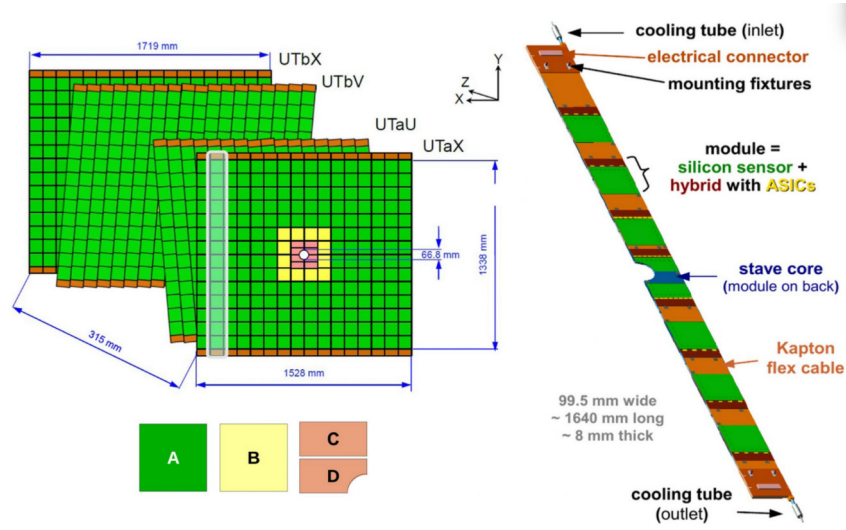


Figure 3.19: Schematic view of the UT modules. The colors in rectangle shapes gives sensor types: A, B,C and D (left). Module and flex arrangement on a stave (right).

- **Scintillating Fibre Tracker (SCiFi) upgrade:**

It is difficult to cope with faster data-taking rate at 40 MHz and higher occupancy due to the increased luminosity with current IT and OT. For that reason, with the upgrade LHCb has chosen a replacement tracker with higher granularity. IT and OT displayed in Figure 3.10 are substituted by a single technology based on scintillating fibre which is known as Scintillating Fibre (SCiFi) tracker which covers the full detector acceptance placed after the magnet [100]. It is downstream from the magnet which consists of three stations (T1, T2, T3) with four detection layers (X-U-V-X, stereo angle $(0°, \pm 5°)$ per station [104]. Each station with the same configuration and make of 11000 km of scintillating optical fibres that emits photons in blue-green wavelength when it interacts with a charged particle passing through a mat. The fibres are of 0.25 mm in diameter and 2.5 m in length which are stacked in six layers with silicon photo-multipliers (SiPM) settled both end (top and bottom) of the each plane. Each detection layer consists of 10 or 12 modules which are composed of 8 fibre mats individually see Figure3.20. In total there are 144 SCiFi modules covering a total area of 360 m$^2$. Photons travelling along the scintillating fibres readout by SiPMs which is 2.5 m away from the beam pipe. The SiPMs are cooled at -40 $°C$ to reduce the expected effects of radiation damage. The readout box (ROB) which holds all the readout electronics, SiPM and the cooling system at the outside of the detector acceptance placed at the top and bottom part of the modules. Figure 3.21 shows the SCiFi tracker. The tracker require spatial precision better than 100 $\mu$m and the single hit efficiency to be larger than 99% [105].
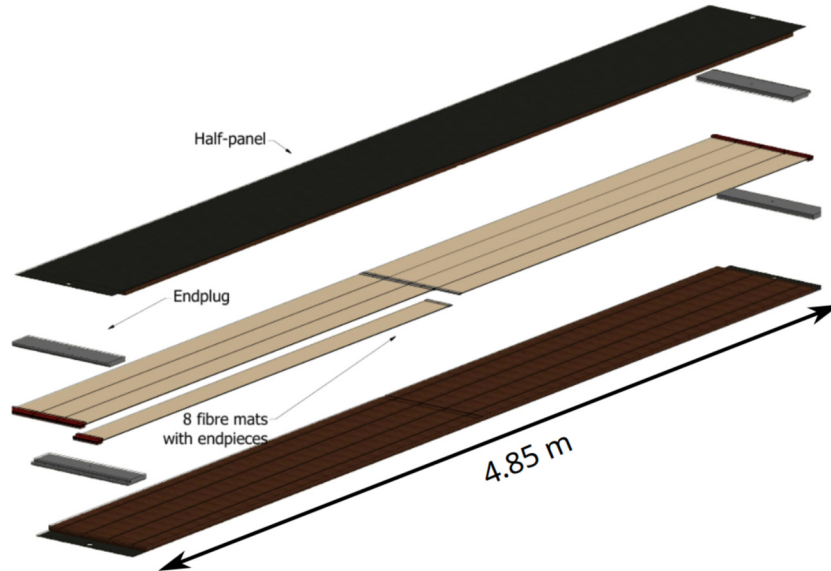


Figure 3.20: Schematic view of a SciFi tracker module. Figure is taken from [104].

- **Ring-imaging Cherenkov (RICH) upgrade:**

49
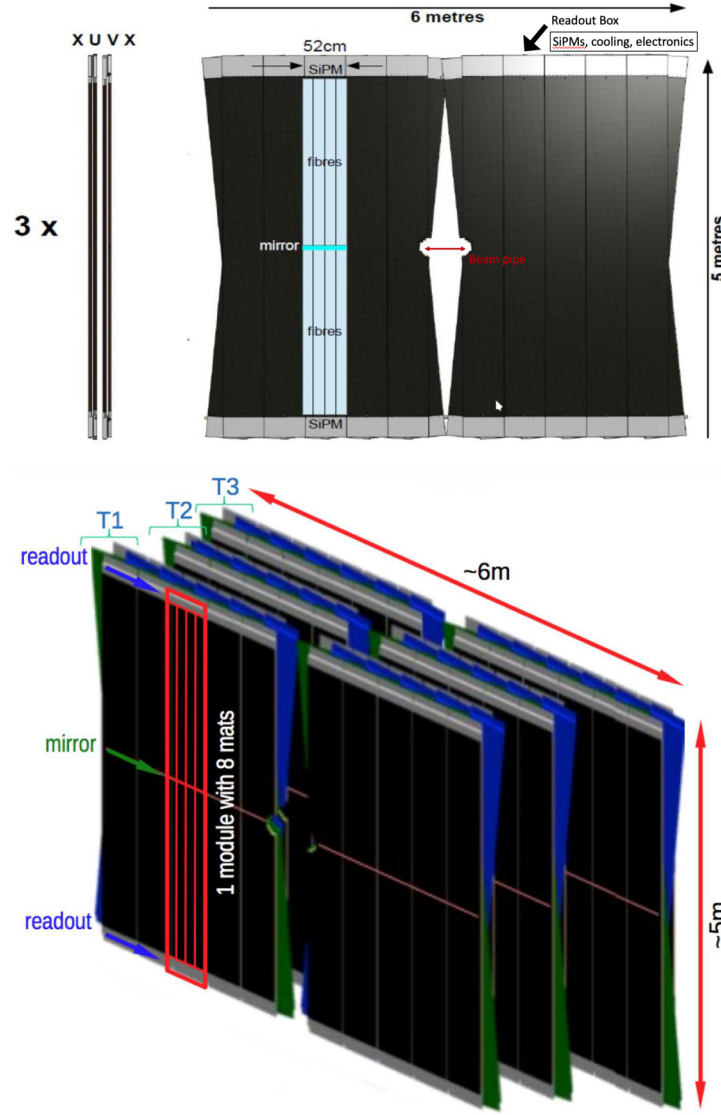
Figure 3.21: (Top) Schematic view of one station SCiFi tracker. It is located upstream of the magnet and downstream of the RICH2 detector. (Bottom) The tracker is composed of 3 stations with 4 layers (X-U-V-X arrangement) which are made of 10 or 12 fibre modules over 6m × 5m detection area. The optical mirrors settled at the inner end of the modules. Figure is taken from [104].

RICH detectors: RICH 1 and RICH 2 are revamped to cope with the increased data taking rate of LHC Run 3 and to maintain better level of particle identification with the increased luminosity of five folded. Excellent performance provided for the particle identification (PID) by LHCb during Run 1 and Run 2. The current

RICH detectors based on Hybrid Photon Detectors(HPDs) is renewed with the installation of new single photon-detectors to read out 40 MHz and optics, mechanics are modified for the upstream RICH1 detector [106].

- **Calorimeters upgrade :**

  The calorimeters (ECAL and HCAL) are mostly kept unchanged during the upgrade and adopted for Run 3. With the removal of L0 hardware trigger, the Preshower (PS) and Scintillating Pad Detector (SPD) before calorimeters has been removed since the informations provided by these systems which are only L0 based. All the electronics of the readout are replaced [107].

- **Muon station M1 :**

  For Run 3, hardware information based muon station M1 has been removed due to the higher occupancy while the rest of the four stations (M2-M5) are retained. All readout electronics of the system is renewed.

- **Trigger upgrade :**

  For Run3 and ahead, the decision is made to maintain with the triggerless system by removing the 1 MHz L0 hardware trigger (advantage of low mass searches). Current detector system will run full software based trigger where pile up sensors readout at 40 MHz [108]. Figure 3.22 shows the trigger scheme of LHCb detector after the upgrade for Run3.

**LHCb Upgrade Trigger Diagram**
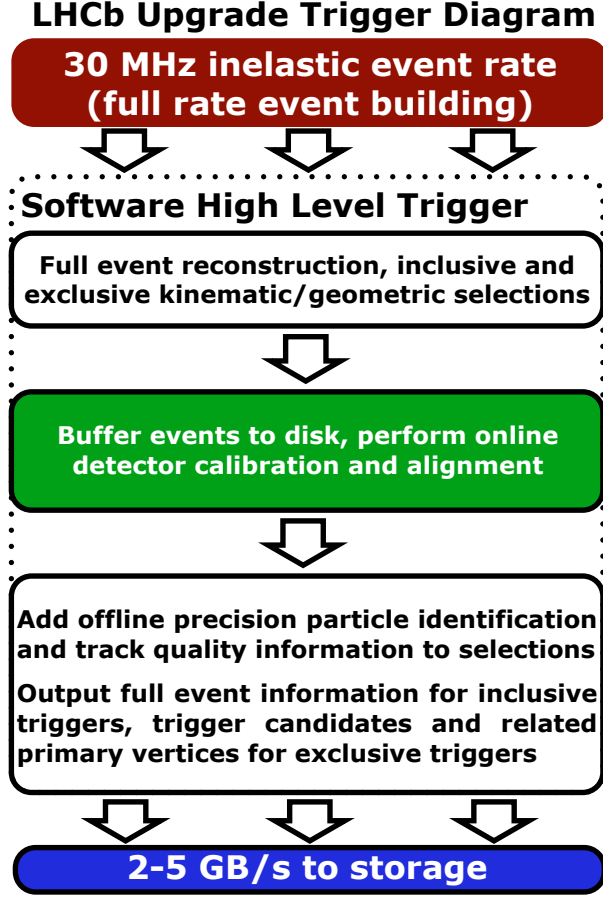


Figure 3.22: The trigger layout of the LHCb upgrade for Run 3.

### 3.2.5 The upgrade phase II of the LHCb detector

The timeline of LHCb detector for the upgrade phase Ib will start with the Run 4 after the LS3. For the phase II upgrade (Run 5 and Run 6) is currently planned to proceed around 2031 and run till 2035, see an overview of data taking periods see in Figure 3.23 [109]. A time scale with the ending of data taking period at the same moment around 2025 [110] is also shown for Belle II detector operate at the energy-asymmetric $e^+e^-$ SuperKEKB accelerator which is a descendant of Belle detector at KEKB. The Belle II is expected to collect 50 $ab^{-1}$ of data [111] by 2025. After LS3 with Run 4 High Luminosity LHC (HL-LHC) term will start up. The LHCb detector will operate at a luminosity of $\mathcal{L} = 2 \times 10^{34} cm^{-2} s^{-1}$ which is ten times more than the one during upgrade phase I. Figure 3.24 gives the instantaneous luminosity and the integrated luminosity for each period [111]. After the phase II upgrade LHCb detector is foreseen to collect a data sample corresponding to a $300 fb^{-1}$ during 3-5 years of run. With the high luminosity upgrade LHCb will reach the opportunities to fully exploit the flavour physics, as well as other physics opportunities in the forward acceptance and leading to the complementary to the improved knowledge

of physics ATLAS and CMS achieved.
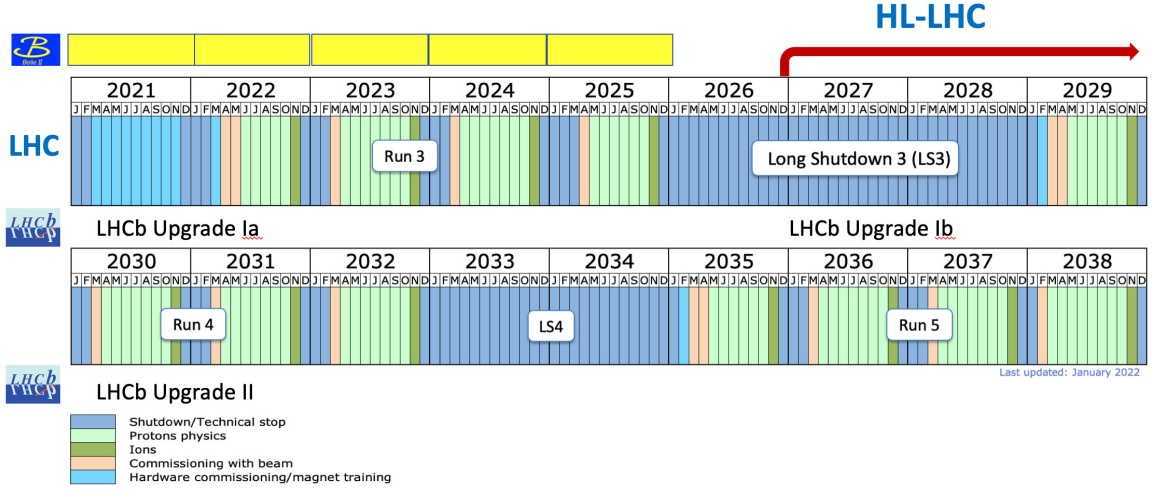


Figure 3.23: A timeline for the LHC operations over the years of 2021-2031. LS3 and LS4 shows the period of Long Shutdown which will take place between 2024-2016 and 2029-2031 respectively. Figure is taken from [109] and [110] and [112].
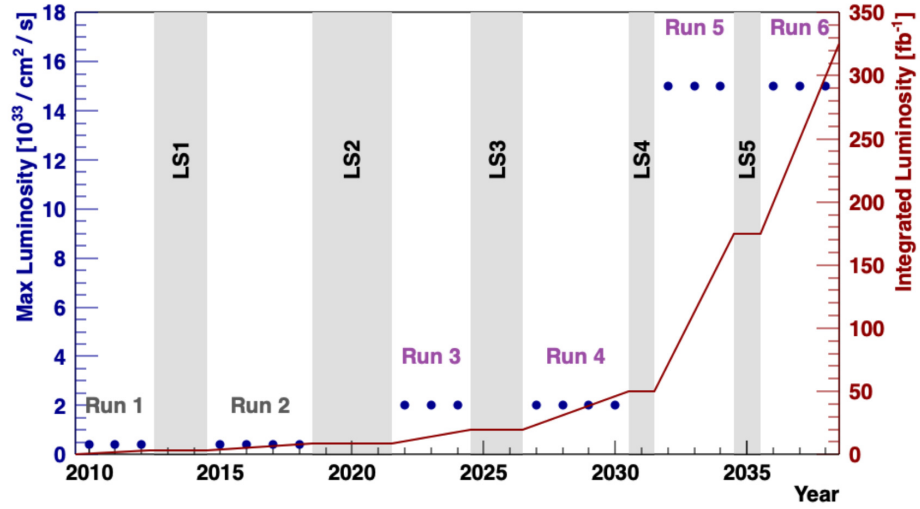


Figure 3.24: Luminosity projections as a function of time for Upgrade Phase I and Phase II of LHCb detector. The integrated luminosity is given with the blue line and the red dots represent the instantaneous luminosity during each period. Figure is taken from [113]

# 4  Analysis of $B_s^0 \to \tilde{D}^{(*)0}\phi$ decays

## 4.1  Motivation

The precise determination of the $\gamma$ angle of the CKM Unitarity Triangle is one of the main goal of the flavour physics. The $B_s^0 \to \tilde{D}^{(*)0}\phi$ decay, where $\tilde{D}^0$ indicates for either a $D^0$ or a $\bar{D}^0$ has been observed by the LHCb experiment [[8], [114]] provides a clear path to measure the $\gamma$ angle precisely. With the earlier sensitivity study [4] on $\gamma$ with the $B_s^0 \to \tilde{D}^{(*)0}\phi$ decay, where $D^0$ decays $KK, \pi\pi, K3\pi, K\pi$ and $K\pi\pi^0$, it has been shown that the precision on $\gamma$ about 8 ° to 9 ° can be achieved with the full dataset Run 1 and Run 2 provided by the LHCb experiment and this precision can be improved with more data. For this analysis we consider the decay of $B_s^0 \to \tilde{D}^{(*)0}\phi$, where $D^0$ decays to $K\pi\pi^0$ sub-decay by using the using full dataset recorded in 2011 and 2012 at a center-of-mass energies of $\sqrt{s}=$ 7 TeV and $\sqrt{s}=$ 8 TeV, respectively, corresponding to an integrated luminosity of $3\,\text{fb}^{-1}$ and $9\,\text{fb}^{-1}$ of data collected during the years between 2015 and 2018 at a center-of-mass energy of $\sqrt{s} = 13$ TeV.

## 4.2  Dataset

### 4.2.1  Data samples

The yields of the decay of $B_s^0 \to \tilde{D}^{(*)0}\phi$ * and $\tilde{D}^0 \to K\pi$ has been measured corresponding to an integrated luminosity of $3\,\text{fb}^{-1}$ of data Run 1 by the LHCb detector. Table 4.1 shows the related cross sections among different center-of-mass energies and corresponding integrated luminosities for different data collected over several years (see [4]).

In this study a sample of neutral-$B$ mesons from $pp$ collisions based on Run 1 and Run 2 Data by the LHCb detector is used. A corresponding integrated luminosity and the stripping $^\dagger$ versions used are given in Table 4.2. The CKM angle $\gamma$ is measured through $B_s^0 \to \tilde{D}^{(*)0}\phi$ decay, where $D$ mesons reconstructed in $K\pi$, $K3\pi$, $K\pi\pi^0$, $KK$ and $\pi\pi$.

---

*Here and the following sections $\tilde{D}^0, D$ indicates $D^0$ and $\bar{D}^0$, unless differently declared

$^\dagger$The first step the data is filtered through the selections called stripping

| Years/Run | $\sqrt{s}$ ( TeV) | int. lum.( fb$^{-1}$) | cross section | equiv. 7 TeV data |
|-----------|-------------------|----------------------|---------------|-------------------|
| 2011 | 7 | 1.1 | $\sigma_{2011} = 38.9$ μb | 1.1 |
| 2012 | 8 | 2.1 | $1.17 \times \sigma_{2011}$ | 2.4 |
| Run 1 | – | 3.2 | – | 3.5 |
| 2015-2018 (Run 2) | 13 | 5.9 | $2.00 \times \sigma_{2011}$ | 11.8 |
| Total | – | 9.1 | – | 15.3 |

Table 4.1: Integrated luminosities and cross-sections of LHCb Run 1 and Run 2 Data. The integrated luminosities come from [4] and cross-sections from [[115], [116]].

| Years/Run | $\sqrt{s}$ ( TeV) | int. lum.( fb$^{-1}$) | Stripping version |
|-----------|-------------------|----------------------|-------------------|
| Run 1 | 7-8 | | |
| 2011 | 7 | 1.1 | 21r1 |
| 2012 | 8 | 2.1 | 21 |
| Run 2 | 13 | | |
| 2015 | | 0.3 | 24r1 |
| 2016 | | 1.6 | 28r1 |
| 2017 | | 1.5 | 29r2 |
| 2018 | | 2.0 | 34 |

Table 4.2: Full dataset corresponding to an integrated luminosity of fb$^{-1}$ and corresponding stripping version used for the analysis of $B_s^0 \to \tilde{D}^{(*)0}\phi$ for each year.

### 4.2.2 Monte Carlo samples

Monte Carlo (MC) simulation are used to model the invariant mass distributions of the signal decay and to determine the selection efficiency. The simulated collision events are used in this work based on MC (2011- 2012) and MC (2015, 2016, 2017, 2018) generated with PYTHIA and SIM09h/k versions only for different years. All MC samples generated with the option DecProdCut which means that all daughters of the decay chain are in the acceptance of the LHCb detector. MC samples (2011-2018) used in the analysis are truth-matched. Table 4.3 shows the number of Monte Carlo simulated samples produced for each decay mode and each year. The decay of $B_s^0$ meson is scalar to two vector particle $S \to VV$. Thus, due to the angular momentum conservation, the HELAMP model is used, which takes the helicity amplitudes as the input of the studied decays for this analysis.

## 4.3 Event preselections

### 4.3.1 Trigger requirements

Trigger selection is made in order to select the signal candidates while rejecting the background, at the detector and data acquisition level trigger exploits quantities characteristic for the signal decay. TriggerTisTos tool classifiers the triggers L0 and HLT as TIS (Trigger

| Decay | Event type | Number of simulated events (year) | | | | | |
|---|---|---|---|---|---|---|---|
| Signal modes | | 2011 | 2012 | 2015 | 2016 | 2017 | 2018 |
| $B_s^0 \to D^0\phi$ | 13164412 | 288941 | 313317 | 571361 | 443811 | 465679 | 107991 |
| $B_s^0 \to D^{*0}((K^-\pi^+\pi^0)\pi^0)\phi$ HELAMP 100 | 13164467 | 33743 | 28066 | 30284 | 27854 | 26436 | 25448 |
| $B_s^0 \to D^{*0}((K^-\pi^+\pi^0)\pi^0)\phi$ HELAMP 010 | 13164468 | 33291 | 28129 | 29229 | 27840 | 26216 | 25887 |
| $B_s^0 \to D^{*0}((K^-\pi^+\pi^0)\gamma)\phi$ HELAMP 100 | 13164664 | 30463 | 26248 | 28022 | 25769 | 27076 | 26082 |
| $B_s^0 \to D^{*0}((K^-\pi^+\pi^0)\gamma)\phi$ HELAMP 010 | 13164665 | 30329 | 26628 | 26962 | 26129 | 27546 | 26311 |

Table 4.3: MC simulated samples used in this analysis, In these samples, all decays with $D^0$ are decaying into Cabibbo-Favoured mode ($\overline{D}^0 \to K^+\pi^-\pi^0$). All samples are generated in detector acceptance (with DecProdCut option). The number contain both MagUp and MagDown. Each line gives the total number of simulated events for each of the year for $B_s^0 \to \bar{D}^0\phi$ and $B_s^0 \to D^{*0}\phi$.

Independent of Signal) or TOS (Trigger On Signal) in the analysis [117] are defined as follows:

- TOS (Trigger On Signal): represent the selected events which are triggered on the signal candidate, independently from the rest of the events.

- TIS (Trigger Independent of Signal): represent the selected events which are triggered independently from the signal candidate.

Events used in this analysis are triggered by the L0_Hadron_TOS or by the L0_Global_TIS L0 trigger.

For the High Level Trigger HLT1 and HLT2, we require this at least one track has fired by the HLT1TrackAllL0_TOS [118]. The HLT2 requirements are this at least one trigger line from the following three has fired [119]:

- HLT2Topo2BodyBBDT_TOS;

- HLT2Topo3BodyBBDT_TOS;

- HLT2Topo4BodyBBDT_TOS;

For events in Run 1 Data, the trigger requirements are:

- L0Hadron_TOS or L0Global_TIS (B_L0HadronDecision_TOS || B_L0Global_TIS).

- Hlt1Track_TOS (B_Hlt1TrackAllL0Decision_TOS).

- Hlt2 2-, 3- or 4-body topological TOS (B_Hlt2Topo2BodyBBDTDecision_TOS || B_Hlt2Topo3BodyBBDTDecision_TOS || B_Hlt2Topo4BodyBBDTDecision_TOS)

The percentage for each trigger line after stripping ($K\pi\pi^0$) for Run 1 are listed in Table 4.4.

For events in Run 2 Data, the trigger requirements are:

- L0Hadron_TOS or L0Global_TIS (B_L0HadronDecision_TOS || B_L0Global_TIS).

| Triggers | Percentage |
|---:|:---|
| L0Hadron_TOS | 52% |
| L0Global_TIS | 65% |
| HLT1TrackAllL0_TOS (L0Hadron_TOS \|\| L0Global_TIS) | 90% |
| HLT2Topo2BodyBBDT_TOS (L0 & Hlt1) | 60% |
| HLT2Topo3BodyBBDT_TOS (L0 & Hlt1) | 72% |
| HLT2Topo4BodyBBDT_TOS (L0 & Hlt1) | 50% |

Table 4.4: Percentage for difference trigger lines obtained after stripping ($K\pi\pi^0$) for MC Run 1

- Hlt1Track_TOS (B_Hlt1TrackMVADecision_TOS \|\| B_Hlt1TwoTrackMVADecision_TOS).

- Hlt2 2-, 3- or 4-body topological TOS (B_Hlt2Topo2BodyDecision_TOS \|\| B_Hlt2Topo3BodyDecision_TOS \|\| B_Hlt2Topo4BodyDecision_TOS)

Note that these stripping lines have HLT2 Topo and inclusive $\phi$ requirements and HLT2 lines requires HLT1 Physics confirmation while HLT1 requires L0 Physics confirmation. It is thus very biased but it can be used for information on where the events come from.The percentage from each line after stripping for Run 2 are listed in Table 4.5.

| Triggers | Percentage |
|---:|:---|
| L0Hadron_TOS | 49% |
| L0Global_TIS | 60% |
| HLT1TrackAllL0_TOS (B_Hlt1TrackMVA_TOS \|\| B_Hlt1TwoTrackMVA_TOS) | 91% |
| HLT2Topo2BodyDecision_TOS (L0 & Hlt1) | 75% |
| HLT2Topo3BodyDecision_TOS (L0 & Hlt1) | 79% |
| HLT2Topo4BodyDecision_TOS (L0 & Hlt1) | 58% |

Table 4.5: Percentage for difference trigger lines obtained after stripping ($K\pi\pi^0$) for MC Run 2.

## 4.3.2 Stripping selections

After the events are reconstructed (HLT2), a first selection is applied to minimise the huge amount of data, this is called as stripping line criteria. The events passing the stripping line `B02D0KKD2Pi0HHResolvedBeauty2CharmLine` are used in order to select decay $B_s^0 \to \tilde{D}^{(*)0}\phi$. The line has been written taking into account the characteristic topologies of $B_s^0 \to \tilde{D}^{(*)0}\phi$ and $\tilde{D}^0 \to K\pi\pi^0$ decay and its kinematics. The analysis uses this line described in section 4.5. The purpose of using this selection to reduce the size of the data-sample (background contamination) without a significant loss of signal after the data registered by the LHCb detector. The selection criteria from this stripping line are summarised in Table 4.6.

| Particle | Quantity | Criteria |
|---|---|---|
| Event | #long tracks | $< 500$ |
| | #PV | $> 0$ |
| | HLT2IncPhi | true |
| | HLT2Topo(2\|\|3\|\|4)Body | true |
| All tracks | Min IP $\chi^2$ | $> 4$ |
| $D^0$ | $\sum p_T$ | $> 1800$ MeV/c |
| | $\delta M(D^0)$ | $< 100$ MeV/c$^2$ |
| | DOCA | $< 0.5$ mm |
| | Vertex: $\chi^2$/nDof | $< 10$ |
| | BPVVDCHI2 | $> 36$ |
| | $\cos(\theta_{dira})$(BPVDIRA) | $> 0$ |
| All $D^0$ daughters | Track: $\chi^2$/nDof | $< 3$ ($< 4$ for Run 2) |
| | $p_T$ | $> 100$ MeV/c |
| | $p$ | $> 1000$ MeV/c |
| At least one $D^0$ daughter | Track: $\chi^2$/nDof | $< 2.5$ ($< 4$ for Run 2) |
| | $p_T$ | $> 500$ MeV/c |
| | $p$ | $> 5000$ MeV/c |
| $X$ | $\sum p_T$ | $> 1000$ MeV/c |
| | Invariant mass ($\pi$ hypothesis)** | $< 5200$ MeV/c$^2$ |
| | DOCA | $< 0.5$ mm |
| | Vertex: $\chi^2$/nDof | $< 16$ |
| | BPVVDCHI2 $\chi^2$ | $> 16$ |
| | $\cos(\theta_{dira})$(BPVDIRA) | $> 0$ |
| All $X$ daughters | Track: $\chi^2$/nDof | $< 3$ ($< 4$ for Run 2) |
| | $p_T$ | $> 100$ MeV/c |
| | $p$ | $> 2000$ MeV/c |
| At least one $X$ daughter | Track: $\chi^2$/nDof | $< 2.5$ ($< 4$ for Run 2) |
| | $p_T$ | $> 500$ MeV/c |
| | $p$ | $> 5000$ MeV/c |
| $\pi^0$ | $\sum p_T$ | $> 1000$ MeV/c |
| | $p$ | $> 1000$ MeV/c |
| | CHILD(CL,1) | $> 0.25$ |
| | CHILD(CL,2) | $> 0.25$ |
| $B^0$ | $\sum p_T$ | $> 5000$ MeV/c |
| | Invariant mass of $D^0$ and $X$ | [4750, 6000] MeV/c$^2$ |
| | Vertex: $\chi^2$/nDof | $< 10$ |
| | $\tau$ | $> 0.2$ ps |
| | BPVIPCHI2 | $< 25$ ($< 9$ for Run 2) |
| | $\cos(\theta_{dira})$(BPVDIRA) | $> 0.999$ ($> 0.99995$ for Run 2) |
| | BBDT | $> 0.05$ |
| One daughter | Track: $\chi^2$/nDof | $< 2.5$ ($< 4$ for Run 2) |
| | $p_T$ | $> 1700$ MeV/c |
| | $p$ | $> 10000$ MeV/c |
| | Min IP$\chi^2$ | $> 16$ |
| | MIPDV | $> 0.1$ mm |
| More than one daughter | Track: $\chi^2$/nDof | $< 2.5$ ($< 4$ for Run 2) |
| | $p_T$ | $> 500$ MeV/c |
| | $p$ | $> 5000$ MeV/c |

Table 4.6: Stripping selections used for the stripping line `B02D0KKD2Pi0HHResolvedBeauty2CharmLine`, `B02D0KKD2HHBeauty2CharmLine` and `B02D0KKD2KPiPiPiBeauty2CharmLine(B02D0KKD2HHHHBeauty2CharmLine)` for both Run 1 and Run 2. BPVVDCHI2 means $\chi^2$ of the distance from PV, BPVIPCHI2 means $\chi^2$ (significance) of the Impact Parameter with PV, MIPDV means Minimal distance to PV. DOCA gives the distance of the closest approach of the two tracks having less than 0.5 mm. For the criteria noted with **, for $B_s^0 \to D\phi$ mode under the $\pi$ hypothesis. X means $B^0 \to \overline{D}^0[\to K^-\pi^+, \pi^+\pi^-, K^+K^-, K^-\pi^+\pi^0, K^-\pi^+\pi^+\pi^-]X[\to H^+H^-]$. The CHILD(CL,1) and CHILD(CL,2) are the confidence level identification variable for the photons from the $\pi^0$ decays. The cosine of the DIRection Angle $\theta_{dira}$ of the candidates means the angle between the $B$ candidate momentum and the direction defined by the Primary Vertex (PV) of the candidate $B$.

## 4.4 Selections for the decay $B_s^0 \to \tilde{D}^{(*)0}\phi$

The stripping selections are applied, following the trigger requirements. As what has been done in [120], and in order to improve the signal to combinatorial background ratio, the stripping selections are tightened displayed in Table 4.6. These initial selections are mainly based on kinematics and topological variables. The discriminating variables used for $B_s^0 \to \tilde{D}^{(*)0}\phi$ signal are the same with the ones used for the measurements of the branching ratio of $B_s^0 \to \tilde{D}^0 K^+ K^-$ as studied and were optimised using the $B^0 \to \tilde{D}^0 \pi^+ \pi^-$ detailed in [9]. In this case we don't use these variables to optimise the branching ratio of $B_s^0 \to \tilde{D}^0 K^+ K^-$, but to optimize the $B_s^0 \to \tilde{D}^{(*)0}\phi$ signal. Then it is necessary to be ensure that these selections are convenient for the $B_s^0 \to \tilde{D}^{(*)0}\phi$ decay. Thus all the selection cuts which has been previously used in the analysis [9] are revisited one by one for this analysis. Further in order to increase the signal over background separation, these selections will be optimised and improved by using multivariate analysis with all the variables to obtain most abundant signal. These studies will be detailed and presented in the next sections. We have five sub-decay modes for the $\tilde{D}^0$ ($K3\pi$, $K\pi$, $K\pi\pi^0$, $KK$, $\pi\pi$) which have been studied and produced for the $\gamma$ sensitivity introduced in [4]. The similar selections are applied to the each sub-decay modes used in the analysis. As shown in the recent $\gamma$ sensitivity study [4], when extracting the angle $\gamma$, we rely on the ratio of the selection efficiencies which is normalized to the most copious mode $\tilde{D}^0 \to K\pi$. This is explained in the supporting document for the branching ratio measurement of $B_s^0 \to \overline{D}^{(*)0}\phi$ decay [121], among these sub-decay modes, the most challenging one is $\tilde{D}^0 \to K^-\pi^+\pi^0$ where the $D^0$ candidates reconstructed in $K^-\pi^+\pi^0$ by the combination of two tracks and photons reconstructed in $\pi^0$. It's a known problem at LHC that operating with $\pi^0$ causes additional constraints than for final states purely made of charged tracks, because of the large combinatorial background emerging from pp collisions as the $\pi^0$ roughly constitute half of the produced particles see [122].

### 4.4.1 Signal box and sidebands

The first strategy is to define which events will be used for the $B_s^0 \to D\phi$ analysis. The final states where the invariant masses are in a certain neighbourhood of the $B_s^0$ invariant mass belong to the signal region; others belong to the so-called sidebands. Here we use signal sample correspond to truth-matched MC events in the Signal Box (SB), while the background is modelled by data candidates localised in upper mass sidebands, in the vicinity of the SB. Here the sidebands are defined for the various considered mesons: $\phi$, $D^0$, $B_s^0$. A Gaussian fit is performed to obtain the masses of the signal shape in the MC sample see the example Figures 4.1 and 4.3 for $B_s^0$ and $\phi$ respectively and in order to extract their resolutions, a double-sided (DSCB) Crystal-Ball function is used for the signal model shown in Figure 4.2. The definition of a single Crystal-Ball function is defined as [[123], [124], [125]] the signal models of the $B_s^0$, $\tilde{D}^0$ and $\pi^0$ mass fit by the Probability Density Function (PDF) superimposition of the double-sided Crystall-Ball function with parameters determined from simulation. We define the SB, as regions where $\phi$, $D^0$, $B_s^0$

candidates are reconstructed within $\pm 2.5\ \sigma$ resolution of their reconstructed mass. For the background, the sideband of the $D^0$ that is all the events are at least $5\sigma$ away from the mean value of the mass of the reconstructed $D^0$ candidates within the limit $[5, 10]\sigma$ as seen in Figure 4.4 where we define SB and sideband zone for the analysis.
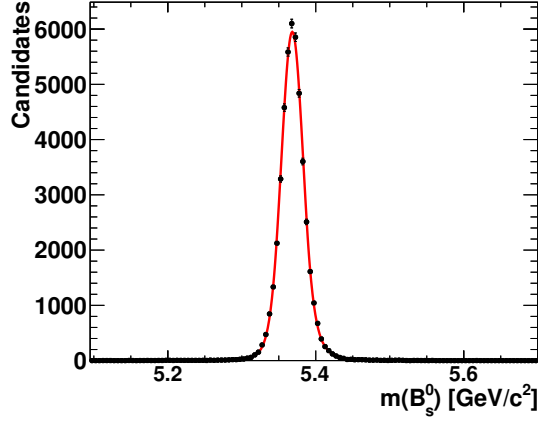


Figure 4.1: Example of reconstructed $B_s^0$ mass in the Run 2 (2015-2018) stripped dataset.

The masses and the resolutions of the reconstructed $\pi^0$, $\tilde{D}^0$ and $\pi^0$ mesons in MC Run 2 are displayed in Table 4.8. And the equivalent for MC Run 1 is given in Table 4.7.

| Particle | PDG [18] | fit. mean ($\mu$) [MeV/$c^2$] | fit. resol. ($\sigma$) [MeV/$c^2$] |
|----------|----------|-------------------------------|-------------------------------------|
| $B_s^0$ | 5366.88±0.14 | 5368.3±0.10 | 15.25±0.10 |
| $D^0$ | 1864.83±0.05 | 1865.1±0.02 | 17.01±0.02 |
| $\pi^0$ | 134.976±0.0005 | 134.90±0.10 | 8.6±0.1 |

Table 4.7: PDG and the reconstructed masses of the $B_s^0$, $\tilde{D}^0$, $\pi^0$ particles for MC Run 1.

| Particle | PDG [18] | fit. mean ($\mu$) [MeV/$c^2$] | fit. resol. ($\sigma$) [MeV/$c^2$] |
|----------|----------|-------------------------------|-------------------------------------|
| $B_s^0$ | 5366.88±0.14 | 5368.30±0.07 | 14.99±0.07 |
| $D^0$ | 1864.83±0.05 | 1865.1±0.3 | 17.4±0.5 |
| $\pi^0$ | 134.976±0.0005 | 135.07±0.06 | 8.44±0.06 |

Table 4.8: PDG [[18]] and the reconstructed masses of the $B_s^0$, $\tilde{D}^0$, $\pi^0$ particles for MC Run 2.

For the $\phi$ resonance, its natural width $\gamma$ is not negligible. $\phi$ is reconstructed in two oppositely charged kaons and its mass is sufficiently large, such that as opposed to $B_s^0$, $\tilde{D}^0$ and $\pi^0$, already after stripping selections a very clear signal can be observed with a
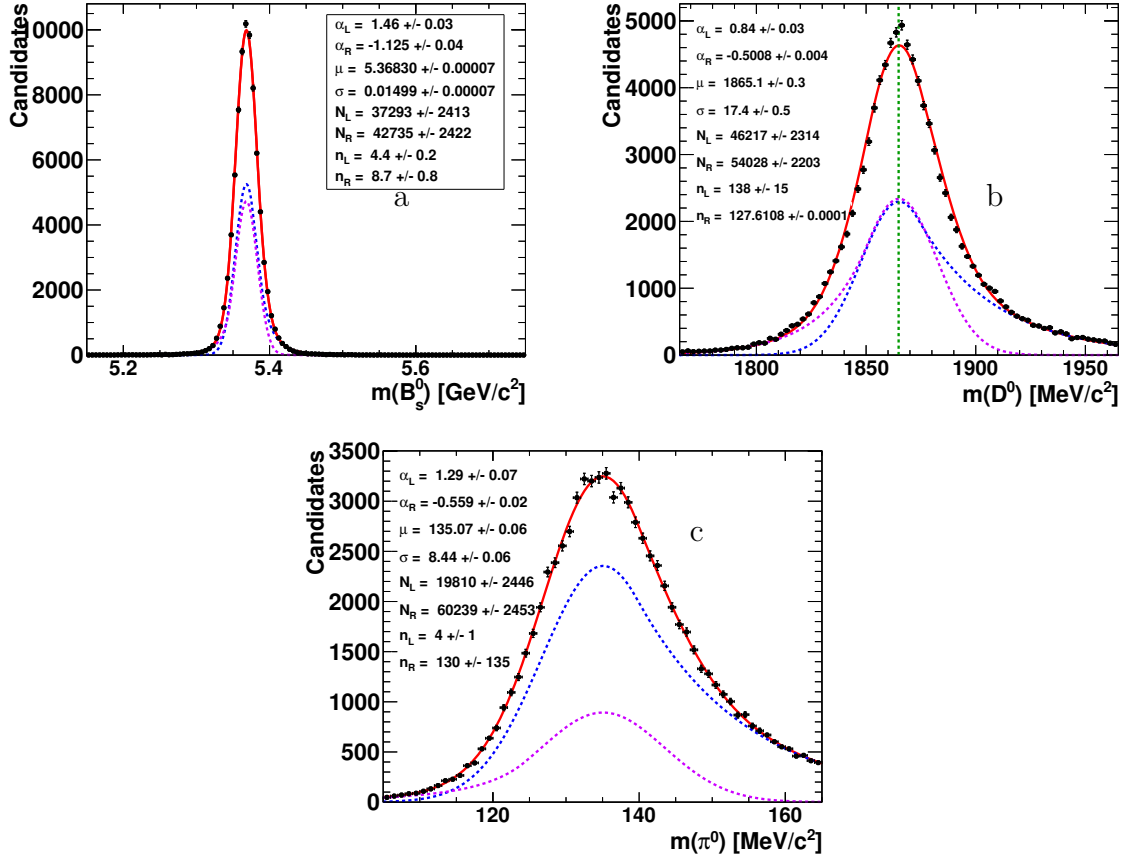
Figure 4.2: Reconstructed mass for $B_s^0$ (a), $\tilde{D}^0$ (b), $\pi^0$ (c) for MC Run 2 simulated $B_s^0 \to D^0(K^-\pi^+\pi^0)\phi$ events. The various distributions are fitted with double-sided Crystall Ball function to account for left and right possible tails.

very quite good signal to background ratio, see Figure 4.3. The natural width of the $\phi$ resonance is $(4.249 \pm 0.013)$ MeV [PDG] [18], so it can't be neglected with respect to (wrt) the resolution of its reconstructed mass. It can be clearly seen the signal peak of the $\phi$ resonance at $(1019.461 \pm 0.016)\,\mathrm{MeV}/c^2$ in the Figure 4.3.

At the phase space limit Figure 4.3, one can see a clear peak, which is probably due to occurrences of misidentified in $f0(980)$ and $a0(980)$ to $KK$ or $\pi\pi$. In the early stage, concept of the sideband for the $K^+K^-$ is not accounted for till the very end of the selections and then we will fit to the $\phi$ invariant mass in this spectrum using the *sPlot* technique [126].

In the next Section 4.4.2, the selections which are specific to $\tilde{D}^0 \to K^-\pi^+\pi^0$ sub-decay mode of our interest will be described and then Section 4.5 the pre-selections on the $B_s^0 \to D^0\phi$ and the discriminators based on TMVA for $\tilde{D}^0 \to K^-\pi^+\pi^0$ will be detailed.
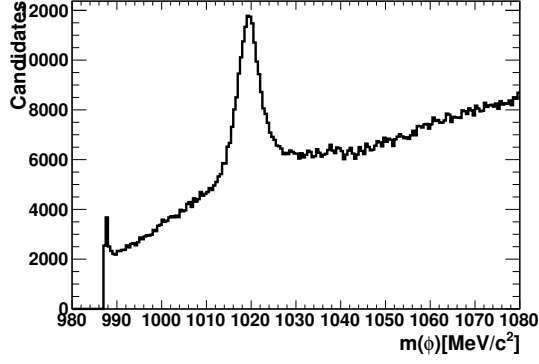
Figure 4.3: Example of reconstructed $\phi$ mass in the Run 2 (2015-2018) stripped dataset.
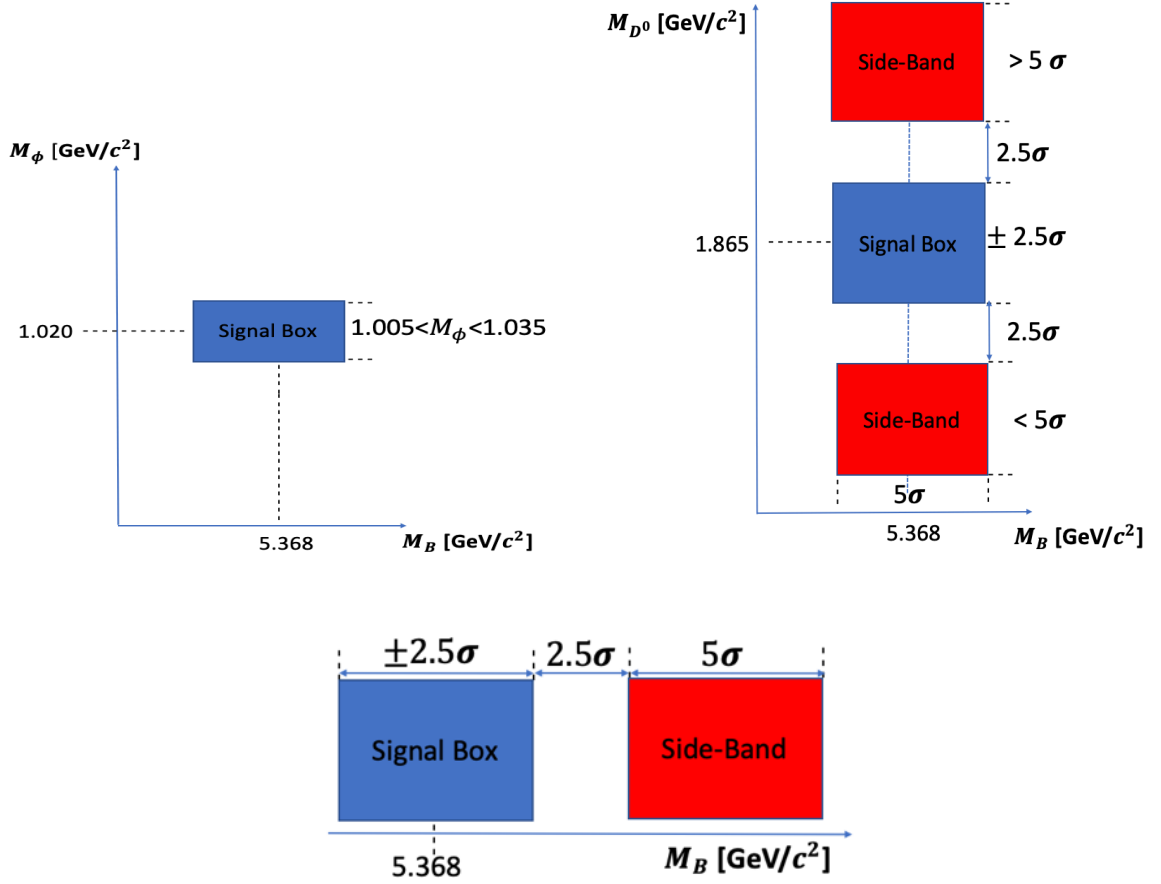


Figure 4.4: Side Band (red) and SB (blue) for $\phi$ (left), $D^0$(right) and $B_s^0$ (bottom) particles.

## 4.4.2   Specific selections for $\tilde{D}^0 \to K^-\pi^+\pi^0$

Specific selections have to be applied for the sub-decay mode $\tilde{D}^0 \to K^-\pi^+\pi^0$ in which we are dealing with neutral $\pi^0$. Neutral three-body decay of $\tilde{D}^0$ meson which lead to the

$K^-\pi^+\pi^0$ has a limited efficiency since the $\pi^0$ has to be reconstructed in reconstructed $B$ decays. The $\pi^0$ can be identified by a decay of two photons with a branching ratio is $(98.823 \pm 0.034\%)$ and detected by the Electromagnetic Calorimeter (ECAL). In the ECAL, the signature of the $\pi^0$ depends on its kinematics. The separation between two photons coming from the decay of $\pi^0$ depends on the momentum of it. The higher is the momentum of the $\pi^0$, the smaller the size of the opening angle of the photon pair (*i.e.*: $\theta_\gamma m \simeq 2m_{\pi^0}/E_{\pi^0}$), thus smaller the distance of the photons' clusters in the ECAL see [127] and [128]. Neutral pions are then reconstructed from these two photons produce two separated clusters called as "**resolved**" $\pi^0$ or share a single cluster in which their individuality are not clearly distinguishable and this is called as "**merged**" $\pi^0$ see [72]. In the case of resolved $\pi^0$, two photons are reconstructed independently to be in the range $[105, 165]\,\mathrm{MeV}/c^2$ and combined them together to build $\pi^0$. The rest of the information for the photon and neutral pion reconstruction can be found in [129]. From this reconstruction point of view, it can be understood that resolved $\pi^0$ provides more precise reconstruction with a better mass resolution of the reconstructed particles than the merged one. Because of the kinematics of the decay we take resolved $\pi^0$ and in this case the goodness of presented signal is that $\pi^0$ is produced in cascade and the momentum of the $\pi^0$ is not too large, means that high momentum $\pi^0$ is more probable to be merged than resolved. Figure 4.5 displays the $p_T$ spectrum for the truth-matched $\pi^0$ produced in the decays $B_s^0 \to \tilde{D}^0(K^-\pi^+\pi^0)\phi$. One can clearly see that $p_T$ is mostly well below $10\,\mathrm{GeV}/c$, therefore only resolved $\pi^0$ are considered for this study in what follows.
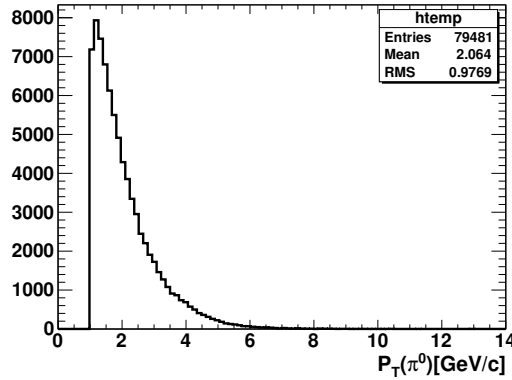


Figure 4.5: Transverse momentum distribution for resolved $\pi^0$ particles from $\tilde{D}^0 \to K^-\pi^+\pi^0$ for MC signal (MC Run 2).

Table 4.6 which shows the stripping selections of $\tilde{D}^0 \to K^-\pi^+\pi^0$, one can see that in the case of resolved $\pi^0$, a minimal $\gamma$ CL cut is imposed for two photons.

Repeating ourself, we are firstly in charge of understanding the effect of sub-decay $\tilde{D}^0 \to K^-\pi^+\pi^0$. The actual problem with the $K^-\pi^+\pi^0$ is the combinatorial background of genuine false $\pi^0$ produced at LHCb. To be able to fight against the combinatorial background forming false $\tilde{D}^0 \to K^-\pi^+\pi^0$ and to reduce the level of false $\pi^0$ as much as possible, we choose specific selections which strategy is actually to deal with the specific

skin of $\pi^0$. The selection cuts that we use for the $\tilde{D}^0 \rightarrow K^-\pi^+\pi^0$ in $B_s^0 \rightarrow D^0\phi$ decays, are based on the discriminating observables: (see TMVA outputs 4.12)

- **gamAsmy:** represents the asymmetry between the transverse energy of the two photons of the $\pi^0$ candidate. The energy asymmetry is defined as

$$\gamma_{asym} = \frac{|E_{\gamma^1}^T - E_{\gamma^2}^T|}{E_{\gamma^1}^T + E_{\gamma^2}^T} \tag{4.1}$$

where $E_{\gamma^1}^T$ and $E_{\gamma^2}^T$ are the transverse energies of the decay photons. For a genuine $\pi^0$ (pseudo scalar mesons decaying to two similar vector bosons) this quantity is expected to be mostly null with a small dispersion as the momentum of two photons should be similar in the $\pi^0$ decay. Fake $\pi^0$ should be mostly uniformed in the range $[0, 1]$.

- **gamisNotETot:** is the probability of the two $\gamma$ of not being an electron see [128].

$$gamisNotETot = gamisNotE_{\gamma^1} \times gamisNotE_{\gamma^2} \tag{4.2}$$

- **gamisNotHTot:** represents the probability of the two $\gamma$ of not being a hadron defines as

$$gamisNotHTot = gamisNotH_{\gamma^1} \times gamisNotH_{\gamma^2} \tag{4.3}$$

isNotE and isNotH are two identification quantities: gamisNotH is an identification of the photons compared to electrons and hadrons based on the shape and quantities of the energies left in the SPD, PS (Preshower), electromagnetic and hadronic calorimeters see [[127] and [130]]. The PID response of LHCb detector to be independent for each of the two photons (*i.e.* "resolved" $\pi^0$), that is the reason why we use their products in the above definition. This definition allows to treat as a combined probability for the $\pi^0$ to be made of two photon candidates that simultaneously are neither electrons nor hadrons.

These two discriminating variables: isNotE and isNotH are formed as follow in [131]) (see Slide 7) and $e^{\pm}$, $\gamma$, $\pi^0$ is identified with information combined (with multivariate tools) from calorimeter sub-detectors:

- Scintillating Pad Detector (SPD)

- Preshower (PS)

- Electromagnetic Calorimeter (ECAL)

– Hadronic Calorimeter (HCAL)

and calibrated with calibration samples [131] (explained in Slide 16) Three different Neural Networks are trained with simulation to separate photon signatures from other species

- photons vs. hadrons (*i.e.* pions, kaons, protons,...): IsNotH

- photons vs.(electrons and positrons): IsNotE where for the training and testing of the MVA

- Signal: Reconstructed photon candidates matching the generated photons $(B \to K^* \gamma)$

- Background: electrons: Reconstructed photons matching generated electrons $(B \to K^* ee$ sample)

- Non-electromagnetic: Reconstructed photon matching non-electromagnetic particles.

It should be noticed in EM calorimetry the calorimetry gamma, the energy longitudinal distribution varies as ln(E), both for electrons and photons (see in [132]).

- **gamEtMoy:** is the mean of the transverse energy of the two photons of the $\pi^0$ candidate. This variable is purely related to the kinematics of the $\pi^0$ in the decay $B_s^0 \to D^0[K^- \pi^+ \pi^0]\phi$ see Figure 4.5

$$\gamma_{E_{Moy}^T} = \frac{E_{\gamma^1}^T + E_{\gamma^2}^T}{2} \tag{4.4}$$

- **Log (Dalitz Weight)**

Among these discriminating variables, the first four variables that we mention above as selections for the $\pi^0$ to describe the kinematics which shows the asymmetry and the particle identification (PID) variables for photons. And the last variable is a unique one named Dalitz Weight, which is quite complicated and special variable coming from a particular Dalitz plot structure of $D^0 \to K^- \pi^+ \pi^0$ decay [18]. This is related to the phenomenology of the decay $D^0 \to K^- \pi^+ \pi^0$ and it is described in detail in next sections. The decay proceeds in majority through the decays of $K^- \rho^+$, $K^*(892)^- \pi^+$, $\overline{K}^*(892)^0 \pi^0$, for which the sum of partial decay width is $(15.6 \pm 0.8)\%$, which is saturating the total fraction $(14.4 \pm 0.5)\%$. Branching ratios for these channels are given in the Table 4.9.

| Mode | Ratio ($\Gamma_i/\Gamma$) |
|---|---|
| $K^-\pi^+\pi^0$ | $(14.4 \pm 0.5)\%$ |
| $K^-\rho^+$ | $(11.2 \pm 0.7)\%$ |
| $K^-\rho(1700)^+$, $\rho^+ \to \pi^+\pi^0$ | $(8.2 \pm 1.8) \times 10^{-3}$ |
| $K^*(892)^-\pi^+$, $K^*(892)^- \to K^-\pi^0$ | $(2.31^{+0.40}_{-0.20})\%$ |
| $\overline{K}^*(892)^0\pi^0$, $\overline{K}^*(892)^0 \to K^-\pi^+$ | $(1.95 \pm 0.24)\%$ |
| $K_0^*(1430)^-\pi^+$, $K_0^{*-} \to K^-\pi^0$ | $(4.8 \pm 2.2) \times 10^{-3}$ |
| $\overline{K}_0^*(1430)^0\pi^0$, $\overline{K}_0^{*0} \to K^-\pi^+$ | $(5.9^{+5.0}_{-1.6}) \times 10^{-3}$ |
| $K^*(1680)^-\pi^+$, $K^{*-} \to K^-\pi^0$ | $(1.9 \pm 0.7) \times 10^{-3}$ |
| $K^-\pi^+\pi^0$ nonresonant | $(1.15^{+0.60}_{-0.20})\%$ |

Table 4.9: Branching ratios measured for the decay of $D^0 \to K^-\pi^+\pi^0$ [18].

## 4.4.3 Dalitz plot formalism of the decay $D^0 \to K^-\pi^+\pi^0$ and computation of the Dalitz Weight (DW)

The Dalitz plot technique is a visual representation of the phase space of a multi body decay involving the parent particle is a spin 0 but the daughter in the multibody decay are spin 0, 1, 2, 3... [133]. It is particulary important to study three-body decays of the heavy-flavoured $D$ and $B$ mesons. It describes the phase-space of the multi-body decay in terms of the three possible two-body invariant mass-squared combinations according to one another. The limits of the plot are, where $M$ is the mass with four-momentum "p" of the original particle and that decays into three final state particles $i$, $j$, $k$: $1, 2, 3$ ($m_1$, $m_2$, $m_3$) can be written with corresponding four-momentum $p_1$, $p_2$, $p_3$.

Using as independent variables, the Eq. 4.5 shows that defining the invariant mass squared of a pair of particles as $p_{ij} = p_i + p_j$ and $m_{ij}^2 = p_{ij}^2$

$$M^2 + m_1^2 + m_2^2 + m_3^2 = m_{12}^2 + m_{13}^2 + m_{23}^2 \tag{4.5}$$

and $m_{12}^2 = (p_1 + p_2)^2 = (p_M - p_3)^2 = M^2 + m_3^2 + 2ME_3$ where $E_i$ stands for the energy of the $i^{th}$ particle in the rest frame of M.

The square of the invariant masses define the boundaries on the axes of the plot (Energy and the momentum is conserved). The extrema (maximal and minimal masses) of this relation within the physical region are given in each invariant axis as Eq. 4.6

$$(m_i + m_j)^2 \leq m_{ij}^2 \leq (M - m_k)^2 \tag{4.6}$$

The partial decay width of the three-body decays of the spin zero particle to a final state 123 (pseudo-scalar final states) is expressed by Eq. 4.7 and Eq. 4.8

$$d\Gamma \propto |M|^2 dm_{12}^2 dm_{13}^2 \tag{4.7}$$

66

$$d\Gamma = \frac{1}{(2\pi)^3 32 M^3} |M|^2 dm_{12}^2 dm_{13}^2 \tag{4.8}$$

where $m_{12} = m_{K^-\pi^0}$ and $m_{23} = m_{K^-\pi^+}$ is the invariant mass of two particle combination(daughter particles) and $M = M_{D^0}$ is the origin particle (parent particle) and $|M|^2$ is the invariant amplitude.

In our case, $D^0 \to K^-\pi^+\pi^0$ decay which involves a spin zero $D^0$ meson into three spin zero particle $1,2,3 = K^-$, $\pi^+$ and $\pi^0$ . Possible pairs of final state particles for the decay are represented in terms of the invariants: $M_{D^0}^2$, $m_{K^-\pi^0}^2$, $m_{K^-\pi^+}^2$, $m_{\pi^+\pi^0}^2$. From the kinematics we defined above Eq. 4.5 we obtain:

$$m_{K^-\pi^+}^2 + m_{K^-\pi^0}^2 + m_{\pi^+\pi^0}^2 = m_{K^-}^2 + m_{\pi^0}^2 + m_{\pi^+}^2 + M_{D^0}^2$$
$$m_{K^-\pi^+}^2 + m_{K^-\pi^0}^2 < m_{K^-}^2 + m_{\pi^0}^2 + m_{\pi^+}^2 + M_{D^0}^2$$

From the mass values given by the PDG [18] we obtain the mass limits for the boundaries of the Dalitz plot:

$$\begin{cases} m_{K^-\pi^+}^2 \geq (m_{K^-} + m_{\pi^+})^2 \to m_{K^-\pi^+}^2 \geq 0.401 \, \text{GeV}/c^2 \\ m_{K^-\pi^0}^2 \geq (m_{K^-} + m_{\pi^0})^2 \to m_{K^-\pi^+}^2 \geq 0.395 \, \text{GeV}/c^2 \end{cases}$$

and

$$\begin{cases} m_{K^-\pi^+}^2 \leq (m_{D^0} - m_{\pi^0})^2 \to m_{K^-\pi^+}^2 \leq 2.98 \, \text{GeV}/c^2 \\ m_{K^-\pi^0}^2 \leq (m_{D^0} - m_{\pi^+})^2 \to m_{K^-\pi^+}^2 \leq 2.99 \, \text{GeV}/c^2 \end{cases}$$

In the rest frame of the $M_{D^0}$, for a given value of the $m_{K^-\pi^+}^2$ mass, we can write the range as a function of kinematic boundaries $m_{K^-\pi^0}^2$ as in Eq 4.9 and Eq 4.10

$$(m_{K^-\pi^0}^2)_{max} = (E_{K^-} + E_{\pi^0})^2 - \left(\sqrt{E_{K^-}^2 - m_{K^-}^2} - \sqrt{E_{\pi^0}^2 - m_{\pi^0}^2}\right)^2 \tag{4.9}$$

$$(m_{K^-\pi^0}^2)_{min} = (E_{K^-} + E_{\pi^0})^2 - \left(\sqrt{E_{K^-}^2 - m_{K^-}^2} + \sqrt{E_{\pi^0}^2 - m_{\pi^0}^2}\right)^2 \tag{4.10}$$

where E is the energy of the particles $K^-$ and $\pi^0$, here $E_{K^-} = (m_{K^-\pi^0}^2 - m_{K^-}^2 + m_{\pi^0}^2)/2m_{K^-\pi^0}$ and $E_{\pi^0} = (M^2 - m_{K^-\pi^0}^2 - m_{\pi^0}^2)/2m_{K^-\pi^0}$. Figure 4.6 shows these boundaries of the phase space has taken the same form used in the Dalitz plot provided by the Particle Data Group [18].

From Eq. 4.8 if the squared invariant amplitude $|M|^2$ is constant, the observed phase space of the plot would be uniformed. Non-constant amplitude allows the non-uniformity which gives the information about physics dynamics in the plot.
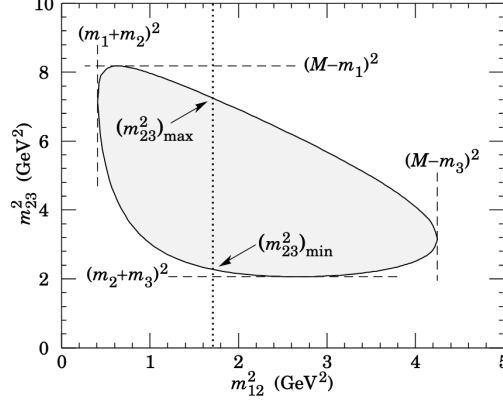
Figure 4.6: Dalitz plane kinematic phase space limits, the masses $m_{1,2,3}$ and $M$ are respectively the mass of the $\pi^0$, $K^-$, $\pi^+$ and $D^0$ mesons. Events constrained in the shaded area [18].

**The Dalitz Weight (DW)**

In order to understand the Dalitz plot structure and to keep in a large majority of the occurences, a variable named Dalitz Weight is used. If there are any resonances in the decay, they will reveal as lines on the plot and their position (horizontal, vertical and diagonal) will indicate the particles come from these resonant particles. In our case, it is $D^0$ decays to final state $K^-\pi^+\pi^0$ through the resonances $K^{*+}(892)$ to $K^-\pi^+$, $K^{*0}(892)$ to $K^-\pi^0$ and $\rho^+(777)$ to $\pi^+\pi^0$. These resonances indicates the structures inside the plot. Resonances are expected in the $m^2_{(K^-\pi^+)}$ and $m^2_{(K^-\pi^0)}$ combinations and the Dalitz plot axes will be defined by these two observables. These invariant observables of Dalitz plot are computed with the masses of the $\tilde{D}^0$ meson constraint to its own PDG mass [18] using the Decay Tree Fitter algorithm (based on the kinematic and geometrical (vertex) constraints) [134]. Events are analyzed on the Dalitz plot by choosing the independent variables: $x \equiv m^2_{K^-\pi^0}$ (horizontal axis) and $y \equiv m^2_{K^-\pi^+}$ (vertical axis). The third variable is $m^2_{\pi^+\pi^0}$ as dependent variable on $x$ and $y$ through the energy and momentum conservation. The values of the $K^-$, $\pi^+$, $\pi^0$ and $D^0$ mesons are known from [18] and one can calculate the masses for each of the resonance from the Eq. 4.11, 4.12, 4.13, 4.14

$$m^2_{K^-\pi^+} + m^2_{K^-\pi^0} + m^2_{\pi^+\pi^0} = m^2_{K^-} + m^2_{\pi^0} + m^2_{\pi^+} + M^2_{D^0} \tag{4.11}$$

$$m^2_{K^-\pi^+} = m^2_{K^-} + m^2_{\pi^0} + m^2_{\pi^+} + M^2_{D^0} - m^2_{K^-\pi^0} - m^2_{\pi^+\pi^0} \tag{4.12}$$

$$m^2_{K^-\pi^0} = m^2_{K^-} + m^2_{\pi^0} + m^2_{\pi^+} + M^2_{D^0} - m^2_{K^-\pi^+} - m^2_{\pi^+\pi^0} \tag{4.13}$$

68

$$m_{\pi^+\pi^0}^2 = m_{K^-}^2 + m_{\pi^0}^2 + m_{\pi^+}^2 + M_{D^0}^2 - m_{K^-\pi^+}^2 - m_{K^-\pi^0}^2 \tag{4.14}$$

Clear resonance structures (signal) $K^{*-}(892)$ appears vertically, decays into $K^-\pi^0$, $m_{K^-\pi^0}^2 = m_{K^{*-}(892)}^2$ and $K^{*0}(892)$ running horizontally which would decay into $K^-\pi^+$, the resonance appear at $m_{K^-\pi^+}^2 = m_{K^{*0}(892)}^2$. And the band appear when $m_{\pi^+\pi^0}^2 = m_{\rho^+(770)}^2$ (anti-diagonal) shows the characteristic of the decay $D^0 \to K^-\pi^+\pi^0 \to K^-\rho^+$. The position of this anti-diagonal segment can easily be computed from Eq. 4.14. Figure 4.7 illustrates the Dalitz plot of all the events passing the selection requirements and these resonances.
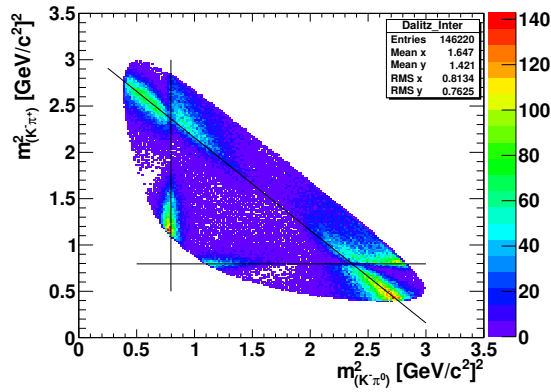


Figure 4.7: Dalitz Plot of the $D^0 \to K^-\pi^+\pi^0$ decay with Signal MC. The resonances are clearly visible in the vertical, horizontal and anti-diagonal directions. $K^{*0}(892)$ (horizontal segment), $K^{*-}(892)$ (vertical segment) and $\rho^+(770)$ (anti-diagonal segment).

In the phase space of the Dalitz plot it is seen that the variation of the population density (signal) is larger near the resonance bands shows that those are spin one resonances since the amplitude for spin one resonances comes with a node in the intermediate of their bands. To reduce the combinatorial background that is mostly distributed uniformly over the phase space, need to calculate the probabilities that a given candidate is actually originated from one of these three resonances that saturate the Branching fraction of the decay $D^0 \to K^-\pi^+\pi^0$. Concerning a resonance particle R ($\rho^+$, $K^{*-}$, $K^{*0}$) decays into ($i$, $j$, $k$: $K^-$, $\pi^+$, $\pi^0$), the decay amplitude for each resonant particle is given by

$$A_R = \frac{C_R e^{i\frac{\phi_R \pi}{180}}\sqrt{\frac{\Gamma_R}{2\pi}}cos\theta_{ij}^*}{m_R - m_{ij} - i\frac{\Gamma}{2}} \tag{4.15}$$

where $\theta_{ij}^*$ represents the two-body angles ($i$, $j$, $k$: $K^-$, $\pi^+$, $\pi^0$), $\Gamma_R$ and $m_R$ are the width and the mass of the resonant particles. $C_R$ and $\Phi_R$ represent the amplitude and the phase. All these parameters are taken from the PDG [18] and E691 experiment [135]. Table 4.10 shows all the values of the parameters.

| Resonance $R$ | $m_R$ ( MeV/$c^2$) | $\Gamma_R$ ( MeV) | $C_R$ | $\Phi_R$ |
|---|---|---|---|---|
| $K^{*0}(892) \to K^-\pi^+$ | 896.10 | 50.70 | 3.19 | $-13°$ |
| $K^{*-}(892) \to K^-\pi^0$ | 891.66 | 50.80 | 2.96 | $68°$ |
| $\rho^+(770) \to \pi^+\pi^0$ | 766.50 | 150.2 | 8.56 | $40°$ |

Table 4.10: Resonance parameters in the decay $D \to K^-\pi^+\pi^0$.

The MC simulation of the $D^0 \to K^-\pi^+\pi^0$ used in the analysis were generated and the probability $P_{D^0 \to K^-\pi^+\pi^0}(x, y)$ is fully computed from the parameters of the decay amplitude model measured by the E691 experiment [135] and confirmed by the CLEO-C experiment [136]. It is defined as:

$$P_{D^0 \to K^-\pi^+\pi^0}(m^2_{-0}, m^2_{-+}) = |\mathcal{A}_0 + \mathcal{A}_{\bar{K}^{*0}} + \mathcal{A}_{K^{*-}} + \mathcal{A}_{\rho^+}|^2. \tag{4.16}$$

Here non-resonant component with $A_0=1$ is taken as a reference. This probability function Eq. 4.16 is convoluted with a resolution function formed by the product of two Gaussians $\mathcal{G}_1$ and $\mathcal{G}_2$ and the Dalitz Weight quantity is used which shows propensity for an event to be near a resonance in the Dalitz phase space

$$\begin{aligned}
DW(m^2_{-0}, m^2_{-+}) &= (\mathcal{G}_1 \times \mathcal{G}_2) \otimes P_{D^0 \to K^-\pi^+\pi^0}(x, y) \\
&= \int_{m^2_{-0}(min.)}^{m^2_{-0}(max.)} \int_{m^2_{-+}(min.)}^{m^2_{-+}(max.)} \frac{1}{\sqrt{2\pi\sigma^2(m^2_{-0})}} e^{\frac{(y-m^2_{-0})^2}{2\sigma^2(m^2_{-0})})} \\
&\quad \times \frac{1}{\sqrt{2\pi\sigma^2(m^2_{-+})}} \exp^{\frac{(x-m^2_{-+})^2}{2\sigma^2(m^2_{-+})}} \times P_{D^0 \to K^-\pi^+\pi^0}(x, y) dx dy,
\end{aligned} \tag{4.17}$$

where $m_{-0} \equiv m(K^-\pi^0) = x$ and $m_{-+} \equiv m(K^-\pi^+) = y$. These two Gaussians represent the experimental resolution of the measured invariant masses: $m^2_{(K^-\pi^+)}$ and $m^2_{(K^-\pi^0)}$.

Figure 4.8 displays that invariant mass squared resolution of scatter plots superimpose with the vertical axis average for each bin in $x$ and $y$. Versus the above defined variables, this resolution is computed as the reconstructed squared masses minus the generated true values as a function of the generated true value. The average of the difference is superimposed on top of the 2D histograms for each bin in $x$ and $y$. From the profiles vs. $x$ and $y$, one can understand that for the charged tracks profile plot (on top $x$ vs. $y$) the resolution is increasing with the increasing mass, since, for the momentum resolution of charged track obey the law

$$\frac{\Delta p_T}{p_T} \propto p_T$$

The momentum resolution of the tracks $\Delta p_T/p_T \sim 0.5\%$ and $0.8\%$ and $\Delta p_T/p_T \sim 0.8$ for the particles of $20\,\text{GeV}/c^2$ and $100\,\text{GeV}/c^2$ respectively. And the function is for the

charged track is increasing function. While for the $\pi^0$, it is decreasing with the increasing mass and this is just because it is dominated by the resolution of the $\pi^0$, i.e. = by that of the two $\gamma$ reconstructed in the ECAL that follow $\sigma E/E \simeq 10\%/\sqrt{(E)} \oplus 1\%$ (E in GeV) [72] and the momentum of $\pi^0$ will be larger.
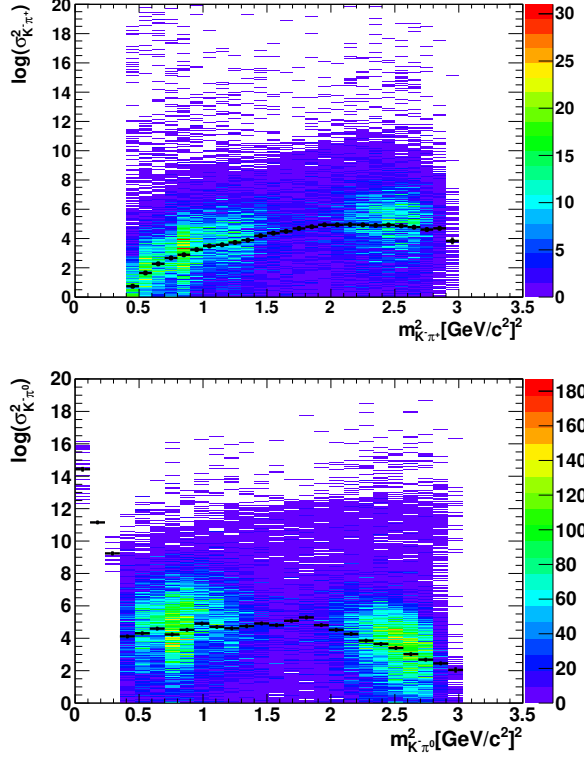


Figure 4.8: Resolution $\sigma$ as a function of invariant mass squared of $(a)$ $m^2_{(K^-\pi^+)}$ (top) and $(b)$ $m^2_{(K^-\pi^0)}$ (bottom) for MC Run 2 signal.

Empirical fits, with multi-degrees polynoms (four for $x$ and five for $y$), are performed for this averaged profiles as a function of $x$ and $y$ to model the experimental resolution of the mass squared $m^2_{(K^-\pi^+)}$ and $m^2_{(K^-\pi^0)}$ (in $(\,\mathrm{GeV}/c^2)^2$ ) for Run 1 and Run 2 are shown in Figure 4.9.

The result of the fitted empirical polynomials with Run 1 and Run 2 MC simulation are (in $log((\,\mathrm{MeV}/c^2)^2))$, for Run 1:

$$log(\sigma^2(x)) = 4.4 - 2.1x + 4.2x^2 - 2.2x^3 + 0.3x^4$$
$$log(\sigma^2(y)) = -6.2 + 25.6y - 28.9y^2 + 17.1y^3 - 4.9y^4 + 0.5y^5$$

for Run 2:

$$log(\sigma^2(x)) = 4.9 - 3.1x + 5.0x^2 - 2.4x^3 + 0.3x^4$$
$$log(\sigma^2(y)) = -6.8 + 28.7y - 34.1y^2 + 21.1y^3 - 6.3y^4 + 0.7y^5$$

71

where $x = (m^2_{-0})$ and $y = (m^2_{-0})$.
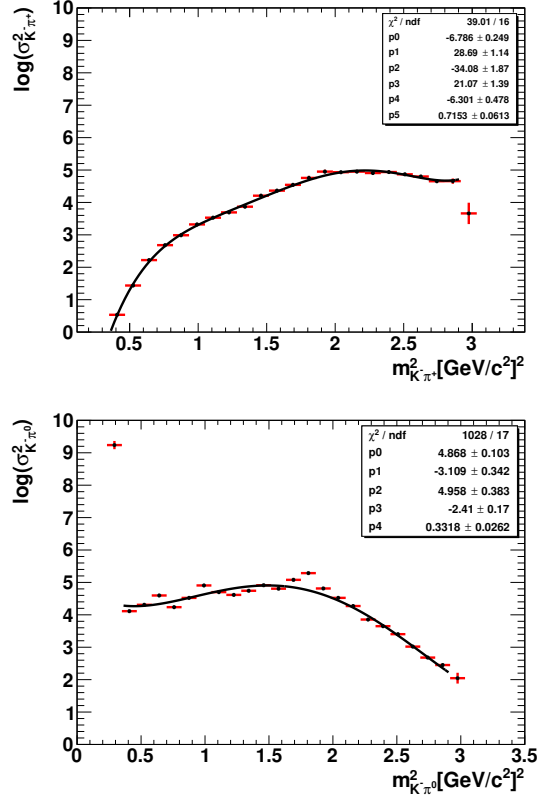


Figure 4.9: Fit to the (a) $log(\sigma^2_{K^-\pi^+})$ and (b) $log(\sigma^2_{K^-\pi^0})$ as a function of the $m^2_{(K^-\pi^+)}$ and $m^2_{(K^-\pi^0)}$ for MC Run 2 signal. Each of the fit plots in the Figure (a)(top) and Figure (b)(bottom) the two aberrant average points at the left (top) and at the right (bottom) sitting at the phase space limit were not included in the fits.

One can see that within the statistical uncertainties of the fitted polynoms, the resolution of $m^2_{(K^-\pi^+)}$ and $m^2_{(K^-\pi^0)}$ is roughly similar for MC simulation is Run 1 and Run 2. The obtained resolutions are used together with the amplitude model by E691 experiment 4.10 in Eq. 4.17.

Distribution of Dalitz Weight (DW) for signal MC and the background Data is shown in Figure 4.10. The background is mainly distributed around the low values of the Dalitz weight while the signal is distributed up to larger DW values and by construction the mean value of the DW is much larger than those of the background (*i.e.*: $7 - 7.5$ with respect to $3 - 3.5$). One can see that from statistics the probability gets closer 1 if it is a signal and smaller if it is background. That's why Dalitz weight larger for signal than the background. We contract the weight such that the points are outside the phase space limits are just considered non-signal and the weight for them is zero. Bin at zero is due to occurrences where the computed of the squared mass of the $m^2_{(K^-\pi^0)}$ and $m^2_{(K^-\pi^+)}$ is just out of the envelope of the kinematic limits shown in Figure 4.7. By definition $DW = 0$

and we first cut those events which are outside the phase space limit with the TMVA with Dalitz weight and the kinematics to keep the non-zero bins in the phase space limit. Figure 4.11 shows the events in the Dalitz plot distribution before and after we apply the Dalitz Weight selection $DW > 0$ for signal MC Run 2 and the background from Data Run 2.

From the Figure 4.11, plot on the top right side after DW selection, we can clearly see the structure of the angular distribution(which is important to understand the events distribution on the Dalitz plane) and the resonances that are shown with the lines for each one: $K^{*-}(892)$(vertical), $K^{*0}(892)$(horizontal) and $\rho^+(770)$ (anti-diagonal) and the decay in terms of angular momentum into: Vector$\rightarrow$Scalar+Scalar. One can understand that the Dalitz Weight gives the regions related with the resonances and the background includes the real $D^0 \rightarrow K^-\pi^+\pi^0$. In the bottom left dalitz plot of data, one can see that the events outside of the phase space limit are genuine fake $D^0$ which can not be computed correctly because the amplitude is defined by the envelope model. This will be explained in the next section before and after applying the TMVA selection.
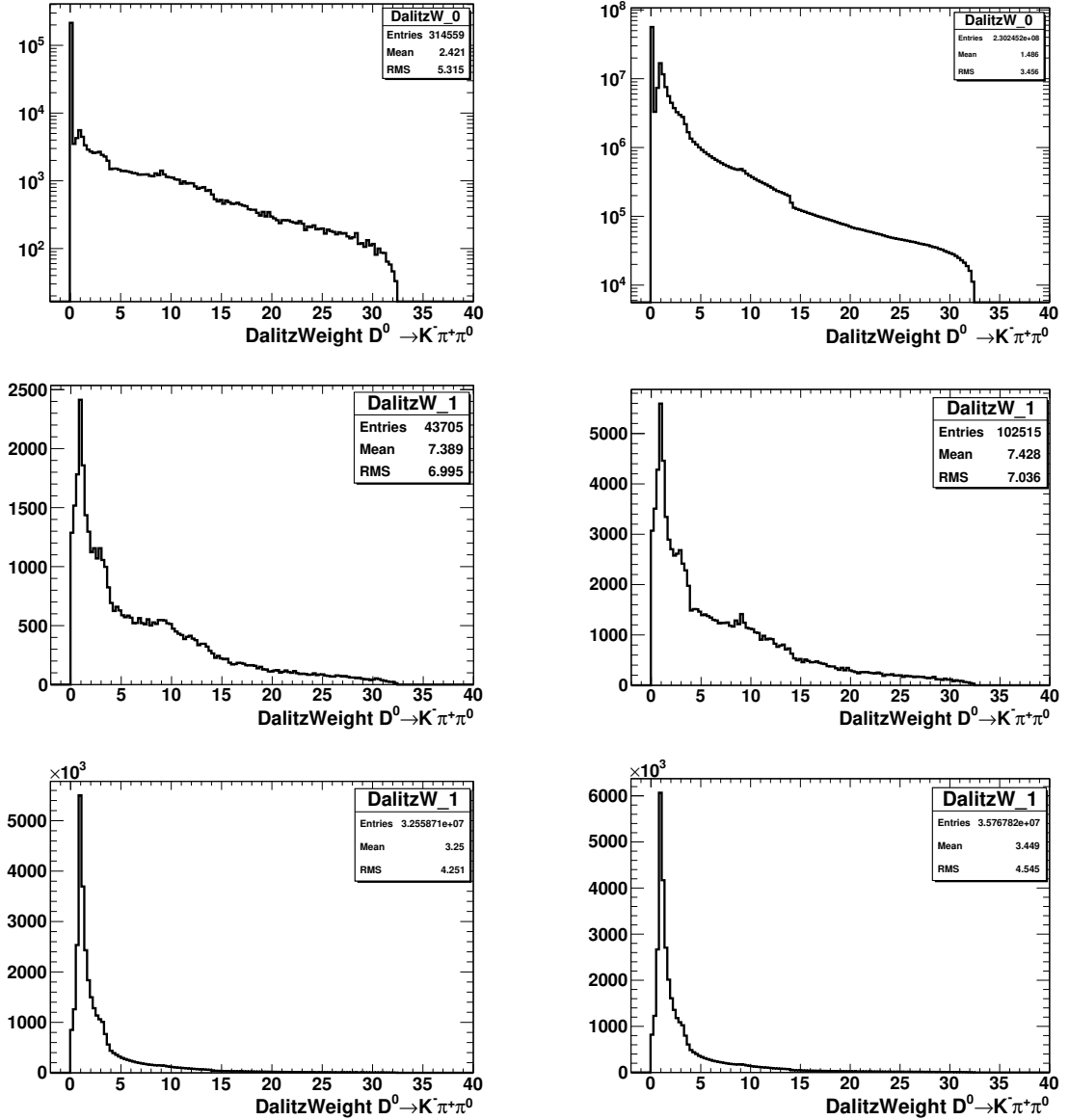
Figure 4.10: Top row shows the logaritmic scale of Dalitz Plots ($DW = 0$) before Dalitz weight selections for MC simulation (left) and Data (right) for Run 2. Middle row for Dalitz plots after Dalitz weight selections for MC simulation and bottom row for Data Run 1 (left side) and Run 2(right side).

### 4.4.4 $D^0 \to K^-\pi^+\pi^0$ candidate selection by multivariate analysis

After the variables are defined in Sect. 4.4.2 to select the photons originated from the $\pi^0$, a Multivariate Analysis (MVA) technique is employed to the Toolkit for Multivariate Analysis (TMVA) software package [137] integrated within ROOT to improve signal over background ratio by using kinematic and topological variables. This technique is
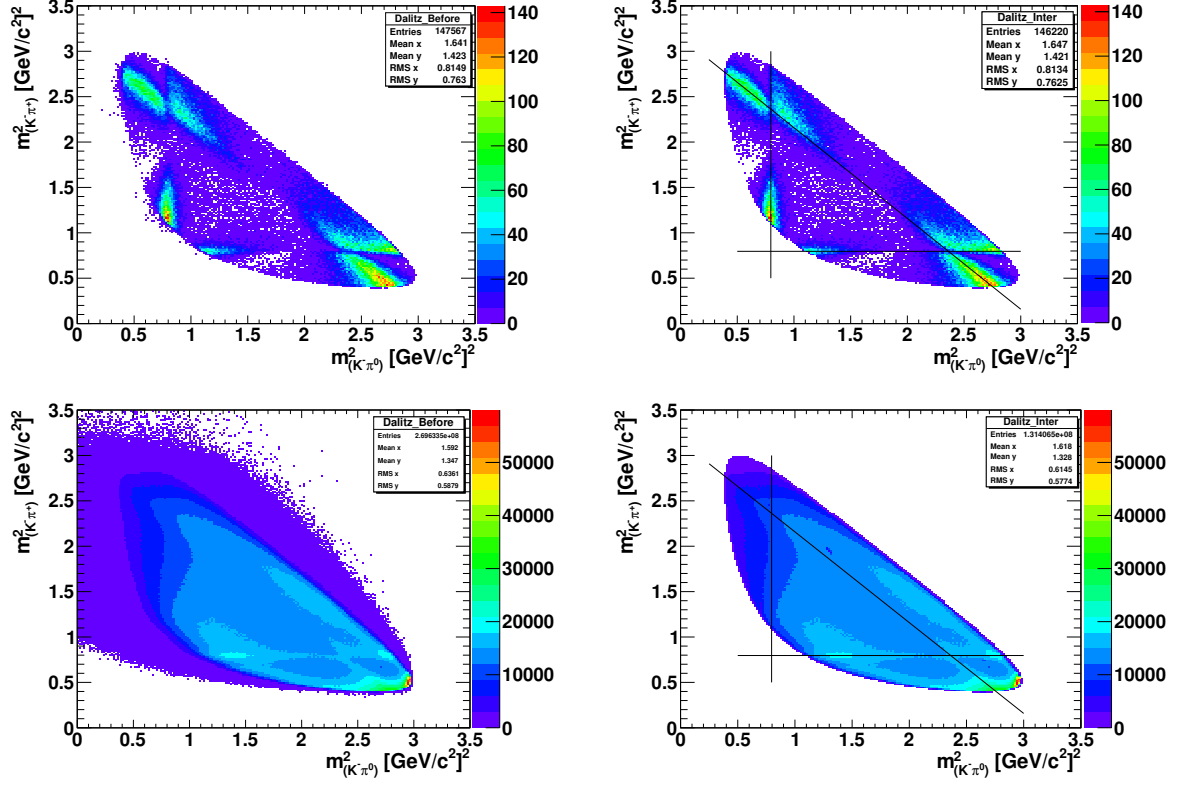
Figure 4.11: Dalitz Plot of the selected sample $D^0 \to K^- \pi^+ \pi^0$ for signal MC Run 2 before DW selection plot (top left) and after selection (top right) for background Data Run 2 before DW selection (bottom left) and after selection (bottom right).

important to reduce the complexity of many problems and allow to account for possible correlations between the different variables. From that point, we choose the selections to fight against the non-$\pi^0$ background.

The multivariate approach allows to combine the variables into a single discriminant. The MVA method is employed to select the $\pi^0$ in the $D^0 \to K^- \pi^+ \pi^0$ candidates. The MVA is computed based on the combination of these five input variables 4.4 and Figure 4.12 shows the distributions of the input variables with the signal and the background events separation. These distributions give the information to check the success of the operations carried out.

The linear correlation matrices between the discriminating input variables for both signal and background events are shown in Figure 4.13. One can see that the correlation between the variables is very low and this will maximise their global power as when the correlations are low additional variables will provide new information.

The variables kept, listed by rank in Table 4.11, are those that have the highest discriminating power. This relative discriminating power of each variable is evaluated by counting how often it is used to split decision nodes, weighting each split by the square of the separation gain and the number of events considered in the node for the BDT.
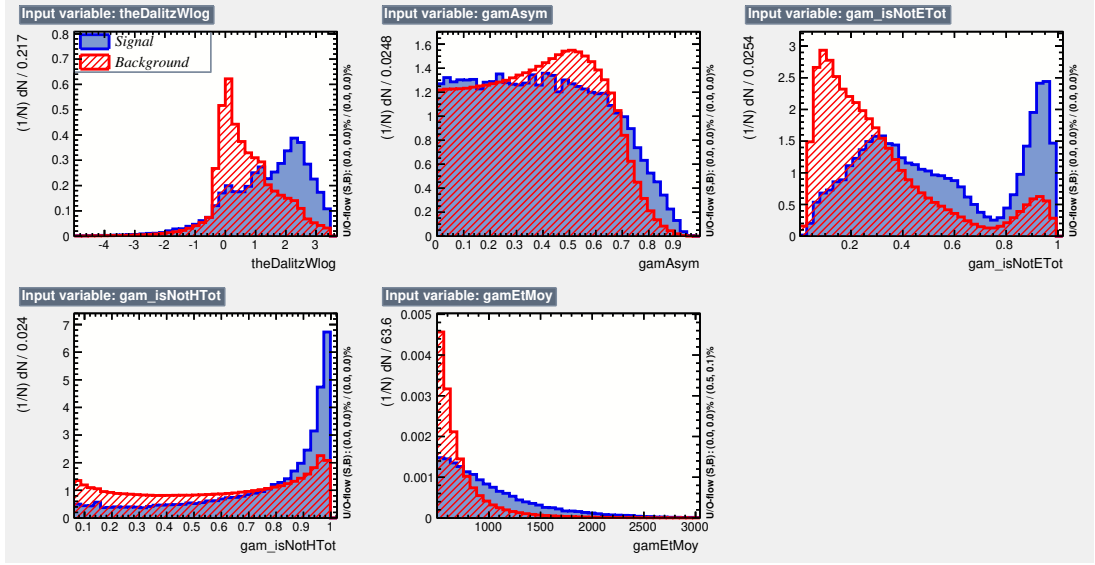
Figure 4.12: Comparison between the selection of input variables distributions. Signal is given in blue and background is in red. First output distribution is the log of DalitzW explicitly mentioned in the figure caption for better numerical behaviour with TMVA (as the distribution has long tail see Figure 4.10). Distribution for the input variable *gam_isNotETot* explain that variable peak at 1 is genuine photon signal, while the bump in the range $[0.1, 0.7]$ corresponds to early showering (i.e. pair conversions) before the PS part of ECAL such that the distribution for those converted photons may look like a bit like an electron.

| Variable | MVA Ranking | Separation |
|---|---|---|
| $gamisNotETot$ | 1 | $1.751 \times 10^{-1}$ |
| $gamEtMoy$ | 2 | $1.702 \times 10^{-1}$ |
| $theDalitzWlog$ | 3 | $1.552 \times 10^{-1}$ |
| $gamisNotHTot$ | 4 | $8.978 \times 10^{-2}$ |
| $gamAsym$ | 5 | $1.443 \times 10^{-2}$ |

Table 4.11: The separation power of input variables.

Among the several multivariate methods exist, three different MVA methods are tested for this analysis: Fisher discriminant (Fisher) (linear correlation between input variables), Multilayer Perceptron (artificial neural network) (MLP) and Boosted Decision Tree (BDT) (non linear correlation). We used TMVA to apply these methods. TMVA provides the user with optimal values for the hyper parameters for each fold, the performance of which can be compared by calculating the area under the Receiver Operating Characteristic (ROC) curve for the corresponding classifier. The three methods have shown relatively similar performances. The performances of given classifiers are illustrated by ROC curve represented in Figure 4.14. The larger the area under the ROC
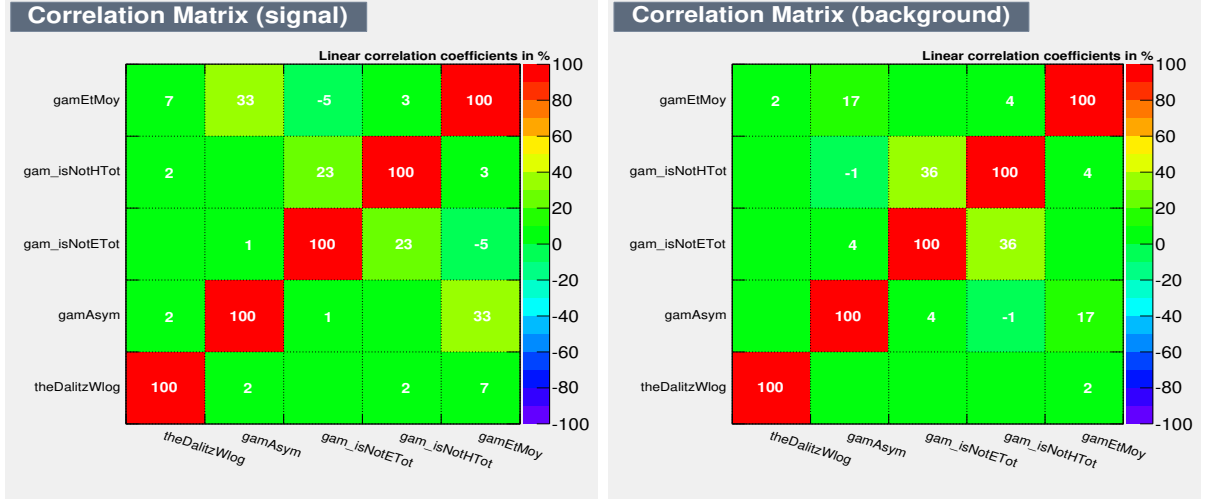
Figure 4.13: The correlation matrices of TMVA input variables for signal (left) and background (right).

curve, the more powerful the classifier. The distribution shows that the BDT is found to be most powerful discriminator to reduce the combinatorial background as it gives the best performance to this analysis.
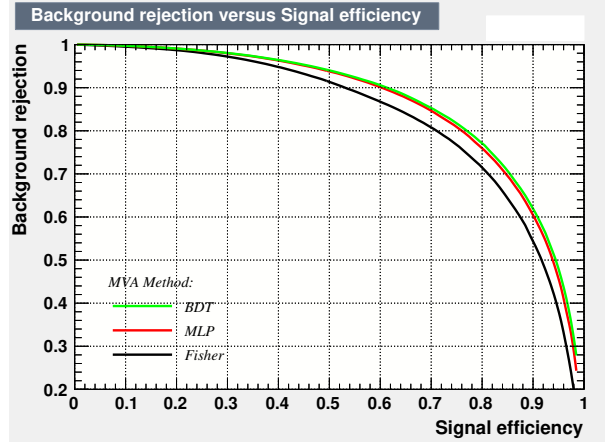


Figure 4.14: Signal Efficiency vs Background Rejection for MVA classifiers. Receiver Operating Characteristic (ROC) curve giving the different range of MVA methods applying on the $D^0 \to K^- \pi^+ \pi^0$ decay. Among the classifiers: the better the performance, the closer to the right hand side corner of the plot.

The signal and the background of the classifiers training in a coefficient called classifier response with the MVA Overtraining plots are shown in Figure 4.15. We have shown overtraining check for three of the classifiers: Fisher, BTD and MLP. This testifies that the performance of the classifier is expected and here we can see that BDT is not overtrained

77

and shows a good separation than MLP and Fisher which we can understand this from the Figure 4.15 (a) and (c). The Kolmogorov-Smirnov test (statistical test) evaluate the difference between the test and the training sample of the signal and the background.
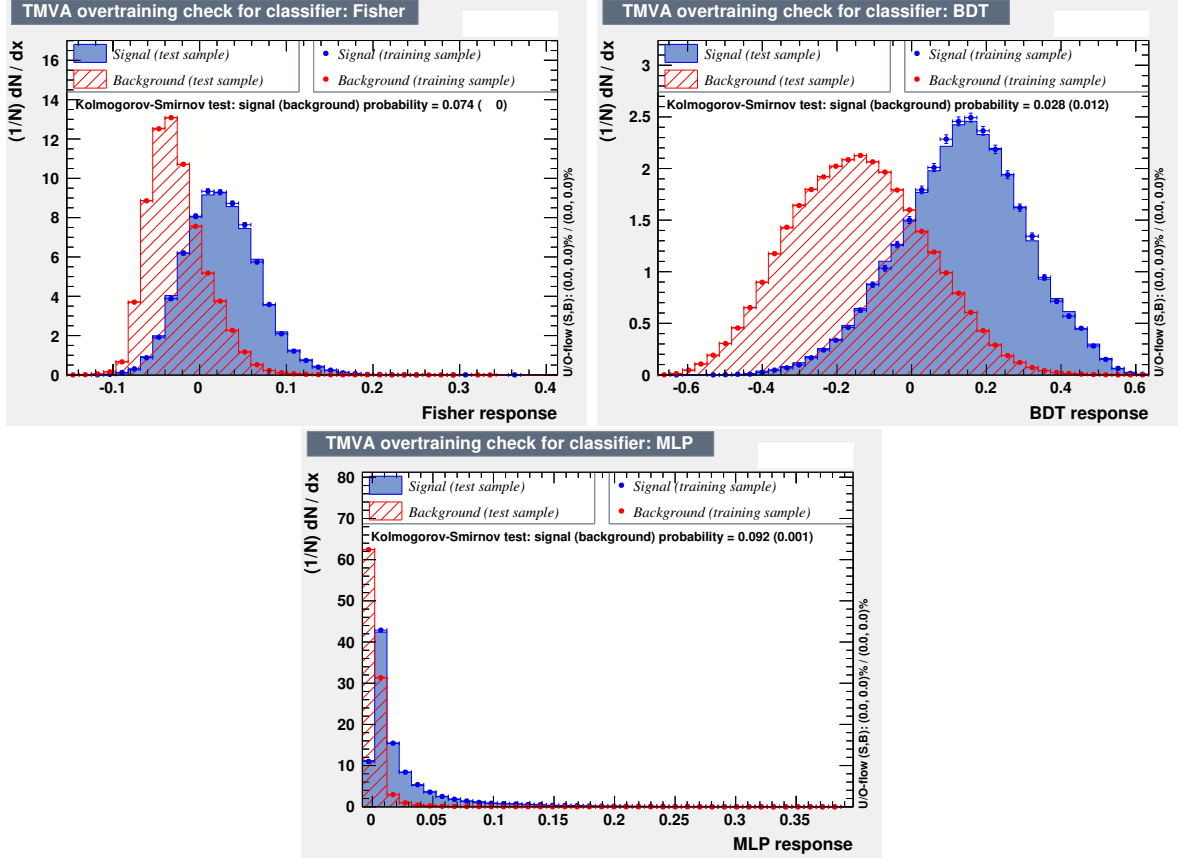


Figure 4.15: Overtraining plots for the classifiers. Distribution of the signal (blue) and background (red) in terms of the BDT response for Run 2, both on the training sample (dots) and the test sample (solid line). From the results of the Kolmogorov-Smirnov test, training and testing sample show that the two signal and the background distributions are in good agreement.

The BDT method is the least linear method, so the most sensitive to possible biases, or discrepancies in Data versus MC simulation of the discriminating variables, and limited statistics of the training samples, nevertheless BDT gives the best performances. Its performances is however similar to that of the artificial Neural network MLP (multi-layer Perception) but one clearly sees in Figure 4.15 (a) and (c) that the background and signal distributions are better split for BDT allowing a smoother behaviour of the signal statistical significance or purity when varying the position of the selection cut for the BDT with respect to the MLP method. After BDT has been trained and tested, Figure 4.16 shows the cut efficiencies and the optimal cut value plot, through this BDT response parameter, we can study to find the optimal cut value for which we have the

maximum of statistical significance defined as $Q = S/\sqrt{(S+B)}$, where $S$ is the number of survival signal and $B$ that for the background for a specific BDT value in signal and background.
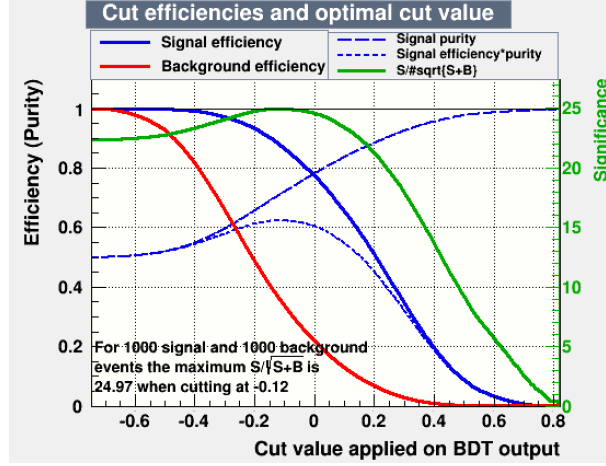


Figure 4.16: Figures of merit used to optimise the cut on BDT output for Run 2. The plot gives the cut value on output as a function of efficiency(purity). The solid red line represents the background efficiency, blue line gives the signal efficiency and the green line is for the significance function.

Table 4.12 shows the final significance values for the signal and background and the cut values which perform on BDT for Run 1 and Run 2. This is our choice to purify the signal and reject the background from data. As our analysis is signal limited, we choose the maintain the signal efficiency very high and to gain at least about order of magnitude on the background level, that's why we choose and operation point where the signal efficiency is 85%, corresponding to a rejection of the background of 69% for the Run 1 and 71% for the Run 2.

| dataset | BDT cut value | Signal eff. | Bkgd reject. |
|---|---|---|---|
| Run1 | -0.08 | 85 % | 69 % |
| Run2 | -0.054 | 85 % | 71 % |

Table 4.12: Signal efficiency and the background rejection, when cutting on BDT for Run 1 and Run 2.

We use these optimal cut values that we defined on the BDT selection for Run 1 and Run 2.

And after the optimisation of BDT, the selection is used to further reduce the combinatorial background, the Dalitz Plots are shown in Figure 4.17 and the Dalitz weight variable distributions can be seen in Figure 4.18 for both signal MC Run 2 and Data Run 2. One can see that thanks to the MVA method the distribution shape in data is tailored to look like that in the MC simulation for the signal. The MVA selection doesn't

change the relative Dalitz structure (i.e. decay amplitude) of the $D^0 \to K^- \pi^+ \pi^0$ signal in data.
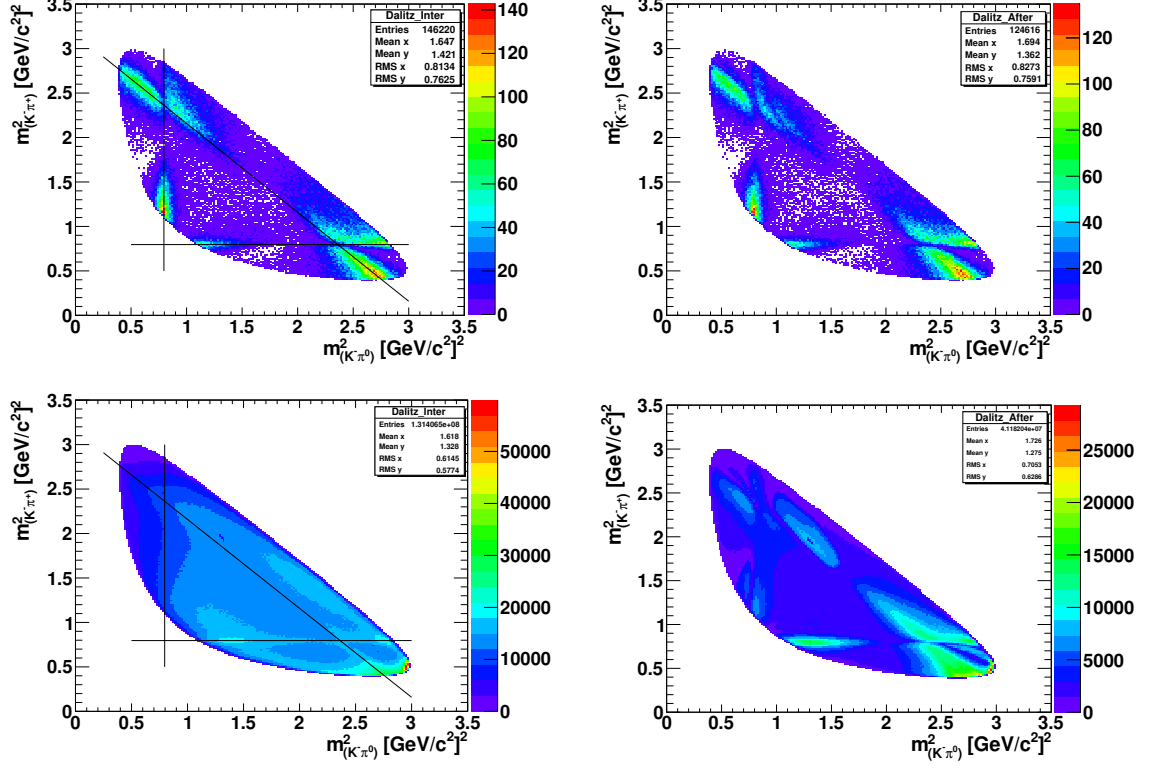


Figure 4.17: Dalitz Plot of the selected sample $D^0 \to K^- \pi^+ \pi^0$ for signal MC Run 2 before BDT selection plot (top left) and after selection (top right) for background Data Run 2 before BDT selection (bottom left) and after selection (bottom right).

From the Figure 4.17 one can see that the Dalitz plot resolution is improved after the BDT selection. We have 85% of signal efficiency and 79% of background rejection.
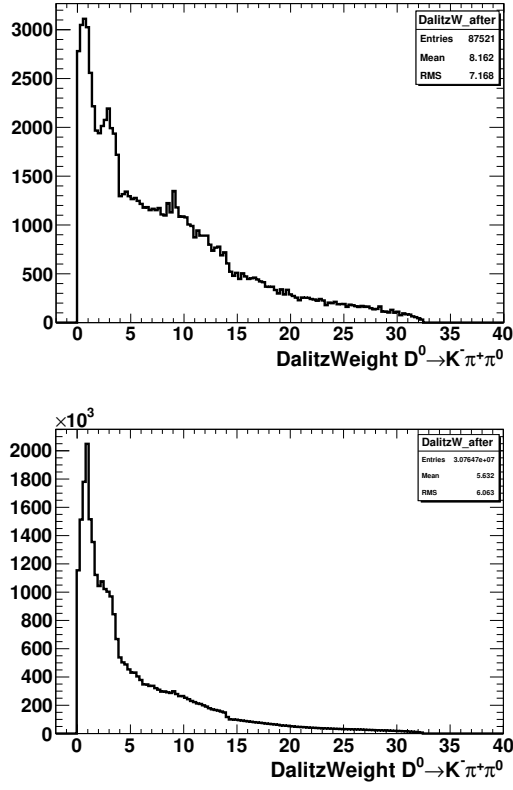
Figure 4.18: Dalitz Weight distribution after the BDT selection for Signal MC (top)(a) and Background Data Run 2 (bottom)(b).
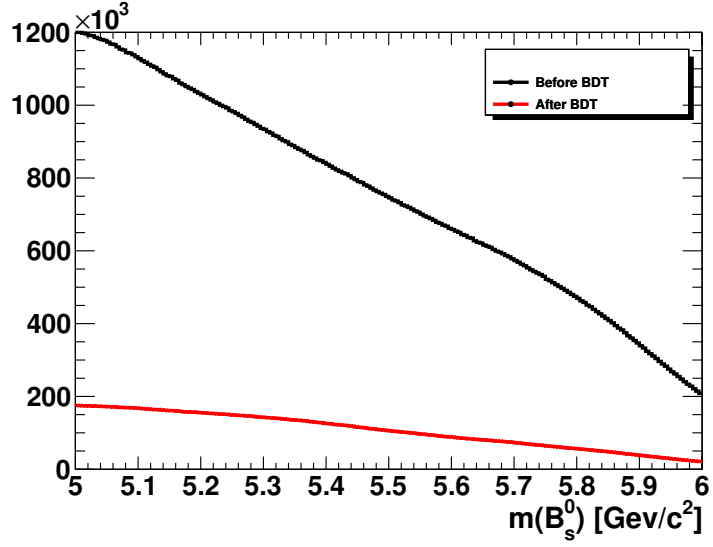


Figure 4.19: Invariant mass spectrum of $B_s^0$ before (black line) and after (red line) the BDT selection for Data Run 2.

$B_s^0$ invariant mass spectrum (with DTF) before and after we apply the BDT selection is shown in Figure 4.19. From Figure 4.19 one can see a factor of 1/70% reduction on the background rate. And the same way we consider $\pi^0$ mass spectrum after BDT selection was implemented (see Figure 4.20). For the $\pi^0$ distribution, one can see the background under the spectrum before BDT selection while after the selection, the background is reduced and $\pi^0$ mass distribution can be seen clearly.
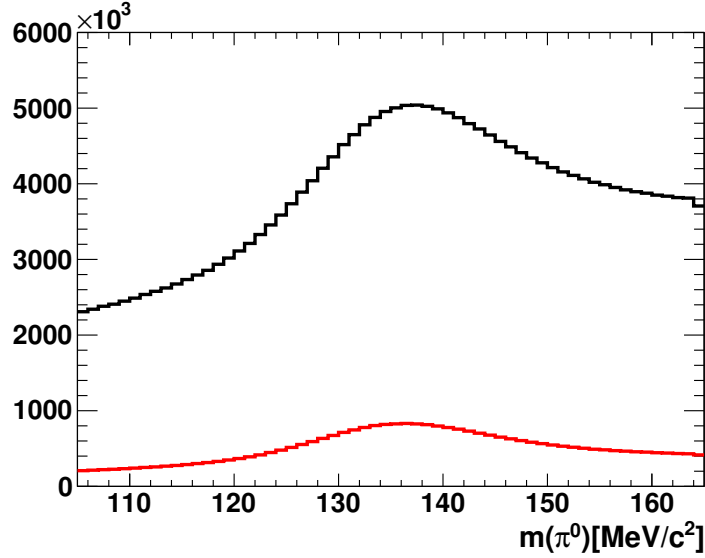


Figure 4.20: Invariant mass spectrum of $\pi^0$ before (black) and after (red) BDT selection for Data Run 2.

From the $\pi^0$ mass distribution it can be seen that we don't have enough sidebands to estimate the shape of the background. And at this point we made an assumption that background should be like an increasing first degree polynomial (straight line).

## 4.4.5  Optimisation of the $\pi^0$ mass window limits

The method we used for the optimisation of the $\pi^0$ is to perform the adjustment to have a very similar distribution both in the Data and the Monte Carlo for the Run 1 & Run 2. Here we use the MC distribution of the particle as a reference to model the data. Figure 4.21 shows the fit to the $\pi^0$ invariant mass distribution for the MC. And for the MC, we can see that the tails are asymmetric and there is more events on the right side than the left side. The asymmetry is due to the fact that at larger $\pi^0$ mass, the intrinsic resolution of the photon pair angle degrades the reconstructed $\pi^0$ mass resolution.

What we have done here is that we have data and from the Figure 4.20, we model the combinatorial background with a simple first order of polynomial from the straight line as shown in Figure 4.22. The red curve is the modelling of the background and the blue curve is the result of the subtraction of the modelled background from the initial data distribution. This resulting distribution is therefore a fair approximation of the signal $\pi^0$

82
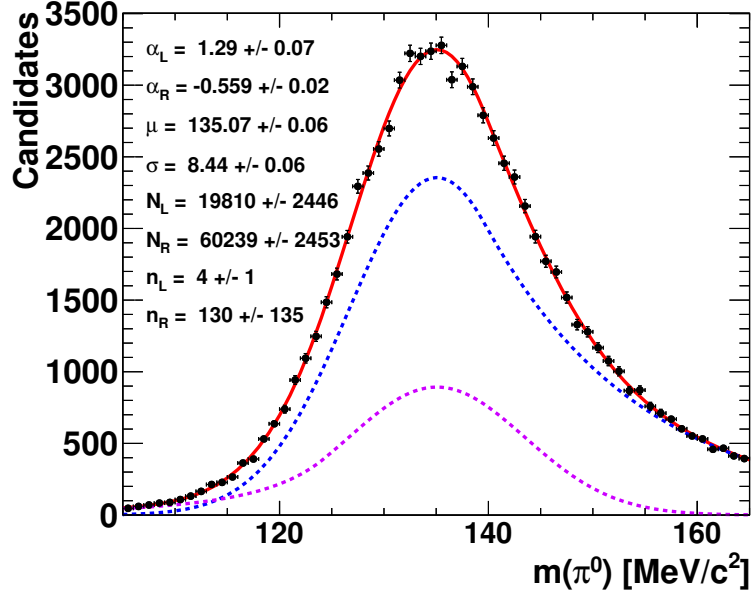
Figure 4.21: Optimisation the mass of $\pi^0$ for signal MC Run 2. Here the $\pi^0$ signal is fitted with a Right (R) and Left (L) side Crystal Ball function, while the two function share the same resolution ($\sigma$) and central value ($\mu$).

spectrum to be used for the study of the investigation for the best $\pi^0$ mass window limits. We subtract bin by bin in the histogram and compute the histogram for background which is subtracted the mass of the $\pi^0$ to get signal very similar to the distribution in the MC. We check what is the relative level (number of events) of tails from left to right at bin 105 and and 165 after the subtraction. This is our best guess on the background. And one can see that the blue histogram in the Figure 4.22 can be compared with the MC fit distribution in Figure 4.21, especially for the bins at 105 MeV/$c^2$ and 165 MeV/$c^2$.

After the subtraction Figure 4.23 shows the fit distribution of the $\pi^0$ mass signal which is given with the red curve in Figure 4.22.

One can see that the tails for the Data are a little bit different than in the Monte Carlo. For the comparison between Data and MC, it is obvious that the resolution is worse in Data because of the limitations of the GEANT4 simulation and due to the variation of the calorimeter response and calibration in real life over time. The results are given (fit values of the mean and the sigma) in Table 4.13 for Run 1 and Run 2, from the Table, we scale the limits on the $\pi^0$ mass window which are obtained in the data to get the corresponding limits in the MC simulation.

After the fit to the $\pi^0$ mass distribution in data, the next step is to find the optimum cut for the data on the mass of the $\pi^0$. For this, the Figure 4.22 is used that shows the plot involving the signal and the background of $m_{\pi^0}$. From the integrals of the signal and the background histograms of the Figure 4.22, one can compute the cumulative efficiency as a function of selection cut that starts from the upper right part or left lower part of the
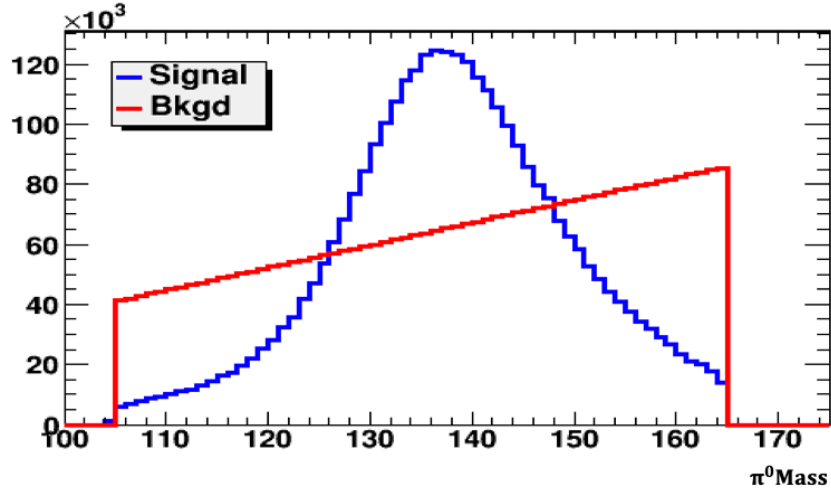
Figure 4.22: The distribution in blue curve gives mass of the $\pi^0$ signal while red straight line shows the subtraction for the $\pi^0$ mass in the Data Run 2.
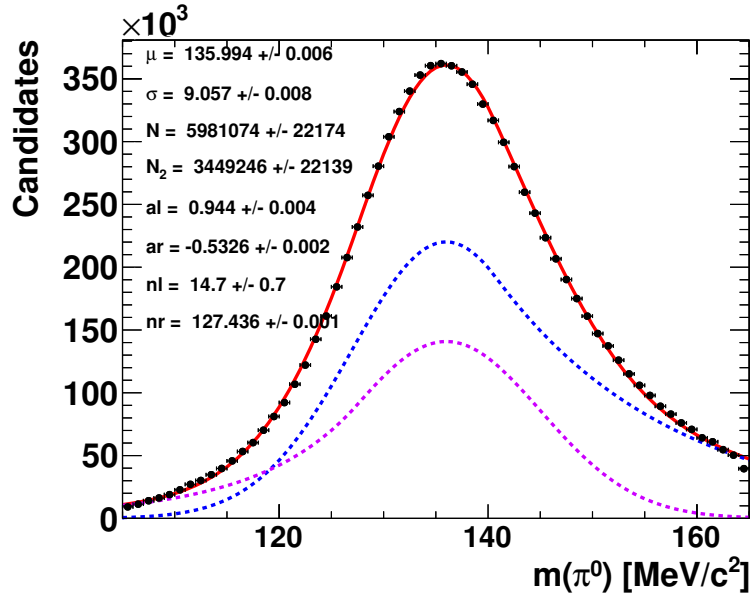


Figure 4.23: Optimisation the mass of $\pi^0$ for signal Data Run 2. The $\pi^0$ signal is fitted with a Right (R) and Left (L) side Crystal Ball function, while the two function share the same resolution ($\sigma$) and central value ($\mu$).

signal and the background histograms. Figure 4.24 shows the signal and the background efficiency plot for the selected cut value.

For the Figure 4.24, the first one (a), one can see that the cumulative efficiency starting from the right side and we obtain the position of the selection cut in the plot. From the bin by bin efficiencies we can compute the significance(Q) $Q = \frac{S}{\sqrt{S+B}}$ at a given position

| | $\mu$ ( MeV/$c^2$) | $\sigma$ ( MeV/$c^2$) |
|---|---|---|
| MC Run 1 | 134.93 ±0.09 | 8.54±0.09 |
| DATA Run 1 | 137.51±0.01 | 9.29±0.01 |
| MC Run 2 | 135.07 ±0.06 | 8.44±0.06 |
| DATA Run 2 | 135.99±0.01 | 9.06±0.01 |

Table 4.13: Mean and Resolutions obtained from the fit to $\pi^0$ mass distribution for the MC and Data Run 1 and Run 2.

from the right hand side of the plot 4.24 (b).
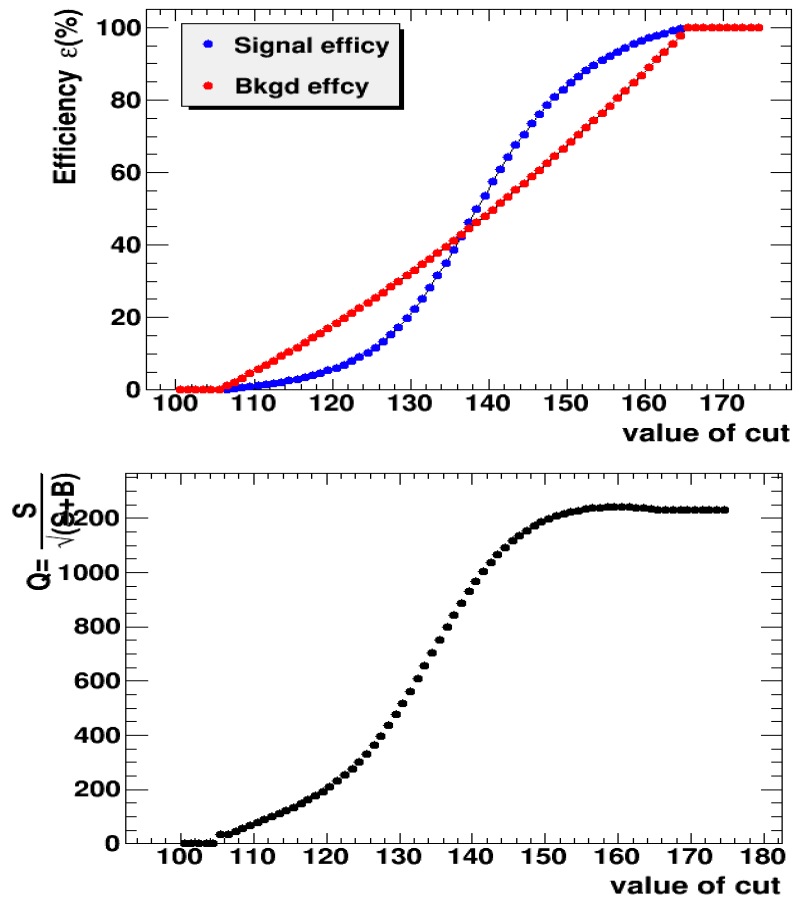


Figure 4.24: Efficiency (top) and the the value of the significance(Q) (bottom) for the optimal cut values Data Run 2.

The upper and lower limits, and the the best (Q) significance within the best position of the selection cut are obtained. Table 4.14 gives the optimum limit cuts and the relevant significance values.

Now we know for the $m_{\pi^0}$, the upper limit should be $m_{\pi^0} < 160 \, \text{MeV}/c^2$. And in order to obtain the lower limit on the $m_{\pi^0}$, the same process is followed. We want to reject

| DATA | Optimal interval $m_{\pi^0}(\,\mathrm{MeV}/c^2)$ | $Q$ at lower limit | $Q$ at higher limit |
|------|--------------------------------------------------|--------------------|---------------------|
| Run1 | $117.5 < m_{\pi^0} < 160.0$ | 1240.2 | 1242.5 |
| Run2 | $117.5 < m_{\pi^0} < 159.0$ | 2116.1 | 2133.9 |

Table 4.14: $\pi^0$ optimum cut limits and their significance for Run 1 and Run 2.

the candidates that have low $m_{\pi^0}$. For the lower limit of the optimum cut, cumulative efficiency starts from the left side and point by point efficiencies in Figure 4.25(a) we compute the significance $\frac{S}{\sqrt{(S+B)}}$ at a given position from the left hand side shown in Figure 4.25(b).
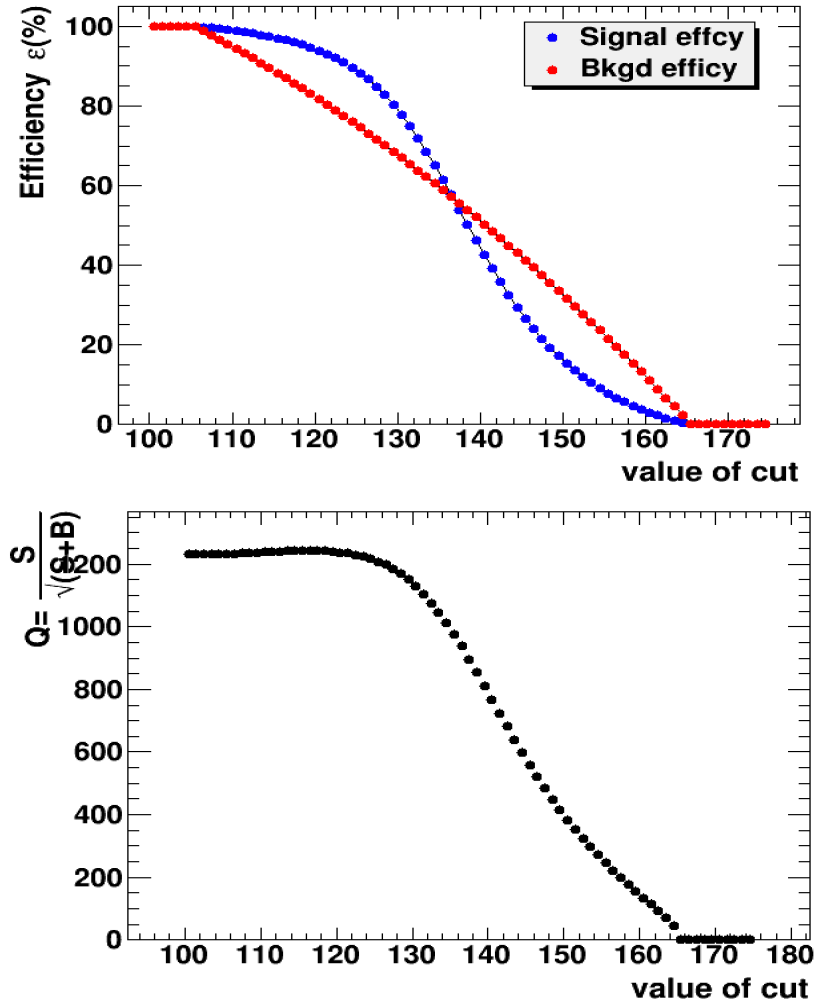


Figure 4.25: Efficiency (top) and the the value of the significance(Q) (bottom) for the lower limit on the optimal cut values of $m_{\pi^0}$(b) Data Run 2.

The best optimum lower limit on the $m_{\pi^0}$ is obtained as $m_{\pi^0} > 116\,\mathrm{MeV}/c^2$. The

optimum selection and the related significance Q for the limit is given in Table 4.14.

Since the aim to to maximise the statistical significance of studied signal $B_s^0 \to D^0 \phi$, which is very small with respect to the background, so in that case Q significance is the best estimator on each step of the selection before (BDT on Dalitz weight) and after, and final optimum selection on the mass of $\pi^0$ is given as in the Table 4.14.

Optimisation is same for both Run 1 and Run 2. And for the MC and Data Run 1, the optimum selections are defined on the mass in the same way. Fit plots are shown in Figure 4.26. For the fitting there is a shift in the Data and it is found that the resolution and the fitted average is not same for Run 1 and Run 2. In Run 1 (see Table 4.13) one can see that from the fit to the Data, the central value is away from the PDG [18] value while in the Run 2, the resolution is likely improved and the central value is much more closer to the PDG value. It is obvious that Data and MC in Run 2 is better. This is because, during the Run 2, there is an online calibration from the Data given in the [26] and the central value is really at the PDG mass. Resolution is improved in Data Run 2 rather than Run 1.
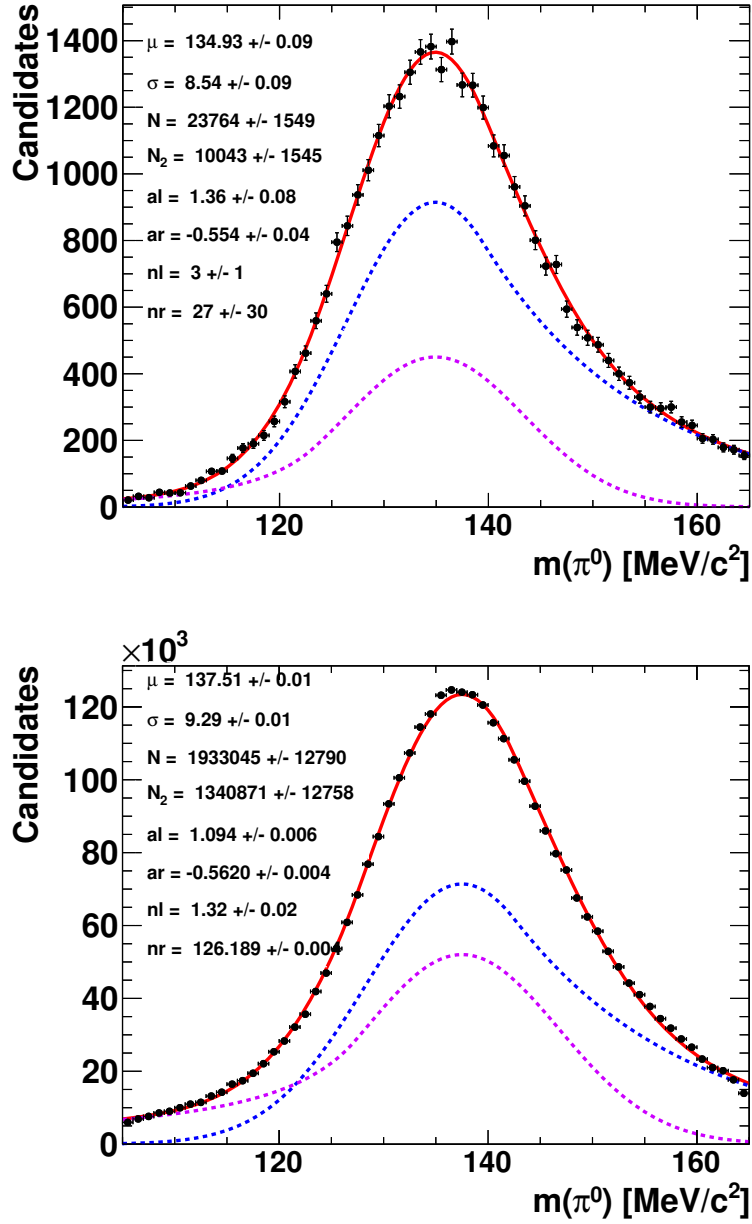
Figure 4.26: Optimisation the mass of $\pi^0$ for signal (a)(top) MC Run 1 and (b)(bottom) Data Run 1.

The result of the optimisation of the $\pi^0$ mass within the range $\in [116.0, 160.0] MeV/c^2$, we keep the candidates in this interval and reject the ones outside. Figure 4.27 shows the candidates mass spectrum in the region for MC and Data. The MC limits have been adapted to obey the difference Data with respect to the MC differences. $\pi^0$ mass effects on the $D^0$ and the $B_s^0$ candidates are shown in Figure 4.28. The corresponding signal (MC signal box) and background (data sideband) are listed in Table 4.15
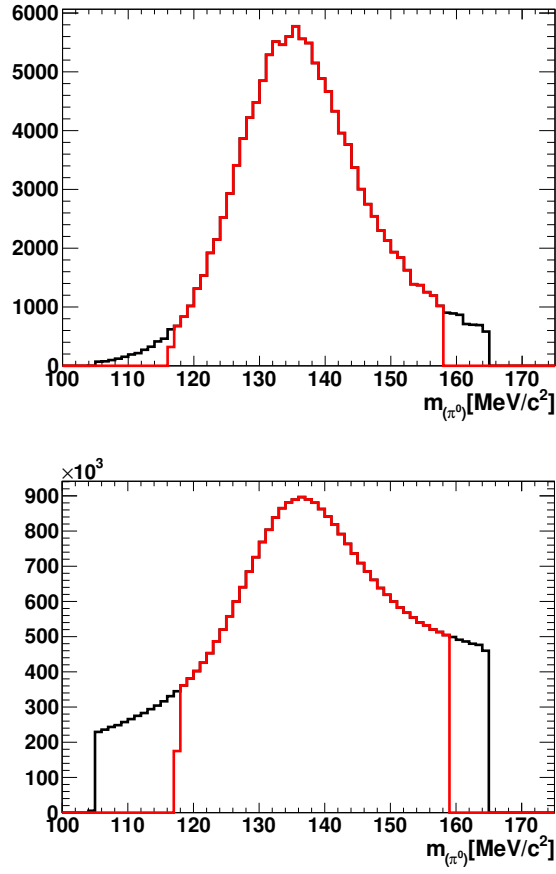
Figure 4.27: $\pi^0$ mass selection for signal MC Run 2 (top) and background Data Run 2 (bottom). Black line shows the distribution before selection cuts and red line after selection cuts.

| Selection on $\pi^0$ Mass Window | Run1 | Run2 |
|---|---|---|
| Signal Efficiency (MC) | 94.29% | 94.14% |
| Background Efficiency (DATA) | 81.31% | 80.15% |

Table 4.15: The corresponding signal and background efficiencies for MC signal and Data background for Run 1 and Run 2.
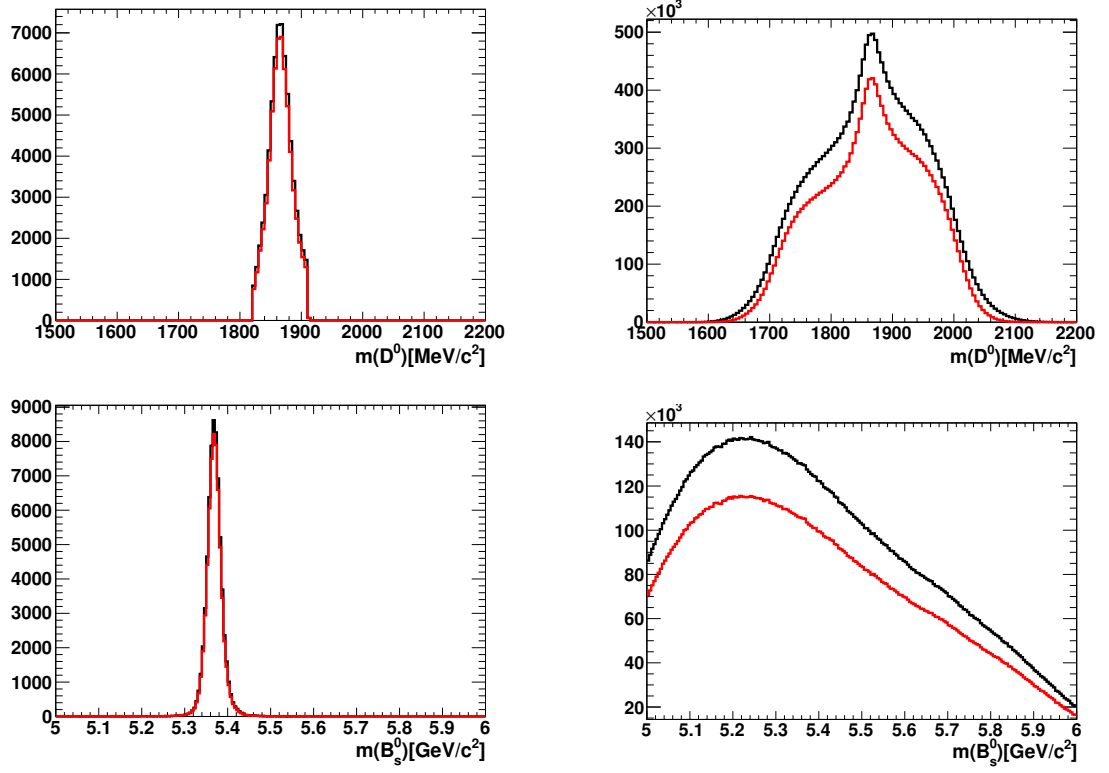
Figure 4.28: $\pi^0$ mass selection effects on $D^0$ mass constraint (top) and $B_s^0$ mass DTF for signal MC Run 2 (right) and background Data Run 2 (left).

# 4.5 Initial selections of the $D^0$ and $B_s^0$ meson candidates

Following the trigger and stripping selections, a separate treat is employed for the $K\pi\pi^0$ with the selection of the MVA variables and $\pi^0$ mass optimisation to strictly suppress the background coming from the $\pi^0$. Then we optimise and apply a few more cuts in common for the $B_s^0 \to \tilde{D}^{(*)0}\phi$ channel with $D$ meson decays to sub-modes: $K\pi$, $KK$, $\pi\pi$, $K3\pi$, $K\pi\pi^0$. This selections have been shown in the supporting document for the measurement of the branching ratio of the decay mode $B_s^0 \to \overline{D}^{(*)0}\phi$ [121]. The point is to have similar conclusion as much as possible, except when the specific behaviour of the background for the signal $D \to K\pi\pi^0$ requires particular treatment.

After trigger requirements, stripping lines has been established as given in Table 4.6 applied, the candidates of the decay of interest $D^0$ have to pass additional criteria in order to reduce the level of background without loosing too much of signal. For the former published analysis [9] the selections were designed to reduce the combinatorial background in $B_s^0 \to DKK$ decays, using the signal $B_d \to D\pi\pi$ as a training sample. For the present analysis, they have been systematically revisited and their usefulness justified and invalidated, while taking the $B_s^0 \to D^{(*)0}\phi$ and $D \to K\pi\pi^0$, signal and data upper sideband training samples as references. The set of pre-selections employed in the 2018 published analysis [9]. These selections are tuned for two-body $B_s^0 \to \tilde{D}^{(*)0}\phi$ analysis for the aim to maximise both the purity and the significance to obtain the best statistical significance for the signal channel of $B_s^0 \to \tilde{D}^{(*)0}\phi$. We want to keep the signal efficiency very high. The signal is modelled by MC signal simulation in the signal box and background from data sideband as defined in Section 4.4.1. The selections applied and optimised for the $B_s \to \overline{D}^0(K3\pi, K\pi, K\pi\pi^0, KK, \pi\pi)\phi$ signal and determined for both Run 1 and Run 2 are summarized in Table 4.16. These selections are rearranged according to the analysis shown with "$*$". While defining the selections we have adopted three selection cuts which were found not to be optimum for the specifically studied signal channel. These selection cuts will be explained in detail in the further.

- $\underline{B_s^0 \text{ mass window}}$ :

  The $B_s^0$ mass window is restricted to be within the range $m_{B_s^0} \in [4.75, 6.0]\,\mathrm{GeV}/c^2$ to search for the signal. The offline algorithm DecayTreeFitter (DTF) package [138] is used to refit the full pp collision. With this requirement, a large upper sideband is retained for both the combinatorial background training and in the final step to fit the combinatorial background with a large enough interval. Figure 4.29 shows the fit to the $B_s^0$ with and without the DTF mass constraint, where in the decay the four-momentum of the particles are recomputed and the $D^0$ and $\pi^0$ are constrained to their PDG mass. Geometrical constraints of the decay vertices of the $B$ and $D$ mesons have been taken into account. For the MC distribution (left distribution) without applying DTF constraint, the resolution improves about $35.96\,\mathrm{MeV}$, while

| Particle | Quantity | Criteria |
|---|---|---|
| $D^0$ | Invariant constrained mass $m_D$ | $\in [1765, 1965]$ MeV/$c^2$ |
| $B^0$ | Invariant mass $m_{\bar{D}^0 h^+ h^-}$ | $\in [4.75, 6.0]$ GeV/$c^2$ |
| $\Phi$ | Invariant mass $m_{KK}$ | $\in [987.354, 1077.354]$ MeV/$c^2$ |
| $\pi^0$ | | $\in [116.0, 160.0]$ MeV/$c^2$ |
| $D^0$ | Vertex $\chi^2$/nDof * | $< 4$ |
| | BPVIPCHI2 | $> 20$ |
| $D^0$ | $SDB = \frac{z_D - z_B}{\sqrt{\sigma_{z_D}^2 + \sigma_{z_B}^2}}$ * | $> 1.25$ (Run 1) |
| | | $> 1.05$ (Run 2) |
| $B^0$ | Vertex $\chi^2$/nDof | $< 4$ |
| | BPVIPCHI2 | $< 4$ |
| | $\cos(\theta_{dira})$(BPVDIRA) | $> 0.99995$ |
| $D^{*-}(2010)$ veto | $m_{D\pi} - m_D$ | $\notin [140.621;\ 150.221]$ MeV/$c^2$ |
| | PID requirements for $D^0$ daughters | |
| $\pi$ | $ProbNN_\pi \times (1 - ProbNN_K) \times (1 - ProbNN_p)$ | $> 2$ % |
| $K$ | $ProbNN_K \times (1 - ProbNN_\pi) \times (1 - ProbNN_p)$ * | $> 5$ % |

Table 4.16: Adapted pre-selections for this analysis are applied to the decay mode $B_s^0 \to \bar{D}^0(K^+\pi^-\pi^0)\phi$.

adding the four-momentum vectors of the $\phi$ daughters and $K\pi\pi^0$ (right distribution), resolution reduces to 14.92 MeV where the DFT is applied and the $D$, $\pi^0$ and vertices are constrained. Figure 4.30 gives the fit to the mass of $D^0$ with and without DTF mass constraint for the signal MC Run 2.
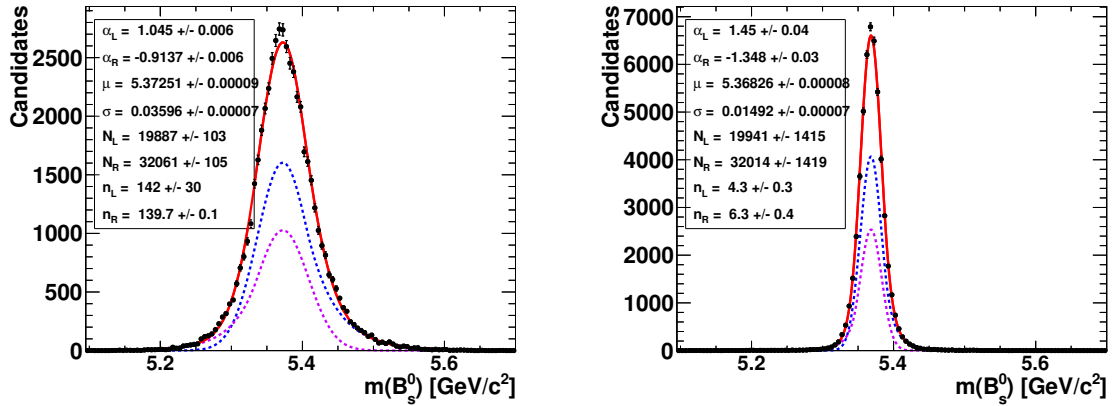


Figure 4.29: $B_s^0$ mass fit without (left) and with (right) DTF mass constrained for signal MC Run 2.
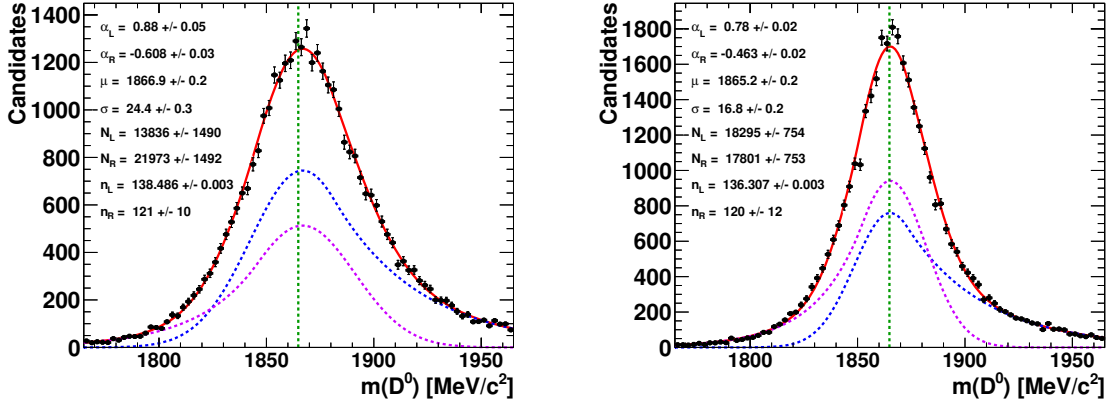
Figure 4.30: Fit to the $D^0$ mass without (left) and with (right) DTF mass constrained for signal MC Run 2. The resolution improves from $24.4\,\mathrm{MeV}$ to $16.8\,\mathrm{MeV}$ where DTF is applied.

- **Particle identification requirements for $D^0$ daughters for $K$ and $\pi$**

  Particle identification (PID) variables, the Probability Neural Network (ProbNN) are used to identify the information for each particle. Those variables provide a probability for each particle and as a probability, for the signal, it is mostly uniformed within the range $[0,1]$ for positive identification or it is peaked at 1 for the veto mode part of their definition below and peaking at 0 for background. They combined all the information coming from the Ring Imaging Cherenkov (RICH) detector for the discrimination between the charged particles like kaon and pion. $ProbNN_\pi$ and $ProbNN_K$ are used to identify $\pi$ and $K$ daughters from the $D^0$ decay. The probability for the charged pion candidate as $ProbNN_\pi > 2\%$ is defined and for the charged kaon, the probability from $ProbNN_K > 2\%$ to $> 5\%$ is changed. This is given in Eq. 4.18 and 4.22. The quantities in the equations are build such that the global variable operates as the product for the charged pion or kaon to be positively identified. While the PID hypotheses kaon, respectively pion, are vetoed as well as that of been identified as a proton. Figures 4.31 and 4.32 show these variables for MC signal and Data background and the cut setting is slightly raised up to further reduce the contamination from charged pions (see the right part in Figure).

$$PID_\pi = ProbNN_\pi \times (1 - ProbNN_K) \times (1 - ProbNN_p) > 2\% \qquad (4.18)$$

$$PID_K = ProbNN_K \times (1 - ProbNN_\pi) \times (1 - ProbNN_p) > 5\% \qquad (4.19)$$

93
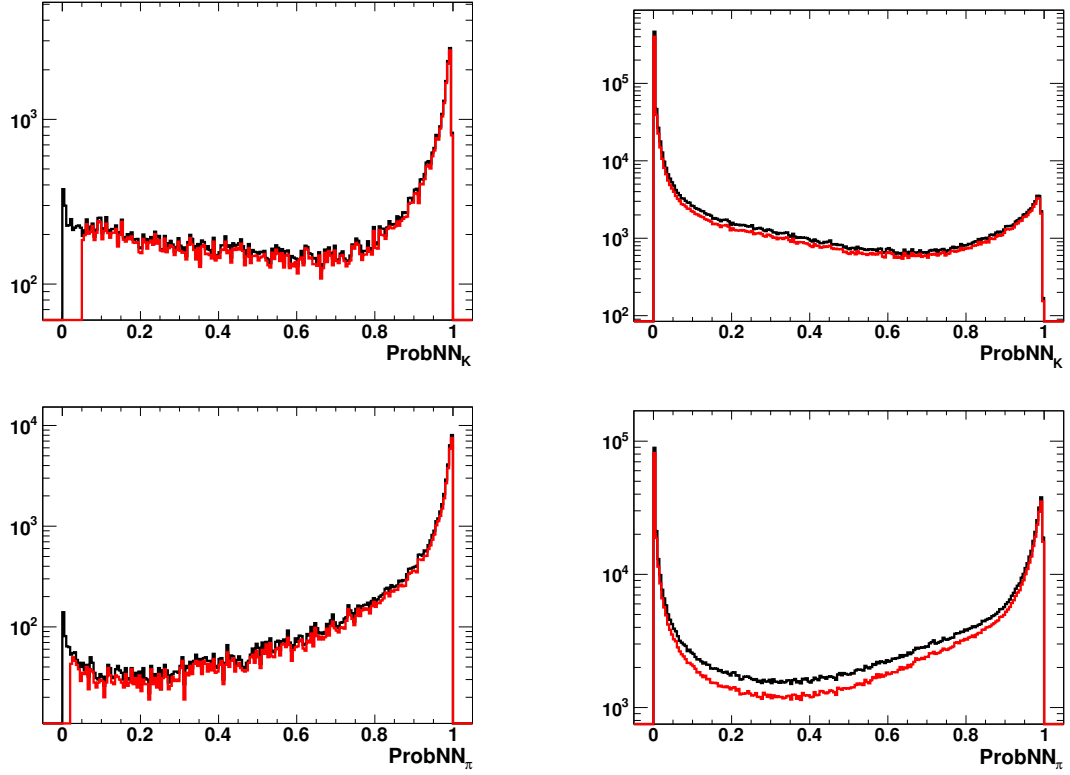
Figure 4.31: PID selection effects on $K$ (top) and $\pi$ (bottom) for signal MC Run 1 (left) and background Data Run 1 (right). The red curve is shown after both PID selections are applied to the charged pion and kaon in the $D$ meson decay.Plots are shown in logarithmic scale.

Figure 4.33 shows the plots after applying the $ProbNN_\pi$ and $ProbNN_K$ selections on the $B_s^0$ and $D^0$ DTF mass constrained for the MC and Data. The corresponding signal (MC signal box) and background (Data sideband) are listed in Table 4.17. From the results one can see that the difference between Run 1 and Run 2 is mainly in the rejection of non pions particles are more abundant in Run 1(see Figure 4.31). This is because from Run 1 to Run 2 the Aerogel layer which was in front of RICH1 was removed and this allows better background rejection at low momentum.
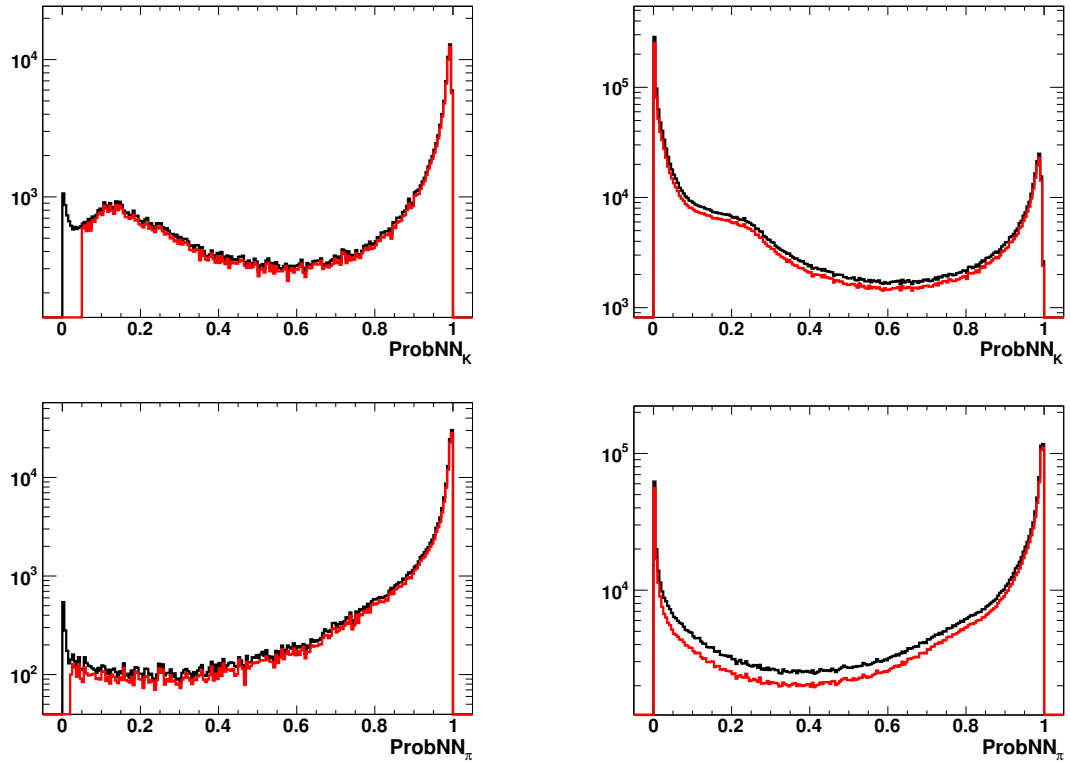
Figure 4.32: PID selection effects on $K$ (top) and $\pi$ (bottom) for signal MC Run 2 (left) and background Data Run 2 (right). The red curve is shown after both PID selections are applied to the charged pion and kaon in the $D$ meson decay. Plots are shown in logarithmic scale.
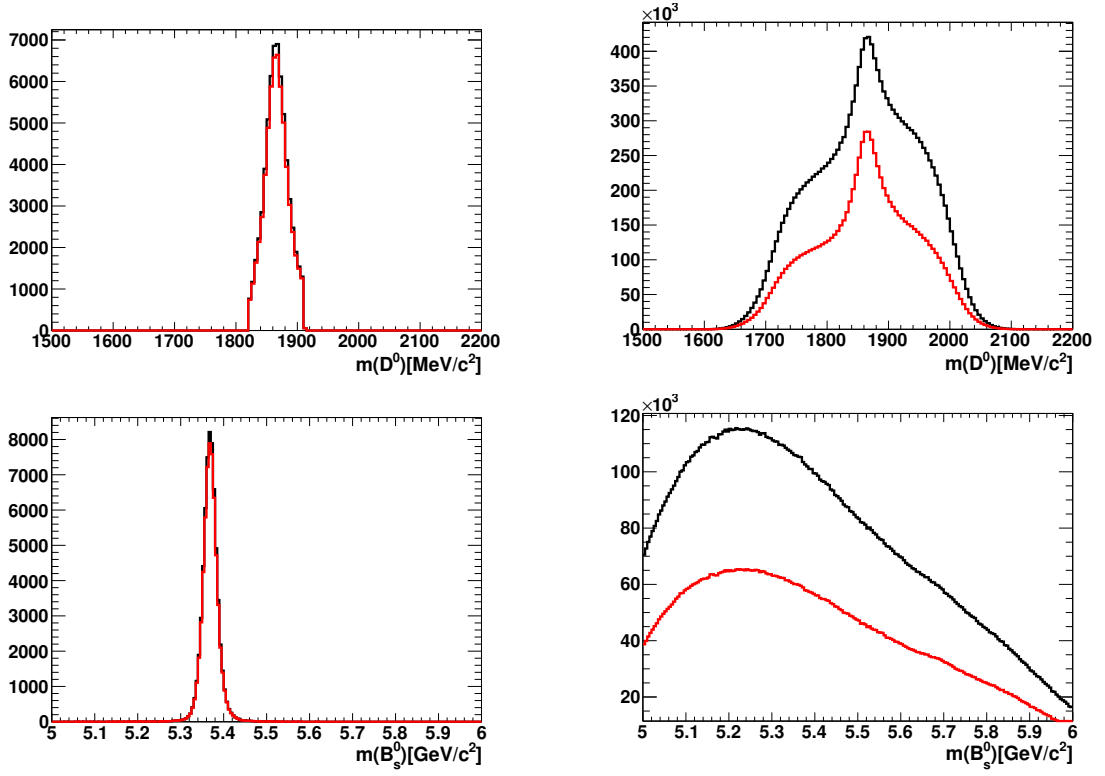
Figure 4.33: PID Kaon and $\pi$ selection effects on $D^0$ mass constraint (top) and $B_s^0$ mass with DTF (bottom) for signal MC Run 2 (right) and background Data Run 2 (left). Black curve represents before applying the $ProbNN_\pi$ and $ProbNN_K$ and red curves are shown after $ProbNN_\pi$ and $ProbNN_K$ selections.

| PID Selection | Run1 | Run2 |
|---|---|---|
| Signal Efficiency (MC) | 94.6% | 96.0% |
| Background rejection (DATA) | 78.0% | 55.0% |

Table 4.17: The corresponding signal efficiency (MC signal) and background rejection (Data sideband) for Run 1 and Run 2.

- $D^0$ **vertex** $\chi^2/nDof$ :

  The $\chi2/nDof$ (D vertex) variable gives the goodness of the fit is the per degree of freedom while combining the charged $K$ and the charged $\pi$ in the decay $D^0 \to K^-\pi^+\pi^0$ to compute the 3D position of the $D$ meson decay vertex. For the $D^0$ meson, a loose cut is applied on $\chi^2/nDof$ (D Vertex). Earlier selection was $\chi^2/nDof < 6$ but we think this selection on $D^0$ vertex is too loose, since it can be seen that in the right side of the Figure 4.34, it looks like there is a step at 4 for Data. The cut is tightened from $\chi^2/nDof < 6$ to $\chi^2/nDof < 4$ to have a better vertex quality and the gain on Signal/Background (S/B) ratio. The reason was investigated in the stripping and DaVinci code selection for what could be the source of such a step, but we found no reason why. The corresponding signal (MC signal box) and background (data sideband) are listed in Table 4.18.
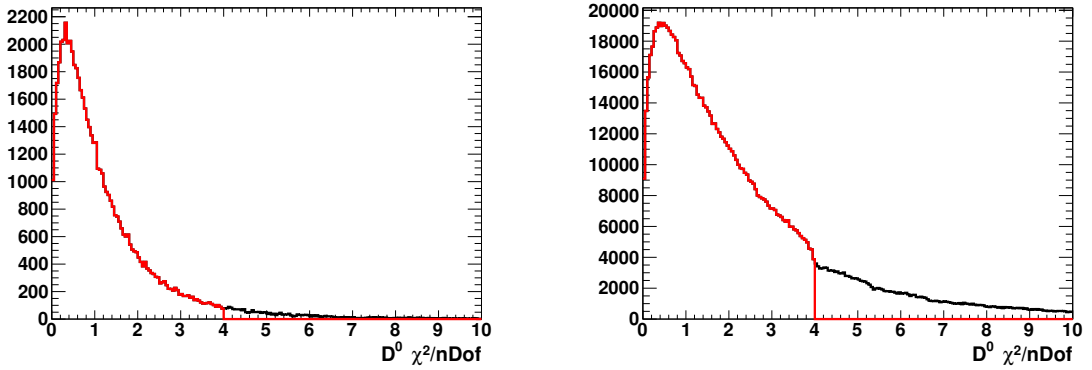


Figure 4.34: $D^0$ vertex $\chi2/nDof$ mass selection for signal MC Run 2 (right) and background Data Run 2 (left). Black curve represents before applying the $\chi^2/nDof$ and red curves are shown after $\chi^2/nDof$ selections.

Figure 4.35 shows the effects of the $D^0$ vertex $\chi2/nDof$ selection on the $D^0$ and $B_s^0$ masses before and after for the signal MC and background Data.
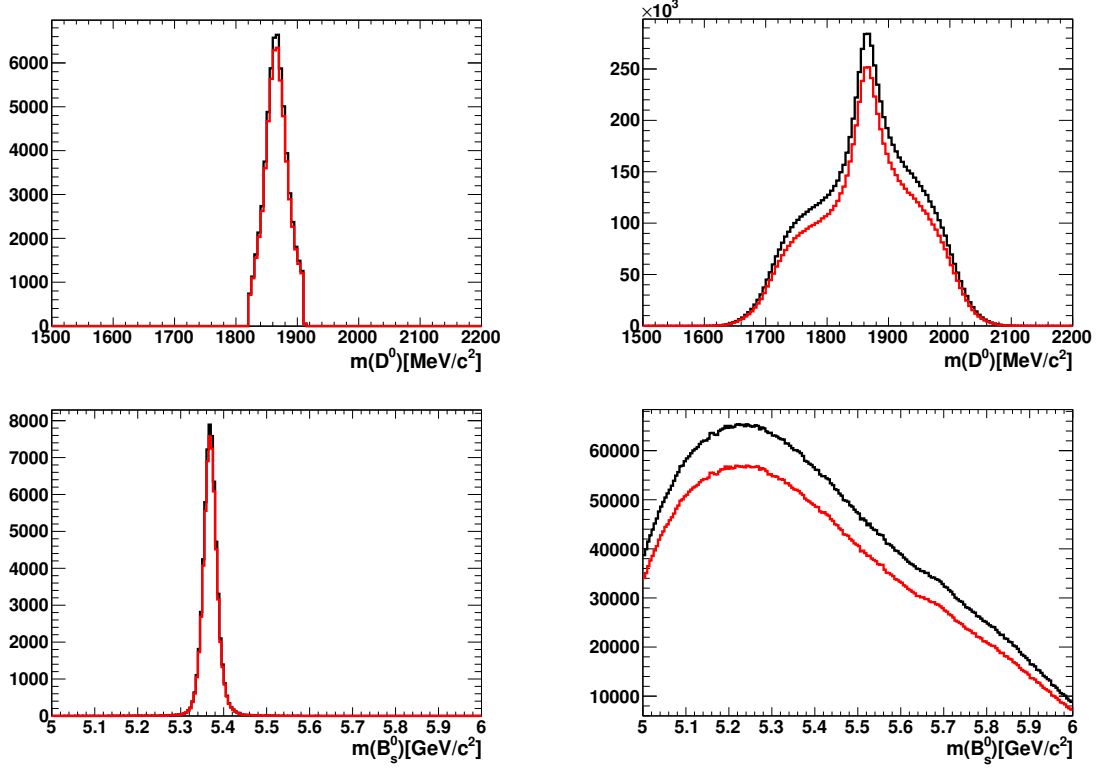
Figure 4.35: $D^0$ vertex $\chi2/nDof$ selection on $D^0$ mass constraint(top) and $B_s^0$ DTF mass for signal MC Run 2(right) and background Data Run 2(left). Black curve represents before applying the $\chi^2/nDof$ and red curves are shown after $\chi^2/nDof$ selection.

| $D^0 Vtx\chi2/nDof$ Selection | Run1 | Run2 |
|---|---|---|
| Signal Efficiency (MC) | 91.1% | 94.0% |
| Background Rejection (DATA) | 86.4% | 89.5% |

Table 4.18: The corresponding signal efficiency (MC signal) and background rejection (Data background) for Run 1 and Run 2.

- **$D^0$ B PV IP $\chi2$** :

  This selection defines the best (primary vertex) PV as a vertex, where the $D^0$ reconstructed candidates with the shortest transverse distance $IP\chi^2$. Impact Parameter (IP) is expected to be bigger for the $D^0$ particles originating from the secondary vertices. Figure 4.36 shows $D^0 BPV IP\chi2$ selection and in the Table 4.19, the corresponding signal (MC signal box) and background (Data sideband) are listed. The selection on DTF mass constrained of the $D^0$ and $B_s^0$ are shown in the Figure 4.37 for the signal MC and background Data.
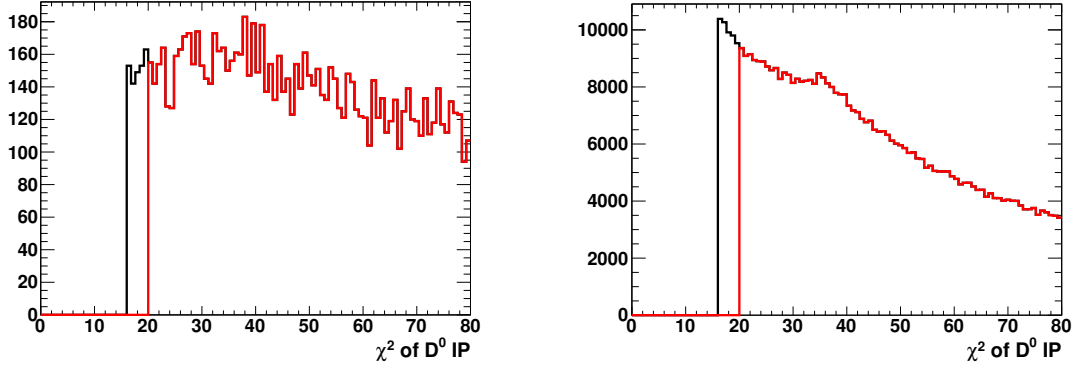
Figure 4.36: Selection on $D^0$ B PV IP $\chi^2$ for signal MC Run 2 (left) and background Data Run 2. Black curve represents before applying the $D^0 BPVIP\chi 2$ and red curves are after the $D^0 BPVIP\chi 2$ selection.
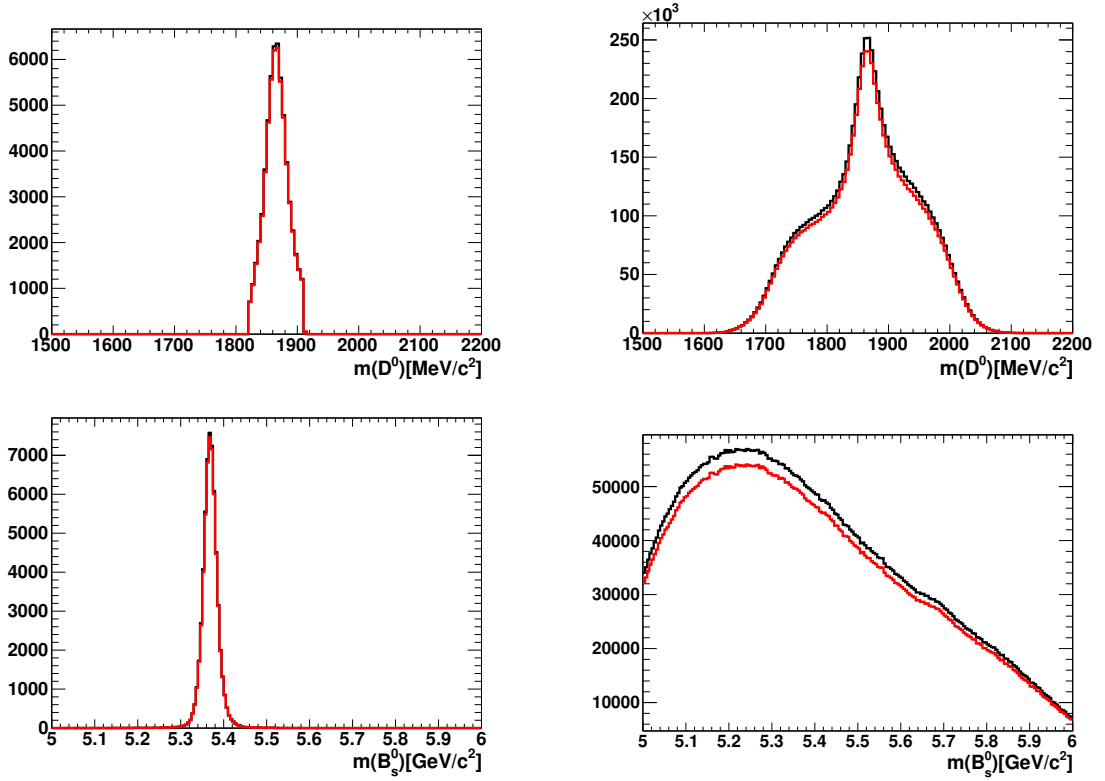


Figure 4.37: $D^0$ B PV IP $\chi^2$ selection on $D^0$ mass constraint (top) and $B_s^0$ DTF mass for signal MC Run 2 (left) and background Data Run 2 (right). Black curve represents before applying the $D^0 BPVIP\chi 2$ and red curves are after the $D^0 BPVIP\chi 2$ selection.

| $D^0 BPVIP$ Selection | Run1 | Run2 |
|---|---|---|
| Signal Efficiency (MC) | 98.9% | 98.6% |
| Background Rejection (DATA) | 95.4% | 95.0% |

Table 4.19: The corresponding signal efficiency (MC signal) and background rejection (Data background) for Run 1 and Run 2.

- $B_s^0 vertex \chi^2 / nDoF$ :

  The quantity $\chi^2$ is a measure for the quality of a performed fit e.g. how accurate the position of the PV could be determined. The $\chi^2/nDoF$ is used as a measure of quality, where $nDoF$ denotes the number of degrees of freedom. The $\chi^2/nDoF$ is required to be $\chi^2/nDoF < 4$ of the reconstructed $B_s^0$ decay vertex is given in Figure 4.38. The corresponding signal (MC signal box) and background (Data sideband) are listed in Table 4.20. Figure 4.39 shows the selection $B_s^0 vertex \chi^2/nDoF$ on $B_s^0$ mass.
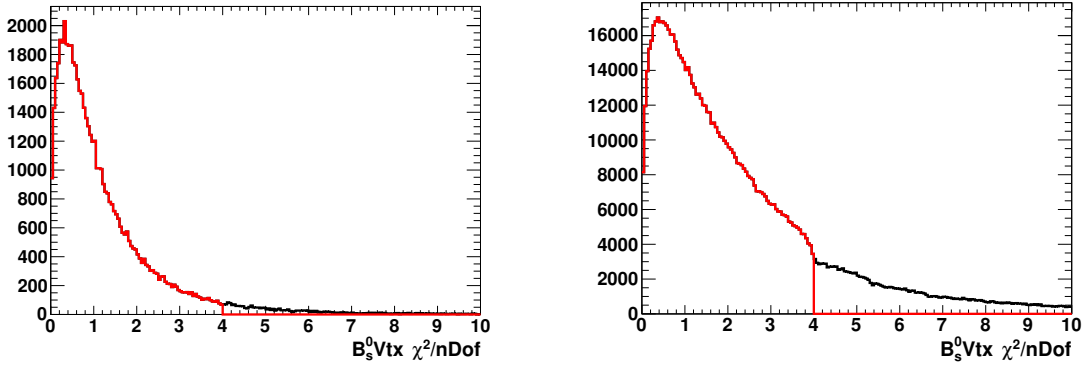


Figure 4.38: Selection on $B_s^0 vertex \chi^2/nDoF$ for signal MC Run 2 (left) and background Data Run 2 (right). Black curve represents before applying the $\chi^2/nDoF$ and red curves are after $\chi^2/nDoF$ selection.

| $B_s^0 Vtx \chi^2/nDof$ Selection | Run1 | Run2 |
|---|---|---|
| Signal Efficiency (MC) | 93.7% | 95.6% |
| Background Rejection (DATA) | 79.5% | 84.2% |

Table 4.20: The corresponding signal efficiency (MC signal) and background rejection (Data background) for Run 1 and Run 2.
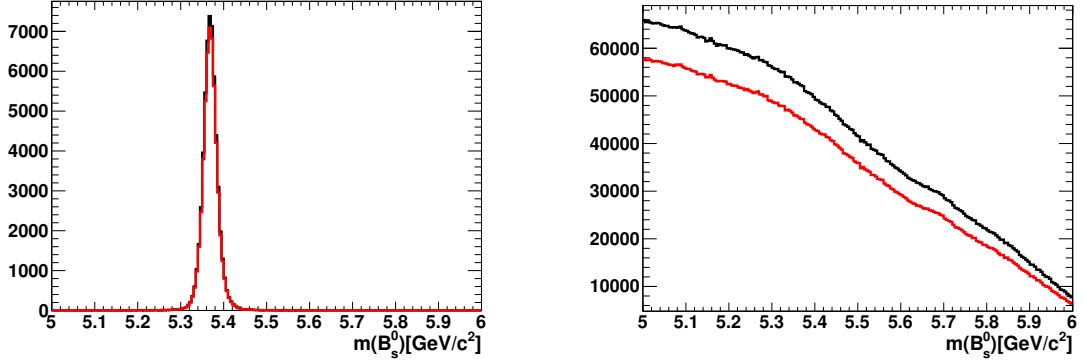
Figure 4.39: $B_s^0 vertex \chi^2/nDoF$ selection on $B_s^0$ DTF mass for signal MC Run 2 (left) and background Data Run 2 (right). Black curve represents before applying the $\chi^2/nDoF$ and red curves are after $\chi^2/nDoF$ selection.

- **The $B_s^0$ direction angle, $B_s^0 PV cos(\theta_{dira})$:**
  A selection is set on the $B_s^0$ direction angle ($cos\theta_{dira}$), which is defined as the cosine of the angle ($cos\theta_{dira}$) that may describe a possible deviation from the momentum direction of the particle and the direction of the flight from the best primary vertex to the decay vertex. A deviation from unity, means that there is a miss-alignment of direction of the reconstructed $B$ momentum with respect to its flight direction, determined by the $B$ vertex and PV positions. This mis-alignment may be due to wrong combinations of particles when reconstructing the $B_s^0$ candidate. Figure 4.40 shows the selection on the cosine of the direction angle of the candidate is tightened the direction angle to $cos\theta_{DIRA} > 0.99995$ (i.e. about 10 mrad) and the selection on $B_s^0$ DTF mass is shown in Figure 4.41. In the Table 4.21, corresponding signal (MC signal box) efficiency and background (Data sideband) rejection are listed.
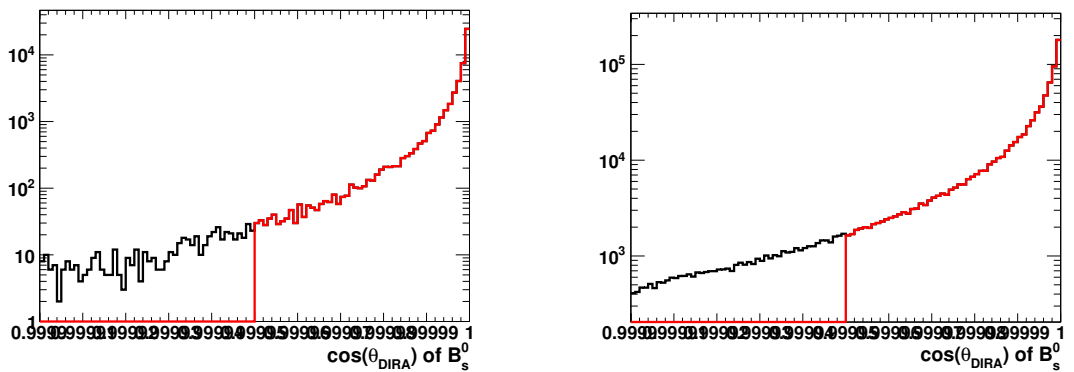


Figure 4.40: $B_s^0 PV cos(\theta_{dira})$ selection for signal MC Run 2 (left) and background Data Run 2 (right). Black curve represents before applying the $cos\theta_{DIRA}$ and red curves are after $cos\theta_{DIRA}$ selection.
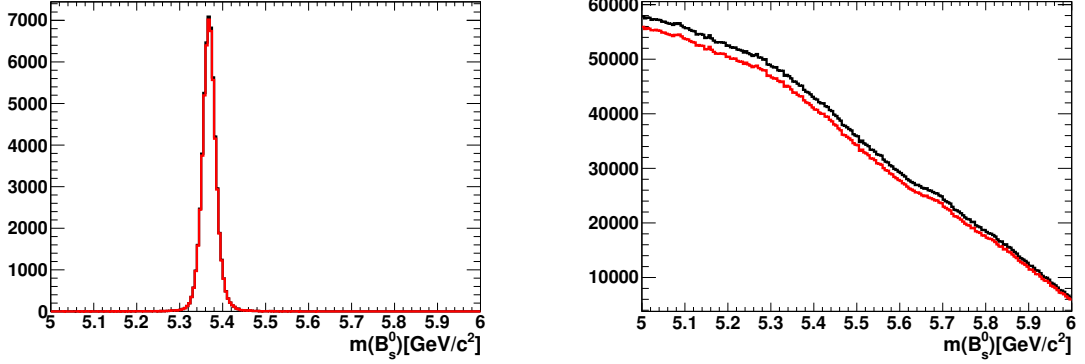
Figure 4.41: $B_s^0 PV cos(\theta_{dira})$ selection on $B_s^0$ DTF mass for signal MC Run 2 (left) and background Data Run 2 (right). Black curve represents before applying the $cos\theta_{DIRA}$ and red curves are after $cos\theta_{DIRA}$ selection.

| $B_s^0 cos\theta_{dira}$ Selection | Run1 | Run2 |
|---|---|---|
| Signal Efficiency (MC) | 98.8% | 98.9% |
| Background Rejection (DATA) | 94.8% | 94.5% |

Table 4.21: The corresponding signal efficiency (MC signal) and background rejection (Data background) for Run 1 and Run 2.

- $\underline{B_s^0 \text{ B PV IP } \chi2}$ :

  This selection defines the best PV as a vertex where the $B_s^0$ reconstructed candidates with the shortest transverse distance $IP\chi^2$. Figure 4.42 shows the decay of $B_s^0 \to D^0\phi$ and represents the IP of the $D^0$ meson. IP is expected to be very small for the $B_s^0$ particles originating from the primary vertices. The selection is represented in the Figure 4.43 and the corresponding signal (MC signal box) efficiency and background (Data sideband) rejection are listed in the Table 4.22.

| $B_s^0 BPVIP\chi2$ Selection | Run1 | Run2 |
|---|---|---|
| Signal Efficiency (MC) | 85.6% | 90.8% |
| Background Rejection (DATA) | 64.4% | 64.4% |

Table 4.22: The corresponding signal efficiency (MC signal) and background rejection (Data background) for Run 1 and Run 2.

- **Vetoing the $D^{*-}(2010)$ resonance**
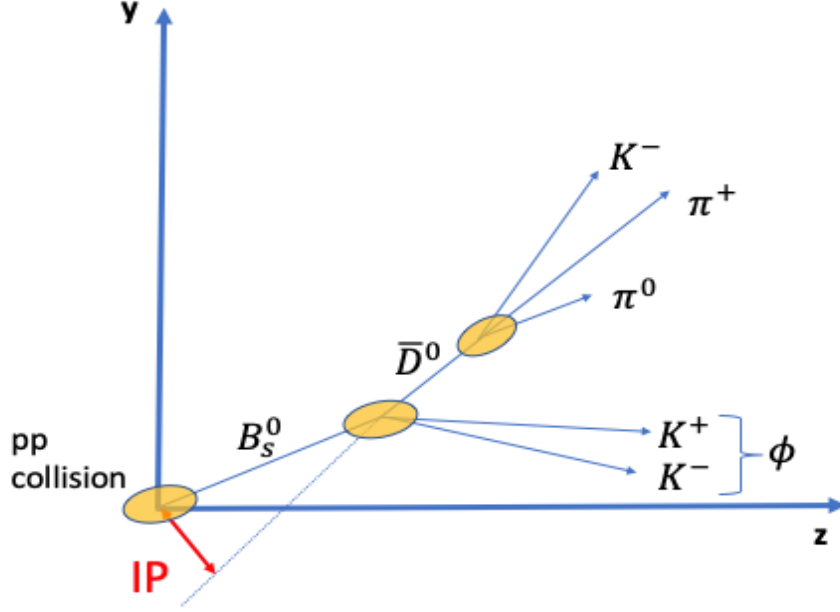
Figure 4.42: Diagram of the impact parameter (IP) of the $D^0$ meson of the decay of $B_s^0 \to D^0(K^-\pi^+\pi^0)\phi(K^+K^-)$.
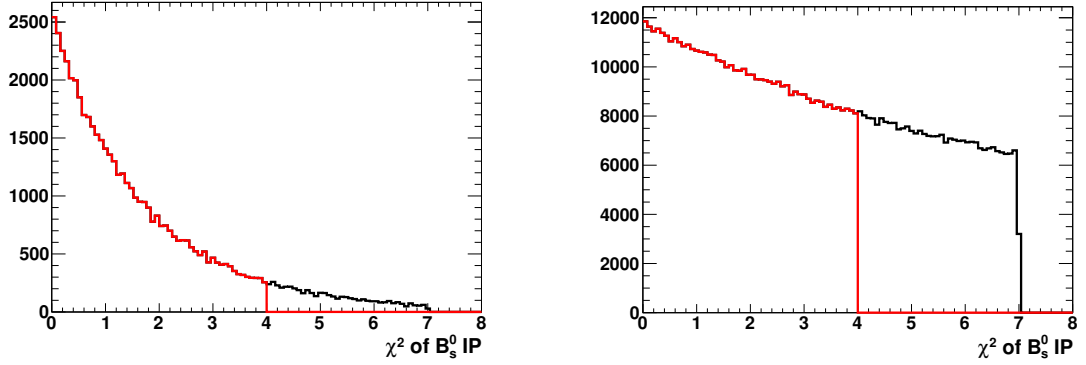


Figure 4.43: $B_s^0$ B PV IP $\chi 2$ selection for signal MC Run 2 (left) and background Data Run 2 (right). Black curve represents before applying the B PV IP $\chi 2$ and red curves are after B PV IP $\chi 2$ selection.

While vetoing $D^{*-}$, a genuine $B^0$ mesons decaying as $B^0 \to D^{*-}(\pi^+/K^+)$ is rejected, where $D^{*-}$ decays in a $\bar{D}^0\pi^-$ pair ($D^{*-} \to \bar{D}^0\pi^-$) and $\bar{D}^0 \to K^+\pi^-\pi^0$, such that $\pi^-(\pi^+K^+)$ pair is doubly or simply misidentified as a $K^+K^-$ pair. In order to reject those events, the four momentum vectors of the $K^+$ and $K^-$ candidates with the $\pi$ mass hypothesis are recomputed. The resulting $m_{D^{*-}} - m_{\bar{D}^0}$ mass difference distributions for Run 1 and Run 2 datasets are presented in Figure 4.44, where clear $B^0 \to D^{*-}\pi^+$ are visible. The veto is defined such that candidates with $m_{D^{*-}} - m_{\bar{D}^0}$

in $[140.621, 150.221]$ MeV/$c^2$ are rejected. The same procedure as that in PRD [89] is used. The branching ratio (BF) of the $B^0 \to D^{*-}(\pi^+/K^+) = (2.74 \pm 0.13) \times 10^{-3}$ and $(2.12 \pm 0.15) \times 10^{-4}$ while BF of $B^0_s \to \tilde{D}^{(*)0}\phi(KK) = (3.0 \pm 0.5) \times 10^{-5}$ (see PDG [18]) so one or two order of magnitude less. The corresponding signal efficiency (MC signal box) and background rejection (Data sideband) are listed in Table 4.23.
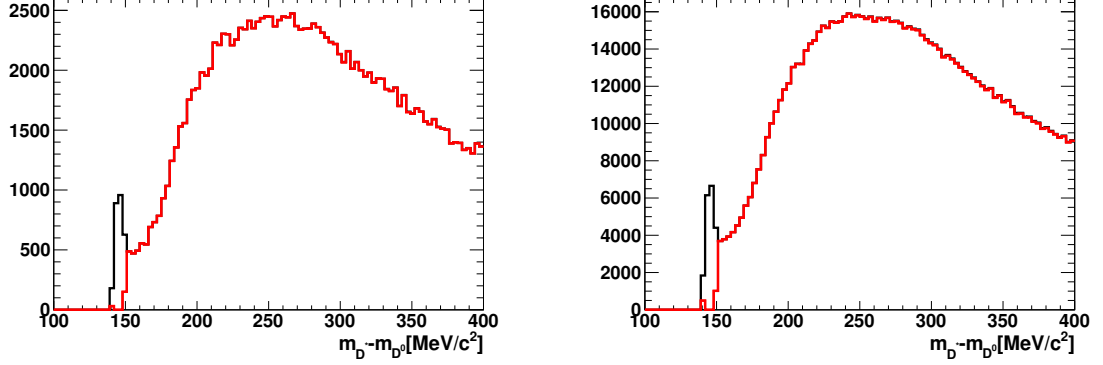


Figure 4.44: Distribution of the mass difference of $m_{D^{*-}} - m_{\bar{D}^0}$ before (black) and after (red) selections for Data Run 1 and Run 2.

| Veto $D^{*-}(2010)$ Selection | Run1 | Run2 |
|---|---|---|
| Signal Efficiency (MC) | 99.6% | 99.6% |
| Background Rejection (DATA) | 99.0% | 98.8% |

Table 4.23: The corresponding signal efficiency and background rejection for Run 1 and Run 2.

- **Selections on the $SDB$ for the charmless background**

  A selection criteria is used on $SDB$ which gives the significance of the distance in $z$ direction between $B$ and $D$ vertices. The variable is defined as follows:

  $$SDB = \frac{z_D - z_B}{\sqrt{\sigma^2_{z_D} + \sigma^2_{z_B}}} \tag{4.20}$$

  This selection helps to reduce the charmless background (events without a real $D^0$ meson) coming from the decay given in previous analysis [9] with Run1. It is applied in the sideband of the $D^0$ in the $m_{D^0 KK} \in [5.1, 6.0]$ GeV/$c^2$. And Figure 4.45 shows the SDB distribution before and after the selection for the MC and the Data.

  The selection was designed to measure the branching ratio of $B^0_s \to \bar{D}^0 K^+ K^-$ which was studied in the previous analysis [89]. The selection requirement optimised relative to that of the topologically similar, abundant and precisely measured decay

104
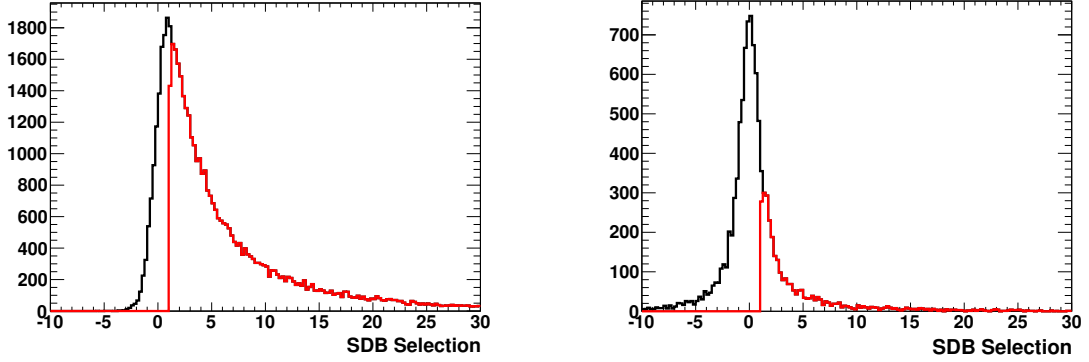
Figure 4.45: $SDB$ selection for signal MC Run 2 (left) and background Data Run 2 (right). For MC signal, one can clearly see that the right hand side are the $D$ meson is decaying at larger z values than the $B^0$ (due to boost in the beam direction). At zero one can see the z vertexing resolution, such that the distribution is an exponential (lifetime of the $D$) convoluted with a resolution function (Gaussian). For the Data the distribution is left and right side distributed and made of a mixture of prompt charm hadron originated from the PV and from charmless decay where the all particles are emitted at the $B$ vertex.

of $B^0 \to \overline{D}^0 \pi^+ \pi^-$ as a normalization channel. In this case the selections were optimised based on the $B^0 \to \overline{D}^0 \pi^+ \pi^-$ where the charmless background of the mode $B^0 \to \overline{D}^0 \pi^+ \pi^-$, $\overline{D}^0 \to K^- \pi^+$ was genuine as shown in the $m_{D_{\pi\pi}}$ distribution of charmless background in Figure 4.46 (taken from the published paper [139]). At that time this requirement was set as $SDB > 3$ which permits to select events with $D^0$ downstream to $B^0$ vertex to fight against the large charmless background and aimed to reduce as much as possible the systematic uncertainties. One can see from the Figure 4.46, without criteria on SDB, some events pile up in the $B^0$ signal region and with the requirement $SDB > 3$, peaking structure in the signal region $m_{D_{\pi\pi}}$ is removed. Distributions involve other criteria on SDB values were also given in the figure. In our case, since we are not optimising the signal channel $B_s^0 \to D^0 \phi$ against to the $B^0 \to \overline{D}^0 \pi^+ \pi^-$, we found that this requirement $SDB > 3$ caused too much loss of signal efficiency. Thus it is loosened because of the dealt with the signal low rate $B_s^0 \to \tilde{D}^{(*)0} \phi$ in the sideband of the $D$. As opposed to Branching fraction paper [121] for $B_s^0 \to D^0 (K\pi)\phi$, based on the maximum, SDB selection $SDB > 1$ is used for Run 1 and Run 2 (see Eq. 4.21). Figures 4.47 and 4.48 show the invariant mass distribution of the $B_s^0$ for MC and Data.

$$SDB = \frac{z_D - z_B}{\sqrt{\sigma_{z_D}^2 + \sigma_{z_B}^2}} > 3 \to > 1.25(Run1) \to > 1.05(Run2) \qquad (4.21)$$

It can be seen that there is no peaking $B$ background around the $B_s^0$ mass. This is because a charmless $B_s^0 \to D^0 (K^- \pi^+ \pi^0) \phi(K^+ K^-)$ state is really improbable.

105
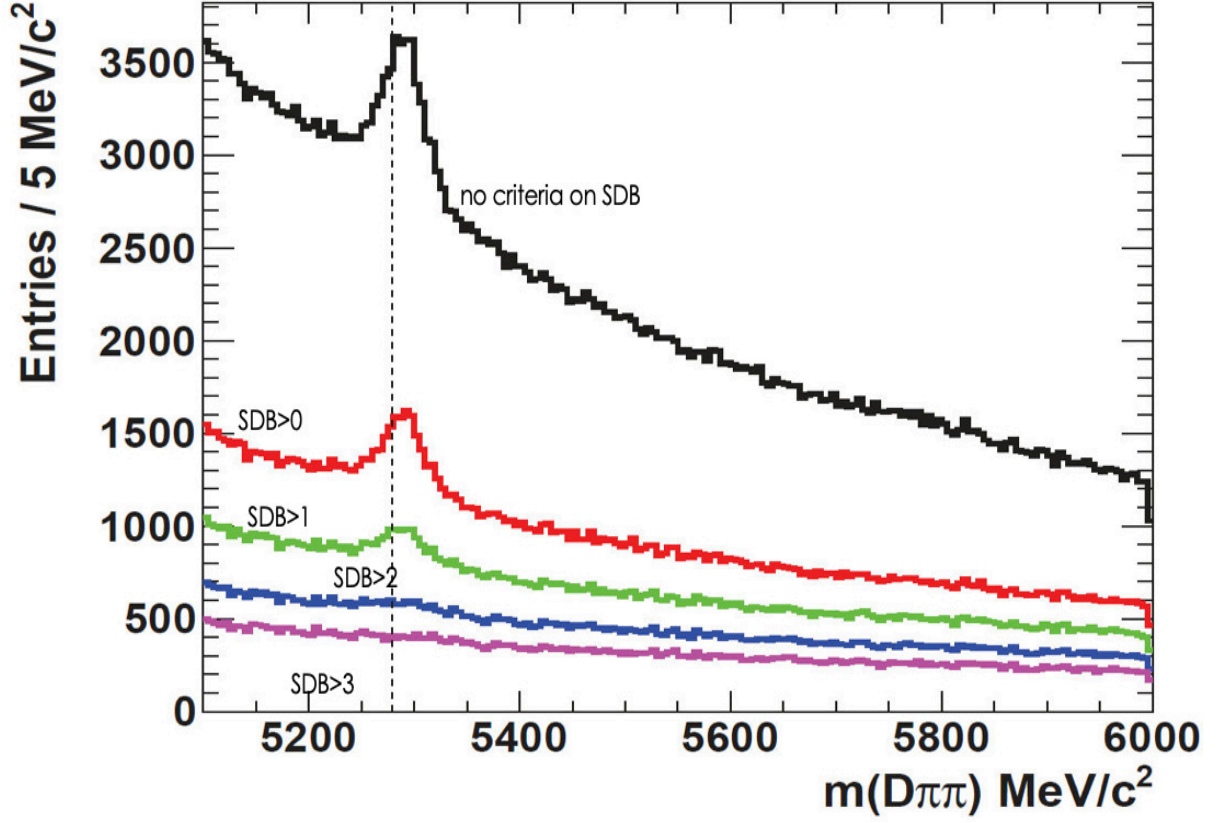
Figure 4.46: Distributions of the invariant mass $m_{D_{\pi\pi}}$ from $D\pi\pi$ data after initial selections for events in $D$ sidebands $m_D \in [1750; 1840] \cup [1890; 1980]$ MeV/$c^2$, with several requirements on $SDB$. In black no criteria on $SDB$, in red $SDB > 0$, green $SDB > 1$, blue $SDB > 2$ and magenta $SDB > 3$. The dashed line shows the $B^0$ mass, $m_{D\pi\pi} = 5279.58$ MeV/$c^2$.
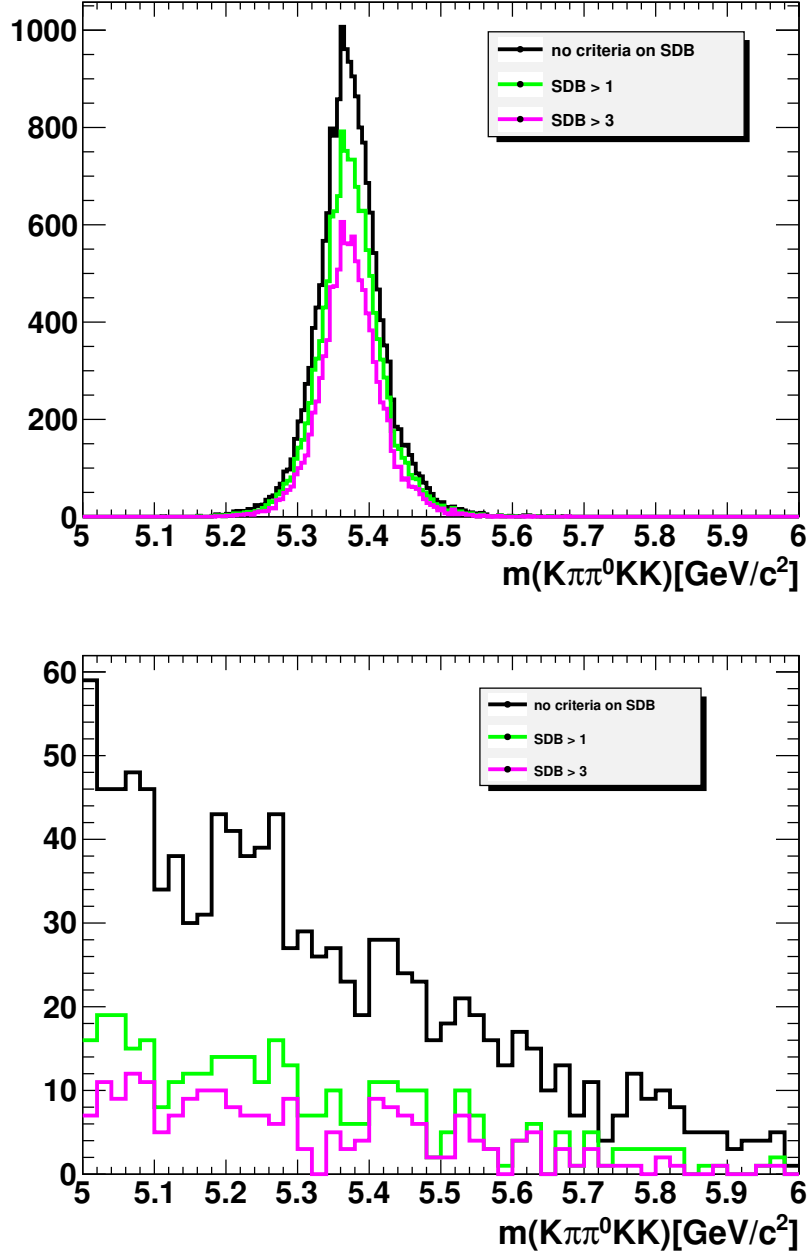
Figure 4.47: SDB selection on the invariant mass distribution of $B_s^0$ in the $D$ sidebands and $m_{KK} < 1080\,\mathrm{MeV}$ for signal MC Run 1 (top) and background Data Run 1 (bottom).
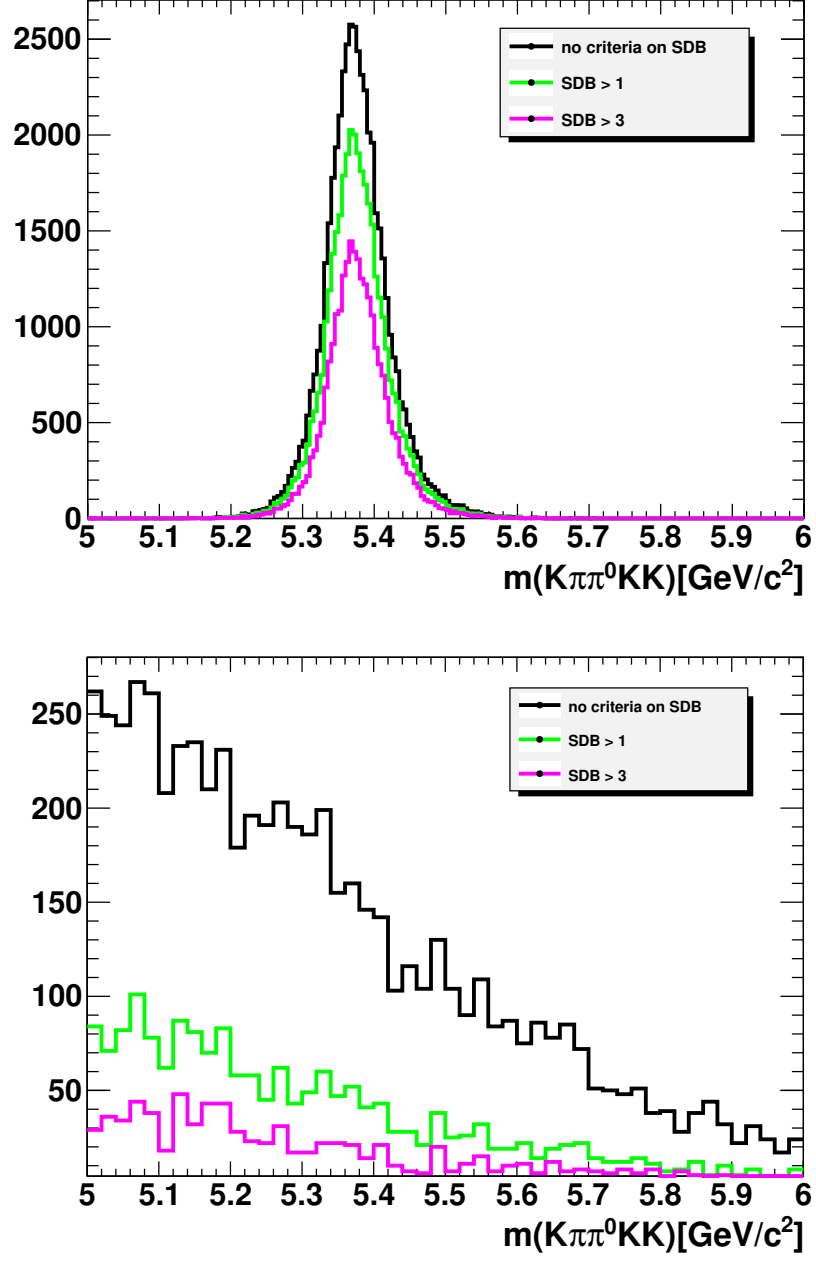
Figure 4.48: SDB selection on the invariant mass distribution of $B_s^0$ in the $D$ sidebands and $m_{KK} < 1080\,\text{MeV}$ for signal MC Run 2 (top) and background Data Run 2 (bottom).

Table 4.24 gives the signal efficiencies and the background rejections $SDB > 1.25$, $SDB > 1.05$ and Table 4.25 gives the corresponding results for $SDB > 1$ for MC and Data Run 1 and Run 2.

| | $K\pi\pi^0$ | |
|---|---|---|
| $SDB$ Selection | Run1 ($SDB > 1.25$) | Run2 ($SDB > 1.05$) |
| Signal Efficiency (MC) | 78% | 77% |
| Background Efficiency (DATA) | 32% | 29% |

Table 4.24: The corresponding signal efficiency (MC signal) and background rejection (Data sideband) when $SDB > 1.25$ for Run 1 and $SDB > 1.25$ for Run 2.

| | $K\pi\pi^0$ | |
|---|---|---|
| $SDB$ Selection | Run1 ($SDB > 1$) | Run2 ($SDB > 1$) |
| Signal Efficiency (MC) | 80.2% | 77.4% |
| Background Efficiency (DATA) | 38.9% | 34.6% |
| | $K\pi$ | |
| Signal Efficiency (MC) | 86.5% | |
| Background Efficiency (DATA) | 52.2% | |

Table 4.25: The corresponding signal efficiency (MC signal) and background rejection (Data background) when $SDB > 1$ for Run 1 and Run 2.

Table 4.26 gives the result for signal efficiency and the background rejection for $SDB > 3$

| | $K\pi\pi^0$ | |
|---|---|---|
| $SDB$ Selection | Run1 ($SDB > 3$) | Run2 ($SDB > 3$) |
| Signal Efficiency (MC) | 58.4% | 53.3% |
| Background Efficiency (DATA) | 19.6% | 14.5% |
| | $K\pi$ | |
| Signal Efficiency (MC) | 66.1% | |
| Background Efficiency (DATA) | 69.1% | |

Table 4.26: The corresponding signal efficiency (MC signal) and background rejection (Data sideband) for Run 1 and Run 2.

Figure 4.49 shows the SDB selection fit distributions for MC simulation and Data Run 1. On the right side of the MC distribution, there is two parts: one is the exponential part which counts for the lifetime of the $D^0$, tail of the distribution goes from 1 to 30 in the $x$ axis. The other part is the Gaussian part $\mu = 1.22$ of the distribution and this is the effect of the resolution on the vertexing z on the $D^0$ and $B_s^0$.

For Data Run 1, from the Figure 4.49 on the right side, it can be seen that this SDB distribution is not the same as it is in the sideband of the $D^0$. Gaussian distribution centered at $\mu = 0.294$. This is because of the association of all tracks coming from the Primary Vertex(PV) or $B_s^0$ vertex (the candidates are a mixture of combinatorial $D$ mesons with $KK$ pairs and the $D$ are produced at the PV and possibly charmless $B$ background with $B_s^0 \to K^- \pi^+ \pi^0 K^+ K^-$ final state see Figures 4.47 and 4.48.) And as seen in the Figure 4.49, there are two Gaussian distributions with tails that are modelled with the Crystal Ball (CB) function, one left and one right hand tails of the CB function. But the behaviour of the distribution is different, since in Data distribution, it doesn't have a long tail going to 30 because it is in the sideband of the $D^0 \to K^- \pi^+ \pi^0$. For Data we have the same resolution $\sigma = 1.388 \pm 0.007$ that we have in the signal MC.
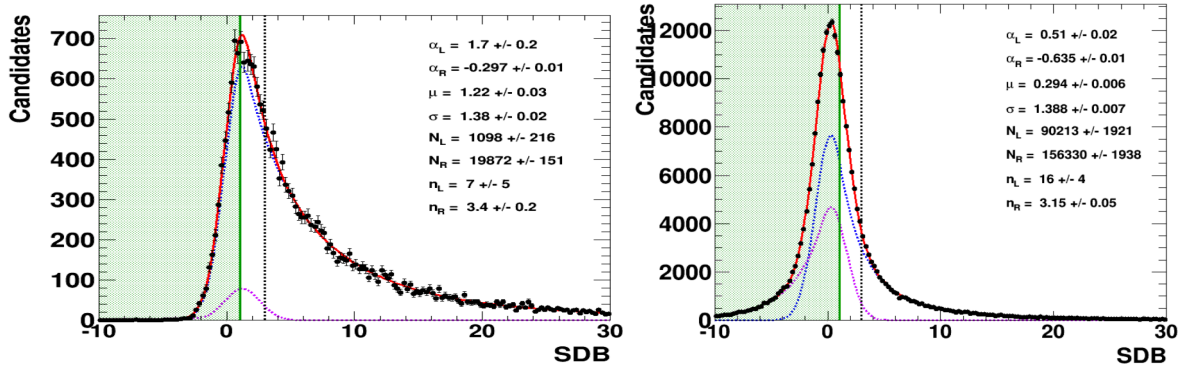


Figure 4.49: SDB selection on the signal MC on the left side and background Data on the right side for Run 1 at 1.25. Green part shows the excluded area for both MC and Data.

In the same way, Figure 4.50 shows the SDB fit results for Monte Carlo and Data Run 2. Either of the fit distribution for MC and Data Run 1&2, there is a vertical green line which cuts exactly the mean value at 1.25 for Run 1 and 1.05 for Run 2. But when the SDB is chosen to be $SDB > 3$ given with black dashed line on the fit distributions, it is seen that we cut much on the signal efficiency on the right side of the green line. That's why we loose too much signal efficiency with this selection and removing this cut to be $SDB \sim 1$ and the cut is fixed to be maximum of the signal distribution for both Run 1 and Run 2.

- **Initial particle identification requirements on $K^+ K^-$ from the $\phi$**

Before training the MVA, a very loose PID is employed to the two charged kaon to
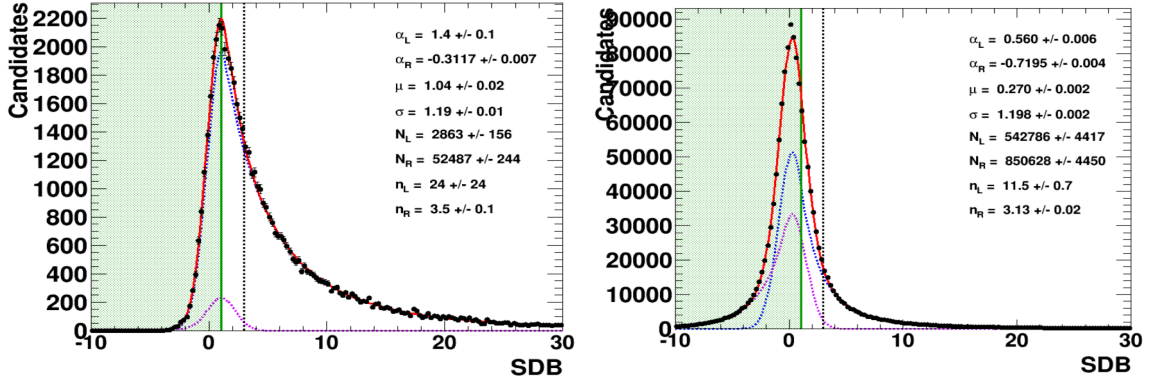
Figure 4.50: SDB selection on the signal MC on the left side and background Data on the right side for Run 2 at 1.05. Green part shows the excluded area for both MC and Data.

reconstruct the $\phi$ candidates $Prob_K > 0.1\%$ to remove genuine non-kaon background originated from charged pions (see peak at zero in Figure 4.31 and 4.32). Before developing the MVA discriminants, $B_s^0 \to \tilde{D}^0 \phi$ events from continuum combinatorial background is modelled from $B$ upper sideband (see Figure 4.4).

For the MVA training and to retain sufficiently large statistics for the continuum background, all the events are kept that satisfy $m_{KK} < 1700\,\mathrm{MeV}/c^2$ and that requirement will be tightened to $m_{KK} < 1800\,\mathrm{MeV}/c^2$ for the signal yield extraction. This will be discussed in the next sections.

$$PID_K = ProbNN_K \times (1 - ProbNN_\pi) \times (1 - ProbNN_p) > 0.1\% \qquad (4.22)$$

Selections on $K^+K^-$ pairs are displayed in Figure 4.51.
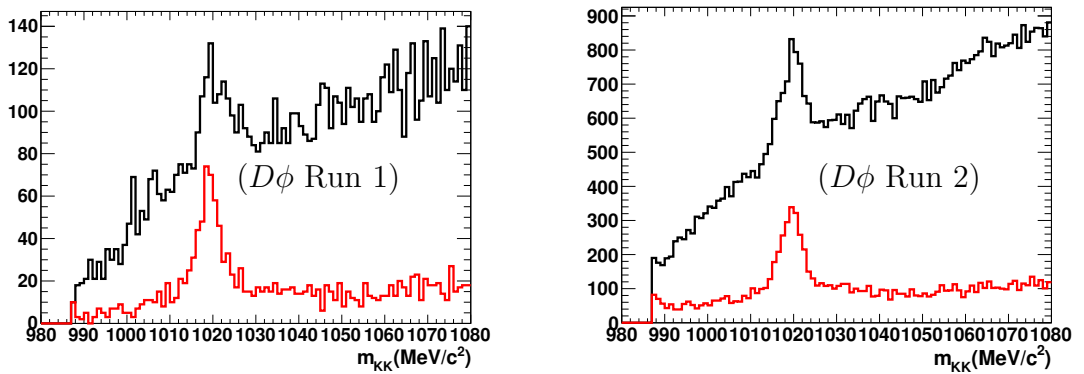


Figure 4.51: $K^+K^-$ pairs before (black) and after (red) applying PID selections.

111

## 4.6 Multivariate analysis (MVA) for $B_s^0 \rightarrow \tilde{D}^0 \phi$

Once all the selections have been applied on the sample, with these, a certain amount of combinatorial background and misidentified events have already been reduced by using variables which allow a separation between signal and background. As a final stage, a set of well-separating multiple input variables has been trained which are explained below to improve the signal and the background separation. A Multivariate Analysis (MVA) is used through ROOT (TMVA) package to discriminate signal from background contributions based on these input variables and during the training procedure, the total number of sample is split in two parts, where the half of the statistics is used in training and the other half is for testing. The first step is to define the six preliminary input variables taken into account:

- *Bdau_log_min_IPCHI2*: minimum Impact Parameter (IP) $\chi^2$ between the $K^\pm$ daughters of the $B_s^0$-meson candidate. The IP is computed with respect to the Primary Vertex (PV).

- *Bdau_log_min_PT*: minimum momentum between two $K^\pm$ daughters of the $B_s^0$-meson candidate transverse to the $pp$ beamline.

- *Tvar*: minimum cosine of the angle between the transverse momentum of the $D^0$ and the transverse momentum of the each $B_s^0$ daughters. This variable illustrated in Figure 4.52.
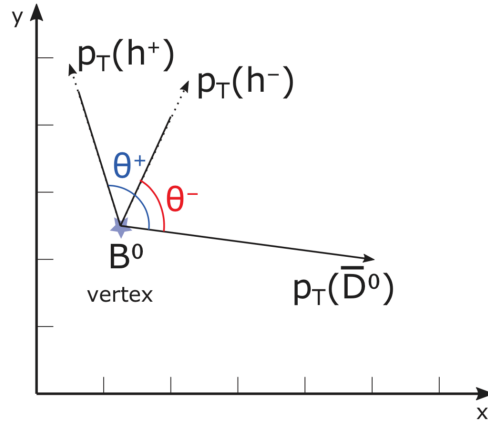


Figure 4.52: Cartoon defining the TVar discriminating variable.

- *B_IPChi2_OWNPV*: $\chi_{IP}^2(B)$ with respect to the most probable Primary Vertex (PV) of the $\chi^2$ of the impact parameter of $B$ meson.

- *D0_IPChi2_OWNPV*: ($\chi_{IP}^2(D)$) $\chi^2$ of the impact parameter of the $D^0$ candidate. Impact parameter is the transverse distance of the closest approach between the particle trajectory and its vertex.

- $BVtxProb$: probabilities of the $B_s^0$-meson daughters $\overline{D}^0$ and the $K^+$ and $K^-$ to originate from the same decay vertex. It includes not only the $\chi^2_{vtx}(B)$ of this geometrical fit but it also includes the number of degrees of freedom of this fit.

As studied earlier in the PRD paper [89], Fisher discriminant based on 4 (+1) of the 6 variables given above was used. In this study, once more these variables are revisited against to $B_s^0 \to D^{(*)0}\phi$ signal. Several MVA methods have been trained, tested and the best performance evaluation is carried out. Initially these preliminary 6 variables prescribed above are trained. After training and testing, Figure[ 4.53] shows the performance of the trained classifiers are given with the Receiver Operating Characteristics (ROC) curve where the background rejection rate as a function of the signal efficiency [140]. From this curve which gives the dependence of a signal efficiency versus the background rejection, an optimum cut point is obtained for three different types of MVA algorithm: Boosted Decision Tree (BDT), Gradient boosted decision tree (BDTG) and Linear discriminant Fisher and the best discriminant eventually.

Among these, Fisher discriminant has been chosen rather than BDT and BDTG (non-linear methods) which use many inputs. As can be seen, the performance of the Fisher doesn't show the best but give the similar performance with its less inputs and simplicity. Fisher discriminant is easy to understand and the classifier is more robust and uses only the width and the mean values which make it more stable. With this selection, the highest background rejection with the best possible signal efficiency is desired.
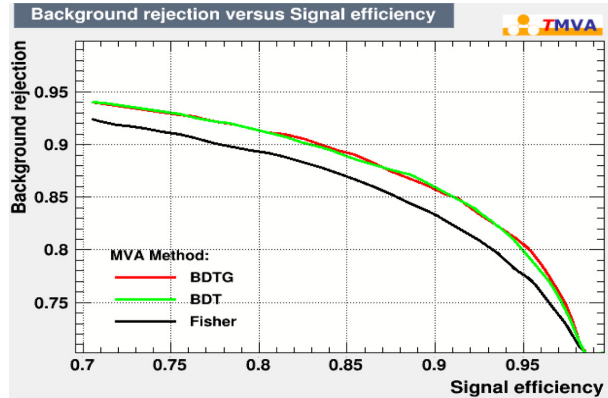


Figure 4.53: Background Rejection vs Signal Efficiency for BDTG, BDT and Fisher for the 5 discriminant variables studied in [89] for Data Run 2.

The input variables described in this part have not been taken as guarantee throughout this study and further selections which are used for different sub-decay modes of $D^0$ and those will be detailed in due course.

## 4.6.1   MVA for $D^0 \to K\pi\pi^0$

For the $K\pi\pi^0$, these intermediate discriminating variables are improved by adding new multiple variables for the $D^0 \to K\pi\pi^0$ mode which was already explained with

the initial MVA optimisation in Section 4.4.4. This is needed to maintain the signal efficiency very high and further to reduce the combinatorial background. While doing MVA optimisation, loose preselections are applied on the PID of the kaon pairs such that $ProbNN_K$ is required to be larger than 0.1% (to remove genuine charged pions) and they are required not to be qualified as muons by the muon PID system based on signal detected in the LHCb muon chamber (to reject the semi-leptonic $B$ decays).

The final set of input variables listed below are tested together with the 6 variables defined above. These variables are chosen according to their ranking as a function of discrimination power, some of them are newly added and some of them are changed with their other correlated variables according to the correlation matrix. Lattermost, the following discriminating variables have been chosen with the aim of improving the signal and background separation. These variables are explained below and Figure 4.56 displays the distributions of input variables chosen to train the MVA classifiers with the goal of improving the signal and the background separation precisely.

- $Ddau\_log\_min\_IPCHI2$: minimum $\chi^2$ impact parameter of the $D^0$ daughters.

- $Ddau\_log\_min\_PT$: minimum momentum of the $D^0$ daughters transverse to the beamline.

- $Ddau\_CosTheta$: the angle between the two $D^0$ daughters in the transverse plane.

- $D0mass\_const$: this discriminating variable is the earlier selection cut that has been revisited and used in the MVA. The mass of the $D^0$ is computed with the constraints of the PV and $\pi^0$ is constrained to its PDG mass. The invariant mass distribution of $D^0$ constraint mass is not the same for the signal in MC and Data. It is need to be corrected in MC, so it looks like the Data. For this, the smear on the Gaussian is used. With smear MC, the position of the reconstructed mass is recomputed event by event and the resolution is corrected. The $D^0$ mass constrained distribution is smeared and shifted in MC with respect to the Data displayed in Figures 4.54 and 4.55 for Run 1 and Run 2. Summary Tables 4.27 and 4.28 gives the parameters before and after smearing for MC and Data Run 1 and Run 2, respectively.
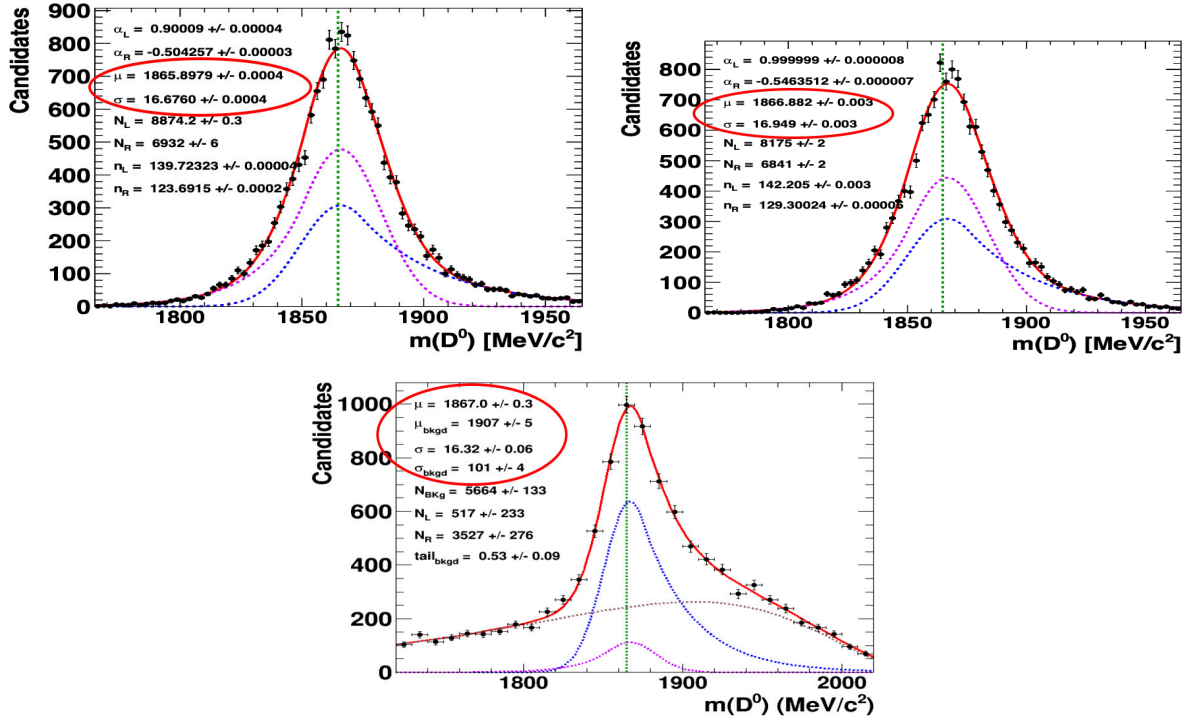
Figure 4.54: (Upper left) shows $D^0$ mass distribution before smear&shift, (Upper right) after smear&shift in MC (better resolution) with respect to the Data (bottom) for Run 1.



Figure 4.55: (Upper feft) shows $D^0$ mass distribution before smear&shift, (Upper right) after smear&shift in MC with respect to the Data (bottom) for Run 2.

|  | Unsmear MC Run 1 | Smear MC Run 1 | DATA Run 1 |
|---|---|---|---|
| Central Value ($\mu$) | 1865.9±0.00 | 1866.9±0.00 | 1867.0±0.3 |
| Resolution ($\sigma$) | 16.7±0.00 | 16.9±0.00 | 16.3±0.06 |

Table 4.27: Comparing results for the $D^0$ DTF smeared and un-smeared MC with Data for Run 1.

|  | Unsmear MC Run 2 | Smear MC Run 2 | DATA Run 2 |
|---|---|---|---|
| Central Value ($\mu$) | 1865.2±0.00 | 1867.2±0.00 | 1867.3±0.3 |
| Resolution ($\sigma$) | 15.8±0.00 | 18.51±0.00 | 18.09±0.1 |

Table 4.28: Comparing results for the $D^0$ DTF smeared and un-smeared MC with Data for Run 2.

- *DVtxProb*: This variable is preselection which is revisited. It gives the probabilities of the $D^0$-meson daughters originate from the same decay vertex. It includes not only the $\chi 2$ of this geometrical fit but also it includes the number degrees of freedom of this fit. In Figure 4.56 the distribution of this variable is displayed.

Several MVA methods are trained: Fisher discriminant, the Boosted Decision Tree (BDT) and Multilayer Perception Neural Network (MLP). The linear correlation matrices of the discriminating variables are presented in Figure 4.57 regarding the both signal and the background. There is no strong correlation observed among the input variables. This yields a powerful classifier which gives a generous separation between signal and background. One can see that in Figure 4.58 among the performance of the trained classifiers, the MLP classifier is chosen and used to classify events in data samples with signal and background composition.
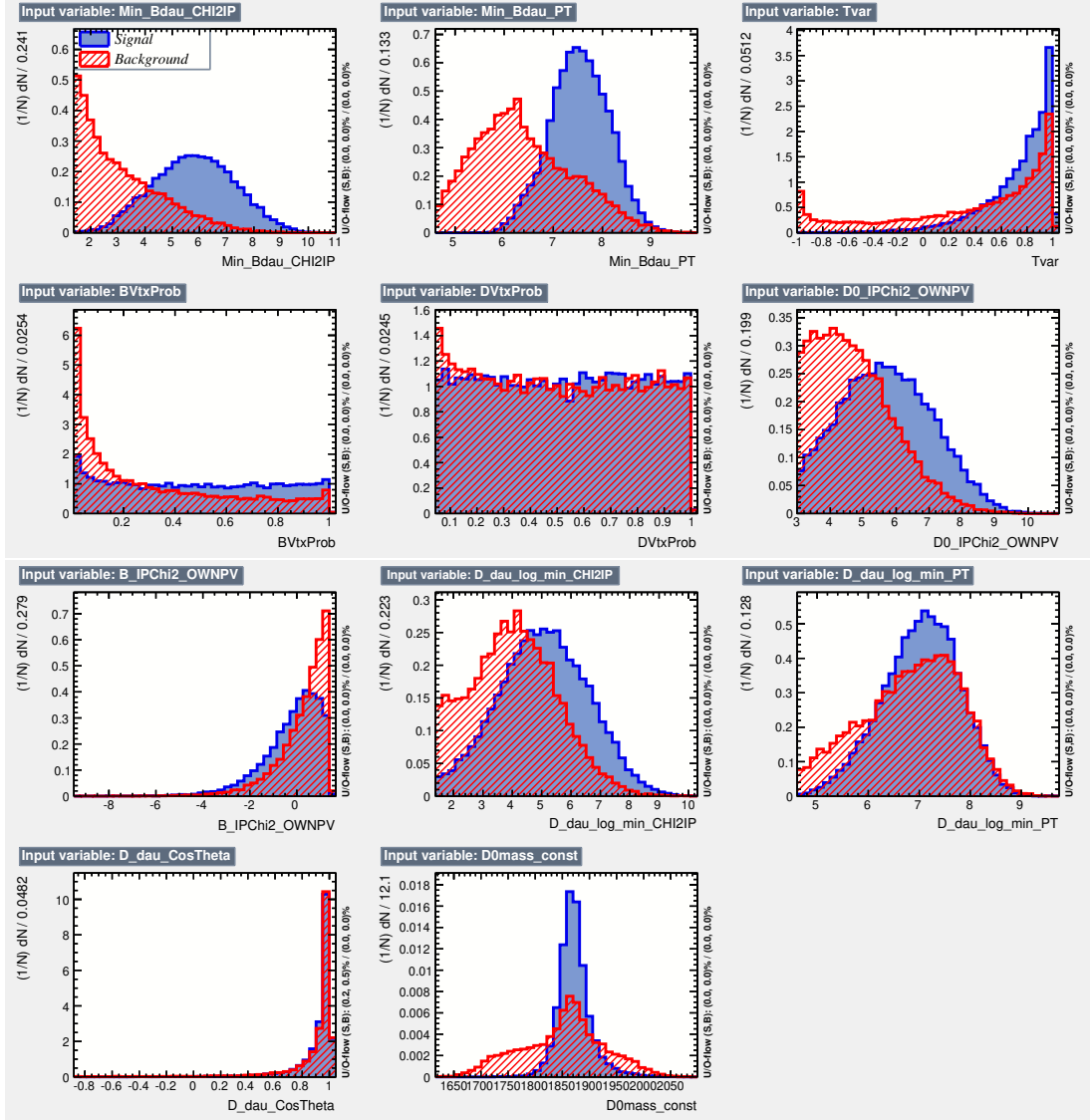
Figure 4.56: Comparison between the signal and the background distributions of final input variables used to train MVA as the signal is in blue and the background is in red. The signal training sample is obtained for MC simulated event in the $B$ signal box and the background from data with candidates in the upper $B$ sideband.
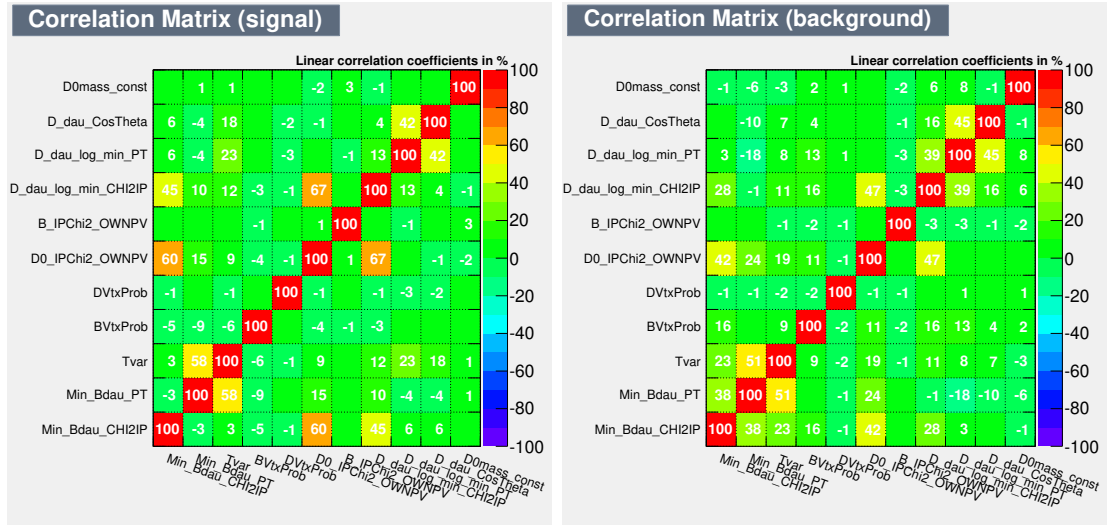
Figure 4.57: Linear correlation matrices for the final eleven input variables used in the MVA. Indicating linear correlation coefficient percentages between each pair of variables for both the signal MC (left) and the background Data (right).
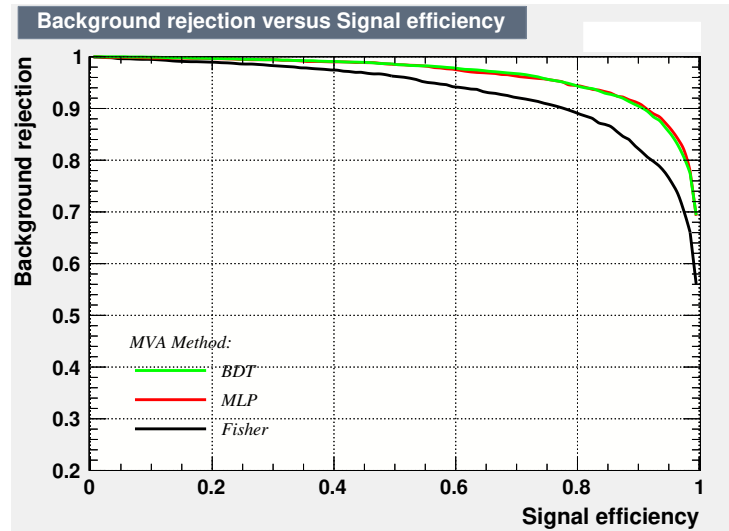


Figure 4.58: The signal efficiency versus background rejection for different classifiers. The ROC curve for the final model.

The MLP classifier which has a better performance than the Fisher and it is as good as BDT which is more complicated. In the Figure 4.56 which shows the input variables distribution, one can see that the last distribution of the $D^0$ mass constraint, there is background on the left and the right side of the signal. MLP gives the best performance with the less parameters and simple systematics to be handled and move the background on the left and the right side of this mass variable. Table 4.29 gives the importance of each variable from the high ranking to less ranking.

| Variable | MVA MLP Ranking | Separation |
|---|---|---|
| $Bdau\_log\_min\_IPCHI2$ | 1 | $4.690 \times 10^{-1}$ |
| $Bdau\_log\_min\_PT$ | 2 | $3.955 \times 10^{-1}$ |
| $D0mass\_const$ | 3 | $2.315 \times 10^{-1}$ |
| $Tvar$ | 4 | $1.430 \times 10^{-1}$ |
| $D0\_IPChi2\_OWNPV$ | 5 | $1.258 \times 10^{-1}$ |
| $Ddau\_log\_min\_IPCHI2$ | 6 | $1.047 \times 10^{-1}$ |
| $BVtxProb$ | 7 | $8.677 \times 10^{-2}$ |
| $B\_IPChi2\_OWNPV$ | 8 | $5.660 \times 10^{-2}$ |
| $Ddau\_log\_min\_PT$ | 9 | $3.777 \times 10^{-2}$ |
| $Ddau\_CosTheta$ | 10 | $4.947 \times 10^{-3}$ |
| $DVtxProb$ | 11 | $2.189 \times 10^{-3}$ |

Table 4.29: The separation power for the 11 variables used to train the MLP, listed in order of the ranking of the variables of $K\pi\pi^0$ for Run 2.

The classifier output distribution for the classifiers Fisher, BDT and MLP are given with Figure 4.59 show the superimposed response of training and testing samples. From this test it can be seen this MLP response is same for both training and the test sample, there is no significant over-training.

Furthermore, the cut is applied to the discriminant, Figure 4.60 shows optimal cut value on the MLP discriminant to obtain the best statistical efficiency and the background rejection. The Table 4.30 gives the optimum cut values ($\frac{S}{\sqrt{S+B}}$) which is applied on the MLP discriminant and it also shows the efficiency for the signal and the rejection for the background with this selection. From the Figure 4.60, the signal efficiency is chosen to be 95% and reject 82% of the background for Run 1, and for Run 2 signal efficiency is 95% vs 87% background rejection with the optimal cut value.
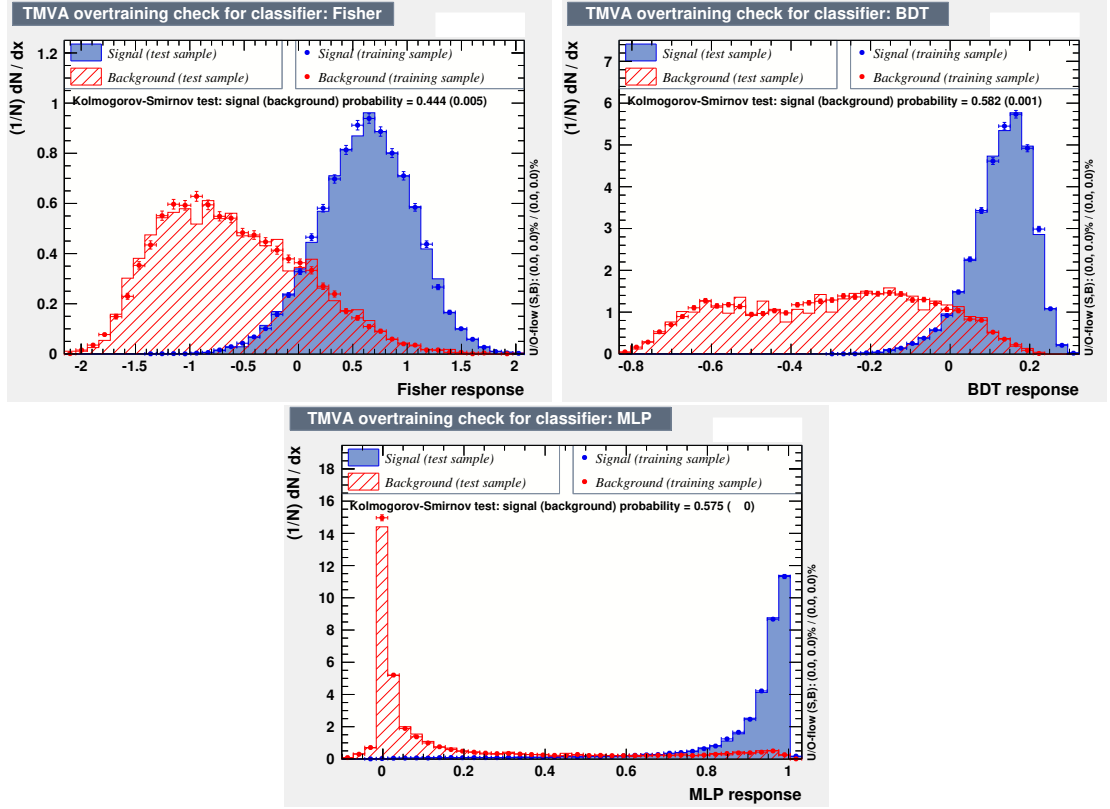
Figure 4.59: The classifier response for Fisher, BDT and MLP for Run 2. Signal test sample is represent by solid histogram and background is given by the dashed histogram. Training samples are given by the data points for both the signal and the background events from the upper mass sideband for Run 2.
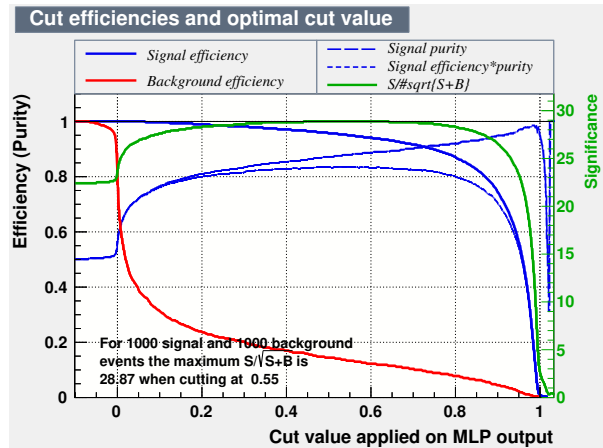


Figure 4.60: The Signal efficiency in blue and the background rejection in red in function of the optimal cut value applied on MLP discriminant.

Figure 4.61 shows the mass spectrum of the $\phi$ and $B_s^0$ after all the selections have

| dataset | MLP cut value | Signal eff. | Bkgd reject. |
|---------|---------------|-------------|--------------|
| Run 1   | 0.65          | 95 %        | 82 %         |
| Run 2   | 0.54          | 95 %        | 87 %         |

Table 4.30: The signal and the background efficiency when cutting on MLP for Run 1 and Run 2.

been optimised. From the $\phi \to K^+K^-$ mass distribution, it can be seen that there is a clear peak at the nominal mass of the $\phi$ resonance $\phi(1020)$. Bottom plot gives the mass spectrum of $B_s^0 \to D\phi$ candidate and from the plot $B^0 \to DKK$ and $B_s^0 \to DKK$ signals can be seen given with the dashed pink and blue lines respectively. This includes the $K^+K^-$ pair in the mass window ($m_{KK} \in [2m_K, 2m_K + 90] \,\mathrm{MeV}/c^2$) and $m_{KK} = 987.354 \,\mathrm{MeV}/c^2$. In order to separate the signal from the background clearly and improve the signal efficiency, sPlot technique is used [126]. This will be explained later in detailed.

## 4.7 Particle identification requirements on $K^+K^-$ from $\phi$

After MLP optimisation, a tighter PID cut is applied on two kaons which is used to reconstruct the $\phi$. A cut on $Prob_K$ at 7% is applied on both tracks inherited from [121]. This criteria has been optimised for the mode $B_s^0 \to D^{*0}(K\pi)\phi(K^+K^-)$. The same criteria is used for the $K\pi\pi^0$ sub-decay mode in order to reduce as much difference as possible with respect to the reference mode $D \to K\pi$.

The statistical significance $Q = \frac{S}{\sqrt{S+B}}$ is optimised by using signal $B_s^0 \to \overline{D}^0(K\pi)\phi$ MC and Data upper sideband region $m_{DKK} \in [5600, 6000] \,\mathrm{MeV}/c^2$ where events with one or two $\pi \to K$ mis-identification are situated. For the simplicity, it is decided to use $Prob_K > 7\%$ for both Run 1 and Run 2 Data. Figure 4.62 shows the $m_{DKK}$ (with and without a cut on the $\phi$-mass window, respectively) and $m_{KK}$ distributions before and after the optimised PID cuts on $KK$ for Run 1 and Run 2.

## 4.8 Veto $D_s^- \to \phi\pi^-$

Since we reconstruct the final state of $B_s^0 \to D^{0(*)}(K\pi\pi^0)\phi$, there is a kind of background originated from the decay of $B_s^0 \to D_s^+\rho^-(\pi^0\pi^-)$, where $D_s^+$ decays to $\phi\pi^+$ which replicate the signal. The $D^*$ candidates can be from $B_s^0 \to D_s^+\rho^-(\pi^0\pi^-)$, and contribute to signal yields since it has a true $\phi$ and $B_s^0$ but a fake $D^0$. The branching ratio of the mode is $\mathcal{B}(B_s^0 \to D_s^+\rho^-(\pi^0\pi^-)) = (6.8 \pm 1.4) \times 10^{-3}$ [18]. This background is vetoed with the reconstruction of the $D_s^+$ mass by $K^+K^-\pi$ mode using kaons from $\phi$ and $\pi$ from $D^0$ and veto the events in the mass window $m_{K^+K^-\pi} \in [1900, 2050] \,\mathrm{MeV}/c^2$. The candidates in the mass window is displayed in Figure 4.64 and the Figure 4.63 shows the $m(K^+K^-)$ candidates before MLP selection.
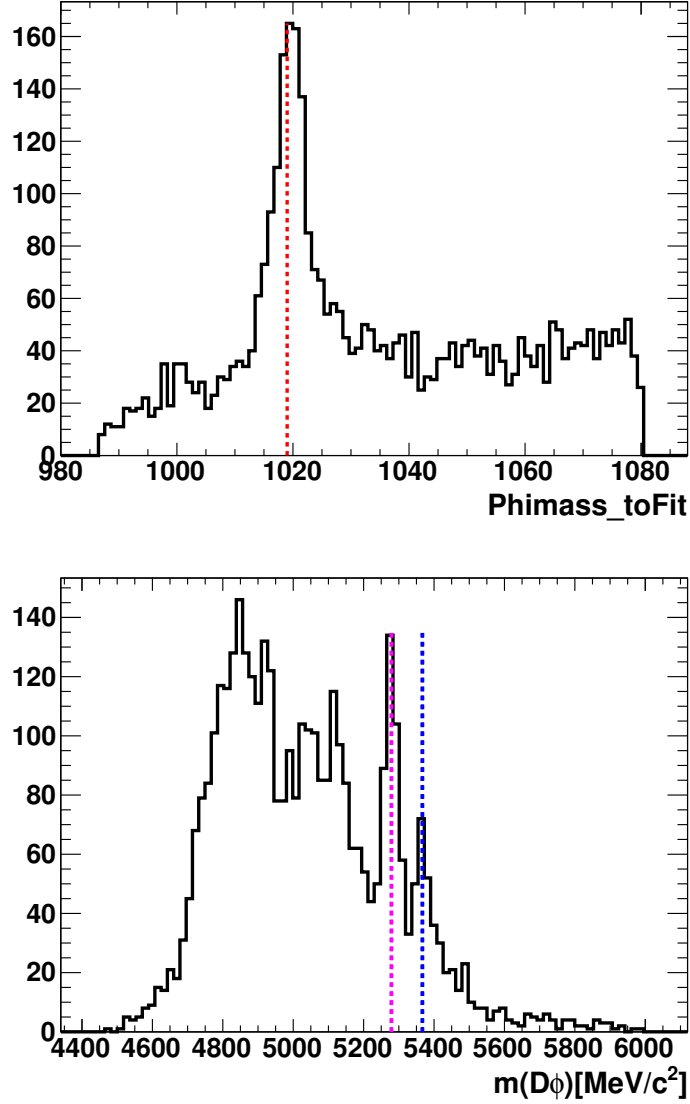
Figure 4.61: Results of the selections. $\phi$ mass spectrum (top)(red dashed line) and $B$ mass spectrum (bottom) shows the $B^0$ PDG mass for $B^0$ (pink dashed line) and $B_s^0$ (blue dashed line) mesons for Data Run 1 + Run 2.

Figure 4.64 shows all the fitted parameters and the veto $D^* \rightarrow \phi\pi$ on $\phi \rightarrow K^+K^-$, where the sPlot subtraction is performed and project the $D_s^+$ mass to define the PDF of the $D^*$ signal where the $42 \pm 10$ number of events are obtained. The veto is performed for the $\phi\pi$ candidates which invariant mass lies within $3\sigma$ (i.e. $\pm 30$ MeV/$c^2$) around the $D^*$ nominal mass 1970 MeV/$c^2$. The efficiency is evaluated with MC signal which is about 100% and the marginal loss of 0.2%. Figure 4.65 and 4.66 shows the given $D_s^+$ PDF obtained for $m(K^+K^-)$ candidates and $m_{K^+K^-\pi} \in [1900, 2050]$ mass window after MLP selection respectively.
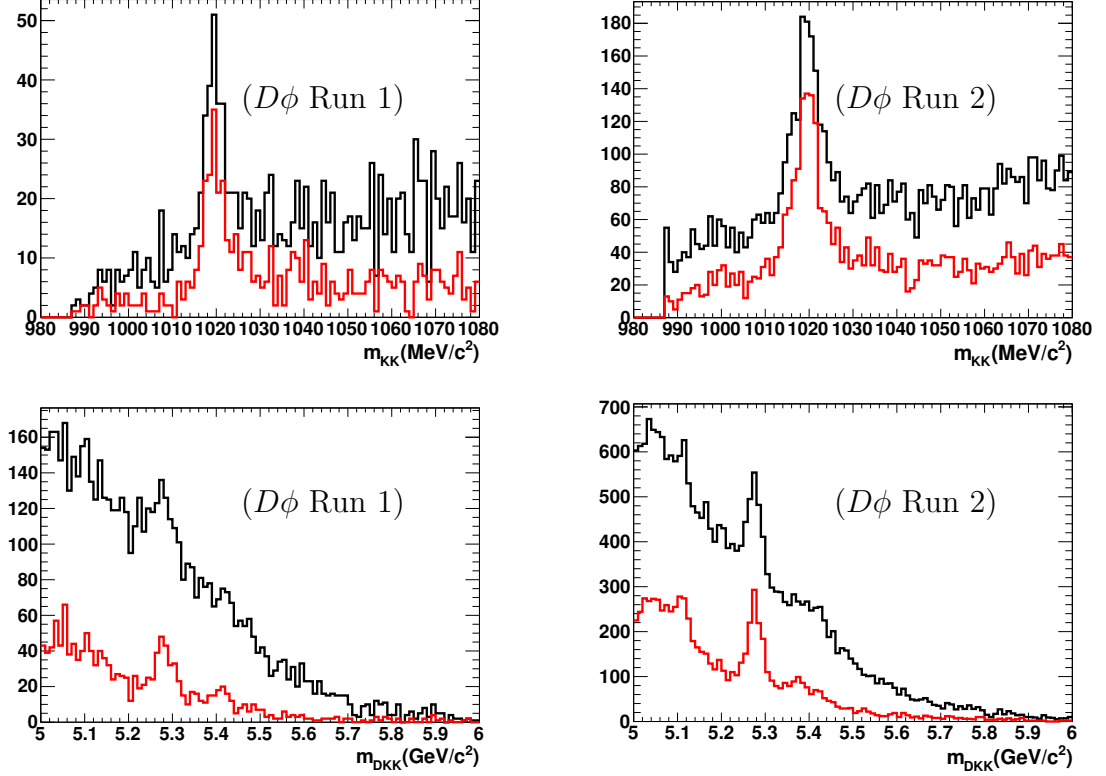
Figure 4.62: Distribution of $m_{KK}$ and $m_{DKK}$ without (black colour) and with a cut (red colour) on the $\phi$-mass window, respectively for Data Run 1 and Run 2 $B_s^0 \rightarrow \overline{D}^0(K\pi\pi^0)\phi$. The black curve represents the distribution after the initial selection and without PID requirement $Prob_K > 0.07$, while the red curve shows the distribution after the initial selection and after adding the optimised PID requirement $Prob_K > 0.07$ for $\phi(1020)$ daughters in $B_s^0 \rightarrow \overline{D}^0\phi$ mode.
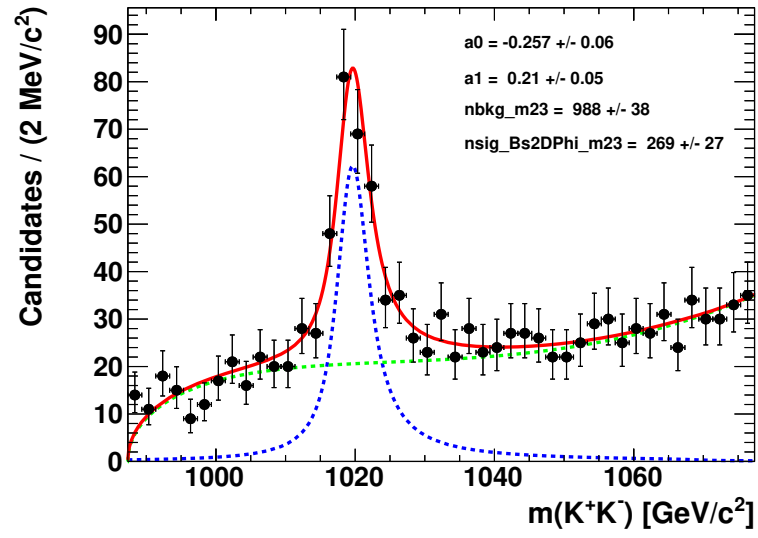
Figure 4.63: Vetoed $D^* \to \phi\pi^+$ mass effects on $m(K^+K^-)$ for Run 1 and Run 2. This fit distribution is obtained after vetoing the $D^* \to \phi\pi^+$ candidates in the given mass region before MLP.
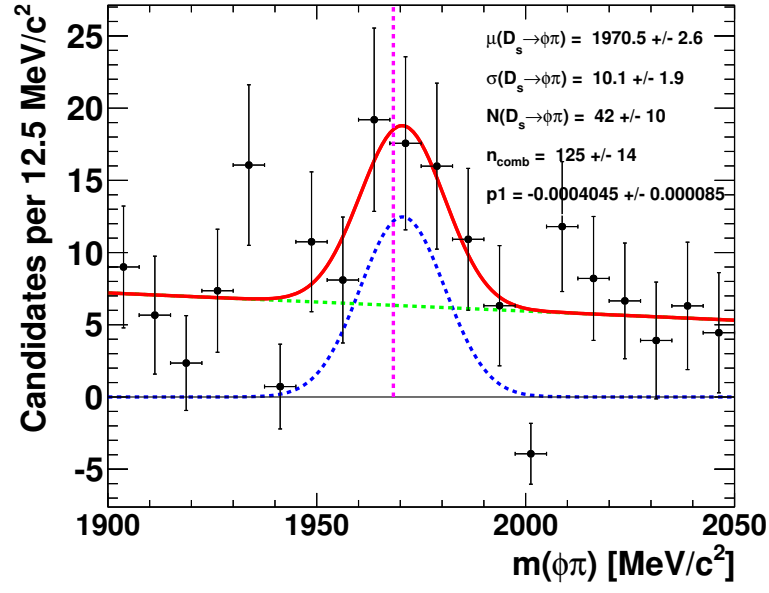
Figure 4.64: Vetoed $D^* \to \phi\pi^+$ mass candidates within the mass region $m_{K^+K^-\pi^+} \in [1900, 2050]$ for Run 1 and Run 2 before MLP.
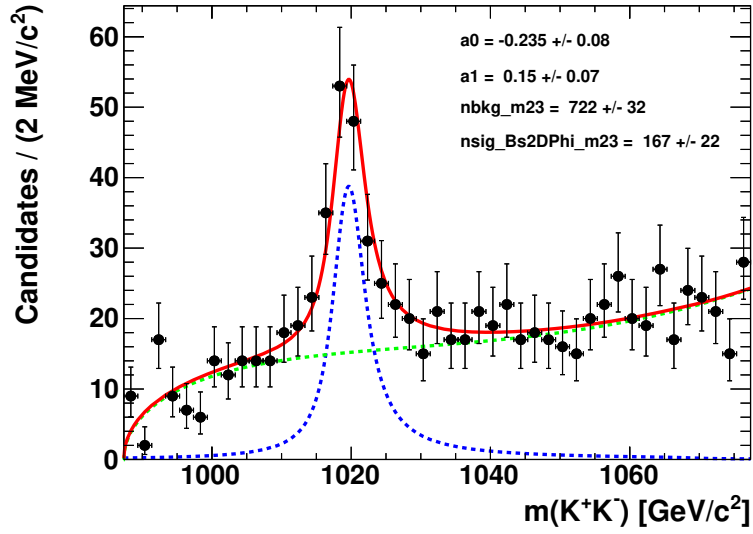


Figure 4.65: Vetoed $D^* \to \phi\pi^+$ mass effects on $m(K^+K^-)$ for Run 1 and Run 2. This fit distribution is obtained after vetoing the $D^* \to \phi\pi^+$ candidates in the given mass region after MLP.
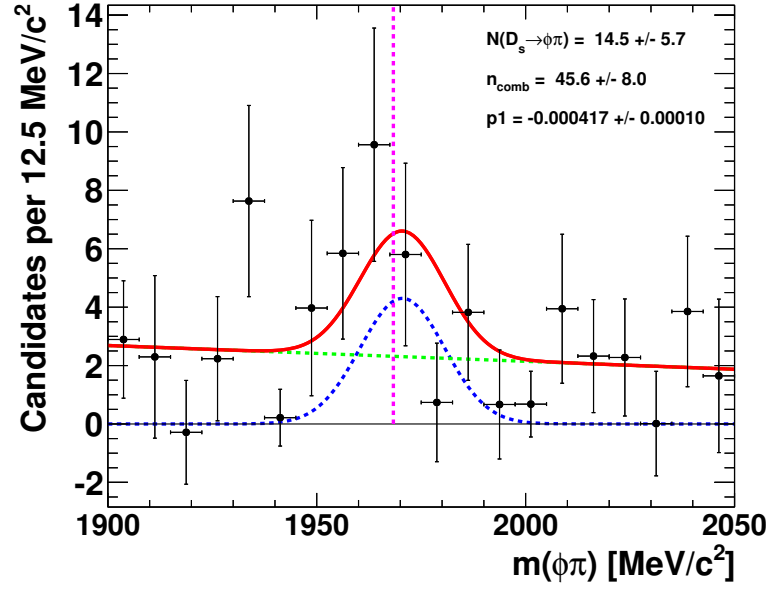
Figure 4.66: Vetoed $D^* \to \phi\pi^+$ mass candidates within the mass region $m_{K^+K^-\pi^+} \in [1900, 2050]$ for Run 1 and Run 2 after MLP.

## 4.9  Multiple Candidates

Once the full selection and MLP has been done, the presence of the multiple candidates per event have been investigated for the surviving candidates in both data and signal. Figure 4.67 shows the distributions of the number of multiple candidates for Run 1 (left) and Run 2 (right) for the same LHCb event in logarithmic scale. One can clearly see that this multiplicity is 1 for Run 1 and about 2 per mille, or less for Run 2. Therefore to ease the following part of the analysis, one single candidate is chosen randomly per event, if more than 1 is found as advised by [141].
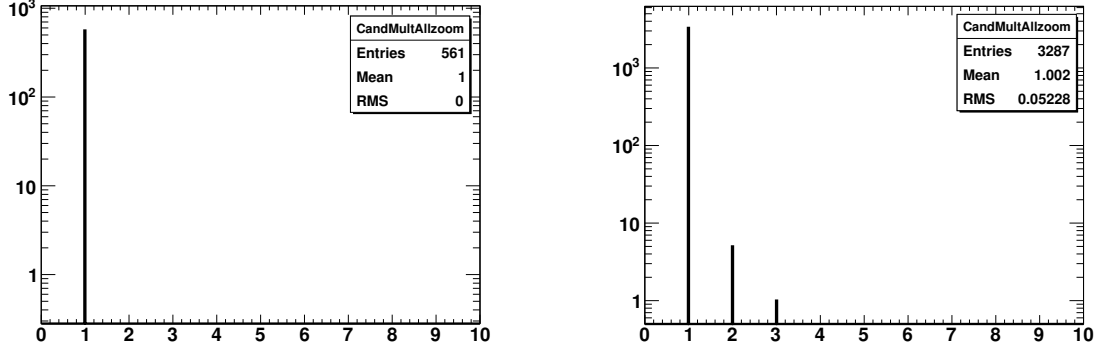
Figure 4.67: Distributions of multiple candidates for Run 1 (left) and Run 2 (right) are given in logarithmic scale.

## 4.10  Extraction of the yields of the $B_s^0 \to \tilde{D}^{(*)0}\phi$, and $D^0$ decays to $K\pi\pi^0$ signals

Following the selections described in previous Section 4.6.1, a method is developed to extract the event yield for the selected $B_s^0 \to \tilde{D}^{(*)0}\phi$ candidates. This method proceed in two steps:

- a fit to the $m_{KK}$ spectrum to seperate $\phi$ signals from non-$\phi$ ($KK$) candidates.

- from the first step sWeights are computed for signal $\phi$ and background non-$\phi$ candidates and each candidate is projected using sPlot technique back to the $m_{DKK}$ distribution.

### 4.10.1  Mass Fit on $m(K^+K^-)$

For signal $\phi(1020)$, as the $\phi$ resonance is expected to be very narrow [18]: $m_\phi = 1019.461 \pm 0.016\,\mathrm{MeV}/c^2$, $\Gamma_\phi = 4.249 \pm 0.013\,\mathrm{MeV}/c^2$ and the threshold to $m_{KK}$ being $987.354\,\mathrm{MeV}/c^2$, considered events are $KK$ candidates near the $\phi$ resonance: $m_{KK} \in [2m_K, 2m_K + 90]\,\mathrm{MeV}/c^2$.

In order to describe the reconstructed $\phi$ invariant mass distribution, a convolution of the Breit-wigner and Crystal Ball PDFs are used. Breit-wigner function is fixed to the $\phi$ meson mass and known $\phi$ width and $\gamma$ is fixed to its PDG value. Considering the phase space, the background shape (events without $\phi$ resonance) is modelled with a phase space threshold PDF (see [9] where p and q are the momentum of $K^+$ in the rest frame of $K^+K^-$ and momentum of $K^+K^-$ in the rest frame of $\overline{D}^0 K^+ K^-$ and $a_0$ is a free parameter. The normalization factor $N_{bkg}$ is also floated during the fit.

Then unbinned maximum likelihood fits are performed. The fit to $m(K^+K^-)$ is shown in Figure 4.68, and the PDFs parameters are fixed. The values of the parameters are shown on Figure 4.68.
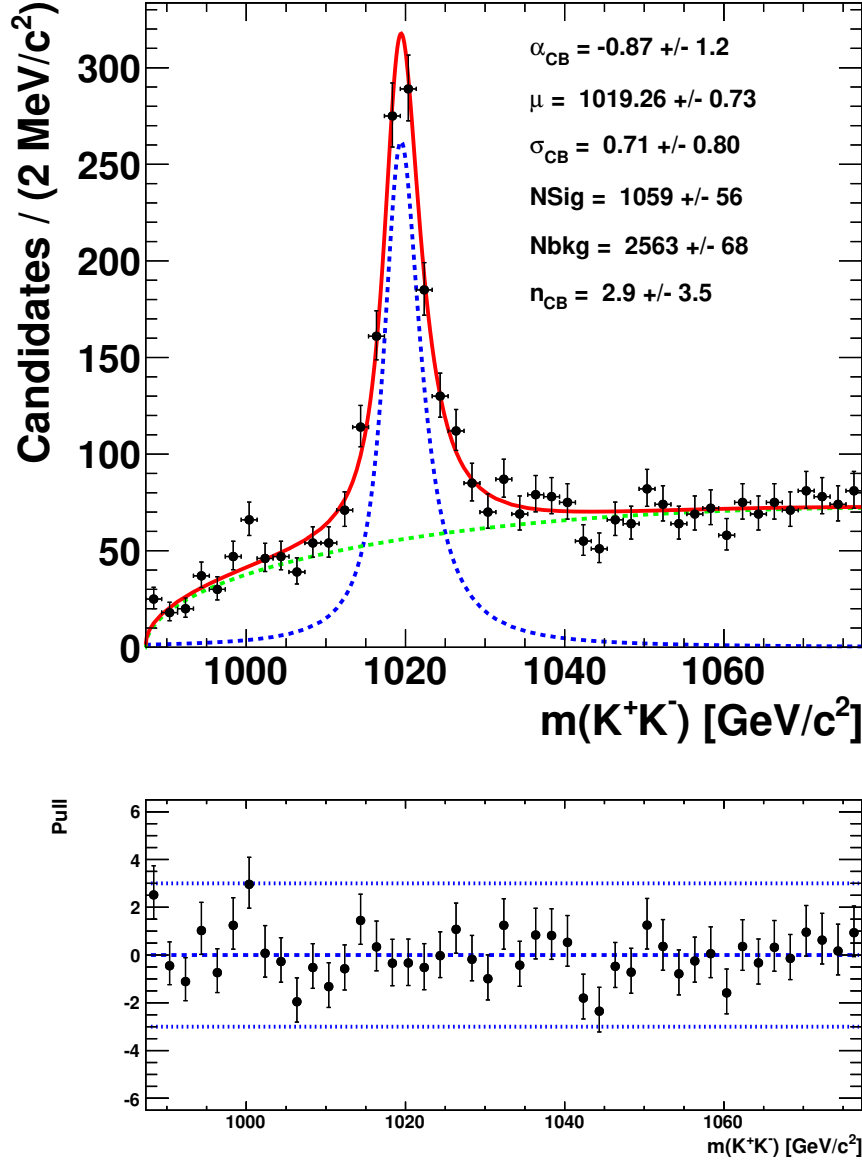
Figure 4.68: Fit to the invariant mass distribution of $m(K^+K^-)$ for Run 1 + Run 2 Data with sPlot technique for $D^0 \to K\pi\pi^0$. Data points are shown as black with error bars, the fitted total PDF is given with the red line. The component PDFs as dashed lines: (green) background and (blue) signal. PDFs parameters are fixed for Signal and Background.

We repeat the fit to the $m(K^+K^-)$, where $D^0 \to K^+\pi\pi^0$ and $D^0 \to K^-\pi\pi^0$ with the fixed parameters and compute the Signal and Background parameters for the fit to the $m(K^+K^-)$ with sub-samples $D^0 \to K^+\pi\pi^0$ and $D^0 \to K^-\pi\pi^0$ separately Figure 4.69. Parameters for two sub-decays are not computed separately but for their combination and these are shown on Figure 4.68.
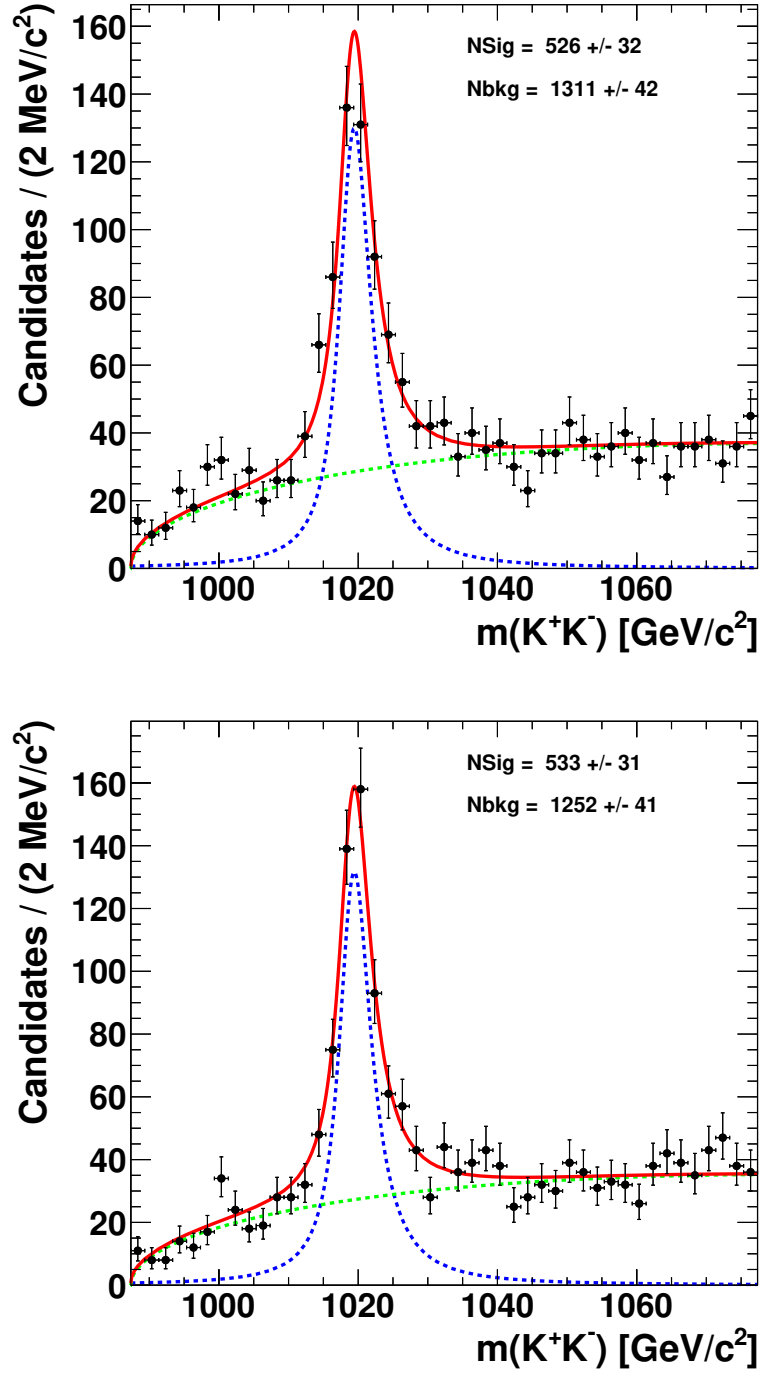
Figure 4.69: Fit to the invariant mass distribution of $m(K^+K^-)$ for Run 1 + Run 2 Data with sPlot technique for $D^0 \rightarrow K^+\pi\pi^0$ (top) and $D^0 \rightarrow K^-\pi\pi^0$ (bottom). Data points are shown as black with error bars, the fitted total PDF is given with the red line. The component PDFs as dashed lines: (green) background and (blue) signal. PDFs parameters are fixed for Signal and Background.

## 4.10.2   The fit of the invariant mass of $m(D\phi)$

Figure 4.71 shows the fit to the $m(DKK)$ invariant distribution of $D\phi$ candidates. An extended unbinned maximum-likelihood fit is performed to extract the yields. The main components are modelled for the final fit: $B_s^0 \to D^0\phi$, $B_s^0 \to D^*\phi$, $B^0 \to D^0\phi$, $B^0 \to D^*\phi$, $B_s^0 \to D\phi X$ and remaining combinatorial background. The $B_s^0 \to D^0\phi$ and $B^0 \to D^0\phi$ partially reconstructed signals, where one or more particles in the signal are not reconstructed properly or failed to reconstruct. These signals are modelled by a Gaussian function, where the mean and resolution are fixed. The invariant mass distribution of peaking $B_s^0 \to D^*\phi$ MC is generated by four components shown in Figure 4.70 where $D^{*0} \to D^0\gamma$ and $D^{*0} \to D^0\pi^0$ where $\gamma$ or $\pi^0$ is not reconstructed and correspond to the two possible extreme polarization states: fully transverse and fully longitudinal component. They are modelled by RooKeys [142] probability density function (PDF) [‡]

---

[‡]which is a method provided by RooFit package where a Gaussian kernel density estimation is performed.
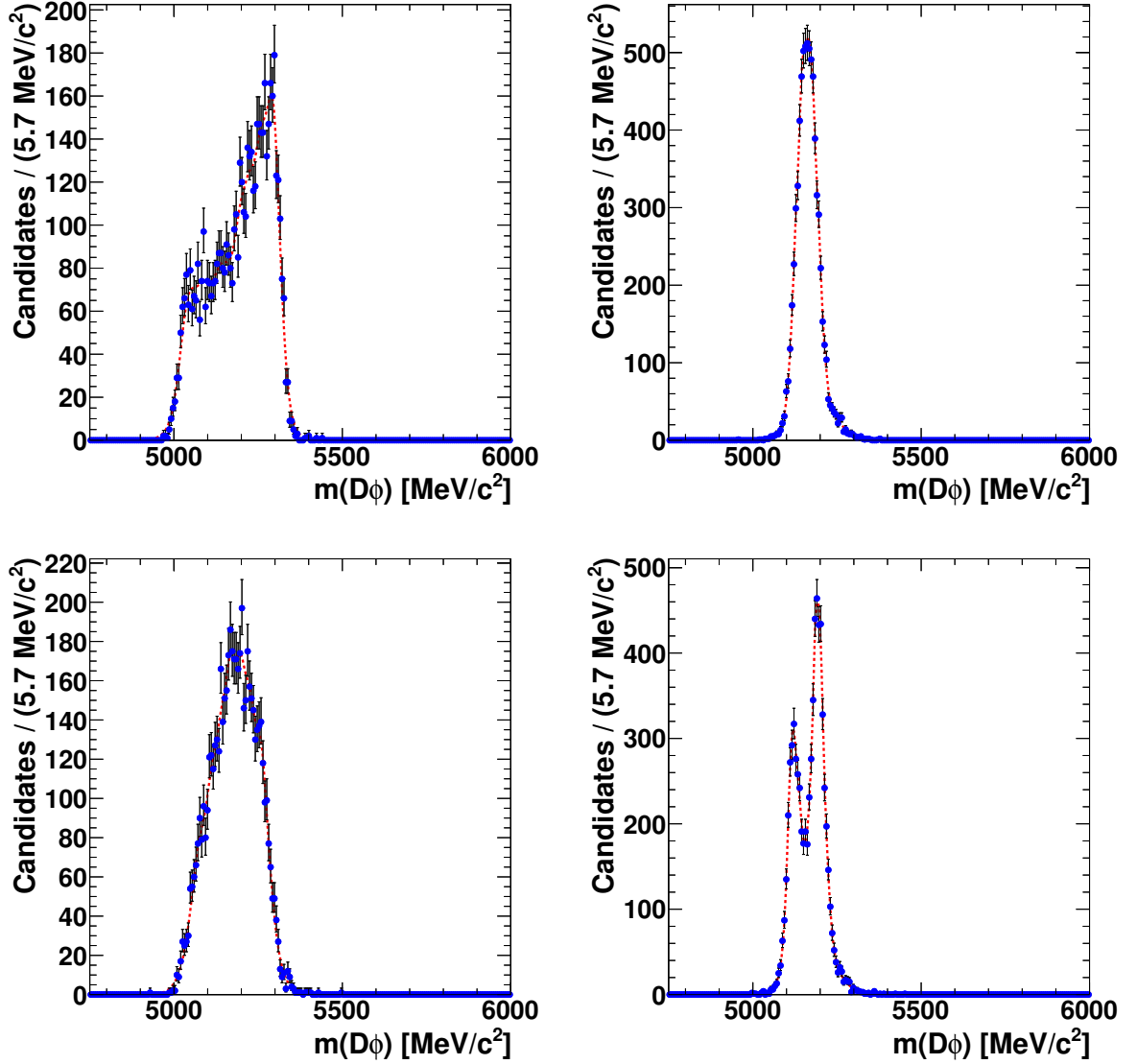
Figure 4.70: Fit to the $DKK$ invariant mass on Monte Carlo samples of $B_s^0 \to D^{*0}(D^0\gamma)\phi$ and $B_s^0 \to D^{*0}(D^0\pi^0)\phi$ decays in helicity state 100 (top figures), where it corresponds to a pure transverse polarization and (bottom figures) $B_s^0 \to D^{*0}(D^0\gamma)\phi$ and $B_s^0 \to D^{*0}(D^0\pi^0)\phi$ decays in helicity state 010, where it corresponds to a pure longitudinal polarization.

When the mass range $m_{DKK} \in [4750, 6000]\,\mathrm{MeV}/c^2$ is taken in the Figure 4.71, we have the nominal fit and in the far recoil a component $B_s^0 \to D\phi X$, where can be associated to the decay $B_s^0 \to D\phi K^0$. The corresponding Feynman diagram is shown in Figure 4.72). This decay (see Figure 4.73) is studied with a fast Monte Carlo simulation "RapidSim" [143] based on EvtGen.
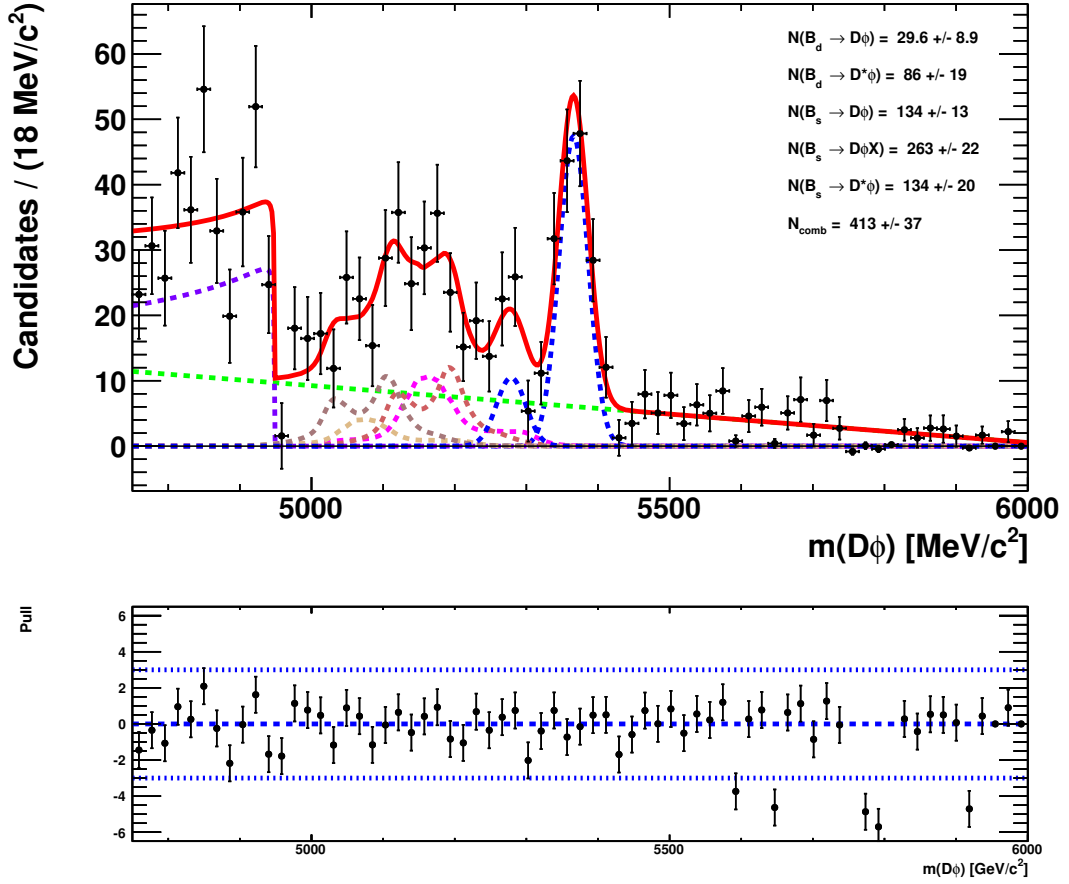
Figure 4.71: Fit to the invariant mass distribution of $B_s^0$ mass $(D\phi)$ in the full Run 1 + Run 2 Data, mass range $m_{DKK} \in [4750, 6000]\,\text{MeV}/c^2$ with sPlot technique. Data points are shown as black with error bars, total PDF is displayed with the red line. The different contributions PDFs are given as dashed lines: (green) combinatorial background and (blue) signal $B_s^0 \to D\phi$, where $D^0 \to K\pi\pi^0$. Small blue dashed $B^0 \to D\phi$, purple dashed is for $B_s^0 \to D\phi X$ signal decay, the peaking contribution $B_s^0 \to D^*\phi$ decay with magenta is for transverse and brown dashed longitudinal polarization.



Figure 4.72: Feynman diagram of the decay $B_s^0 \to D\phi X$ signal and $X$ represents the $K^0$ meson.
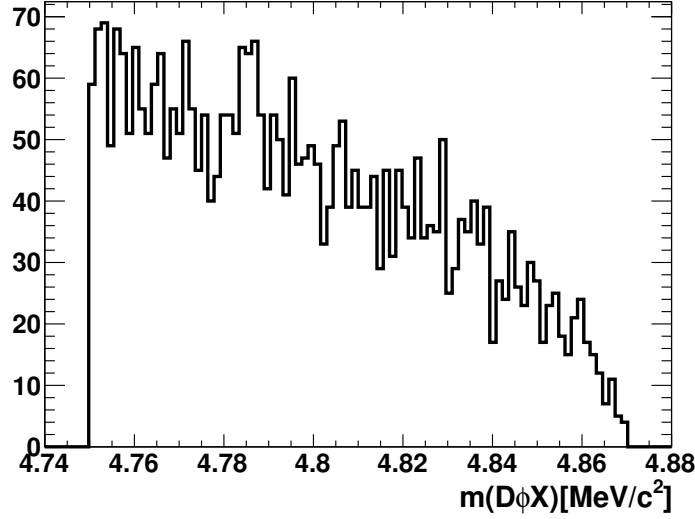
Figure 4.73: $B_s^0 \to D\phi X$ signal where $X$ represents the $K^0$ meson.

All parameters and the yields obtained from the nominal fit are given in Table 4.31.

| Parameter | $D^0 \to K\pi\pi^0$ |
|---|---|
| **Signal Modelling** | |
| $\mu(B_s^0)$ | $5365.9 \pm 2.2$ |
| $\sigma(B_s^0)$ | $20.4 \pm 1.7$ |
| $N_{(B^0 \to D\phi)}$ | $29.6 \pm 8.9$ |
| $N_{(B^0 \to D^*\phi)}$ | $86 \pm 19$ |
| $N_{(B_s^0 \to D\phi)}$ | $134 \pm 13$ |
| $N_{(B_s^0 \to D\phi X)}$ | $263 \pm 22$ |
| $N_{(B_s^0 \to D^*\phi)}$ | $134 \pm 20$ |
| **Background Modelling** | |
| $N_{comb}$ | $413 \pm 37$ |

Table 4.31: Combined fit values of the signal yields and shape parameters for Run 1 and Run 2. $f_{L,d}$ and $f_{L,s}$ values are taken from [121].

For the merged sample($D^0 \to K^-\pi\pi^0$ and $D^0 \to K^+\pi\pi^0$) shown in Figure 4.71, we set the mean value on the $B_s^0$ and the $\sigma + P_{comb}$, $B^0$ mass is constrained to the known mass difference to the (PDG difference [18]) $m_{B_s^0}$ mass and PDG $m_{B_s^0} - m_{B^0}$. The longitudinal polarisation fraction is fixed to be $f_L(B_s^0 \to \overline{D}^{*0}\phi) = (53.1 \pm 6.0 \pm 1.0)\%$ and $f_L(B^0 \to \overline{D}^{*0}\phi) = (65.7 \pm 21.6 \pm 2.9)\%$. This value is fixed from the internal LHCb analysis note of branching fraction measurement of $B_{(s)} \to \overline{D}^{(*)0}\phi$ decay mode to be published see [121]. From the combined fit gives within $\pm 3\sigma$, the significance is obtained as $\frac{S}{\sqrt{(S+B)}} = 10.16$ and the purity is $\frac{S}{(S+B)} = 77.67$. The combinatorial background is modelled with a Chebyshev polynomial. The fitted values of all the yields and the parameters are shown in the legend of the fit distributions. The shape of the corresponding

133

likelihood function distributions are displayed for each of the corresponding decay mode in the fit displayed in Figure4.75 and 4.76. These parameters from the nominal fit can be fixed and the fit is redone separately for both $D^0$ decays to $K^+\pi\pi^0$ and $K^-\pi\pi^0$ shown in Figure 4.74 respectively for Run 1 and Run 2. For the $\gamma$ sensitivity study which has been published [4], a naive expectation has been done on the signal yields for each sub-modes where $D^0$ decays to. And for the $K\pi\pi^0$ sub-mode, we had only 58 number of events for $B_s^0 \to D\phi$ and 52 number of events for the $B_s^0 \to D^*\phi$. While now from the Table 4.31, one can see that those yields from the signal are improved by a factor of 2. In the 2018 PRD publication $B_s^0 \to \tilde{D}^{(*)0}\phi$ [9] with only Run 1 Data for the $B_s^0 \to D\phi$ where $D^0$ to $K\pi$, the yields obtained from the fit was $132 \pm 13$ and for $B_s^0 \to D^*\phi$ was $163 \pm 19$ while with the current analysis for the combined Run1 + Run2 Data, the yields are obtained $920 \pm 32$ and $1090 \pm 42$, respectively.
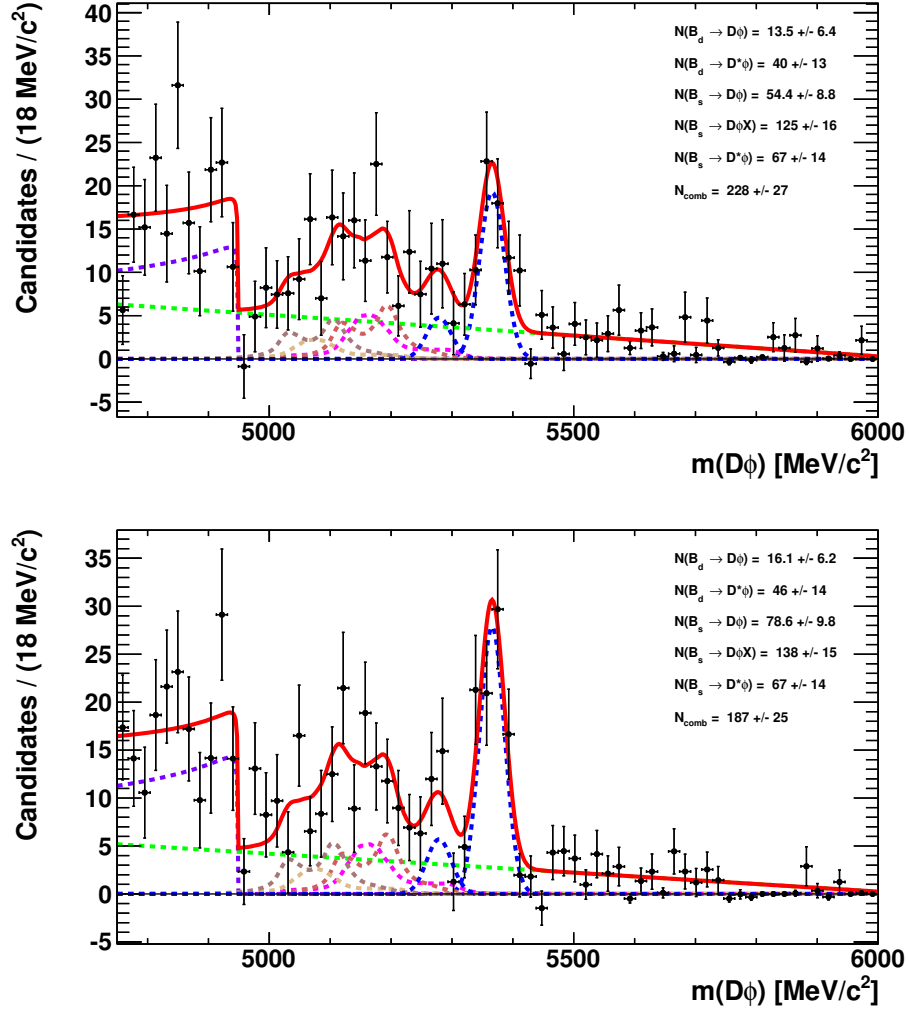
Figure 4.74: Fit to the invariant mass distribution of $B_s^0$ mass ($D\phi$), where $D^0$ decays to $K^+\pi^-\pi^0$ (top) and $K^-\pi^-\pi^0$ (bottom) in the full Run 1 + Run 2 Data with sPlot technique. Data points are shown as black with error bars, the full fitted PDF is displayed with the red line. The different contributions PDFs are given as dashed lines: (green) combinatorial background and (blue) signal $B_s^0 \to D\phi$, where $D^0 \to K\pi\pi^0$. Small blue dashed $B^0 \to D\phi$, purple dashed is for $B_s^0 \to D\phi X$ signal decay, the peaking contribution $B_s^0 \to D^*\phi$ decay with magenta is for transverse and brown dashed longitudinal polarization.
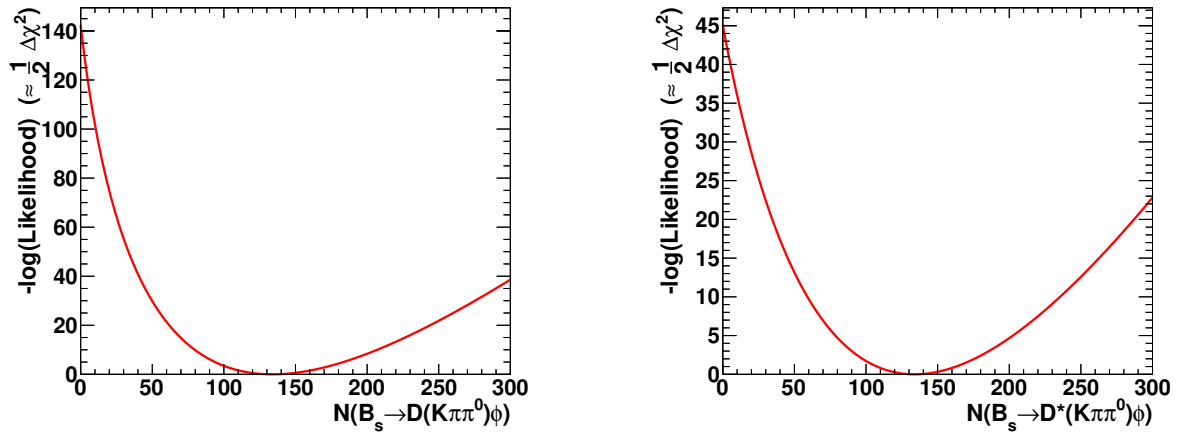
Figure 4.75: Log-Likelihood profile of the $B_s^0 \rightarrow D\phi$ (left), $B_s^0 \rightarrow D^*\phi$ (right) candidates from the fit to the data. From the $B_s^0 \rightarrow D\phi$, it is seen about $18\sigma$ significant and for $B_s^0 \rightarrow D^*\phi$ it is about $10\sigma$ significance.
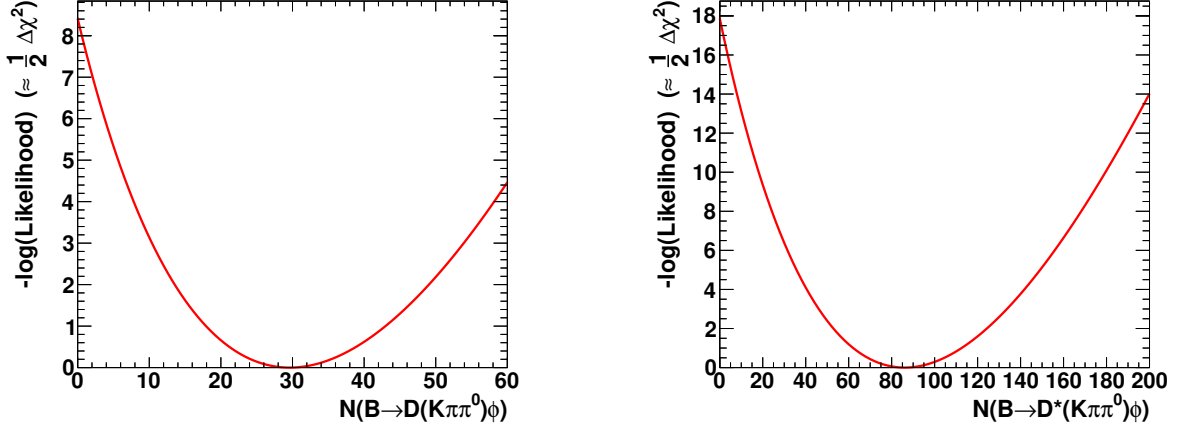
Figure 4.76: Log-Likelihood profile of the $B^0 \rightarrow D\phi$ and $B^0 \rightarrow D^*\phi$ candidates from the fit to the data. From the $B^0 \rightarrow D\phi$, it is seen about 4.2 $\sigma$ significant and for $B^0 \rightarrow D^*\phi$ it is about 5.5 $\sigma$ significance.

### 4.10.3 Validation of the fits: pseudo Monte Carlo study (toy)

The validation of the reliability of the invariant mass fit model is performed using simulated pseudo-experiments, known as "toys". Toy MC is generated to check if there is any bias on the yields and then to validate the statistical uncertainties on the yields. 4000 toy samples ($N_{SigToy}$) are performed from the nominal fit model displayed on nominal fit Figures 4.68 and 4.71 using the parameters, number of signal events($N_{sig}$) according to the uncertainties on our nominal fit. For the toy study all of the parameters displayed in Figures 4.68 and 4.71 are left free to vary within their fitted 1 $\sigma$ confidence interval according to Gaussian statistics.

When the parameters of the pull distributions $\frac{N_{SigToy} - N_{sig}}{\sigma_{N_{sig}}}$ are fitted with a Gaussian model, they are expected to be a Gaussian distribution with $\mu = 0$ and $\sigma = 1$ to determine the parameter which is unbiased in the measurement and consider as good. In other case, the pull distribution is obtained as biased within the statistical errors. According to this probability, systematic uncertainties are estimated where the toy fits differ from the nominal fit source. Figure 4.77 shows the results from the Toy studies and seen that there is no bias for the fits to the $B^0_s \rightarrow D\phi$, $B^0 \rightarrow D\phi$ and $B^0_s \rightarrow D^*\phi$, $B^0 \rightarrow D^*\phi$. The obtained parameters are given in the Table 4.32 and it is shown that the fitted values are stable (mean values of the pulls are compatible with 0) while the RMS of the pull distributions are slightly above 1 for $B^0_s \rightarrow D\phi$, $B^0 \rightarrow D\phi$ and $B^0_s \rightarrow D^*\phi$, $B^0 \rightarrow D^*\phi$. it means that all the statistical uncertainties will have to be inflated by these numbers 1.195±0.014, 1.357±0.015 for $B^0_s \rightarrow D\phi$, $B^0_s \rightarrow D^*\phi$.

137
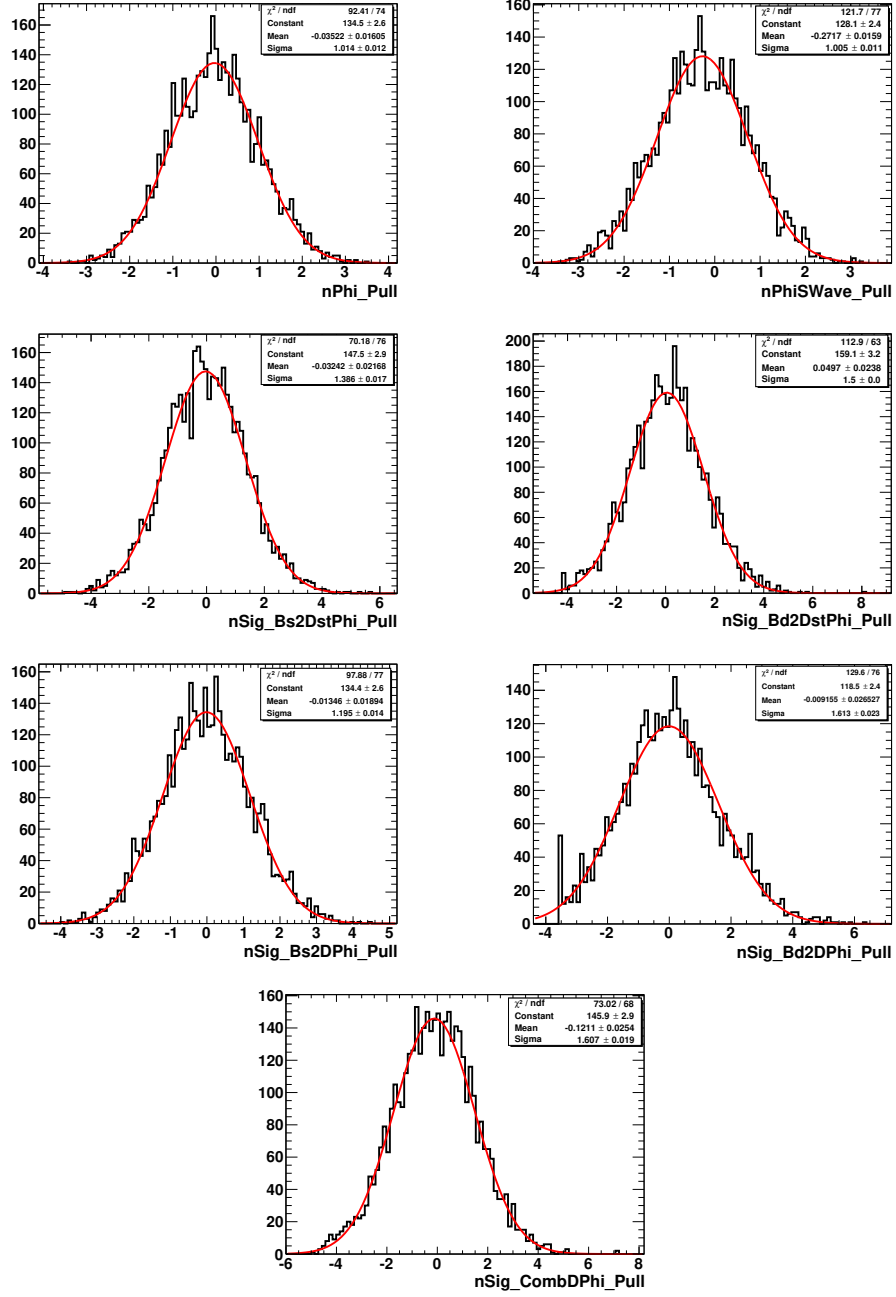
Figure 4.77: Pull distribution parameters obtained from 4000 pseudo-toy experiments study which is generated using the parameters extracted from the MC sample. The pulls are fitted with a Gaussian function. Here one can see that all the central (mean) values are coherent with zero, which means that there is no shift.

| Parameter | $N_{pull}(B_s^0 \rightarrow D\phi)$ |
|---|---|
| mean | $-0.014 \pm 0.019$ |
| standard deviation | $1.195 \pm 0.014$ |
| | $N_{pull}(\phi)$ |
| mean | $-0.035 \pm 0.016$ |
| standard deviation | $1.014 \pm 0.012$ |
| | $N_{pull}(PhiSWave)$ |
| mean | $-0.272 \pm 0.016$ |
| standard deviation | $1.005 \pm 0.011$ |
| | $N_{pull}(B_s^0 \rightarrow D^*\phi)$ |
| mean | $-0.032 \pm 0.023$ |
| standard deviation | $1.386 \pm 0.017$ |
| | $N_{pull}(B^0 \rightarrow D^*\phi)$ |
| mean | $0.049 \pm 0.024$ |
| standard deviation | $1.5 \pm (\ < 0.1)$ |
| | $N_{pull}(B^0 \rightarrow D\phi)$ |
| mean | $-0.009 \pm 0.027$ |
| standard deviation | $1.613 \pm 0.023$ |
| | $N_{pull}(ComD\phi)$ |
| mean | $-0.121 \pm 0.025$ |
| standard deviation | $1.607 \pm 0.019$ |

Table 4.32: Parameters of the fit to the pull distributions.

### 4.10.4 Validation of the Rookey PDF versus analytical function for the recoil partially reconstructed $B_s^0 \rightarrow D^{(*)0}\phi$ on the nominal B mass fit

A cross check is performed with an alternate fit to the invariant mass distribution, which is shown in Figure 4.79. Peaking $B_s^0 \rightarrow D^*\phi$ MC is modelled with four components shown in Figure 4.78, where $D^{*0} \rightarrow D^0\gamma$ and $D^{*0} \rightarrow D^0\pi^0$, $\gamma$ and $\pi^0$ is not reconstructed,

correspond to the two polarization: purely transverse polarization and longitudinal polarization. They are modelled by analytical shapes, which derive their shapes from angular distribution of vector decays (RooHORNSdini and RooHILLdini [144]) and detailed informations are given in Appendix D. The parameters and the yields from the fit are given in Table 4.33. From these two Tables 4.31 and 4.33, it can be seen that the same rates for $N(B_s^0 \to D\phi)$, $N(B^0 \to D\phi)$ and $N(B_s^0 \to D^*\phi)$, $N(B^0 \to D^*\phi)$ are obtained for the nominal fit and this alternate model to describe the partially reconstructed signals $B_s^0 \to D^*\phi$.
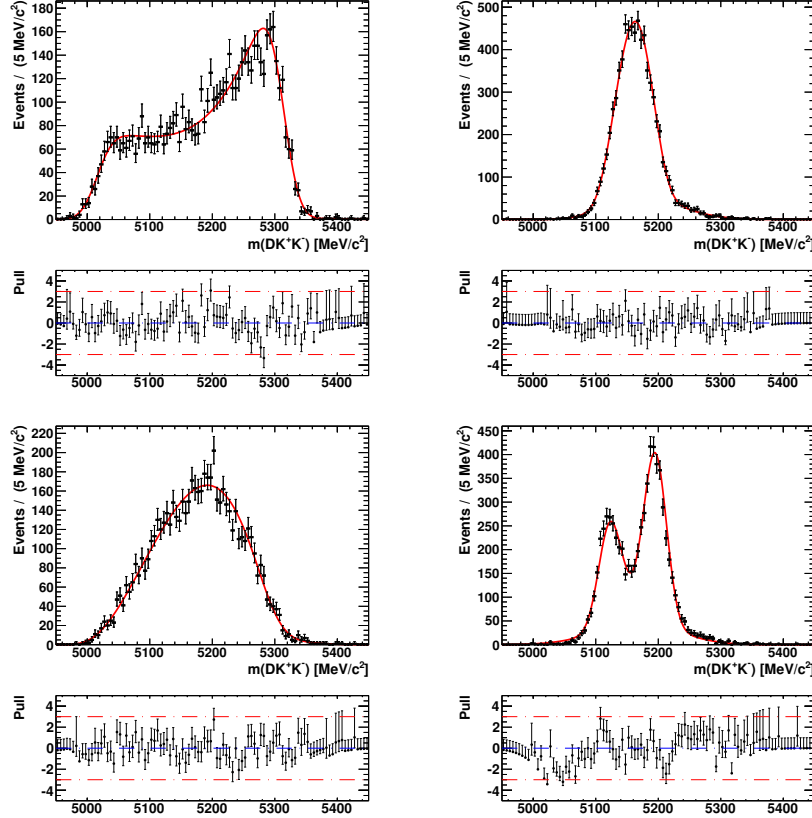


Figure 4.78: Reconstructed $D\phi$ candidate invariant mass distributions and their kernel estimation superimposed, from the simulated (top figures) $B_s^0 \to D^{*0}(D^0\gamma)\phi$ and $B_s^0 \to D^{*0}(D^0\pi^0)\phi$ decays in helicity state 100 where it corresponds to a pure transverse polarization and (bottom figures) $B_s^0 \to D^{*0}(D^0\gamma)\phi$ and $B_s^0 \to D^{*0}(D^0\pi^0)\phi$ decays in helicity state 010 where it corresponds to a pure longitudinal polarization.

140

Figure 4.79: Fit to the invariant mass distribution of $B_s^0$ mass ($D\phi$) in the full Run 1 + Run 2 Data, mass range $m_{DKK} \in [4750, 6000]\,\mathrm{MeV}/c^2$ with sPlot technique. Data points are given in black with error bars, total PDF is displayed with the red line. The different contributions PDFs are given as dashed lines: (green) combinatorial background and (blue) signal $B_s^0 \to D\phi$, where $D^0 \to K\pi\pi^0$. Small blue dashed $B^0 \to D\phi$, purple dashed is for $B_s^0 \to D\phi X$ signal decay, the peaking contribution $B_s^0 \to D^*\phi$ decay with magenta is for transverse and brown dashed longitudinal polarization.

| Parameter | $D^0 \to \pi\pi^0$ |
|---|---|
| | **Signal Modelling** |
| $\mu(B_s^0)$ | $5366.7 \pm 2.2$ |
| $\sigma(B_s^0)$ | $19.8 \pm 1.8$ |
| $N_{(B^0 \to D\phi)}$ | $29.1 \pm 9.0$ |
| $N_{(B^0 \to D^*\phi)}$ | $84 \pm 20$ |
| $N_{(B_s^0 \to D\phi)}$ | $134 \pm 13$ |
| $N_{(B_s^0 \to D\phi X)}$ | $260 \pm 23$ |
| $N_{(B_s^0 \to D^*\phi)}$ | $134 \pm 20$ |
| $f_{L,d}$ | $0.72 \pm 0.18$ |
| $f_{L,s}$ | $0.514 \pm 0.06$ |
| | **Background Modelling** |
| $N_{comb}$ | $420 \pm 41$ |
| $p_{comb}$ | $-0.9327 \pm 0.057$ |

Table 4.33: Combined fit values of the signal yields and shape parameters for Run 1 and Run 2. The values of $f_{L,d}$ and $f_{L,s}$ are taken from [121].

## 4.10.5 Selection with and without the Dalitz Weight (DW) variable

This section contains an additional study has been done on the Dalitz weight which was detailed in the early stage of the analysis 4.4.2. The purpose of this part is to clarify the use of the Dalitz Weight variable may effect the coherence factor $R_{K\pi\pi^0}$ and the strong phase distribution $\delta_{K\pi\pi^0}$ over the Dalitz plane $(m^2_{K\pi^0}, m^2_{K\pi})$. In the nominal selection Sect.4.4.2 specific selections with five variables have been defined and taken into account in order to cope with the vast background from $\pi^0$ coming from $D^0 \rightarrow K\pi\pi^0$ sub-decay mode. Among these variables there is a specific selection implemented which is called as "Dalitz weight amplitude". The amplitude model is from E691 Experiment [135] and confirmed by CLEO-c Experiment [136]. Therefore the dataset of selected candidates for the $B^0_s \rightarrow D^{(*)0}\phi$ channel is adjusted according to the amplitude model. MVA BDT selections with Dalitz weight variable at nominal efficiency of this five variables may affect the 2D distribution without biasing the strong phase of $D^0 \rightarrow K\pi\pi^0$. With this study, MVA selections are tested to be chosen with and without Dalitz variable and if this bias the effective values of the hadronic parameters $R_{K\pi\pi^0}$ and $\delta_{K\pi\pi^0}$, and affects in cascade the relative amplitude of the two dominant interfering diagrams that contribute to the $B^0_s \rightarrow D^{(*)0}\phi$ decays through $b \rightarrow c$ and $b \rightarrow u$ transitions. At first in order to demonstrate the influence of the Dalitz Weight variable we compare in Figures 4.80 and 4.81 the Dalitz plane $(m^2_{K\pi^0}, m^2_{K\pi})$ distributions of candidates in MC simulation of signal and in data, before and after the selection cut at 85% efficiency of the MVA five variables. Figure 4.82 gives the efficiency ratio of without MVA selection/MVA selection (85%) for both selection with and without Dalitz weight respectively for MC Run 1 + Run 2.
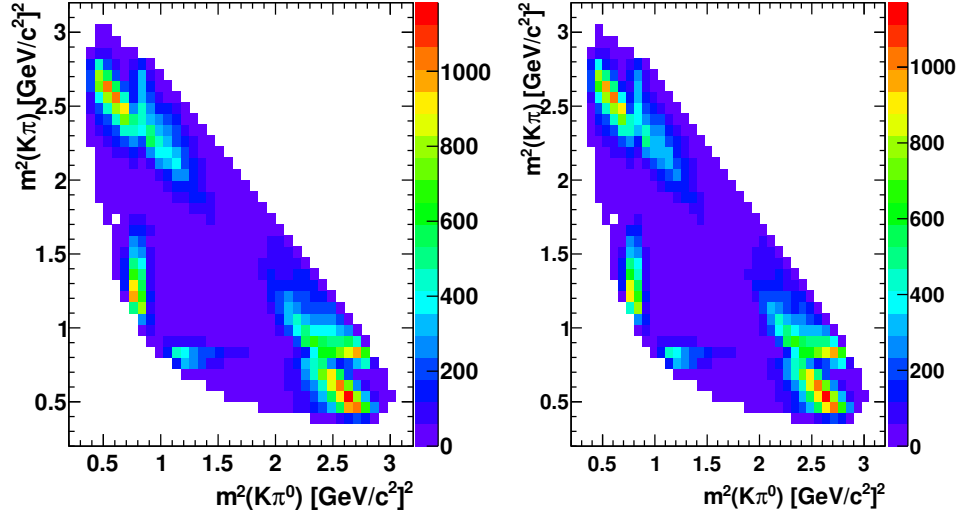
Figure 4.80: Distributions in the Dalitz plane $(m^2_{K\pi^0}, m^2_{K\pi})$ of the candidates for Run 1 + Run 2 MC simulation, with the Dalitz Weight variable included in the five variables nominal MVA, and before selection (left) and after the selection cut on TMVA (85% efficiency applied).
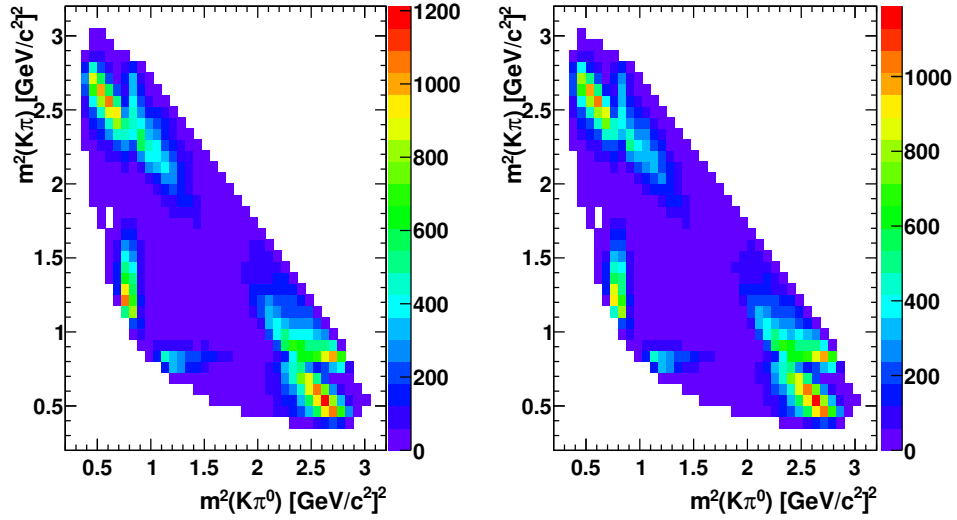


Figure 4.81: Distributions in the Dalitz plane $(m^2_{K\pi^0}, m^2_{K\pi})$ of the candidates for Run 1 + Run 2 MC simulation, without the Dalitz Weight variable included in the five variables nominal MVA, and before selection (left) and after the selection cut on TMVA (85% efficiency applied).
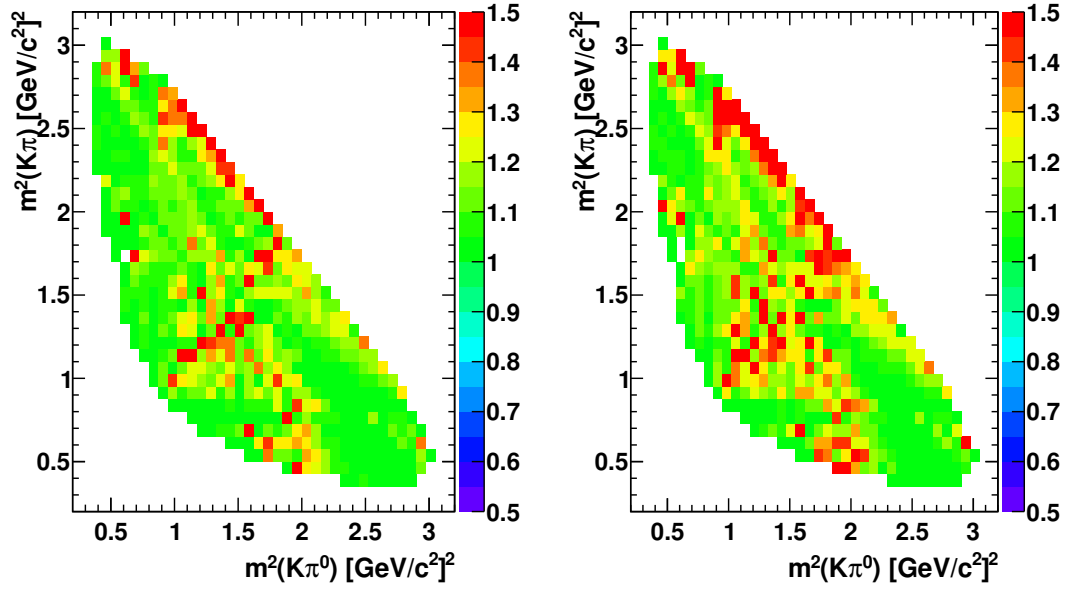
Figure 4.82: Distributions in the Dalitz plane $(m^2_{K\pi^0}, m^2_{K\pi})$ of the candidates for Run 1 + Run 2 MC simulation, with (left) and without (right) Dalitz weight.

And Figure 4.83 displays the ratio between the Dalitz plane "with Dalitz weight" and "without Dalitz weight" for MC Run 1 + Run 2. One can see that the distribution is uniformly distributed which showing that the incorporation of the Dalitz Weight variable in the MVA discriminant is not an issue.
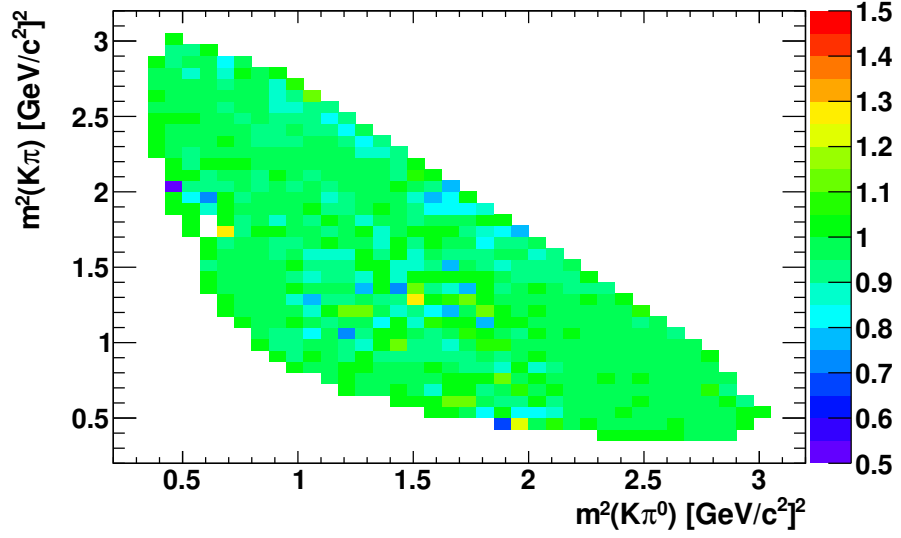
Figure 4.83: The ratio of the selections with Dalitz weight and without Dalitz weight for MC Run 1 + Run 2

The previous successful sanity check is not a surprise for the Monte Carlo simulation as the simulation samples in Evtgen where precisely produced accordingly to the E691 amplitude model. Therefore, we have proceed to the same study with the candidates in Data Run 1 and Run 2 as displayed in Figures 4.84 and 4.85 respectively. And Figure 4.86 displays the efficiency ratio of without MVA selection/MVA selection (85%) for both selection with and without DW respectively, for Run 1 + Run 2.
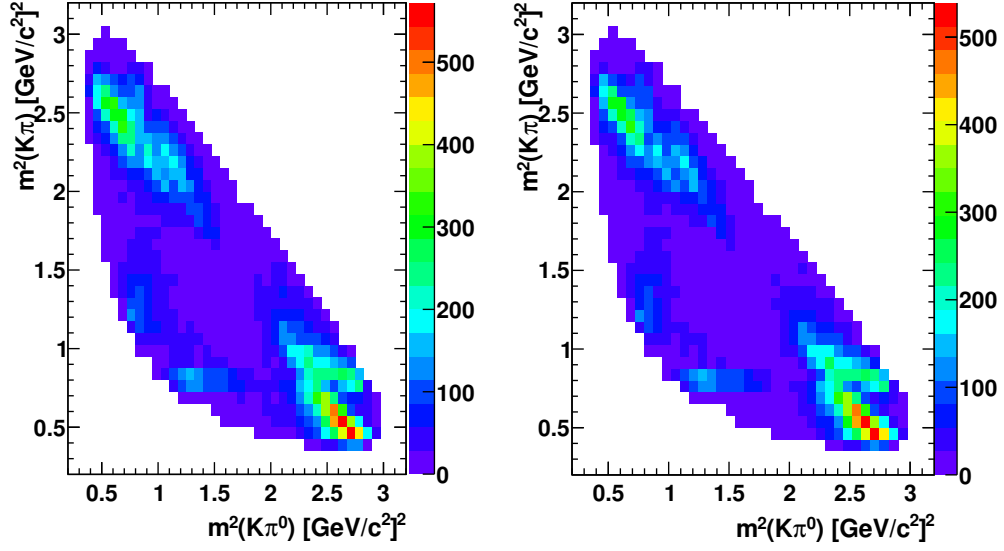
Figure 4.84: Distributions in the Dalitz plane $(m^2_{K\pi^0}, m^2_{K\pi})$ of the candidates for Data Run 1 + Run 2, with the Dalitz Weight variable included in the five variables nominal MVA, and before selection (left) and after the selection cut on TMVA (85% efficiency applied).
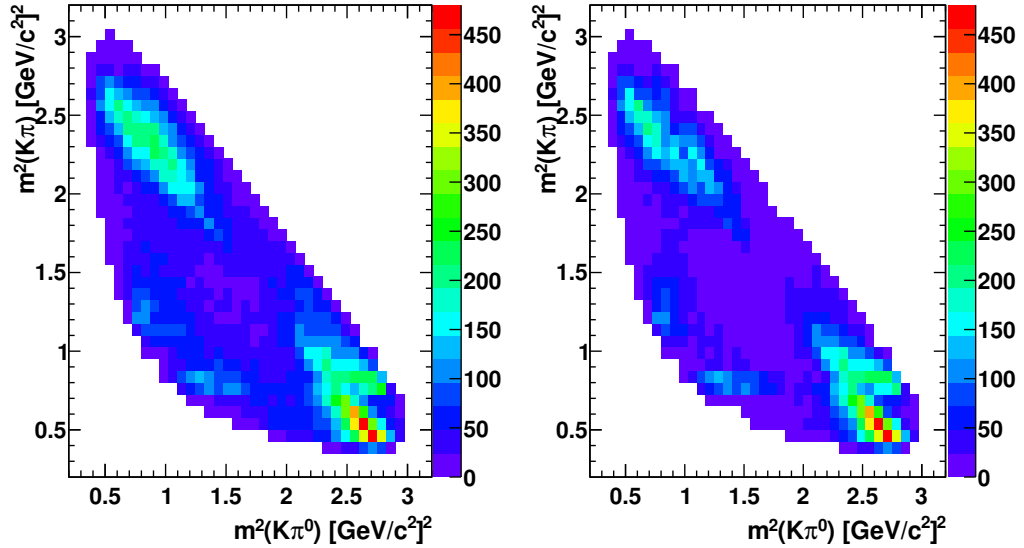


Figure 4.85: Distributions in the Dalitz plane $(m^2_{K\pi^0}, m^2_{K\pi})$ of the candidates for Data Run 1 + Run 2, without the Dalitz Weight variable included in the five variables nominal MVA, and before selection (left) and after the selection cut on TMVA (85% efficiency applied).
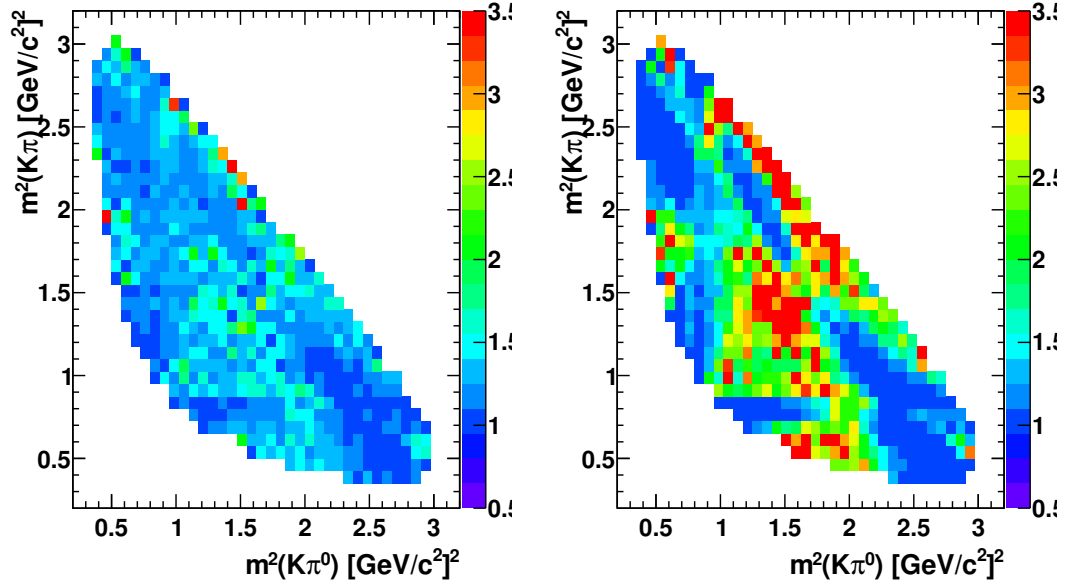
Figure 4.86: Distributions in the Dalitz plane $(m^2_{K\pi^0}, m^2_{K\pi})$ of the candidates for Data Run 1 + Run 2, with (left) and without (right) Dalitz weight.

For Data Run 1 + Run 2 the ratio between the two Dalitz plan with and without Dalitz weight variables is displayed in Figure 4.87. It can be seen that the distribution is mostly flat and the ratio is equal to 1 in the regions where the $D^0 \rightarrow K\pi\pi^0$ decay occurs from dominating three $K^{*-}$, $\rho^-$ and $K^{*0}$ resonances, such that at the level of precision we work, i.e. $N(B_s^0 \rightarrow D\phi)=134\pm13$, a possible impact to modify the coherence factor $R_{K\pi\pi^0}$ and strong phase $\delta_{K\pi\pi^0}$ can safely be neglected in the forthcoming extraction of the CKM angle $\gamma$.
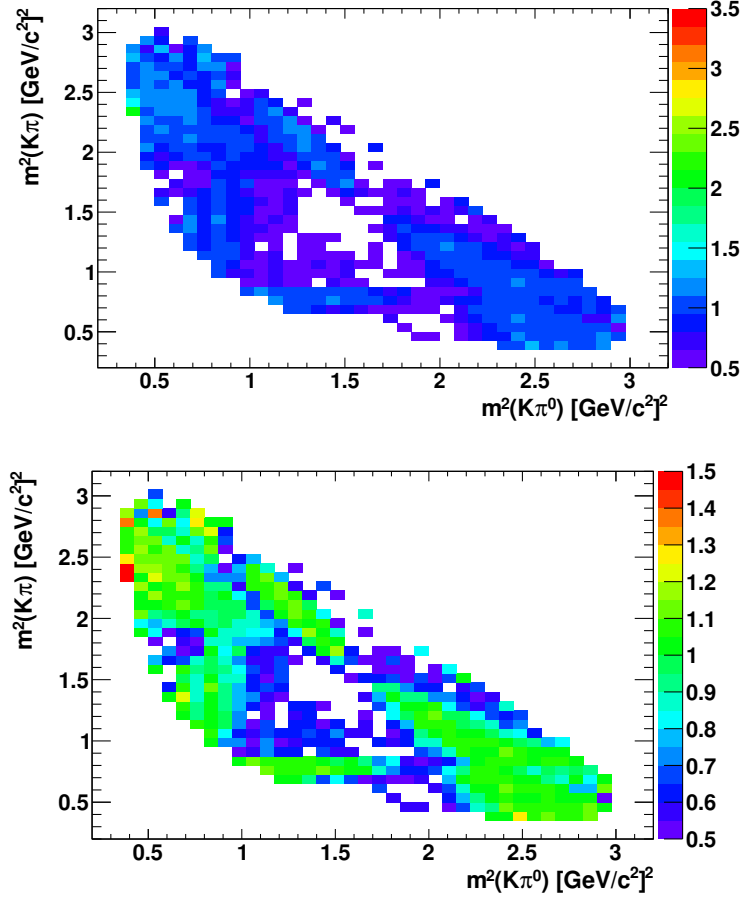
Figure 4.87: The ratio of the selections with Dalitz weight and without Dalitz weight for Data Run 1 + Run 2. Bottom figure is the same figure with the interval cut in the range [0.5, 1.5] on the z vertical scale.

We show that without Dalitz weight variable BDT selection with four variables have been chosen to fit to the invariant mass distribution for $m(K^+K^-)$ and $B_s^0$ mass $(D\phi)$ candidates which are represented in Figures 4.88 and 4.89 used to extract the signal yields in the signal region and sidebands for Run 1 + Run 2 respectively.
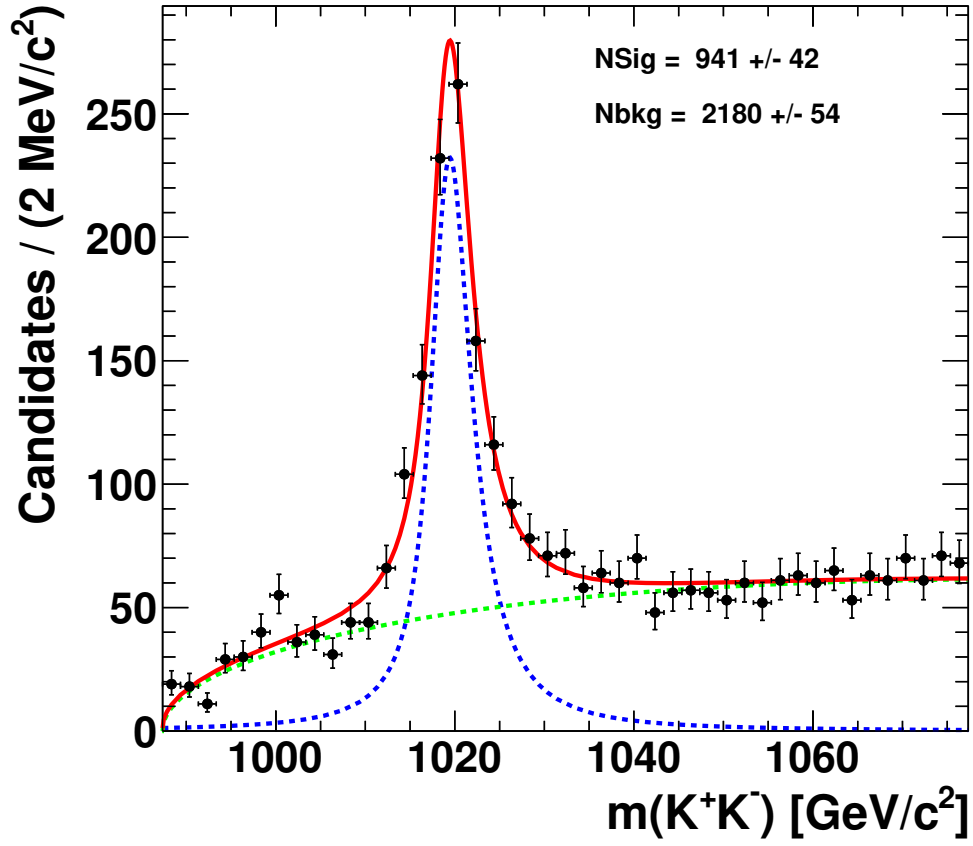
Figure 4.88: Fit to the invariant mass distribution of $m(K^+K^-)$ for Run 1 + Run 2 Data with sPlot technique for $D^0 \to K\pi\pi^0$. Data points are shown as black with error bars, the fitted total PDF is given with the red line. The component PDFs as dashed lines: (green) background and (blue) signal. PDFs parameters are fixed for Signal and Background.
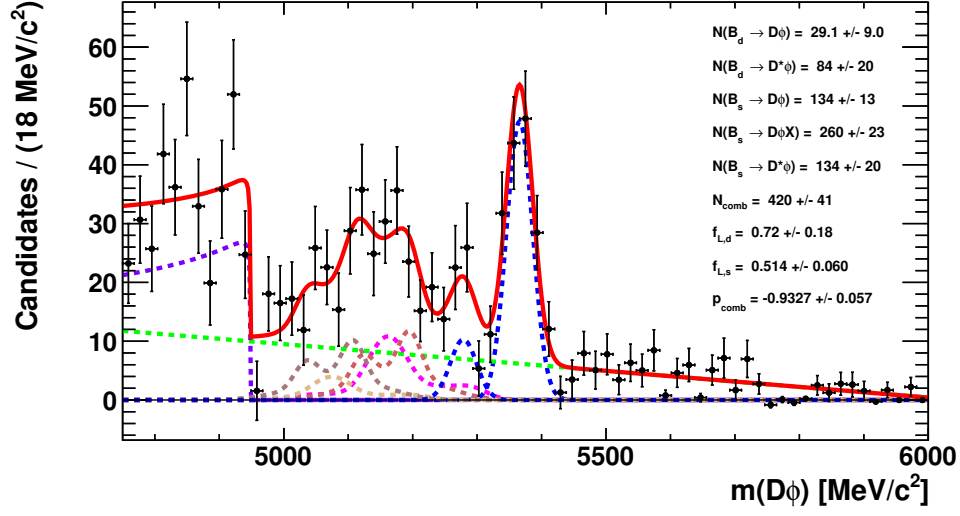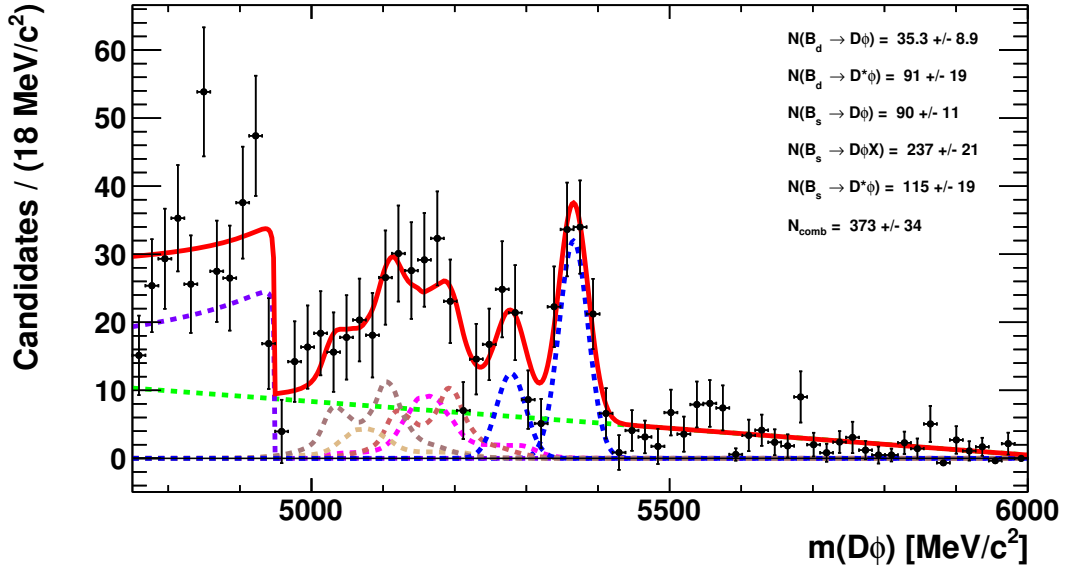
Figure 4.89: Fit to the invariant mass distribution of $B_s^0$ mass $(D\phi)$ in the full Run 1 + Run 2 Data, mass range $m_{DKK} \in [4750, 6000]\,\text{MeV}/c^2$ with sPlot technique. Data points are shown as black with error bars, total PDF is displayed with the red line. The different contributions PDFs are given as dashed lines: (green) combinatorial background and (blue) signal $B_s^0 \to D\phi$, where $D^0 \to K\pi\pi^0$. Small blue dashed $B^0 \to D\phi$, purple dashed is for $B_s^0 \to D\phi X$ signal decay, the peaking contribution $B_s^0 \to D^*\phi$ decay with magenta is for transverse and brown dashed longitudinal polarization.

Table 4.34 shows the values of the parameters from the fit.

| Parameter | $D^0 \to K\pi\pi^0$ |
|---|---|
| | **Signal Modelling** |
| $\mu(B_s^0)$ | $5366.7 \pm 2.2$ |
| $\sigma(B_s^0)$ | $19.8 \pm 1.8$ |
| $N_{(B^0 \to D\phi)}$ | $35.3 \pm 8.9$ |
| $N_{(B^0 \to D^*\phi)}$ | $91 \pm 19$ |
| $N_{(B_s^0 \to D\phi)}$ | $90 \pm 11$ |
| $N_{(B_s^0 \to D\phi X)}$ | $237 \pm 21$ |
| $N_{(B_s^0 \to D^*\phi)}$ | $115 \pm 19$ |
| | **Background Modelling** |
| $N_{comb}$ | $373 \pm 34$ |

Table 4.34: Combined fit values of the signal yields and shape parameters for four variables without Dalitz weight for Run 1 and Run 2.

One can see that the number of $B_s^0 \to D\phi$ candidates drop from $134\pm13$ candidates in the nominal fit to $90\pm11$ in the modified case of the early stage "$\pi^0$" MVA. Even if the remaining part of the selection optimisation that adding the Dalitz weight variable in the early stage of the event selection helps much in filtering and purifying the dominant

combinatorial background contribution from fake $\pi^0$. Without the Dalitz weight variable, from the combined fit which is given within $\pm 3\sigma$, the significance is obtained as $\frac{S}{\sqrt{(S+B)}} = 8.04$ and the purity is $\frac{S}{(S+B)} = 72.19$.

## 4.11 Efficiency

After the fit to the m($\phi$) and m($D\phi$) mass has been described and validated, now the total selection efficiency is computed for the studied $B_s^0$ decay modes. It is mandatory in view of the extraction of the CKM angle $\gamma$ which is described in the next chapter, and where, it has to be determined more precisely relatively to the normalisation mode $B_s^0 \to \tilde{D}^0 \phi$ and the D meson decays to the $K\pi$ final state. Therefore the efficiency for the signal mode $B_s^0 \to \overline{D}^0 \phi$ gives the proportion of the signal candidates which are produced in the LHCb detector acceptance, pass the selection steps and all the reconstructions. Total efficiency contributions can be computed according to the following product of contributions:

$$\epsilon_{TOT} = \epsilon^{geom} \times \epsilon^{sel|geom} \times \epsilon^{PID|sel\ \&\ geom} \times \epsilon^{Trigger|PID\ \&\ sel\ \&\ geom}. \qquad (4.23)$$

where:

- $\epsilon_{geom.}$ : is the efficiency of the signal events produced in acceptance of the LHCb detector. This is determined from the MC simulation events generated log files for the particular channel of interest to pass selection criteria.

- $\epsilon_{sel|geom.}$ : is the efficiency with respect to the initial cut-based selection and the MLP-based selection candidates in the acceptance of the detector and includes filtering (stripping) efficiency, tracking corrections from data.

- $\epsilon_{PID|sel\&geom}$ : is the Particle Identification (PID) efficiency relative to the selection along with the geometrical efficiency, determined from MC samples with calibration data using PIDCalib tool provided by LHCb [145].

- $\epsilon_{Trigger|PID\&sel\&geom}$ : is the efficiency of the selected events that pass the trigger requirements. It is divided for the L0 which is obtained from calibration data and HLT is from MC.

Here, each of the efficiency term $x|y$ denotes that events pass the conditions under x are relative to the y. All the efficiencies except PID efficiency are obtained using truth-matched MC simulation samples. PID efficiency is calculated with a data-driven method explained in the following sections.

### 4.11.1 Selection efficiency

Selection efficiency is calculated using MC simulation samples after passing stripping, initial and MVA selections. This efficiency includes the events which are filtered and fully reconstructed and pass the trigger requirements. Filtering includes generator (EvtGen + Pythia) level pre-selections and stripping selections are on the many simulated events and plus an additional cut on the $P_T(\pi^0)$ which was previously generated with a lower $P_T$ cut (500 MeV/$c$). The tracking efficiency is obtained from the MC differs from what it has

been measured in the data. The related efficiency needs to be corrected for each reconstructed charged track while using the LHCb centralized corrections Tables for the various data taking periods [130]. The efficiency results for filtering (stripping), geometrical, offline selection, tracking (efficiency is corrected between data and MC) are summarized in the Table 4.35.

| $\epsilon^{sel|geom}$(%) | 2011 | 2012 | 2015 | 2016 | 2017 | 2018 |
|---|---|---|---|---|---|---|
| | | | $B_s^0 \to \overline{D}^0(K^-\pi^+\pi^0)\phi$ | | | |
| filter | $0.29 \pm 0.01$ | $0.30 \pm 0.01$ | $0.57 \pm 0.01$ | $0.45 \pm 0.01$ | $0.71 \pm 0.01$ | $0.69 \pm 0.00$ |
| geom | $15.51 \pm 0.28$ | $16.06 \pm 0.21$ | $17.07 \pm 0.23$ | $16.95 \pm 0.23$ | $17.04 \pm 0.23$ | $17.05 \pm 0.05$ |
| offline sel. | $39.47 \pm 0.29$ | $37.39 \pm 0.31$ | $43.33 \pm 0.21$ | $41.62 \pm 0.25$ | $41.27 \pm 0.25$ | $40.97 \pm 0.31$ |
| tracking | $100.87 \pm 0.30$ | $104.57 \pm 0.32$ | $98.94 \pm 0.22$ | $96.66 \pm 0.24$ | $98.21 \pm 0.24$ | $97.51 \pm 0.88$ |
| | | | $B_s^0 \to D^{*0}(K^-\pi^+\pi^0)\pi^0(100)\phi$ | | | |
| filter | $0.35 \pm 0.02$ | $0.36 \pm 0.02$ | $0.71 \pm 0.04$ | $0.52 \pm 0.03$ | $0.56 \pm 0.03$ | $0.79 \pm 0.01$ |
| geom | $14.11 \pm 0.03$ | $14.40 \pm 0.04$ | $15.41 \pm 0.05$ | $15.41 \pm 0.05$ | $15.43 \pm 0.05$ | $15.45 \pm 0.05$ |
| offline sel. | $28.24 \pm 0.70$ | $26.63 \pm 0.84$ | $31.87 \pm 0.79$ | $29.88 \pm 0.85$ | $29.02 \pm 0.64$ | $30.55 \pm 0.57$ |
| tracking | $100.14 \pm 2.38$ | $103.55 \pm 3.08$ | $98.71 \pm 2.63$ | $96.50 \pm 2.83$ | $97.81 \pm 3.06$ | $97.57 \pm 1.92$ |
| | | | $B_s^0 \to D^{*0}(K^-\pi^+\pi^0)\pi^0(010)\phi$ | | | |
| filter | $0.35 \pm 0.02$ | $0.35 \pm 0.02$ | $0.65 \pm 0.04$ | $0.52 \pm 0.03$ | $0.53 \pm 0.03$ | $0.77 \pm 0.01$ |
| geom | $14.06 \pm 0.03$ | $14.37 \pm 0.04$ | $15.38 \pm 0.05$ | $15.42 \pm 0.05$ | $15.39 \pm 0.05$ | $15.44 \pm 0.05$ |
| offline sel. | $28.00 \pm 0.70$ | $27.28 \pm 0.84$ | $31.59 \pm 0.81$ | $29.24 \pm 0.85$ | $29.12 \pm 0.64$ | $29.57 \pm 0.58$ |
| tracking | $100.17 \pm 2.40$ | $103.69 \pm 3.02$ | $98.71 \pm 2.73$ | $96.35 \pm 2.86$ | $97.93 \pm 3.25$ | $97.52 \pm 1.96$ |
| | | | $B_s^0 \to D^{*0}(K^-\pi^+\pi^0)\gamma(100)\phi$ | | | |
| filter | $0.31 \pm 0.02$ | $0.32 \pm 0.02$ | $0.64 \pm 0.04$ | $0.47 \pm 0.03$ | $0.49 \pm 0.03$ | $0.71 \pm 0.00$ |
| geom | $15.68 \pm 0.03$ | $16.01 \pm 0.04$ | $17.04 \pm 0.06$ | $16.99 \pm 0.05$ | $17.03 \pm 0.03$ | $17.02 \pm 0.06$ |
| offline sel. | $29.15 \pm 0.79$ | $27.73 \pm 0.96$ | $32.81 \pm 0.89$ | $30.54 \pm 0.96$ | $30.99 \pm 0.94$ | $30.57 \pm 0.62$ |
| tracking | $100.19 \pm 2.66$ | $103.52 \pm 3.51$ | $98.78 \pm 2.91$ | $96.60 \pm 3.15$ | $100.20 \pm 2.65$ | $97.58 \pm 2.09$ |
| | | | $B_s^0 \to D^{*0}(K^-\pi^+\pi^0)\gamma(010)\phi$ | | | |
| filter | $0.32 \pm 0.02$ | $0.32 \pm 0.02$ | $0.62 \pm 0.04$ | $0.47 \pm 0.03$ | $0.50 \pm 0.03$ | $0.71 \pm 0.00$ |
| geom | $15.68 \pm 0.03$ | $15.99 \pm 0.05$ | $16.99 \pm 0.00$ | $17.00 \pm 0.05$ | $16.96 \pm 0.06$ | $16.98 \pm 0.06$ |
| offline sel. | $27.71 \pm 0.74$ | $28.15 \pm 0.93$ | $30.40 \pm 0.89$ | $28.51 \pm 1.34$ | $31.27 \pm 0.95$ | $29.52 \pm 0.61$ |
| tracking | $100.10 \pm 2.53$ | $103.60 \pm 3.38$ | $98.74 \pm 3.05$ | $96.19 \pm 4.70$ | $100.09 \pm 2.51$ | $97.54 \pm 2.09$ |

Table 4.35: Selection efficiencies for the signal mode $B_s^0 \to \overline{D}^0\phi$ and $B_s^0 \to \tilde{D}^{*0}\phi$ of MC Run 1 and Run 2.

## 4.11.2 PID efficiency

For this analysis the efficiency of PID cuts is determined by the weights from the calibration sample generated by the PIDCalib package [146] using data calibration samples of decays $D^{*+} \to D^0\pi^+$ and $D^0 \to K^-\pi^+$, where the PID system is not used. But the kaons and pions are identified from the pure kinematic criteria is such that the two pions have the same electric charge (and the $\pi$ from the $D^{*+}$ decay has the lowest momentum ("slow momentum") as the mass difference $m_{D^*} - m_{D^0}$ which is about 145.5 MeV/$c^2$, so it is just above the mass of the pion which is 139.6 MeV/$c^2$) and the kaon is the daughter of the D with opposite charge.

MC sample of $D^{*+} \to D^0\pi^0$ in dependence of total momentum ($p$), pseudorapidity ($\eta$), and number of tracks ($n_{Tracks}$) [§] variables for Run 1 and Run 2. The corresponding efficiencies are given in the Table 4.36. In this analysis PIDCalib scripts version v8r0 is used.

---

[§]referred as best tracks

| $\epsilon^{PID|sel\&geom}$ (%) | 2011 | 2012 | 2015 | 2016 | 2017 | 2018 |
|---|---|---|---|---|---|---|
| $B_s^0 \to \tilde{D}^0(K^-\pi^+\pi^0)\phi$ | | | | | | |
| D daughter | $92.62 \pm 0.28$ | $93.23 \pm 0.29$ | $95.44 \pm 0.21$ | $95.39 \pm 0.23$ | $94.92 \pm 0.23$ | $95.65 \pm 0.86$ |
| $K^+K^-$ from $\phi$ $(Prob_K >)$ | $83.33 \pm 0.25$ | $84.02 \pm 0.26$ | $90.13 \pm 0.20$ | $89.05 \pm 0.22$ | $87.56 \pm 0.21$ | $90.94 \pm 0.82$ |
| total | $77.29 \pm 0.24$ | $78.44 \pm 0.24$ | $86.04 \pm 0.19$ | $84.98 \pm 0.21$ | $83.18 \pm 0.20$ | $87.04 \pm 0.79$ |
| $B_s^0 \to D^{*0}(K^-\pi^+\pi^0)\pi^0(100)\phi$ | | | | | | |
| D daughter | $93.76 \pm 2.23$ | $94.24 \pm 2.80$ | $96.26 \pm 2.56$ | $96.12 \pm 2.82$ | $95.59 \pm 3.00$ | $95.62 \pm 1.88$ |
| $K^+K^-$ from $\phi$ $(Prob_K >)$ | $86.36 \pm 2.07$ | $87.11 \pm 2.61$ | $92.81 \pm 2.47$ | $92.11 \pm 2.71$ | $91.74 \pm 2.88$ | $90.84 \pm 1.79$ |
| total | $81.02 \pm 1.94$ | $82.14 \pm 2.46$ | $88.55 \pm 2.61$ | $88.55 \pm 2.61$ | $87.74 \pm 2.76$ | $86.95 \pm 1.72$ |
| $B_s^0 \to D^{*0}(K^-\pi^+\pi^0)\pi^0(010)\phi$ | | | | | | |
| D daughter | $93.93 \pm 2.25$ | $94.65 \pm 2.76$ | $96.06 \pm 2.66$ | $95.97 \pm 2.85$ | $95.68 \pm 3.17$ | $95.62 \pm 1.93$ |
| $K^+K^-$ from $\phi$ $(Prob_K >)$ | $86.14 \pm 2.08$ | $87.89 \pm 2.57$ | $92.87 \pm 2.58$ | $92.32 \pm 2.75$ | $91.57 \pm 3.05$ | $90.82 \pm 1.83$ |
| total | $80.98 \pm 1.96$ | $83.22 \pm 2.44$ | $89.24 \pm 2.48$ | $88.61 \pm 2.64$ | $87.67 \pm 2.92$ | $86.90 \pm 1.76$ |
| $B_s^0 \to D^{*0}(K^-\pi^+\pi^0)\gamma(100)\phi$ | | | | | | |
| D daughter | $93.84 \pm 2.49$ | $94.39 \pm 3.20$ | $96.14 \pm 2.83$ | $96.11 \pm 3.14$ | $93.82 \pm 2.49$ | $95.75 \pm 2.05$ |
| $K^+K^-$ from $\phi$ $(Prob_K >)$ | $86.53 \pm 2.32$ | $87.25 \pm 2.98$ | $92.81 \pm 2.74$ | $91.83 \pm 3.00$ | $86.50 \pm 2.31$ | $91.24 \pm 1.96$ |
| total | $81.30 \pm 2.18$ | $82.46 \pm 2.82$ | $89.24 \pm 2.64$ | $88.29 \pm 2.89$ | $81.28 \pm 2.18$ | $87.41 \pm 1.88$ |
| $B_s^0 \to D^{*0}(K^-\pi^+\pi^0)\gamma(010)\phi$ | | | | | | |
| D daughter | $93.83 \pm 2.37$ | $94.14 \pm 3.07$ | $96.07 \pm 2.97$ | $96.11 \pm 4.69$ | $93.81 \pm 2.36$ | $95.67 \pm 2.06$ |
| $K^+K^-$ from $\phi$ $(Prob_K >)$ | $86.33 \pm 2.20$ | $87.71 \pm 2.88$ | $92.36 \pm 2.86$ | $91.63 \pm 4.48$ | $86.41 \pm 2.19$ | $90.83 \pm 1.96$ |
| total | $81.10 \pm 2.07$ | $82.65 \pm 2.72$ | $88.75 \pm 2.75$ | $88.08 \pm 4.31$ | $81.17 \pm 2.06$ | $86.95 \pm 1.88$ |

Table 4.36: Particle identification efficiency (PID) for the signal mode $B_s^0 \to \tilde{D}^0\phi$ and $B_s^0 \to \tilde{D}^{*0}\phi$ for MC Run 1 and Run 2.

### 4.11.3 Trigger efficiency

This gives the efficiency of the events pass the trigger requirements. Trigger efficiency is obtained from the reconstructed simulation.

#### 4.11.3.1 L0 trigger efficiency

For this analysis trigger efficiency ($\epsilon_{Trigger}$) is obtained using HLT and both L0 tigger L0Hadron_TOS ($N_{TOS}$) and L0Global_TIS ($N_{TIS}$) are used. Schematic view of $N_{TOS}$, $N_{TIS}$ and $N_{TOS\&!TIS}$ are given in Figure 4.90. Trigger efficiency for the signal modes $B_s^0 \to \tilde{D}^0\phi$ and $B_s^0 \to \tilde{D}^{*0}\phi$ are shown in Table 4.37. This part is mainly driven by the Monte Carlo as for the HLT triggers Level 1 and Level 2, which are software based. Nevertheless L0 trigger that based on detector hardware can not be directly driven from simulation.
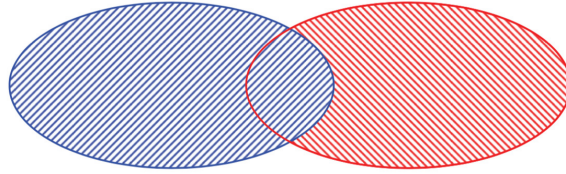


Figure 4.90: These diagrams shows the number of events $N_{TIS}$ of L0 Global TIS (blue) and $N_{TOS}$ events of L0 Hadron TOS (red) and the crossing part of the diagrams (blue & red) correspond to the events for both L0 Global TIS and L0 Hadron TOS.

| $\epsilon^{TOS\|PID\&sel\&geom}$(%) | 2011 | 2012 | 2015 | 2016 | 2017 | 2018 |
|---|---|---|---|---|---|---|
| | | | $B_s^0 \to \bar{D}^0(K^-\pi^+\pi^0)\phi$ | | | |
| $\epsilon^{TOS}$ | $35.58 \pm 0.14$ | $32.77 \pm 0.14$ | $30.19 \pm 0.09$ | $39.71 \pm 0.12$ | $40.21 \pm 0.12$ | $41.53 \pm 0.12$ |
| | | | $B_s^0 \to D^{*0}(K^-\pi^+\pi^0)\pi^0(100)\phi$ | | | |
| $\epsilon^{TOS}$ | $33.14 \pm 0.39$ | $30.04 \pm 0.43$ | $25.94 \pm 0.39$ | $36.55 \pm 0.47$ | $37.73 \pm 0.49$ | $37.99 \pm 0.32$ |
| | | | $B_s^0 \to D^{*0}(K^-\pi^+\pi^0)\pi^0(010)\phi$ | | | |
| $\epsilon^{TOS}$ | $32.31 \pm 0.31$ | $31.02 \pm 0.44$ | $26.26 \pm 0.40$ | $36.09 \pm 0.46$ | $37.12 \pm 0.54$ | $37.69 \pm 0.32$ |
| | | | $B_s^0 \to D^{*0}(K^-\pi^+\pi^0)\gamma(100)\phi$ | | | |
| $\epsilon^{TOS}$ | $32.32 \pm 0.40$ | $29.39 \pm 0.47$ | $25.68 \pm 0.42$ | $36.56 \pm 0.51$ | $37.20 \pm 0.50$ | $36.65 \pm 0.33$ |
| | | | $B_s^0 \to D^{*0}(K^-\pi^+\pi^0)\gamma(010)\phi$ | | | |
| $\epsilon^{TOS}$ | $32.02 \pm 0.40$ | $29.38 \pm 0.47$ | $26.56 \pm 0.42$ | $35.74 \pm 0.51$ | $36.82 \pm 0.50$ | $37.11 \pm 0.33$ |

Table 4.37: Trigger efficiencies for the signal mode $B_s^0 \to \tilde{D}^0\phi$ and $B_s^0 \to \tilde{D}^{*0}\phi$ for MC Run 1 and Run 2.

The total efficiency of the L0 trigger is calculated as

$$\epsilon^{L0|PID \ \& \ sel \ \& \ geom} = \frac{N_{TIS} + N_{TOS\&TIS}}{N_{gen}} \tag{4.24}$$

$$= \frac{N_{TIS}}{N_{gen}} + \frac{N_{TOS\&!TIS}}{N_{gen}} \tag{4.25}$$

$$= \frac{N_{TIS}}{N_{gen}} + \frac{N_{TOS\&!TIS} \times N_{TOS}}{N_{gen} \times N_{TOS}} \tag{4.26}$$

$$= \frac{N_{TIS}}{N_{gen}} + \frac{N_{TOS\&!TIS}}{N_{TOS}} \times \frac{N_{TOS}}{N_{gen}} \tag{4.27}$$

$$= g + f \times \epsilon^{TOS|PID \ \& \ sel \ \& \ geom} \tag{4.28}$$

$$f = \frac{N_{TOS\&!TIS}}{N_{TOS}}, \tag{4.29}$$

and

$$g' = \frac{N_{TIS}}{N_{TOS}}, \tag{4.30}$$

$$g = \frac{N_{TIS}}{N_{gen}} = \frac{N_{TIS}}{N_{TOS}} \times \frac{N_{TOS}}{N_{gen}} = g' \times \epsilon^{TOS|PID \ \& \ sel \ \& \ geom} \tag{4.31}$$

$N_{TOS}/N_{gen}$ gives the $\epsilon^{TOS}$. $N_{gen}$ denotes the number of events that passes the selections. The $f$ and $g$ are determined by the number of $N_{TIS}$, $N_{TOS}$, $N_{gen}$ and $N_{TOS\&!TIS}$ which represents the number of events triggered only by L0Hadron_TOS (not by TIS). The values of f and g are computed using the number of events in the control mode $B_s^0 \to \bar{D}^0 K^+ K^-$ extracted from the fit to the data for each trigger requirement taken from [121]. The values for $f$ and $g'$ are obtained for Run 1 and Run 2 as shown in the

| DATA | $f$ | $g'$ |
|------|-----|------|
| RUN1 | $67.35 \pm 2.1$ | $99.28 \pm 4.16$ |
| RUN2 | $65.96 \pm 0.96$ | $102.94 \pm 2.28$ |

Table 4.38: $f$ and $g'$ values for the signal $B_s^0 \to \tilde{D}^0 \phi$ for Run 1 and Run 2. The values were computed based on the reference mode $D^0 \to K\pi$ [121].

Table 4.38. These values were computed based on the large dataset of the sub-decay mode $D^0 \to K\pi$ and explained in [121].

When we study the efficiency on the $\tilde{D}^0 \to K\pi\pi^0$ mode, we compute the values for $f$ and $g'$ fractions which shown in Table 4.39 and Table 4.40 which are compatible with the values in Table4.38 for $D^0 \to K\pi$. And one can see that the values are obtained with very large error bars as the statistic is much lower in our sub-decay $\tilde{D}^0 \to K\pi\pi^0$ with respect to the $D^0 \to K\pi$.

| $f$ | RUN1 | RUN2 | RUN1+2 |
|------|------|------|--------|
| MC | $59.49 \pm 0.00$ | $56.64 \pm 0.00$ | $-$ |
| DATA | $85.90 \pm 71.39$ | $63.98 \pm 30.59$ | $68.67 \pm 27.15$ |

Table 4.39: $f$ values for the signal $B_s^0 \to \tilde{D}^0 \phi$ for Run 1 and Run 2. These values are computed based on the $\tilde{D}^0 \to K\pi\pi^0$ mode.

| $g'$ | RUN1 | RUN2 | RUN1+2 |
|------|------|------|--------|
| MC | $119.56 \pm 0.00$ | $116.28 \pm 0.00$ | $-$ |
| DATA | $102.56 \pm 39.83$ | $89.69 \pm 18.69$ | $92.04 \pm 16.91$ |

Table 4.40: $g'$ values for the signal $B_s^0 \to \tilde{D}^0 \phi$ for Run 1 and Run 2. These values are computed based on the $\tilde{D}^0 \to K\pi\pi^0$ mode.

### 4.11.4 Total efficiency

Total efficiency is obtained from different contributions defined as follows:

- discrepancies between Monte Carlo and Data for PID : data-driven method (PID-Calib) to determine $\epsilon_{PID|sel\&geom}$ ;

- discrepancies between Monte Carlo and Data for L0 TOS trigger : data driven method to determine $\epsilon_{Trigger|PID\&sel\&geom}$;

- small discrepancies between Monte Carlo and Data for tracking : data-driven method to correct tracking efficiency in $\epsilon^{sel|geom}$ ;

Table 4.41 shows the total efficiency of the each selections which pass the requirements for the signal mode $B_s^0 \to \tilde{D}^0\phi$ and Table 4.42 is the total efficiency from the different contributions to the final selection for $B_s^0 \to \tilde{D}^{*0}\phi$ for Run 1 and Run 2.

| | 2011 | 2012 | 2015 | 2016 | 2017 | 2018 |
|---|---|---|---|---|---|---|
| | | | $B_s^0 \to \overline{D}^0(K^-\pi^+\pi^0)\phi$ | | | |
| $\epsilon^{geom}(\%)$ | $15.51 \pm 0.28$ | $16.06 \pm 0.21$ | $17.07 \pm 0.23$ | $16.95 \pm 0.23$ | $17.04 \pm 0.23$ | $17.05 \pm 0.05$ |
| $\epsilon^{sel|geom}(\%)$ | $0.12 \pm 0.00$ | $0.12 \pm 0.00$ | $0.24 \pm 0.00$ | $0.18 \pm 0.00$ | $0.29 \pm 0.01$ | $0.28 \pm 0.00$ |
| $\epsilon^{PID|sel\&geom}(\%)$ | $77.29 \pm 0.24$ | $78.44 \pm 0.24$ | $86.04 \pm 0.19$ | $84.98 \pm 0.21$ | $83.18 \pm 0.20$ | $87.04 \pm 0.79$ |
| $\epsilon^{TOS|PID\&sel\&geom}(\%)$ | $35.58 \pm 0.14$ | $32.77 \pm 0.14$ | $30.19 \pm 0.09$ | $39.71 \pm 0.12$ | $40.21 \pm 0.12$ | $41.54 \pm 0.12$ |
| $\epsilon^{tot}(10^{-4})$ | $0.84 \pm 0.05$ | $0.81 \pm 0.05$ | $1.79 \pm 0.10$ | $1.73 \pm 0.99$ | $2.71 \pm 0.15$ | $2.83 \pm 0.16$ |

Table 4.41: Summary of the total efficiency for the signal mode $B_s^0 \to \tilde{D}^0\phi$.

| | 2011 | 2012 | 2015 | 2016 | 2017 | 2018 |
|---|---|---|---|---|---|---|
| | | | $B_s^0 \to D^{*0}(K^-\pi^+\pi^0)\pi^0(100)\phi$ | | | |
| $\epsilon^{geom}(\%)$ | $14.11 \pm 0.03$ | $14.40 \pm 0.04$ | $15.41 \pm 0.05$ | $15.41 \pm 0.05$ | $15.43 \pm 0.05$ | $15.45 \pm 0.05$ |
| $\epsilon^{sel|geom}(\%)$ | $0.09 \pm 0.01$ | $0.10 \pm 0.01$ | $0.22 \pm 0.02$ | $0.15 \pm 0.01$ | $0.16 \pm 0.01$ | $0.24 \pm 0.01$ |
| $\epsilon^{PID|sel\&geom}(\%)$ | $81.02 \pm 1.94$ | $82.14 \pm 2.46$ | $89.36 \pm 2.38$ | $88.55 \pm 2.61$ | $87.74 \pm 2.76$ | $86.95 \pm 1.72$ |
| $\epsilon^{TOS|PID\&sel\&geom}(\%)$ | $33.14 \pm 0.39$ | $30.04 \pm 0.43$ | $25.94 \pm 0.39$ | $36.55 \pm 0.47$ | $37.73 \pm 0.49$ | $37.99 \pm 0.32$ |
| $\epsilon^{tot}(10^{-4})$ | $0,62 \pm 0.05$ | $0.59 \pm 0.06$ | $1.33 \pm 1.12$ | $1.25 \pm 0.12$ | $1.35 \pm 1.13$ | $2.00 \pm 0.13$ |
| | | | $B_s^0 \to D^{*0}(K^-\pi^+\pi^0)\pi^0(010)\phi$ | | | |
| $\epsilon^{geom}(\%)$ | $14.06 \pm 0.03$ | $14.37 \pm 0.04$ | $15.38 \pm 0.05$ | $15.42 \pm 0.05$ | $15.39 \pm 0.05$ | $15.44 \pm 0.05$ |
| $\epsilon^{sel|geom}(\%)$ | $0.09 \pm 0.01$ | $0.10 \pm 0.01$ | $0.20 \pm 0.01$ | $0.15 \pm 0.01$ | $0.15 \pm 0.01$ | $0.22 \pm 0.01$ |
| $\epsilon^{PID|sel\&geom}(\%)$ | $80.98 \pm 1.96$ | $83.22 \pm 2.44$ | $89.24 \pm 2.48$ | $88.61 \pm 2.64$ | $87.67 \pm 2.92$ | $86.90 \pm 1.76$ |
| $\epsilon^{TOS|PID\&sel\&geom}(\%)$ | $32.31 \pm 0.31$ | $31.03 \pm 0.44$ | $26.26 \pm 0.40$ | $36.09 \pm 0.46$ | $37.12 \pm 0.54$ | $37.69 \pm 0.32$ |
| $\epsilon^{tot}(10^{-4})$ | $0.60 \pm 0.05$ | $0.62 \pm 0.06$ | $1.22 \pm 0.11$ | $1.21 \pm 0.11$ | $1.26 \pm 0.12$ | $1.88 \pm 0.12$ |
| | | | $B_s^0 \to D^{*0}(K^-\pi^+\pi^0)\gamma(100)\phi$ | | | |
| $\epsilon^{geom}(\%)$ | $15.67 \pm 0.03$ | $16.01 \pm 0.04$ | $17.04 \pm 0.06$ | $16.99 \pm 0.05$ | $17.03 \pm 0.03$ | $17.02 \pm 0.06$ |
| $\epsilon^{sel|geom}(\%)$ | $0.09 \pm 0.01$ | $0.09 \pm 0.01$ | $0.21 \pm 0.02$ | $0.14 \pm 0.01$ | $0.16 \pm 0.01$ | $0.21 \pm 0.01$ |
| $\epsilon^{PID|sel\&geom}(\%)$ | $81.30 \pm 2.18$ | $82.46 \pm 2.82$ | $89.24 \pm 2.64$ | $88.29 \pm 2.89$ | $81.28 \pm 2.18$ | $87.41 \pm 1.88$ |
| $\epsilon^{TOS|PID\&sel\&geom}(\%)$ | $32.32 \pm 0.40$ | $29.39 \pm 0.47$ | $25.68 \pm 0.42$ | $36.56 \pm 0.51$ | $37.19 \pm 0.50$ | $36.65 \pm 0.33$ |
| $\epsilon^{tot}(10^{-4})$ | $0.63 \pm 0.06$ | $0.59 \pm 0.06$ | $1.35 \pm 0.13$ | $1.26 \pm 0.12$ | $1.33 \pm 0.13$ | $1.93 \pm 0.13$ |
| | | | $B_s^0 \to D^{*0}(K^-\pi^+\pi^0)\gamma(010)\phi$ | | | |
| $\epsilon^{geom}(\%)$ | $15.68 \pm 0.03$ | $15.99 \pm 0.05$ | $16.99 \pm 0.00$ | $17.00 \pm 0.05$ | $16.96 \pm 0.06$ | $16.98 \pm 0.06$ |
| $\epsilon^{sel|geom}(\%)$ | $0.09 \pm 0.01$ | $0.09 \pm 0.01$ | $0.19 \pm 0.01$ | $0.13 \pm 0.01$ | $0.16 \pm 0.01$ | $0.20 \pm 0.01$ |
| $\epsilon^{PID|sel\&geom}(\%)$ | $81.10 \pm 2.07$ | $82.65 \pm 2.72$ | $88.75 \pm 2.75$ | $88.08 \pm 4.31$ | $81.17 \pm 2.06$ | $86.95 \pm 1.88$ |
| $\epsilon^{TOS|PID\&sel\&geom}(\%)$ | $32.02 \pm 0.40$ | $29.38 \pm 0.47$ | $26.56 \pm 0.42$ | $35.74 \pm 0.51$ | $36.82 \pm 0.50$ | $37.11 \pm 0.33$ |
| $\epsilon^{tot}(10^{-4})$ | $0.59 \pm 0.05$ | $0.61 \pm 0.06$ | $1.24 \pm 0.12$ | $1.15 \pm 1.13$ | $1.32 \pm 0.12$ | $1.86 \pm 0.12$ |

Table 4.42: Summary of the total efficiency for the signal mode $B_s^0 \to \tilde{D}^{*0}\phi$.

## 4.12 Systematic uncertainties

After the efficiency studies, a study on the systematic uncertainties is performed. In this section, systematics are studied selections-induced for the special mode $\tilde{D}^0 \to K\pi\pi^0$ with respect to the reference mode $\tilde{D}^0 \to K\pi$. For the extraction of the CKM angle $\gamma$ [4], we only need to know the relative systematic uncertainties survived with respect to the reference mode $\tilde{D}^0 \to K\pi$. We develop the selections of our sub-decay mode $\tilde{D}^0 \to K\pi\pi^0$ such that they are mostly similar to the reference mode $\tilde{D}^0 \to K\pi$. Most of the selections therefore vanish in the ratio of efficiencies. In this part, we only study those that differ from the reference mode $\tilde{D}^0 \to K\pi$ and that are specific to the final state mode $\tilde{D}^0 \to K\pi\pi^0$ of interest. The following sections explains the potential sources of systematic uncertainties considered during the $B_s^0 \to \overline{D}^{(*)0}\phi$ analysis.

### 4.12.1 Uncertainties on $K^-\pi^+\pi^0$ candidate selection by multivariate analysis BDT

The nominal signal efficiency (for the early stage MVA (5 variables)) optimised for the $\tilde{D}^0 \to K^-\pi^+\pi^0$ is 85%. For the systematics, the variations around this nominal efficiency are investigated and set at 80% and 90% for MC and Data. The systematic is computed as the average deviation from this two tested option with respect to the nominal value of 85%. The number of events for these variations are given in Table 4.43. From this variation, the systematics for the MC and for Data are obtained.

| | Number of events(80%) | Number of events(Nominal 85%) | Number of events(90%) | Systematic Uncertainty |
|---|---|---|---|---|
| MC (count) | 47.624 | 50.543 | 53.346 | 1.3% |
| DATA (fitted) | $122.04 \pm 11.94$ | $134 \pm 13$ | $145, 18 \pm 13, 54$ | |

Table 4.43: Number of events for 80%, 85% and 90% variations for the BDT with five variables.

### 4.12.2 Uncertainties on $m_{\pi^0}$ mass interval

In the section 4.4.5, a study has been done for the optimisation of the $\pi^0$ mass adjustment to have the similar distributions for both in the Data and MC. For the systematics on the mass of the $\pi^0$, the range of the mass window is chosen as $\pm 2\,\text{MeV}/c^2$. Table 4.44 shows the result for the systematics.

| | Number of events $[-2, +2]\,\text{MeV}/c^2$ | Number of events $[+2, -2]\,\text{MeV}/c^2$ | Number of events(Nominal value 85%) | Systematic Uncertainty |
|---|---|---|---|---|
| MC (count) | 51.781 | 48.993 | 50.543 | 1.6% |
| DATA (fitted) | $141.98 \pm 13.16$ | $123.82 \pm 12.59$ | $134 \pm 13$ | |

Table 4.44: Number of events for the $\pi^0$ mass systematic uncertainties.

### 4.12.3 Uncertainties on the final selection with the MLP selection with $D^0 \to K^- \pi^+ \pi^0$ vs Fisher selection for $D^0 \to K^+ \pi^-$

Systematics on the final selection for the $D^0 \to K^- \pi^+ \pi^0$ MLP with 11 variables and analysis on $K\pi$ with the final MVA Fisher 6 variables for the measurements of the branching ratio of the decay modes $B_s^0 \to \overline{D}^{(*)0}\phi$ [121] are examined. Differences between the MC efficiencies are taken of these two selections. We take half of the difference as systematic. The results for the systematics are given in the Table 4.45.

| | Number of events ( with 6 variable) | Number of events ( with 11 variable) | Systematic Uncertainty |
|---|---|---|---|
| MC (count) | 53.683 | 50.543 | 2.6% |
| DATA (fitted) | $137.06 \pm 13.56$ | $134 \pm 13$ | |

Table 4.45: Number of events for $B_s^0 \to \tilde{D}^0 \phi$ with MLP 11 variables and $D^0 \to K\pi$ with Fisher 6 variables.

### 4.12.4 Uncertainties on stripping $\gamma(CL, 1)$ and $\gamma(CL, 2)$

In the stripping, for two photons $gamisNotH$, there is $\gamma(CL, 1) > 25\%$ and $\gamma(CL, 2) > 25\%$. This is changed as $\gamma(CL) > 30\%$ to see the variation on this efficiency. The systematic is computed as half of the tested alternate option to the nominal value of 25%. Number of events for MC and Data are given in Table 4.46

| | Number of events (%30) | Number of events (%25) | Systematic Uncertainty |
|---|---|---|---|
| MC (count) | 47.885 | 50.543 | 3.5% |
| DATA (fitted) | $119.07 \pm 11.93$ | $134 \pm 13$ | |

Table 4.46: Number of events for the stripping $\gamma(CL) > 25\%$ for two photons.

### 4.12.5 Total relative systematic uncertainty

The total systematic uncertainties for the all sources taken into account are listed in Table 4.47 for the specific decay $D^0 \to K^- \pi^+ \pi^0$ and $B_s^0 \to \tilde{D}^0 \phi$. The total relative systematic is about 4.8% and corresponding to about $\pm 6.5$ events to be compared to the $134 \pm 13$ fitted $N(B_s^0 \to D\phi)$ events, where the latter uncertainty is only statistical.

159

| Source of Systematic | $F_{K^-\pi^+\pi^0}$ |
| --- | --- |
| BDT selection for $\pi^0$ at 80% and $\pi^0$ at 90% | 1.3% |
| $m_{\pi^0}$ mass selection at $[-2,+2]\,\mathrm{MeV}/c^2$ | 1.6% |
| MLP vs Fisher 6 vars.(95%)+$m(D^0)$ | 2.6% |
| Stripping $\gamma(CL) > 25\%$ | 3.5% |
| TOTAL | 4.8% |

Table 4.47: Summary of total systematics for all the sources. The above effects are independent therefore summed in quadrature for the Total.

## 4.13   Extraction of the CKM angle $\gamma$ from $B_s^0 \to \tilde{D}^{(*)0}\phi$ and results

In this part of the thesis, the results are presented where the weak phase $\gamma$ is extracted from time-integrated and untagged measurement of $B_s^0 \to \tilde{D}^{(*)0}\phi$ decays, with the combination of D meson decays to five sub-modes: $KK, \pi\pi, K\pi, K\pi\pi, K\pi\pi^0$. In addition to the angle $\gamma$, the values on the unknown nuisance strong interaction parameters: $r_B, r_B^*$ and $\delta_B, \delta_B^{(*)}$ are determined. The strategy is here to obtain the observables for $B_s^0 \to \tilde{D}^{(*)0}\phi$ decays and to determine the angle $\gamma$ with the high sensitivity and the earlier study on this has been introduced in the recent sensitivity paper on $\gamma$ [[4], [7]]. The sensitivity study has been relying on rough extrapolation based on the analysis developed for the $B_s^0 \to \overline{D}^0 K^+ K^-$ decay [9]. Now we repeat this study and optimise the selections for the various $B_s^0 \to \tilde{D}^{(*)0}\phi$ channels to obtain a very high purity and the most abundant signal of $B_s^0 \to D^0\phi$ to achieve the best sensitivity on $\gamma$ angle. We use the formalism to determine the observables for $B_s^0 \to \tilde{D}^{(*)0}\phi$ and the choice of the D-meson final states introduced in the recent sensitivity study of the CKM angle $\gamma$ [[4], [7]] and the details are given in the Appendix A. Number of yields are calculated and the longitudinal polarisation fraction considered for $B_s^0 \to \tilde{D}^{*0}\phi$ is $f_L(B_s^0 \to \overline{D}^{*0}\phi) = (53.1 \pm 6.0 \pm 1.0)\%$ (taken from [121]). The corresponding signal yields for $B_s^0 \to \tilde{D}^{(*)0}\phi$, where $D^{(*)0}$ decays to final states $f^-(f)$ quasi flavour-specific modes and their CP conjugates $f^+(\bar{f})$: $K^-\pi^+, K^+\pi^-, K^-3\pi, K^+3\pi, K^-\pi^-\pi^0, K^-\pi^+\pi^0$ and CP-eigenstates $f_{CP}$: $K^+K^-, \pi^+, \pi^-$ obtained with full datasets Run 1 and Run 2 are shown in Table 4.48. Any observed asymmetry for the $D^0$-meson decays rate to final state $f$ and $\bar{f}$ are considered and the asymmetry is defined as

$$A_{CP} = \frac{N(B_s^0 \to [f]_D\phi) - N(B_s^0 \to [\bar{f}]_D\phi)}{N(B_s^0 \to [f]_D\phi) + N(B_s^0 \to [\bar{f}]_D\phi)}. \tag{4.32}$$

where N gives the number of the observed decays and $\phi$ decays to $K^+K^-$. The details are given how to calculate signal yields from the Eq. A.17, A.20, A.18, A.21 for each observed decays in Appendix A. Any differences observed on the yields of the signal

which will lead to the explanation of the CP violation. The asymmetry determined for the $D \to K\pi$, $D \to K3\pi$, $D \to K\pi\pi^0$ and $D^* \to D\pi^0$, $D^* \to D\gamma$, where $D$ decays to $K\pi, K3\pi, K\pi\pi^0$ are given in Table 4.48.

| $B_s^0 \to \tilde{D}^0\phi$ | Yields | Asymmetry |
|---|---|---|
| $D \to K^-\pi$ | 449.49±22.44 | (-2.0±3.5)% |
| $D \to K^+\pi$ | 467.63±22.66 | |
| $D \to K^-3\pi$ | 267.33±17.91 | (11.7±5.0)% |
| $D \to K^+3\pi$ | 211.20±16.06 | |
| $D \to K^-\pi^+\pi^0$ | 79.00±11.88 | (18.8±11.9)% |
| $D \to K^+\pi^-\pi^0$ | 53.98±10.52 | |
| $D \to KK$ | 158.75±13.98 | |
| $D \to \pi\pi$ | 41.75±7.06 | |

| $B_s^0 \to \tilde{D}^{*0}\phi$ | $D^0\gamma$ | | $D^0\pi^0$ | |
|---|---|---|---|---|
| $\tilde{D}^{*0} \to K^-\pi$ | 181.36±56.95 | (49.56±30.1)% | 195.28±33.01 | (-16.2±10.3)% |
| $\tilde{D}^{*0} \to K^+\pi$ | 61.16±44.95 | | 270.78±34.28 | |
| $\tilde{D}^{*0} \to K^-3\pi$ | 106.08±50.69 | (-15.6±28.8)% | 75.33±27.08 | (-22.3±20.4)% |
| $\tilde{D}^{*0} \to K^+3\pi$ | 145.45±50.36 | | 118.62±28.21 | |
| $\tilde{D}^{*0} \to K^-\pi^+\pi^0$ | 3.25±204.03 | (-61.5±1953.0)% | 23.58±38.64 | (100.0±165.3)% |
| $\tilde{D}^{*0} \to K^+\pi^-\pi^0$ | 13.65±45.56 | | 0.00±19.49 | |
| $\tilde{D}^{*0} \to KK$ | 79.06±27.76 | | 84.07±18.23 | |
| $\tilde{D}^{*0} \to \pi\pi$ | 50.45±19.04 | | 17.13±10.86 | |

Table 4.48:  The yields obtained for each mode with $9.1\,\text{fb}^{-1}$ (Run 1 and Run 2 data). The yields for the $B_s^0 \to \tilde{D}^*\phi$ are scaled by the longitudinal fraction of polarisation $f_L(B_s^0 \to \overline{D}^{*0}\phi) = (53.1 \pm 6.0 \pm 1.0)\%$ [121]) in order to determine the final state similar to the $B_s^0 \to \tilde{D}^0\phi$ [4]. The asymmetry is calculated for the $D \to K\pi$, $D \to K3\pi$, $D \to K\pi\pi^0$ and $D^* \to D\pi^0$, $D^* \to D\gamma$, where $D$ decays to $K\pi, K3\pi, K\pi\pi^0$.

The normalisation factors $C_{K\pi}$ are calculated from the Eq. A.15 for $B_s^0 \to \tilde{D}^0\phi$ and $C_{K\pi,D\pi^0}$, $C_{K\pi,D\gamma}$ for $B_s^0 \to \tilde{D}^{*0}\phi$ are determined in the same way of $C_{K\pi}$ defined in Appendix A.2 and A.3. The values for the inputs are taken from PDG [18]. The normalisation factors are obtained as $C_{K\pi}$, $C_{K\pi,D\pi^0}$, $C_{K\pi,D\gamma}$ are 966.3±106, 431.4±69, 193±31 respectively. They should be compared to the sum of $D \to K\pi$, $D^* \to D^0\pi^0(K\pi)$, $D^* \to D^0\gamma(K\pi)$ columns which are respectively: 917±32, 466±47 and 242±72 given in the Table 4.48. The scale factors for each decay mode are calculated through the Eq. A.19, where it depends on the detection efficiencies and the branching fractions (taken from [18]) of the corresponding final states and the obtained values are given in Table 4.49.

Using the same statistical method as been described in [4] based on the CKMfitter code and, when minimizing a global $\chi2$, we obtain Figures 4.91 show the one-dimensional p-profile value of the nuisance parameters: $r_B^{(*)}$, $\delta_B^{(*)}$ respectively. From the Figure 4.91, it can be clearly seen that $r_B^{(*)}$ is obtained away from being 0 and obtained as $r_B = 0.19^{+0.15}_{-0.13}$ and $r_B^* = 0.52^{+0.19}_{-0.22}$ at 68% CL (1$\sigma$). For the bottom plots: $\delta_B$ (left) and $\delta_B^*$ (right) parameters are shown respectively. One can see that p-value is maximum for $\delta_B$ at $\delta_B = 0.86$ rad and $\delta_B = 4.00$ rad, for the $\delta_B^*$ peaked at $\delta_B^* = 1.93$ rad and $\delta_B^* = 5.07$ rad. The fit parameters obtained are given in Table 4.50

| Parameter | Value |
|---|---|
| $-2\beta_S$ [mrad] | $-36.86 \pm 0.82$ [147] |
| $y = \Delta\Gamma_s/2\Gamma_s$ (%) | $6.40 \pm 0.45$ [148] |
| $r_D^{K\pi}$ (%) | $5.87^{+0.02}_{-0.02}$ |
| $\delta_D^{K\pi}$ [deg] | $189.9^{+4.2}_{-4.1}$ |
| $r_D^{K3\pi}$ (%) | $5.56 \pm 0.06$ |
| $R_D^{K3\pi}$ (%) | $48 \pm 6.4$ |
| $\delta_D^{K3\pi}$ [deg] | $153.95^{14.95}_{15.99}$ |
| $r_D^{K\pi\pi^0}$ (%) | $4.48 \pm 0.08$ |
| $R_D^{K\pi\pi^0}$ (%) | $79 \pm 3$ |
| $\delta_D^{K\pi\pi^0}$ [deg] | $197 \pm 10.26$ |
| Scale factor (wrt $K\pi$) | (stat. uncertainty only) |
| $F_{K3\pi}^{-}$ (%) | $57.3 \pm 1.24$ |
| $F_{K3\pi}^{+}$ (%) | $57.3 \pm 1.24$ |
| $F_{K\pi\pi^0}^{-}$ (%) | $28.5 \pm 1.9$ |
| $F_{K\pi\pi^0}^{+}$ (%) | $28.5 \pm 1.9$ |
| $F_{KK}$ (%) | $10.8 \pm 0.2$ |
| $F_{\pi\pi}$ (%) | $3.2 \pm 0.1$ |

Table 4.49: Other external parameters used in the analysis. The scale factors $F$ are also listed for each sub-decay mode. The value of $R_D$ is one for two-body decays and the value of $r_D$ is one for the CP-eigenstates.
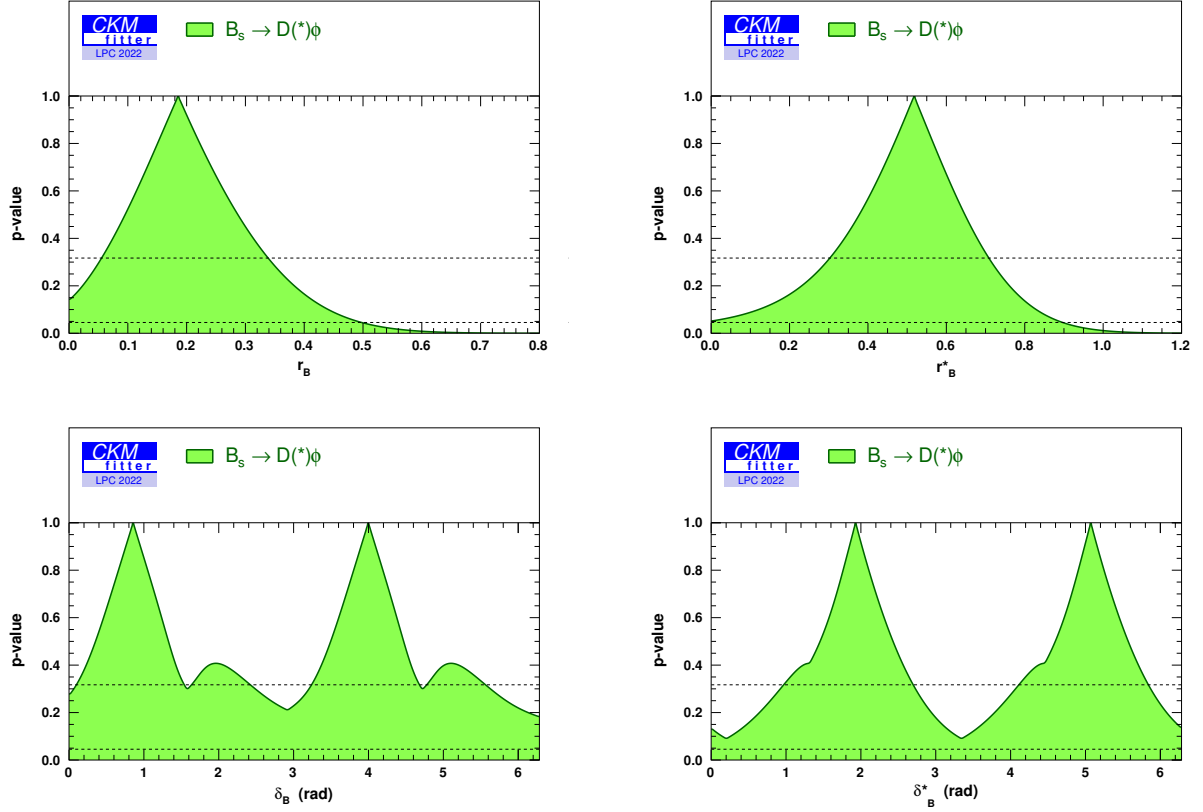
Figure 4.91: (Top) Profile of the p-value distribution of the global $\chi 2$ fit to $r_B$ (top left) and $r_B^*$ (topright) after observables are computed, for fitted parameters: $\gamma = 75.06°(1.31$ rad), $r_B = 0.19^{+0.15}_{-0.13}$ $(1\sigma)$, $r_B = 0.19^{+0.31}_{-\infty}$ $(2\sigma)$, $r_B = 0.19^{+0.48}_{-\infty}$ $(3\sigma)$, and $r_B^* = 0.52^{+0.19}_{-0.22}(1\sigma)$, $r_B^* = 0.52^{+0.38}_{-\infty}(2\sigma)$, $r_B^* = 0.52^{+0.58}_{-\infty}(3\sigma)$. The two horizontal dashed black lines refer to 68.3 % (1 $\sigma$) and 95.4 % CL (2 $\sigma$,) respectively. (Bottom) Profile of the p-value distribution of the global $\chi 2$ fit to $\delta_B$ (bottom left) and $\delta_B^*$ (bottom right) after observables are computed, for fitted parameters: $\gamma = 75.06°(1.31$ rad), $\delta_B = 49.27°(0.86$ rad), $229°(4.00$ rad) (1 $\sigma$) respectively and $\delta_B^* = 111°(1.93$ rad) and $\delta_B^* = 291°(5.07$ rad) (1$\sigma$). The horizontal two dashed black lines refer to 68.3 % (1 $\sigma$) and 95.4 % CL (2 $\sigma$), respectively.

| Parameter | Value ($1\sigma$) | Value ($2\sigma$) |
|---|---|---|
| $\gamma$ (UT) | $1.31^{+0.26}_{-0.51}$ | $1.3^{+1.8}_{-1.2}$ |
| $r_B$ | $0.19^{+0.15}_{-0.13}$ | $0.19^{+0.31}_{-\infty}$ |
| $r_B^*$ | $0.52^{+0.19}_{-0.22}$ | $0.52^{+0.38}_{-\infty}$ |
| $\delta_B$ | $4.00^{+0.68}_{-0.76}\|5.10^{+0.46}_{-0.32}\|1.96^{+0.46}_{-0.32}\|0.86^{+0.68}_{-0.76}$ | |
| $\delta_B^*$ | $5.07^{+0.77}_{-0.96}\|1,93^{+0.77}_{-0.96}$ | |

Table 4.50: Values of the fit parameters.

After having displayed the nominal fits of the parameters $\gamma$, $r_B$, $r_B^*$, $\delta_B$, $\delta_B^*$, we have performed a few studies to evaluate the sensitivity of the nominal results as a function of the various employed observables. Figure 4.92 (left) displays the constraint on $\gamma$ from $B_s^0 \to \tilde{D}^0 \phi$ decay where D reconstructed in $KK, \pi\pi, K\pi, K\pi\pi, K\pi\pi^0$ is given with the green curve combining all the yields and the latest $\gamma$ combination measurement by the LHCb [2] is shown with the blue straight line. For the fitted parameters $\gamma=(75^{+15}_{-29})^\circ$, $r_B$ =0.19, $\delta_B$ =0.86 rad, $r_B^*$ =0.52, $\delta_B^*$ =1.93 rad. Also a distribution is presented in Figure 4.92 (right) with a full frequentist treatment on Monte Carlo (MC) simulation basis performed which is referred as PLUGIN method [[149] and [150]], where $\gamma$ =$(75^{+23}_{-21})^\circ$. It can be seen that both values obtained for the CKM angle $\gamma$ are quite in agreement, and demonstrating that the fits based on global $\chi 2$ minimization can be trusted and used to extract the relevant physics parameters displayed in this thesis work. One can see that the obtained precision on $\gamma$ is compatible to that one expects as written in the paper on the preliminary sensitivity study [4](see Figure 4.93)



Figure 4.92: Profile of the p-value distribution of the global $\chi 2$ fit to $\gamma$ after observables are computed, where the decay mode $B_s^0 \to \tilde{D}^{(*)0} \phi$ is considered. The $D^0$ decays to five sub-decay modes: $KK$, $\pi\pi$, $K\pi$, $K3\pi$, $K\pi\pi^0$ are taking into account. (Top figure) For fitted parameters: $\gamma$ value at maximum is $\gamma$ =$1.31^{+0.26}_{-0.51}$ rad, and $r_B$ =0.19, $\delta_B$ =0.86 rad, $r_B^*$ =0.52, $\delta_B^*$ =1.93 rad. The latest $\gamma$ combination is displayed on the plot for the comparison [2]. (Right) Profile of the p-value distribution of the $\chi 2$ fit to the $\gamma$ for the decay mode $B_s^0 \to \tilde{D}^{(*)0} \phi$ is obtained for the fitted parameters $\gamma$ =$1.31^{+0.40}_{-0.36}$ rad, $r_B$ =0.18, $\delta_B$ =0.86 rad, $r_B^*$ =0.52, $\delta_B^*$ =1.93 rad. The corresponding distribution obtained from a full frequentist treatment(PLUGIN method) on Monte Carlo simulation basis is superimposed to the same distribution. The horizontal two dashed black lines refer to 68.3 % (1 $\sigma$) and 95.4 % CL (2 $\sigma$).

Figure 4.94 displays the constraint on the CKM angle $\gamma$ for the full combination of $B_s^0 \to \tilde{D}^{(*)0} \phi$ shown in green curve combining the decay modes: $KK$, $\pi\pi$, $K\pi$, $K3\pi$, $K\pi\pi^0$ and the corresponding fitted value of $\gamma$ is obtained $\gamma=(75^{+15}_{-29})^\circ$, and we also show a distribution for $\gamma$ superimposed to the same $B_s^0 \to \tilde{D}^{(*)0} \phi$ without $K\pi\pi^0$ given with the
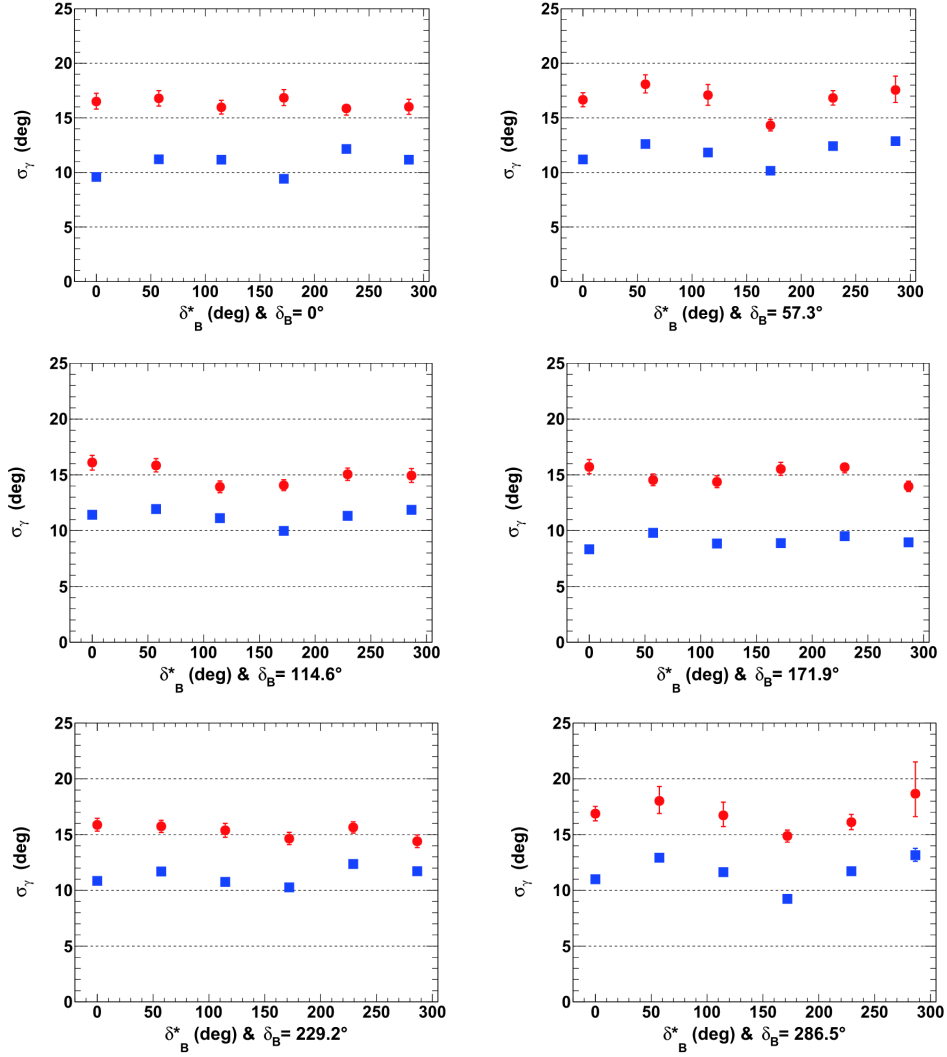
Figure 4.93: Fitted resolution of $\gamma$ ($\sigma_\gamma$), for $r_B^*$=0.22 (red circles) and 0.4 (blue squares), as a function of $\delta_B^*$, for an initial true value of 65.66° (1.146 rad). All the listed values are in [deg]. On each figure, the horizontal dashed black lines are guide for the eye at $\sigma_\gamma$=5°, 10°, 15° and 20°. All the plotted uncertainties are statistical only. Taken from [4].

red dashed line with the corresponding $\gamma=(72.77^{+10.89}_{-24.64})°$with the slight better precision. On the right side plot the p-profile value of $\gamma$ provided by keeping the only distribution of $B_s^0 \to \tilde{D}^{(*)0}\phi$ excluding the information from $B_s^0 \to D^*\phi$, the value of $\gamma=(74^{+18}_{-53})°$with the $r_B$ =0.19, $\delta_B$ =0.85 rad (49°). And one can see that from the Figure 4.94, the distribution for $B_s^0 \to D\phi$ CL interval is enlarged.
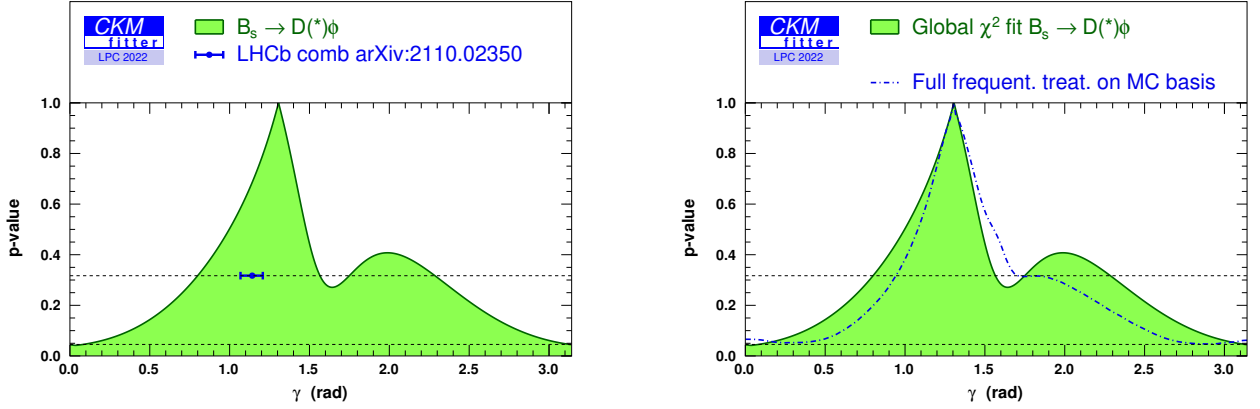
Figure 4.94: Profile of the p-value distribution of the global $\chi 2$ fit to $\gamma$ after observables are computed, where the decay mode $B_s^0 \to \tilde{D}^{(*)0}\phi$ is considered, where the $D^0$ decays to five sub-decay modes: $KK$, $\pi\pi$, $K\pi$, $K3\pi$, $K\pi\pi^0$ are taking into account. (Left) For the green curve fitted parameters: $\gamma$ value at maximum is $\gamma = 1.31^{+0.26}_{-0.51}$ rad and $r_B$ =0.19, $\delta_B$ =0.86 rad (49.27°), $r_B^*$ =0.52, $\delta_B^*$ =1.93 rad (111°). The $B_s^0 \to \tilde{D}^{(*)0}\phi$ decay without sub-decay mode $K\pi\pi^0$ is shown with the dashed red line superimposed to the same distribution. The fitted parameters: $\gamma$ value at maximum is $\gamma = 1.27^{+0.19}_{-0.43}$ rad, $r_B$ =0.21, $\delta_B$ =0.56 rad (32°), $r_B^*$ =0.56, $\delta_B^*$ =1.96 rad (112°). (Right) The $B_s^0 \to \tilde{D}^{(*)0}\phi$ decay without $B_s^0 \to D^*\phi$ is shown with the dashed red line superimposed to the same distribution. Fitted parameters for the $B_s^0 \to D\phi$: $\gamma = 1.30^{+0.31}_{-0.93}$ rad, $r_B$ =0.19, $\delta_B$ =0.85 rad (49°). The horizontal two dashed black lines refer to 68.3 % (1 $\sigma$) and 95.4 % CL (2 $\sigma$).

The one dimension p-profile value of $\gamma$ for the $B_s^0 \to \tilde{D}^{(*)0}\phi$ with the $D^0$ decay modes is given with the corresponding value of $\gamma=(75^{+15}_{-29})°$. We also performed one dimension p-profile value of $\gamma$ overlap the same distribution while keeping only $B_s^0 \to \tilde{D}^0\phi$ and excluding the information provided by $K\pi\pi^0$ mode and $B_s^0 \to \tilde{D}^{*0}\phi$ displayed in Figure 4.95. In that case, the corresponding fitted value of $\gamma$ is obtained equal to $\gamma=(73^{+11}_{-59})°$ with $r_B$ =0.21, $r_B^*$ =0.52, $\delta_B$ =6.84 rad, $\delta_B^*$ =1.93 rad.
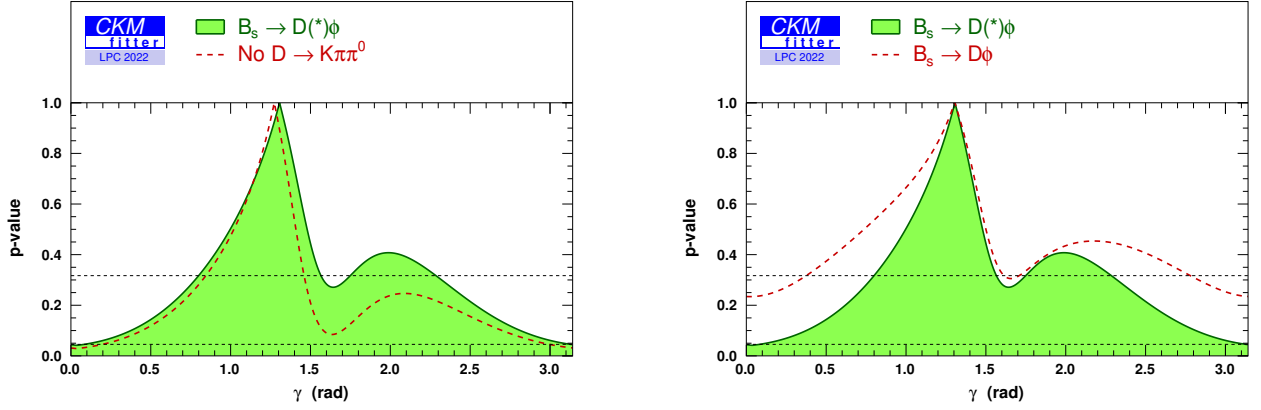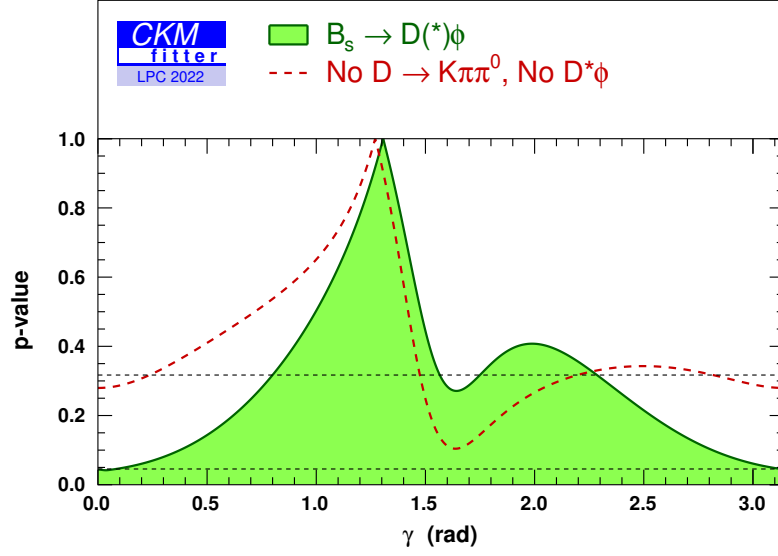
Figure 4.95: Profile of the p-value distribution of the global $\chi 2$ fit to $\gamma$ after observables are computed, where the decay mode $B_s^0 \to \tilde{D}^{(*)0}\phi$ is considered, where the $D^0$ decays to five sub-decay modes: $KK$, $\pi\pi$, $K\pi$, $K3\pi$, $K\pi\pi^0$ are taking into account. For the green curve fitted parameters: $\gamma$ value at maximum is $\gamma = (1.31^{+0.26}_{-0.51})$ rad, $r_B = 0.19$, $\delta_B = 0.86$ rad, $r_B^* = 0.52$, $\delta_B^* = 1.93$ rad. The $B_s^0 \to \tilde{D}^{(*)0}\phi$ decay without sub-decay mode $K\pi\pi^0$ and $B_s^0 \to D^*\phi$ is shown with the dashed red line superimposed to the same distribution. Fitted parameters for $B_s^0 \to D\phi$: $\gamma = 1.27^{+0.20}_{-1.03}$ rad, $r_B = 0.21$, $\delta_B = 6.84$ rad (392°). The horizontal two dashed black lines refer to 68.3 % (1 $\sigma$) and 95.4 % (2 $\sigma$) CL.

Figure 4.96 corresponds to the one dimension p-profile value of $\gamma$ provided by the $B_s^0 \to \tilde{D}^{(*)0}\phi$, where $D^0$ decay to $KK$, $\pi\pi$, $K\pi$, $K3\pi$, $K\pi\pi^0$ in green curve and the corresponding $\gamma$ value of $\gamma=(75^{+15}_{-29})°$ and the value from $B_s^0 \to \tilde{D}^{(*)0}\phi$ when we exclude the $K\pi\pi^0$ decay, the $\gamma$ is obtained as $\gamma=(73^{+11}_{-25})°$, we also display the measurement from the decay $B_s^0 \to D_s^\mp K^\pm(\pi\pi)$ with the value of $\gamma$ angle is to be $\gamma=(79^{+21}_{-24})°$ decays [2]. The recent combination provided by the LHCb gives $\gamma(\text{direct}) = (65.4^{+3.8}_{-4.2})°$. One can see that from the Figure 4.96, $\gamma$ value from $B_s^0 \to \tilde{D}^{(*)0}\phi$ without $K\pi\pi^0$ is slightly better than the one obtained from the untagged $B_s^0 \to \tilde{D}^{(*)0}\phi$ decay with the full sub-decay modes combination and the $\gamma$ value from the time-dependent tagging analysis of $B_s^0 \to D_s^\mp K^\pm(\pi\pi)$ decay. The value of $\gamma$ obtained from $B_s^0 \to \tilde{D}^{(*)0}\phi$ is in good agreement with the current $\gamma$ combination determined from the LHCb [2]. This new result in $B_s^0 \to \tilde{D}^{(*)0}\phi$ will provide the improvement of $\gamma$ measurements from $B_s^0$ decays $B_s^0 \to D_s^\mp K^\pm(\pi\pi)$ which is involved in current LHCb combination and help to understand the differences from $B^0$ and $B^\pm$ decays.
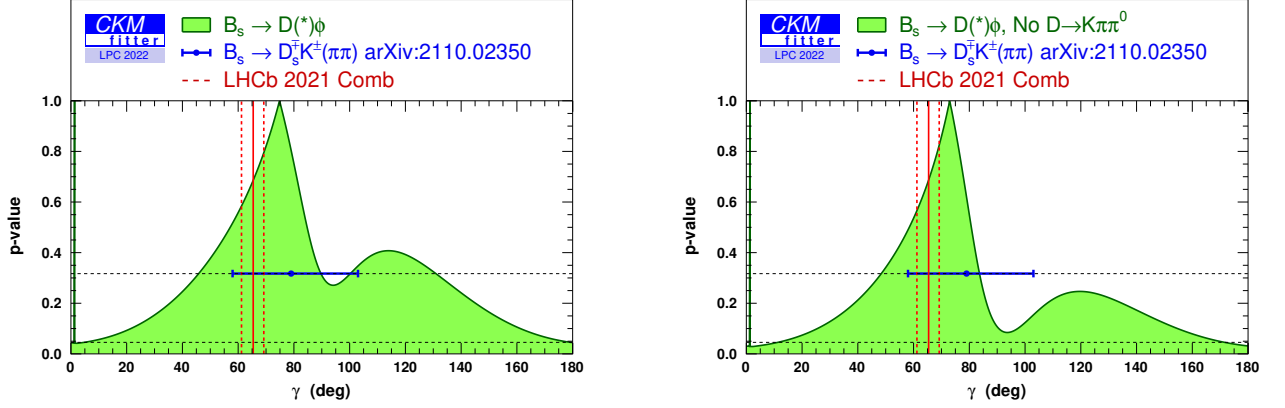
Figure 4.96: Profile of the p-value distribution of the global $\chi 2$ fit to $\gamma$ after observables are computed, where the decay mode $B_s^0 \to \tilde{D}^{(*)0}\phi$ is considered, where the $D^0$ decays to five sub-decay modes: $KK$, $\pi\pi$, $K\pi$, $K3\pi$, $K\pi\pi^0$ are taking into account is shown in green curve with the corresponding value $\gamma=(75^{+15}_{-29})°$. Measurement through the $B_s^0 \to D_s^\mp K^\pm(\pi\pi)$ decay with the $\gamma=(79^{+21}_{-24})°$ decays [2] with horizontal blue straight line and the LHCb $\gamma$ combination $\gamma(\text{direct}) = (65.4^{+3.8}_{-4.2})°$ with the vertical dashed red line are represented for the comparison. (Right) Profile of the p-value distribution of the global $\chi 2$ fit to $\gamma$ after observables are computed, where the decay mode $B_s^0 \to \tilde{D}^{(*)0}\phi$ is considered dropping the information from $K\pi\pi^0$ are taking into account is shown in green curve with the value of $\gamma=(73^{+11}_{-25})°$, and the measurement through the $B_s^0 \to D_s^\mp K^\pm(\pi\pi)$ decays [2] is shown with the horizontal blue straight line and the LHCb $\gamma$ combination with the vertical dashed red line are represented for the comparison. The horizontal two dashed black lines refer to 68.3 % ($1\sigma$) and 95.4 % CL ($2\sigma$).

Figures 4.97 and 4.98 shows the two dimensional p-value profile of the nuisance parameters $r_B^{(*)}$ and $\delta_B^{(*)}$ as a function of $\gamma$ for the full combination of $B_s^0 \to \tilde{D}^{(*)0}\phi$, where $D^0$ decays to $KK$, $\pi\pi$, $K\pi$, $K3\pi$, $K\pi\pi^0$ sub-decay modes. The fitted parameters: $\gamma = 1.31^{+0.26}_{-0.51}$ rad, $r_B =0.19$, $r_B^* =0.52$, $\delta_B =0.86$ rad, $\delta_B^* =1.93$ rad, respectively.
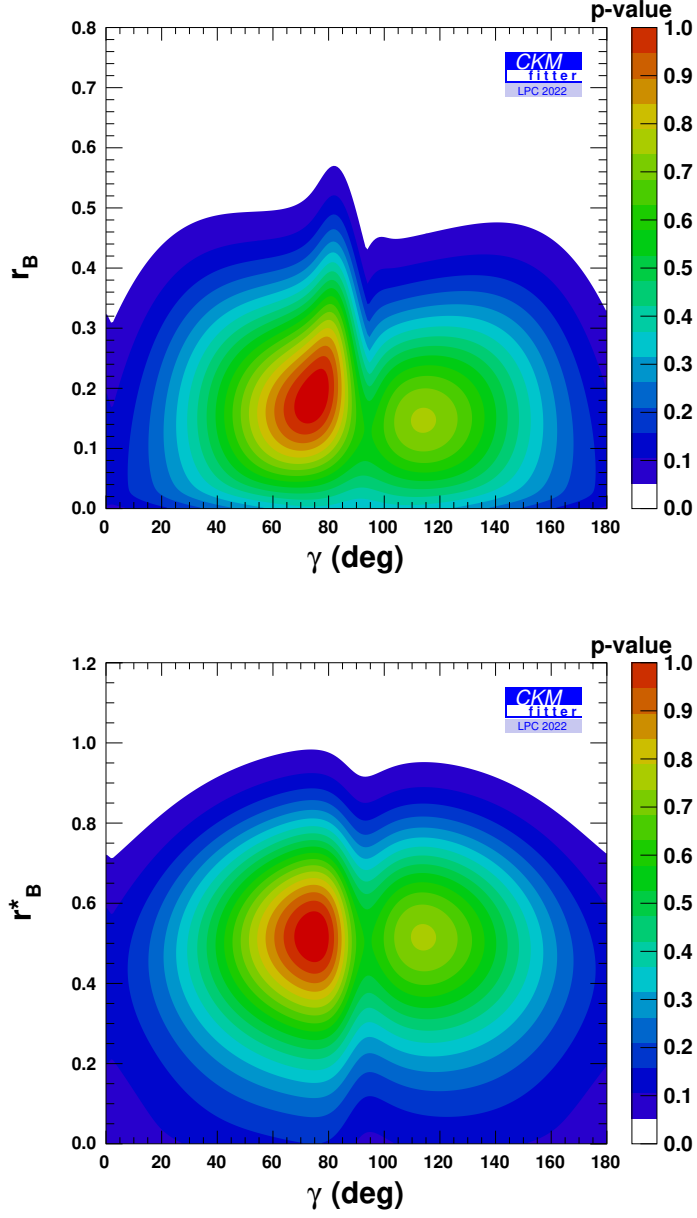
Figure 4.97: Two dimensional (p-value) projections distribution of the physics parameters: $r_B$ (top) and $r_B^*$ (bottom) as a function of $\gamma$. On each figure the fitted values are given for $\gamma = 75.05°$ (1.31 rad), $r_B = 0.19$, and $r_B^* = 0.52$.
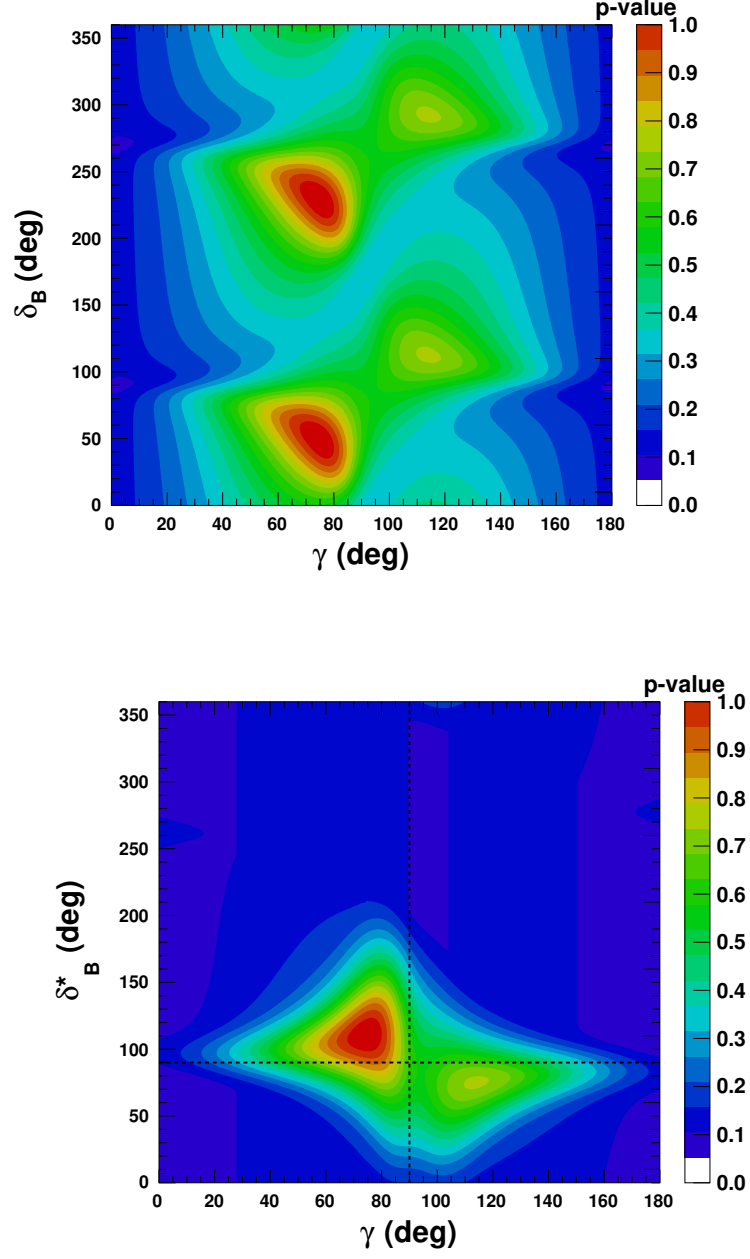
Figure 4.98: Two dimensional (p-value) projections distribution of the physics parameters: $\delta_B$ (top) and $\delta_B^*$ (bottom) as a function of $\gamma$. On each figure the fitted values are given for $\gamma = 75.05°$ (1.31 rad), $\delta_B = 49.27°(0.86$ rad), $\delta_B^* = 111°(1.93$ rad).

# 4.14 Conclusion for $B_s^0 \to \tilde{D}^0 \phi$

We have shown for the first time the constraint on the CKM angle $\gamma$ with the modes $B_s^0 \to \tilde{D}^{(*)0}\phi$, where D meson reconstructed in the sub-decays $K\pi, K3\pi, K\pi\pi^0, KK, \pi\pi$. The obtained constraint on the CKM angle $\gamma$ is quite compatible with the charged $B$ constraint by LHCb [2]. The precision that we obtain is similar to what was anticipated in a phenomenological study that we performed in 2021 [4] and allows to obtain a precision of the order or better than the so far flagship modes with $B_s^0 \to D_s^{\mp}K^{\pm}$, $B_s^0 \to D_s^{\mp}K^{\pm}\pi^+\pi^-$ [2] decays. It should be improved with better statistics allowed by the already started Run3 data taking campaign (i.e. since Spring 2023) of the LHCb experiment.

# 5 Analysis of $B^{\pm} \to \tilde{D}^0 K^{*\pm}$ decay

## 5.1 Motivation

The $B^{\pm} \to \tilde{D}^0 K^{*\pm}$ decay, where $\tilde{D}^0$ stands for either a $D^0$ or a $\bar{D}^0$ meson, has previously been studied by the BaBar collaboration using a variety of two-body $D$ decay modes [151]. In 2017, LHCb published the $B^{\pm} \to \tilde{D}^0 K^{*\pm}$ results using two- and four-body $D^0$ final states using Run 1, and Run 2 (including only 2015-2016) datasets [40]. Both studies reconstruct the $K^{*-} \to K_s^0 \pi^-$, which has a smaller branching fraction with respect to the $K^{*-} \to K^- \pi^0$ 5.1.

$$\mathcal{BF}(K^{*-} \to K_s^0(\pi^+ \pi^-)\pi^-) \approx \frac{2}{3} \times BF(K^{*-} \to K^- \pi^0) \tag{5.1}$$

but the $\pi^0$ reconstruction efficiency is much lower (about 5% reduction due to the $\pi^0$ reconstruction), while the charged kaon $K^-$ in the latter case is more easy to detect than $K_s^0$ and offers a cleaner signature.

However, the two $K^{*-}$ decay channels correspond to two statistically independent and complementary ways of measuring the same parameter: $\gamma$, of course and the two same strong parameters: $r_B$, $\delta_B$. Therefore we can expect this mode could make a large contribution to the precision of $\gamma$ measurement at LHCb. For this analysis we consider the decay of $D^0$ meson reconstructed in four different final states and the methods depending on the final states which are separated as ADS modes: $K^- \pi^+$ (RS), the ADS mode $K^+ \pi^-$ (WS) and GLW modes (CP-eigenstates): $K^+ K^-$, $\pi^+ \pi^-$. Optimising all selections for each of the final states we calculate the CP observables: $R_{CP+}$ ($R_{KK}$, $R_{\pi\pi}$), $A_{CP+}$ ($A_{KK}$, $A_{\pi\pi}$), $R_{K\pi}^+$, $R_{K\pi}^-$ and $A_{ADS}$. The CP violation phase $\gamma$, the two physics parameters: the ratio of the magnitude between the suppressed and favoured $B$ decays amplitudes $r_B$ and strong phase between the two interfering amplitudes $\delta_B$ can be determined by using the values of the CP observables. This analysis uses the dataset recorded in 2011 and 2012 at a center-of-mass energies of $\sqrt{s} = 7$ TeV and $\sqrt{s} = 8$ TeV, respectively, corresponding to an integrated luminosity of $3 \, \text{fb}^{-1}$ and $9 \, \text{fb}^{-1}$ of data collected during the years between 2015 and 2018 at a center-of-mass energy of $\sqrt{s} = 13$ TeV.

In this chapter performed on the $B^{\pm} \to \tilde{D}^0 K^{*\pm}$ decay

## 5.2 Dataset

### 5.2.0.1 Data samples

The analysis uses proton-proton collision data collected by the LHCb detector in the Run 1 and Run 2 stages, corresponding to an integrated luminosity of $9\,\mathrm{fb}^{-1}$. The data used in the analysis in summarized in Table 5.1. All data is processed using DAVINCI and $B^{\pm} \to DK^{*\pm}$ candidates, where the $K^{*\pm}$ decays to $K^{\pm}\pi^0$, are taken from stripping.

| Year | $\sqrt{s}/\,\mathrm{TeV}$ | Luminosity | Stripping |
|------|------|------|------|
| 2011 | 7.0  | 1.0  | S21r1p1 |
| 2012 | 8.0  | 2.0  | S21 |
| 2015 | 13.0 | 0.3  | S24 |
| 2016 | 13.0 | 1.5  | S28 |
| 2017 | 13.0 | 1.6  | S29 |
| 2018 | 13.0 | 1.6  | S34 |

Table 5.1: Summary of the data used in the analysis for Run 1 and Run 2.

### 5.2.1 Monte Carlo samples

This analysis uses the simulated collision events based on MC, generated with PYTHIA8 and SIM09i/j versions for different years corresponding to Run 1 (2011 - 2012) and Run 2 (2015-2016-2017-2018). All MC samples generated with the option DecProdCut which means that all daughters of the decay chain are in the acceptance of the LHCb detector. MC samples (2011-2018) used in the analysis are truth-matched. Table 5.2 shows the Monte Carlo simulated samples and the number of generated events for each run years.

| Decay | Event type | Number of simulated events (year) | | | | | |
|-------|------------|------|------|------|------|------|------|
| Signal modes | | 2011 | 2012 | 2015 | 2016 | 2017 | 2018 |
| $B^- \to D^0 K^{*-} - (K\pi)(K\pi^0)$ | 12163495 | 211678 | 210982 | 42420 | 92715 | 96258 | 94871 |
| $B^- \to D^0 K^{*-} - (KK)(K\pi^0)$ | 12163496 | 207673 | 209780 | 42695 | 73062 | 110970 | 93559 |
| $B^- \to D^0 K^{*-} - (\pi\pi)(K\pi^0)$ | 12163497 | 219152 | 207390 | 43738 | 69370 | 81029 | 107900 |
| $B^- \to D^{*0}(D^0\gamma)K^{*-} - (K\pi)(K\pi^0)$ | 12163601 | 224909 | 204745 | 307299 | 1708899 | 86571 | 81658 |
| $B^- \to D^{*0}(D^0\pi^0)K^{*-} - (K\pi)(K\pi^0)$ | 12163422 | 224869 | 225453 | 303099 | 1709696 | 83894 | 89747 |
| $B^- \to D^{*-}(D^0\pi^-)K^{*+} - (K\pi)(K\pi^0)$ | 11164461 | 219742 | 211659 | 48048 | 68584 | 87432 | 81697 |
| $B^- \to D^0\rho - (K\pi)(\pi\pi^0)$ | 12163473 | 203584 | 204287 | 600999 | 3407995 | 99117 | 91071 |
| $B^- \to KKK^{*-} - (K\pi^0)$ | 12103411 | 208212 | 200953 | 19216 | 80995 | 83143 | 84135 |
| $B^- \to \pi\pi K^{*-} - (K\pi^0)$ | 12103421 | 208741 | 209003 | 18548 | 71950 | 82949 | 83496 |

Table 5.2: Monte Carlo simulated samples for signal and background and the number of generated events for Run 1 and Run 2.

## 5.3   Event selections

### 5.3.1   Signal Box and the sideband

Signal Box (SB) and sideband zones considered for the events in this analysis are displayed in Figure 5.1. We define three main zones for the analysis. The signal region using the MC simulation for the events is shown the red box within the while upper sideband data for B meson and the sideband regions for $B$ & $D$ mesons is displayed with green and blue boxes respectively. As in the same way explained in the previous analysis of $B_s^0 \to \tilde{D}^{(*)0}\phi$, based on the kinematic and topological characteristics of the decay modes of $B^\pm \to D^0 K^{*\pm}$, the discriminating variables are chosen.
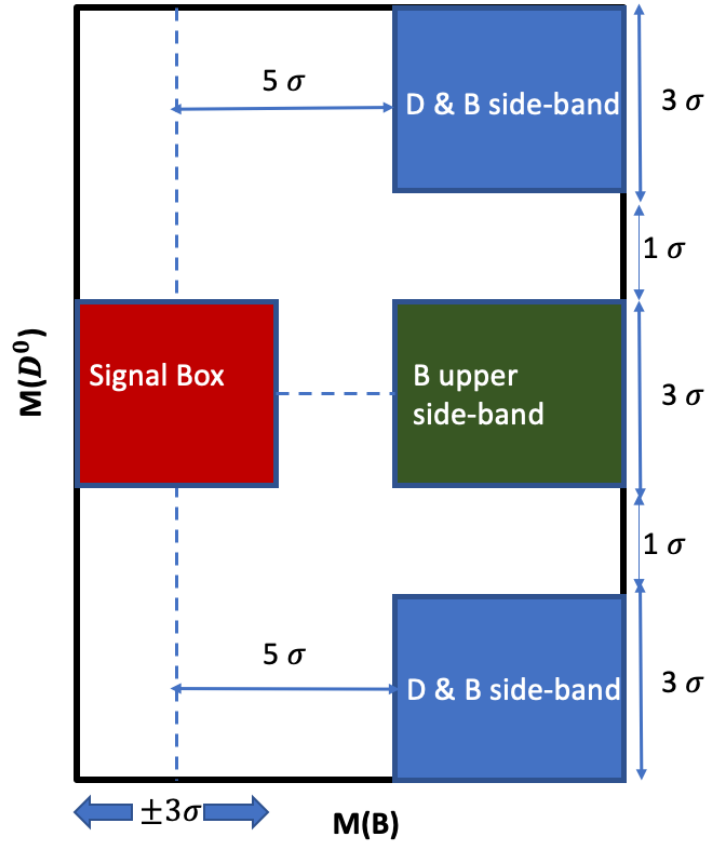


Figure 5.1: Signal and mass sidebands for $M(D^0)$ and $M(B)$ (PDG mass [18]) used in the analysis. The red box correspond to the signal, upper sideband for the $B$ meson is given with green color and sideband for $D$ & $B$ mesons are given with the blue color. $K^*$ mass sideband is from m($K\pi^0$) in [1.1, 1.3]( GeV/$c^2$).

## 5.3.2 Trigger selection

Events in both simulation and data samples are required to be selected by any L0 trigger line either due to the $B^+$ candidates Trigger on Signal (TOS) or the rest of the events Trigger Independent of Signal (TIS), and by at least one high-level trigger lines on the $B^+$ candidates (TOS).

All $B^\pm$ candidates are required to passed the following triggers for both Run 1 and Run 2 samples:

- `L0Global_TIS` or `L0Global_TOS`

- `Hlt1Global_TOS`

- `Hlt2Global_TOS`

## 5.3.3 Stripping

In this analysis the stripping line `B2D0KPi0ResolvedD2HHBeauty2CharmLineDecision` for Run 1 and Run 2 data samples is used to select $B^\pm \to DK^{*\pm}$ candidates. The standard selection criteria for this stripping line are summarised in Table 5.3.

## 5.3.4 Pre-selection

Following the premier stage through the stripping-selections, two step of selections are applied in order to reduce the data sample size: first one is the pre-selection applied on each selected variables and as second one a multivariate analysis applied. The pre-selection are summarized in Table 5.4

In order to fight against the combinatorial background, to improve the signal ratio over background, on top of the pre-selections, several methods of the offline selections are taken into consideration :

- **Multivariate analysis (MVA)**

- **Particle identification (PID) selections**

- **Selections for the background**

| Selection variable | $B^- \to D^0 K^{*-}$ |
|---|---|
| | all basic particles |
| $\chi^2_{trk}/\mathrm{ndof}$ | $< 4$ |
| $P(\mathrm{ghost})$ | $< 0.4$ |
| $p_{\mathrm{T}}$ | $> 100\,\mathrm{MeV}/c$ |
| $p$ | $> 1000\,\mathrm{MeV}/c$ |
| $\chi^2_{IP}$ | $> 4$ |
| | $D^0$ selection |
| $p_{\mathrm{T}}\,(K)+p_{\mathrm{T}}\,(p)+p_{\mathrm{T}}\,(\pi)$ | $> 1800\,\mathrm{MeV}/c$ |
| $|M_{rec} - M_{pdg}|$ | $< 100\ \mathrm{MeV}/c^2$ |
| $\chi^2_{vtx}/\mathrm{ndof}$ | $< 10$ |
| $\chi^2_{FD}$ | $> 36$ |
| one track with | $p_{\mathrm{T}} > 500\,\mathrm{MeV}/c,\ p > 5000\,\mathrm{MeV}/c$ |
| DOCA two tracks | $< 0.4\,\mathrm{mm}$ |
| | $\pi^0$ selection |
| $p_{\mathrm{T}}$ | $> 2000\ \mathrm{MeV}/c$ |
| $p$ | $> 500\ \mathrm{MeV}/c$ |
| CL of two $\gamma$ | $> 0.25$ |
| | $B^- \to D^0 \pi^0 K^-$ selections |
| sum of $p_{\mathrm{T}}$ | $> 5000\ \mathrm{MeV}/c$ |
| $BPV\,cos(\theta_p)$ | $> 0.999$ |
| $\chi^2_{IP}$ | $< 25$ |
| $\tau$ | $> 0.2\,\mathrm{ps}$ |
| one track with | $p_{\mathrm{T}} > 1.7\,\mathrm{GeV}/c,\ p > 10\,\mathrm{GeV}/c,\ \chi^2_{minIP} > 16,\ \mathrm{minIP} > 0.1\,\mathrm{mm}$ |
| $\chi^2_{vtx}/\mathrm{ndof}$ | $< 10$ |

Table 5.3: Stripping selection criteria applied on the **B2D0KPi0ResolvedD2HHBeauty2CharmLineDecision** stripping line.

| Particle | Variable | Selections |
|---|---|---|
| $\gamma$ | $CL$ | $> 0.2$ |
| $D^0$ | Mass window | (-80,+80) around $D^0$ known mass( $\mathrm{MeV}/c^2$) |
| $\pi^0$ | Mass window | (-30,+30) around $\pi^0$ known mass( $\mathrm{MeV}/c^2$) |
| $B^-$ | Mass window | (-600, +600) around $B^-$ known mass ( $\mathrm{MeV}/c^2$) |

Table 5.4: Pre-selection of $B^+ \to D^0 K^+ \pi^0$ candidates.

### 5.3.5 Selections of the $B$ daughters: $K^*$ and $D$, and then $B$ with Multivariate analysis

Initially, toolkit for MVA is performed for Run 1 and Run 2 samples individually for signal and background classification. Training is done with MC for the signal and Data within the upper sideband of the reconstructed $B^-$ mass spectrum and $D^0$ & $B^-$ sideband for the background. In order to estimate and fight against the combinatorial background, the strategy is to use $D$ and $K^*$ sidebands. The 4-vector momentum of $D^0$ and $\pi^0$ is constrained in the mother particles to Primary Vertex (PV). At this stage, the idea is to proceed with three MVA algorithm based on $K^{*-}$, $D^0$ and $B^-$ respectively in order to further suppress the background. These three steps to train MVAs for each are given in the following sections in detail. Defined PID criteria have been applied on all the three charged daughters in the decays of $B^- \to D(h^+h^-)K^{*-}(K^-\pi^0)$, such that they are incompatible with muons (muons chambers) or electrons (electromagnetic calorimeter).

#### 5.3.5.1 MVA based on $\pi^0$ and $K^{*-}$ discrimination

The MC signal sample is the decay of $K^{*-} \to K^-\pi^0$, while the background is obtained with the sideband of the $K^{*-}$ mass spectrum with $m_{K^{*-}(K^-\pi^0)} \in [1.1, 1.3]\,\mathrm{GeV}/c^2$. MVA based on $\pi^0$ and $K^*$ discriminating variables using MC and data (see Figure 5.1). This requires $\pi^0$ to be in $[117.5, 159]\,\mathrm{GeV}/c^2$ (optimisation for $\pi^0$ is explained in $B_s^0 \to \tilde{D}^0\phi$ analysis) and m($K^*$) to be in $\pm225\,\mathrm{MeV}/c^2$. Candidates from the MC simulated events and the data in the sideband are used as signal and background. Both signal and background samples are randomly divided into two parts.

A set of discriminating variables chosen as input against the combinatorial background are listed in Table 5.5 with their definitions. The distributions for the signal and the background of the input variables are shown in Figure 5.2.

Discrimination between signal and background is obtained with the multivariate analysis classifiers trained on MC signal samples and the data.

| Name of variable | Meaning of variable |
|---|---|
| cosThetaHely_bach | Helicity angle of bachelor track |
| BachIPChi2 | Quality ($\chi^2$) of the impact parameter of a given particle (bachelor particle) |
| KstarPT | transverse momentum of Kaon |
| gamAsym | asymmetry between the transverse energy of the two photons of the $\pi^0$ candidate |
| gam_isNotETot | probability of the two $\gamma$ of not being an electron |
| gam_isNotHTot | probability of the two $\gamma$ of not being a hadron |
| gamEtMoy | the average of the transverse energy of the two photons of the $\pi^0$ candidate |

Table 5.5: Discriminating variables for $K^{*-} \to K^-D^0$ decay mode used in the MVA training.

Figure 5.3 shows the ROC curves for all different classifiers studied in TMVA package : MLP, BDTG, MLPBNN, Fisher. In order to reject combinatorial background, a multivariate classifier, especially multilayer perceptron MLP [152] which gives the best performance is chosen.
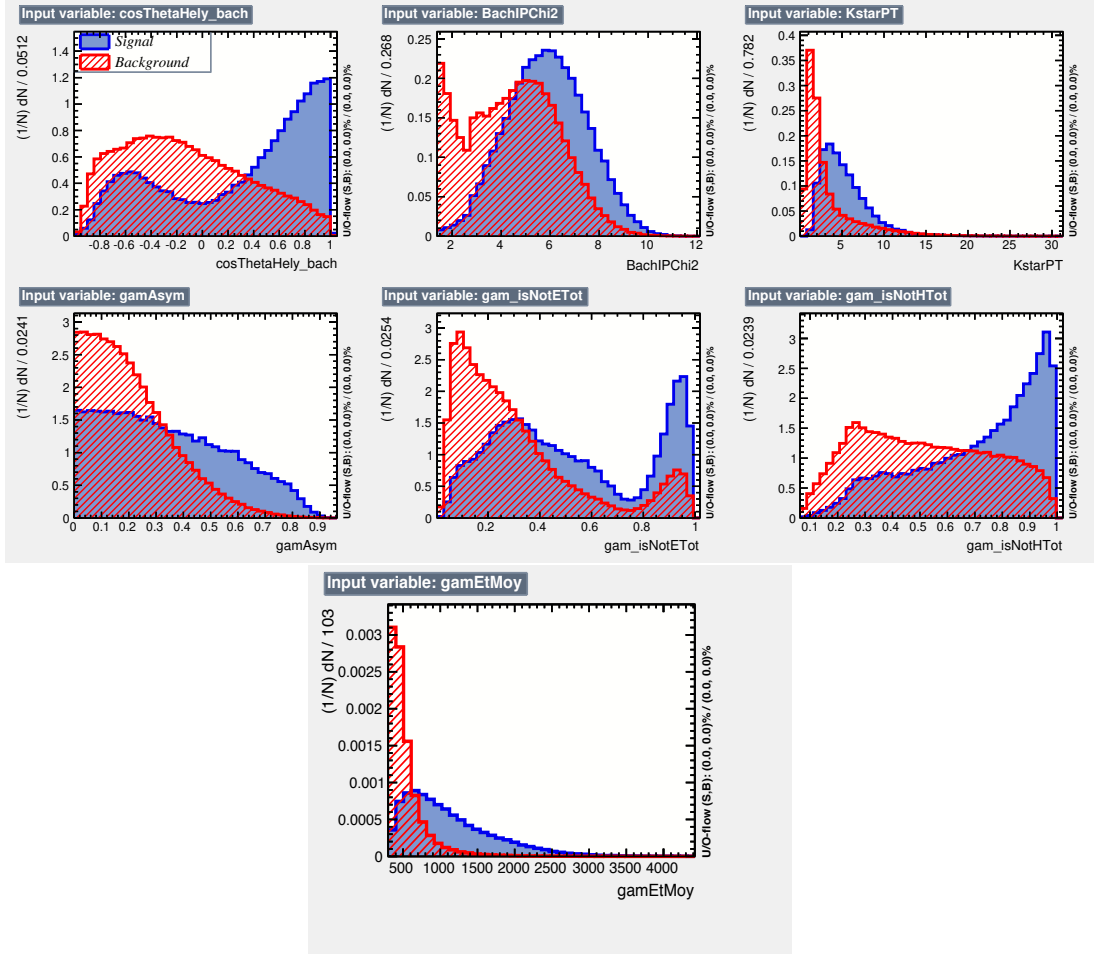
Figure 5.2: $K^{*-} \to K^- \pi^0$ discriminating variables used by the MVA for Run 2. The signal and the background distributions are given in blue and red respectively. For the first distribution of cosThetaHely_bach variable: $K^*$ is a vector decays to two pseudo-scalar, so that for the signal one can expect to have a $\cos^2$theta distribution and the asymmetry is due to stripping cuts on the $p_T$ of the $\pi^0$ and K track (see Table 5.3). For the second variable of BachIPChi2: the K track is originated from the $B$ vertex and not primary vertex PV. For the KstarPT variable: combinatorial background combined $K$ and $\pi^0$ such that lower momentum of particles originated from a massive object as $K^* = 892\,\mathrm{MeV}$. The distribution for gamEtMoy variable: the combinatorial gamma spectrum has an exponential decaying spectrum. For the gamAsym, $\pi^0$ is a pseudo-scalar which decays to two similar vector bosons and have the same transverse energy of $E_{\gamma^1}^T$ and $E_{\gamma^2}^T$.

The correlation matrices for MLP discriminating variables for both signal and background samples are shown in Fig. 5.4. In Table 5.6 the ranking of importance of the input variables are given, where they are ordered from the most important to the least. The MLP output displays good agreement between the signal and the background events see Figure 5.5.
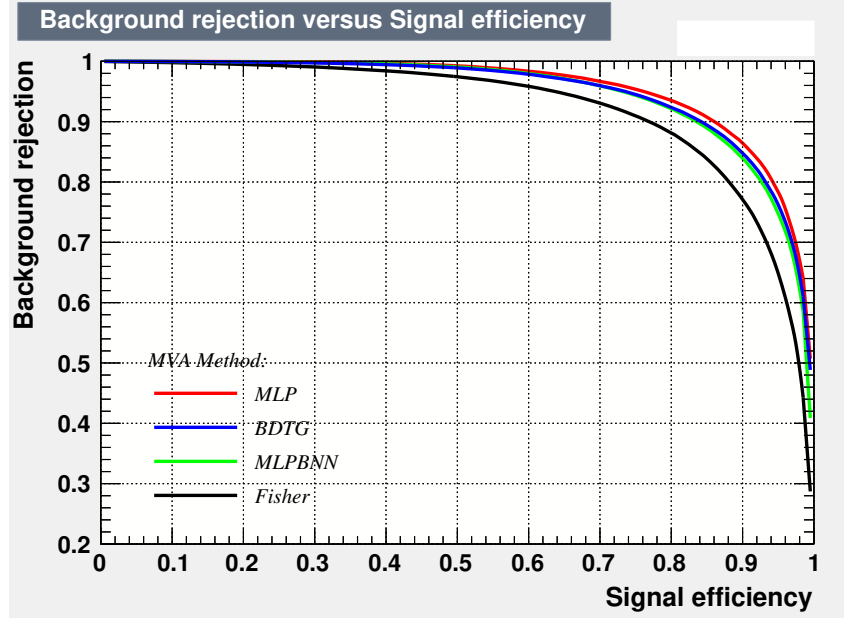
Figure 5.3: Signal efficiency vs background rejection of $K^{*-} \to K^-\pi^0$ candidates (ROC curve) for Run 2. Performances of the four MVA classifiers have been tested and MLP which gives the best background rejection for a given signal efficiency.
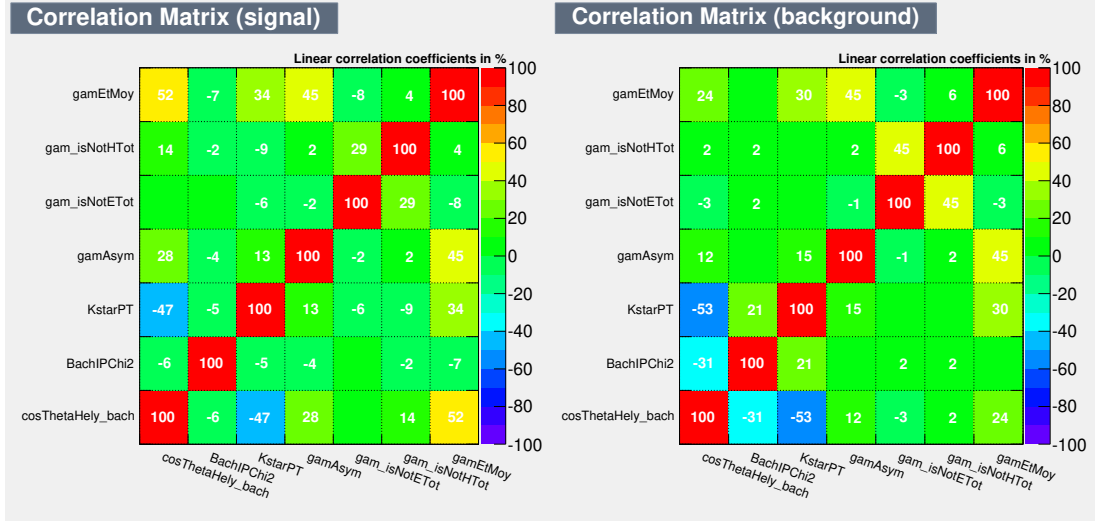


Figure 5.4: Correlation matrix of input variables in signal samples (left) and background samples (right) in $K^{*-} \to K^-\pi^0$ decays.

As it has been mentioned earlier, the best result among the all tested classifiers yield by the MLP algorithm throughout the analysis for all the selection. This performance can be seen in Figure 5.6. Figure 5.6 shows the variation of signal and background efficiency vs the MLP value. Here we use a cut with the signal efficiency 96% (cut is chosen to gain as much efficiency on signal as possible) to reject as much genuine non $K^* \to K\pi^0$

| Variable | MVA Ranking | Separation |
|----------|-------------|------------|
| $gamEtMoy$ | 1 | $3.923 \times 10^{-1}$ |
| $KstarPT$ | 2 | $3.111 \times 10^{-1}$ |
| $cosThetaHely\_bach$ | 3 | $1.787 \times 10^{-1}$ |
| $BachIPChi2$ | 4 | $1.496 \times 10^{-1}$ |
| $gamisNotHTot$ | 5 | $1.491 \times 10^{-1}$ |
| $gamisNotETot$ | 6 | $1.461 \times 10^{-1}$ |
| $gamAsym$ | 7 | $1.104 \times 10^{-1}$ |

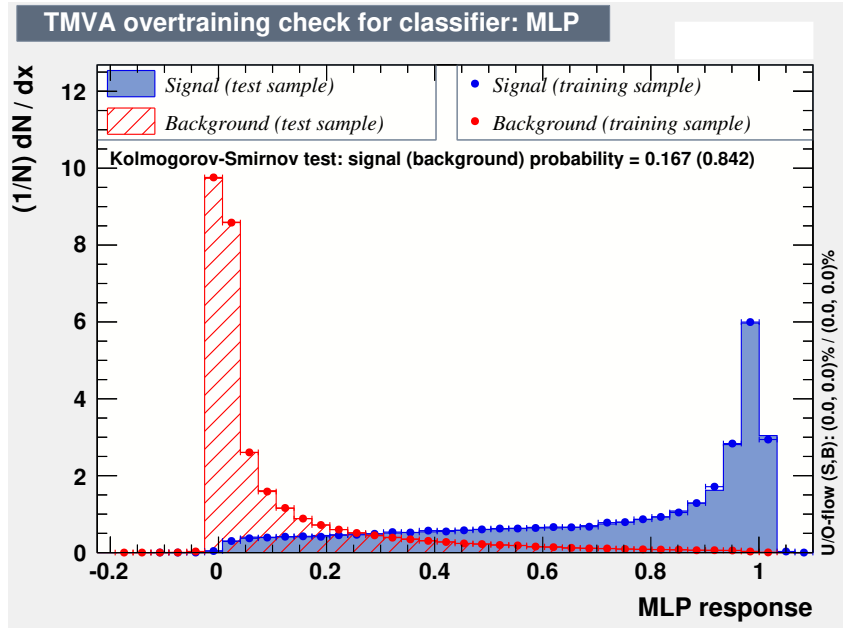Table 5.6: Input variables separation power for $K^{*-}$.



Figure 5.5: $K^*$ MLP response for the signal (in blue) and background (in red) samples. Training samples are shown in dots and test samples are seen as histograms. No evidence of over training is found through the confirmation of Kolmogorov-Smirnov tests which is a measure of agreement between two distributions

background, i.e. about 76%. Then this MLP will be used as a discriminating variable for the final $B$ MVA selection. Table 5.7 shows the chosen optimum cut value on the MLP output with the signal efficiency and the background rejection.

| Candidate | Cut MVA MLP | Signal Efficiency | Background Rejection |
|-----------|-------------|-------------------|----------------------|
| $K^*$ | 0.113 | 96% | 75.6% |

Table 5.7: The signal efficiency and the background rejections are obtained when cutting on the MLP for Run2.
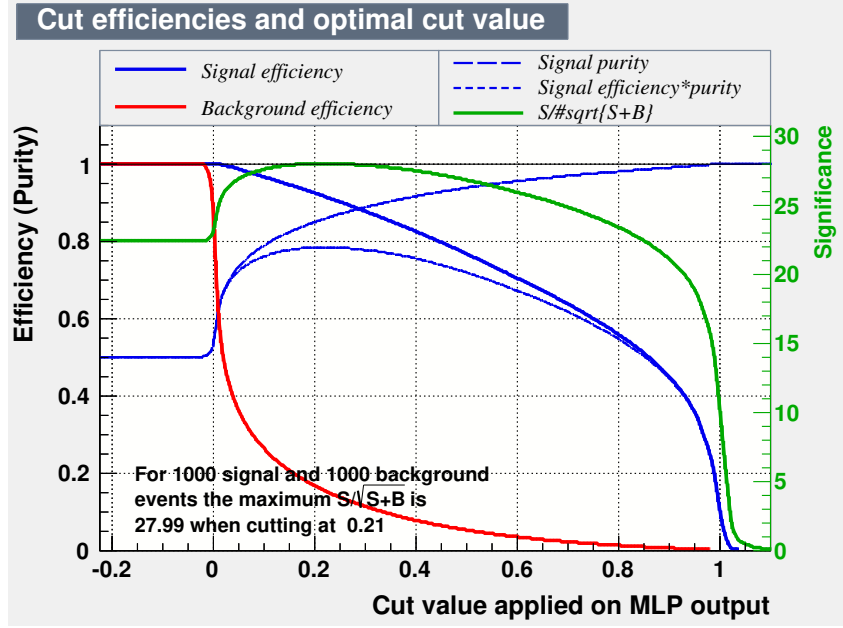
Figure 5.6: Optimisation of the MLP cut value for $K^*$ to maximise the figure of merit. Signal efficiency, background rejection, signal purity, signal efficiency purity and figures of merit are plotted against the classifier output value for MLP at the training-evaluation phase.

We select $K\pi^0$ pairs with a mass range in $\pm$ 300 of $K^*$ (892) PDG mass and the $\pi^0$ mass for this analysis are optimised within the intervals as it was optimised for the $B_s^0 \to \tilde{D}^{(*)0}\phi$ analysis (see 4.4.5), where $D^0$ decays to $K\pi\pi^0$.

### 5.3.5.2 MVA based on $D^0$ discrimination

Table 5.8 lists all discriminating variables and their definitions used as inputs to the adopted algorithm MLP for $D^0$. Figure 5.7 shows the tested classifiers Fisher, BDTG and MLP and the MLP gives the best performance, therefore it is retained both for performances and relatively simple configuration. For the training of the MLP, the signal sample is the full simulation sample of $D^0$ with all selections applied and the background sample is obtained from the sideband of the $D^0$ mass spectrum with $M_{D^0}$ sideband mass window $\pm 105\,\mathrm{MeV}/c^2$ (i.e. keep sideband for later use) see Figure 5.1. The 50% of the events are used for training, while the other 50% are used for test. Figure 5.8 compares the signal and the background distributions of these six input variables.

The linear correlation between these kinematical and topological input variables of $D^0$ decay for signal and background are displayed in Figure 5.9 and from the correlation matrices it can be seen that there is a bit more correlation among the input variables but sanity computation has been done for the $K^*$, $B^-$ input variables and with the consideration of different discriminators and the mass of the particle we select. And as a result of this sanity check we conclude that there is less than few percent of correlation

182

| Name of variable | Meaning of variable |
|---|---|
| DDIRA | The direction angle of $D$ meson |
| D0_IPChi2 | quality ($\chi^2$) of the impact parameter (IP) of the $D^0$ meson |
| D0_VTXProb | Probability of the vertex of the $D^0$ meson |
| DhIPChi2_min | quality ($\chi^2$) of the impact parameter (IP) of the daughter of $D$ meson |
| DhPT_min | minimum transverse momentum ($p_T$) of the daughter of $D$ meson |
| D0PT | transverse momentum of $D^0$ meson |

Table 5.8: Discriminating variables for $D^0 \rightarrow hh$ decay mode used in the MVA training. All variables are used for 2-body $D^0$ meson decays.
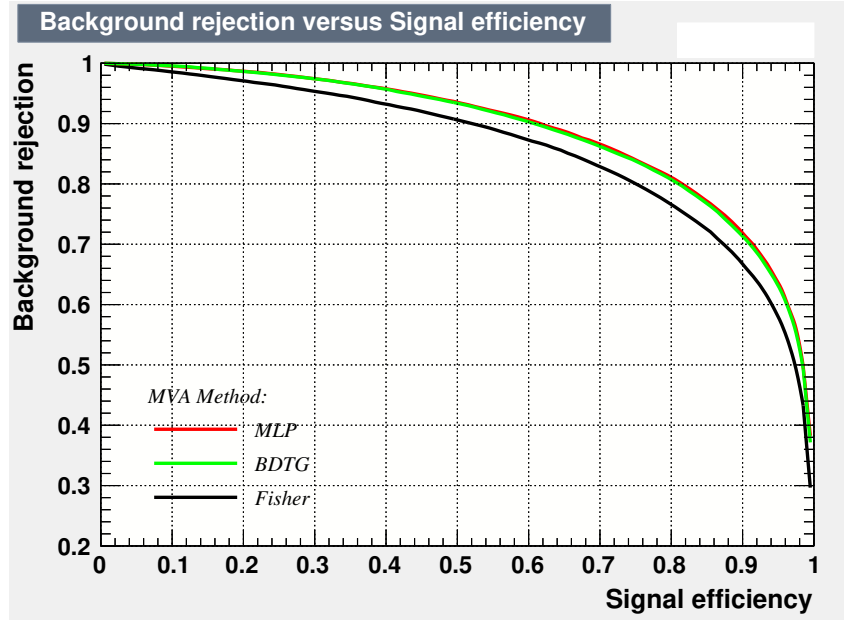


Figure 5.7: Signal efficiency vs background rejection of $D^0 \rightarrow hh$ candidates (ROC curves) for Run 2. Performances of the three MVA classifiers have been tested and MLP which gives the best performance is chosen.

which doesn't produce any bias in the final mass fit study. In Table 5.9 the separation powers of the input variables are given.

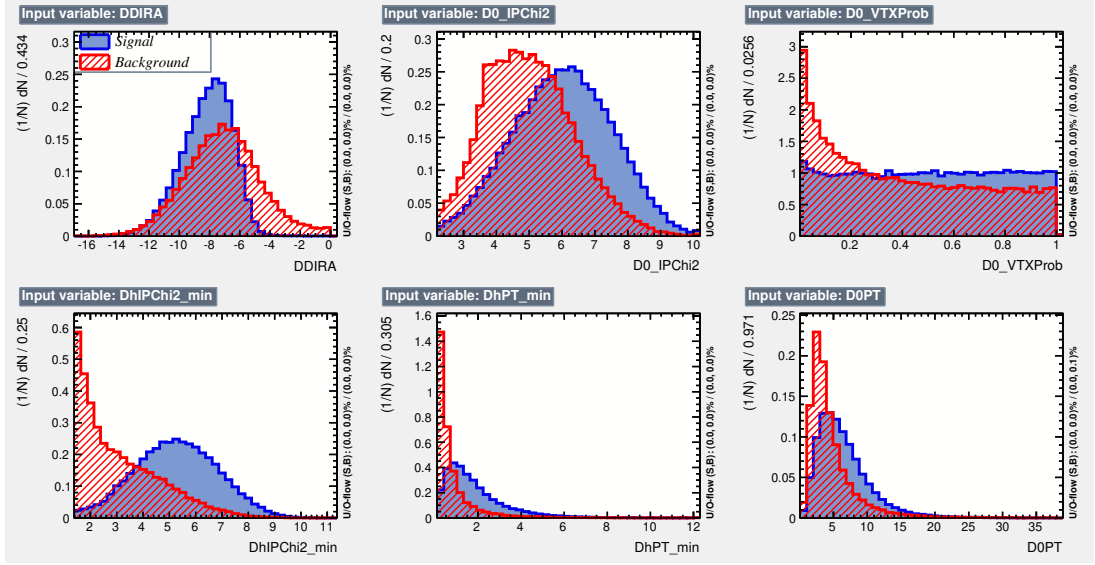| Variable | MVA Ranking | Separation |
|---|---|---|
| $DhIPChi2\_min$ | 1 | $3.466 \times 10^{-1}$ |
| $DhPT\_min$ | 2 | $2.808 \times 10^{-1}$ |
| $DDIRA$ | 3 | $1.152 \times 10^{-1}$ |
| $D0\_IPChi2$ | 4 | $1.136 \times 10^{-1}$ |
| $D0PT$ | 5 | $1.038 \times 10^{-1}$ |
| $D0\_VTXProb$ | 6 | $3.116 \times 10^{-2}$ |

Table 5.9: Input variables separation power.

Figure 5.8: Distributions of the $D^0 \to hh$ input variables of the MLP used for Run 2. The MC signal and the sideband background distributions are given in blue shaded and red shaded areas respectively. So one can see the distribution of probability variable D0_VTXProb is flat between [0,1] for two tracks from the same vertex and peaked at zero for not associated. For the DDIRA discriminating variable: the momentum of the reconstructed $D$ direction is aligned for signal to the $B$ and $D$ vertex direction (not for background) and here DDIRA is defined as DDIRA = $\ln(1-\cos\theta)$ for a better numerical behaviour. The variable of D0_IPChi2: $D^0$ doesn't come from the Primary Vertex (PV) but from the $B$ vertex such that IPChi2 is larger and D0_IPChi2 is defined log() for a better numerical behaviour. For DhPT_min variable: the min. $p_T$ of the two $D^0$ daughter is larger than the combinatorial background as the $D$ gets in the $B$ decays and $p_T$ is large about $p_T > 30$ GeV/$c$ and the same for D0PT.

The MLP classifier response for $D^0$ selections is shown in Figure 5.10.

In Figure 5.11 the cut applied on the MLP is shown as a function of efficiency (purity). Again the MLP output for $D^0$ will be an input for the last stage $B$ final MVA in order to reject the combinatorial background as modelled by the $B$ upper sideband, a very loose cut is set on MLP_$D^0$, such that 96% of the signal is kept while 39% of the $D^0$ background is rejected. Optimum choice on the MLP classifier with the signal efficiency and the background rejection are given in the Table 5.10.

| Candidate | Cut MVA MLP | Signal Efficiency | Background Rejection |
|-----------|-------------|-------------------|----------------------|
| $D^0$ | 0.36 | 96% | 39% |

Table 5.10: The signal efficiency and the background rejections are obtained when cutting on the MLP for Run2.
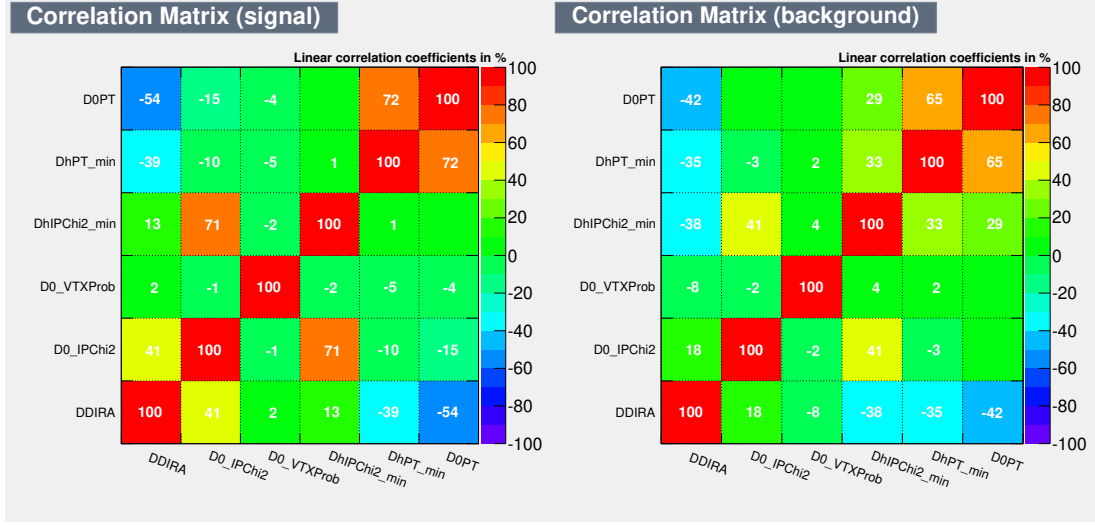
Figure 5.9: Correlation matrix of discriminating variables of training samples for the signal (left) and the background (right).
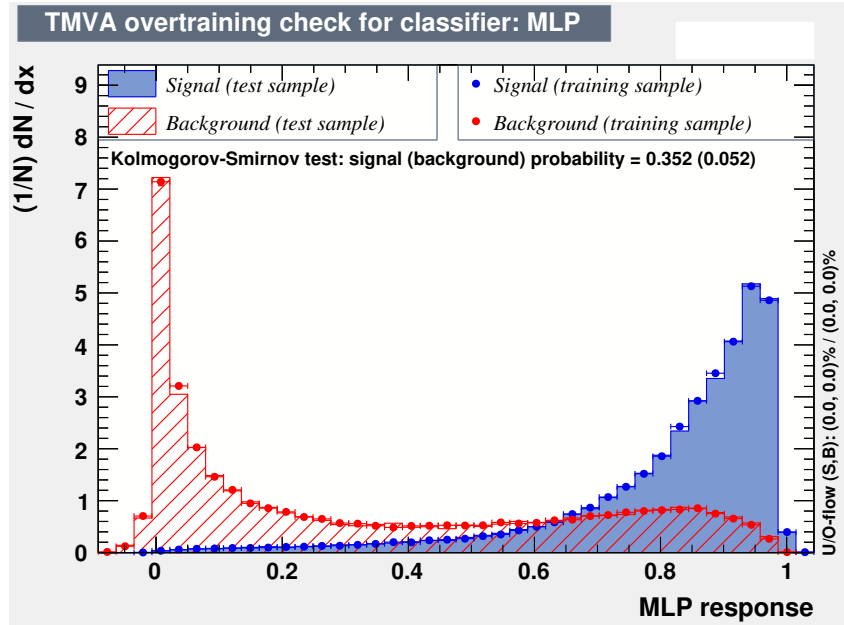


Figure 5.10: $D^0$ MLP response for the signal (in blue) and background (in red) samples. Training samples are shown in dots and test samples are seen as histograms. No evidence of over training is found through the confirmation of Kolmogorov-Smirnov tests which is a measure of agreement between two distributions

### 5.3.5.3 MVA based on $B^-$ discrimination

All the input variables with their meaning are listed in Table 5.11 and Fig. 5.12 provides the distribution of the input variables. As a final selection of $B^-$ candidates, for the

Figure 5.11: Optimisation of the MLP cut value for $D^0$ to maximise the figure of merit. Signal efficiency, background rejection, signal puri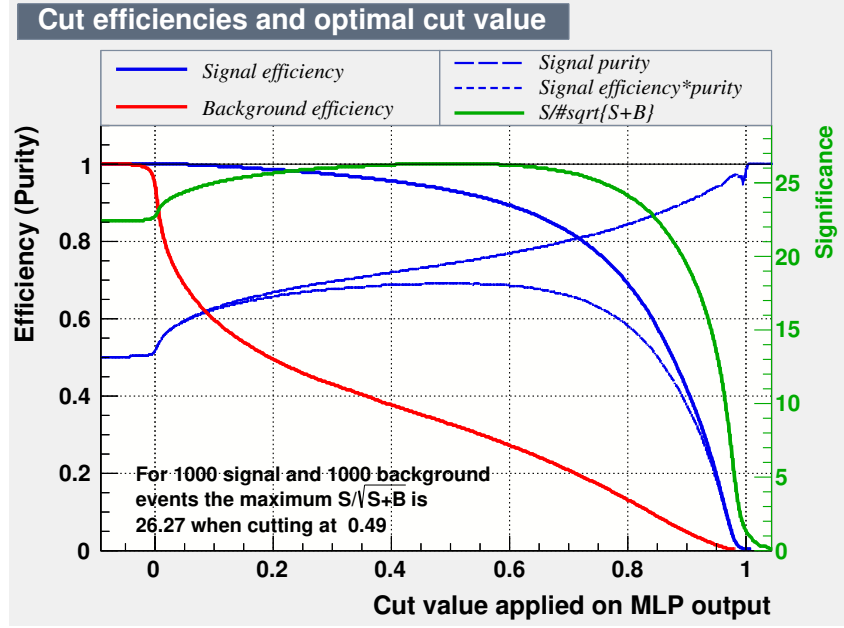ty, signal efficiency purity and figures of merit are plotted against the classifier output value for MLP at the training-evaluation phase.

training of the chosen MLP algorithm see in Figure 5.13, the signal is the full simulation sample of $B^- \rightarrow D^0 K^{*-}$ with the MLP of $K^{*-}$, $\pi^0$ and $D^0$ decays with their all the aforementioned selections are applied. Because the MLP selections of $K^*$ and $D$ are efficient for different sideband and the background zone to be considered in the final $B^-$ MLP selection. The background sample is obtained from the upper sideband of the $B$ mass as it is shown in the Figure 5.1. The correlation between different input variables are computed for the signal and the background are shown in Fig. 5.14 and the Fig. 5.15 shows MLP output response for signal and background .

| Name of variable | Meaning of variable |
|---|---|
| TheMLP_KstarSel | MLP output for $K^*$ selection MVA |
| TheMLP_DSel | MLP output for $D^0$ selection MVA |
| cosThetaHely_D | Helicity angle of $D^0$ meson |
| cosD_bachT_xy | Cos ($D$ wrt $K$ in $K^*$ rest frame in xy) |
| B_IPchi2 | Quality ($\chi^2$) of the Impact Parameter (IP) of $B$ meson |
| BDIRA | angle between the $B$ momentum and the flight distance (FD) from $B$ meson decay vertex to the PV |
| BPT | Transverse momentum ($p_T$) of $B$ meson |
| B_VTXProb | Vertex probability of $B$ meson |
| cosThetaHely_Kstar | Helicity angle of $K^*$ |
| LogDiffZ_DvsB_Err | Logarithm of z difference between $B^-$ and $D^0$ |

Table 5.11: Discriminating variables for $B^-$ decay mode used in the MVA training.

The power of separation of the input variables to the MLP are given in Table 5.12 and Figure 5.15 covering the testing and the training results for the MLP classifier. Note
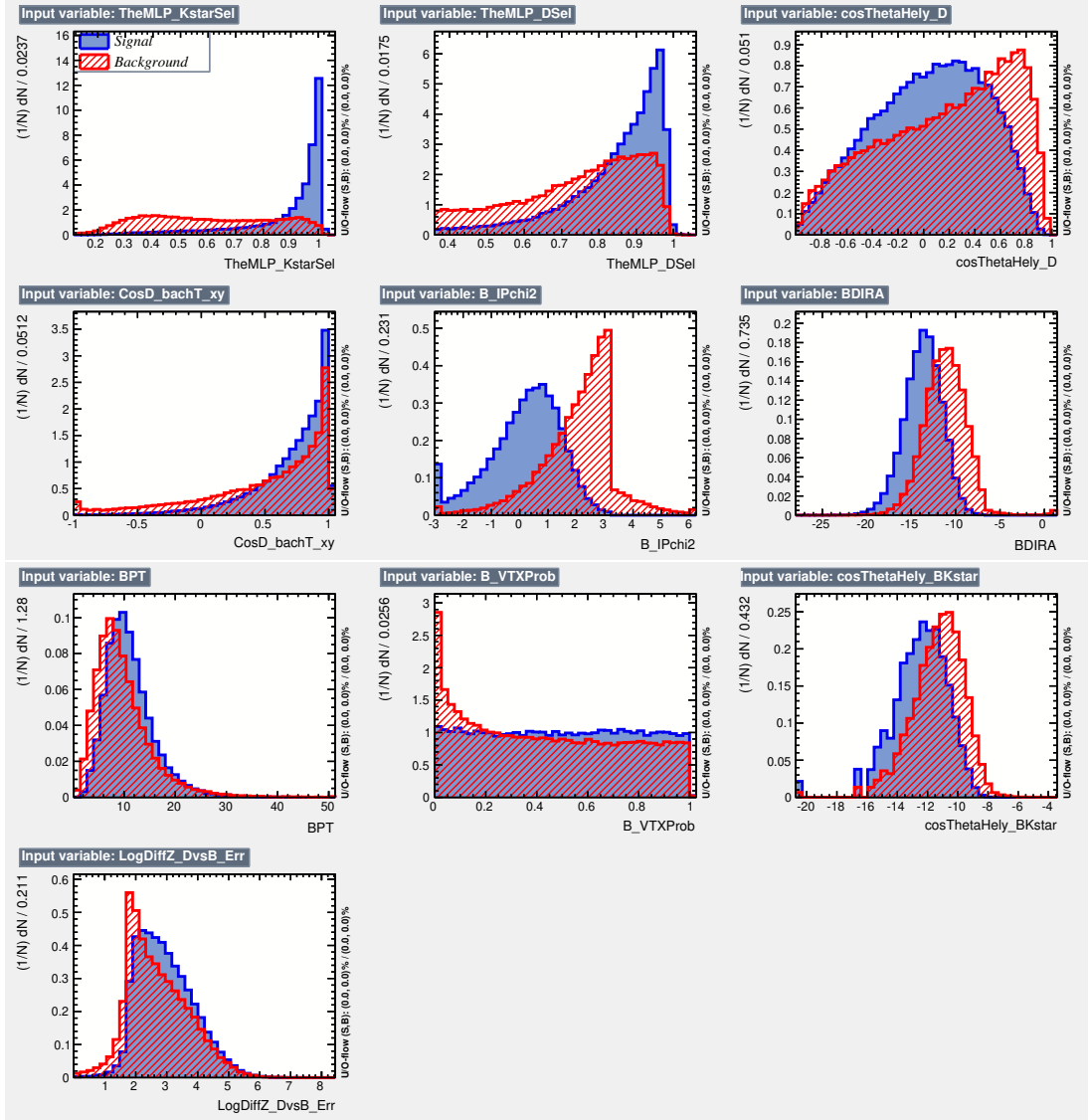
186

Figure 5.12: $B^-$ discriminating variables of the TMVA used with their distributions for signal and background for Run 2. For the expected distributions of the input variables: The cosThetaHely_D is defined as the angle between the momentum of $D$ and $B$ mesons. The signal shape is is proportional to 1-$cos^2\theta$ since $B^- \to DK^{*-}$ is S → S + V. For the B_IPchi2 : transformed to log() for a better numerical behaviour. The $B$ should have a Impact parameter (IP) back to the PV while the background is not. For the BDIRA, it is log(1-BDIRA) the direction of the reconstructed momentum should be parallel to the $B$ vertex and PV. The transverse momentum of $B$ meson BPT discriminating variable should be larger for signal.

that enough amount of signal and background events used during the training, it can be seen that there is no overtraining occured during the training phase.
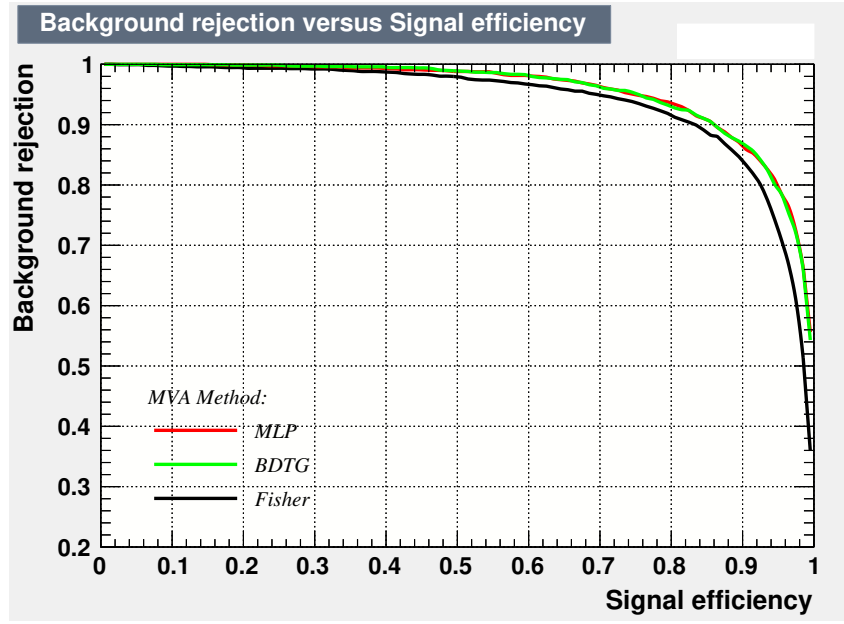
Figure 5.13: Signal efficiency plotted vs background rejection of $B^-$ candidates for Run 2. Different TMVA classifiers have been tested and MLP which gives the best background rejection for a given signal efficiency is chosen.
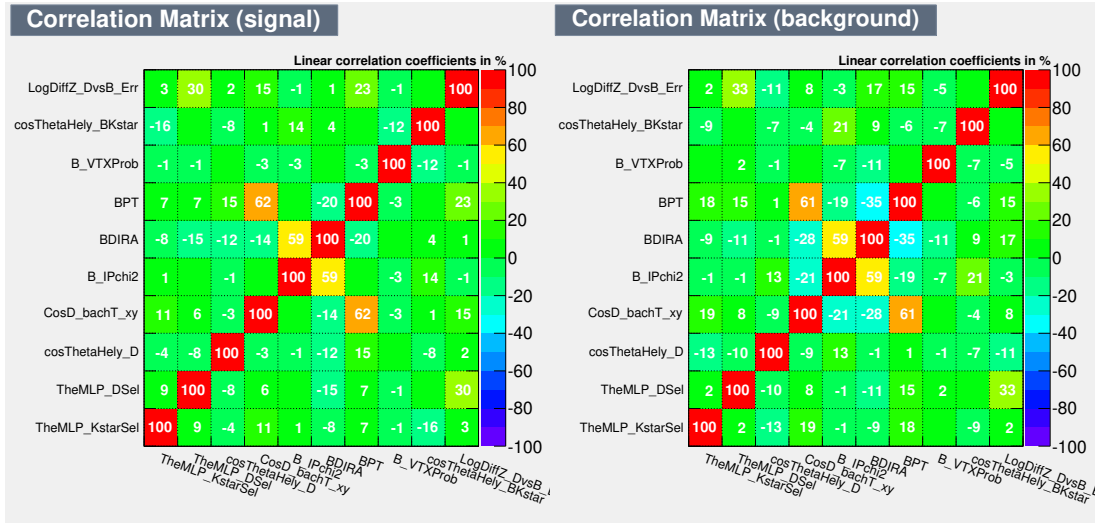


Figure 5.14: Correlation matrix of input variables for the signal samples (left) and background samples (right) in $B^-$ decays.

Figure 5.16 shows the optimisation of the MLP cut value in order to magnify the figure of merit. The last stage of MVA a cut is chosen as a working point and this retain 80% of signal efficiency and reject 93.8% background. The optimum cut value with its signal efficiency and background rejection is specified in Table 5.13.

Subsequently in this part, in order to get rid of majority of the background and retain

| Variable | MVA Ranking | Separation |
|---|---|---|
| $B\_IPChi2$ | 1 | $4.235 \times 10^{-1}$ |
| $TheMLP\_KstarSel$ | 2 | $3.945 \times 10^{-1}$ |
| $BDIRA$ | 3 | $2.528 \times 10^{-1}$ |
| $cosThetaHely\_BKstar$ | 4 | $1.095 \times 10^{-1}$ |
| $TheMLP\_DSel$ | 5 | $1.029 \times 10^{-1}$ |
| $CosD\_bachT\_xy$ | 6 | $6.335 \times 10^{-2}$ |
| $CosThetaHely\_D$ | 7 | $5.738 \times 10^{-2}$ |
| $BPT$ | 8 | $5.383 \times 10^{-2}$ |
| $LogDiffZ\_DvsB\_Err$ | 9 | $3.990 \times 10^{-2}$ |
| $B\_VTXProb$ | 10 | $1.731 \times 10^{-2}$ |

Table 5.12: Input variables separation power.
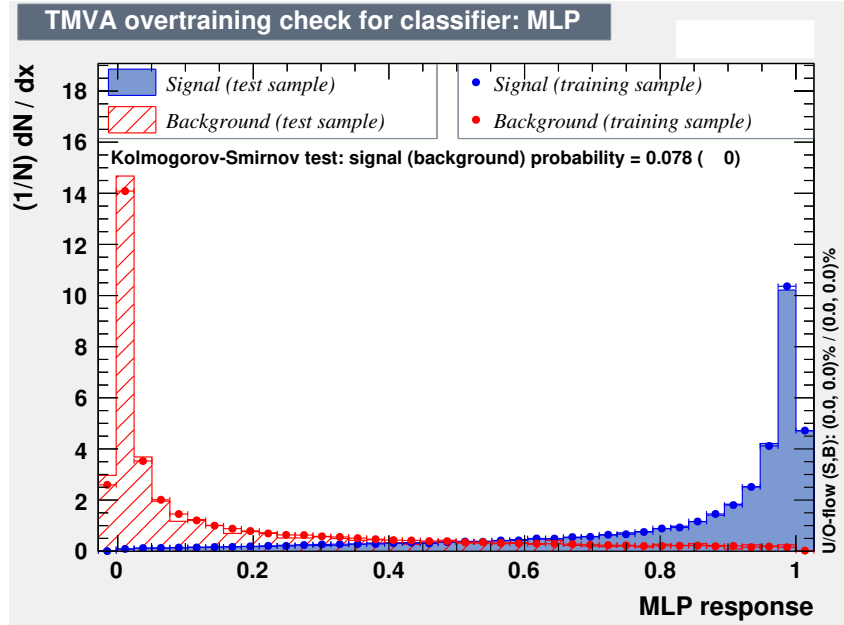


Figure 5.15: $B^-$ MLP response for the signal (in blue) and background (in red) samples. Training samples are shown in dots and test samples are seen as histograms. No evidence of over training is found through the confirmation of Kolmogorov-Smirnov tests which is a measure of agreement between two distributions.

the most of the signal events, TMVA requirements with MLP algorithm optimisation on each of the $B^-$, $K^*$ and $D^0$ candidates has been provided and following this there are still selections based on $\Delta z(B - D)$ and PID of charged tracks which will be detailed in the next sections.

Figure 5.16: Optimisation of the MLP cut value for $B^-$ to maximise the figure of merit. Signal efficiency, background rejection, signal purity, signal efficiency purity and figures of merit plotted against the classifier output value for MLP at the training-evaluation phase.
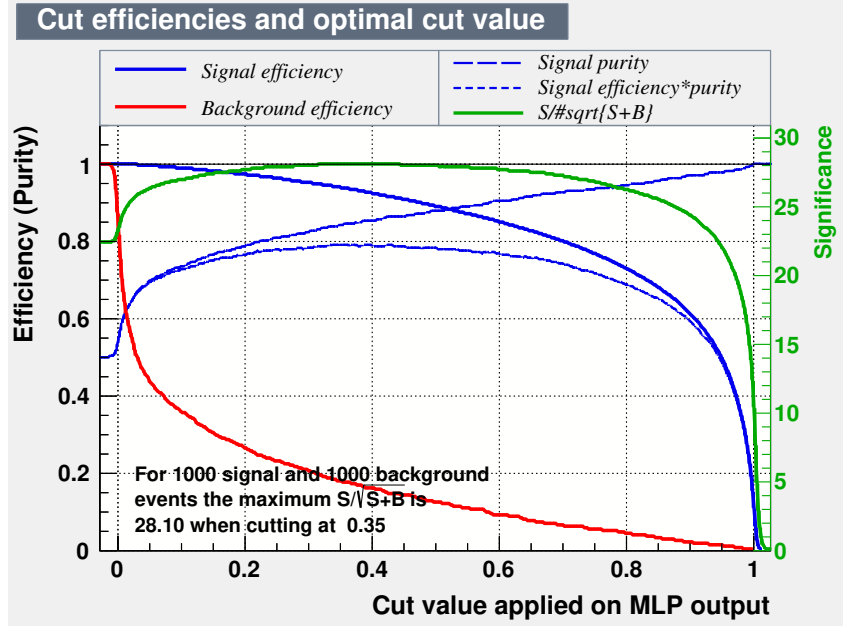
| Candidate | Cut MVA MLP | Signal Efficiency | Background Rejection |
|-----------|-------------|-------------------|----------------------|
| B | 0.83 | 80% | 93.8% |

Table 5.13: The signal efficiency and the background rejections are obtained when cutting on the MLP for Run2.

## 5.3.6  Particle identification (PID) requirements for $B^- \to D^0 K^{*-}$ $(K^-\pi^0)$

After applying all the identical selections on the $D^0$ meson final states, it is important to apply two standard particle identification (PID) variables which LHCb used : ProbNN* and Difference in Log-Likelihood (DLL). For this analysis, we use the DLL variables in order to distinguish the kaons and pions in the final states. The likelihoods are calculated by combining of all the information from the RICH, calorimeters and the muon systems 5.3. The DLL variable is defined with the likelihood function $\mathcal{L}$: $\mathcal{L}_\pi$, $\mathcal{L}_K$ 5.2.

$$DLL_{K-\pi} = ln\mathcal{L}_\pi - ln\mathcal{L}_\mathcal{K}, \qquad (5.2)$$

---

*PID particle identification provided by the ProbNN variables. These variables are based on multi-variate algorithm and explained earlier with the $B_s^0 \to D\phi$ analysis.

$$\mathcal{L}(h) = \mathcal{L}^{\mathcal{RICH}}.\mathcal{L}^{\mathcal{CALO}}.\mathcal{L}^{\mathcal{MUON}} \tag{5.3}$$

A tight cut on both $D$ daughter tracks $DLL\_K$ and $DLL\_\pi$ is applied from $D^0$ where decay modes are reconstructed in the $K\pi$ (RS), $K^-K^+$, $\pi^-\pi^+$, $K\pi$ (WS) final states to improve the purity. The $D^0$ mass to be in $[1.8421, 1.8883]\,\mathrm{GeV}/c^2$ and the mass range is $\pm\,20.5$ in the data selection.

For the $B^- \to D^0 K^-$, where $D^0$ decays to $D^0 \to hh$, $h \in [\pi, K]$ [35], [38], relatively loose cut on the $D$ charged track daughter has been set to reduce the miss-ID crossfeed from other $D$ modes, even if a $\pm 3\sigma$ cut is set on the mass of $m(D^0)$ that should suppress the mixing of $D^0 \to KK$, $D^0 \to \pi\pi$ and $D^0 \to K\pi$ modes seen in Figure 5.17. From this figure one can see the $D^0$ mass distribution after the $D$ MVA selection for 2018 Data and this is for the $D$ decays to $D^0 \to K^-\pi^+$. From the Figure 5.17, on the left (right) of the signal peak, one can clearly see the $D^0 \to KK(\pi\pi)$ signal peak, without PID criteria on the $D$ daughter. It is clear that a mass cut for the signal to be in $[1.8421, 1.8883]\,\mathrm{GeV}/c^2$ allow to avoid the $D^0 \to K\pi$, $D^0 \to KK$, $D^0 \to \pi\pi$ mixing of the various signals, the additional PID cuts on $D^0$ daughters allow to reduce the combinatorial background below the $D$ signal peak.
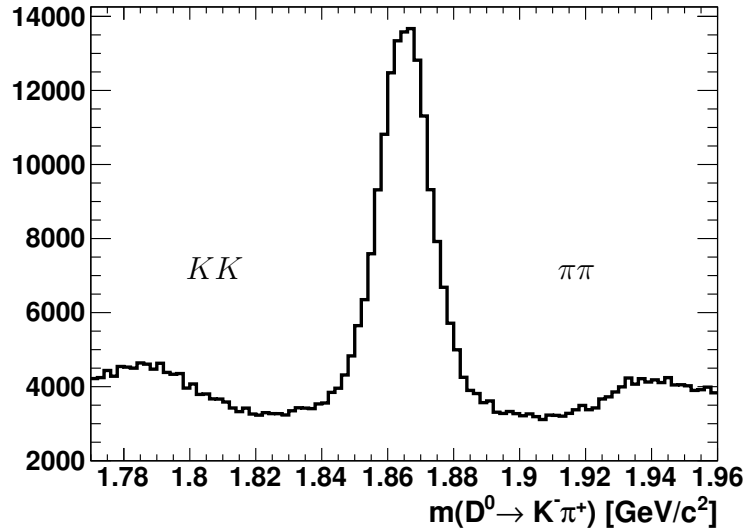


Figure 5.17: $D^0$ mass distribution after the D MVA selection for Data 2018. This distribution shows $D^0 \to KK$ on the left side of the signal peak and $D^0 \to \pi\pi$ on the right side of the signal peak without PID selection on the $D^0$ daughter.

The PID criterions applied on the $K^{*-}$ daughters are somewhat tighter but not too much, since we have to deal with the different levels of backgrounds for the various analysis where $D^0 \to K^-\pi^+$ (Right Sign (RS)/ADS) or $D^0 \to K^+\pi^-$ (Wrong Sign (WS)/ADS) and $D^0 \to K^-K^+$, $D^0 \to \pi^-\pi^+$ (CP-eigenstates/GLW). Nevertheless, the fact that a fit is performed to $K^{*-} \to K^-\pi^0$, sPlot subtraction of the backgrounds allows us to set these

criterions to be reasonably loose for $D^0$ decays to $K^-\pi^+$(RS), $K^-K^+$, $\pi^-\pi^+$ and to set a tighter value. All of the above retained choices allow a large background rejection, while keeping the signal efficiency as much as high possibly achievable. We have slightly tuned this criterion for the various mode: $K^-\pi^+$, $K^-K^+$, $\pi^-\pi^+$, $K^+\pi^-$(WS) to accommodate the combinatorial background in the $D$ and $K^{*-}$ decays.

#### 5.3.6.0.1 PID requirements for Right Sign (RS): $D^0 \to K^-\pi^+$

- $DLL\_K > 4$ for $K^*$ daughter

- $DLL\_K > 2$ for the D daughter if kaon

- $DLL\_K < -2$ for the D daughter if pion

#### 5.3.6.0.2 PID requirements for $K^-K^+$

- $DLL\_K > 4$ for $K^*$ daughter

- $DLL\_K > 2$ for the daughters $(KK)$

#### 5.3.6.0.3 PID requirements for $\pi^-\pi^+$

- $DLL\_K > 4$ for $K^*$ daughter

- $DLL\_K < -2$ for the daughters $(\pi\pi)$

#### 5.3.6.0.4 PID requirements for Wrong Sign (WS): $D^0 \to K^+\pi^-$

- $DLL\_K > 8$ for $K^*$ daughter

- $DLL\_K > 4$ for the $D$ daughter if kaon

- $DLL\_K < -4$ for the $D$ daughter if pion

- $|D^0{}_{swapped} - 1865\,\mathrm{MeV}/c^2|$ for ADS modes $m_{D^0}$ is in the range of [1.8421, 1.8883] $\mathrm{GeV}/c^2$, see the next section for the detailed discussion.

### 5.3.7 Double miss-ID and Kaon/pion swapping in $D \to K\pi$ decays

A veto is performed on the possible background originated from $D^0 \to K^-\pi^+$ (Cabibbo Favoured (CF)) decays that could mimic $D^0 \to K^+\pi^-$ (Doubly Cabibbo suppressed (DCS)) (WS) decays if the kaon and pions daughters are swapped. For the reminder, branching fraction of $D^0 \to K^+\pi^-$ is $\mathcal{BF}(D^0 \to K^+\pi^-) = (3.947 \pm 0.030)\%$ and the branching fraction of $D^0 \to K^-\pi^+$ is $\mathcal{BF}(D^0 \to K^-\pi^+) = (1.50 \pm 0.07) \times 10^{-4}$ (more than a factor of 25°!) [18]. It is therefore quite probable that a double miss-ID $K$ to $\pi$

192

and vice-versa may happen in the decays of $D \to K\pi$. Selection requirements for the sub-decays of $D^0$ have been defined in the previous sections. There is need to have a tighter PID selections just to avoid having the CF mode $D^0 \to K^-\pi^+$ polluted the $D^0 \to K^+\pi^-$ signal. We veto the $D$ candidates for which the mass of the pion and kaon have been swapped $K \longleftrightarrow \pi$: a kaon can be mis-identifed as a pion or a pion can be mis-identified as a kaon. In order to apply the veto events, the reconstructed mass window of swapped $D^0$ mass is within the range $[1.8421, 1.8883]$ GeV/$c^2$. And with the swap which Figure 5.18 shows, a study is performed with $B^- \to D^0 K^{*-}$ and $D^0 \to K^-\pi^+$ simulated signal Monte Carlo (MC)(Run 1 and Run 2), distribution on the left side of the Figure 5.18 gives the $D^0 \to K^+\pi^-$ mass distribution and the swap of the mass of the kaon and the mass of the pion, while computing the $D^0$ candidate mass, right side distribution of Figure 5.18 for the $D^0 \to K^+\pi^-$ WS mass distributions before and after the veto. And resultinf from this, there are 3163 and 2769 events before and after the veto which saves 88% of $D^0$ true events respectively. This safe requirement will eliminate more than 99.7%, as we have chosen a $\pm 3\sigma$ veto interval for the $D$ ($K/\pi$ swapped) mass and it costs about 12% signal efficiency loss on the ADS signal.
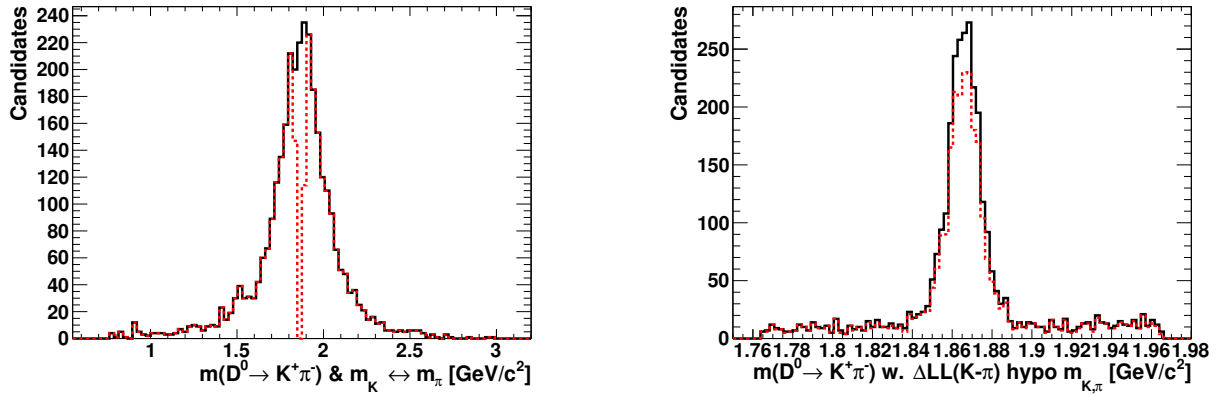


Figure 5.18: Distributions represent the veto performed. (Left) Distribution for the $D^0 \to K^+\pi^-$ mass distribution and the swap of the mass of the kaon and the mass of the pion hypotheses, while computing the $D^0$ candidate mass. (Right) The distribution shows the $K\pi$ WS mass distributions before and after the veto, after using the $K\pi$ RS mass hypotheses for MC Run 1 and Run 2.

## 5.4    Background contributions

The goal of this part to define the numerous background sources contribute to the invariant mass fit. There MC backgrounds peaking at the low-mass region of the phase space of the signal of interest and a combinatorial background. One of the background sources comes from charmless decays. Three of these MC background sources from the partially recon-structed decays i.e. $B^- \to D^{*0}[D^0\pi^0]K^{*-}$, $B^- \to D^{*0}[D^0\gamma]K^{*-}$, $B^0 \to D^{*+}[D^0\pi^+]K^{*-}$,

where $D^0$ meson is reconstructed while the one particle in the final state in the decay i.e $\pi^0$, $\gamma$ and $\pi^+$ is reconstructed partially only. We have one source is from copious peaking decays of $B^- \to D^{(*)0}\rho[\pi^-\pi^0]$ and a pure combinatorial background. The different background sources will be detailed in the following parts.

## 5.4.1 Charmless peaking background

This background sources comes from the decay processes which don't involve $D$ meson i.e. $B^- \to (h_1 h_2)_{D^0} K^{*-}$ where $h_1 = K, \pi$ and $h_2 = \pi, K$ and $h_1 h_2$ looks like $D^0$. For this type of charmless decays, the decay of the $B$ meson can then directly give the decay products of the $D^0$: i.e $B^\pm \to D^0 K^{*\pm}[K^\pm\pi^0]$. These decays has been measured by BaBar collaboration and have been included in the PDG [18]. Charmless decays and their branching ratios are given in the Table 5.14. Each of these decay channels in the table represent a background in one of the channels studied in this thesis.

| Decay Channel | Branching fraction |
|---|---|
| $B^- \to K^+ K^- K^{*-}$ | $(B^- \to K^+ K^- K^{*-}) = (3.6 \pm 0.5) \times 10^{-5}$ |
| $B^- \to \pi^+ \pi^- K^{*-}$ | $(B^- \to \pi^+ \pi^- K^{*-}) = (7.5 \pm 1.0) \times 10^{-5}$ |
| $B^- \to \pi^- K^+ K^{*-}$ | $(B^- \to \pi^- K^+ K^{*-}) < 6.1 \times 10^{-6}$ |
| $B^- \to \pi^+ K^- K^{*-}$ | $(B^- \to \pi^+ K^- K^{*-}) < 1.18 \times 10^{-5}$ |

Table 5.14: Branching ratios of the decays constitute the physical background [18].

These large number of events corresponding to the decay modes contribute to the background represent the danger of these signals. With the requirements has been applied on the mass of $D^0$ candidates $\pm 23\,\mathrm{MeV}/c^2$ around the mass of $D^0$ which is given by the PDG [18] and the kinematic requirements performed on the $B$ meson mass constraint and thus the background contribution from these decays are peaking at the $B$ mass spectrum. These decays has the final state with the decay mode interest of this study and has contribution from charmless background. These contributions show itself peaking in the invariant $B^-$ mass spectrum. And in order to avoid charmless contamination a dedicated selection criteria is used to remove this background and for this we have $D^0$ sidebands to check the charmless background and it can be subtracted directly in the $D$ sideband where the region is defined $\pm 5\,\sigma$ away from the nominal $D^0$ mass as displayed in Figure 5.19. We don't rely on the MC signal and just measure in the sideband, so directly subtract the signal that can be likely found in the sideband of the $D^0$. The yield from this peaking background is measured in the sidebands of $D^0$ and fixed in the fit. The requirement for the charmless background is set on $SDB$ which gives the significance of the distance in $z$ direction (so-called flight distance significance) between $B$ and $D$ vertices and given as an input variable within the MVA for $B$ meson (see in Table 5.11). What really matter here is the resolution on the $z$ vertex position, $D$ decay vertex must be very well separated from the $B$ decay vertex. The variable is defined as in the Eq. 5.4
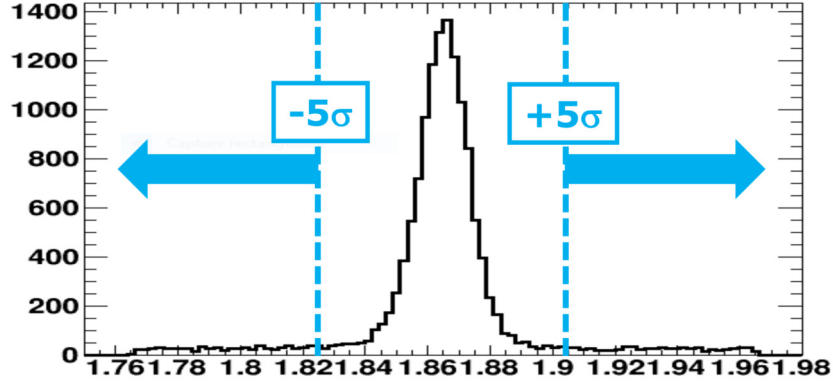
Figure 5.19: Distribution for the $D^0$ mass sidebands. The blue dashed lines define the regions $5\sigma$ away from the nominal $D^0$ mass.

$$Signif[\Delta z(DB)] = SDB = \frac{\Delta z_{vtx}(D - B)}{[\sigma z_{vtx}(D) \oplus \sigma z_{vtx}(B)]} \quad (5.4)$$

where $\Delta z_{vtx}(D - B)$ is the $z$ position of the decay vertex of the $D$ and $B$. $\sigma z_{vtx}(D)$ and $\sigma z_{vtx}(B)$ gives the uncertainty on the $z$ position of the $D$ and $B$ decay vertex. The requirement is optimised on the $B^- \to D^0 K^{*-}$, where $D^0$ reconstructed in the decay modes of $K^-\pi^+$ (RS), $K^+\pi^-$ (WS), $K^+K^-$ and $\pi^+\pi^-$ and the same requirement for each of these decay modes as listed below:

$$Signif[\Delta z(DB)]_{D^0} > 1 \quad (5.5)$$

## 5.4.2  Partially reconstructed background

This background source is based on three MC samples listed below. Information about these decay modes has been given within the scope of previous $B_s^0 \to \tilde{D}^0 \phi$ analysis.

1. $B^- \to D^{*0}[D^0\pi^0]K^{*-}$

2. $B^- \to D^{*0}[D^0\gamma]K^{*-}$

3. $B^0 \to D^{*+}[D^0\pi^+]K^{*-}$

where the first and second one the $\pi^0$ and $\gamma$ formed in the decay of $D^{*0}$ meson is not reconstructed in the final state.

Table 5.15 shows the branching ratios for these decay modes taken from [18] which are similar to the signal decay. That's why it is important to study these decays since they mimic like signal and populate as a peak in the low mass region lies below the nominal B mass spectrum.

| Decay Channel | Branching fraction |
|---|---|
| $D^{*0} \to D^0\pi^0$ | $(D^{*0} \to D^0\pi^0) = (64.7 \pm 0.9)\%$ |
| $D^{*0} \to D^0\gamma$ | $(D^{*0} \to D^0\gamma)= (35.3 \pm 0.9)\%$ |
| $D^{*+} \to D^0\pi^+$ | $(D^{*+} \to D^0\pi^+) = (67.7 \pm 0.5)\%$ |
| $B^- \to D^{*0}K^{*-}$ | $(B^- \to D^{*0}K^{*-}) = (8.1 \pm 1.4) \times 10^{-4}$ |
| $B^0 \to D^{*+}K^{*-}$ | $(B^- \to D^{*+}K^{*-}) = (21.6 \pm 4.2)\%$ |

Table 5.15: Branching fractions for the considered partially reconstructed decay channels [18].

Non-parametric and unbinned PDFs so-called RooKeysPDF [142] are used to model the background distributions. Gaussian function is used with an exponential tail to constraint these background shapes defined in the invariant mass fit after all selections are applied. These shapes of the partially reconstructed decays modelled by RookeysPDf are shown in Figures 5.20 and 5.21. The dangerous parts are those who leak in to the $B^-$ mass region at $5.279\,\mathrm{GeV}/c^2$, within about $\pm 100\,\mathrm{MeV}/c^2$. In Figure 5.20, one can see that the $D^0\gamma K^{*-}$ (right side figure) is the most potentially dangerous as a non neglecting part of it (right side wall) is located in the $B$ mass region $5.28\pm0.1\,\mathrm{GeV}/c^2$.
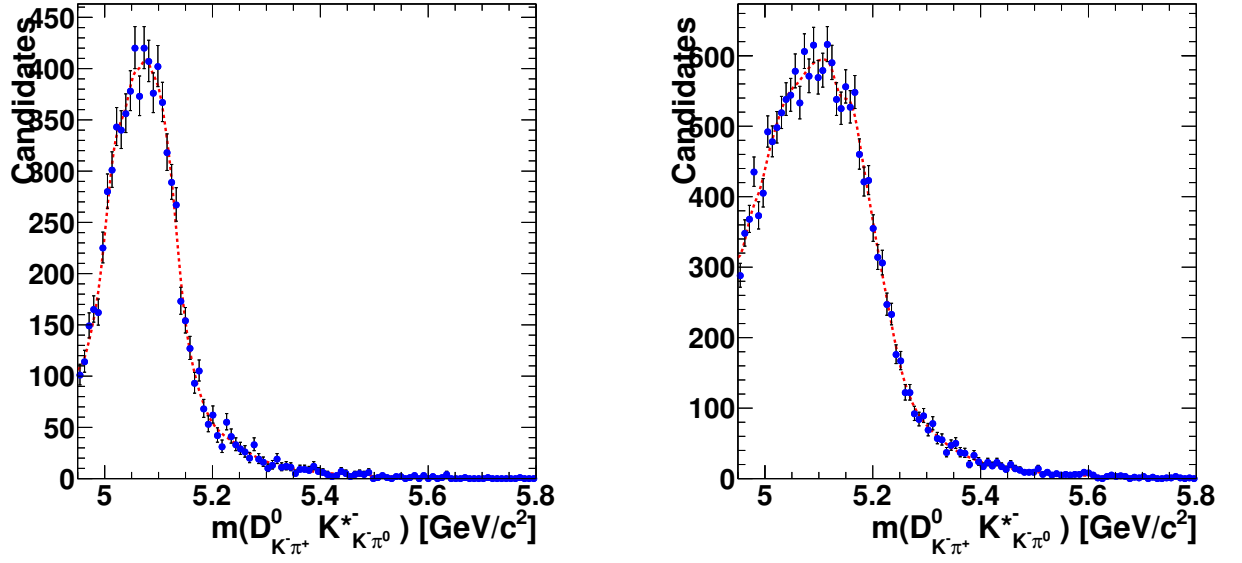
Figure 5.20: Partially reconstructed decays of $B^- \to D^{*0}[D^0\pi^0]K^{*-}$ (left) and $B^- \to D^{*0}[D^0\gamma]K^{*-}$ (right). The $D^{*0} \to D^0\gamma$ is more dangerous as a non neglecting part falls into the $B$ mass region i.e. $5.28 \pm 0.100\,\text{GeV}/c^2$.
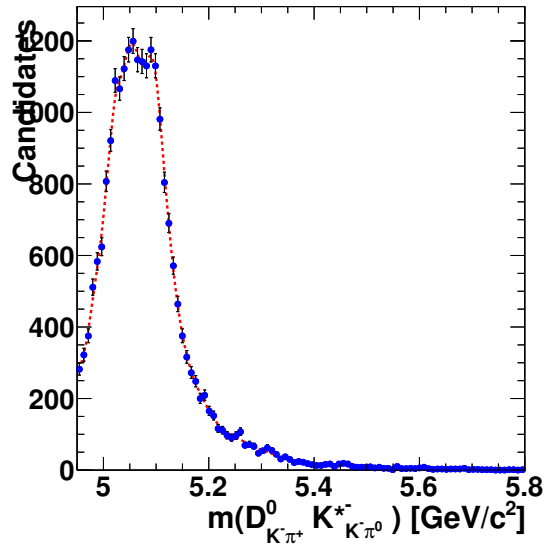


Figure 5.21: Partially reconstructed decays of $B^0 \to D^{*+}[D^0\pi^+]K^{*-}$.

### 5.4.3 Background from $B^0 \to D^{*+}[D^0\pi^+]\rho^-[\pi^-\pi^0]$ and $B^- \to D^{(*)0}\rho^-[\pi^-\pi^0]$

We have further three MC background sources which arises from such decay modes as $B^- \to D^0\rho^- (\pi^-\pi^0)$ and $B^- \to D^*(\pi^0)\rho^-$ and $B^- \to D^*(\gamma)\rho^-$ for which neutral pion is reconstructed as photons and one or more final state particles, in this case, pions are missing. Table 5.16( [18]) shows the branching ratios of the decay modes studied. These background sources are the most dangerous since it has similarity with the $B^- \to D^0K^{*-}$ $(K^-\pi^0)$ signal decay of interest and contribute to the background within its vicinity. The danger is that the $\rho$ $(\pi^-\pi^0)$ will mimic a $K^{*-}$ as the pions mis-ID even at a few percent can really satisfy the log-likelihood differences DDL requirements for $K$ as the branching fraction of the $B$ decays are two order of magnitude larger than $B^- \to DK^{*-}$. Even if we apply PID criterion of $K^*$ daughter this is not enough, therefore a fit to the $m(K\pi)$ candidates is performed to perform a sPlot subtraction of the non-$K^*$ components. Figures 5.22 show the spectrum of surviving $B^- \to D^{(*)}\rho^-$ backgrounds for MC signal samples and even after applying PID on the $K^{*-}$ charged daughter. We will eventually account for the $D^0\rho^-$ that peaks at higher mass than the $B^-(\text{m}(\pi)\longleftrightarrow\text{m}(K)$ swap) with a RookeyPDF in the final $B$ mass fits. But a method will be applied by fitting the m$(K\pi^0)$ spectra in order to exclude $\rho^-$ mesons contributions as much as possible see Figure 5.26 (This will be detailed in the Section 5.5.3).

| Mode | Branching fraction |
|---|---|
| $B^- \to D^0\rho^-$ | $(B^- \to D^0\rho^-) = (1.34 \pm 0.18) \times 10^{-2}$ |
| $B^- \to D^0K^{*-}$ | $(B^- \to D^0K^{*-}) = (5.3 \pm 0.4) \times 10^{-4}$ |
| $B^0 \to D^{*+} (D^0\pi^+)\rho^-$ | $(B^0 \to D^{*+}(D^0\pi^+)\rho^-) = (6.8 \pm 0.9) \times 10^{-3}$ |
| $B^- \to D^{*0}(D^0\pi^0/\gamma)\rho^-$ | $(B^- \to D^{*0}(D^0\pi^0/\gamma)\rho^-) = (9.8 \pm 1.7) \times 10^{-3}$ |
| $\rho^- \to \pi^-\pi^0$ | $(\rho^- \to \pi^-\pi^0) = 100\%$ |
| $K^{*-} \to K^-\pi^0$ | $(K^{*-} \to K^-\pi^0) = \frac{1}{3}$ |

Table 5.16: Branching fractions for the considered decay modes. Taken from [18].
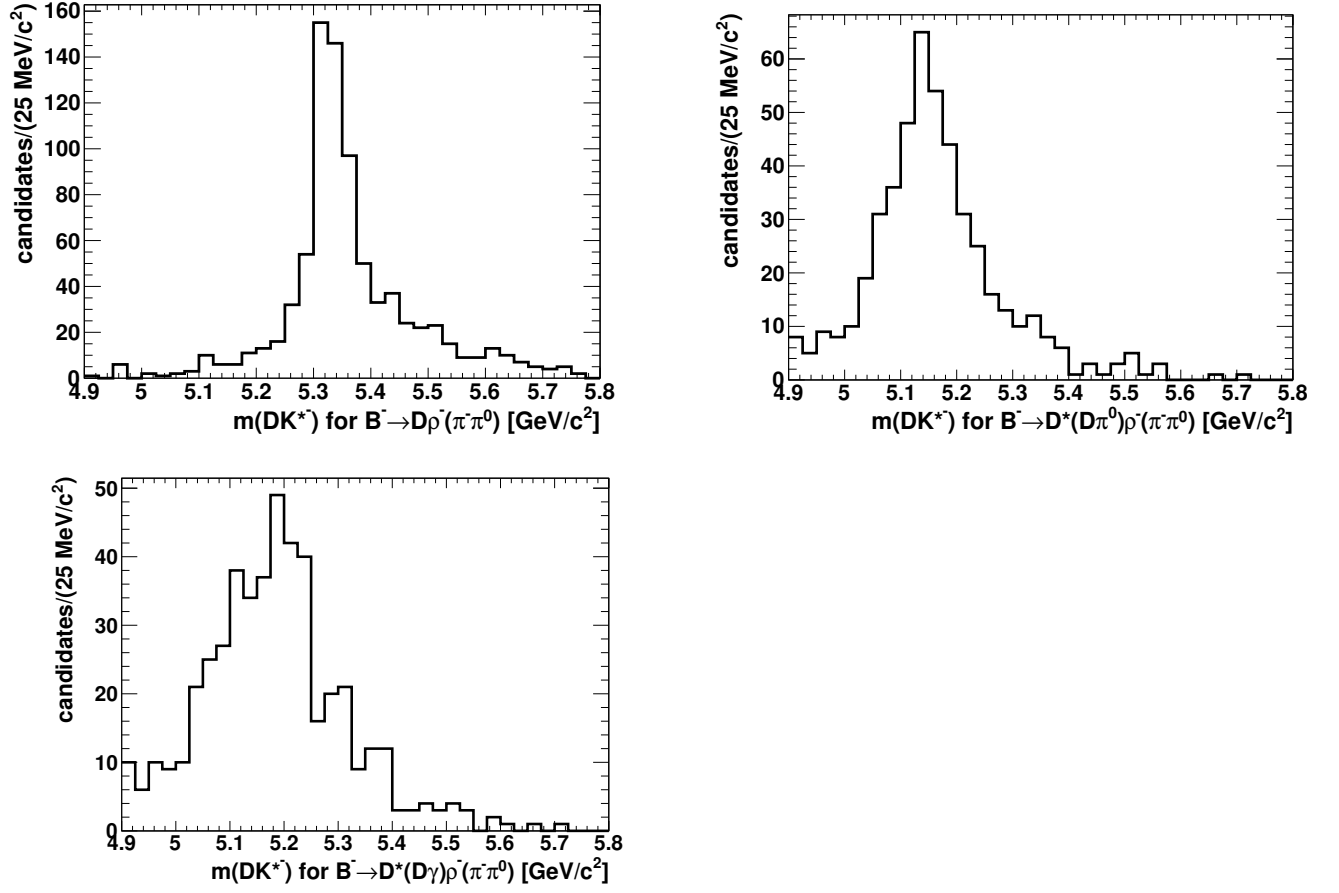
Figure 5.22: Mass distributions for the $B^- \to D^{(*)}\rho^-$ background components for MC simulation. Upper left side distribution is for the $B^- \to D^0\rho^-(\pi^-\pi^0)$, upper right side is for the $B^- \to D^*(D\pi^0)\rho^-$ and bottom distribution is for the $B^- \to D^*(D\gamma)\rho^-$.

The shape of this background is fitted with Novosibirsk function which represents better description RookeyPDF displayed in Figure 5.23.
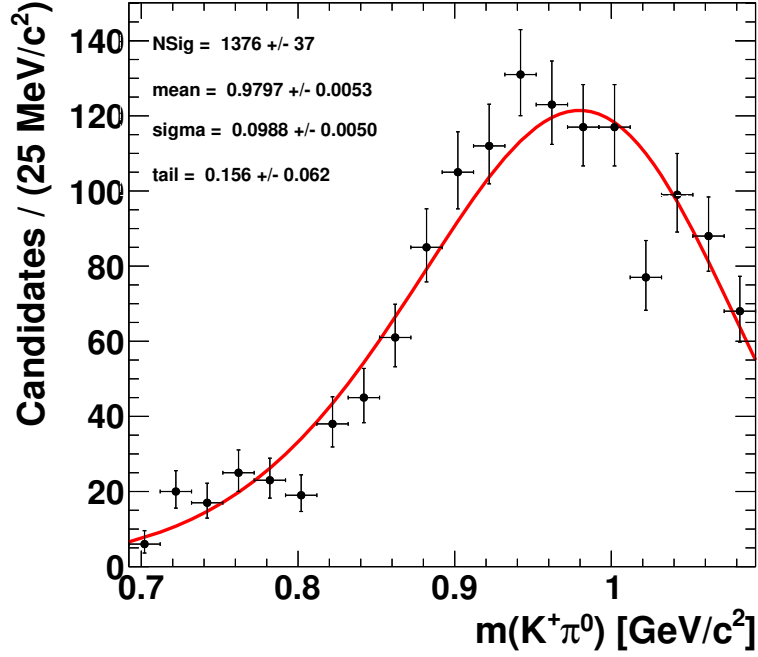
Figure 5.23: Background model of $\rho^+ \to \pi^+\pi^0$ is improved for m$K^*$. The signal is fitted with Novosibirsk function with 1376 events after only surviving selections.

## 5.4.4 Combinatorial background

This type of background category is dominant emerges from the combination of the random tracks which are not originating from the same $B^-$ in the pp collision but from the $D$ and $K^*$ companion with random $\pi^0$ or charged particles in the event and they mimic the signal. The combinatorial background doesn't peak. It is important to have a good invariant mass resolution in order to lower the search window and decrease the level of background. These background contamination has been reduced by the help of the multivariate selection and its behaviour is described by using polynomial function.

## 5.5 Extraction of the number of $B^+/B^-$ events yields

After applying all the selections including: preselections, PID selections, different background categories to the decay of interest $B \to D^0 K^{*-}$ are described which will be used in the mass fit model. Then a fit to the invariant mass of $K^*$ and $B$ decays is performed. For the analysis we make use of RooFit Package [153] where unbinned extended maximum likelihood (UML) fit is constructed to the data to extract the signal and the background yields individually for each of the $K^* \to K^- \pi^0$ and $B \to D^0 K^{*-}$ where $D^0$ meson decays to modes: non-CP eigenstates $K^- \pi^+$, $K^+ \pi^-$ (ADS/WS) and CP-eigenstates GLW modes: $\pi^+ \pi^-$, $K^+ K^-$. Each fits performed to these decay modes are explained separately.

### 5.5.1 Fit strategy and suppression of non-$K^*$ components

After all selections, in the previous section it has been shown that a few background components will survive and this will complicate the fit to the selected $B \to D^0[hh]K^{*-}(K^-\pi^0)$ candidates. Therefore, as for the $B_s^0 \to \tilde{D}^{(*)0}\phi$, we will take advantage of the non negligible natural width of the $K^*$ meson to suppress or at least to reduce the non-$K^{*-}$ components (i.e. $B \to D^{(*)}\rho^-$), the combinatorial $K\pi^0$, including possible S-wave (non P-wave as the $K^*$) that will dilute our CP observables measurement and bias the extraction of the angle $\gamma$. It has been shown in [58] for the companion analysis of $B^\pm \to DK^{*\pm}$, where $K^{*\pm}$ reconstructed in $K_S^0 \pi^\pm$, which after the selection in a $\pm 70\,\mathrm{MeV}/c^2$ mass window, $K\pi$ S-wave represent the order of $[100\text{-}(95\pm6)]\%$, as estimated from a dedicated analysis based on the LASS line-shape [154]. In order to avoid to rely on such a model we develop a special fit strategy. This fit strategy proceeds in two steps:

- In a first step, we retain only $K^{*-} \to K^- \pi^0$ candidates in the mass window [0.692, 1.092] $\mathrm{GeV}/c^2$ and perform a fit to the $K^*$ mass on top of $K\pi^0$ combinatorial background and miss-identified $\rho^- \to \pi^- \pi^0$.

- From the previous fit, sWeight is determined to project into the m($DK^{*-}$) $B$ mass plot only the $K^{*-}$ signal components.

It will be shown that as an illustration, with the $B^- \to D(K^-\pi^+)K^{*-}(K^-\pi^0)$ abundant and pure signal how the above strategy is deployed.

### 5.5.2 Fit to the invariant mass of $K^* \to K^-\pi^0$ and $B \to D^0[K^-\pi^+]K^{*-}$ (RS)

Selections are defined for the $B \to D^0[K^-\pi^+]K^{*-}$ (RS) decay

- $Signif[\Delta z(DB)]_{D^0} > 1$

- $m_D \in [1.8421, 1.8883]\,\mathrm{GeV}/c^2$ ($\pm\, 3\sigma$)

- $DLL\_K > 4$ for the charged $K^*$ daughter

- $DLL\_K > 2$ for the D daughter if kaon

- $DLL\_K < -2$ for the D daughter if pion

Figure 5.24a a fit performed to the invariant mass of $K^* \to K^-\pi^0$ candidates, where the MC $K^*$ signal is described by the convolution of a Breit-Wigner function with the natural width fixed to the known PDG mass of $K^*$ is $\Gamma(K^*) = 51.4\,\text{MeV}$ with the sum of two alleged Novosibirsk functions (PDFs) can be seen and the fit in Figure 5.24b to the DATA $K^*$ samples before the sPlot subtraction, the Breit-Wigner function with the mean value is adjusted to $883.2\,\text{MeV}/c^2$, the parameters of the two Novosibirsk (Left and Right) functions are set to their MC simulation values (see Figure 5.24a). Here it can be seen that the combinatorial background is reasonably low (green curve) and the brown dashed curve is for the $\rho$ background where we have $K^*$ decays to $K^-\pi^0$ and the branching ratio of the $B \to D\rho$ is much larger than the $B^- \to D^0K^{*-}$. What we really care is to split the pure combinatorial background and $\rho$ background. This is studied by using the sPlot weights obtained from a fit to the $K^{*-}$ distribution. This will be detailed in the following section 5.5.3. The number of combinatorial background candidates is evaluated by fitting the first degree of polynomial function which is given with the only three parameters. And the fraction of the total background $f(\rho)$ comes from the external fit of peaking background. All the fit parameters for each PDFs are listed on the plots for both MC and DATA. Invariant mass distribution of $B^- \to DK^{*-}$ ($K^-\pi^0$) with the fit on the MC where all the survivors are taken after all the selections which have been described in the previous sections is shown in Figure 5.25. The PDF MC shape is computed from the Monte Carlo signal $B^- \to DK^{*-}$ and $D \to K\pi$, $D \to KK$, $D \to \pi\pi$ all together with all the candidates surviving the selections. The signal is described by the Double-Crystal-Ball function. The region corresponding a range of $m_B \in [4.9, 5.8]\,\text{MeV}/c^2$ and $m_D \in [1.8421, 1.8883]\,\text{GeV}/c^2$ ($\pm\,3\,\sigma$) for the $B$ and $D$ candidates are required. We use the RookeyPDF obtained from Figures 5.20 and 5.21. The relative rate of $D^{*+}K^{*-}$, $D^{(*)0}K^{*-}$ and $D^{(*)0} \to D^0\pi^0$ and $D^{(*)0} \to D^0\gamma$ are fixed according to the PDG rates, varies within their uncertainties as what has been done in the analysis [59], [15].
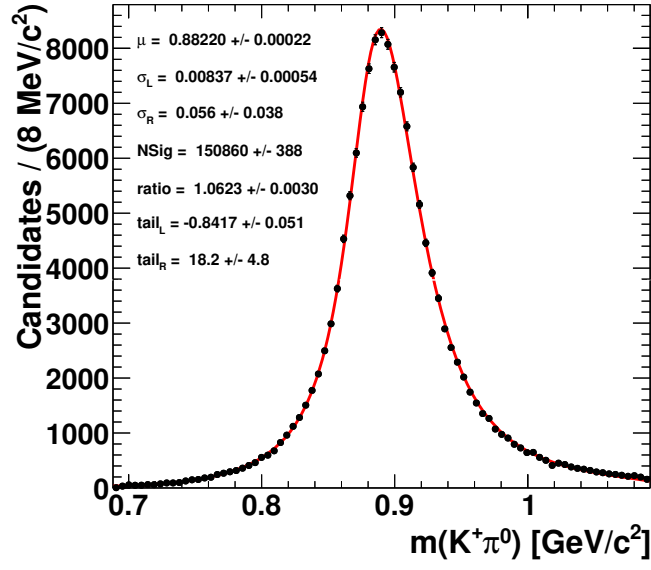
(a)
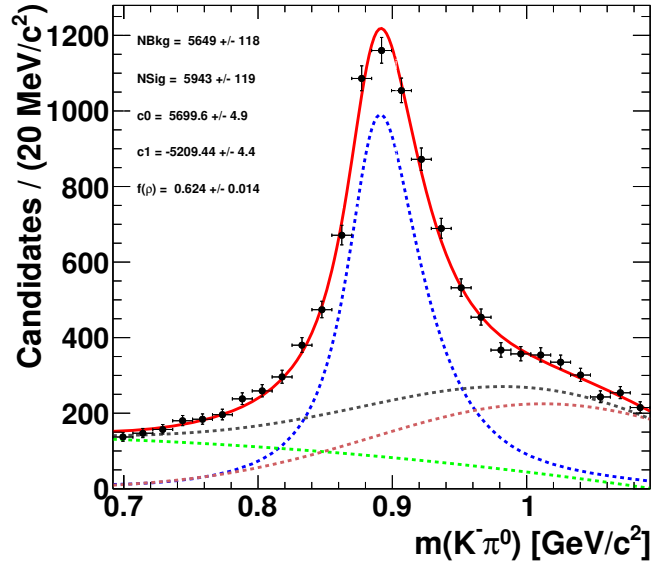


(b)

Figure 5.24: Fit to the invariant mass distribution of $K^{*-} \to K^- \pi^0$ candidates of $B^- \to DK^{*-}$, where $D^0 \to K^- \pi^+$ (RS) for MC (a) and DATA Run 1 and Run 2 (b). The fit parameters are listed on the plots. Bottom: green dashed curve represents the combinatorial background, brown dashed curve is the contribution from $B \to D\rho^-$ decay. The blue dashed line is for the signal and the total PDF is given with the red line.
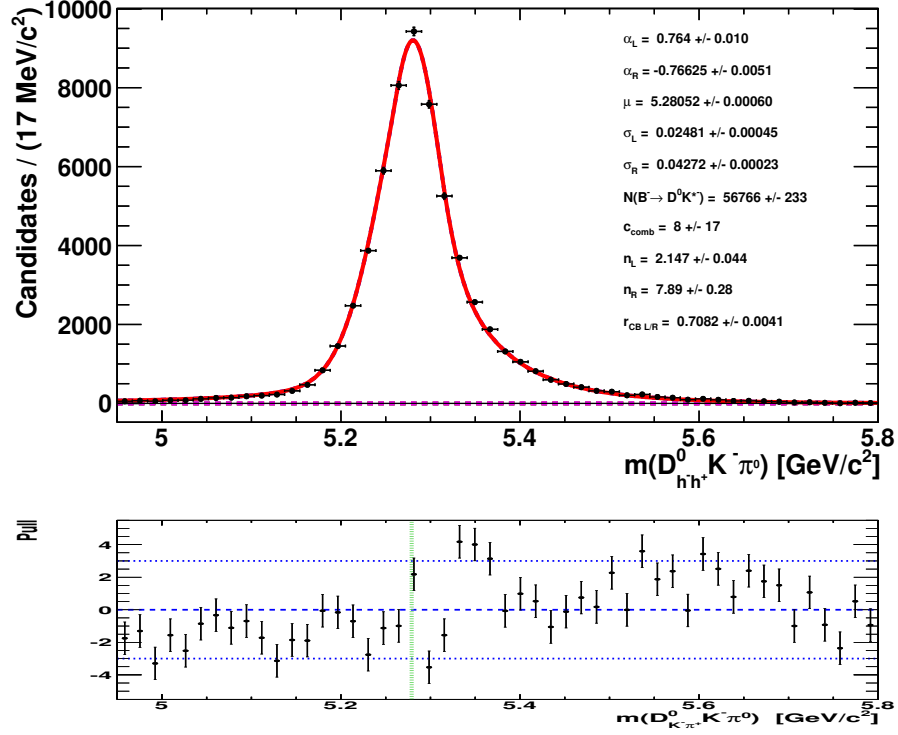
Figure 5.25: Fit to the invariant mass distribution of $B^- \to DK^{*-}$ $(K^-\pi^0)$ for MC signal Run 1 and Run 2. The fit parameters are listed on the plot.

### 5.5.3 Effect of sWeight subtraction of non $K^*$ background

In this part, in order to polish off the background contaminations from signal, the sPlot method which provides statistical subtraction is studied. Here we describe as much as possible pedagogical effect of subtracting non-$K^*$ background with sWeight method. After all the selections, Figure 5.24b shows that there are backgrounds which lies below the signal peak of $K^*$ and with the sPlot method we have a reduction of the both combinatorial background given with green curve modelled by polynomial PDF and the abundant signal $B^- \to D^*\rho$ displayed in brown dashed curve. Therewith, the non-$K^{*-}$ backgrounds are subtracted from the $K^{*-}$ by using sPlot weights obtained from a fit to the $K^{*-}$. Here in the Figure 5.26 we have usual sPlot subtraction for the fitted $K^{*-}$ where Figure 5.26a shows the raw invariant mass distribution of $B$ and the Figure 5.26b is for the $B$ mass background where we can see the non-$K^{*-}$ peaking background contributions from $B \to D^{(*)0}\rho^-$ decay are really obvious. And here there is non-resonant $DK\pi^0$ decay which is so-called S-wave structure in the $K^{*-}$ fit treated as a combinatorial background in the sideband of $K^{*-}$. This decay is not measured before and not included in the PDG. And the combinatorial background is given with the blue dashed curve. When these two plots are subtracted from each, we obtain this Figure 5.26c which shows the final subtracted invariant mass distribution of $B$ candidates with the combinatorial background $(+K\pi$ S-wave) and the $D^{(*)0}\rho^-$ contamination is almost fully removed in the $K^{*-}$ and

thus the fit is more simplified and there are mainly the signal $B^- \to DK^{*-}$. And the $B^- \to D^*K^{*-}$ partially reconstructed decays in the lower mass and they are as expected and unfortunately survive the non-$K^*$ sWeight subtraction and therefore we have to fit to them and especially to account for contributions sneaking into the $B$ mass signal region $5.28\pm \text{GeV}/c^2$. Here we also check the $K^*$ upper-sideband in $[1.1,\ 1.4]\,\text{GeV}/c^2$ to justify the model of the non-resonant $K\pi^0$ component in a reverse approach: we fit the $B$ mass and watch back the sWeight subtracted $\text{m}(K\pi^0)$ mass spectrum shown in Figure 5.27. One should also include possible $B \to DK\pi^0$ non-resonant background that may bias the CP content as the $K\pi^0$ could be S-wave component under the $K^*$ P-wave. For this background, the use of helicity angles already impact the contribution (see Table 5.5 and 5.11), while our fit strategy also reduces its contribution. This can be possibly studied and measured the branching fraction of non-resonant $K\pi^0$ S-wave $B \to DK\pi^0$ (i.e. above the $K^*(892)$ and below the $K^*(1410)$).
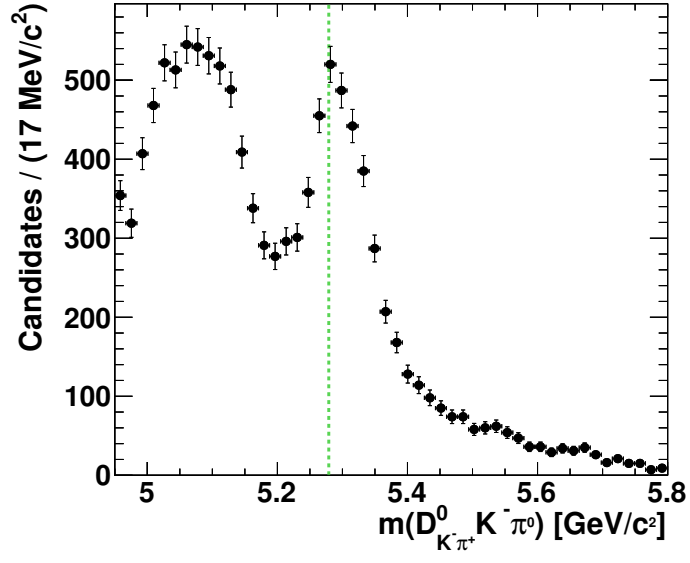
(a)
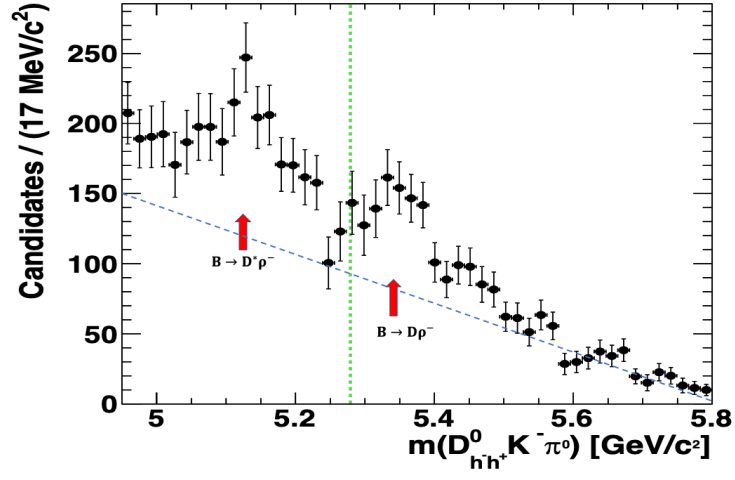


(b)
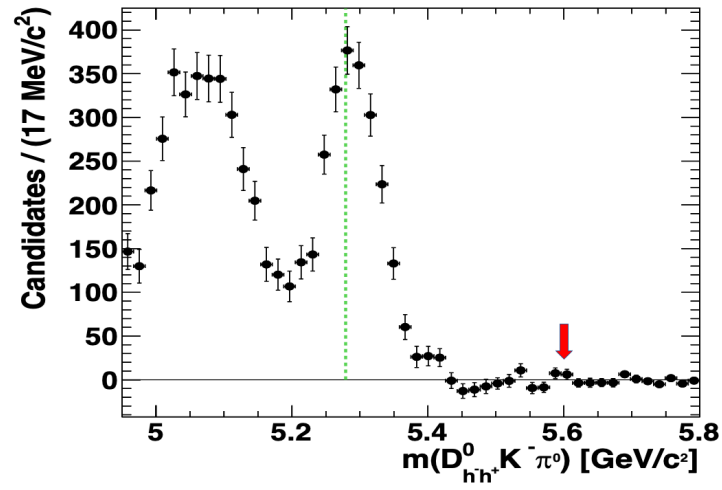
Figure 5.26: sWeight subtraction of two-body modes of $B^- \to DK^{*-}$, where $(K^-\pi^0)$ for MC Run 1 and Run 2.
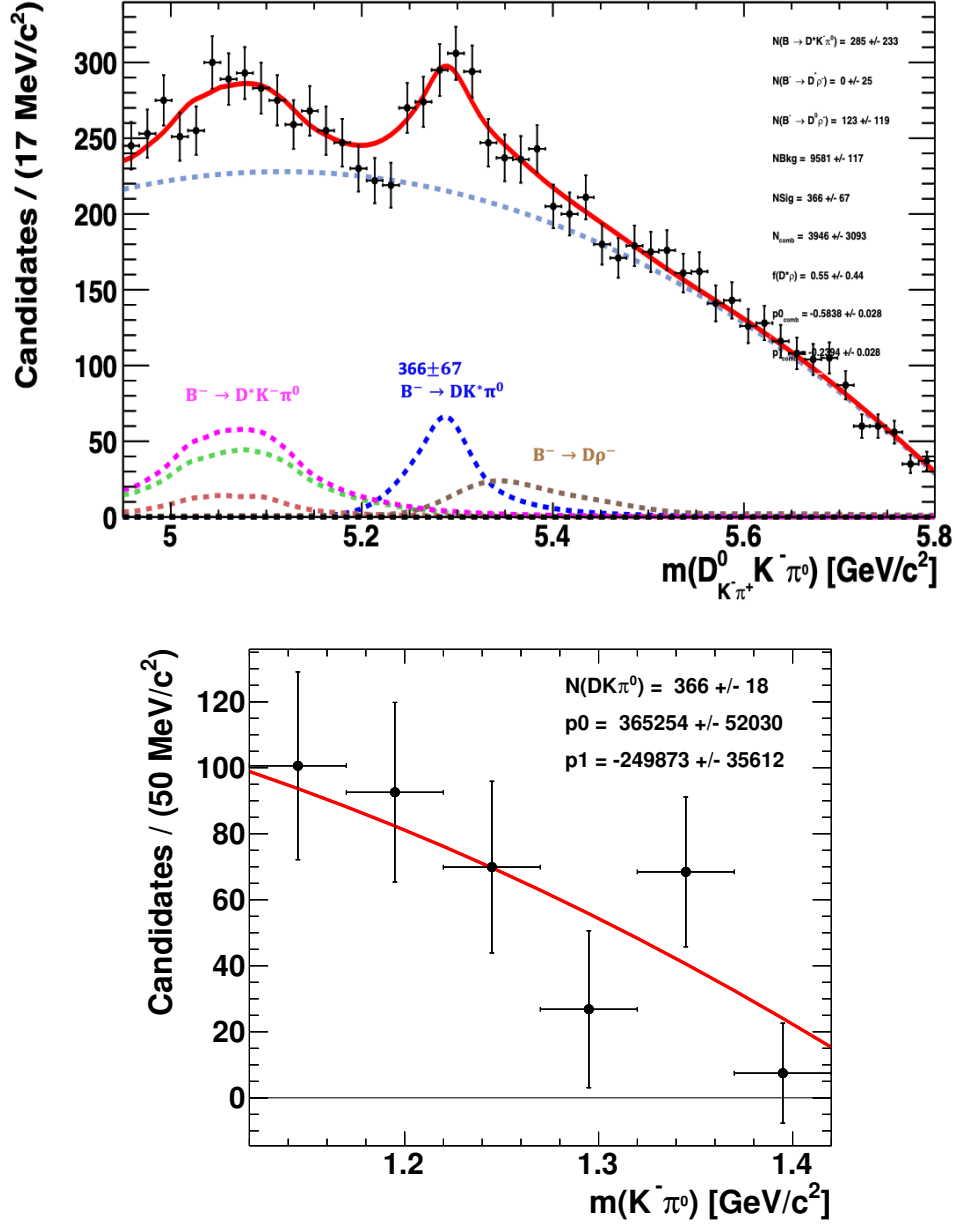
Figure 5.27: Fit to the $B$ mass to check the sWeight subtracted m($K\pi^0$) spectrum. The $K^*$ upper-sideband is in $[1.1, 1.4]\,\mathrm{GeV}/c^2$ to justify the non-resonant $K\pi^0$.

After the sPlot subtraction, an unbinned extended maximum likelihood fit to the invariant mass of $B^- \to DK^{*-}$ ($K^-\pi^0$), where $D^0$ decays to $D^0 \to K^-\pi^+$ is performed for Data Run 1 and Run 2 displayed in Figure 5.28. According to the Figure 5.25 some parameters are readjusted to accommodate the data and some parameters are frozen: mean of the signal distribution $\mu = 5.286\,\mathrm{GeV}/c^2$ and the two $\sigma$ of the Crystal-Ball functions (CBs) to $26.11\,\mathrm{MeV}/c^2$, $36.83\,\mathrm{MeV}/c^2$ and the fraction of two of them is given 69.5%. All the

other parameters of the two Crystal Ball functions (left and right) for the signal are frozen to their values as obtained from a fit to MC and as listed in Figure 5.25. In Figure 5.28, one can see that we obtain $2168\pm51$ $B \rightarrow D(K^-\pi^+)K^{*-}(K^-\pi^0)$ signal candidates and $3775 \pm 65$ partially reconstructed $B^- \rightarrow D^*K^{*-}(K^-\pi^0)$ background candidates. While, in the nominal fit a possible contribution from combinatorial residual background is compatible with zero, as well as that for a possible residual $B^- \rightarrow D^0(K^-\pi^+)\rho^-(\pi^-\pi^0)$ background.
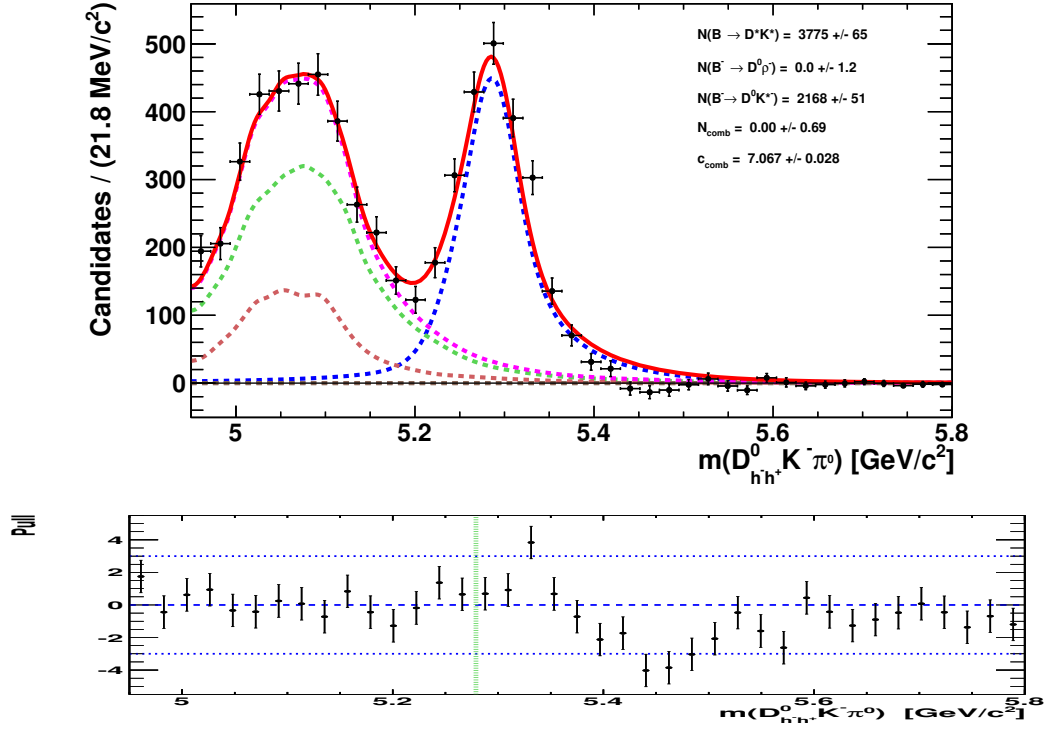


Figure 5.28: Fit to the invariant mass distribution of $B^- \rightarrow D^0K^{*-}$ $(K^-\pi^0)$, where $D^0$ decays to $D^0 \rightarrow K^-\pi^+$ (RS) for DATA Run 1 and Run 2 after sWeight subtraction. Signal shown in blue dashed curve and Data shown in black dots, partially reconstructed background shown $B \rightarrow D^*K^*$ in green dashed curve, the peaking background $B^- \rightarrow D^0\rho^-$ is indicated with brown dashed curve and the overall fit is represented by the solid red line. The distribution of the pull shown beneath the fit distribution and represent the good agreement between the data and the fit functions.

In order to estimate the possible contributions from the charmless (non-$D$)($K^-\pi^+$) background, a fit is performed with the same PDF functions and same selections as for Figures 5.24b and 5.28, but where the invariant mass of the $K\pi$ pair is non compatible with $D$ meson. The m($K\pi$) mass should be $> 40$ MeV/$c^2$ away ($+5\sigma$) from the $D$ PDG mass and $< 86$ MeV/$c^2$ ($+11\sigma$). The chosen $D$ sidebands (on the lower and upper side of the $D$ signal box) size is twice as large as the signal $D$ box ($\pm23$ MeV/$c^2$). Therefore, a fit to the $K^{*-} \to K^-\pi^0$ is performed for candidates lying above the defined $D$ sidebands, sWeights are computed and in cascade a fit to the corresponding $B^- \to D(K^-\pi^+)K^{*-}$ invariant masses of the candidate is also performed. Figures 5.29a and 5.29b display the result of these fit for the $K^{*-} \to K^-\pi^0$ signal and for the $B$ mass after sWeight subtraction of non-$K^*$ candidates respectively. One can see that a peaking background from $K^-\pi^+K^{*-}$ signal at the nominal $B$ mass compatible with $28.7 \pm 6.7$ $B^- \to K^-\pi^+K^{*-}$ charmless events. Accounting for the double size of the $D$-sidebands ($\times2$ the sigBox size), one can conclude that within the 2168$\pm$51 signal candidates, one should subtract $(28.7/2 \pm 6.7/\sqrt{(2)}) = 14.4 \pm 4.7$ corresponding irreducible peaking background at that stage. This corresponds to 0.7% of the signal and therefore very small.

(a)



(b)
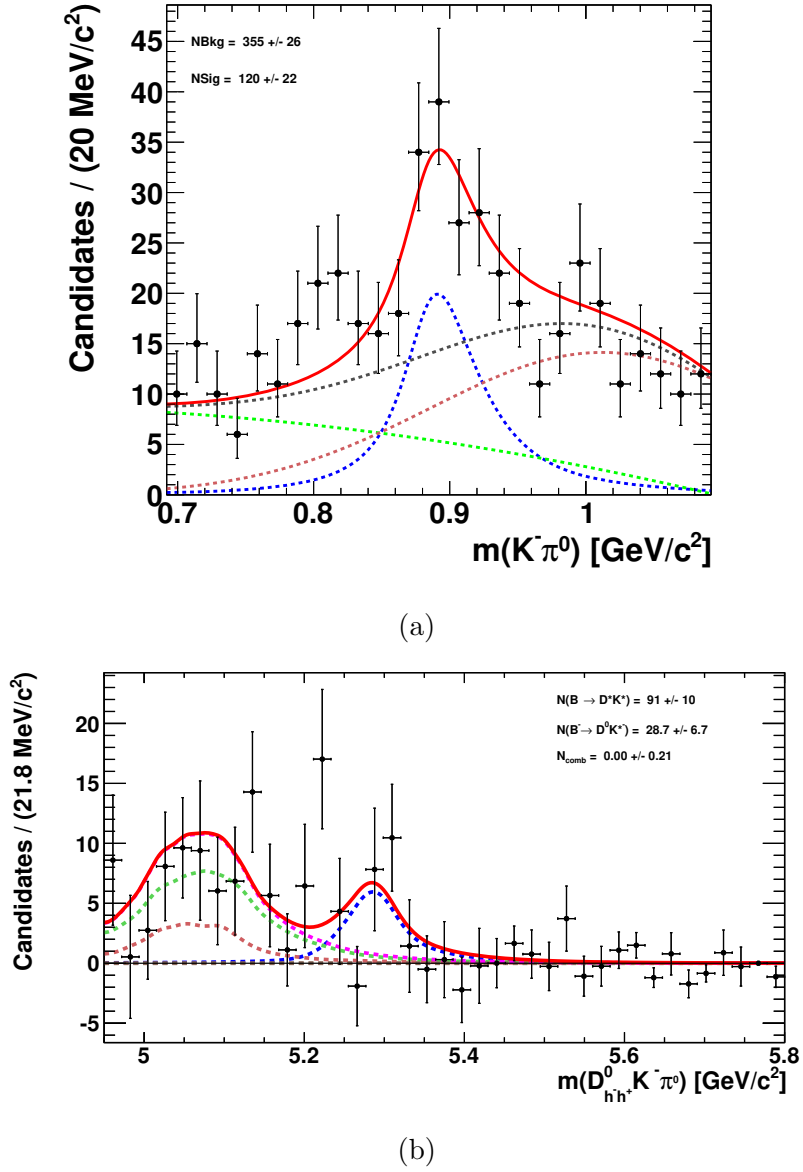
Figure 5.29: Fit to the invariant mass of the $K^{*-}$ ($K^-\pi^0$) and the $B^- \rightarrow DK^{*-}$ ($K^-\pi^0$) where $D^0$ decays to two body RS mode $D^0 \rightarrow K^-\pi^+$ for Data Run 1 and Run 2 in $D$-sideband charmless background. Fit components are as described in the legend.

In Figure 5.30, for candidates in the $D$ signal box, we display the fits to the $K^{*-}$ for $B^-$ 5.30a and for $B^+$ 5.30a, the PDF and the fit parameters except the normalisation of components are fixed to that of the reference nominal fit displayed in Figure 5.25. Then Figures 5.31a and 5.31b show the fit to the $B$ candidates originated from the sWeight signal part of the population extracted from the fits presented in Figures 5.30, for $B^-$ and $B^+$ candidates, respectively. One can see that a slight excess of $B^+$ that needs to be corrected for various effects:

1. Subtraction of the charmless background as estimated from the $D$ sidebands

2. Accounting for the $B^{\pm}$ production asymmetries in the pp LHC collisions and detection asymmetries, while reconstructing the $K^-$ and $K^+$, and $\pi^-$ or $\pi^+$ [155].
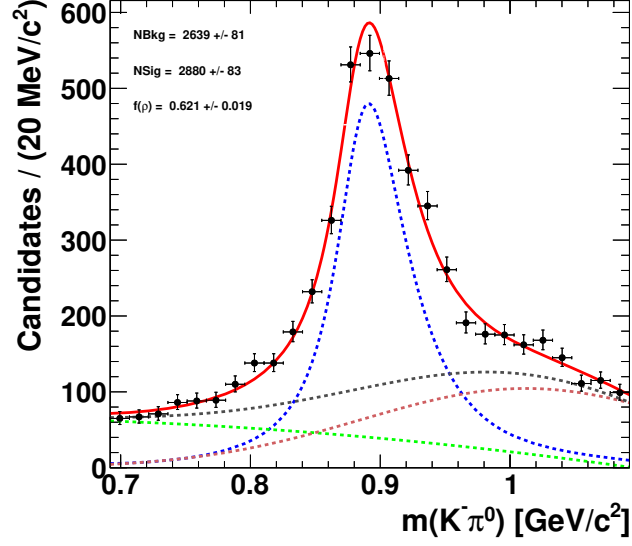


(a)
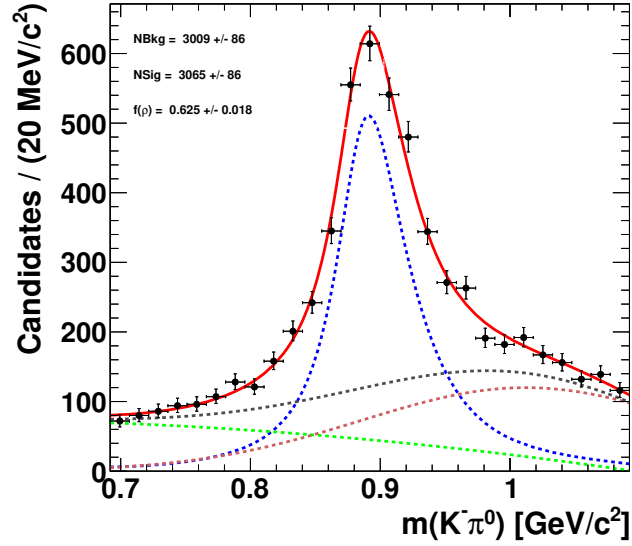


(b)

Figure 5.30: Fit to the invariant mass distribution of $K^{*-} \to K^- \pi^0$ for $B^- \to D^0 K^{*-}$ and $B^+ \to D^0 K^{*+}$ candidates. And $D^0$ decays to $D^0 \to K^- \pi^+$.
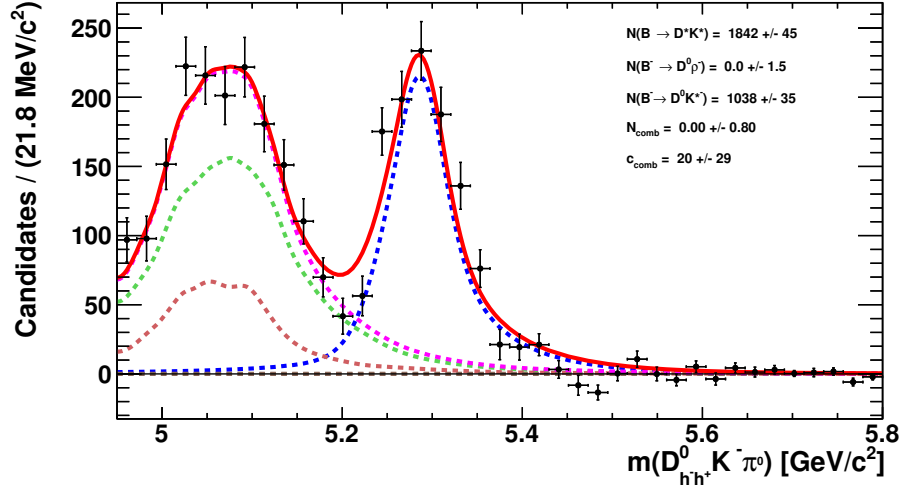
(a)
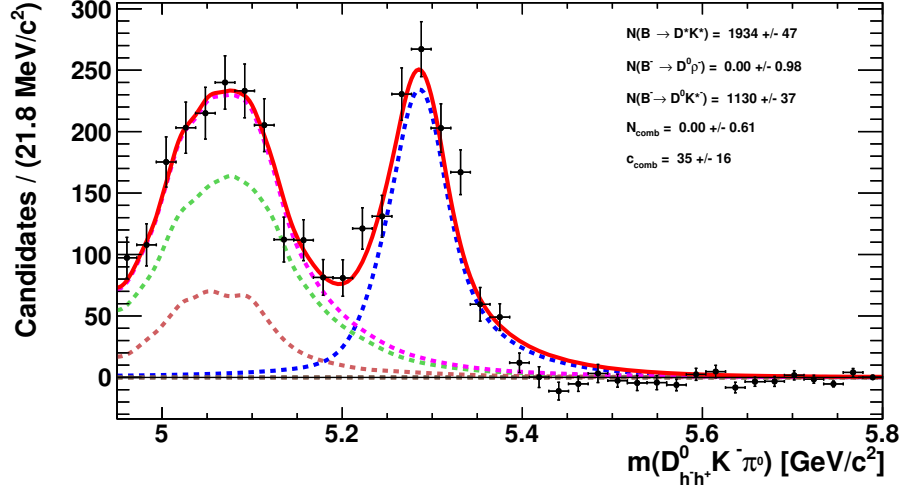


(b)

Figure 5.31: Fit to the invariant mass distribution $B^- \to D^0 K^{*-}$ and $B^+ \to D^0 K^{*+}$ candidates, where $D^0$ decays to $D^0 \to K^- \pi^+$. Blue dashed line represents the signal for $B^-$ (top) and $B^+$ (bottom). Green dashed line is for the partially reconstructed background decay $B^- \to D^* K^{*-}$ and the brown dashed curve is for the background contribution from the $B^- \to D^0 \rho$ decay. Combinatorial background is almost fully removed. Number of events for $B^-$ is $NB^-_{sig} = 1038 \pm 35$ and for $B^+$ is $NB^+_{sig} = 1130 \pm 37$.

Figures 5.32a and 5.32b show the fit to the possible contribution of $B$ charmless $K^- \pi^+ K^{*-}$ background for $B^-$ and $B^+$, respectively after having followed the same procedure as for the result displayed in Figure 5.29b. The sum of the two $B^-$ and $B^+$ components, $13.7 \pm 4.7$ and $15.0 \pm 4.9$ is clearly compatible with the fit is shown in Figure 5.29b.
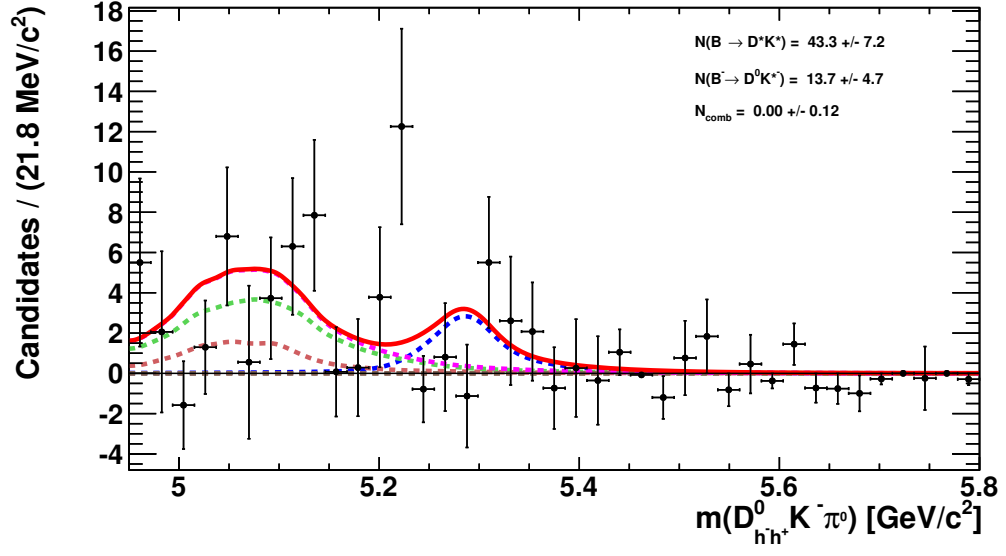
(a)
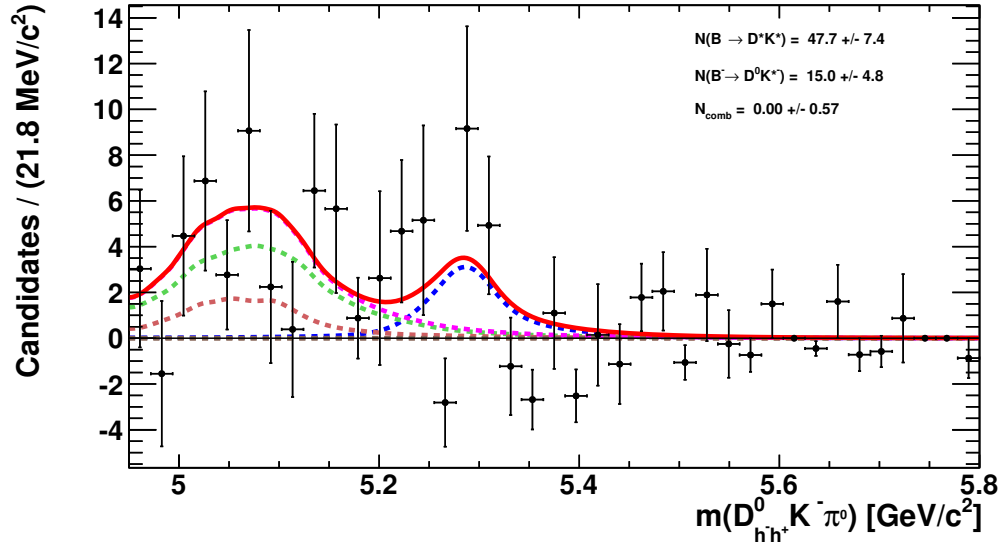


(b)

Figure 5.32: Fit to the possible $B$ charmless background $K^-\pi^+K^{*\mp}$ for $B^-$ and $B^+$ candidates in $D$ sideband.

To conclude, the numbers of $B^-$ and $B^+$ signal decaying to the mode $D^0(K^-\pi^+)K^{*\mp}(K^-\pi^0)$, and conjugate, before and after correction of the contributions from $B$ charmless backgrounds are:

$$NB_{sig}^- = 1038 \pm 35 \; \& \; NB_{peak}^- = 7 \pm 3 \rightarrow NB_{sig}^- = 1031 \pm 35 \tag{5.6}$$

$$NB^+_{sig} = 1130 \pm 37 \ \& \ NB^+_{peak} = 8 \pm 3 \rightarrow NB^+_{sig} = 1122 \pm 37 \tag{5.7}$$

where the statistical uncertainties are the quadratic sum of the individual statistical uncertainties of the fits in the $D$ signal box and the sidebands of the $D$ (double size, i.e. divided by two) and their central value differences.

In order to validate the uncertainties as obtained from the fit displayed in Figures 5.24b and 5.28, a crosscheck with a toy study is performed, where 4000 pseudo Monte Carlo experiments were generated with the given number of signal and background, where the various fitted background and signal components of the fits of Figures 5.24b and 5.28 were left free to vary within their Gaussian uncertainties. Based on those 4000 pseudo Monte Carlo experiments, the fit procedure is repeated for each of the generated samples ($K^{*-}$ and after sWeighted signal sample projection to the $B$ mass, the fit to the $B$ candidates.) Figure 5.33 shows the pull distributions for the fit results to the 4000 generated samples by pseudo-experiment generated values. One can clearly see that the mean value of the number of fitted $K^*$ is relatively unbiased, while from the residual cascade fit to the number of $B^- \rightarrow DK^{*-}$ signal, the ratio ($\mathrm{N}_{fitted}$ - $\mathrm{N}_{gen}$)/$\mathrm{N}_{gen}$ is equal to 1.12%, which correspond to about 1.12% of 2168, so an underestimation of about 25 events, while the statistical uncertainty of the $B$ mass fit displayed in Figure 5.28 is obtained as 51. This is not really reason for us to worry about, but the bias should be corrected and assign a $1/\sqrt{(12)}\times$bias as a systematic uncertainty. After the bias correction, in the bottom of Figure 5.33, one can see the resulting pull distribution for the fitted number of $\mathrm{N}(B^- \rightarrow DK^{*-})$ signals. The central value of the pull is centered at zero (as expected after the bias correction) and the $\sigma$ of the pull is larger than one and equal to $\sigma = 1.34$, which means statistical uncertainty as obtained in the fit displayed in Figure 5.28 is underestimated (under-coverage by the same factor).

| $\chi^2$ / ndf | 44.38 / 47 |
| --- | --- |
| Constant | 160.4 ± 3.7 |
| Mean | 0.2094 ± 0.0189 |
| Sigma | 1.012 ± 0.014 |

**NKstar_Pull**

| $\chi^2$ / ndf | 39.96 / 47 |
| --- | --- |
| Constant | 210.5 ± 4.8 |
| Mean | -0.01122 ± 0.00057 |
| Sigma | 0.03082 ± 0.00041 |

**NBtoDKstar_Resid**

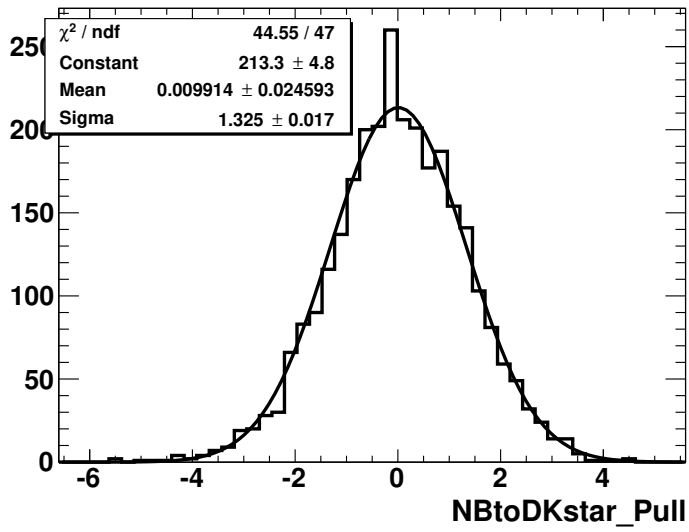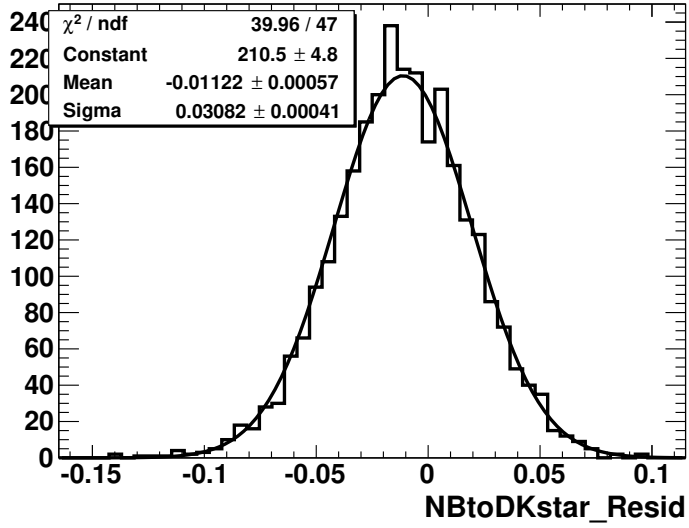| $\chi^2$ / ndf | 44.55 / 47 |
| --- | --- |
| Constant | 213.3 ± 4.8 |
| Mean | 0.009914 ± 0.024593 |
| Sigma | 1.325 ± 0.017 |

**NBtoDKstar_Pull**
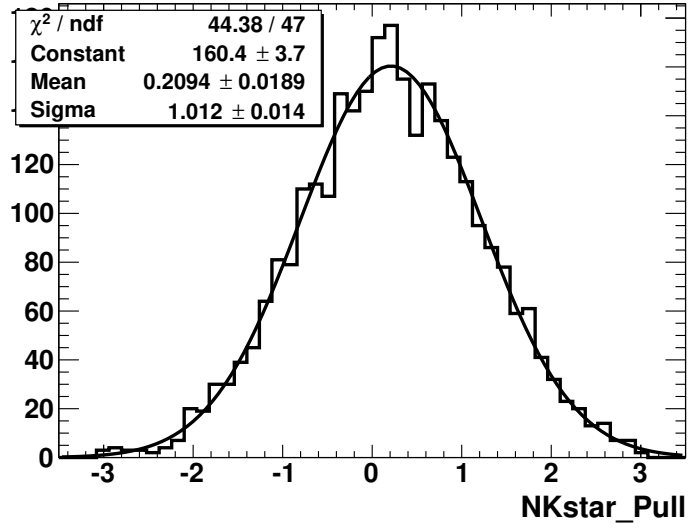
Figure 5.33: Pull distributions for $K^*$ (top) $B^- \to D^0 K^{*-}$ (middle) and $B^- \to D^0 K^{*-}$ (bottom) candidates, where $D^0$ decays to $D^0 \to K^- \pi^+$ (RS) using 4000 generated pseudo-experiments.

Finally, the numbers of $B^-$ and $B^+$ candidates listed in Eq. 5.6 and 5.7 have to be corrected after this study accounting for the fit bias and the under-estimation of their statistical uncertainties.

$$NB^-_{sig} = 1042 \pm 47 \pm 3 \tag{5.8}$$

$$NB^+_{sig} = 1134 \pm 50 \pm 3 \tag{5.9}$$

In the following sections same process will be performed and repeated for all the decay modes of interest: $K^+\pi^-$ (WS), $K^-K^+$ and $\pi^-\pi^+$.

## 5.5.4 Fit to the invariant mass of $K^* \rightarrow K^-\pi^0$ and $B^- \rightarrow D^0[K^+\pi^-]K^{*-}$ ADS like signal (WS)

The same procedure described for the $D^0[K^-\pi^+]$ (RS) is performed for the $D^0[K^+\pi^-]$ (WS) decay. Selections are defined for $B^- \rightarrow D^0[K^+\pi^-]K^{*-}$ (WS)

- $Signif[\Delta z(DB)]_{D^0} > 1$

- $m_D \in [1.8421, 1.8883]\, \mathrm{GeV}/c^2$ ($\pm\, 3\sigma$)

- $DLL\_K > 8$ for the charged $K^*$ daughter

- $DLL\_K > 4$ for the $D$ daughter if kaon

- $DLL\_K < -4$ for the $D$ daughter if pion

Figure 5.34 shows the fit to the invariant mass of $K^*$ before the sPlot technique is implemented ( Sweight subtraction has been explained in detail in Section 5.5.3). Additionally we perform a veto to the viable background events from $D$ candidates $K\pi$ RS signal for which the mass of the $\pi$ and the kaon are swapped. This study has been discussed particularly in Section 5.3.7. After the background (non-$K^*$) flows below the signal peak reduced by using the sWeights from the fit to the $K^*$ mass, and performing the veto to the $K\pi$ (RS) signal which could mimic $K\pi$ (WS), we obtain Figure 5.35 which displays the unbinned maximum likelihood fit to the invariant mass of the $B$ candidates for Data Run 1 and Run 2.

NBkg = 1028 +/- 43

NSig = 134 +/- 30

c0 = 4274 +/- 2224

c1 = 3342 +/- 1743
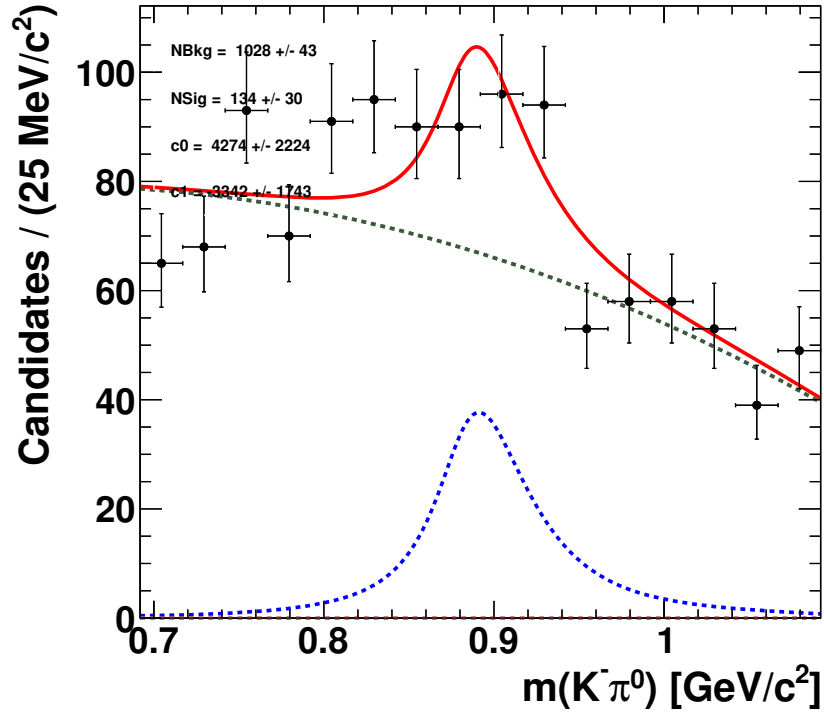
(a)
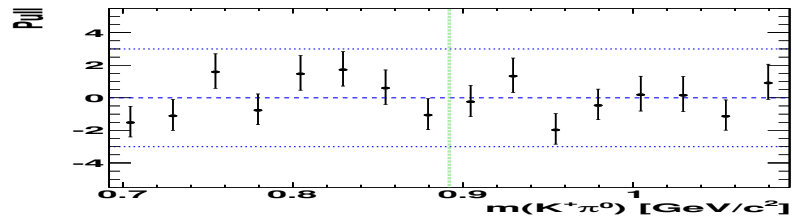
(b)

Figure 5.34: (a)Fit to the $K^{*-} \to K^- \pi^0$ invariant mass for Data Run 1 and Run 2. Blue dashed line represents the signal, green dashed line is for the background and overall fit is given with the red straight line. Corresponding pull plot for the fit to the $K^{*-} \to K^- \pi^0$.
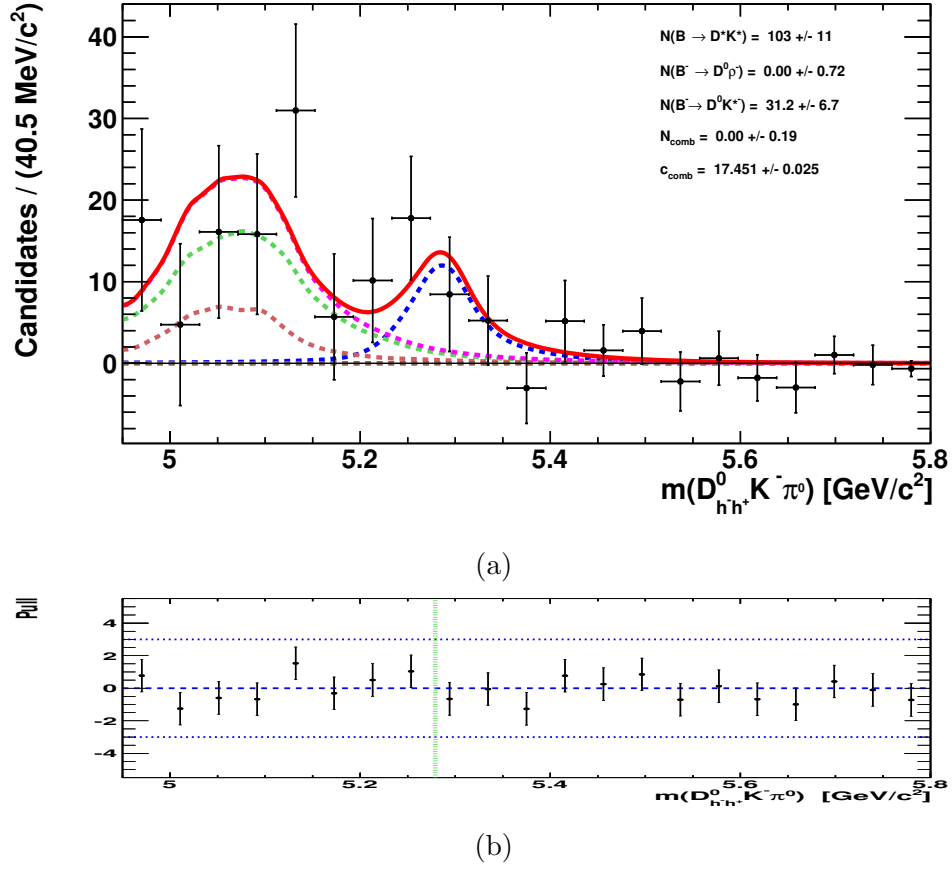
Figure 5.35: (a)Fit to the $B^- \to DK^{*-}$ invariant mass for DATA Run 1 and Run 2 to obtain the yields. Blue dashed line represents the signal, green dashed line is for the partially reconstructed background $B \to D^*K^*$ and the brown dashed curve is for the $B^- \to D^0\rho^-$ background. The overall PDF is given with the red straight line. The number of signal and the background events are given on the plot. Corresponding pull plot for the fit to the $B^- \to DK^{*-}$.

The study is also performed in the sidebands of the $D$ meson candidates (which size twice larger than the signal box $\pm 23\,\mathrm{MeV}/c^2$) decays to $K\pi$ (WS) to eliminate the possible charmless background contributions peaking in the signal region. As mentioned for the $K\pi$(RS), we apply the same PDF functions and the same selections as we did for Figures 5.34 and 5.35. The mass of the $K\pi$ is chosen to be $>40\,\mathrm{MeV}/c^2$ ($5\sigma$) and $<86\,\mathrm{MeV}/c^2$ ($11\sigma$) away from the $D$ mass (PDG). A fit performed to the mass of the $K^*$ shown in Figure 5.36 to compute the sWeights for the backgrounds below the signal peak and after subtraction, we perform the fit to the invariant mass of $B$ candidates displayed in Figure 5.37. An here it can be seen that peaking background from $K^+\pi^- K^*$ in the nominal $B$ mass region is obtained as $2.3\pm2.8$. Taking into account the size of the sideband, with respect to the number of signal which is $31.2\pm6.7$, from this we should subtract the $(2.3/2\pm2.8/\sqrt{(2)}) = 1.2 \pm 1.9$ final peaking background and correspond to 3.9% of the

signal. Here we see the ADS signal on the invariant mass fit at 4.5 $\sigma$.
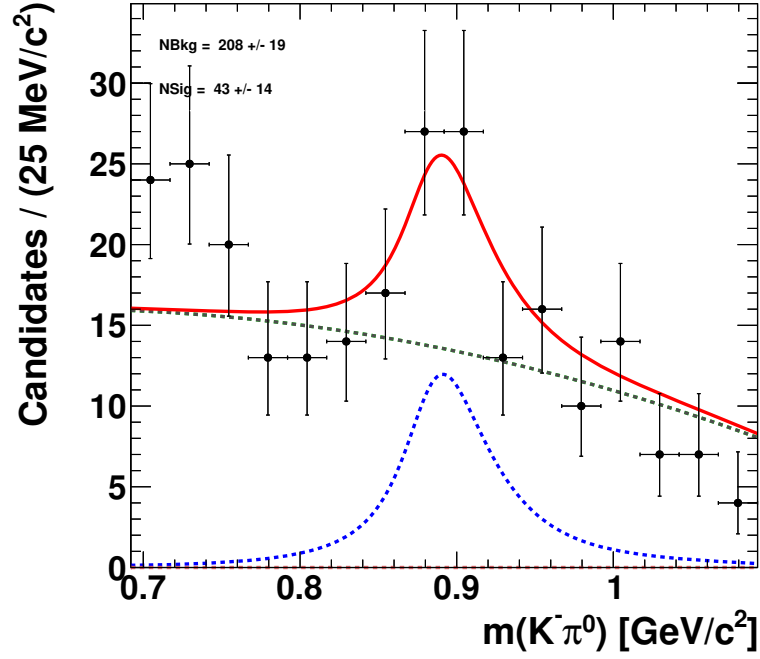


Figure 5.36: Fit to the invariant mass of $K^{*-} \to K^-\pi^0$ for DATA Run 1 and Run 2 in the sideband of the $D$.
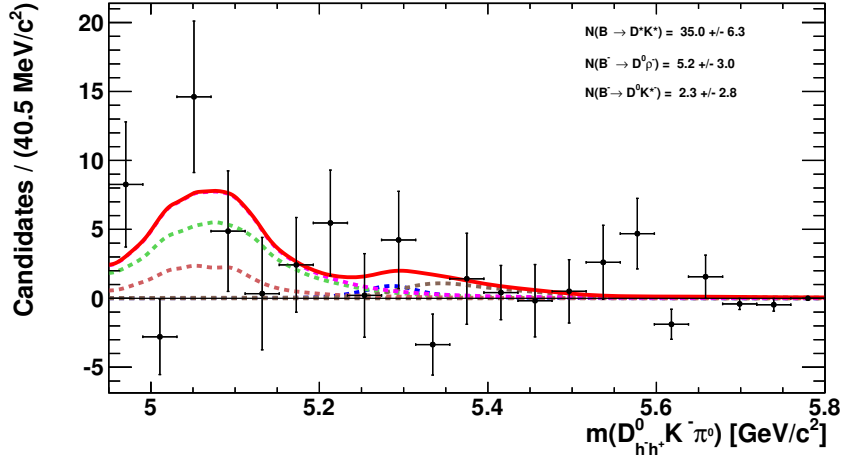


Figure 5.37: Fit to the invariant mass distribution to the $B^- \to DK^{*-}$ $(K^-\pi^0)$ where $D^0$ decays $D^0 \to K^+\pi^-$ for DATA Run 1 and Run 2 in the sideband of the $D$.

Figures 5.38 displays the invariant mass fit to the $K^{*-} \to K^-\pi^0$ for the $B^-$ and $B^+$ candidates which can be obtained $NB^-_{sig} = 49\pm21$ for $B^-$ and $NB^+_{sig} = 85\pm22$ for $B^+$.

NBkg = 512 +/- 30

NSig = 49 +/- 21

(a)



NBkg = 516 +/- 30

NSig = 85 +/- 22
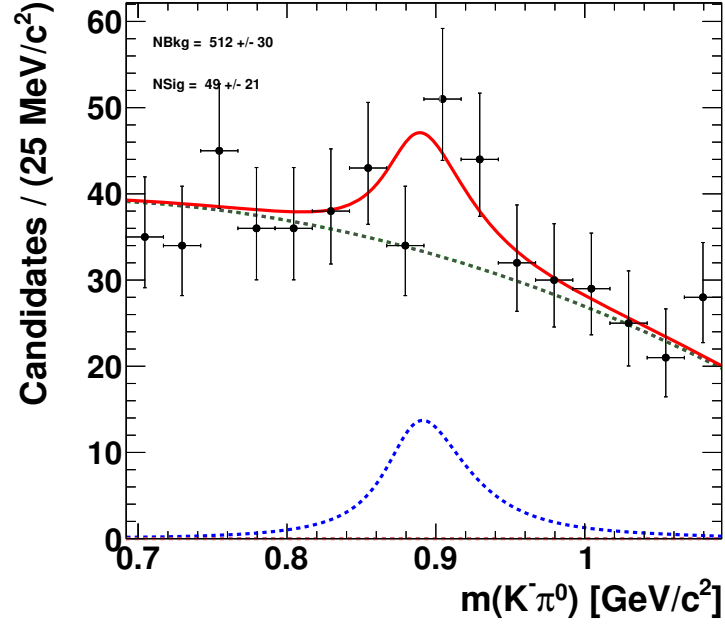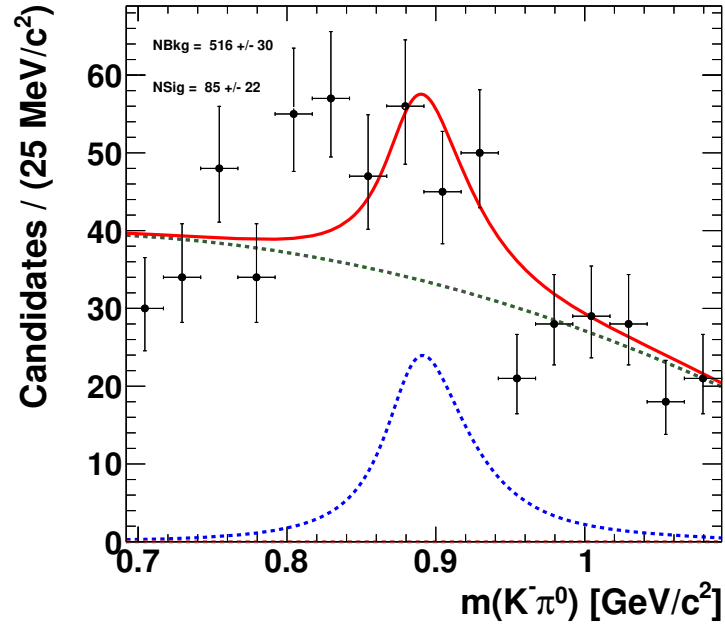
(b)

Figure 5.38: Fit to the invariant mass of $K^{*-} \to K^- \pi^0$ for $B^-$ and $B^+$ candidates.

The invariant mass fit of $B^- \to D^0 K^{*-}$ and $B^+ \to D^0 K^{*+}$, where $D^0$ decays $K^+ \pi^-$ is shown in Figures 5.39a and 5.39b, respectively. It can be seen that there is a very large

asymmetry observed (almost 100%) for $B^-$ ( 0 events fitted) and for $B^+$ (31.4±6.3 events fitted).
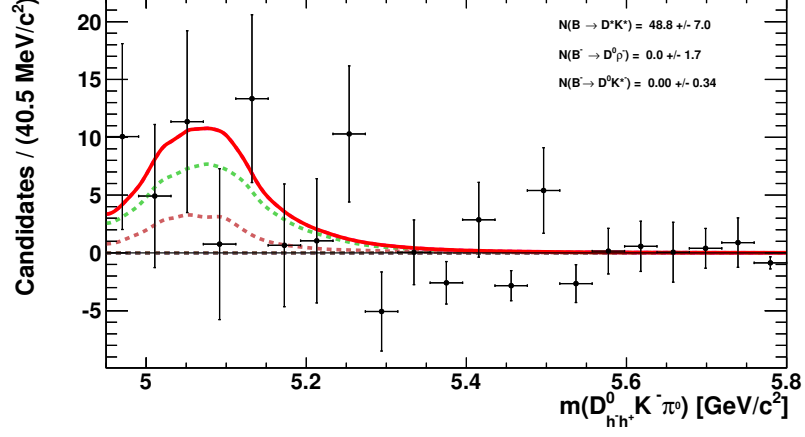


(a)
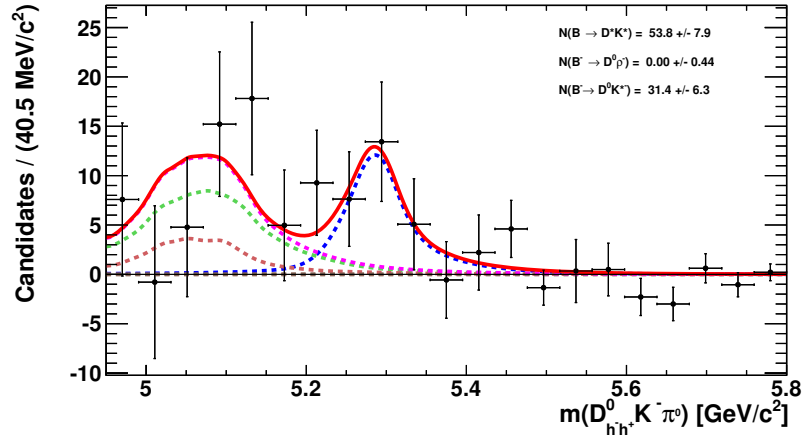


(b)

Figure 5.39: Fit to the invariant mass distribution $B^- \to D^0 K^{*-}$ and $B^+ \to D^0 K^{*+}$ candidates, where $D^0$ decays to $D^0 \to K^+ \pi^-$. Blue dashed line represents the signal for $B^-$ (top) and $B^+$ (bottom). Green dashed line is for the partially reconstructed background decay $B^- \to D^* K^{*-}$ and the brown dashed curve is for the background contribution from the $B^- \to D^0 \rho$ decay which can be seen almost fully removed. Number of events for $B^-$ is $NB^-_{sig} = 0.00 \pm 0.34$ and for $B^+$ is $NB^+_{sig} = 31.4 \pm 6.3$.

We also show the fit to the $B$ charmless $K^+ \pi^- K^{*-}$ background for $B^-$ and $B^+$ candidates in the sideband of the $D$ in Figure 5.40a and 5.40b.
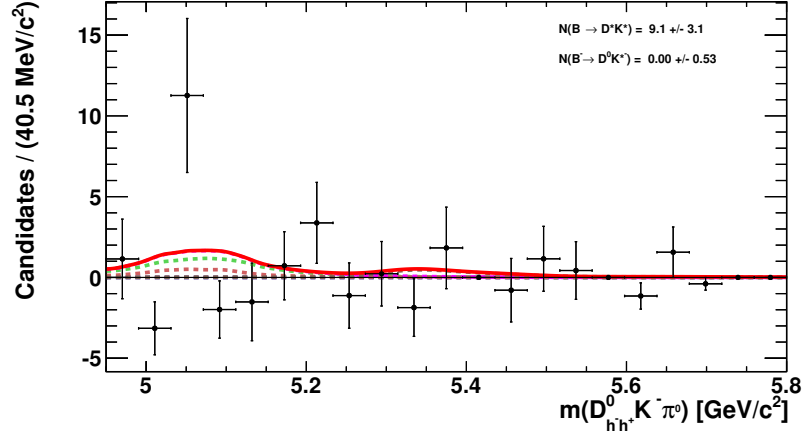
(a)
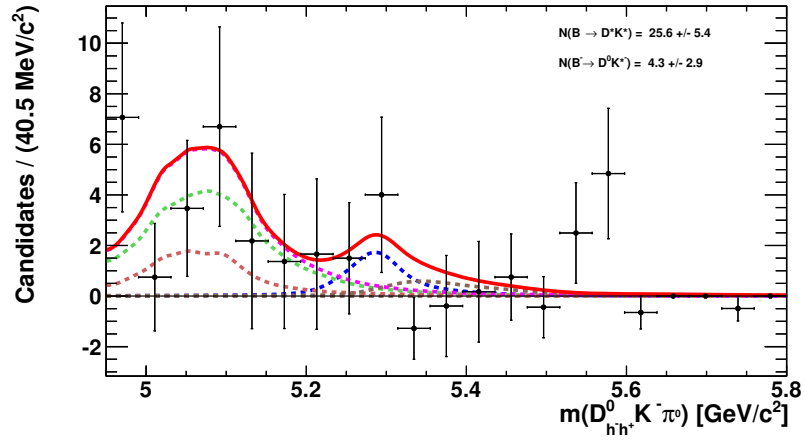


(b)

Figure 5.40: Fit to the possible $B$ charmless background $K^+\pi^- K^{*\mp}$ for $B^-$ and $B^+$ candidates in $D$ sideband.

The number of signals for $B^-$ and $B^+$ decays to $D^0 \to (K^+\pi^-)K^{*\mp}(K^-\pi^0)$ and, before and after the correction of the contributions from the charmless backgrounds are obtained as

$$NB^-_{sig} = 0.0 \pm 0.34 \ \& \ NB^-_{peak} = 0.0 \pm 0.4 \to NB^-_{sig} = 0.0 \pm 0.5 \qquad (5.10)$$

$$NB^+_{sig} = 31.4 \pm 6.3 \ \& \ NB^+_{peak} = 2.2 \pm 2.1 \to NB^+_{sig} = 29.2 \pm 6.6 \qquad (5.11)$$

The correction proceeds in the same way as explained earlier with $K\pi$ (RS), a toy study is performed and Figure 5.41 gives the distributions for 4000 pseudo-experiments.
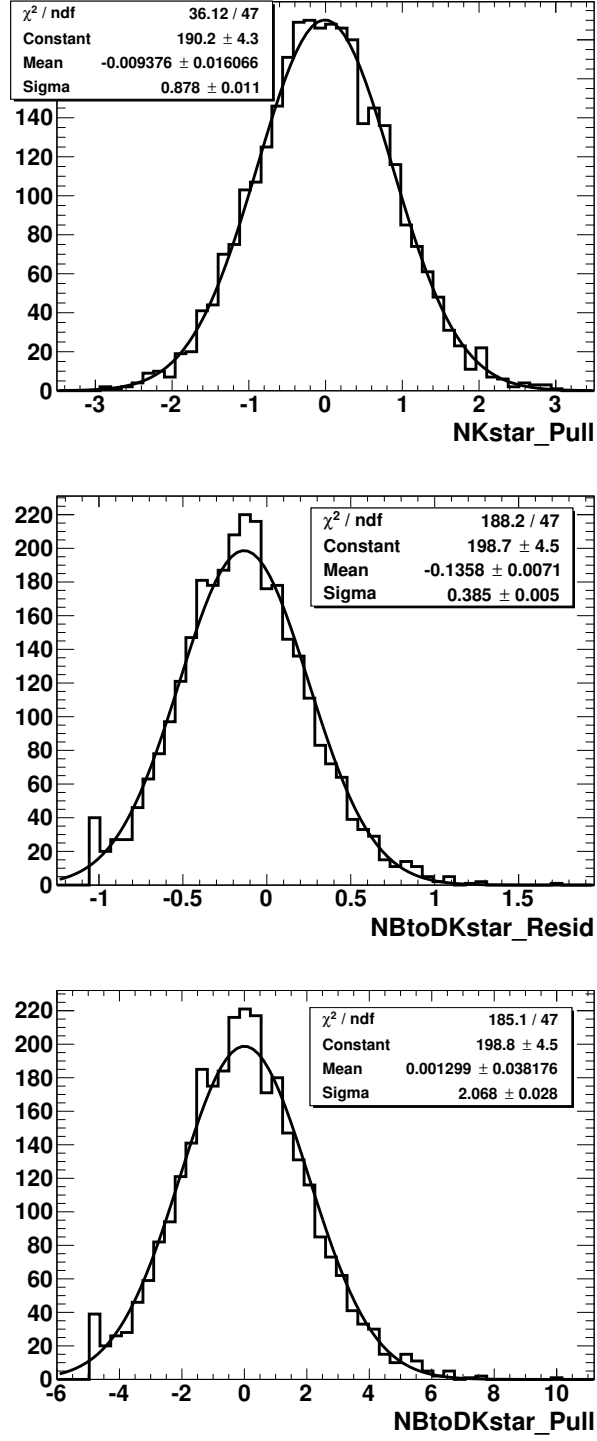
Figure 5.41: Pull distributions for $K^*$ (top) $B^- \rightarrow D^0 K^{*-}$ (middle) and $B^- \rightarrow D^0 K^{*-}$ (bottom) candidates, where $D^0$ decays to $D^0 \rightarrow K^+\pi^-$ with toy/pull study.

From the distributions it can be seen that the $K^*$ is ok, the mean value is relatively

unbiased. From the residual cascade fit to the number of $B^- \to DK^{*-}$ signal, the bias obtained with the ratio $(N_{fitted}\text{-}N_{gen})/N_{gen}$ = - 13.6% and this correspond to the 31.2 number of $B^- \to D^0 K^{*-}$ signal, underestimation of 4.2 events and the statistical uncertainty is 6.7 as shown in the Figure 5.35. After the bias correction, in the bottom distribution of Figure 5.41, the central value is centered to be at zero and the $\sigma$ is ok but it's uncertainty is 2.07 times underestimated. Eventually taking into account the bias correction and the under-estimation of the statistical uncertainties, the number of $B^-$ and $B^+$ signals are calculated:

$$NB^-_{sig} = 0.0 \pm 0.7 \pm 0.0. \tag{5.12}$$

$$NB^+_{sig} = 31.4 \pm 13.04 \pm 1.4. \tag{5.13}$$

## 5.5.5 Fit to the invariant mass of $K^* \to K^- \pi^0$ and $B \to D^0[K^- K^+]K^{*-}$

In this part, we study the GLW method which considers $B^\pm \to D^0 K^{*\pm}$, where $D^0$ decays to CP-even eigenstates $K^- K^+$ and $\pi^- \pi^+$(this will be detailed in this Section 5.5.6). Selections applied on $B^\pm \to D^0[K^- K^+]K^{*\pm}$ decay are defined.

- $Signif[\Delta z(DB)]_{D^0} > 1$

- $m_D \in [1.8421, 1.8883]\,\text{GeV}/c^2\ (\pm\ 3\sigma)$

- $DLL\_K > 4$ for the charged $K^*$ daughter

- $DLL\_K > 2$ for the daughters $(KK)$

We apply the selections on the decay of interest and perform the sWeight subtraction to remove the non-$K^*$ backgrounds from the signal $K^*$ as seen in Figure 5.42a. After sWeight subtraction, an unbinned extended maximum likelihood fit is performed to the invariant mass of $B^- \to D^0 K^{*-}$ decays, where $D^0$ decays to GLW mode $K^- K^+$ for Data Run 1 and Run 2 is shown in Figure 5.42b. Number of events for the signal and the background are given on the plots. In order to remove contamination of the charmless background a fit is performed to the $K^*$ as shown in Figure 5.43a for the candidates present in the sideband region which is the double size of the signal $D$ region $(\pm\ 23\ \text{MeV}/c^2)$ and performed sWeight subtraction. Then after the sWeight subtraction, in Figure 5.43b from the fit to the $B^- \to D^0 K^{*-}$ one can see that there is a peaking background originated from $B^- \to K^- K^+ K^{*-}$ signal in the nominal $B$ mass with the number of 39±13 $B^- \to K^- K^+ K^{*-}$ charmless events. We subtract $(39/2\pm13/\sqrt{2})$ withing the 317±21 $B$ signal candidates and 19.5±9.2 number of peaking backgrounds obtained, which correspond to the 6.2% of the signal.
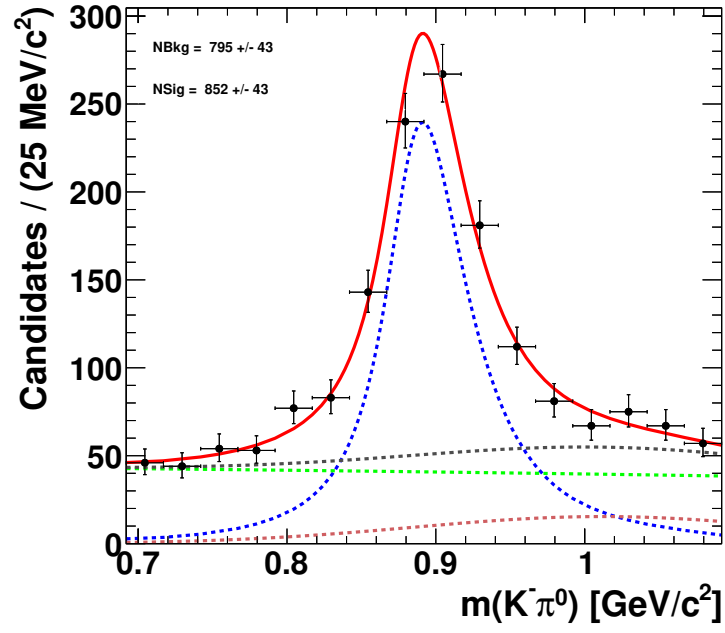
(a)
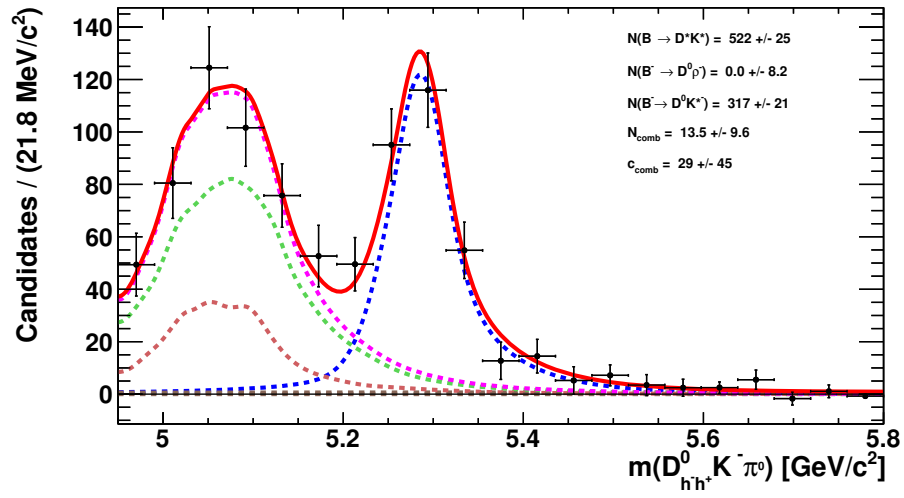


(b)

Figure 5.42: Fit to the invariant mass of $K^{*-} \rightarrow K^- \pi^0$ (top) and $B^- \rightarrow DK^{*-}$ $(K^- \pi^0)$ where $D^0$ decays to $D^0 \rightarrow K^- K^+$ for Data Run 1 and Run 2.
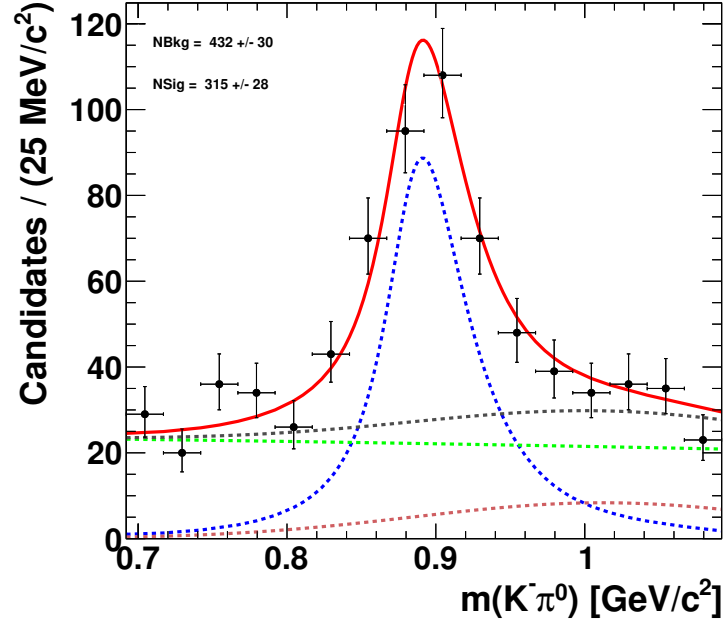
(a)
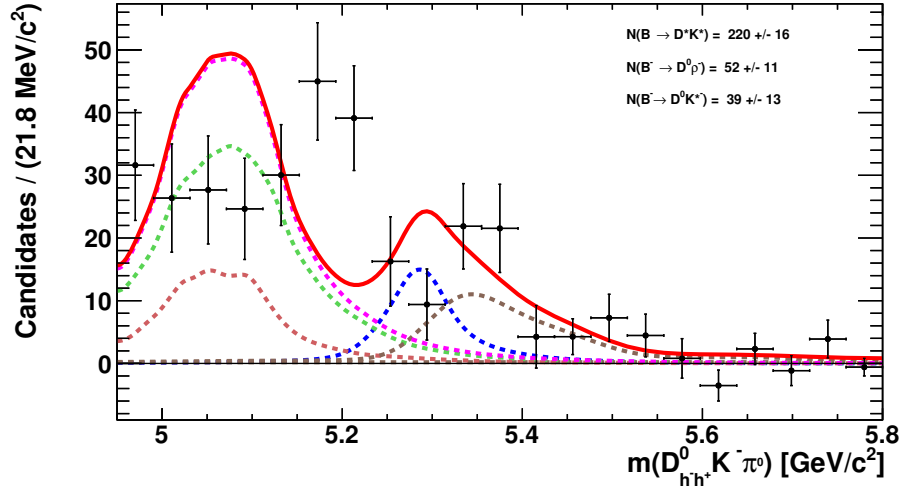


(b)

Figure 5.43: Fit to the invariant mass of $K^{*-} \to K^- \pi^0$ (top) and $B^- \to DK^{*-}$ $(K^- \pi^0)$ (bottom) where $D^0$ decays to $D^0 \to K^- K^+$ in the $D$ sideband for Data Run 1 and Run 2.

Figures 5.44a and 5.44b shows the fit to the $K^{*-}$ for $B^-$ and $B^+$ candidates separately. And as can be seen in the Figure 5.45 a fit is performed to the $B^- \to DK^{*-}$ $(K^- \pi^0)$ for $B^-$ (Figure 5.45a) and $B^+$ (Figure 5.45b). It can be seen that number of $B^-$ signal $NB^-_{sig} = 170 \pm 18$ is slightly larger than $B^+$ signal $NB^+_{sig} = 144 \pm 14$.
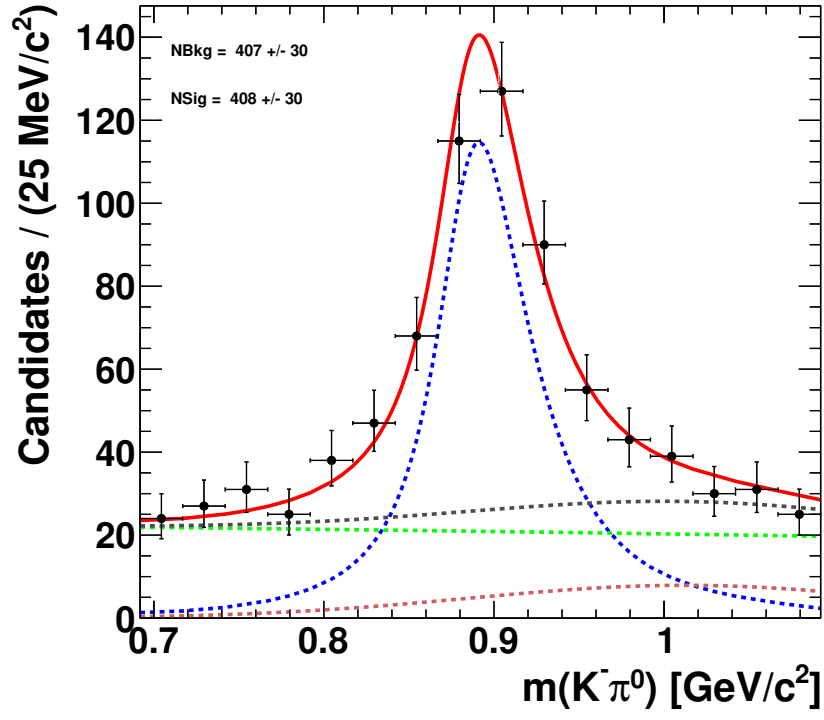
(a)
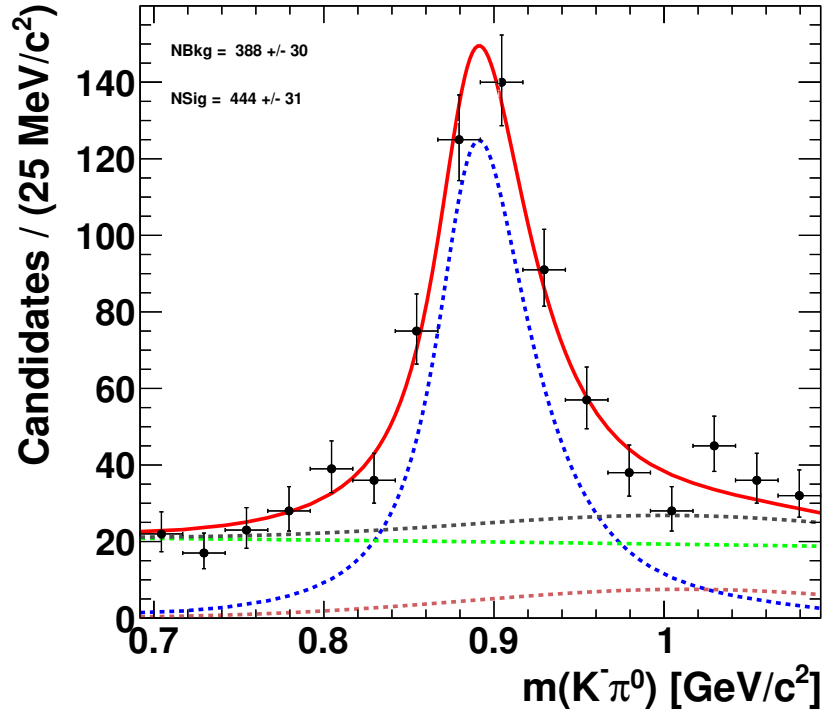


(b)

Figure 5.44: Fit to the invariant mass of $K^{*-} \to K^- \pi^0$ for $B^-$ (top) and $B^+$ (bottom) candidates for Data Run 1 and Run 2.

227
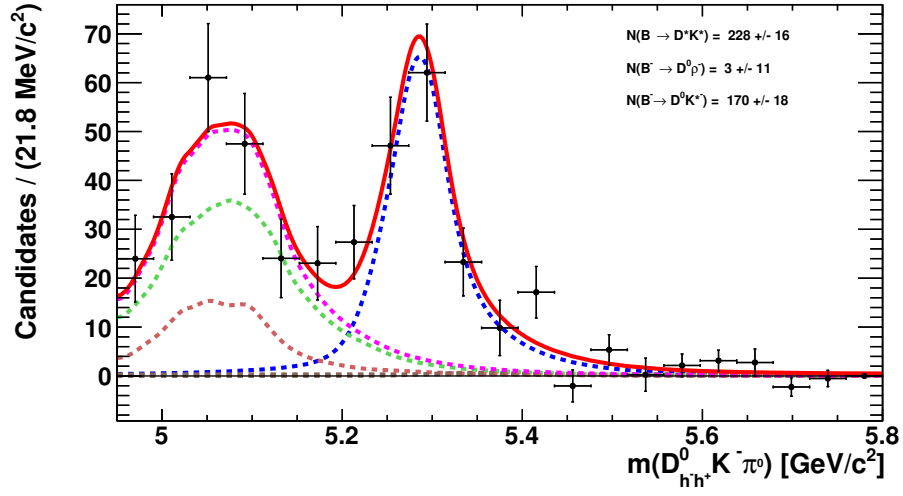
(a)
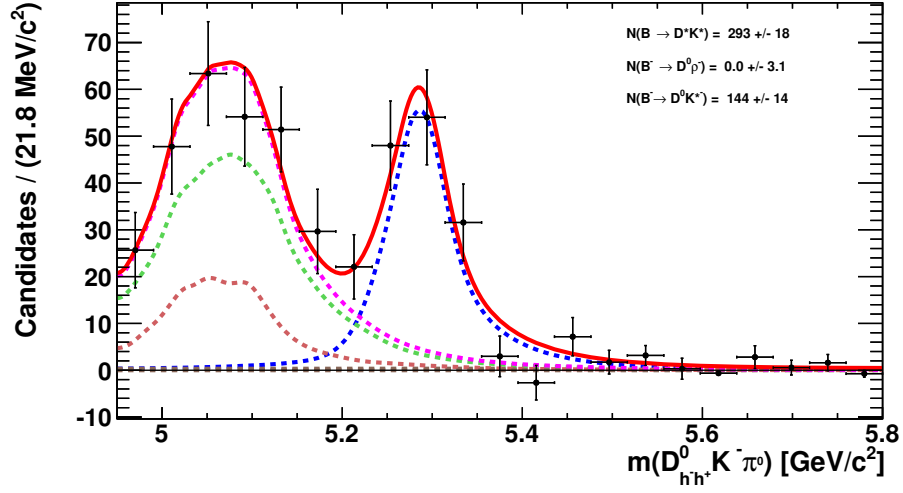


(b)

Figure 5.45: Fit to the invariant mass of $B^- \to D^0 K^{*-}$ (top) and $B^+ \to D^0 K^{*+}$ (bottom) candidates, where $D^0$ decays to $D^0 \to K^- K^+$ for Data Run 1 and Run 2.

In the sideband of $D$, Figure 5.46 displays the invariant mass fit for $B^-$ and $B^+$ candidates. The number of signal from charmless background for $B^-$ is $NB^-_{sig} = 24.6 \pm 8.1$ and for $B^+$ is $NB^+_{sig} = 14.1 \pm 7.4$ which is compatible with the one in Figure 5.43b.
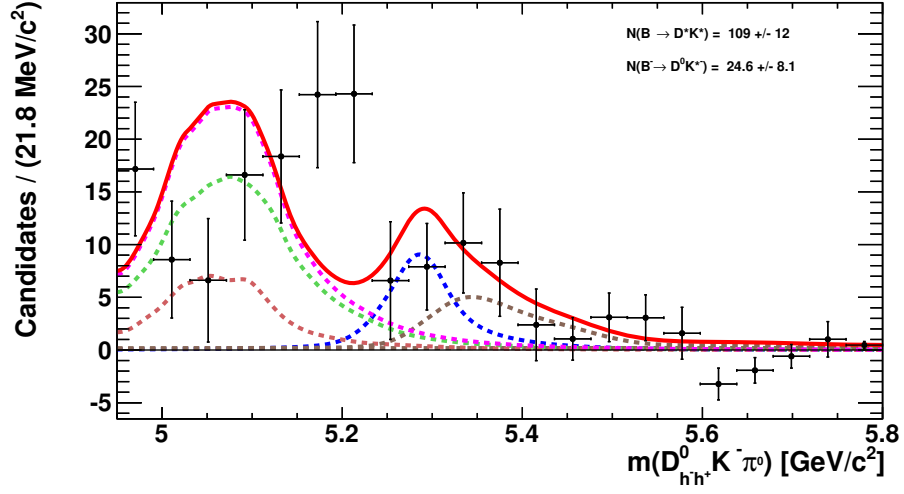
(a)
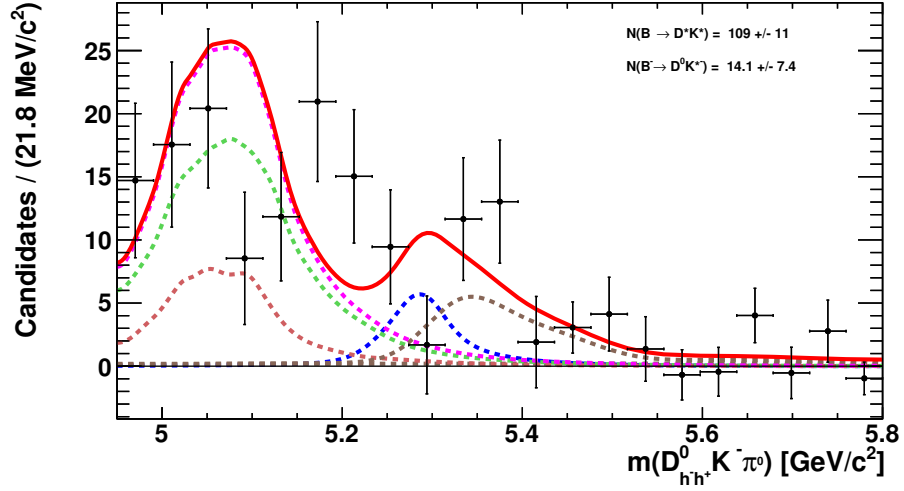


(b)

Figure 5.46: Fit to the invariant mass of $B^- \to D^0 K^{*\mp}$ for $B^-$ (top) and $B^+$ (bottom) candidates in $D$ sideband for Data Run 1 and Run 2.

To conclude, the number of events for $B^-$ and $B^+$ signal before the corrections are obtained as:

$$NB^-_{sig} = 170 \pm 18 \ \& \ NB^-_{peak} = 12 \pm 6 \to NB^-_{sig} = 158 \pm 19 \tag{5.14}$$

$$NB^+_{sig} = 144.0 \pm 14 \ \& \ NB^+_{peak} = 7 \pm 5 \to NB^+_{sig} = 137 \pm 15 \tag{5.15}$$

We perform a toy study for $K^- K^-$ to validate the uncertainties as it was studied in the earlier sections for $K\pi$ (RS) and $K\pi$ (WS) and corresponding distributions are presented

in Figure 5.47. From the first distribution one can clearly see that fitted $K^*$ is okay and there is no sign of bias found. From the residual fit to the $B^- \rightarrow D^0 K^{*-}$ signal, the ratio ($N_{fitted}$ - $N_{gen}$)/$N_{gen}$ is equal to -3.3%, this correspond about3.3% of 317±21 signal, which makes an underestimation of about 11 event, and the uncertainty is within 317±21 signal is 21 (see Figure 5.42b). The bias needs to be corrected with $1/\sqrt{(12)} \times$bias and is added systematic uncertainty. After the correction, bottom pull distribution Figure 5.47 is corrected to be centered at zero ( this is what we expect after the bias correction), and the $\sigma$ is 1.163, meaning that the statistical uncertainty in Figure 5.42b is underestimated. And with respect to these informations after the bias corrections and the under-estimation of the statistical uncertainty one can obtain the number of events for $B^-$ and $B^+$ to be

$$NB^-_{sig} = 176 \pm 22 \pm 2. \tag{5.16}$$

$$NB^+_{sig} = 149 \pm 17 \pm 2. \tag{5.17}$$
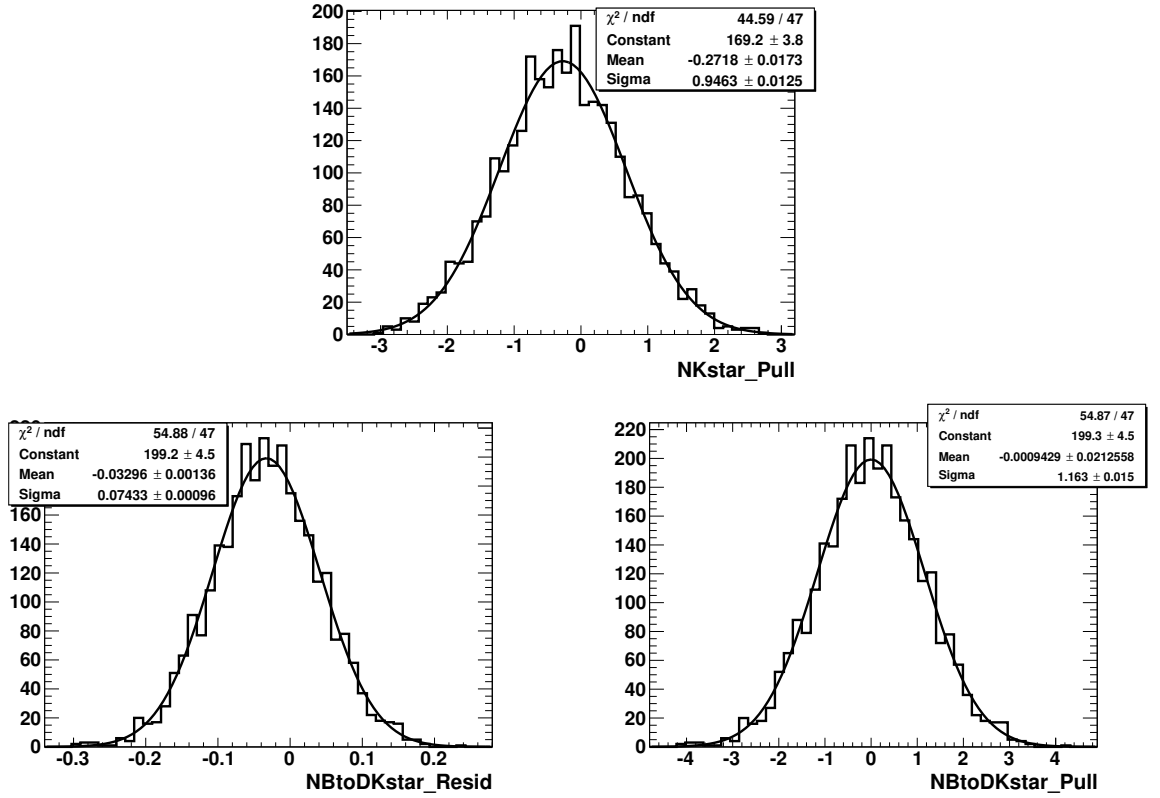


Figure 5.47: Pull distributions obtained for $K^*$ (top), the residual $B^- \rightarrow D^0 K^{*-}$ (middle) and the pull of $B^- \rightarrow D^0 K^{*-}$ (bottom) candidates, where $D^0$ decays to $D^0 \rightarrow K^- K^+$. The pull distributions for the fits results to the 4000 generated samples by pseudo experiment

## 5.5.6 Fit to the invariant mass of $K^* \rightarrow K^-\pi^0$ and $B \rightarrow D^0[\pi^-\pi^+]K^{*-}$

The selections defined for the $B \rightarrow D^0[\pi^-\pi^+]K^{*-}$ decay is listed below:

- $Signif[\Delta z(DB)]_{D^0} > 1$

- $m_D \in [1.8421, 1.8883] \,\mathrm{GeV}/c^2 \ (\pm \ 3\sigma)$

- $DLL\_K > 4$ for the charged $K^*$ daughter

- $DLL\_K < -2$ for the daughters $(\pi\pi)$

After the sWeight subtraction (see Figure 5.26) as it has been explained in the Section 5.5.3 aiming to remove the non-$K^{*-}$ background from the fit to the invariant mass of $K^{*-} \rightarrow K^-\pi^0$ shown in Figure 5.48a, a fit is performed to the $B^- \rightarrow D^0 K^{*-}$ signal, where $D^0$ decays to $\pi^-\pi^+$ represented in Figure 5.48b. Number of events for the signal is obtained to be $NB_{sig} = 105 \pm 15$. In order to estimate the possible charmless background contribution peaking below the signal region, an unbinned maximum likelihood fit is performed to the $B$ invariant mass distribution, where the mass of $D^0$ kept to be in the region of $> 40 \,\mathrm{MeV}/c^2 \ (+ \ 5\sigma)$ and $< 86 \,\mathrm{MeV}/c^2 \ (+ \ 11 \ \sigma)$ away from the nominal $D^0$ mass. As it is indicated before, the chosen $D$ sideband (upper and lower) is twice as large as the $D$ signal box considered $(\pm 23 \,\mathrm{MeV}/c^2)$. Hence a fit to the mass $K^{*-} \rightarrow K^-\pi^0$ for the candidates lying above the chosen $D$ sideband is performed. sPlot tecnique is used for the subtraction, calculating the weights and a corresponding mass fit of $B^- \rightarrow D^0 K^{*-}$ is also performed. Figures 5.49a and 5.49b display the result of $K^{*-}$ and $B^-$ mass after the sWeight subtraction. From the Figures, it can be seen that the peaking background for $\pi^-\pi^+K^{*-}$ at the nominal $B$ mass is 84±18 charmless events. Considering the double size of the $D$ sideband, the number of signal candidates within $105 \pm 15$ and in order to obtain the number of peaking background events in the signal region $(84/2 \pm 18/\sqrt{2})=$ 42±12.73 candidates should be subtracted.

Figure 5.50 shows the fit to the invariant mass of $K^{*-}$ for $B^-$ 5.50a and $B^+$ 5.50b. Fit parameters are fixed from the nominal reference fit in 5.25. Invariant mass fit to the signal is displayed in the Figures 5.51a and 5.51b for the $B^-$ and $B^+$ candidates separately. It can be seen that the number of $B^-$ candidates is slightly larger than $B^+$ candidates before the correction and as noted in the previous sections for the $K\pi$ (RS), $KK$ and $K\pi$ (WS) decays. It is required to be corrected for the charmless background subtraction in the $D$ sideband and the production asymmetry of $B^\pm$ and the detection asymmetry of $K^\pm$ and $\pi^\pm$.
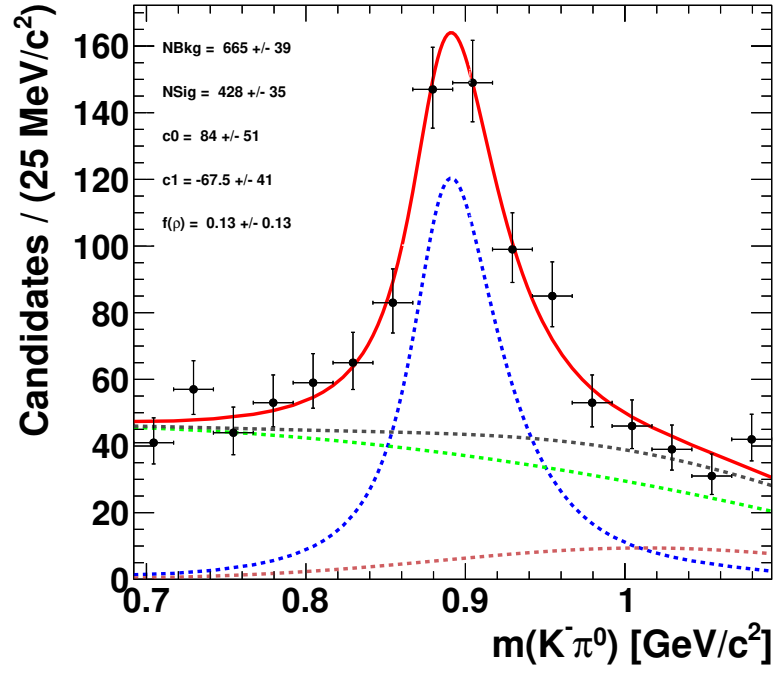
(a)
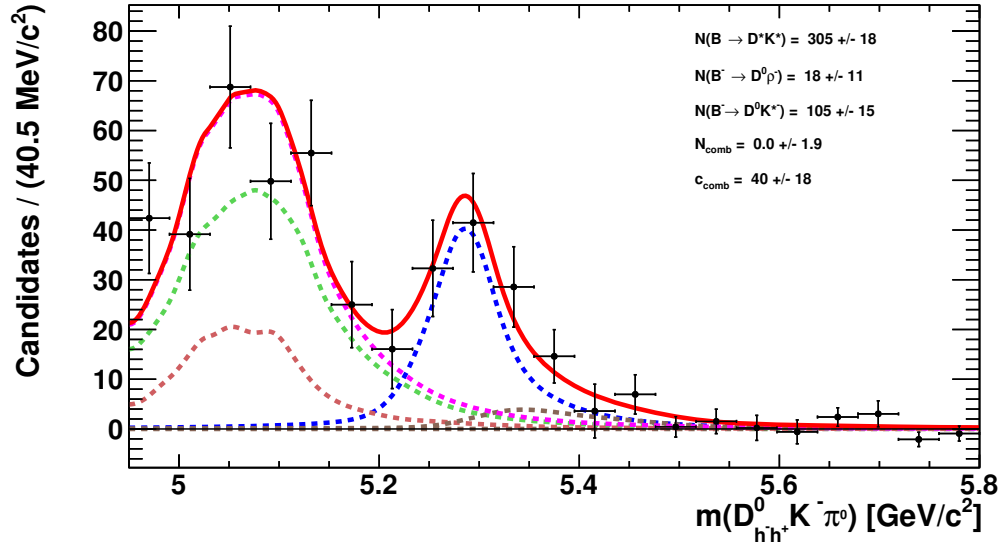


(b)

Figure 5.48: Fit to the invariant mass of $K^{*-} \to K^- \pi^0$ (top) and $B^- \to D^0 K^{*-}$ (bottom) for Data Run 1 and Run 2. The signal is given with the blue dashed line. Over all PDF is shown with the red straight line. The various background contributions are with the different colors.
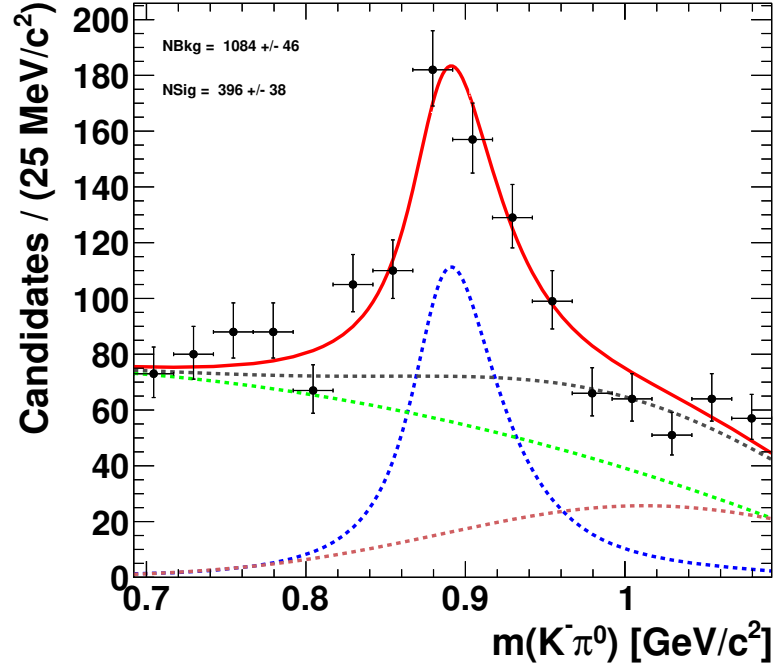
(a)
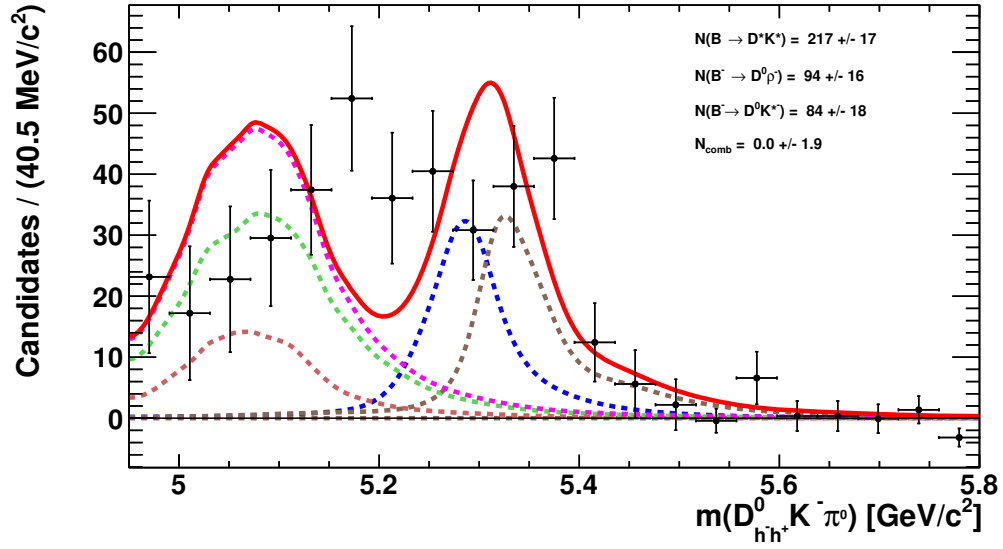


(b)

Figure 5.49: Fit to the invariant mass of $K^{*-} \to K^- \pi^0$ (top) and $B^- \to D^0 K^{*-}$ (bottom) in the sideband for Data Run 1 and Run 2. The signal is given with blue dashed line and various background contributions are indicated with the different colors. Total PDF is given with the red straight line.
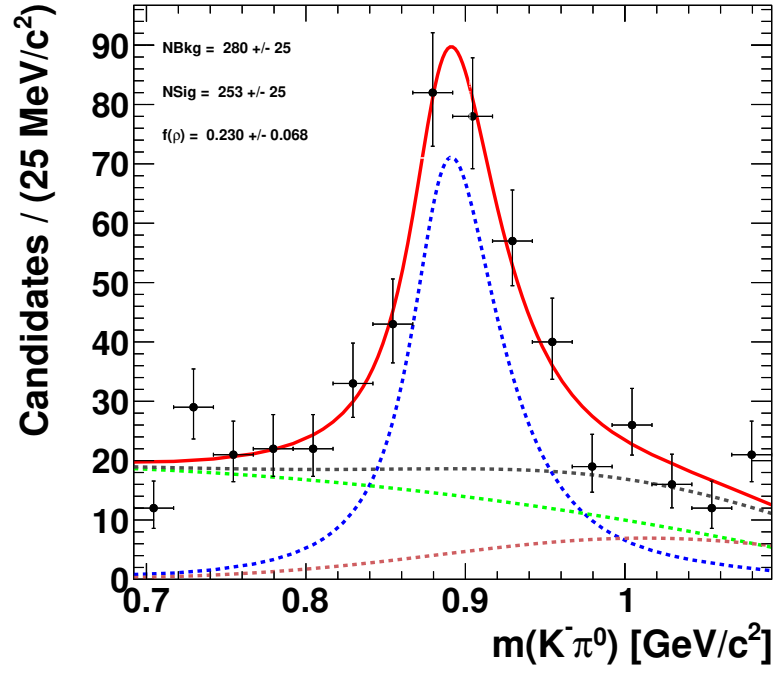
(a)
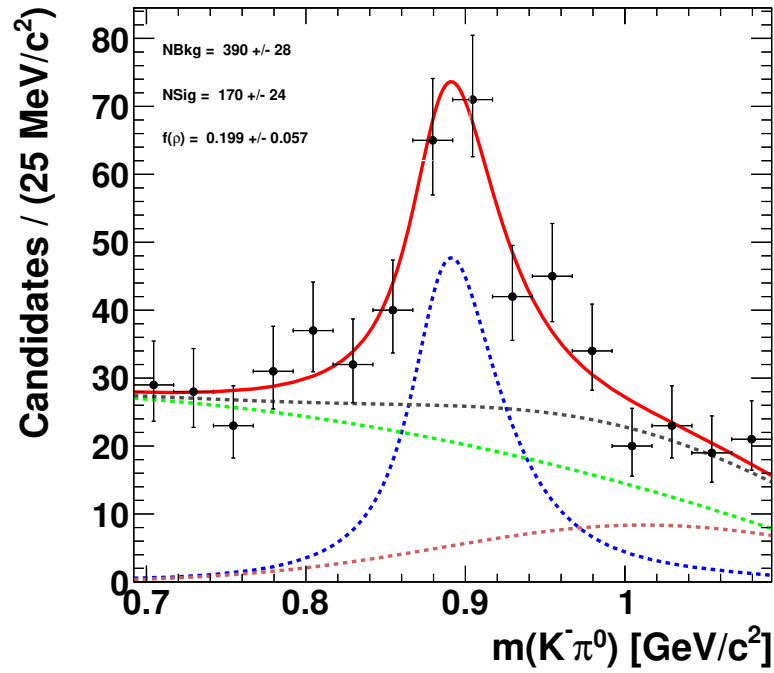


(b)

Figure 5.50: Fit to the invariant mass distribution of $K^{*-} \rightarrow K^{-}\pi^{0}$ for $B^{-}$ (top) and $B^{+}$ (bottom) candidates for Data Run 1 and Run 2
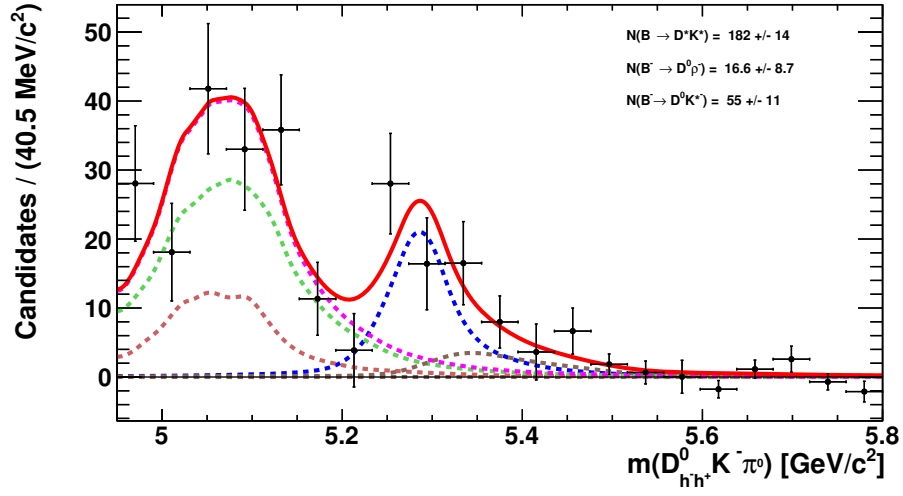
(a)
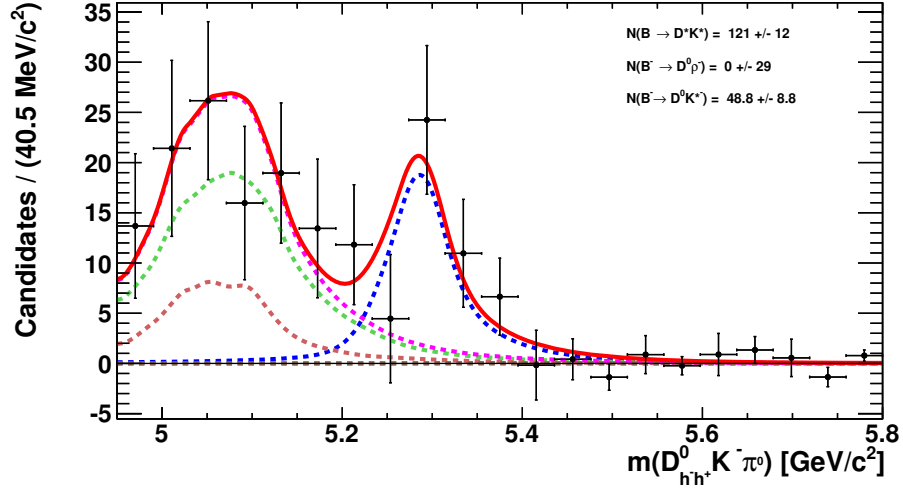


(b)

Figure 5.51: Fit to the invariant mass of $B^- \to D^0 K^{*-}$ (top) and $B^+ \to D^0 K^{*+}$ (bottom) candidates, where $D^0$ decays to $D^0 \to \pi^- \pi^+$ for Data Run 1 and Run 2. Number of events for $B^-$ is $NB_{sig}^- = 55 \pm 11$ and for $B^+$ is $NB_{sig}^+ = 48.8 \pm 8.8$.

The corresponding mass fit for the possible contribution of $B$ charmless $\pi^+ \pi^- K^{*\mp}$ background for $B^-$ and $B^+$ is shown in Figure 5.52a and 5.52b and this is obtained repeating the same procedure as we did for the result in Figure 5.49. The number of $B^-$ candidates is $69 \pm 13$ and for the $B^+$ to be $30 \pm 12$. One can see that the sum of number of the candidates $B^-$ and $B^+$ are compatible with the one given in Figure 5.49
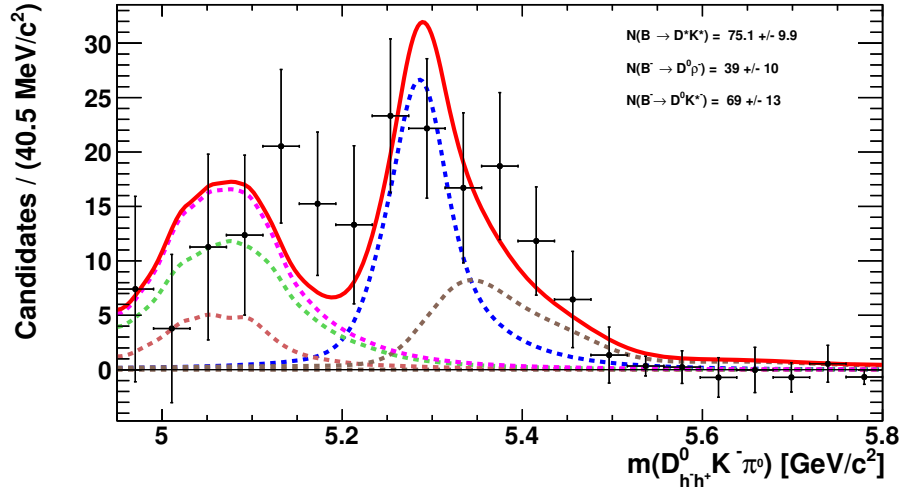
(a)
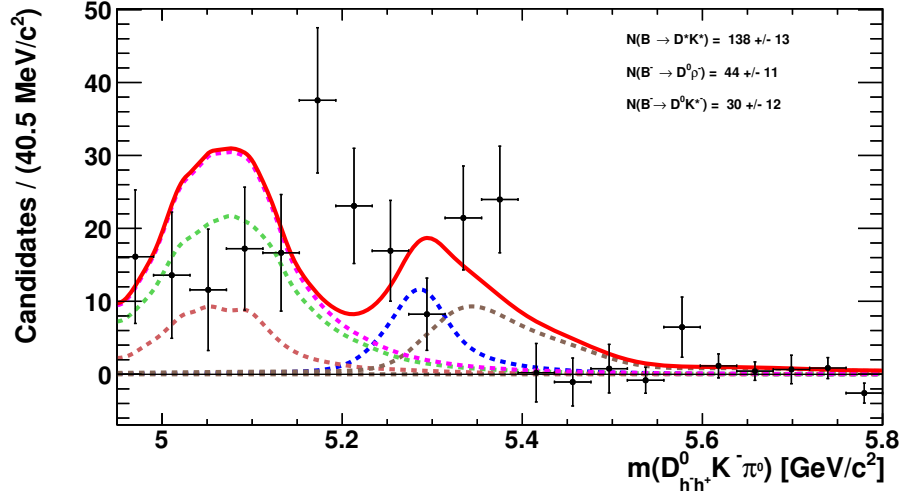


(b)

Figure 5.52: Fit to the invariant mass distribution of $B^- \to D^0 K^{*-}$ (top) and $B^+ \to D^0 K^{*+}$ (bottom) candidates, where $D^0$ decays to $D^0 \to \pi^- \pi^+$ in $D$ sideband for Data Run 1 and Run 2.

As a result, the number of candidates for $B^-$ and $B^+$ signal are obtained before and after the correction of the contributions from the charmless backgrounds

$$NB_{sig}^- = 55.1 \pm 11.6 \& NB_{peak}^- = 34.5 \pm 9.2 \to NB_{sig}^- = 20.6 \pm 14.8. \tag{5.18}$$

$$NB_{sig}^+ = 48.8 \pm 8.8 \& NB_{peak}^+ = 15.0 \pm 8.5 \to NB_{sig}^+ = 33.8 \pm 12.2. \tag{5.19}$$

where the uncertainties are quadratic sums of statistical uncertainties from the fits in the signal box and the sideband of $D$.

236

The validation of the uncertainties is performed with the toy studies. The same procedure is implemented as it was performed for the $K^-\pi^+$ (RS), $K^-K^+$, $K^+\pi^-$ (WS). 4000 pseudo-experiments are generated for the toy study based on the nominal fit for the signal $K^{*-}$ 5.24b and the $B$ mass 5.48b. We perform the fit for each of the generated samples and the pull distributions correspond to the mass fit of $K^{*-}$ and $B$ are displayed in Figure 5.53. From the pull distribution, it can be seen that the mean value of fitted $K^{*-}$ indicate almost unbiased and from the residual fit to the number of $B^- \to D^0 K^{*-}$ signal, the bias in the $B^\pm \to D^0 K^{*\pm}$ is observed ($N_{fitted}$ - $N_{gen}$)/$N_{gen}$ equal to 0.4%, and this is about 0.4% of $105 \pm 15$ signal candidates (see 5.48b). The bias is corrected and assign $1/\sqrt{(12)}\times$bias as a systematic uncertainty. With the correction, the pull distribution to the $B^- \to D^0 K^{*-}$ signal is obtained 5.53, where the mean value centered at zero (as expected) but $\sigma$ is at 1.34 (expected to be $\sigma = 1$) shows deviation which means statistical uncertainty in 5.48b is underestimated. Finally, after the corrections the number of $B^-$ and $B^+$ candidates are calculated and obtained to be

$$NB^-_{sig} = 19.4 \pm 20.0 \pm 0.1 \tag{5.20}$$

$$NB^+_{sig} = 33.6 \pm 15.7 \pm 0.1. \tag{5.21}$$
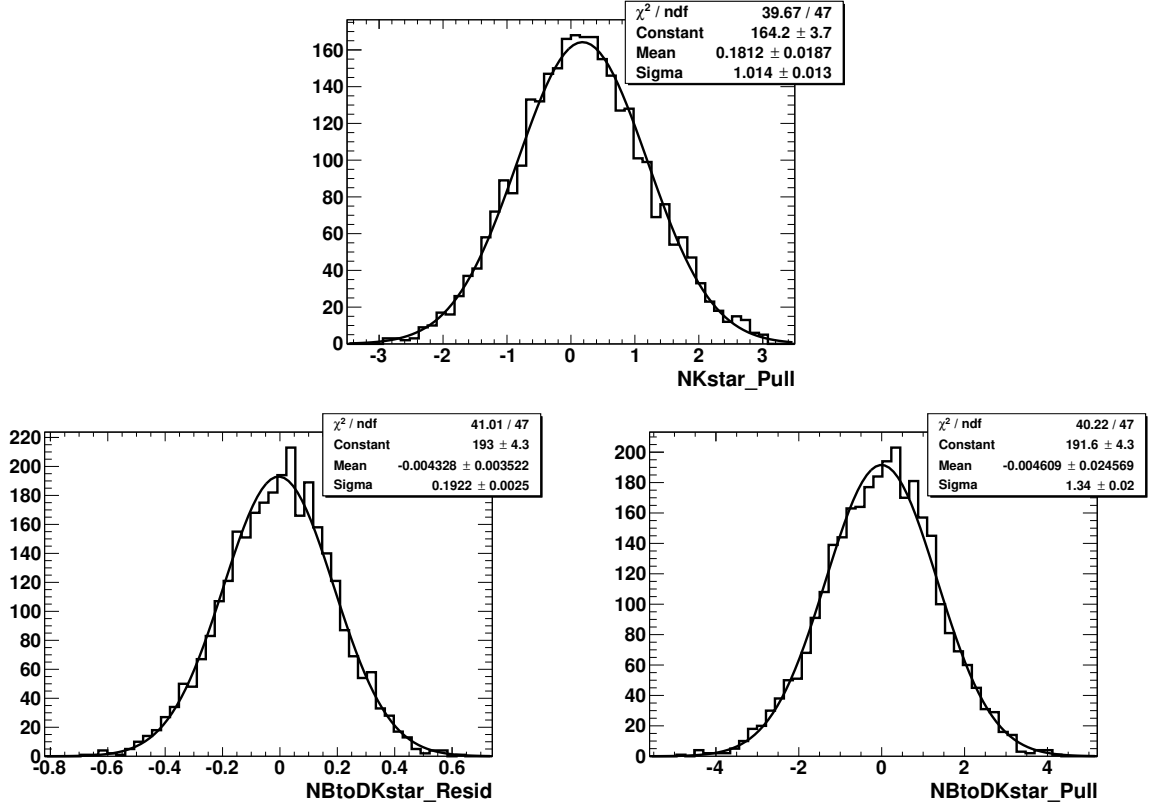
Figure 5.53: Pull distributions for $K^*$ (top) $B^- \to D^0 K^{*-}$ (middle) and $B^- \to D^0 K^{*-}$ (bottom) candidates, where $D^0$ decays to $D^0 \to \pi^- \pi^+$ with toy/pull study.

## 5.6 Measurement of the CP asymmetry(physical asymmetry) for the $K\pi$ (RS), $K\pi$ (WS), $KK$ and $\pi\pi$

After performing the fit to the invariant masses of $KK, \pi\pi$, $K\pi$ (RS) and $K\pi$ (WS) decay modes and obtaining the number of yields for these considered decays, we calculate the various asymmetries contribute to the derivation of the CP asymmetry (physical asymmetry) $A_{CP}$ which is actually what we want to measure. The asymmetries to be scrutinized in the analysis defined as

$$A_{CP} = A_{raw} - A_{det} - A_{prod} \tag{5.22}$$

where $A_{raw}$ indicates raw asymmetry, $A_{det}$ and $A_{prod}$ stands for the detector and the production effects. The production and the detector asymmetries are respectively due to the fact that LHC is a pp machine that produces slightly more $B^+$ than $B^-$ and because pions and kaons have different cross section values according to their electric charges,

238

when they interact with the LHCb detector. These asymmetries will be detailed in the following parts.

## 5.6.1  Raw asymmetry

The raw asymmetry is determined through the fit performed to the invariant masses of $B^+$ and $B^-$ candidates. The definition of the measured raw asymmetry to the final state is given by

$$A_{raw}(B^\pm \to \bar{f}) = \frac{N(B^- \to f) - N(B^+ \to \bar{f})}{N(B^- \to f) + N(B^+ \to \bar{f})} \tag{5.23}$$

where N denotes the number of decays observed for $B^-$ and $B^+$.

## 5.6.2  Production asymmetries

In order to measure the CP asymmetry, it is important to determine the $b$ and $\bar{b}$ hadrons in proton-proton (pp) collisions at LHC, for which in fact they are not expected to be identical in size. The production asymmetry of the $B^\pm$ mesons is measured exploited the analysis of $B^+ \to \bar{D}^0 \pi^+$ decay mode in bins of momentum $p_T$ and the pseudorapidity $\eta$ [[156], [15], [59]]. We define the production asymmetry between the $B^+$ and $B^-$ mesons cross sections as given below

$$A_{prod} = \frac{\sigma(B^-) - \sigma(B^+)}{\sigma(B^-) + \sigma(B^+)} \tag{5.24}$$

where $\sigma$ indicates the production cross-section for $B^+$ and $B^-$. We use the production asymmetry $A_{prod}(B^-/B^+)$ is measured to be (0.014±0.099)% from [157] for $B^- \to DK^{*-}$ analysis.

## 5.6.3  Detection asymmetries

Detection asymmetries arise from the differences between the matter and the antimatter in the pp collision with the detector effects (i.e. tracking, particle identification RICH). It is important to determine the detection asymmetries, since we have two main contributions in the final state are kaons and the pions to be identified. And the asymmetry difference is defined by

$$A_{det}^{K\pi} = \frac{\epsilon(K^-\pi^+) - \epsilon(K^+\pi^-)}{\epsilon(K^-\pi^+) + \epsilon(K^+\pi^-)} \tag{5.25}$$

The detection asymmetry for kaon and pion is determined to be $A_{det}^{K\pi}$ =(-0.96±0.13)%, while the detection asymmetry for pions are $A_{det}^{\pi}$ =(-0.064±0.018)% [[157], [35]]. These values for the detection asymmetry for kaons and pions are taken [[157], [35], [158]]. We measure the efficiency of the detection asymmetry for each decay mode for $B^\pm$ where the effect is obtained small.

- $B^\pm \to D^0[K\pi]K^{*\pm}$ (RS)

$$A_{det}B^\pm = -0.020 \pm 0.003$$

- $B^\pm \to D^0[KK]K^{*\pm}$

$$A_{det}B^\pm = -0.010 \pm 0.002$$

- $B^\pm \to D^0[\pi\pi]K^{*\pm}$

$$A_{det}B^\pm = -0.010 \pm 0.002$$

- $B^\pm \to D^0[K\pi]K^{*\pm}$ (WS)

$$A_{det}B^\pm = 1.001 \pm 0.000$$

## 5.7 Efficiency Studies

This section factorizes out the efficiency studies performed on different terms which are obtained from the simulated signal samples. Both magnet polarities are generated with Pythia 8 and Sim09j/l. In this part we obtained the efficiency on the stripping, geometry, offline selections and the total efficiency can be expressed in a given form as being a product of different contributions

$$\epsilon^{tot} = \epsilon^{geom} \times \epsilon^{sel|geom} \times \epsilon^{PID|sel} \tag{5.26}$$

where each of the term (except geometrical efficiency as $\epsilon^{geom}$) calculated within the scope of the previous one. The first term $\epsilon^{geom}$ require to have all the final state particles of decay in the acceptance of the LHCb detector. As opposed to the $B_s^0 \to \tilde{D}^{(*)0}\phi$ analysis, we don't consider the trigger part as it was described in Sec. 4.11 Eq. 4.23. Indeed triggering is performed the same way, for the same topology in the various subdecay modes: $B \to D[h_1 h_2]K^{*-}[K^-\pi^0]$ and $h_{1,2} = K$ or $\pi$ in the extraction of the observables $R_{CP}$/ADS and $A_{CP}$/ADS. In the following sections detailed informations will be given on the studied efficiencies.

### 5.7.1 Selection efficiency

Efficiencies on the filtering, geometrical acceptance and the offline selections have been computed for MC signals. It should be noted that all of the four sub-decays selections which are mostly developed and optimised together until that we differentiate them from PID criteria, and a veto for the WS $D^0 \to K^+\pi^-$ decay. Therefore we have to study the PID efficiency with its specific differences in the next section. In Table 5.17, geometrical, filtering and the selection efficiencies are given before the PID correction of MC.

| $\epsilon^{sel|geom}$(%) | 2011 | 2012 | 2015 | 2016 | 2017 | 2018 |
|---|---|---|---|---|---|---|
| | | | $B^- \to D^0(K^\mp\pi^\pm)K^{*-}$ | | | |
| geom | $7.33 \pm 0.06$ | $7.39 \pm 0.06$ | $7.91 \pm 0.08$ | $7.75 \pm 0.08$ | $7.85 \pm 0.08$ | $7.84 \pm 0.08$ |
| filter | $2.11 \pm 0.01$ | $2.18 \pm 0.01$ | $2.44 \pm 0.012$ | $3.18 \pm 0.01$ | $3.19 \pm 0.01$ | $2.87 \pm 0.01$ |
| offline selection $(K^-\pi^+(RS))$ | $29.28 \pm 0.17$ | $29.06 \pm 0.25$ | $28.32 \pm 0.41$ | $29.93 \pm 0.28$ | $30.57 \pm 0.32$ | $29.72 \pm 0.33$ |
| offline selection $(K^+\pi^-(WS))$ | $20.66 \pm 0.16$ | $22.28 \pm 0.22$ | $22.31 \pm 0.37$ | $23.63 \pm 0.26$ | $23.98 \pm 0.29$ | $23.07 \pm 0.30$ |
| | | | $B^- \to D^0(K^+K^-)K^{*-}$ | | | |
| geom | $7.33 \pm 0.1$ | $7.39 \pm 0.1$ | $7.85 \pm 0.1$ | $8.01 \pm 0.1$ | $7.74 \pm 0.1$ | $7.89 \pm 0.1$ |
| filter | $2.04 \pm 0.004$ | $2.13 \pm 0.01$ | $2.44 \pm 0.012$ | $3.03 \pm 0.01$ | $3.17 \pm 0.01$ | $2.78 \pm 0.01$ |
| offline selection | $30.57 \pm 0.18$ | $31.25 \pm 0.26$ | $29.39 \pm 0.41$ | $30.51 \pm 0.31$ | $31.65 \pm 0.30$ | $30.39 \pm 0.33$ |
| | | | $B^- \to D^0(\pi^+\pi^-)K^{*-}$ | | | |
| geom | $7.19 \pm 0.1$ | $7.46 \pm 0.1$ | $7.94 \pm 0.1$ | $7.99 \pm 0.1$ | $7.93 \pm 0.1$ | $7.94 \pm 0.1$ |
| filter | $2.15 \pm 0.01$ | $2.20 \pm 0.01$ | $2.53 \pm 0.01$ | $3.17 \pm 0.01$ | $3.26 \pm 0.01$ | $2.93 \pm 0.01$ |
| offline selection | $27.19 \pm 0.16$ | $26.41 \pm 0.24$ | $28.02 \pm 0.40$ | $27.59 \pm 0.31$ | $29.19 \pm 0.35$ | $27.68 \pm 0.30$ |

Table 5.17: Selection efficiencies for the signal mode $B^- \to D^0 K^{*-}$, where $D^0$ decays to $KK, \pi\pi, K\pi$ (RS) and $K\pi$ (WS) of MC Run 1 and Run 2. Selections are not including PID calibration.

## 5.7.2  PID efficiency

PID variables of kaons and pions are not perfectly well described by the simulation, therefore the data-driven method called as PIDCalib to evaluate the efficiencies of the variables is used. As explained in the previous analysis 4.11.2 for the $B_s^0 \to D\phi$, the efficiency of the PID values has been obtained by correcting the MC PID variables with the more traditional method called PIDCalib [145]. For each year and each magnet polarity the correction is performed. For this analysis a different method known as PIDCorr based on correcting the PID variables with an unbinned approach in the Monte Carlo simulation sample is considered. This method perform an alteration for the MC PID variables to disperse alike as in the data sample (calibration sample). As in the PIDCalib, PID correction is a function of track kinematics and event multiplicity $(p, \eta, NTracks)$. For the analysis, only difference between the decay modes : $KK, \pi\pi, K\pi$ (RS) and the $K\pi$ (WS) are just PID requirements because we develop the selections in parallel. In order to determine the PID efficiency for these decays, we run Meerkat tool which is the kernel density estimation procedure describes the calibration PDFs in four dimension (PID, $p_T, \eta, Ntrack$) [[159], [160], [161]].

## 5.7.3  Total efficiency

Here is the Table 5.18 summarizes the total efficiency for $KK, \pi\pi, K\pi$ (RS) and $K\pi$ (WS). Total efficiency are calculated considering the efficiencies from geometrical acceptance, selections and the PID efficiencies.

| | 2011 | 2012 | 2015 | 2016 | 2017 | 2018 |
|---|---|---|---|---|---|---|
| $B^\pm D^0[K^-\pi^+]K^{*\pm}[K^-\pi^0]$ **(RS)** | | | | | | |
| offline selection (%) | $27.16 \pm 0.17$ | $27.06 \pm 0.25$ | $28.16 \pm 0.41$ | $29.75 \pm 0.28$ | $30.57 \pm 0.32$ | $29.53 \pm 0.33$ |
| $\epsilon^{tot}$(%) | $0.042 \pm 0.001$ | $0.044 \pm 0.001$ | $0.054 \pm 0.002$ | $0.073 \pm 0.002$ | $0.077 \pm 1.002$ | $0.067 \pm 0.002$ |
| $B^\pm D^0[K^+\pi^-]K^{*\pm}[K^-\pi^0]$ **(WS)** | | | | | | |
| offline selection (%) | $22.65 \pm 0.16$ | $20.42 \pm 0.22$ | $21.14 \pm 0.37$ | $22.91 \pm 0.26$ | $23.62 \pm 0.29$ | $22.66 \pm 0.30$ |
| $\epsilon^{tot}$(%) | $0.035 \pm 0.001$ | $0.033 \pm 0.001$ | $0.041 \pm 0.001$ | $0.057 \pm 0.001$ | $0.059 \pm 0.001$ | $0.051 \pm 0.001$ |
| $B^\pm D^0[K^-K^+]K^{*\pm}[K^-\pi^0]$ | | | | | | |
| offline selection (%) | $31.34 \pm 0.18$ | $31.59 \pm 0.26$ | $29.23 \pm 0.41$ | $29.86 \pm 0.31$ | $31.34 \pm 0.30$ | $30.17 \pm 0.33$ |
| $\epsilon^{tot}$(%) | $0.047 \pm 0.001$ | $0.049 \pm 0.001$ | $0.056 \pm 0.002$ | $0.073 \pm 0.002$ | $0.077 \pm 0.002$ | $0.066 \pm 0.002$ |
| $B^\pm D^0[\pi^-\pi^+]K^{*\pm}[K^-\pi^0]$ | | | | | | |
| offline selection (%) | $22.35 \pm 0.16$ | $22.63 \pm 0.24$ | $27.50 \pm 0.40$ | $27.74 \pm 0.31$ | $29.27 \pm 0.35$ | $27.58 \pm 0.30$ |
| $\epsilon^{tot}$(%) | $0.035 \pm 0.001$ | $0.037 \pm 0.001$ | $0.055 \pm 0.002$ | $0.070 \pm 1.002$ | $0.076 \pm 0.002$ | $0.064 \pm 0.002$ |

Table 5.18: Total efficiency for the decay modes: $K\pi$ (RS), $KK$, $\pi\pi$, $K\pi$ (WS). The offline selections efficiencies are given after PID selection. The total efficiency obtained through the correction on the PID variables through the PIDCorr.

Possible differences for the PID efficiency before and after PID correction and as the PID criteria that is applied on the decays are quite loose, it can be seen that the differences before (see Table 5.17) and after (see Table 5.18) the PID corrections are not too large and that half of the differences are taken as systematic uncertainties. The average of the total efficiencies normalized to the number of $B$ candidates after the PID correction for

2011-2018 years of data taking displayed in the Table 5.19 for each decays of interest of this analysis.

| Average of Total efficiency (%)×100 |
|---|
| $B^{\pm}D^0[K^-\pi^+]K^{*\pm}[K^-\pi^0]$ **(RS)** |
| $6.44 \pm 0.16$ |
| $B^{\pm}D^0[K^+\pi^-]K^{*\pm}[K^-\pi^0]$ **(WS)** |
| $4.96 \pm 0,16$ |
| $B^{\pm}D^0[K^-K^+]K^{*\pm}[K^-\pi^0]$ |
| $6.55 \pm 0,16$ |
| $B^{\pm}D^0[\pi^-\pi^+]K^{*\pm}[K^-\pi^0]$ |
| $6.12 \pm 0.21$ |

Table 5.19: Average of total efficiency for the decay modes: $K\pi$ (RS), $K\pi$ (WS), $KK$, $\pi\pi$ for 2011-2018 years of data taking.

## 5.8 Systematic uncertainties

In this section main sources of systematic uncertainties that effect the measurements of $B^- \to D^0 K^{*-}$ decay of interest are discussed. Different sources contribute to the systematics will be addressed in the following sections.

### 5.8.1 Uncertainties from the charmless background and the fit biases

The systematic uncertainties are determined for the possible charmless backgrounds and the fit biases, as estimated from the fits performed to the D sidebands for each of the sub-decays: $K\pi$ (RS), $K\pi$ (WS), $KK$ and $\pi\pi$ and from the pull studies the signal $B^- \to D^0 K^{*-}$. A crosscheck with the toy study with 4000 pseudo-experiments is performed to validate the uncertainties obtained from the fit. The residual biases involved in the systematic uncertainties are calculated for the $B^- \to D^0 K^{*-}$, where $D^0$ decays to $KK, \pi\pi$, $K\pi$ (RS) and $K\pi$ (WS). This is explained in Sec. 5.5.2 for the decay modes considered. The pull distributions and the residuals for the fits to the invariant mass of $K^{*-}$ and $B^- \to D^0 K^{*-}$ for each decay modes are obtained and the bias for $B^- \to D^0 K^{*-}$ is calculated through the $(N_{fitted} - N_{gen})/N_{gen}$, where $N_{gen}$ is the residual. After correcting the bias and the fitted number, the bias assign to $1/\sqrt{12} \times$bias of correction is taken as a systematic uncertainty. Table 5.21 displays the systematic uncertainties from the charmless background and the fit biases for the $B^-$ and $B^+$ candidates.

| Source of systematic | $K\pi$ (RS) | $KK$ | $\pi\pi$ | $K\pi$ (WS) |
|---|---|---|---|---|
| Fit model | 3.0 | 2.0 | 0.1 | 0.0 |

Table 5.20: Systematic uncertainties from the possible charmless backgrounds and the fit biases for $B^-$ candidates and their magnitudes.

| Source of systematic | $K\pi$ (RS) | $KK$ | $\pi\pi$ | $K\pi$ (WS) |
|---|---|---|---|---|
| Fit model | 3.0 | 2.0 | 0.1 | 1.4 |

Table 5.21: Systematic uncertainties from the possible charmless backgrounds and the fit biases for $B^+$ candidates and their magnitudes.

### 5.8.2 Uncertainties on production $A_{prod}$ and detection asymmetries $A_{det}$

In this part, systematic uncertainties on the production asymmetry $A_{prod}$ and the detection asymmetry $A_{det}$ has been studied. Table 5.22 shows the systematics on the detection asymmetries determined for the two-body $D^0$ decays of $B^- \to D^0 K^{*-}$. The production asymmetry doesn't depend on the decay mode of interest. The measured value for the

production asymmetry is $A_{prod}=(0.014\pm0.099)\%$ where gives the combination of statistics and systematics taken from the [157].

| Source of systematic | $K\pi$ (RS) | $KK$ | $\pi\pi$ | $K\pi$ (WS) |
|---|---|---|---|---|
| $A_{det}$ for $B^{\pm}$ | 0.003 | 0.002 | 0.002 | 0.000 |

Table 5.22: Systematic uncertainties on the production and the detection asymmetry with their magnitudes.

### 5.8.3  Uncertainties on branching fractions

The systematics on the branching fractions of various sub-decay modes used in the analysis to be considered in the fit. In Tables 5.15 and 5.16, the branching fractions of the related decays are given [18]. These decays are fixed in the fit with their uncertainties. Table 5.23 shows the systematic uncertainties determined on the branching fractions for the $D^0$ sub-decays.

| Source of systematic (%) | $K\pi$ (RS) | $KK$ | $\pi\pi$ | $K\pi$ (WS) |
|---|---|---|---|---|
| Branching fraction | 3.946±0.030 | 0.408±0.006 | 0.145±0.002 | 0.014±0.000 |

Table 5.23: Systematic uncertainties due to the branching fractions of decay modes studied in the analysis. Uncertainties are obtained from the PDG [18].

### 5.8.4  Uncertainties on the efficiency

We calculate the efficiencies for each $D^0$ decay modes considered. These efficiency studies has been detailed in the previous sections. When we calculate selections as already explained earlier, we take the possible differences for the PID efficiency before and after the PID correction and these differences are taken as systematics. Here in the Table 5.24, systematics which come from the selections including geometric, stripping and PID efficiencies defined for the each decay modes. We are applying loose criterion on PID and the systematics are not too large.

| Source of systematic (%) | $K\pi$ (RS) | $KK$ | $\pi\pi$ | $K\pi$ (WS) |
|---|---|---|---|---|
| Efficiency | 0.068 | 0.043 | 0.1421 | 0.096 |

Table 5.24: Systematic uncertainties due to the selection efficiency of $D^0$ decay modes studied in the analysis. Relative difference between with and wo PID correction is taken as systematics.

# 5.9 Results for the CP observables

In this section the results for the observables and the parameters are presented. The results are obtained by CKMfitter [162].

## 5.9.1 Results for $B^\pm \to DK^{*\pm}$

Results for the analysis of $B^- \to DK^{*-}$ decay are given, where $D$ meson decays to :$K^-\pi^+$ (RS), $K^+\pi^-$ (WS) and, where $D$ meson decays to CP-eigenstates: $K^+K^-$, $\pi^+\pi^-$. Through the CP observables, information on the physics parameters are extracted: $r_B, \delta_B$ and $\gamma$. Number of the yields obtained in this analysis are displayed in Table 5.25. These numbers are corrected for the possible charmless backgrounds and fit biases, as estimated from the fits performed to the $D$ meson sidebands and from the pull studies.

| Number of events | $NB^\pm$ | $NB^-$ | $NB^+$ |
|---|---|---|---|
| $K\pi$ (RS) | $2176 \pm 69 \pm 4.2$ | $1042.0 \pm 47.0 \pm 3.0$ | $1134.0 \pm 50.0 \pm 3.0$ |
| $KK$ | $325 \pm 28 \pm 2.8$ | $176.0 \pm 22.0 \pm 2.0$ | $149.0 \pm 17.0 \pm 2.0$ |
| $\pi\pi$ | $53 \pm 26 \pm 0.14$ | $19.4 \pm 20.0 \pm 0.1$ | $33.6 \pm 15.7 \pm 0.1$ |
| $K\pi$ (WS) | $31.4 \pm 13 \pm 1.4$ | $0.0 \pm 0.7 \pm 0.0$ | $31.4 \pm 13.04 \pm 1.4$ |

Table 5.25: Number of yields for $B^- \to DK^{*-}$ $N_{B-}$ and $B^+ \to DK^{*+}$ $N_{B+}$ where $D^0$ decays to $K\pi$ (RS), $KK$, $\pi\pi$, $K\pi$ (WS). The given uncertainties are statistical only.

### 5.9.1.1 Observables with GLW method

The $\gamma$ angle determined by GLW method. The $D^0$ is reconstructed in CP-eigenstates $KK$ and $\pi\pi$. The CP asymmetry and the ratio of the rate for the $D^0$ meson decays to $K^+K^-$ (scaled by branching fraction) are defined by the Eq.

$$A_{KK} = A_{CP\pm} = \frac{\Gamma(B^- \to D(K^+K^-)K^{*-}) - \Gamma(B^+ \to D(K^+K^-)K^{*+})}{\Gamma(B^- \to D(K^+K^-)K^{*-}) + \Gamma(B^+ \to D(K^+K^-)K^{*+})} \tag{5.27}$$

$$R_{KK} = R_{CP\pm} = \frac{\Gamma(B^- \to D(K^+K^-)K^{*-}) + \Gamma(B^+ \to D(K^+K^-)K^{*+})}{\Gamma(B^- \to D(K^-\pi^+)K^{*-}) + \Gamma(B^+ \to D(K^+\pi^-)K^{*+})} \times \frac{\mathcal{B}(D^0 \to K^-\pi^+)}{\mathcal{B}(D^0 \to K^+K^-)} \tag{5.28}$$

The yield ratios after the efficiency corrections can be written

$$R_{KK} = R_{CP\pm} = \frac{N(B^- \to D(K^+K^-)K^{*-})}{N(B^- \to D(K^-\pi^+)K^{*-})} \times \frac{\mathcal{B}(D^0 \to K^-\pi^+)}{\mathcal{B}(D^0 \to K^+K^-)}$$
$$\times \frac{\epsilon_{sel}(K\pi)}{\epsilon_{sel}(KK)} \times \frac{\epsilon_{PID}(K\pi)}{\epsilon_{PID}(KK)} \tag{5.29}$$

The relative ratio of the efficiency wrt to the normalisation mode $D^0 \to K^- \pi^+$ have to be accounted for in the $R_{CP}$ observables. The $\epsilon_{sel}$ and $\epsilon_{PID}$ are for the selection and the PID efficiencies.

The CP results obtained with the full Run 1 and Run 2 LHCb dataset for the $D^0$ decays to $KK$ mode for $B^- \to D^0 K^{*-}[K\pi^0]$. The results are given for the $KK$ and the asymmetry results are given in %

- $A_{KK} = A_{CP\pm} = 9.3 \pm 8.4 \pm 0.9$

- $R_{KK} = R_{CP\pm} = 1.420 \pm 0.129 \pm 0.051$

where the first uncertainty stands for statistical and the second uncertainty is systematics.

For the $D^0$ decays to $\pi\pi$, the CP asymmetry and the ratio rate are given by

$$A_{\pi\pi} = A_{CP\pm} = \frac{\Gamma(B^- \to D(\pi^+\pi^-)K^{*-}) - \Gamma(B^+ \to D(\pi^+\pi^-)K^{*+})}{\Gamma(B^- \to D(\pi^+\pi^-)K^{*-}) + \Gamma(B^+ \to D(\pi^+\pi^-)K^{*+})} \tag{5.30}$$

$$R_{\pi\pi} = R_{CP\pm} = \frac{\Gamma(B^- \to D(\pi^+\pi^-)K^{*-}) + \Gamma(B^+ \to D(\pi^+\pi^-)K^{*+})}{\Gamma(B^- \to D(K^-\pi^+)K^{*-}) + \Gamma(B^+ \to D(K^+\pi^-)K^{*+})} \times \frac{\mathcal{B}(D^0 \to K^-\pi^+)}{\mathcal{B}(D^0 \to \pi^+\pi^-)} \tag{5.31}$$

The yield ratios after the efficiency corrections can be written

$$R_{\pi\pi} = R_{CP\pm} = \frac{N(B^- \to D(\pi^+\pi^-)K^{*-})}{N(B^- \to D(K^-\pi^+)K^{*-})} \times \frac{\mathcal{B}(D^0 \to K^-\pi^+)}{\mathcal{B}(D^0 \to \pi^+\pi^-)} \\ \times \frac{\epsilon_{sel}(K\pi)}{\epsilon_{sel}(\pi\pi)} \times \frac{\epsilon_{pid}(K\pi)}{\epsilon_{pid}(\pi\pi)} \tag{5.32}$$

The results for $D^0 \to \pi\pi$ are determined

- $A_{\pi\pi} = A_{CP\pm} = -25.8 \pm 52.5 \pm 0.3$

- $R_{\pi\pi} = R_{CP\pm} = 0.696 \pm 0.335 \pm 0.040$

where the first uncertainty indicate statistical and the second is systematic. The combined results of the $KK$ and $\pi\pi$ for the $A_{CP\pm}$ and $R_{CP\pm}$ for the $B^\pm \to D^0 K^{*\pm}$ are determined using the BLUE method [163] in order to account for systematic uncertainties common to the two statistically independent measurement.

- $A_{CP\pm}$ (Combined) $= 8.4 \pm 8.3 \pm 0.3$

- $R_{CP\pm}$ (Combined) $= 1.326 \pm 0.121 \pm 0.031$

where the first uncertainty is for statistical and the second uncertainty for the systematic.

Table 5.26 displays the results for the asymmetry and the ratio for the CP observables and following this we also perform the combination of two analysis with the results of the $K^{*-} \to K^0_\text{S}\pi^-$ [[59], [15]] and our $K^-\pi^0$ analysis.

| Observables GLW modes | $K^{*-}(K^-\pi^0)$ | $K^{*-}(K_s\pi^-)$ | $K^-\pi^0 + K^0_\text{S}\pi^-$ Combination |
|---|---|---|---|
| $A_{KK}$ | $9.3 \pm 8.4 \pm 0.9$ | $6.0 \pm 7.0 \pm 1.0$ | - |
| $A_{\pi\pi}$ | $-25.8 \pm 52.5 \pm 0.3$ | $15 \pm 13 \pm 1$ | - |
| $R_{KK}$ | $1.420 \pm 0.129 \pm 0.051$ | $1.22 \pm 0.09 \pm 0.01$ | - |
| $R_{\pi\pi}$ | $0.696 \pm 0.335 \pm 0.040$ | $1.08 \pm 0.14 \pm 0.03$ | - |
| $A_{CP\pm}$(Combined) | $8.4 \pm 8.3 \pm 0.3$ | $8.0 \pm 6.0 \pm 1.0$ | $8.2 \pm 4.9 \pm 0.3$ |
| $R_{CP\pm}$(Combined) | $1.326 \pm 0.121 \pm 0.031$ | $1.18 \pm 0.08 \pm 0.02$ | $1.224 \pm 0.067 \pm 0.017$ |

Table 5.26: Observables used in the analysis for $B^- \to D^0 K^{*-}(K^-\pi^0)$ and $B^- \to D^0 K^{*-}(K_s\pi^-)$ [15], where $D^0$ decays to CP-even eigenstates $KK$ and $\pi\pi$, and the combination of both analysis is given. The uncertainties are statistical and systematic are included, respectively. Asymmetry is given in %.

And it can be seen that the asymmetry for $KK$ and $\pi\pi$ in our analysis is compatible and in the same direction with the published reference analysis of $B^- \to D^0 K^{*-}$ decay, where $K^{*-}$ decays to $K^0_\text{S}\pi^-$ [59].

### 5.9.1.2   Observables with ADS method

The angle $\gamma$ is determined by the ADS method through the Doubly Cabibbo suppressed mode $D^0 \to K^+\pi^-$ mode and Cabibbo favoured mode $\bar{D}^0 \to K^+\pi^-$.

The asymmetry for the $D^0$ decays to favoured $K^-\pi^+$ mode is given by

$$A_{K\pi} = \frac{\Gamma(B^- \to D(K^+\pi^-)K^{*-}) - \Gamma(B^+ \to D(K^-\pi^+)K^{*+})}{\Gamma(B^- \to D(K^+\pi^-)K^{*-}) + \Gamma(B^+ \to D(K^-\pi^+)K^{*+})} \quad (5.33)$$

The ratio for the ADS mode to the favoured mode for $B^+$ and $B^-$

$$R^+_{K\pi} = \frac{\Gamma(B^+ \to D(K^-\pi^+)K^{*+})}{\Gamma(B^+ \to D(K^+\pi^-)K^{*+})} \quad (5.34)$$

$$R^-_{K\pi} = \frac{\Gamma(B^- \to D(K^+\pi^-)K^{*-})}{\Gamma(B^- \to D(K^-\pi^+)K^{*-})} \quad (5.35)$$

The results for the CP observables for $D^0 \to K\pi$

- $A_{K\pi} = -2.3 \pm 3.1 \pm 0.3$

where the statistical and the systematic uncertainties are given respectively. This number is for the $D^0 \to K\pi$ (RS) and it can be seen that as this is not sensitive to the direct CP violation at that precision $A(K\pi)$ is really compatible with zero as we expect

and so that our method is introducing no bias, while it was almost 2 $\sigma$ as from the initial fit for $B^-$ and $B^+$ candidates displayed in Figure 5.31 and this was coming from the production and detection asymmetry as well that we corrected now. The asymmetry obtained perfectly compatible with zero. The systematics are basically factor of 10 below the statistics.

The results for the $A_{ADS}$ and $R_{ADS}$ are determined

$$A_{ADS} = \frac{(R_{K\pi}^- - R_{K\pi}^+)}{(R_{K\pi}^- + R_{K\pi}^+)} \tag{5.36}$$

$$R_{ADS} = \frac{(R_{K\pi}^- + R_{K\pi}^+)}{2} \tag{5.37}$$

- $A_{ADS} = -100.0 \pm 20.8 \pm 0.1$

- $R_{ADS} = 2.908 \pm 1.186 \pm 0.240$

where statistical and systematic uncertainties are given respectively. Here one can see that the asymmetry is (-100$\pm$21$\pm$0.1)% and it is quite compatible with the 2017 reference publication [59], which provides the asymmetry $A_{ADS} = -81 \pm 17 \pm 4$. Table 5.27 gives the CP results for the analysis and it shows the combined measurements for the $K^+\pi^-$ and $K^-\pi^+$. The results for the $D^0 \to K_s^0\pi^-$ analysis and the combined results for the $K^-\pi$ and $K_s^0\pi^-$ are also included.

| Observable | $K^{*-}(K^-\pi^0)$ | $K^{*-}(K_s\pi^-)$ | $K^-\pi^0 + K_s^0\pi^-$ Combination |
|---|---|---|---|
| $A_{K\pi}$ | $-2.3 \pm 3.1 \pm 0.3$ | $-0.4 \pm 2.3 \pm 0.8$ | - |
| $R_{K\pi}$ | $0.000 \pm 0.003 \pm 0.159$ | $0.020 \pm 0.006 \pm 0.001$ | - |
| $A_{ADS}$ | $-100.0 \pm 20.8 \pm 0.1$ | $-81.0 \pm 17.0 \pm 4.0$ | $-88.2 \pm 13.14 \pm 0.1$ |
| $R_{ADS}$ | $2.908 \pm 1.186 \pm 0.240$ | $0.011 \pm 0.004 \pm 0.001$ | $0.011 \pm 0.004 \pm 0.001$ |

Table 5.27: Observables used in the analysis for $B^- \to DK^{*-}(K^-\pi^0)$ and $B^- \to DK^{*-}(K_s\pi^-)$ [15] where $D$ decays to $K\pi$ (RS), $K\pi$ (WS), and the combination of both analysis are given. The statistical and systematic uncertainties are included, respectively. Asymmetry is given in %.

It can be seen that the results from $K^{*-}(K^-\pi^0)$ analysis are competitive with the published reference $K^{*-}(K_s\pi^-)$ analysis [59].

## 5.10    Extraction of $\gamma$ CKM angle

After having the results for the CP observables which has been explained in the previous Section 5.9, we determine the constraint on the $\gamma$ angle from the $B^- \to D^0 K^{*-}$ decay mode, where $D^0$ decays to GLW modes: $KK$, $\pi\pi$ and ADS modes: $K\pi$ (RS) and $K\pi$ (WS) with the $K^{*-} \to K^-\pi^0$ and also the related physics parameters: $r_B$ and $\delta_B$. The constraint on $\gamma$ angle is obtained from the analysis of the decay mode $B^- \to D^0 K^{*-}$, where $D^0$ decays to $KK$, $\pi\pi$, $K\pi$ (RS) and $K\pi$ (WS) with the $K^{*-}$ modes: $K^-\pi^0$. And we also show the study here for the published reference mode $B^- \to D^0 K^{*-}$, where $K^{*-}$ decays to $K_S^0\pi$ [59]. The purpose here is to make the comparison between the two analysis and to show the validity of our measurement from the reference mode $K_S^0\pi^-$. For this study, in order to extract the $\gamma$ and the physics parameters, we use the CKMfitter [162] which is based on a global $\chi 2$ minimisation of a system of equation that relates the observables and the physics parameters. The results obtained from ADS and GLW modes are combined for both analysis $B^- \to D^0 K^{*-}$, where $K^{*-}$ decays to $K^-\pi^0$ (red dashed line) and $K_S^0\pi^-$ (blue dashed line) and the combination is displayed in Figure 5.54 with the green curve and the current LHCb $\gamma$ combination with the blue straight line to be compared is shown on the same plot. The combination is obtained from both analysis with the $K^-\pi^0$ and $K_S^0\pi^-$ give a constraint at 2 $\sigma$ while it was not the case with the $K_S^0\pi^-$ alone. The value for the angle $\gamma$ is determined to be $\gamma=(33^{+24}_{-36})^\circ$ for $K^-\pi^0$ and for $K_S^0\pi^-$, it is $\gamma=(46^{+22}_{-16})^\circ$. The combined value from this two analysis is to be $\gamma=(45^{+14}_{-11})^\circ$. It can be seen that the results are for $\gamma$ from the two analysis are compatible. And the related physics parameters $\delta_B$ and $r_B$ are displayed in Figure 5.55 for both analysis with the $K^-\pi^0$ (red dashed line) and $K_S^0\pi^-$ and their combination. The fitted physics parameters are determined to be $r_B=7.8^{+3.6}_{-2.7}$, $\delta_B =(26^{+27}_{-26})^\circ$ for $K^-\pi^0$. And for the $K_S^0\pi^-$ $r_B=11.1^{+2.3}_{-2.4}$, $\delta_B =(38^{+23}_{-19})^\circ$, for which one can see that the values for the physics parameters as well from the two analysis are compatible and the combined values from the two analysis are obtained as for $r_B=10.3^{+1.8}_{-1.7}$, $\delta_B =(37^{+15}_{-13})^\circ$.
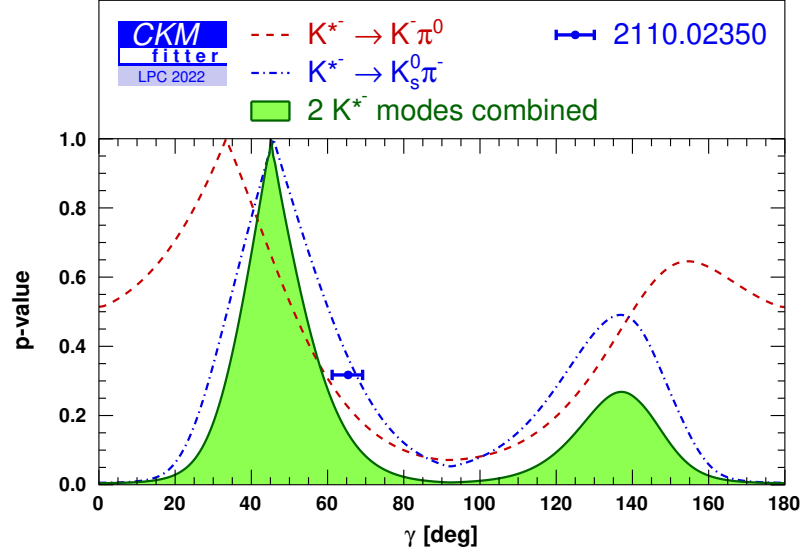
Figure 5.54: Profile of the p-value of the global $\chi 2$ fit to $\gamma$ angle from the analysis of $B^{\pm} \to D^0 K^{*\pm}[K_s^0 \pi^-]$ in blue dashed line and the $B^{\pm} \to D^0 K^{*\pm}[K^{\pm}\pi^0]$ is in red dashed line are obtained with the full LHCb dataset Run 1 and Run 2. Constraint on $\gamma$ is given in degree. The combination for both analysis is given with the green curve. The LHCb $\gamma$ combination is also shown with the horizontal blue straight line [2]. For the fitted parameters: $\gamma=(33^{+24}_{-36})°$ for $K^-\pi^0$ and for $K_s^0\pi^-$, it is $\gamma=(46^{+22}_{-16})°$. The combined *gamma* result from the $K^-\pi^0$ and $K_s^0\pi^-$ is determined as $\gamma=(45^{+14}_{-11})°$. For the LHCb combination, $\gamma=(65.4^{+3.8}_{-4.2})°$ and for the CKMfitter $\gamma=(65.5^{+1.1}_{-2.5})°$.
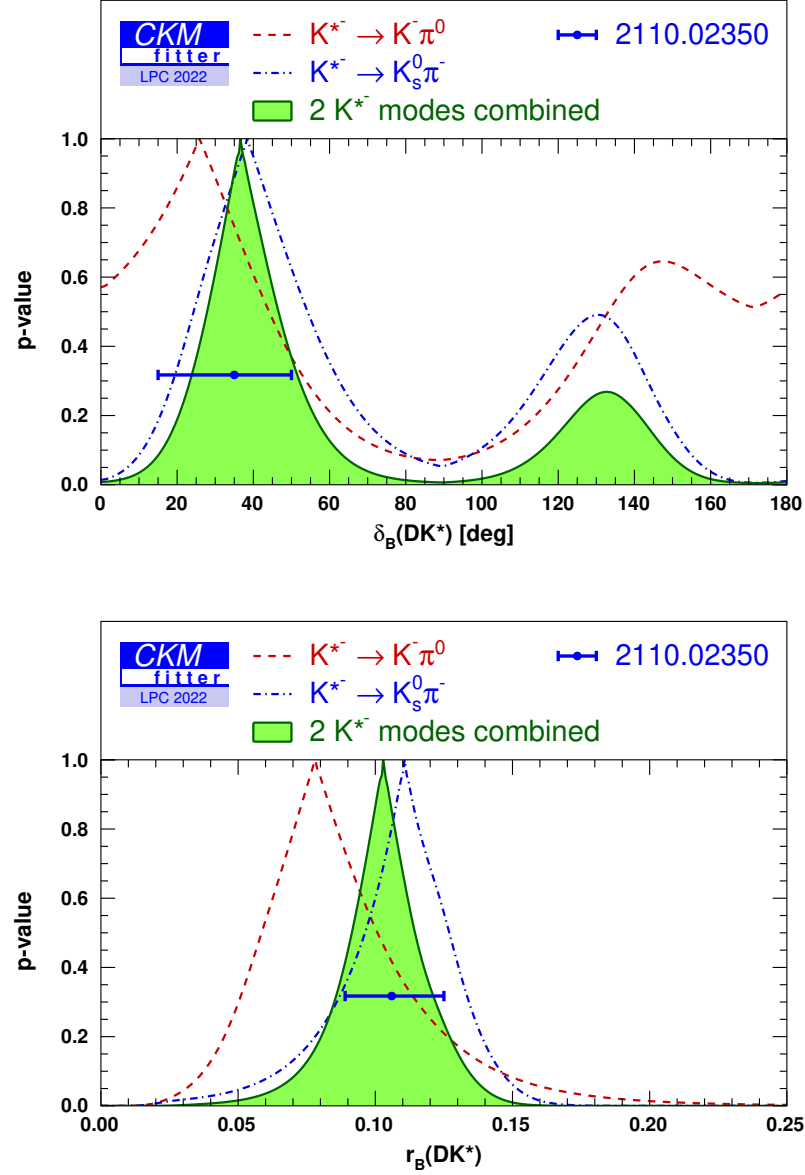
Figure 5.55: Profile of the p-value distribution of $\delta_B$(top) and $r_B$(bottom). Blue dashed line is for the $K^{*-} \to K^0_s \pi^-$ and red dashed line is for the $K^{*-} \to K^- \pi^0$. The combination of these two modes given with the green color. The LHCb $\gamma$ combination is also shown with the horizontal blue straight line [2]. The fitted paramaters: $r_B = 7.8^{+3.6}_{-2.7}$, $\delta_B = (26^{+27}_{-26})°$ for $K^- \pi^0$ and $r_B = 11.1^{+2.3}_{-2.4}$, $\delta_B = (38^{+23}_{-19})°$ for $K^0_s \pi^-$. The combined result for the fitted parameters from the $K^- \pi^0$ and $K^0_s \pi^-$: $r_B = 10.3^{+1.8}_{-1.7}$, $\delta_B = (37^{+15}_{-13})°$.

The physics parameters determined through the observables are provided in Table 5.28 includes the results for the analysis of $K^{*-} \to K_s\pi^-$, the prediction from 2021 CKMfitter of $\gamma$ from the global coherence fit [31] and the LHCb combination [2]. The HFLAV combinations for $r_B$ and $\delta_B$ are also given in Table 5.29.

| $B^- \to DK^{*-}$ | $K^{*-} \to K_s\pi^-$ | $K^{*-} \to K^-\pi^0$ | All ($K^{*-}$ modes combined) | **CKMfitter 2021** | **LHCb 2021** |
|---|---|---|---|---|---|
| $\gamma(°)$ | $46^{+22}_{-16}$ | $33^{+24}_{-36}$ | $45^{+14}_{-11}$ | $65.5^{+1.1}_{-2.5}$ | $65.4^{+3.8}_{-4.2}$ |
| $r_B$ | $11.1^{+2.3}_{-2.4}$ | $7.8^{+3.6}_{-2.7}$ | $10.3^{+1.8}_{-1.7}$ | | |
| $\delta_B(°)$ | $38^{+23}_{-19}$ | $26^{+27}_{-26}$ | $37^{+15}_{-13}$ | | |

Table 5.28: The values of the physics parameters are given for the both analysis of $B^- \to D^0K^{*-}[K_S^0\pi^-]$ and $B^- \to D^0K^{*-}[K^-\pi^0]$. The results for the combination of both and the results for the the 2021 CKMfitter with the LHCb combination are presented for the comparison.

| Parameter | Value |
|---|---|
| $\gamma \equiv \phi_3$ | $(65.9^{+3.3}_{-3.5})°$ [148] |
| $r_B^{DK^+}$ | $0.0994 \pm 0.0026$ |
| $\delta_B^{DK^+}$ | $(127.7^{+3.6}_{-3.9})°$ |
| $r_B^{D^*K^+}$ | $314.8^{+7.9}_{-9.9}$ |
| $\delta_B^{D^*K^+}$ | $(127.7^{+3.6}_{-3.9})°$ |
| $r_B^{DK^{*+}}$ | $0.101^{+0.016}_{-0.034}$ |
| $\delta_B^{DK^{*+}}$ | $(48^{+59}_{-16})°$ |
| $r_B^{DK^{*0}}$ | $0.257^{+0.021}_{-0.023}$ |
| $\delta_B^{DK^{*0}}$ | $(194.1^{+9.6}_{-8.8})°$ |

Table 5.29: HFLAV results for $r_B$ and $\delta_B$

Figures 5.56 and 5.57 display two-dimension contour plots of the $\gamma$ angle as a function of the $\delta_B$ and $r_B$ for two analysis of $B^- \to DK^{*-}$ decay with $K^-\pi^0$ and $K_S^0\pi^-$. Blue dashed line represents the analysis with the $K^{*-} \to K_S^0\pi^-$ while the red dashed one is for the $K^{*-} \to K^-\pi^0$ decay. The combination is provided by the green zones (light and dark) correspond to the $1\sigma$ and $2\sigma$ level. The LHCb $\gamma$ combination is also provided on the same distribution for the comparison. One can see that we improve the picture and the results for analysis of $K^-\pi^0$ (red dashed/straight line) decay is quite compatible with the $K_S^0\pi^-$ (blue dashed/straight line) analysis [59] at $1~\sigma$ and $2~\sigma$ level. The precision is also improved by having the $K^-\pi^0$ analysis which is statistically and technically independent.
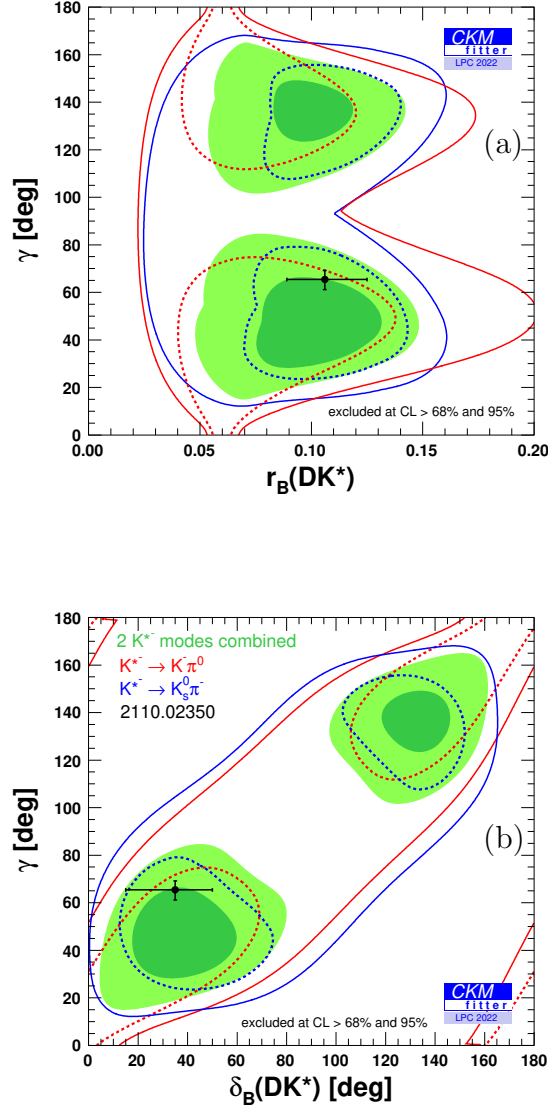
Figure 5.56: Two-dimension contour plots of the angle $\gamma$ as a function of the $r_B$(a) and $\delta_B$(in degree)(b). Red dashed contour displays the $K^{*-} \rightarrow K^-\pi^0$ while blue dashed contour is for the $K^{*-} \rightarrow K^0_s\pi^-$. Dashed lines are for 1 $\sigma$ and straight lines for 2 $\sigma$. The combination of two modes is given with the dark and light green contours. The contours displays two-dimensional boundaries corresponding to 68.3% CL (1 $\sigma$) and 95.4% CL (2 $\sigma$). LHCb $\gamma$ combination [2] is shown with the with the straight black line.
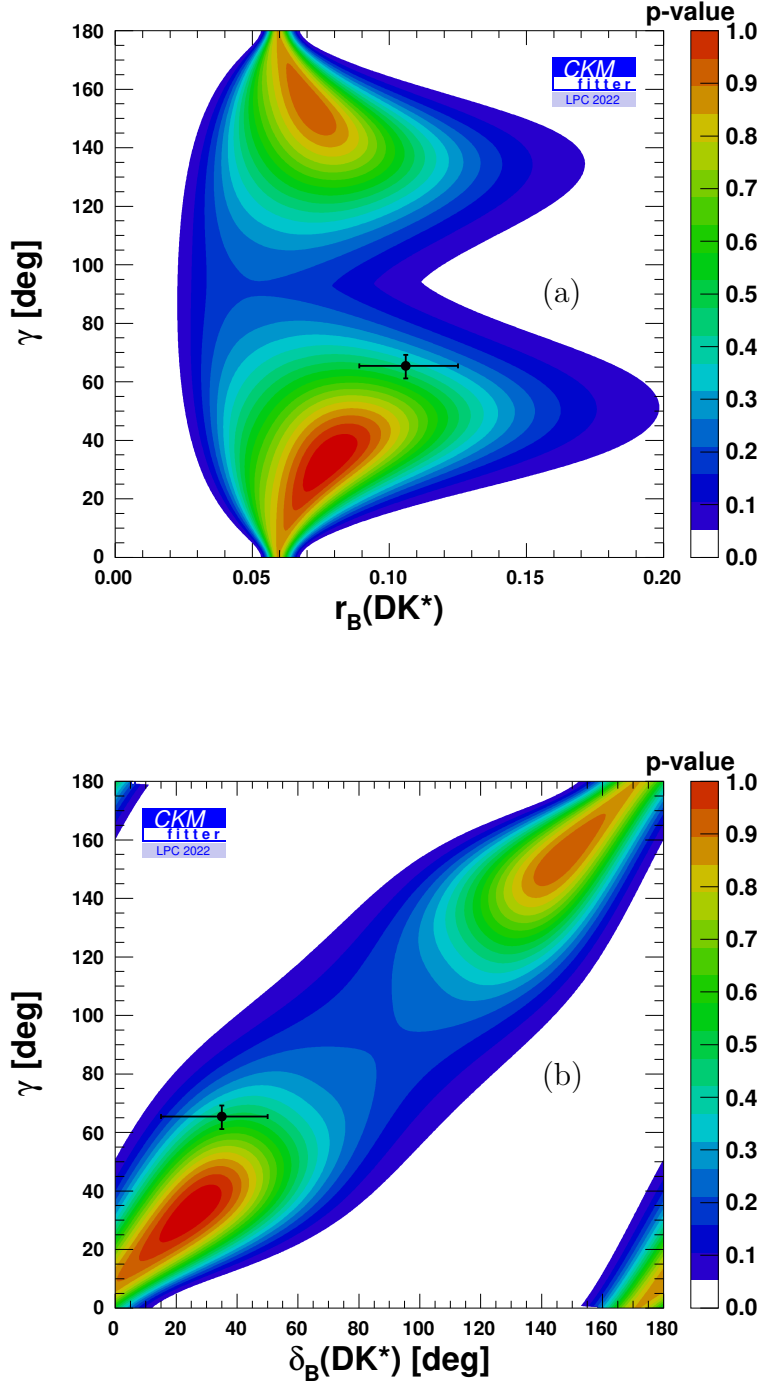
Figure 5.57: Two-dimension contour plots of the fitted physics parameters $r_B$ (a) and $\delta_B$ (b) as a function of $\gamma$. LHCb $\gamma$ combination [2] is shown with the straight black line.

# 5.11 Conclusion for $B^{\pm} \to \tilde{D}^0 K^{*\pm}$

We have performed a study of CP violation with the $B^{\pm} \to \tilde{D}^0 K^{*\pm}$ mode, where the $D^0$ meson is reconstructed in two body decays with the ADS modes: $K\pi$ (RS), $K\pi$ (WS), and the GLW modes: $KK$ and $\pi\pi$ with the $K^{*\pm}$ decays to $K^-\pi^0$ using the full LHCb dataset of Run 1 (2011-2012)and Run 2 (2015-2018). This study based on the another analysis with the same decay with $K^{*\pm}$ decays to $K_{\text{S}}^0\pi^-$ has been studied and published by the LHCb collaboration using Run 1 and Run 2 (only 2015-2016) dataset [59]. We take this reference analysis for the comparison to validate our analysis. CP observables (ADS/GLW) are measured which provides the asymmetry and the ratio of the yields. The results are obtained as

- $A(K\pi) = -2.3 \pm 3.1 \pm 0.3$,

- $A_{\pi\pi} = -25.8 \pm 52.5 \pm 0.3$,

- $A_{KK} = 9.3 \pm 8.4 \pm 0.9$,

- $R_{\pi\pi} = 0.696 \pm 0.335 \pm 0.040$,

- $R_{KK} = 1.420 \pm 0.129 \pm 0.051$

where the first uncertainty is statistical and the second is systematic. The results are found to be compatible with the reference published analysis by LHCb [59]. These results combined by the global $\chi 2$ minimisation to obtain the CKM angle $\gamma$ and the relative physics parameters $r_B$ and $\delta_B$

$$\gamma = (33^{+24}_{-36})^{\circ}$$

$$r_B = 7.8^{+3.6}_{-2.7}$$

$$\delta_B = (26^{+27}_{-26})^{\circ}$$

The results presented in this thesis show that the analysis of $B^{\pm} \to \tilde{D}^0 K^{*\pm}$ decay mode is quite competitive with the published reference LHCb analysis results [59]. This decay mode will help to improve the precision on the CKM $\gamma$ significantly. Direct measurements for the CKM $\gamma$ angle are one of the most important test of the CP violation in the SM and any inconsistency observed between the direct and the indirect measurements will provide the evidence of new physics Beyond the Standard Model.

# Appendices

# A Formalism to determine the CKM angle $\gamma$ for $B_S^0 \to \tilde{D}^{(*)0}\phi$

In this part of the appendix, the formalism that we used for the determination of the angle $\gamma$ from time-integrated untagged measurement of $B_s^0 \to \tilde{D}^{(*)0}\phi$ are provided.

Following the formalism introduced in [5], we define the amplitudes:

$$A(B_s^0 \to \overline{D}^{(*)0}\phi) = A_B, \tag{A.1}$$

$$A(B_s^0 \to D^{(*)0}\phi) = A_B r_B^{(*)} e^{i(\delta_B^{(*)}+\gamma)}, \tag{A.2}$$

where $A_B^{(*)}$ and $r_B^{(*)}$ are the magnitude of the $B_s^0$ decay amplitude and the amplitude magnitude ratio between the suppressed over the favoured $B_s^0$ decay modes, respectively, while $\delta_B^{(*)}$ and $\gamma$ are the strong and weak phases, respectively. Neglecting mixing and $CP$ violation in $D$ decays (see for example [164, 165]), the amplitudes into the final state $f$ (denoted below as $[f]_D$) and its $CP$ conjugate $\bar{f}$ are defined as

$$A(\overline{D}^0 \to f) = A(D^0 \to \bar{f}) = A_f, \tag{A.3}$$

$$A(D^0 \to f) = A(\overline{D}^0 \to \bar{f}) = A_f r_D^f e^{i\delta_D^f}, \tag{A.4}$$

where $\delta_D^f$ and $r_D^f$ are the strong phase difference and relative magnitude, respectively, between the $D^0 \to f$ and the $\overline{D}^0 \to f$ decay amplitudes.

The amplitudes of the full decay chains are given by:

$$A_{Bf} \equiv A(B_s^0 \to [f]_{D^{(*)}}\phi) = A_B A_f \left[1 + r_B^{(*)} r_D^f e^{i(\delta_B^{(*)}+\delta_D^f+\gamma)}\right], \tag{A.5}$$

$$A_{B\bar{f}} \equiv A(B_s^0 \to [\bar{f}]_{D^{(*)}}\phi) = A_B A_f \left[r_B^{(*)} e^{i(\delta_B^{(*)}+\gamma)} + r_D^f e^{i\delta_D^f}\right]. \tag{A.6}$$

The amplitudes for the $CP$-conjugate decays are given by changing the sign of the weak phase $\gamma$:

$$\bar{A}_{Bf} \equiv A(\overline{B}_s^0 \to [f]_{D^{(*)}}\phi) = A_B A_f \left[r_B^{(*)} e^{i(\delta_B^{(*)}-\gamma)} + r_D^f e^{i\delta_D^f}\right], \tag{A.7}$$

$$\bar{A}_{B\bar{f}} \equiv A(\overline{B}_s^0 \to [\bar{f}]_{D^{(*)}}\phi) = A_B A_f \left[1 + r_B^{(*)} r_D^f e^{i(\delta_B^{(*)}+\delta_D^f-\gamma)}\right]. \tag{A.8}$$

Using the standard notations:

$$\tau = \Gamma_s t, \quad \Gamma_s = \frac{\Gamma_L + \Gamma_H}{2}, \quad \Delta\Gamma_s = \Gamma_L - \Gamma_H, \quad y = \frac{\Delta\Gamma_s}{2\Gamma_s}, \quad \lambda_f = \frac{q}{p}\frac{\bar{A}_{Bf}}{A_{Bf}},$$

and assuming $|q/p| = 1$ ($|q/p| = 1.0003 \pm 0.0014$ [166]), the untagged decay rate for the decay $B_s^0/\bar{B}_s^0 \to [f]_{D^{(*)}}\phi$ is given by (Eq. (10) of [167]):

$$\frac{d\Gamma(B_s^0(\tau) \to [f]_{D^{(*)}}\phi)}{d\tau} + \frac{d\Gamma(\bar{B}_s^0(\tau) \to [f]_{D^{(*)}}\phi)}{d\tau} \propto e^{-\tau}|A_{Bf}|^2 \times$$
$$\left[(1 + |\lambda_f|^2)\cosh(y\tau) - 2\mathrm{Re}(\lambda_f)\sinh(y\tau)\right]. \quad (A.9)$$

## A.1   Time acceptance

Experimentally, due to trigger and selection requirements and to inefficiencies in the reconstruction, the decay time distribution is affected by acceptance effects. The acceptance correction has been estimated from pseudoexperiments based on a related publication by the LHCb collaboration [168]. It is described by an empirical acceptance function:

$$\varepsilon_{ta}(\tau) = \frac{(\alpha\tau)^\beta}{1 + (\alpha\tau)^\beta}(1 - \xi\tau), \quad (A.10)$$

with $\alpha = 1.5$, $\beta = 2.5$ and $\xi = 0.01$.

Taking into account this effect, the time-integrated untagged decay rate is

$$\Gamma(\tilde{B}_s^0 \to [f]_{D^{(*)}}\phi)$$
$$= \int_0^\infty \left[\frac{d\Gamma(B_s^0(\tau) \to [f]_{D^{(*)}}\phi)}{d\tau}\right.$$
$$+\left.\frac{d\Gamma(\bar{B}_s^0(\tau) \to [f]_{D^{(*)}}\phi)}{d\tau}\right]\varepsilon_{ta}(\tau)d\tau. \quad (A.11)$$

Defining the function

$$g(x) = \int_0^\infty \frac{e^{-x\tau}(1 + \xi\tau(\alpha\tau)^\beta)}{1 + (\alpha\tau)^\beta}d\tau, \quad (A.12)$$

and using Eq. (A.9), one gets

$$\Gamma(B_s^0 \to [f]_D\phi) \propto |A_{Bf}|^2 \left[(1 + |\lambda_f|^2)\mathcal{A} - 2y\mathrm{Re}(\lambda_f)\mathcal{B}\right], \quad (A.13)$$

where $A = 1 - (f(1-y) + f(1+y))/2$ and $B = 1 - (f(1-y) - f(1+y))/2y$. With $y = 0.064 \pm 0.0045$ for the $B_s^0$ meson [148], one gets $A = 0.488 \pm 0.005$ and $B = 0.773 \pm 0.008$. Examples of decay-time acceptance distributions are displayed in Figure A.1.
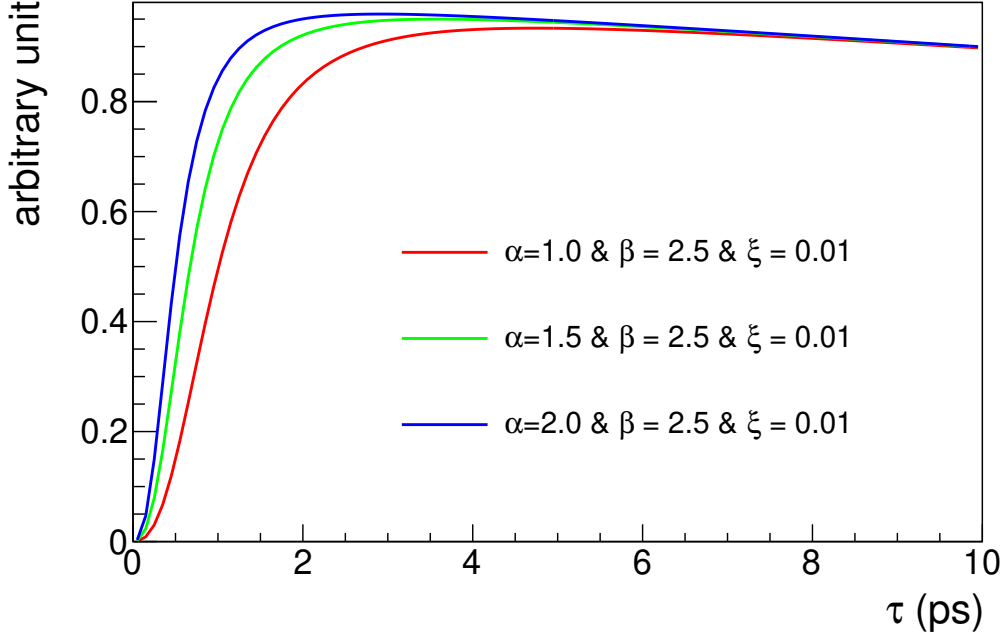
Figure A.1: Examples of decay-time acceptance distributions for three different sets of parameters $\alpha$, $\beta$, and $\xi$ (nominal in green).

## A.2 Observables for $D^0$ decays

The $D$-meson decays are reconstructed in quasi flavour-specific modes: $f^-(\equiv f) = K^-\pi^+$, $K^-3\pi$, $K^-\pi^+\pi^0$, and their $CP$-conjugate modes: $f^+(\equiv \bar{f}) = K^+\pi^-$, $K^+3\pi$, $K^+\pi^-\pi^0$ as well as $CP$-eigenstate modes: $f_{CP} = K^+K^-$, $\pi^+\pi^-$.

In the following, we introduce the weak phase $\beta_s$ is defined as $\beta_s = \arg\left(-\frac{V_{ts}V_{tb}^*}{V_{cs}V_{cb}^*}\right)$. From Eqs. (A.5), (A.7), (A.13) and with $\lambda_f = e^{2i\beta_s}\frac{\bar{A}_{Bf}}{A_{Bf}}$, for a given number of untagged $B_s^0$ mesons produced in the $pp$ collisions at the LHCb interaction point, $N(B_s^0)$, we can compute the number of $B_s^0 \to \overline{D}^0\phi$ decays with the $D$ meson decaying into the final state $f^-$. For the reference decay mode $f^- \equiv K^-\pi^+$ we obtain

$$
\begin{aligned}
N\left(B_s^0 \to \left[K^-\pi^+\right]_D \left[K^+K^-\right]_\phi\right) = \\
C_{K\pi}\Big[ -2\mathcal{B}yr_B\cos\left(\delta_B + 2\beta_s - \gamma\right) \\
+ \mathcal{A}\left(1 + r_B{}^2 + 4r_Br_D^{K\pi}\cos\delta_B\cos\left(\delta_D^{K\pi} + \gamma\right)\right)\Big], \quad \text{(A.14)}
\end{aligned}
$$

where, the terms proportional to $(r_D^{K\pi})^2 \ll 1$ and $yr_D^{K\pi} \ll 1$ have been neglected ($r_D^{K\pi} =$

$5.90^{+0.34}_{-0.25}$ % [148]). The best approximation for the scale factor $C_{K\pi}$ is

$$C_{K\pi} = N(B_s^0) \times \varepsilon(B_s^0 \to \left[K^-\pi^+\right]_D \left[K^+K^-\right]_\phi)$$
$$\times Br(B_s^0 \to \left[K^-\pi^+\right]_D \left[K^+K^-\right]_\phi), \quad \text{(A.15)}$$

where, $\varepsilon(B_s^0 \to \left[K^-\pi^+\right]_D \left[K^+K^-\right]_\phi)$ is the global detection efficiency of this decay mode, and $Br(B_s^0 \to \left[K^-\pi^+\right]_D \left[K^+K^-\right]_\phi)$ its branching fraction. The value of the scale factor $C_{K\pi}$ is estimated from the LHCb Run 1 data [9], the average $f_s/f_d$ of the $b$-hadron production fraction ratio measured by LHCb [169] and the different branching fractions [18].

For a better numerical behaviour, we use the Cartesian coordinates parametrisation

$$x_\pm^{(*)} = r_B^{(*)} \cos(\delta_B^{(*)} \pm \gamma) \quad \text{and} \quad y_\pm^{(*)} = r_B^{(*)} \sin(\delta_B^{(*)} \pm \gamma). \quad \text{(A.16)}$$

Then, Eq (A.14) becomes

$$N\left(B_s^0 \to \left[K^-\pi^+\right]_D \left[K^+K^-\right]_\phi\right) =$$
$$C_{K\pi}\Big[ -2\mathcal{B}y\left[x_- \cos(2\beta_s) - y_- \sin(2\beta_s)\right] +$$
$$\mathcal{A}\Big(1 + x_-^2 + y_-^2 +$$
$$2r_D^{K\pi}[(x_+ + x_-)\cos\delta_D^{K\pi} - (y_+ - y_-)\sin\delta_D^{K\pi}]\Big)\Big]. \quad \text{(A.17)}$$

For three and four body final states $K3\pi$ and $K\pi\pi^0$, there are multiple interfering amplitudes, therefore their amplitudes and phases $\delta_D^f$ vary across the decay phase space. However, an analysis which integrates over the phase space can be performed in a very similar way to two body decays with the inclusion of an additional parameter, the so-called coherence factor $R_D^f$ which has been measured in previous experiments [170]. The strong phase difference $\delta_D^f$ is then treated as an effective phase averaged over all amplitudes. For these modes, we have an expression similar to (A.17)

$$N\left(B_s^0 \to \left[f^-\right]_D \left[K^+K^-\right]_\phi\right) =$$
$$C_{K\pi}F_f\Big[ -2\mathcal{B}y\left[x_- \cos(2\beta_s) - y_- \sin(2\beta_s)\right] +$$
$$\mathcal{A}\Big(1 + x_-^2 + y_-^2$$
$$+ 2r_D^f R_D^f \left[(x_+ + x_-)\cos\delta_D^f - (y_+ - y_-)\sin\delta_D^f\right]\Big)\Big], \quad \text{(A.18)}$$

where $F_f$ is the scale factor of the $f$ decay relative to the $K\pi$ decay and depends on

the ratios of detection efficiencies and branching fractions of the corresponding modes

$$F_f = \frac{C_f}{C_{K\pi}} = \frac{\varepsilon(D \to f)}{\varepsilon(D \to K\pi)} \times$$

$$\frac{[Br(D^0 \to f) + Br(\overline{D}^0 \to f)]}{[Br(D^0 \to K^-\pi^+) + Br(\overline{D}^0 \to K^-\pi^+)]}. \quad (A.19)$$

The value of $F_f$ for the different modes used in this study is determined from LHCb measurements in $B^\pm \to DK^\pm$ and $B^\pm \to D\pi^\pm$ modes, with two or four-body $D$ decays [

The time-integrated untagged decay rate for $B_s^0 \to [\bar{f}]_D \phi$ is given by Eq. (A.13) by substituting $A_{Bf} \to \bar{A}_{B\bar{f}}$ and $\lambda_f \to \bar{\lambda}_{\bar{f}} = \lambda_f^{-1} = e^{-2i\beta_s}(A_{B\bar{f}}/\bar{A}_{B\bar{f}})$ which is equivalent to the change $\beta_s \to -\beta_s$ and $\gamma \to -\gamma$ (i.e. $x_\pm \to x_\mp$ and $y_\pm \to y_\mp$). Therefore, the observables are

$$N\left(B_s^0 \to \left[K^+\pi^-\right]_D \left[K^+K^-\right]_\phi\right) =$$

$$C_{K\pi}\Big[ -2\mathcal{B}y\left[x_+\cos\left(2\beta_s\right) + y_+\sin\left(2\beta_s\right)\right] +$$

$$\mathcal{A}\Big(1 + x_+^2 + y_+^2 +$$

$$2r_D^{K\pi}\left[(x_+ + x_-)\cos\delta_D^{K\pi} + (y_+ - y_-)\sin\delta_D^{K\pi}\right]\Big)\Big], \quad (A.20)$$

and for the modes $f^+ \equiv K^+3\pi$, $K^+\pi^-\pi^0$

$$N\left(B_s^0 \to \left[f^+\right]_D \left[K^+K^-\right]_\phi\right) =$$

$$C_{K\pi}F_f\Big[ -2\mathcal{B}y\left[x_+\cos\left(2\beta_s\right) + y_+\sin\left(2\beta_s\right)\right] +$$

$$\mathcal{A}\Big(1 + x_+^2 + y_+^2 +$$

$$2r_D^f R_f\left[(x_+ + x_-)\cos\delta_D^f + (y_+ - y_-)\sin\delta_D^f\right]\Big)\Big]. \quad (A.21)$$

Obviously, any significant asymmetries on the yield of observable corresponding to Eq. A.17 with respect to Eq. A.20, or Eq. A.18 with respect to Eq. A.21, is a clear signature for $CP$ violation.

For the $CP$-eigenstate modes $D \to h^+h^-$ ($h \equiv K, \pi$), we have $r_D = 1$ and $\delta_D = 0$. Following the same approach than for quasi flavour-specific modes, the observables can be written as

$$N\left(B_s^0 \to \left[h^+h^-\right]_D \left[K^+K^-\right]_\phi\right) =$$

$$4C_{K\pi}F_{hh}\Big[\mathcal{A}\left(1 + x_+^2 + y_+^2 + x_+ + x_-\right) -$$

$$\mathcal{B}y\Big((1 + x_+ + x_- + x_+x_- + y_+y_-)\cos\left(2\beta_s\right) +$$

$$(y_+ - y_- + y_+x_- - x_+y_-)\sin\left(2\beta_s\right)\Big)\Big]. \quad (A.22)$$

In analogy with $F_f$, $F_{hh}$ is defined as

$$F_{hh} = \frac{C_{hh}}{C_{K\pi}} = \frac{\varepsilon(D \to hh)}{\varepsilon(D \to K\pi)} \times$$

$$\frac{Br(D^0 \to hh)}{[Br(D^0 \to K^-\pi^+) + Br(\overline{D}^0 \to K^-\pi^+)]} \quad \text{(A.23)}$$

and their values are determined in the same way than $F_f$.

For the modes $K_{\mathrm{S}}^0\pi^+\pi^-$ and $K_{\mathrm{S}}^0K^+K^-$ (*i.e.* $K_{\mathrm{S}}^0hh$) one obtains

$$N\left(B_s^0 \to \left[K_{\mathrm{S}}^0hh\right]_D \left[K^+K^-\right]_\phi\right) = 2C_{K\pi}F_{K_{\mathrm{S}}^0hh} \times$$

$$\Big[ - \mathcal{B}y\left[(x_+ + x_-)\cos(2\beta_s) + (y_+ - y_-)\sin(2\beta_s)\right] +$$

$$\mathcal{A}\Big(1 + x_-^2 + y_-^2 + 2(x_+ + x_-)$$

$$r_D^{K_{\mathrm{S}}^0hh}(m_+^2, m_-^2)\kappa_D^{K_{\mathrm{S}}^0hh}(m_+^2, m_-^2)\cos\delta_D^{K_{\mathrm{S}}^0hh}(m_+^2, m_-^2)\Big)\Big], \quad \text{(A.24)}$$

where $F_{K_{\mathrm{S}}^0hh}$ is defined as for Eq. A.23. The strong parameters $r_D^{K_{\mathrm{S}}^0hh}(m_+^2, m_-^2)$, $\kappa_D^{K_{\mathrm{S}}^0hh}(m_+^2, m_-^2)$, and $\cos\delta_D^{K_{\mathrm{S}}^0hh}(m_+^2, m_-^2)$ vary over the Dalitz plot $(m_+^2, m_-^2) \equiv (m^2(K_{\mathrm{S}}^0\pi^+), m^2(K_{\mathrm{S}}^0\pi^-))$ and are defined in Section 3 for the Expected yields.

## A.3 Observables for $D^{*0}$ decays

For the $D^{*0}$ decays, we considered the two modes: $D^{*0} \to D^0\pi^0$ and $D^{*0} \to D^0\gamma$, where the $D^0$ mesons are reconstructed, as in the above, in quasi flavour-specific modes: $K\pi$, $K3\pi$, $K\pi\pi^0$ and $CP$-eigenstate modes: $\pi\pi$ and $KK$. As shown in [171], the formalism for the cascade $B_s^0 \to \overline{D}^{*0}\phi$, $\overline{D}^{*0} \to \overline{D}^0\pi^0$ is similar to the $B_s^0 \to \overline{D}^0\phi$. Therefore, the relevant observables can be written similarly to Eqs. (A.17), (A.18), (A.20), (A.21) and (A.22), by substituting $C_{K\pi} \to C_{K\pi,D\pi^0}$, $r_B \to r_B^*$ and $\delta_B \to \delta_B^*$ (*i.e.* $x_\pm \to x_\pm^*$ and $y_\pm \to y_\pm^*$)

$$N\left(B_s^0 \to \left[\left[K^-\pi^+\right]_D \pi^0\right]_{D^*} \left[K^+K^-\right]_\phi\right) =$$

$$C_{K\pi,D\pi^0}\Big[ - 2\mathcal{B}y\left[x_-^* \cos(2\beta_s) - y_-^* \sin(2\beta_s)\right] +$$

$$\mathcal{A}\Big(1 + x_-^{*2} + y_-^{*2} +$$

$$2r_D^{K\pi}\left[(x_+^* + x_-^*)\cos\delta_D^{K\pi} - (y_+^* - y_-^*)\sin\delta_D^{K\pi}\right]\Big)\Big], \quad \text{(A.25)}$$

$$N\left(B_s^0 \to \left[\left[K^+\pi^-\right]_D \pi^0\right]_{D^*} \left[K^+K^-\right]_\phi\right) =$$
$$C_{K\pi,D\pi^0}\Big[ -2\mathcal{B}y\left[x_+^* \cos\left(2\beta_s\right) + y_+^* \sin\left(2\beta_s\right)\right] +$$
$$\mathcal{A}\Big(1 + x_+^{*2} + y_+^{*2} +$$
$$2r_D^{K\pi}\left[\left(x_+^* + x_-^*\right)\cos\delta_D^{K\pi} + \left(y_+^* - y_-^*\right)\sin\delta_D^{K\pi}\right]\Big)\Big], \quad \text{(A.26)}$$

$$N\left(B_s^0 \to \left[\left[f^-\right]_D \pi^0\right]_{D^*} \left[K^+K^-\right]_\phi\right) =$$
$$C_{K\pi,D\pi^0}F_f\Big[ -2\mathcal{B}y\left[x_-^* \cos\left(2\beta_s\right) - y_-^* \sin\left(2\beta_s\right)\right] +$$
$$\mathcal{A}\Big(1 + x_-^{*2} + y_-^{*2} +$$
$$2r_D^f R_f\left[\left(x_+^* + x_-^*\right)\cos\delta_D^f - \left(y_+^* - y_-^*\right)\sin\delta_D^f\right]\Big)\Big], \quad \text{(A.27)}$$

$$N\left(B_s^0 \to \left[\left[f^+\right]_D \pi^0\right]_{D^*} \left[K^+K^-\right]_\phi\right) =$$
$$C_{K\pi,D\pi^0}F_f\Big[ -2\mathcal{B}y\left[x_+^* \cos\left(2\beta_s\right) + y_+^* \sin\left(2\beta_s\right)\right] +$$
$$\mathcal{A}\Big(1 + x_+^{*2} + y_+^{*2} +$$
$$2r_D^f R_f\left[\left(x_+^* + x_-^*\right)\cos\delta_D^f + \left(y_+^* - y_-^*\right)\sin\delta_D^f\right]\Big)\Big], \quad \text{(A.28)}$$

$$N\left(B_s^0 \to \left[\left[h^+h^-\right]_D \pi^0\right]_{D^*} \left[K^+K^-\right]_\phi\right) =$$
$$4C_{K\pi,D\pi^0}F_{hh}\Big[\mathcal{A}\left(1 + x_+^{*2} + y_+^{*2} + x_+^* + x_-^*\right) -$$
$$\mathcal{B}y\Big( \left(1 + x_+^* + x_-^* + x_+^* x_-^* + y_+^* y_-^*\right)\cos\left(2\beta_s\right)$$
$$+ \left(y_+^* - y_-^* + y_+^* x_-^* - x_+^* y_-^*\right)\sin\left(2\beta_s\right)\Big)\Big]. \quad \text{(A.29)}$$

In the case $D^{*0} \to D^0\gamma$, the formalism is very similar, except that there is an effective strong phase shift of $\pi$ with respect to the $D^{*0} \to D^0\pi^0$ [171]. The observables can be derived from the previous ones substituting $C_{K\pi,D\pi^0} \to C_{K\pi,D\gamma}$ and $\delta_B^* \to \delta_B^* + \pi$ (*i.e.* $x_\pm^* \to -x_\pm^*$ and $y_\pm^* \to -y_\pm^*$)

$$N\left(B_s^0 \to \left[\left[K^-\pi^+\right]_D \gamma\right]_{D^*} \left[K^+K^-\right]_\phi\right) =$$
$$C_{K\pi,D\gamma}\Big[2\mathcal{B}y\left[x_-^* \cos\left(2\beta_s\right) - y_-^* \sin\left(2\beta_s\right)\right] +$$
$$\mathcal{A}\Big(1 + x_-^{*2} + y_-^{*2} +$$
$$2r_D^{K\pi}\left[-\left(x_+^* + x_-^*\right)\cos\delta_D^{K\pi} + \left(y_+^* - y_-^*\right)\sin\delta_D^{K\pi}\right]\Big)\Big], \quad \text{(A.30)}$$

$$N\left(B_s^0 \to \left[\left[K^+\pi^-\right]_D \gamma\right]_{D^*} \left[K^+K^-\right]_\phi\right) =$$

$$C_{K\pi,D\gamma}\left[2\mathcal{B}y\left[x_+^* \cos\left(2\beta_s\right) + y_+^* \sin\left(2\beta_s\right)\right] + \right.$$

$$\mathcal{A}\left(1 + x_+^{*2} + y_+^{*2} + \right.$$

$$\left.\left. 2r_D^{K\pi}\left[-\left(x_+^* + x_-^*\right)\cos\delta_D^{K\pi} - \left(y_+^* - y_-^*\right)\sin\delta_D^{K\pi}\right]\right)\right], \quad (A.31)$$

Table A.1: Integrated luminosities and cross-sections of LHCb Run 1 and Run 2 data. The integrated luminosities come from [4] and cross-sections from [[115], [172]]

| Years/Run | $\sqrt{s}$ (TeV) | int. lum.( fb$^{-1}$) | cross section | equiv. 7 TeV data |
|---|---|---|---|---|
| 2011 | 7 | 1.1 | $\sigma_{2011} = 38.9$ μb | 1.1 |
| 2012 | 8 | 2.1 | $1.17 \times \sigma_{2011}$ | 2.4 |
| Run 1 | – | 3.2 | – | 3.5 |
| 2015-2018 (Run 2) | 13 | 5.9 | $2.00 \times \sigma_{2011}$ | 11.8 |
| Total | – | 9.1 | – | 15.3 |

$$N\left(B_s^0 \to \left[\left[f^-\right]_D \gamma\right]_{D^*} \left[K^+K^-\right]_\phi\right) =$$

$$C_{K\pi,D\gamma}F_f\left[2\mathcal{B}y\left[x_-^* \cos\left(2\beta_s\right) - y_-^* \sin\left(2\beta_s\right)\right] + \right.$$

$$\mathcal{A}\left(1 + x_-^{*2} + y_-^{*2} + \right.$$

$$\left.\left. 2r_D^f R_f\left[-\left(x_+^* + x_-^*\right)\cos\delta_D^f + \left(y_+^* - y_-^*\right)\sin\delta_D^f\right]\right)\right], \quad (A.32)$$

$$N\left(B_s^0 \to \left[\left[f^+\right]_D \gamma\right]_{D^*} \left[K^+K^-\right]_\phi\right) =$$

$$C_{K\pi,D\gamma}F_f\left[2\mathcal{B}y\left[x_+^* \cos\left(2\beta_s\right) + y_+^* \sin\left(2\beta_s\right)\right] + \right.$$

$$\mathcal{A}\left(1 + x_+^{*2} + y_+^{*2} + \right.$$

$$\left.\left. 2r_D^f R_f\left[-\left(x_+^* + x_-^*\right)\cos\delta_D^f - \left(y_+^* - y_-^*\right)\sin\delta_D^f\right]\right)\right], \quad (A.33)$$

$$N\left(B_s^0 \to \left[\left[h^+h^-\right]_D \gamma\right]_{D^*} \left[K^+K^-\right]_\phi\right) =$$

$$4C_{K\pi,D\gamma}F_{hh}\left[\mathcal{A}\left(1 + x_+^{*2} + y_+^{*2} - x_+^* - x_-^*\right) - \right.$$

$$\mathcal{B}y\left(\left(1 - x_+^* - x_-^* + x_+^*x_-^* + y_+^*y_-^*\right)\cos\left(2\beta_s\right)\right.$$

$$\left.\left. + \left(-y_+^* + y_-^* + y_+^*x_-^* - x_+^*y_-^*\right)\sin\left(2\beta_s\right)\right)\right]. \quad (A.34)$$

$C_{K\pi,D\pi^0}$ and $C_{K\pi,D\gamma}$ are determined in the same way $C_{K\pi}$, *i.e.* from the LHCb Run 1 data [9] and taking into account the fraction of longitudinal polarization in the decay $B_s^0 \to D^{*0}\phi$: $f_L = (73 \pm 15 \pm 4)\%$ [9] and the branching fractions $Br(\overline{D}^{*0} \to \overline{D}^0\pi^0)$ and $Br(\overline{D}^{*0} \to \overline{D}^0\gamma)$ [18].

# B  Track types

Below different track types reconstructed in the LHCb detector are defined:

- **Velo tracks** have hits only in the VELO. The VELO tracks have crucial importance to use of primary vertex reconstruction.

- **Upstream tracks** which have hits in the VELO and TT. New tracks are reconstructed in new tracker (UT) with high granularity and closer to the beam line.

- **Long tracks** leaves hits in the VELO along with TT and T (T1-T2-T3) tracking stations with excellent spatial and momentum resolution.

- **Downstream tracks** have hits in T and T stations with worse vertex and momentum resolution. These tracks are mainly from the decay of long-lived particles.

- **T tracks** have hits only in the T stations.

# C  Crystal Ball function

$$PDF_{DCB}(x; \alpha, n, \bar{x}, \sigma) \begin{cases} e^{-\frac{(x-\bar{x})^2}{2\sigma^2}}, & for \frac{(x-\bar{x})^2}{2\sigma^2} > -\alpha, \\ A \times (B - \frac{x-\bar{x}}{\sigma})^{-n} & for \frac{(x-\bar{x})^2}{2\sigma^2} \leq -\alpha \end{cases} \tag{C.1}$$

where A and B given by:

$$A = (\frac{n}{|\alpha|}) \times e^{-\frac{1}{2}|\alpha|^2}, \qquad B = \frac{n}{|\alpha|} - |\alpha|. \tag{C.2}$$

The signal probability density function (PDF) (given with Eq. C.3)is parametrized by a double Crystal-Ball function with $(\alpha, n, \bar{x}, \sigma)$ which is set of parameters fitted with the data. The Crystal-ball function consist of a Gaussian core which is described by the mean $\bar{x}$ ($\mu$) and the width $\sigma$. And the other two parameters $\alpha$ and n are to define the Gaussian tail and the shape parameter of the power-law tail respectively. Figure C.1 shows the different Crystal-Ball functions depending on the $\alpha$ and n parameters.

$$PDF_{total} = N \times (nsig[cPDF_{DCB}(x; \alpha, n, \bar{x}, \sigma_1) + (1-c)PDF_{DCB}(x; \alpha, n, \bar{x}, \sigma_2)] + n_{bkg}e^{\lambda m} \tag{C.3}$$

where $n_{sig}$ and $n_{bkg}$ give the number of fitted signal and number of combinatorial background events respectively. $c$ is the fraction of the Crystal Ball function and $\lambda$ is the exponent's tail parameter.
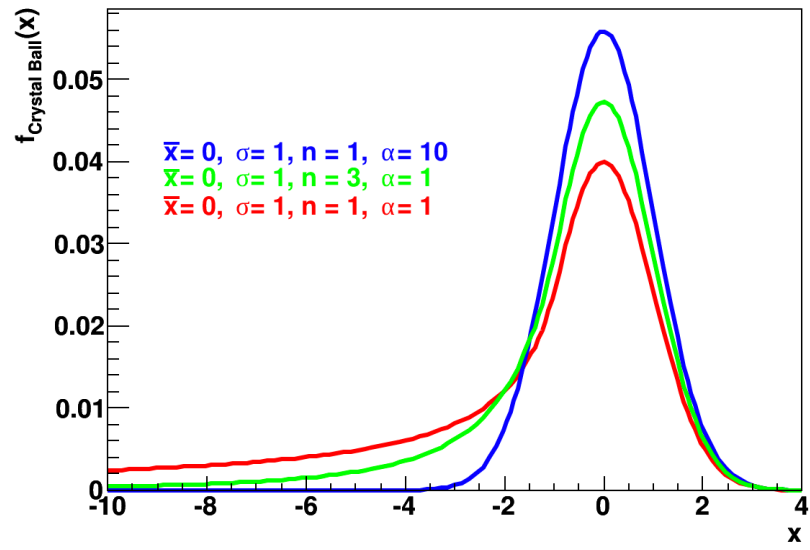
Figure C.1: Examples of different Crystal Ball functions depending on their $\alpha$ and n parameters.

# D  Background Modelling

The HORNSdini shape consists of a Gaussian-like double-peak structure:

$$HORNS(m_{B_s^0}) = \int_a^b (m_{B_s^0} - \frac{a+b}{2})^2 (\frac{1-\xi}{b-a} m_{B_s^0} + \frac{b\xi-a}{b-a}) DG(m_{B_s^0}|\mu,\sigma,f_G) dm_{B_s^0}, \text{(D.1)}$$

where $a$ and $b$ are the kinematic endpoint of the distribution and $\xi$ is the positive, real fraction of the two peak heights. $DG$ function is the double Gaussian function which account for resolution effects. For the mode of $B_s^0 \to \overline{D}^{*0}\phi$ with $\overline{D}^{*0} \to \overline{D}^0\gamma$, with longitudinal polarization, an advanced HORNSdini [173] is used (RooLITTLEHORNSdini) to describe the effect of different efficiencies loss on the two peaks.

The HILLdini model in the mass distribution of $B_s^0$ candidates follows a parabolic curve without any peaking structure. To accommodate for this shape, the HILLdini model consists of a parabolic curve between the kinematic endpoints $a$ & $b$:

$$HILL(m_{B_s^0}) = \int_a^b -(m_{B_s^0} - a)(m_{B_s^0} - b)(\frac{1-\xi}{b-a} m_{B_s^0} + \frac{b\xi-a}{b-a}) DG(m_{B_s^0}|\mu,\sigma,f_G) dm_{B_s^0} \text{(D.2)}$$

This shape is also convoluted with a Gaussian resolution function. The fit to MC the is shown in Fig

Parameters of the RooHORNSdini/RooHILLdini distribution are list below:

- $a$ and $b$: low and upper kinematic endpoints. Fully determined by the specific particle masses in the decay chain;

- $\xi$: relative height of the two peaks, allowing for invariant mass dependent selection effects that remove more of one peak than the other. When $\xi = 1$, both peaks are of equal height. When $\xi > (<)1$, the lower(upper) peak is largest;

- $shift(shift_g$ in RooLITTLEHORNSdini): rigid shift of the entire shape along $m_{B_s^0}$, allowing for differences between the analytical endpoints and the reconstructed endpoints;

- $\sigma$: width of the core resolution Gaussian. The core Gaussian is the Gaussian of narrowest width in the overall double Gaussian convolution;

- $ratio_\sigma$: ratio of wide Gaussian and core Gaussian widths in the double Gaussian resolution function;

- $frac_\sigma$: fractional amount of the main Gaussian in resolution double-Gaussian;

# Bibliography

[1] M. Kobayashi and T. Maskawa, *CP-Violation in the Renormalizable Theory of Weak Interaction*, Progress of Theoretical Physics **49** (1973) 652, online document.

[2] LHCb Collaboration, R. Aaij *et al.*, *Simultaneous determination of CKM angle $\gamma$ and charm mixing parameters*, JHEP **2112** (2021) 141. 32 p, `arXiv:2110.0235`, All figures and tables, along with any supplementary material and additional information, are available at https://cern.ch/lhcbproject/Publications/p/LHCb-PAPER-2021-033.html (LHCb public pages).

[3] LHCb Collaboration, M. Kenzie and M. Withehead, *Update of the LHCb combination of the CKM angle $\gamma$*, CERN-LHCb-CONF-2020-003 (2020), online document.

[4] D. Ao *et al.*, *Study of CKM angle $\gamma$ sensitivity using flavor untagged $B_s^0 \to \tilde{D}^{(*)0}\phi$ decays*, Chinese Physics C **45** (2021) 023003.

[5] M. Gronau *et al.*, *Using untagged $B^0 \to DK_S^0$ to determine $\gamma$*, Physical Review D **69** (2004) .

[6] M. Gronau, Y. Grossman, Z. Surujon, and J. ZupanPhysics Letters B **649** (2007) 61.

[7] LHCb Collaboration, S. Ricciardi, *Measuring the CKM angle $\gamma$ at LHCb using untagged $B_s^0 \to D\phi$ decays*, , CERN-LHCb-PUB-2010-005 (2010), online document.

[8] LHCb Collaboration, R. Aaij *et al.*, *Observation of the decay $B_s^0 \to \overline{D}\phi$*, Physics Letters B (2013) 403.

[9] LHCb Collaboration, R. Aaij *et al.*, *Observation of $B_s^0 \to \overline{D}^{*0}\phi$ and search for $B^0 \to \overline{D}\phi$ decays*, Physical Review D **98** (2018), no. 071103(R) .

[10] M. Gronau and D. London, *How to determine all the angles of the unitarity triangle from $B^0 \to DK_S$ and $B_s^0 \to D\phi$*, Physics Letters B **253** (1991), no. 3 483 .

[11] M. Gronau and D. Wyler, *On determining a weak phase from charged b decay asymmetries*, Physics Letters B **265** (1991), no. 1 172 .

[12] D. Atwood, I. Dunietz, and A. Soni, *Enhanced CP Violation with $B \to K\tilde{D}^0$ Modes and Extraction of the Cabibbo-Kobayashi-Maskawa Angle $\gamma$*, Physical Review Letters **78** (1997) 3257.

[13] D. Atwood, I. Dunietz, and A. Soni, *Improved methods for observing CP violation in $B^{\pm} \to$ KD and measuring the CKM phase $\gamma$*, Phys. Rev. D **63** (2001) 036005.

[14] LHCb Collaboration, R. Aaij *et al.*, *Measurement of CP observables in $B^{\pm} \to DK^{\pm}$ and $B^{\pm} \to D\pi^{\pm}$ with two- and four-body D decays*, Physics Letters B **760** (2016) 117.

[15] A. Nandi, *CP violation measurements using $B\pm \to DK*\pm$ decays at LHCb*, Available at `https://ora.ox.ac.uk/catalog/uuid: 1ebe3ed5-cee1-4157-af24-1374568247fc/download_file?file_format= application%2Fpdfsafe_filename=Oxford_Thesis.pdf`.

[16] *Wikipedia contributors, Fermi–dirac statistics — Wikipedia, the free encyclopedia,* `https://en.wikipedia.org/w/index.php?title=Fermi%E2%80% 93Dirac_statistics&oldid=1093053303`*, 2022. [Online; accessed 3-July-2022].*

[17] *Wikipedia contributors, Bose–einstein statistics — Wikipedia, the free encyclopedia,* `https://en.wikipedia.org/w/index.php?title=Bose%E2%80% 93Einstein_statistics&oldid=1095289619`*, 2022. [Online; accessed 3-July-2022].*

[18] *Particle Data Group, R. L. Workman and Others, Review of Particle Physics, PTEP* **2022** *(2022) 083C01.*

[19] *W. S. Sheldon Stone, B DECAYS, , Available at* `https://cds.cern.ch/ record/257420?ln=en`*.*

[20] *Wikipedia contributors, Cp violation — Wikipedia, the free encyclopedia, 2022. [Online; accessed 23-August-2022].*

[21] *CLEO Collaboration, D. Besson* et al.*, Improved measurements of d meson semileptonic decays to $\pi$ and k mesons, Phys. Rev. D* **80** *(2009) 032005.*

[22] *Belle Collaboration, L. Widhalm* et al.*, Measurement of $D^0 \to \pi l\nu(kl\nu)$ form factors and absolute branching fractions, Phys. Rev. Lett.* **97** *(2006) 061804.*

[23] *BABAR Collaboration, B. Aubert* et al.*, Measurement of the hadronic form factor in $D^0 \to K^- e^+ \nu_e$ decays, Phys. Rev. D* **76** *(2007) 052005.*

[24] *BESIII Collaboration, M. Ablikim* et al.*, Study of dynamics of $D^0 \to K^- e^+ \nu_e$ and $D^0 \to \pi^- e^+ \nu_e$ decays, Phys. Rev. D* **92** *(2015) 072012.*

[25] BESIII Collaboration, M. Ablikim et al., *Study of the $D^0 \to K^- \mu^+ \nu_\mu$ dynamics and test of lepton flavor universality with $D^0 \to K^- \ell^+ \nu_\ell$ decays*, Phys. Rev. Lett. **122** (2019) 011804.

[26] C. A. Beteta et al., *Calibration and performance of the LHCb calorimeters in Run 1 and 2 at the LHC*, 2020. Available at `https://arxiv.org/pdf/2008.11556.pdf`.

[27] A. D. Sakharov, *Violation of CP Invariance, C asymmetry, and baryon asymmetry of the universe*, Pisma Zh. Eksp. Teor. Fiz. **5** (1967) 32.

[28] V. A. Kuzmin, M. E. Shaposhnikov, and I. I. Tkachev, *Strong cp violation, electroweak baryogenesis, and axionic dark matter*, Phys. Rev. D **45** (1992) 466.

[29] Wikipedia contributors, *Cp violation — Wikipedia, the free encyclopedia*, `https://en.wikipedia.org/w/index.php?title=CP_violation&oldid=1100551699`, 2022. [Online; accessed 2-September-2022].

[30] P. S. B. Dev et al., *Searches for Baryon Number Violation in Neutrino Experiments: A White Paper*, `arXiv:2203.0877`.

[31] J. Charles et al., *CP violation and the CKM matrix: assessing the impact of the asymmetric b factories*, The European Physical Journal C **41** (2005) 1, updated results and plots available at: `http://ckmfitter.in2p3.fr`.

[32] M. Bona and et al. UTfit collaboration, *The Unitarity Triangle Fit in the Standard Model and Hadronic Parameters from Lattice QCD: A Reappraisal after the Measurements of $\Delta m_s$ and $BR(B \to \tau\nu_\tau)$*, Available at `https://arxiv.org/abs/hep-ph/0606167` `http://dx.doi.org/10.1088/1126-6708/2006/10/081` `http://www.utfit.org` `http://www.utfit.org/UTfit/ResultsSummer2018SM`.

[33] LHCb, *Simultaneous determination of the CKM angle $\gamma$ and parameters related to mixing and CP violation in the charm sector*, tech. rep., CERN, Geneva, 2022.

[34] LHCb Collaboration, M. Kenzie and M. Withehead, *Update of the LHCb combination of the CKM angle $\gamma$*, CERN-LHCb-CONF-2018-002 (2018), online document.

[35] LHCb, R. Aaij et al., *Measurement of CP observables in $B^\pm \to D^{(*)}K^\pm$ and $B^\pm \to D^{(*)}\pi^\pm$ decays using two-body D final states*, JHEP **04** (2021) 081, `arXiv:2012.0990`.

[36] R. Aaij et al., *Measurement of cp observables in $b\pm\to dk\pm$ and $b\pm\to d\pm$ with two- and four-body d decays*, Physics Letters B **760** (2016) 117.

[37] LHCb Collaboration, R. Aaij et al., *Study of cp violation in $B^\mp \to dh^\mp$ ($h = k, \pi$) with the modes $d \to K^\mp \pi^\pm \pi^0$, $d \to \pi^+ \pi^- \pi^0$ and $d \to K^+ K^- \pi^0$*, Phys. Rev. D **91** (2015) 112014.

274

[38] LHCb, R. Aaij et al., *Measurement of the CKM angle $\gamma$ in $B^\pm \to DK^\pm$ and $B^\pm \to D\pi^\pm$ decays with $D \to K_S^0 h^+ h^-$*, JHEP **02** (2021) 169, `arXiv:2010.0848`.

[39] LHCb, R. Aaij et al., *Measurement of CP observables in $B \to DK$ and $B \to D\pi$ with $D \to K_S^0 K^\pm \pi^\mp$ decays*, JHEP **06** (2020) 058, `arXiv:2002.0885`.

[40] LHCb, R. Aaij et al., *Measurement of CP observables in $B^\pm \to DK^{*\pm}$ decays using two- and four-body $D$ final states*, JHEP **11** (2017) 156, `arXiv:1709.0585`, [Erratum: JHEP 05, 067 (2018)].

[41] LHCb Collaboration, R. Aaij et al., *Study of $B^- \to dK^-\pi^+\pi^-$ and $B^- \to d\pi^-\pi^+\pi^-$ decays and determination of the ckm angle $\gamma$*, Phys. Rev. D **92** (2015) 112005.

[42] LHCb, R. Aaij et al., *Measurement of CP observables in the process $B^0 \to DK^{*0}$ with two- and four-body $D$ decays*, JHEP **08** (2019) 041, `arXiv:1906.0829`.

[43] LHCb, R. Aaij et al., *Measurement of the CKM angle $\gamma$ using $B^0 \to DK^{*0}$ with $D \to K_S^0 \pi^+ \pi^-$ decays*, JHEP **08** (2016) 137, `arXiv:1605.0108`.

[44] LHCb, R. Aaij et al., *Measurement of CP violation in $B^0 \to D^\mp \pi^\pm$ decays*, JHEP **06** (2018) 084, `arXiv:1805.0344`.

[45] LHCb, R. Aaij et al., *Measurement of CP asymmetry in $B_s^0 \to D_s^\mp K^\pm$ decays*, JHEP **03** (2018) 059, `arXiv:1712.0742`.

[46] LHCb, R. Aaij et al., *Measurement of the CKM angle $\gamma$ and $B_s^0$-$\bar{B}_s^0$ mixing frequency with $B_s^0 \to D_s^\mp h^\pm \pi^\pm \pi^\mp$ decays*, JHEP **03** (2021) 137, `arXiv:2011.1204`.

[47] LHCb Collaboration, R. Aaij et al., *Observation of cp violation in charm decays*, Phys. Rev. Lett. **122** (2019) 211803.

[48] LHCb Collaboration, R. Aaij et al., *Measurement of the difference of time-integrated cp asymmetries in $D^0 \to K^-K^+$ and $D^0 \to \pi^-\pi^+$ decays*, Phys. Rev. Lett. **116** (2016) 191601.

[49] LHCb Collaboration, R. Aaij et al., *Measurement of the charm-mixing parameter $y_{CP}$*, Phys. Rev. Lett. **122** (2019) 011802.

[50] LHCb, R. Aaij et al., *Measurement of indirect CP asymmetries in $D^0 \to K^-K^+$ and $D^0 \to \pi^-\pi^+$ decays using semileptonic $B$ decays*, JHEP **04** (2015) 043, `arXiv:1501.0677`.

[51] LHCb Collaboration, R. Aaij et al., *Search for time-dependent cp violation in $D^0 \to K^+K^-$ and $D^0 \to \pi^+\pi^-$ decays*, Phys. Rev. D **104** (2021) 072010.

[52] LHCb Collaboration, R. Aaij et al., *Measurements of charm mixing and cp violation using $D^0 \to K^\pm \pi^\mp$ decays*, Phys. Rev. D **95** (2017) 052004.

[53] LHCb Collaboration, R. Aaij et al., *Updated determination of $D^0 - \overline{d}^0$ mixing and cp violation parameters with $D^0 \to K^+\pi^-$ decays*, Phys. Rev. D **97** (2018) 031101.

[54] LHCb Collaboration, R. Aaij et al., *First observation of $D^0 - \overline{d}^0$ oscillations in $D^0 \to K^+\pi^-\pi^+\pi^-$ decays and measurement of the associated coherence parameters*, Phys. Rev. Lett. **116** (2016) 241801.

[55] LHCb, R. Aaij et al., *Model-independent measurement of mixing parameters in $D^0 \to K_S^0 \pi^+\pi$ decays*, JHEP **04** (2016) 033, `arXiv:1510.0166`.

[56] LHCb Collaboration, R. Aaij et al., *Measurement of the mass difference between neutral charm-meson eigenstates*, Phys. Rev. Lett. **122** (2019) 231802.

[57] LHCb Collaboration, R. Aaij et al., *Observation of the mass difference between neutral charm-meson eigenstates*, Phys. Rev. Lett. **127** (2021) 111801.

[58] and R. Aaij et al., *Measurement of CP observables in $b\pm \to DK*\pm$ decays using two- and four-body d final states*, Journal of High Energy Physics **2017** (2017) .

[59] T. L. Collaboration, *Study of the decay $B\pm \to DK*\pm$ with two-body D decays*, Available at `https://cds.cern.ch/record/2240147/files/LHCb-CONF-2016-014.pdf?version=2`.

[60] M. Gronau and D. Wyler, *On determining a weak phase from CP asymmetries in charged B decays*, Phys. Lett. B **265** (1991) 172.

[61] M. Gronau and D. London, *How to determine all the angles of the unitarity triangle from bd0 → dks andbs0 → d*, Physics Letters B **253** (1991), no. 3 483.

[62] D. Atwood, I. Dunietz, and A. Soni, *Enhanced cp violation with $B \to \mathrm{k}d^0(\overline{d}^0)$ modes and extraction of the cabibbo-kobayashi-maskawa angle $\gamma$*, Phys. Rev. Lett. **78** (1997) 3257.

[63] D. Atwood, I. Dunietz, and A. Soni, *Improved methods for observing CP violation in $B^\pm \to \mathrm{KD}$ and measuring the ckm phase $\gamma$*, Phys. Rev. D **63** (2001) 036005.

[64] A. Giri, Y. Grossman, A. Soffer, and J. Zupan, *Determining $\gamma$ using $B^\pm \to \mathrm{DK}^\pm$ with multibody D decays*, Phys. Rev. D **68** (2003) 054018.

[65] LHCb Collaboration, R. Aaij et al., *Measurement of the CKM angle $\gamma$ using $B^\pm \to DK^\pm$ with $D \to K_S^0\pi^+\pi^-$, $K_S^0 K^+K^-$ decays*, JHEP **08** (2018) 176. 36 p, `arXiv:1806.0120`, *All figures and tables, along with any supplementary material and additional information, are available at https://lhcbproject.web.cern.ch/lhcbproject/Publications/LHCbProjectPublic/LHCb-PAPER-2018-017.html*.

276

[66] Wikipedia contributors, *Large hadron collider — Wikipedia, the free encyclopedia*, 2022. [Online; accessed 3-October-2022].

[67] C. A. science, *The Large Hadron Collider*, Available at `https://home.cern/science/accelerators/large-hadron-collider`.

[68] L. Evans and P. Bryant, *LHC machine*, Journal of Instrumentation **3** (2008) S08001.

[69] L. CERN, *LINAC4 IN VERY SHORT*, Available at `https://lhc-closer.es/taking_a_closer_look_at_lhc/0.linac4`.

[70] T. A. Collaboration et al., *The ATLAS experiment at the CERN large hadron collider*, Journal of Instrumentation **3** (2008) S08003.

[71] T. C. Collaboration et al., *The CMS experiment at the CERN LHC*, Journal of Instrumentation **3** (2008) S08004.

[72] LHCb Collaboration, A. A. Alves et al., *The LHCb Detector at the LHC*, JINST **3** (2008) S08005, Also published by CERN Geneva in 2010.

[73] T. A. Collaboration et al., *The ALICE experiment at the CERN LHC*, Journal of Instrumentation **3** (2008) S08002.

[74] Wikipedia contributors, *Cern — Wikipedia, the free encyclopedia*, 2022. [Online; accessed 14-September-2022].

[75] E. Mobs, *The CERN accelerator complex. Complexe des accélérateurs du CERN*, , General Photo.

[76] L. Collaboration, *The LHCb detector at the LHC*, Available at `https://doi.org/10.1142/S0217751X15300227`.

[77] H. Dijkstra, H. J. Hilke, T. Nakada, and T. Ypsilantis, *LHCb Letter of Intent*, LHCb Collaboration, .

[78] R. Aaij et al., *Performance of the LHCb vertex locator*, Journal of Instrumentation **9** (2014) P09007.

[79] P. d'Argent et al., *Improved performance of the LHCb outer tracker in LHC run 2*, Journal of Instrumentation **12** (2017) P11016.

[80] LHCb RICH Group, M. Adinolfi et al., *Performance of the LHCb RICH detector at the LHC*, Eur. Phys. J. C **73** (2013) 2431, `arXiv:1211.6759`.

[81] A. A. Alves et al., *Performance of the LHCb muon system*, Journal of Instrumentation **8** (2013) P02022.

[82] LHCb collaboration, C. Elsässer, $\overline{b}b$ production angle plots, .

[83] T. L. collaboration, *Measurement of the track reconstruction efficiency at LHCb,* Journal of Instrumentation **10** (2015) P02007.

[84] M. Borsato et al., *Unleashing the full power of lhcb to probe stealth new physics,* 05, 2021.

[85] R. Aaij et al., *Performance of the LHCb vertex locator,* Journal of Instrumentation **9** (2014) P09007.

[86] L. S. Tracker, *Material for Publications,* Available at `https://lhcb.physik.uzh.ch/ST/public/material/index.php`.

[87] LHCb Collaboration, P. R. Barbosa-Marinho et al., LHCb inner tracker: Technical Design Report. *Technical design report. LHCb.* CERN, Geneva, 2002. revised version number 1 submitted on 2002-11-13 14:14:34.

[88] *Performance of the LHCb outer tracker,* Journal of Instrumentation **9** (2014) P01002.

[89] LHCb Collaboration, R. Aaij et al., *Observation of the decay* $B_s^0 \rightarrow \overline{D}^0 K^+ K^-$, Phys. Rev. D **98** (2018) 072006.

[90] L. Collaboration, *LHCb VELO Upgrade Technical Design Report,* tech. rep., 2013.

[91] L. Collaboration, *LHCb Tracker Upgrade Technical Design Report,* tech. rep., 2014.

[92] LHCb, L. Collaboration, *Performance of the LHCb RICH detector at the LHC,* `arXiv:1211.6759`.

[93] A. Papanestis, *Performance of the rich detectors of lhcb,* Physics Procedia **37** (2012) 613.

[94] on behalf of the LHCb collaboration, E. Picatoste Olloqui, *LHCb Preshower(PS) and Scintillating Pad Detector (SPD): commissioning, calibration, and monitoring,* J. Phys. : Conf. Ser. **160** (2009) 012046. 8 p.

[95] M. Calvo Gomez et al., *A tool for* $\gamma/\pi^0$ *separation at high energies,* tech. rep., CERN, Geneva, 2015.

[96] LHCb collaboration, R. Aaij et al., *LHCb Detector Performance,* Int. J. Mod. Phys. A **30** (2015) 1530022. 73 p, `arXiv:1412.6352`.

[97] R. Aaij et al., *The LHCb trigger and its performance in 2011,* Journal of Instrumentation **8** (2013) P04022.

[98] A. P. Navarro and M. F. and, *Event reconstruction in the LHCib/ionline cluster,* Journal of Physics: Conference Series **219** (2010) 022020.

[99] L. E. LHCb Collaboration, *Future physics potential of LHCb*, tech. rep., CERN, Geneva, 2022.

[100] L. Collaboration, *LHCb Tracker Upgrade Technical Design Report*, tech. rep., 2014.

[101] O. A. de Aguiar Francisco et al., *Microchannel cooling for the lhcb velo upgrade i*, Nuclear Instruments and Methods in Physics Research Section A: Accelerators, Spectrometers, Detectors and Associated Equipment **1039** (2022) 166874.

[102] M. Brice, *LHCb's VELO metrology*, , General Photo.

[103] LHCb Collaboration, M. S. Rudolph, *The LHCb Upstream Tracker Upgrade*, PoS **Vertex2019** (2020) 013. 9 p.

[104] LHCb SciFi Tracker Collaboration, P. Hopchev, *SciFi: A large Scintillating Fibre Tracker for LHCb. SciFi: A large Scintillating Fibre Tracker for LHCb*, tech. rep., 2017. Presented at The Fifth Annual Conference on Large Hadron Collider Physics.

[105] A. Massafferri, *SciFi, the new tracker of the LHCb experiment*, Journal of Instrumentation **15** (2020) C08006.

[106] LHCb Rich, M. Fiorini, *The LHCb RICH Detector Upgrade*, PoS **EPS-HEP2017** (2018) 494. 4 p.

[107] A. Piucci, *The LHCb upgrade*, Journal of Physics: Conference Series **878** (2017) 012012.

[108] *LHCb Trigger and Online Upgrade Technical Design Report*, tech. rep., 2014.

[109] LHCb Collaboration et al., *Physics case for an lhcb upgrade ii - opportunities in flavour physics, and beyond, in the hl-lhc era*, 2018. doi: 10.48550/ARXIV.1808.08865.

[110] T. Abe et al., *Belle ii technical design report*, 2010. doi: 10.48550/ARXIV.1011.0352.

[111] N. Neri, *The LHCb Upgrade II*, PoS **BEAUTY2018** (2018) 057.

[112] M. Borsato et al., *Unleashing the full power of LHCb to probe Stealth New Physics*, Rep. Prog. Phys. **85** (2022) 024201. 45 p, `arXiv:2105.1266`, 82 pages, 31 figures. This is the version of the article before peer review or editing, as submitted by an author to Reports on Progress in Physics. IOP Publishing Ltd is not responsible for any errors or omissions in this version of the manuscript or any version derived from it. The Version of Record is available online at doi:10.1088/1361-6633/ac4649.

[113] C. M. LHCb Collaboration, *Framework TDR for the LHCb Upgrade II - Opportunities in flavour physics, and beyond, in the HL-LHC era*, tech. rep., CERN, Geneva, 2021.

[114] LHCb, R. Aaij et al., *Observation of the decay $B_s^0 \to \bar{D}^0\phi$, Phys. Lett.* **B727** *(2013) 403*, `arXiv:1308.4583`.

[115] R. Aaij et al., *Measurement of B meson production cross-sections in proton-proton collisions at $\sqrt{s} = 7$ TeV, Journal of High Energy Physics* **2013** *(2013)* .

[116] R. Aaij et al., *LHCb collaboration - measurement of the b-quark production cross section in 7 and 13 TeV pp collisions, Physical Review Letters* **118** *(2017)* .

[117] A. Camboni et al., *Measurement of $\sigma(b\bar{b})$ with inclusive final states in LHCb*, , *Available at* `https://cds.cern.ch/record/1418162`.

[118] V. V. Gligorov, C. Thomas, and M. Williams, *The HLT inclusive B triggers, CERN-LHCb-PUB-2011-016 (2011), online document*.

[119] V. V. Gligorov and M. Williams, *Efficient, reliable and fast high-level triggering using a bonsai boosted decision tree, JINST* **8** *(2013) P02013*, `arXiv:1210.6861`.

[120] LHCb collaboration, R. Aaij et al., *Measurement of the CKM angle $\gamma$ from a combination of LHCb results, JHEP* **12** *(2016) 087. 58 p*, `arXiv:1611.0307`, *Comments: All figures and tables, along with any supplementary material and additional information, are available at https://lhcbproject.web.cern.ch/lhcbproject/Publications/LHCbProjectPublic/LHCb-PAPER-2016-032.html*.

[121] LHCb Collaboration, D. Ao and et al., *Measurements of the branching fractions of the decay modes $B_s^0 \to D^{(*)0}\phi$*, , *Available at* `https://twiki.cern.ch/twiki/pub/LHCbPhysics/D0Phi/Br_v0.2.pdf` *online document*.

[122] R. K. Ellis, W. J. Stirling, and B. R. Webber, *QCD and collider physics. Cambridge monographs on particle physics, nuclear physics, and cosmology. Cambridge University Press, Cambridge, 2003. Photography by S. Vascotto, doi: 10.1017/CBO9780511628788*.

[123] J. E. Gaiser et al., *Charmonium spectroscopy from inclusive $\psi'$ and $j/\psi$ radiative decays, Phys. Rev. D* **34** *(1986) 711*.

[124] M. Oreglia et al., *Study of the reaction $\psi' \to \gamma\gamma\frac{J}{\psi}$, Phys. Rev. D* **25** *(1982) 2259*.

[125] T. Skwarnicki, *A study of the radiative CASCADE transitions between the Upsilon-Prime and Upsilon resonances, PhD thesis, Cracow, INP, 1986, Available at* `https://inspirehep.net/files/e31108fa63ba2754e30038cccdf9e3a7`.

[126] M. Pivk and F. R. Le Diberder, *SPlot: A Statistical tool to unfold data distributions, Nucl. Instrum. Meth.* **A555** *(2005) 356*, `arXiv:physics/0402083`.

[127] M. Hoballah, *Measurement of the photon polarization using $B_s^0 \to \phi\gamma$ at LHCb, theses, Université Blaise Pascal - Clermont-Ferrand II, Mar., 2015*.

[128] B. Quintana, *Search for radiative B decays to orbitally excited mesons at LHCb*, theses, Université Clermont Auvergne [2017-2020], Nov., 2019, Available at `https://tel.archives-ouvertes.fr/tel-02476983`.

[129] O. Deschamps et al., *Photon and neutral pion reconstruction*, , Available at `https://cds.cern.ch/record/691634`.

[130] R. Aaij et al., *Selection and processing of calibration samples to measure the particle identification performance of the LHCb experiment in Run 2*, EPJ Techniques and Instrumentation **6** (2019) .

[131] Alex Seuthe on behalf of the LHCb collaboration, *PID Performance in Run 2 at LHCb*, Available at `https://indico.cern.ch/event/856696/contributions/3742260/attachments/2044209/3424226/LHCP_Alex_Seuthe.pdf`.

[132] C. W. Fabjan and F. Gianotti, *Calorimetry for particle physics*, Rev. Mod. Phys. **75** (2003) 1243.

[133] Wikipedia contributors, *Dalitz plot — Wikipedia, the free encyclopedia*, 2022. Available at `https://en.wikipedia.org/w/index.php?title=Dalitz_plot&oldid=1098868445`.

[134] W. D. Hulsbergen, *Decay chain fitting with a kalman filter*, Nuclear Instruments and Methods in Physics Research Section A: Accelerators, Spectrometers, Detectors and Associated Equipment **552** (2005) 566–575.

[135] J. C. Anjos et al., *E691 collaboration - Dalitz plot analysis of $D \to K\pi\pi$ decays*, Phys. Rev. D **48** (1993) 56.

[136] CLEO Collaboration, S. Kopp et al., *Dalitz analysis of the decay $D^0 \to K^-\pi^+\pi^0$*, Phys. Rev. D **63** (2001) 092001.

[137] A. Hoecker et al., *TMVA: Toolkit for Multivariate Data Analysis*, PoS **ACAT** (2007) 040, `arXiv:physics/0703039`.

[138] W. D. Hulsbergen, *Decay chain fitting with a kalman filter*, Nuclear Instruments and Methods in Physics Research Section A: Accelerators, Spectrometers, Detectors and Associated Equipment **552** (2005) 566–575.

[139] LHCb Collaboration, R. Aaij et al., *Dalitz plot analysis of $B^0 \to \overline{D}^0 \pi^+\pi^-$ decays*, Phys. Rev. D **92** (2015) 032002.

[140] O. Behnke, K. Kröninger, G. Schott, and T. Schörner-Sadenius, *Data analysis in high energy physics: a practical guide to statistical methods*. Wiley-VCH, Weinheim, 2013. doi: 10.1002/9783527653416.

[141] P. Koppenburg, *Statistical biases in measurements with multiple candidates*, 2019.

[142] K. Cranmer, *Kernel estimation in high-energy physics*, Computer Physics Communications **136** (2001) 198–207.

[143] G. Cowan, D. Craik, and M. Needham, *Rapidsim: An application for the fast simulation of heavy-quark hadron decays*, Computer Physics Communications **214** (2017) 239.

[144] D. Hill, M. John, and P. Gandini, *A study of partially reconstructed $B^{\pm} \to D^{*0}h^{\pm}$ decays using the $D^0 \to K\pi, KK, \pi\pi$ final states*, , Available at `https://cds.cern.ch/record/2253246`.

[145] L. Anderlini et al., *The PIDCalib package*, tech. rep., CERN, Geneva, 2016.

[146] L. Anderlini et al., *The PIDCalib package*, tech. rep., CERN, Geneva, Jul, 2016. Available at `http://cds.cern.ch/record/2202412`.

[147] Charles, J. and others, *Ckmfitter summer 2019 update*, 2019. Available at `http://ckmfitter.in2p3.fr/www/results/plots_summer19/num/ckmEval_results_summer19.pdf`.

[148] Heavy Flavor Averaging Group, Y. Amhis et al., *Averages of b-hadron, c-hadron, and $\tau$-lepton properties as of 2018*, 2019. arXiv:1909.12524 [hep-ex].

[149] S. Bodhisattva, M. Walker, and M. Woodroofe, *On the Unified Method with Nuisance Parameters*, Statist. Sinica **19** (2009) 301, Available at `https://www3.stat.sinica.edu.tw/statistica/oldpdf/A19n116.pdf`.

[150] A. van der Vaart, *Asymptotic statistics (cambridge series in statistical and probabilistic mathematics) by a. w. van der vaart*, Cambridge University Press, 1998. Available at `https://doi.org/10.1017/CBO9780511802256` online document, doi: https://doi.org/10.1017/CBO9780511802256.

[151] BaBar, B. Aubert et al., *Measurement of CP violation observables and parameters for the decays B+- —> D K*+-*, Phys. Rev. D **80** (2009) 092001, arXiv:0909.3981.

[152] Wikipedia contributors, *Multilayer perceptron — Wikipedia, the free encyclopedia*, `https://en.wikipedia.org/w/index.php?title=Multilayer_perceptron&oldid=1091164596`, 2022. [Online; accessed 21-July-2022].

[153] W. Verkerke and D. P. Kirkby, *The RooFit toolkit for data modeling*, eConf **C0303241** (2003) MOLT007, arXiv:physics/0306116.

[154] D. Aston et al., *A study of k+ scattering in the reaction kp→k+n at 11 gev/c*, Nuclear Physics B **296** (1988), no. 3 493.

[155] *LHCb Collaboration, Measurement of the CKM angle  with $B^{\pm} \to D[K^{\mp}\pi^{\pm}\pi^{\pm}\pi^{\mp}]h^{\pm}$ decays using a binned phase-space approach,  tech. rep., CERN, Geneva, 2022. All figures and tables, along with any supplementary material and additional information, are available at* `https: // cern. ch/ lhcbproject/ Publications/ p/ LHCb-PAPER-2022-017. html` *(LHCb public pages).*

[156] *LHCb Collaboration, R. Aaij et al., Measurement of the $B^{\pm}$ production asymmetry and the cp asymmetry in $B^{\pm} \to j/\psi K^{\pm}$ decays, Phys. Rev. D* **95** *(2017) 052005.*

[157] *LHCb Collaboration, M. J. Donal Hill, Measurement of CP observables in $B^{\pm} \to D^{(*)}K^{\pm}$ and $B^{\pm} \to D^{(*)}\pi^{\pm}$ decays using two-body D final states, , Available at* `https: // twiki. cern. ch/ twiki/ pub/ LHCbPhysics/ B2D0K/ LHCb_ ANA_ 2020_ 024_ v9. pdf` *online document.*

[158] *A. Davis et al., Measurement of the instrumental asymmetry for $K^{-}\pi^{+}$-pairs at LHCb in Run 2,  tech. rep., CERN, Geneva, 2018.  Available at* `https: // cds. cern. ch/ record/ 2310213` *online document.*

[159] *A. Poluektov, Kernel density estimation of a multidimensional efficiency profile, Journal of Instrumentation* **10** *(2015) P02011.*

[160] *LHCb Collaboration, A. Poluektov, Unbinned PID resampling using kernel density estimation , , Available at* `https: // twiki. cern. ch/ twiki/ bin/ view/ LHCb/ MeerkatPIDResampling` *online document.*

[161] *Anton Poluektov. Available at* `https: // meerkat. hepforge. org/` *.*

[162] *J. Charles et al., 2005. updated results and plots available at* `http: // ckmfitter. in2p3. fr` *.*

[163] *L. Lyons, D. Gibaut, and P. Clifford, How to combine correlated estimates of a single physical quantity,  tech. rep., Oxford Univ. Nucl. Phys., Oxford, 1987. Available at* `https: // cds. cern. ch/ record/ 183996` *.*

[164] *Y. Grossman, A. Soffer, and J. Zupan, Effect of $D - \overline{D}$ mixing on the measurement of $\gamma$ in $B \to DK$ decays, Physical Review D* **72** *(2005) .*

[165] *M. Martone and J. Zupan, $B^{\pm} \to dK^{\pm}$ with direct cp violation in charm, Phys. Rev. D* **87** *(2013) 034005.*

[166] *Particle Data Group, P. Zyla et al., Review of Particle Physics, PTEP* **2020** *(2020), no. 8 083C01.*

[167] *M. Gronau, Y. Grossman, Z. Surujon, and J. Zupan, Enhanced effects on extracting $\gamma$ from untagged $B^{0}$ and $B_{s}$ decays, Physics Letters B* **649** *(2007), no. 1 61 .*

[168] *LHCb Collaboration, R. Aaij et al., Measurement of the cp-violating phase $\phi_{s}$ in the decay $B_{s}^{0} \to j/\psi\phi$, Phys. Rev. Lett.* **108** *(2012) 101803.*

[169] LHCb Collaboration, *Measurement of the fragmentation fraction ratio $f_s/f_d$ and its dependence on B meson kinematics*, JHEP 1304 (2013) 001 (2013), online document.

[170] T. Evans et al., *Improved determination of the $d{\to}k{+}{+}$ coherence factor and associated hadronic parameters from a combination of $e{+}e{\to}(3770){\to}cc^-$ and $pp{\to}cc^-x$ data*, Physics Letters B **757** (2016) 520.

[171] A. Bondar and T. Gershon, *On $\phi_3$ measurements using $B^- \to D^*K^-$ decays*, Phys. Rev. D **70** (2004) 091503.

[172] LHCb Collaboration, R. Aaij et al., *Measurement of the b-quark production cross section in 7 and 13 tev pp collisions*, Phys. Rev. Lett. **118** (2017) 052002.

[173] M. Stahl, *RooHILLdini and RooHORNSdini functions*, Available at `https://gitlab.cern.ch/mstahl/beef/tree/master/include`.